NASA Contractor Report 178288

ANALYSES AND ASSESSMENTS OF SPAN WISE GUST GRADIENT DATA FROM NASA B-57B AIRCRAFT

WALTER FROST
HO-PEN CHANG
ERIK A. RINGNES

FWG ASSOCIATES,INC.
Tullahoma, TN. 37388

Contract NAS1-17989
AUGUST 1987

(NASA-CR-178288) ANALYSES AND ASSESSMENTS OF SPAN WISE GUST GRADIENT DATA FROM NASA B-57B AIRCRAFT Final Report (FWG Associates) 350 p Avail: NTIS HC A15/MF A01 CSCL 01A 33/02 N88-10007 Unclas 0103504

NASA
National Aeronautics and Space Administration

Langley Research Center
Hampton, Virginia 23665-5225

ACKNOWLEDGEMENTS

This research was supported under NASA Contract NAS1-17989. The authors are grateful for the support of A. Richard Tobiason of the Office of Aeronautical and Space Tennology, NASA Headquarters, Washington, D.C. Special thanks go to Harold N. Murrow and Robert K. Sleeper of the Loads and Aeroelasticity Division, NASA Langley Research Center, Hampton, Virginia, who monitored the research program and made many useful suggestions. Also, the authors want to thank L. Jack Ehernberger, NASA Dryden Research Center, for his valuable inputs and suggestions, and Dennis W. Camp, NASA Marshall Space Fl.ght Facility, for directing and managing the overall program.

TABLE OF CONTENTS

PAGE

LIST OF TABLES

LIST OF FIGURES

PAGE

PAGE

<u>NOMENCLATURE</u>

ASL	Above sea level
b	Bias error
$B_L(\zeta), B_T(\zeta)$	Normalized von Karman one-point auto-correlation functions for longitudinal and transverse velocity components, respectively
$B_x(\vec{\xi},\tau)$	Normalized for two-point correlation function = $R_x(\vec{\xi},\tau)/\sigma_x\sigma_x'$
$B_x(\tau), B_x(\ell)$	Normalized one-point correlation function in temporal/spatial domain
$B_{xy}(\tau)$	Normalized one-point cross-correlation function = $R_{xy}(\tau)/\sigma_x\sigma_y$
$B_{xy}(\vec{\xi},\tau)$	Normalized two-point cross-correlation function = $R_{xy}(\vec{\xi},\tau)/\sigma_x\sigma_y$
c	Constant = $2^{2/3}/\Gamma(1/3)$
$C_x(\vec{\xi},f), C_{xy}(\vec{\xi},f)$	Coincident spectral density functions (co-spectra)
$e_i(\xi), e_j(\xi+\zeta)$	Direction cosines of the velocity vectors at positions ξ and $\xi+\zeta$ with respect to ith and jth axes, respectively
f	Frequency, Hz (cycle per second)
g	Gravitational acceleration
$h(\tau)$	An example function for any correlation function
$H(f)$	Fourier transform of $h(\tau)$
k	A constant between 0.5 and ∞
$K_n(z)$	nth order of a modified Bessel function of the second kind
ℓ	Spatial lag used in correlation functions = $V\tau$
ℓ_{xC}	Distance parallel to airplane x-axis from INS measuring element to α, β, or q_C measuring station at nose boom
L	Turbulence integral length scale
M	A specific lag time for a correlation function to reduce variance error in calculating the corresponding spectral function

	Probability density function of a time history record $x(t)$
PST	Pacific standard time
$Q_x(\vec{\zeta},f), Q_{xy}(\vec{\zeta},f)$	Quadrature spectral density functions (quad-spectra)
r	Degree of non-Gaussian in an analytical function of the probability density function
R	Distance between a flying airplane and center of the earth
$\tilde{R}(\tau)$	An estimate of a correlation function, $R(\tau)$
$R_{ij}(\xi,\zeta)$	Tensor form of a general non-isotropic velocity correlation between velocity fluctuations $u_i(\xi)$ and $u_j(\xi+\zeta)$ at positions ξ and $\xi+\zeta$, respectively
$R_x(\vec{\zeta},\tau)$	Correlation function between common velocity components at two positions separated by a vector distance, $\vec{\zeta}$
$R_x(\tau)$	One-point auto-correlation function
$R_{xy}(\tau)$	One-point cross-correlation function
$R_{xy}(\vec{\zeta},\tau)$	Cross-correlation function between the different velocity components at two positions separated by a vector distance, $\vec{\zeta}$
$\tilde{S}(\omega)$	An estimate of a spectral function, $S(\omega)$
$S_x(f)$	One-point two-sided auto-spectral density function
$S_x(\vec{\zeta},f)$	Two-sided spectral density function between common velocity components at two positions separated by a vector distance, $\vec{\zeta}$
$S_{xy}(f)$	One-point two-sided cross-spectral density function
$S_{xy}(\vec{\zeta},f)$	Two-sided cross-spectral density function between the different velocity components at two positions separated by a vector distance, $\vec{\zeta}$
T	Duration of a time history record; oscillation period of a specific Schuler-adjusted system $T = k \cdot 2\pi\sqrt{R/g}$
u,v,w	Derived gust velocity components (longitudinal, lateral, and vertical)
$\overline{u_R u_L}$	Two-point correlation function

[illegible]	One-point auto-correlation function
$\overline{u_R v_L}$	Two-point cross-correlation function
$\overline{u_R v_R}$	One-point cross-correlation function
$\overline{u_R u_L}/\sigma_{u_R}\sigma_{u_L}$	Normalized two-point common velocity component correlation function
$\overline{u_R u_R}/\sigma_{u_R}\sigma_{u_R}$	Normalized one-point auto-correlation function
$\overline{u_R v_L}/\sigma_{u_R}\sigma_{v_L}$	Normalized two-point cross-correlation function
$\overline{u_R v_R}/\sigma_{u_R}\sigma_{v_R}$	Normalized one-point cross-correlation function
V	True airspeed at nose boom
V_E	East-west component of airplane inertial velocity measured at INS (positive toward east)
V_N	North-south component of airplane inertial velocity measured at INS (positive toward north)
$\overline{V}_L, \overline{V}_C, \overline{V}_R$	Mean aircraft airspeed at left wing tip, nose, and right wing tip, respectively
$w(\tau)$	A truncation function (window)
W	$(W_E^2 + W_N^2)^{1/2}$
$W(f)$	Fourier transform of $w(\tau)$
$W(\omega)$	Spectral window
W_E, W_N	East-west and north-south components of horizontal mean wind speed, W
$\overline{x}$	Mean value of a time history record, $x(t)$
$x(t)$	Random variable, a time history record

Greek Symbols

α_C, β_C	Angle of attack and sideslip angle measured at nose boom
β	Variance ratio
Γ	Gamma function
$\Delta\tau$	Time-lag increment

	A comb function
$\Delta_0(f)$	Fourier transform of $\Delta_0(\tau)$
ζ	Spatial lag used in the normalized von Karman one-point auto-correlation functions
$\vec{\zeta}$	A vector distance used in expression of two-point correlation functions
$\theta_x(\vec{\zeta},f),\theta_{xy}(\vec{\zeta},f)$	Phase angles of spectral density functions $\Phi_x(\zeta,f)$ and $\Phi_{xy}(\vec{\zeta},f)$, respectively
σ	Standard deviation of a random variable
τ	Temporal lag used in correlation functions
$\Phi_u(s,f),\Phi_v(s,f)$, $\Phi_w(s,f)$	Houbolt and Sen theoretical (one-sided) spectral density functions for longitudinal, lateral, and vertical components at two positions separated by a distance, s
$\Phi_x(f)$	One-point one-sided auto-spectral density function
$\Phi_x(\vec{\zeta},f)$	One-sided spectral density function between common velocity components at two positions separated by a vector distance, $\vec{\zeta}$
$\Phi_{xy}(f)$	One-point one-sided cross-spectral density function
$\Phi_{xy}(\vec{\zeta},f)$	One-sided spectral density function between the different velocity components at two positions separated by a vector distance, $\vec{\zeta}$
χ_n^2	Chi-square variable with n degrees of freedom
ψ	Aircraft heading, measured from true north
$\dot{\psi}$	Aircraft yaw rate
ψ_W	Direction from which wind is blowing, measured clockwise from true north, $\tan^{-1}(W_E/W_N) + \pi$
ω	$= 2\pi f$

Symbols

( )	Deviation from the mean value
(¯)	Average value
E{ }	Ensemble average
*	Convolution integration; complex conjugate
Δ	Difference
var[ ]	Variance

Subscripts

L,T	Longitudinal and transverse components
L,C,R	Left, center, and right probes
u,v,w	Velocity components in longitudinal, lateral, and vertical directions

1.0 INTRODUCTION

Spatial variation of turbulence over aircraft is known to strongly influence the structural and control design of the aircraft (Houbolt, 1973; Etkin, 1972; Bisplinghoff and Ashley, 1957). Techniques for computing rolling and pitching moments and other aerodynamic forces, which are influenced by spatial turbulence, have been developed theoretically and, in general, utilize isotropic homogeneous turbulence (Diederich and Drischler, 1957; Eichenbaum, 1972; Eggleston and Diederich, 1956; Houbolt, 1973; Lichtenstein, 1978; Kordes and Houbolt, 1953; Houbolt and Sen, 1972; Pastel, et al., 1981; Akkari and Frost, 1982; Diederich, 1957; Ringnes and Frost, 1985; Frost and Lin, 1983). It is normally accepted, however, that the turbulence in the atmospheric boundary layer close to the earth's surface, which is encountered by an aircraft during approach and takeoff, and turbulence associated with thunderstorms and clear-air roll waves is generally not isotropic. Additionally, turbulence shed by orographic features can also create relatively large-scale turbulence that is typically not isotropic nor homogeneous.

Spatial turbulence statistics have been computed from data measured with single tower to heights not exceeding much more than 100 m. Towers, however, provide spatial turbulence information only in the vertical (Davenport, 1961; Brook, 1975), which is uninteresting to aircraft design. Some studies have been carried out with tower arrays based on two or three towers located at various horizontal separation distances. The data normally reported from these studies is the coherence function for longitudinal velocities (Panofsky and Mizuno, 1975; Panofsky, et al., 1974; Kristensen and Jensen, 1979; Pielke and Panofsky, 1970; Frost and Lin, 1983). These towers are normally less than

30 m in height. Due to the fact that turbulence information required for aircraft design is at much higher altitudes (even in the terminal area data to heights of roughly 500 m are required), tower data are somewhat limited in their application.

For this reason a NASA program has been underway to determine time histories and various statistical characteristics of three components of gust velocity measured simultaneously at the wing tips and at the nose of a specially instrumented B-57B airplane. The instrumentation system has been designed and installed on the airplane and several flights have been carried out (see Table 1.1). The flights include turbulence samples taken near storms in the Denver-Boulder, Colorado, area. Results from Flights 21, 22, and 26* are reported in considerable detail in Frost, et al. (1985a), Camp, et al. (1984), Frost (1983), Campbell, et al. (1983), and Chang, et al. (1986). Turbulence measurements with the aircraft during Flights 40, 44, 64, and 65 have been compared with data obtained using remote radar sensing techniques (Frost, et al., 1985b; Huang, et al., 1985; Frost and Huang, 1983). Also, measurements of turbulent fluxes of momentum, heat, and moisture relative to orographic features were made during Flights 60, 61, 63, and 66. Analyses are presented in Chang and Frost (1985), Theon, et al. (1986), and Frost, et al. (1985c).

The purpose of the present study is threefold:

1. Perform statistical analyses of the acquired flight data with emphasis on long data runs in continuous turbulence and glide slope runs for simulated takeoffs and landing approaches. Flight 31 flown at NASA Dryden was carried out specifically for this purpose.

---

*Flights 21, 22, and 26 were originally numbered 6, 7, and 10 respectively, and are so referred to in the references cited.

Table 1.1. NASA B57-B Gust Gradient Flight Record.*

Flight No.	Date	Flight Site	Flight Duration (hrs)	Comments
1	27Oct81	Edwards	1.6	Functional check flight; no data
2	02Nov81	Edwards	1.6	Functional check flight; no data
3-4	09Nov81	Edwards-Langley	4.9	Ferry flight; no data
5	22Mar82	Langley	0.8	Functional check flight; no data
6	23Mar82	Langley	1.8	Instrumentation check flight
7-11	22Jun82	Langley-Houston	5.6	Instrumentation check flight; ferry flight
12-13	23Jun82	Houston-Edwards	3.4	Ferry flight; no data
14	02Jul82	Edwards	1.3	Instrumentation check flight
15	06Jul82	Edwards-Denver	1.6	Ferry flight; no data
16	07Jul82	Denver	1.3	JAWS-1 fam. flight; light turb.
17	08Jul82	Denver	1.8	JAWS-2; light to mod. turb.
18	09Jul82	Denver	2.5	JAWS-3; light to mod. turb.
19	11Jul82	Denver	2.3	JAWS-4; light to mod. turb.
20	13Jul82	Denver	1.4	JAWS-5; light to mod. turb.
21	14Jul82	Denver	2.3	JAWS-6; light to mod. turb. severe
22	15Jul82	Denver	2.3	JAWS-7; light to severe turb.
23	17Jul82	Denver	1.5	JAWS-8; light to mod. turb.
24	19Jul82	Denver	0.8	Fam. flight; no data
25	20Jul82	Denver	2.3	JAWS-9; light to mod. turb.
26	21Jul82	Denver	2.0	JAWS-10; mod. to severe turb.
27	22Jul82	Denver	1.8	JAWS-11; light to mod. turb.
28	23Jul82	Denver-Edwards	2.7	Ferry flight; no data
29	07Oct82	Edwards	2.3	Mod. to severe turb.; high winds
30	19Nov82	Edwards	2.3	Mod. to severe turb.; high winds
31	29Nov82	Edwards	2.1	Mod. to severe turb.; strong winds
Ground run	20Dec82	Edwards	0	Instrumentation ground run; check
Ground run	21Dec82	Edwards	0	Instrumentation ground run; check
32	04Jan83	Edwards	1.3	Instrumentation flight check
Ground run	05Jan83	Edwards	0	Instrumentation ground run; check
Ground run	07Jan83	Edwards	0	Instrumentaion ground run; check
33	31Mar83	Edwards	1.7	Instrumentation check-out maneuver
34	20Apr83	Edwards	2.2	Light turb.; maneuvers for instrumentation

*For more information, please contact the Aeroservoelasticity Branch, NASA Research Center.

Table 1.1. (continued).

Flight No.	Date	Flight Site	Flight Duration (hrs)	Comments
35	25Apr83	Edwards	1.8	Light to mod. turb.
36	28Apr83	Edwards	1.1	Smooth flight; no turb.
37	04May83	Edwards	2.1	Light turb. & fam. flight
38-39	09May83	Edwards-Huntsville	3.7	Ferry flight; no data
40	10May83	Huntsville	1.51	Tower fly-bys & lidar
41	11May83	Huntsville	0.7	Tower fly-bys
42-43	11May83	Huntsville-Birmingham	1.0	To fill oxygen bottles; no data
44	12May83	Huntsville	--	Tower fly-bys and lidar
45	13May83	Huntsville-Oklahoma City	1.5	Ferry flight; no data
46	16May83	Oklahoma City	1.4	Fam. flight
47	17May83	Oklahoma City	1.6	Light to mod. turb.; rain
48	20May83	Oklahoma City	1.3	Light turb.; light rain
49	25May83	Oklahoma City	2.3	Light turb.; heavy rain
50	27May83	Oklahoma City	1.5	Light to mod. turb.; light rain
51	02Jun83	Oklahoma City	1.5	Light turb.
52	03Jun83	Oklahoma City-Edwards	3.3	Ferry flight; no data
53	29Jul83	Edwards	2.1	Light turb.
54	13Sep83	Edwards	1.9	Light turb.
55	01Jan84	Edwards	1.0	Instrumentation check-out
56	01Jan84	Edwards	0.5	Instrumentation check-out no data
57	16Jan84	Edwards-Buckley	Unk.	Ferry flight; no data

Flight No.	Date	Flight Site	Flight Duration (hrs)	Comments
58	19Jan84	Back Edwards	2.8	Ferry flight
59	29Jan84	Edwards-Col. Spgs.	2.6	Ferry flight
60	01Feb84	Boulder	3.0	Orographic data (flux box pattern)
61	02Feb84	Boulder	2.8	Orographic data (flux box pattern)
62	03Feb84	Boulder	2.6	High altitude wave activity data
63	06Feb84	Boulder	2.7	Orographic data (flux box pattern)
64	07Feb84	Boulder	2.5	Lidar approaches & depart. (4.8° slope)
65	09Feb84	Boulder	2.3	Lidar approaches & depart. (4.8° slope)
66	10Feb84	Boulder	2.5	Orographic data (flux box pattern)
67	10Feb84	Col. Spgs.-Edwards	2.6	Ferry flight
69	08May85	Edwards	1.1	INS check
70	09May85	Edwards	1.9	Mod. to severe turb.
71	15May85	Edwards	1.8	Mod. to severe turb.
72	29May85	Edwards	2.3	Mod. turb.
73	03Jun85	Edwards	0.8	INS check; box pattern; light to med. turb.
74	03Jun85	Edwards	0.9	INS check; box pattern; light to med. turb.
75	14Jun85	Edwards	1.8	Level and glide slope data; light turb.
76	28Jun85	Edwards	2.0	INS check; instrumentation light turb.

Study, develop, and/or modify statistical models, as necessary, from the standpoint of providing an analytical expression for use in design analysis.

3. Analyze effects of instrumentation characteristics and data processing effects on reduced gust velocity data.

Flight 31 contained runs over sufficiently long distances at level flight to provide turbulence time histories long enough to assure a high statistical degree of freedom and to determine spectral characteristics for wavelengths as great as 10,000 ft (3000 m). The meteorological correlations and statistical analyses of data from Flight 31 is the primary thrust of this report. Plans for Flight 31 were also to include takeoff and touch-and-go runs to investigate non-stationary turbulence along the glide slope associated with the vertical variation of the horizontal wind in the atmospheric boundary layer (Panofsky and Dutton, 1984; Haugen, 1973). Non-stationary data calls for statistical ensemble analysis techniques (see Frost and Moulden, 1977; Wang and Frost, 1982). Ensemble statistics requires a collection, or ensemble, of sample records of the turbulence process. Wang and Frost (1982) have shown that a minimum of six flights down the glide slope under similar prevailing meteorological conditions are required to assure meaningful results. Unfortunately, ensemble analyses could not be carried out because during Flight 31 only one touch-and-go and one takeoff run were recorded. Thus, insufficient approaches or takeoffs were made under similar prevailing meteorological conditions to permit ensemble averaging.

Another problem associated with the turbulence measurements carried out along non-level flight paths is that the system of equations presently utilized to remove the airplane motions from the recorded data are based on a linearized model which assumes only small perturbations about wing level, horizontal flight. Analysis using the full non-linear system of equations

...een carried out for typical data and compared with the computations from the linearized system (Frost, et al., 1983). In general, the effects of a glide slope or climb-out angle less than 10° are negligible on the computed turbulence gust velocities.

Data for all runs in Flight 31 including the touch and go are provided in Appendix A. Details of the flight path, the time histories, and selected statistical analyses including probability distributions, correlations, spectra, etc. are given in this appendix. The statistical analyses described in Section 2 were applied to the turbulence measurements for all runs. Although these analyses are strictly applicable to statistically stationary data, little evidence of non-stationary effects is observed in any of the data except for Run 10 as described later. This observation is true for the touch-and-go runs and takeoff run, also.

The philosophy associated with Appendix A is to provide the data after applying sufficient statistical analysis to allow the reader to distinguish data sets which are of interest to his specific application. The complete data can then be obtained on magnetic tape from NASA Langley Research Center (LaRC) for conducting the reader's own analysis. With this in mind, the complete data from Runs 1 through 16 of Flight 31 have been given in the appendix. Selected runs, however, are analyzed in more detail throughout Section 2 and compared with theoretical and empirical models currently available for correlating turbulence data. In general, it was not necessary to develop new theoretical models because the data fit existing models quite well, as also described in Section 2. There were, however, a few exceptions where modifications to two-point correlation and spectrum models were required. These are also described in Section 2.

this study, a distinction is made between a two-point spatial correlation and the commonly used term "cross-correlation." The terminology cross-correlation in this report is reserved for a correlation between different velocity components; for example, between the lateral and longitudinal components or the vertical and longitudinal components, etc. The terminology "two-point" spatial correlation refers to a correlation between velocity components measured at stations separated in space (e.g., at different probe locations on the aircraft). This can be either a two-point cross-correlation between dissimilar velocity components separated spatially or it can be a two-point correlation between like velocity components separated spatially.* A single-point spatial correlation termed an auto-correlation is defined as a correlation between like velocity components measured at the same location (e.g., with the same wing tip probe) but separated in time. Note that a two-point spatial correlation can also be separated in time (i.e., time dependent or lagged in time).

Procedures for estimating two-point spectra from finite digitized time histories are not straightforward. Considerable insight to these procedures which is not readily accessible in the literature was gained during this study. This insight is described in detail in Section 3.

The von Karman analytical correlation and spectrum model for atmospheric turbulence frequently referred to in the literature (Hinze, 1975; Houbolt,

---

*The authors prefer the terminology two-point auto-correlation for a correlation between like velocity components measured at spatially separated positions. In deference to the reviewers, however, who found this terminology confusing and concluded that an auto-correlation must be a correlation of a signal with itself, the correlation between the same velocity components measured at different positions in space is called a two-point common component correlation or, where no confusion exists, simply a two-point correlation in this report.

1964; Etkin, 1972; Panofsky and Dutton, 1984) is used extensively in this study. In Section 2, comparison of this model is made with the experimental data. In general, agreement with the von Karman auto-correlation and the one-point auto-spectrum is good. This is surprising in view of the fact that von Karman's model is generally assumed valid only for isotropic homogeneous turbulence. It should be noted in this regard that for the long duration, level runs of Flight 31 analyzed in the current study, the turbulence is not expected to be isotropic nor even homogeneous. Most runs were carried out over both flat desert and mountainous regions (peaks of 6000 ft ASL) at low altitude (2500 to 10,000 ft ASL) or during touch-and-go flights at the airport. It was therefore surprising that a model based on the assumption of homogeneous isotropic turbulence correlated the data well.

Although one-point spectra are addressed in some detail, emphasis in this report is on the two-point spectra and correlation functions. Comparison of the two-point correlations and spectra with a theoretical model (based on the von Karman model) originally proposed by Houbolt and Sen (1972) is made in some detail. Correction to this model was required and made as described in Section 2. In general, the experimental data agree with the theoretical model after the corrections. Appropriate care must be exercised, however, in computing the two-point spectra from the digitized data. This issue is described in-depth in Section 3.

During analysis of several of the flights, a number of instrumentation characteristics were uncovered which influenced the accuracy of the data. Although significant effort in the past has been devoted to evaluating effects of instrumentation characteristic and of data reduction procedures on the accuracy of the measured turbulence data, some additional factors were ed (Rhyne, 1980; Murrow and Rhyne, 1981; Meissner, 1976; Crooks, et al., 1967). The addition of the wing tip booms and the interest in measuring wind speeds as contrasted to fluctuations about the mean wind were, in general, responsible for the new instrumentation problems. These problems along with recommended correction or removal procedures are discussed in Section 4. In particular, the INS Schuler position and velocity drift errors and the suspected flow vane sensor misalignment problems are addressed.

Data from Flights 63, 66, 73, and 74 were used for analyzing the instrumentation errors. Data from these flights are used only for purposes of analyzing errors in this study. Also, a discussion of the influence of departure from straight and level flight on the computed turbulence when the data are reduced using the linearized equations which are strictly valid only for level flight is given in Section 4 and in Appendix B.

2.0 STATISTICAL ANALYSIS OF DATA

A statistical analysis of the B-57B aircraft data for 16 runs (Runs 1 through 16) of Flight 31 on November 29, 1982, is described in this section. The procedures for analyzing the turbulence data as well as interpreting the analyzed results are strongly influenced by the stationarity of the data. Non-stationary or non-homogenous data represent all classes of data whose statistical properties change with time or with position. Figure 2.1 illustrates three different examples of non-stationary data; these include data with a time-varying mean, data with a time-varying mean square, and data with a time-varying frequency structure (Bendat and Piersol (1971)). The vast majority of physical data actually fall into the former category.

The theoretical ideas and processing techniques for the stationary data do not, for the most part, apply to data which are non-stationary. A totally adequate methodology does not exist yet for the analysis of all types of non-stationary data. In general, an ensemble-averaging technique (Bendat and Piersol, 1971) provides a method to analyze the statistical properties of the non-stationary data (see application of this by Frost and Huang (1983)). By inspecting the time histories of the aircraft-measured turbulence data (shown in Section 2.2), one can easily see considerable patchiness and non-stationarity in these data sets. However, only one sample record of turbulence over common terrain and similar prevailing meteorological conditions is available for analysis from each run of the B-57B aircraft data. Therefore, through necessity the statistical properties of the data presented in this report are calculated by assuming that the measured data are stationary.

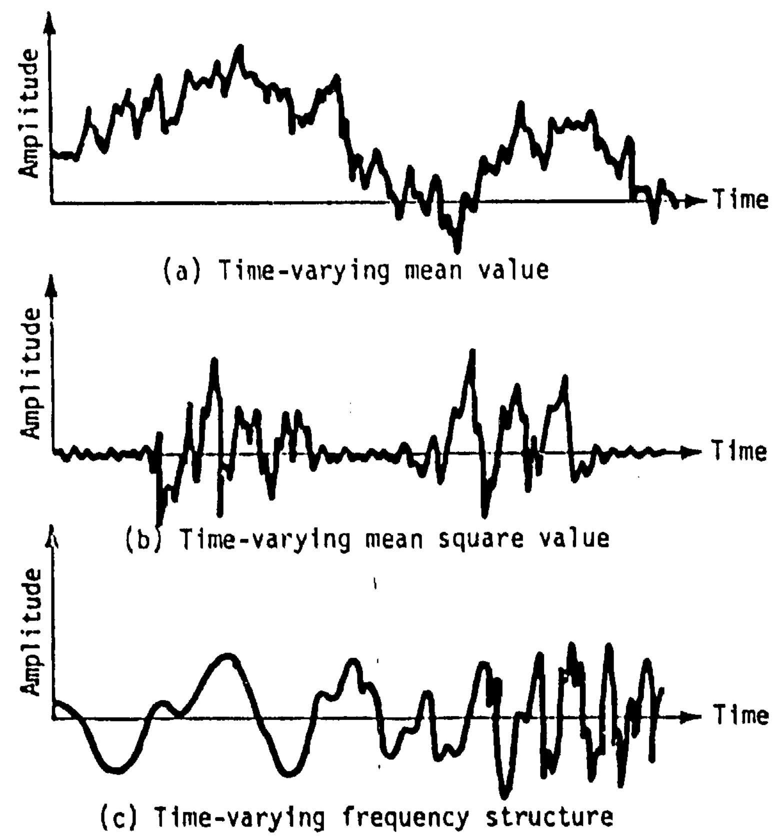

Figure 2.1. Examples of nonstationary data (Bendat & Piersol, 1971).

General information and statistical values for each of the 16 runs are given in Appendix A. The analysis for each run presented in the appendix consists of seven parts as follows:

1. Flight altitude and horizontal wind velocity along the flight path.
2. Time histories of gust velocities, gust velocity differences between wing tips, and the aircraft's normal acceleration.
3. Average turbulence parameters, integral length scales, and correlation coefficients of gust velocities.
4. Probability density functions for gust velocities and gust velocity differences.
5. Normalized one- and two-point correlation functions of gust velocities.
6. Normalized one- and two-point spectral density functions of gust velocities.
7. List of all parameters measured and the range of their extreme and average values.

A map illustrating all ground tracks for Flight 31 over terrain as recorded by the INS during the flight is provided in Figure 2.2. The cross section of the vertical profile of the terrain beneath the flight path is given for each run in Appendix A.

The atmospheric stability is of importance in turbulence considerations. The temperature gradient in the atmospheric boundary layer is a measure of the stability of the atmosphere. Figure 2.3 shows the temperature recorded for all runs of Flight 31 superimposed on the temperature profile measured by the weather balloon. Each "*" represents a 5-second averaged temperature. A scattering of the averaged temperature at different altitudes is seen in the figure. This scattering is believed to represent the spatial temperature variations along a flight path which usually covers more than 10 miles horizontally. Temperature profiles measured during the takeoff run and during the touch-and-go run, Run 2, were converted to potential temperature profiles

ORIGINAL PAGE IS
OF POOR QUALITY

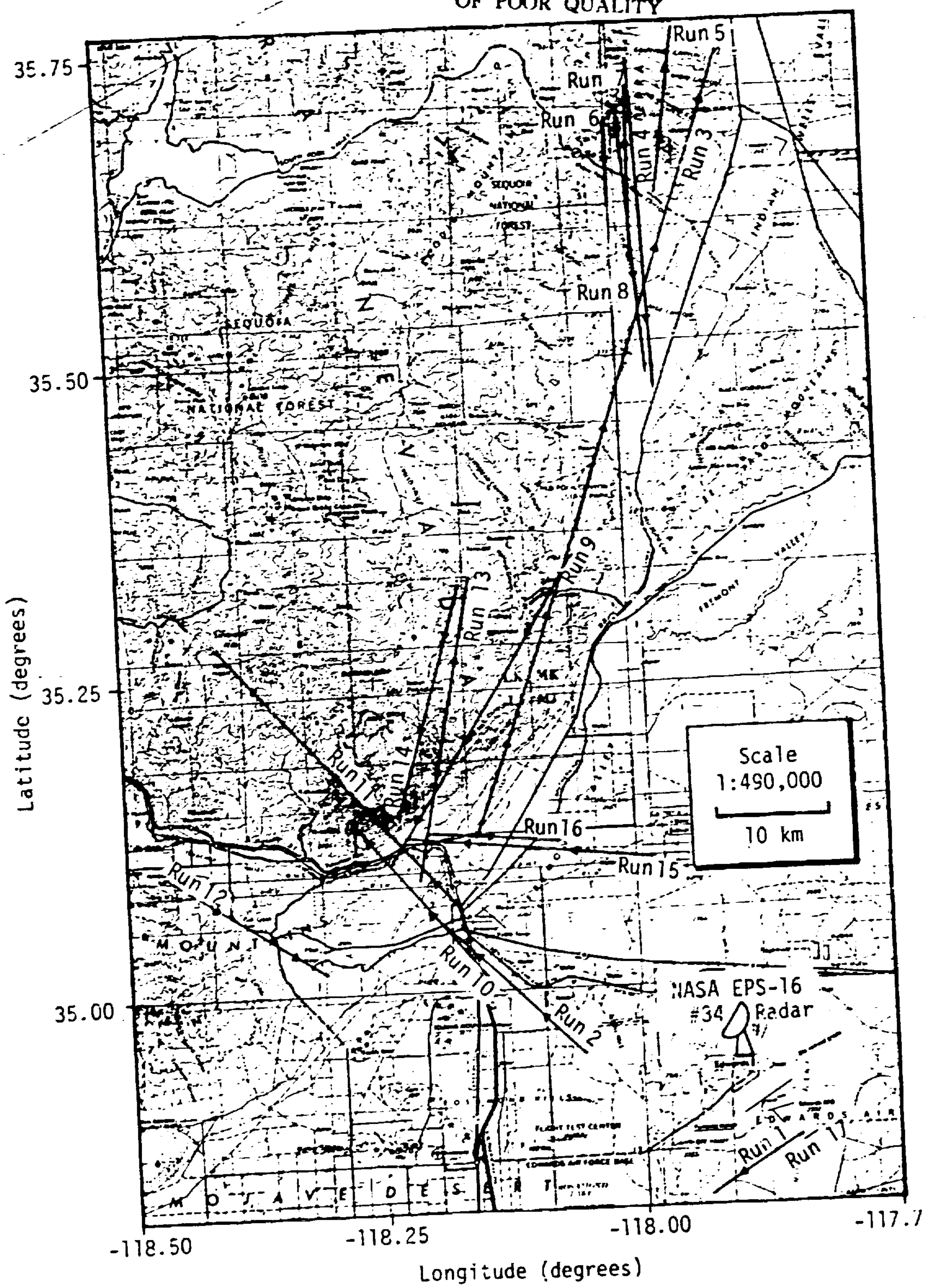

Figure 2.2. Map of the vicinity near Edwards AFB, California, showing ground tracks of 16 runs from Flight 31, November 29, 1982.

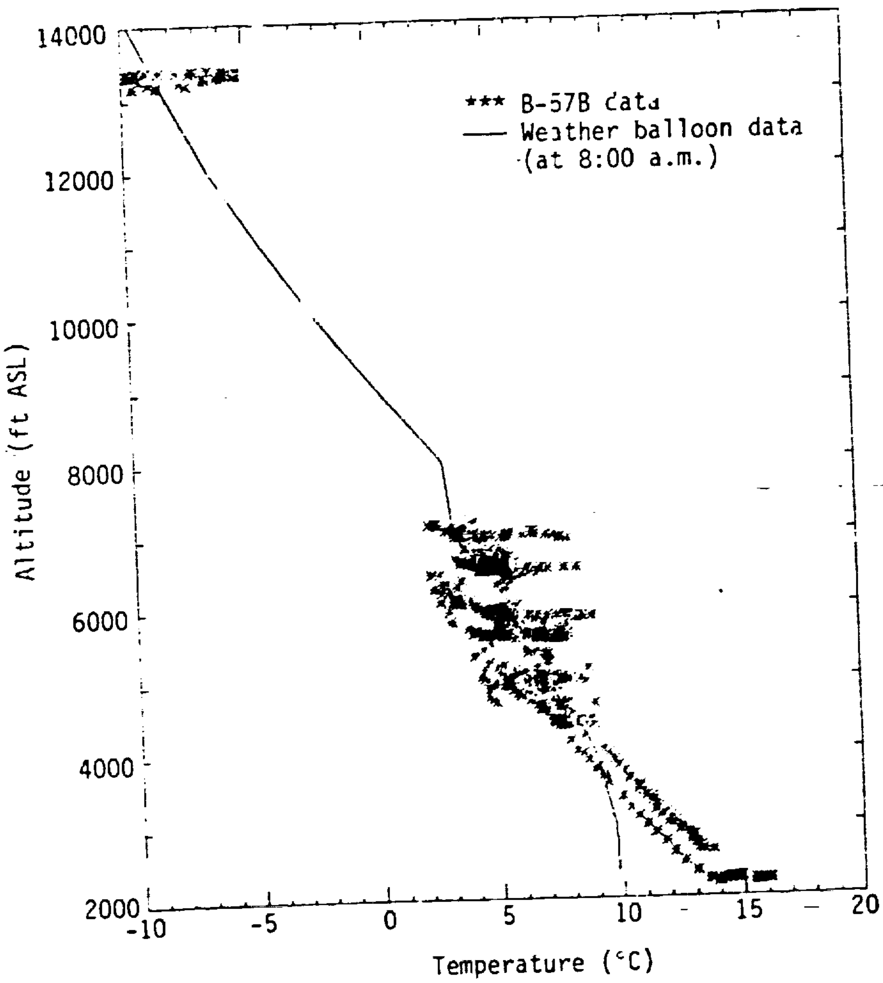

Figure 2.3. Atmospheric temperature profile at Edwards AFB, California, November 29, 1982, with flight data superimposed.

and are plotted in Figure 2.4. The arrows indicate climb or descent. The strong negative temperature gradient near 3700 ft, characteristic of an unstable boundary layer, as shown in the second half of Run 2 is believed to be associated with wake flow generated by a mountain peak up-wind of the flight path (see the terrain contours in Figure 2.2).

The methods and results of the statistical analyses given in Appendix A are described and discussed in detail in the following subsections. The experimental data are also compared with theoretical models.

2.1 Flight Altitude and Horizontal Wind Velocity Along the Flight Path

The first part of the analysis for each run in Appendix A includes flight altitude (ASL), the corresponding terrain height (ASL), the flight direction, and five-second averaged horizontal wind vectors recorded along the flight path. The terrain height is obtained from digitizing a large-scale contour map along each ground track of the flight as shown in Figure 2.2. Also, tabulated are the date, the time (PST) at which the run began, and the duration of the run in seconds.

Run 1 is the takeoff leg of the flight. Run 2 started with an approach and then made a go-around at approximately 100 ft above the ground. The approach and go-around flight path were at a glide slope angle of approximately three degrees. The terrain features over which the majority of the B-57B Flight 31 experiment was flown are characterized by regions of low and high mountainous terrain (Runs 1 and 2 were over flat terrain).

Data from these two runs, however, cannot be expected to be statistically stationary since they represent ascent and descent through variable wind conditions associated with the atmospheric boundary layer. There is no clear evidence in the results of the statistical analysis of these data sets, however, that suggest non-stationary or even non-isotropic effects.

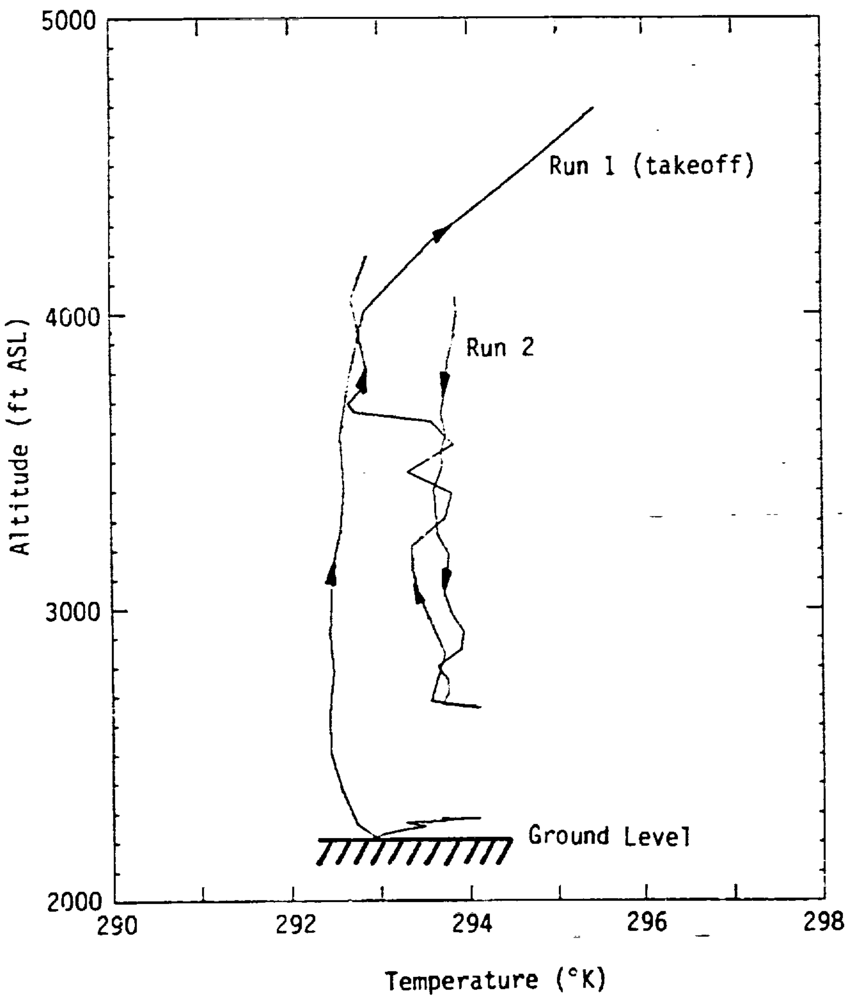

Figure 2.4. Potential temperature profiles from Flight 31.

ORIGINAL PAGE IS
OF POOR QUALITY

Note also in Runs 3, 4, 8, 9, and 11 there are what appear to be relatively large excursions from level flight. This is primarily an illusion due to the exaggeration of the vertical scale in the plot. The apparent climb and descent paths are in all cases less than seven degrees, elevational angle.

Inspection of the flight paths given in Figure 2.2 shows that they may be categorized as occurring over a flat region, a low mountainous regions, and a high mountainous regions. The low mountainous region is further subdivided into two subregions. The first, subregion is that for which the underlying terrain includes gradual and monotonic increase or decrease in elevation. The second subregion is one which includes terrain having more than one peak or valley. Table 2.1 categorizes the type of terrain associated with each run.

TABLE 2.1. Terrain Category for Flight 31.

Terrain Category	Run Number
Flat Region	1, 2
Low Mountain Region	
Single Peak	10, 15, 16
Multi-Peak	5, 6, 9, 11, 12, 13, 14
High Mountain Region	3, 4, 7, 8

The flight paths plotted from the INS data for Runs 4, 8, 11, 13, and 14 shown in Figures A.16, A.36, A.51, A.61 and A.66 suggest that the aircraft flew through mountain peaks. The cause of this obviously impossible result is associated with an INS drift problem which is discussed in Section 4. Errors in the recorded longitude and latitude measurements result in an incorrect aircraft position relative to the fixed terrain features (see Figure 2.2). However, only when the influence of terrain on the turbulence is to be assessed does the error influence the data analysis.

Table 2.2 shows the time duration of each run and the effective mean wind direction relative to the airplane. In most runs the effective mean wind direction is nearly perpendicular to the flight path. The measured mean wind speed in Flight 31 ranges from 5 m/s to over 20 m/s. Run 3 is the longest of the 17 runs making up Flight 31. The landing leg of the flight was recorded as Run 17. This run was only 47 seconds, which is not statistically meaningful and, therefore, is not analyzed in this report.

TABLE 2.2. Time Duration and Mean Wind Direction.

Run Number	Length of Record (sec)	Wind Direction Observed by the Airplane
1	135	Head wind
2	213	Cross wind (left to right)
3	694	Cross wind (left to right)
4	283	Cross wind (right to left)
5	144	Cross wind (left to right)
6	63	Cross wind (right to left)
7	203	Cross wind (left to right)
8	226	Cross wind (right to left)
9	334	Cross wind (right to left)
10	172	Cross wind (left to right)
11	333	Cross wind (left to right)
12	138	Tail wind
13	270	Cross wind (left to right)
14	209	Cross wind (right to left)
15	233	Head wind
16	100	Tail wind
17	47	Head wind

2.2 Time Histories of Gust Velocities, Gust Velocity Differences Between Wing Tips, and the Aircraft's Normal Acceleration

The second part of the analysis for each run recorded in Appendix A shows the gust velocity time histories for the three probes located at the aircraft's nose and wing tips. The left, center, and right probes are designated with subscripts L, C, and R, respectively. The time histories of the spatial velocity differences between the right and left probes are plotted for the longitudinal (u), lateral (v), and vertical (w) velocity components. The definition of longitudinal, lateral, and vertical are along and perpendicular to the mean flight path, respectively. Also plotted with the vertical velocity time histories is the time history of the aircraft's normal acceleration along its flight path. The sampling rate is 40 samples per second.

Figure 2.5 shows a plot of the time histories for Run 3 of Flight 31. Run 3 was the longest record lasting 694 seconds. The velocity fluctuations are typical of the measured data. One observes from the data that there are no significant variations between velocities measured at the three probes. Therefore, one can surmise that length scales associated with these turbulence data are typically larger than the wing span (19.5 m). In Run 3, the aircraft encountered significantly more intense turbulence from 560 seconds to 640 seconds. The turbulence was encountered at approximately 11:00 a.m. (PST) just after the aircraft had climbed from 5600 ft to 6600 ft at an approximate 7° climb angle. During the climb, which started at 530 seconds, visual inspection shows no discernable change in the turbulence during the climb and for roughly a half mile after leveling off at 547 seconds. During the period from 560 seconds to 640 seconds, however, the aircraft encountered much stronger turbulence as it flew over a high mountainous area with well

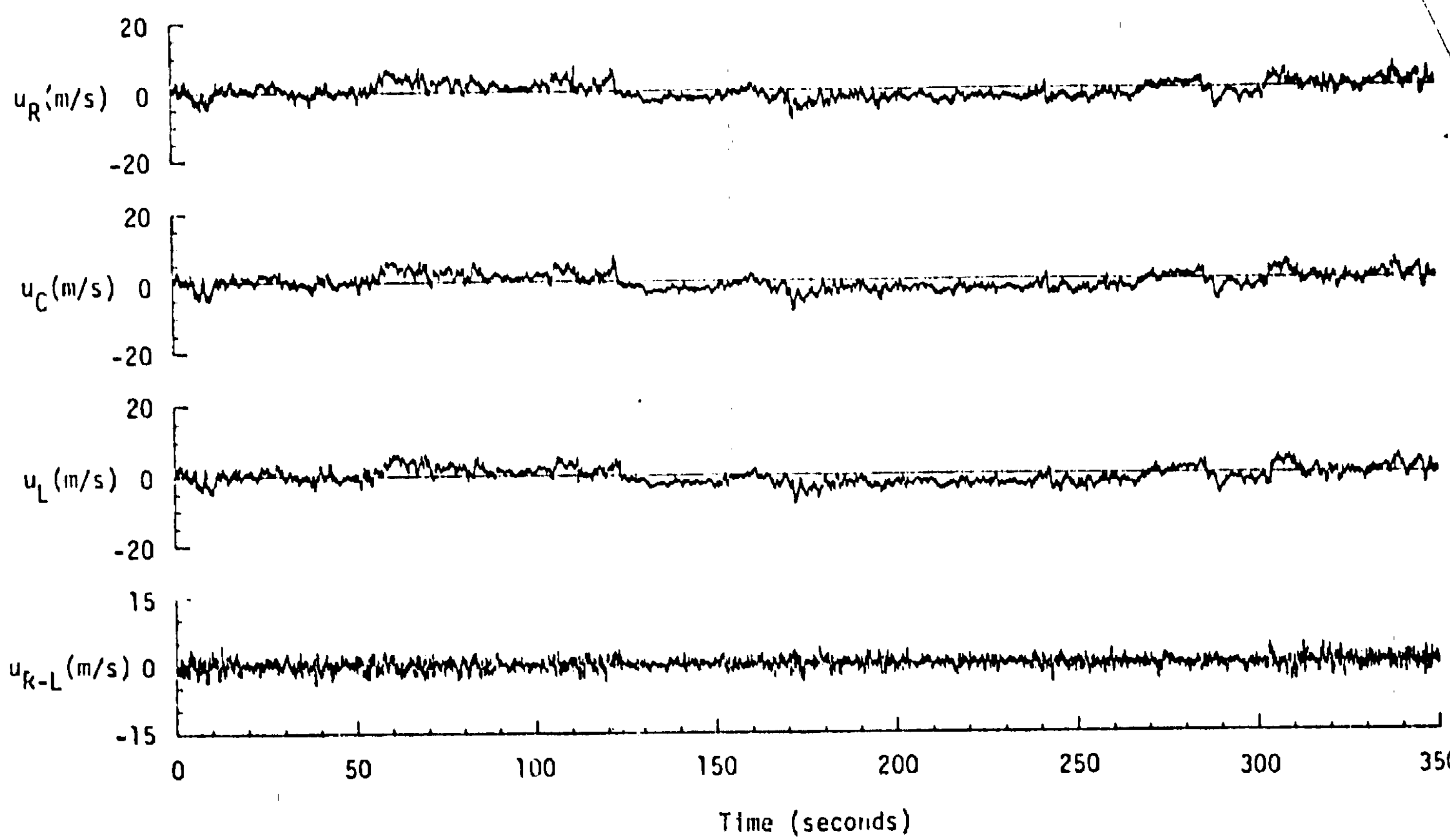

(a) Longitudinal component

Figure 2.5. Time histories of gust velocities, gust velocity differences, and the aircraft's normal acceleration for Run 3 in Flight 31, November 29, 1982.

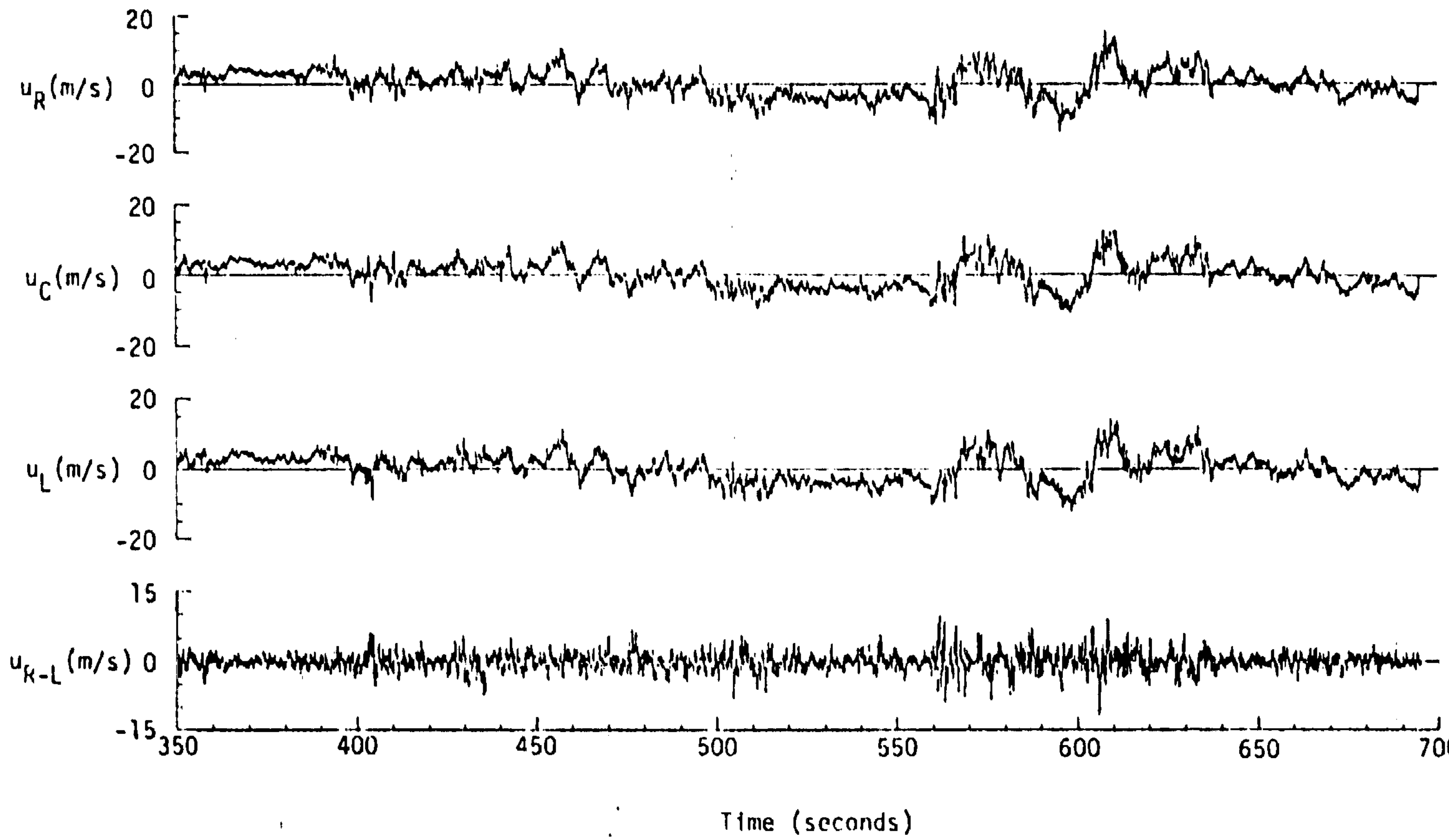

(a) Longitudinal component

Figure 2.5. (continued).

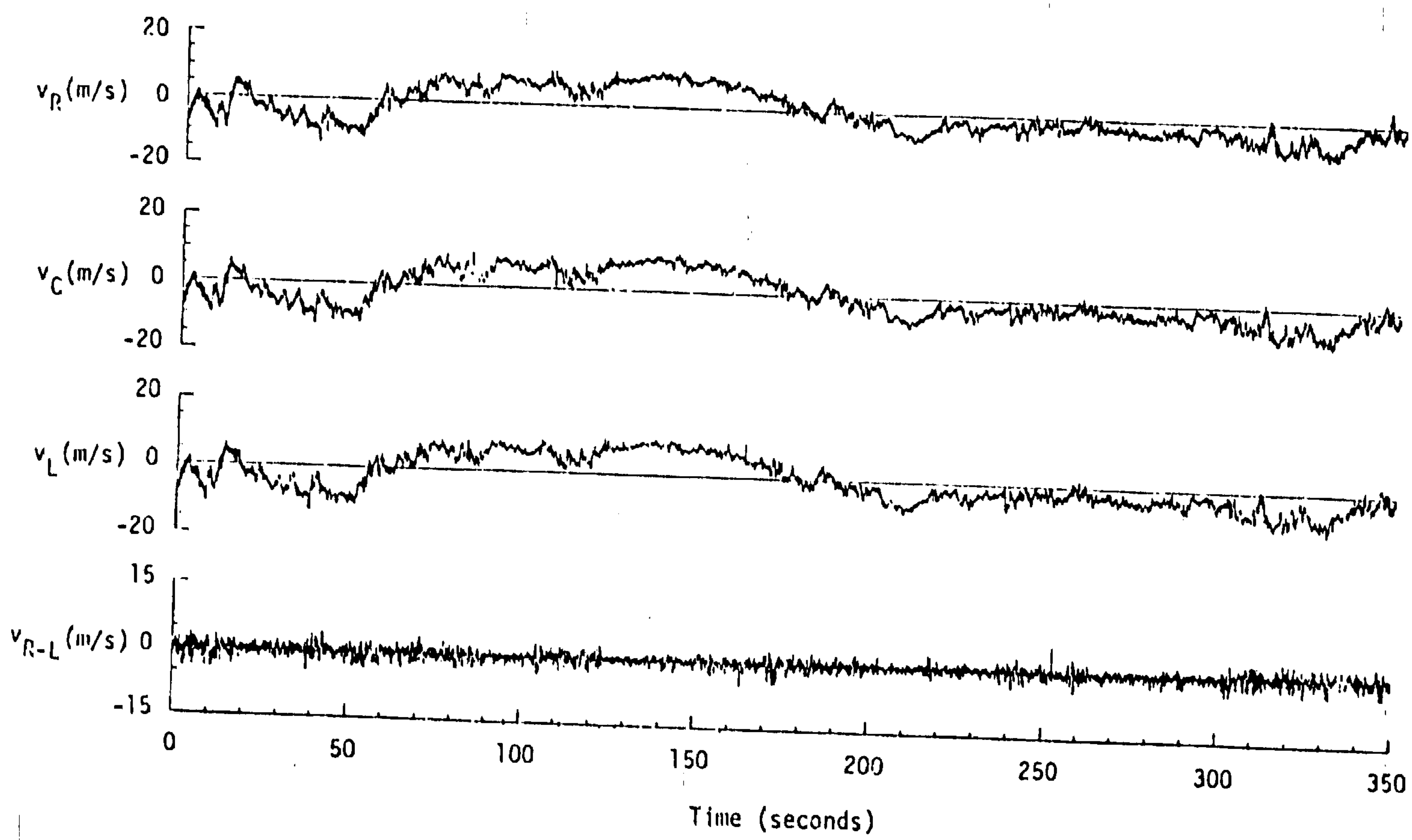

(b) Lateral component

Figure 2.5. (continued).

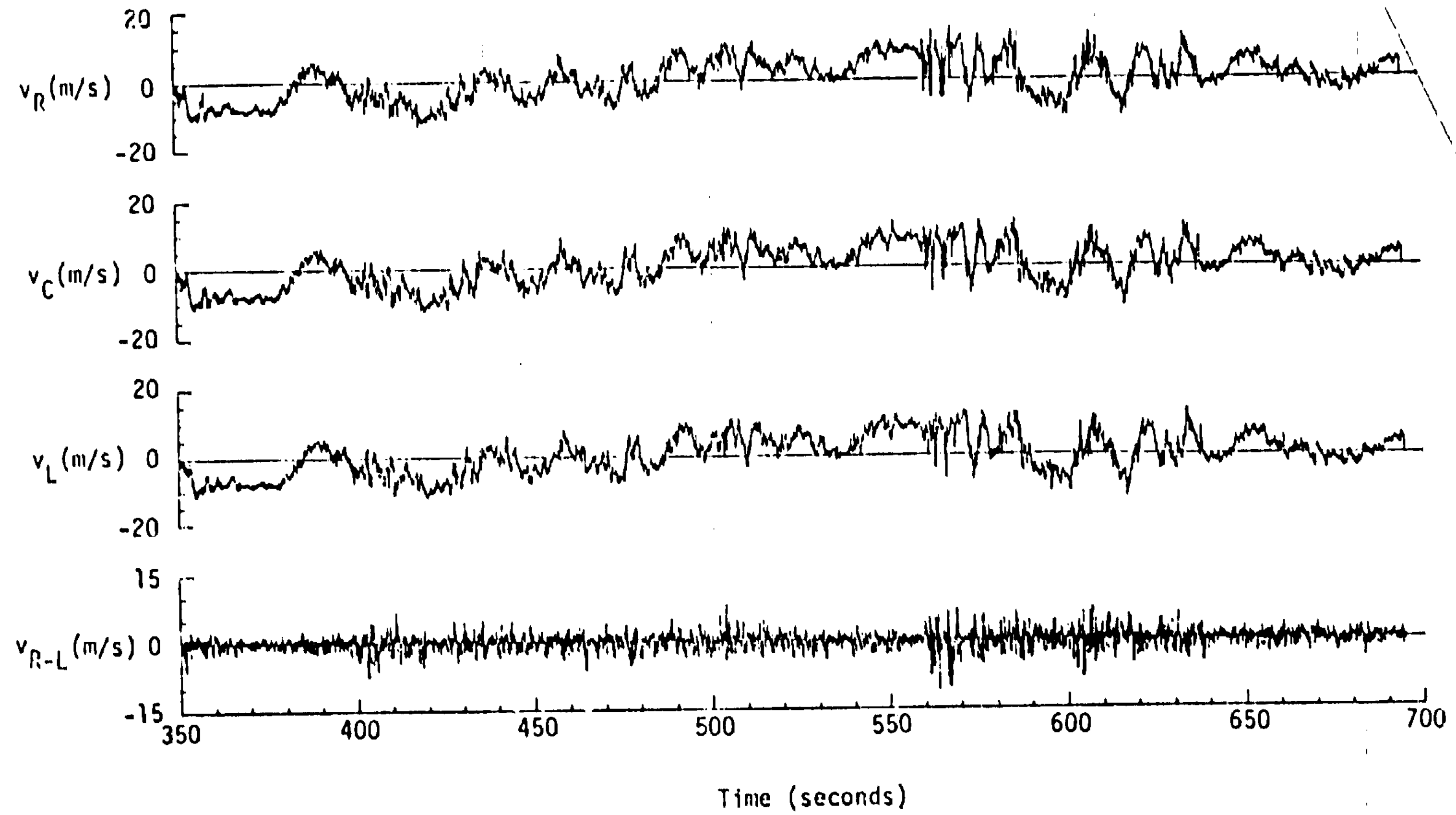

(b) Lateral component

Figure 2.5. (continued).

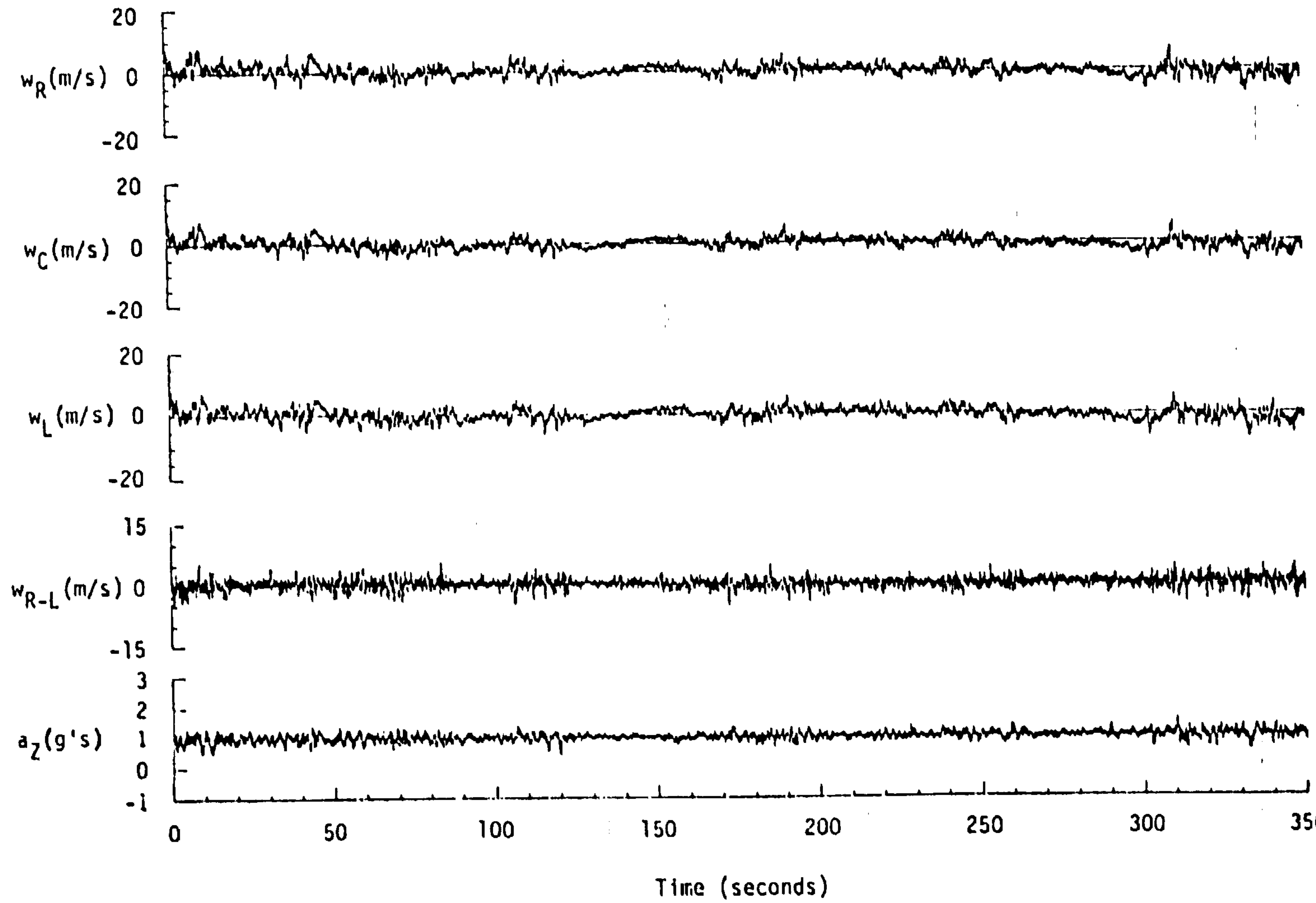

(c) Vertical component and aircraft's normal acceleration

Figure 2.5. (continued).

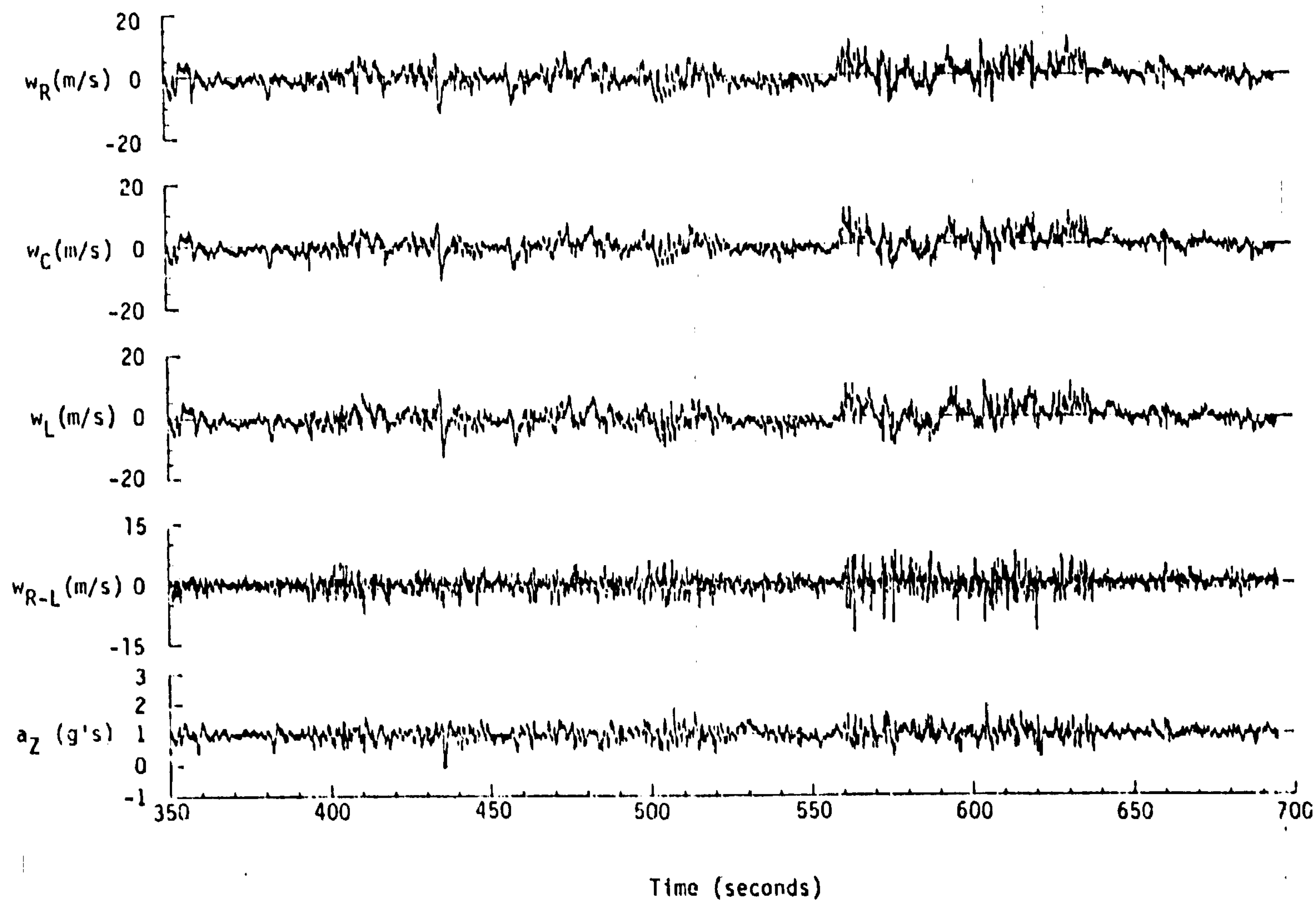

(c) Vertical component and aircraft's normal acceleration.

Figure 2.5. (continued).

pronounced peaks reaching up to 6500 ft. The wind was blowing over the mountains perpendicular to the aircraft flight path (see Figure 2.2). It is believed that the intense turbulence encountered by the aircraft during this time period was associated with the disturbed air flow from the nearby mountain peaks. The strong vertical turbulence induced an increased fluctuation to the aircraft's normal accelerations.

2.3 Average Turbulence Parameters, Integral Length Scales, and Correlation Coefficient of Gust Velocities

The third part of the analysis for each run in Appendix A is a tabulated listing of the average values of several important turbulence parameters for the left, center, and right probes. The statistical parameters include mean airspeed, standard deviation of gust velocity, standard deviation of gust velocity difference, integral length scale, and the correlation coefficient of the gust velocity. The mean airspeed and the standard deviations of the gust velocities and their differences are calculated on the basis of the total time history. However, in analyzing the data to obtain the correlation coefficient and the integral length scale, the total time history is segmented such that the total record is a multiple of segments of 1024 datum points. In computing the correlation coefficients and the length scales, (modify: . . . . scales, the spectrum was first computed by a technique which applied the Fourier transform directly to the original digitalized data. The correlation is then . . . .). The approach first computes the spectrum directly from the turbulence time history. The correlation is then computed from the inverse Fourier transform of the spectrum. Finally, the length scale is computed by integrating the normalized correlation function as described later.

Table 2.3 lists the mean airspeed for all 16 runs in Flight 31. The average mean airspeed for all runs is 102 m/s. The mean airspeeds at the

TABLE 2.3. Mean Airspeed (m/s) for Flight 31, November 29, 1982.

Run Number	$\overline{V}_L$	$\overline{V}_C$	$\overline{V}_R$	Run Number	$\overline{V}_L$	$\overline{V}_C$	$\overline{V}_R$
1	81.13	78.92	81.21	9	103.15	100.84	102.84
2	87.82	85.79	87.51	10	117.27	115.20	116.70
3	104.21	102.52	104.60	11	107.01	104.47	106.49
4	104.78	102.62	104.32	12	101.03	98.55	100.56
5	105.79	103.53	105.33	13	103.30	101.40	103.30
6	104.31	102.19	104.01	14	103.38	101.07	102.99
7	101.47	99.23	100.93	15	107.74	105.40	107.23
8	103.22	101.05	102.86	16	109.41	107.07	108.82

individual right, center, and left probes are 102.8 m/s, 100.6 m/s, and 102.5 m/s. The mean airspeeds measured at the right and left probes are larger than that at the nose by about 2 m/s. This difference can possibly be due to flow deceleration in front of the aircraft nose and/or flow acceleration over the wingtips. Approximate potential flow analysis for a Rankine body (Karmacheti, 1966) suggests the former mechanisms. Similar velocity differences were also found by Frost, et al. (1985a) in the analysis of Flight 21 for the same experimental aircraft.

Table 2.4 lists the standard deviation of gust velocities for all 16 runs of Flight 31. The standard deviation of the gust velocities varies from 1.68 to 7.46 m/s for the longitudinal component, and from 1.42 to 5.57 m/s for the lateral component. The vertical gust component standard deviation ranges from 1.08 to 3.45 m/s. Table 2.4 also lists the standard deviations of the gust velocity differences between the right and left probes. The standard deviation of the gust velocity differences has a high of 1.75 m/s for the longitudinal component, 1.68 m/s for the lateral component, and 2.00 m/s for the vertical component. The standard deviation of the gust velocity, itself,

TABLE 2.4. Standard Deviation (m/s) of Gust Velocity and Gust Velocity Difference for Flight 31.

Run Number	σ_{uR}	σ_{vR}	σ_{wR}	σ_{uC}	σ_{vC}	σ_{wC}
1	2.12	2.11	2.31	1.69	1.99	2.33
2	3.23	2.03	1.16	3.20	2.01	1.08
3	3.17	5.25	2.36	3.15	5.20	2.18
4	3.73	4.07	2.80	3.73	4.09	2.61
5	2.49	4.06	2.76	2.47	4.04	2.66
6	3.64	3.67	3.41	3.54	3.65	3.00
7	3.03	3.00	2.23	3.03	3.03	2.15
8	3.93	5.17	2.52	3.89	5.18	2.36
9	4.10	5.12	2.40	4.10	5.10	2.21
10	2.04	4.57	2.40	1.99	4.58	2.34
11	3.74	2.10	2.25	3.76	2.15	1.99
12	1.68	1.43	1.66	1.68	1.47	1.54
13	2.49	5.57	2.43	2.48	5.57	2.29
14	2.51	3.54	2.37	2.47	3.50	2.12
15	7.46	2.84	3.45	7.31	2.89	3.29
16	5.68	3.21	3.21	5.59	3.44	3.02

Run Number	σ_{uL}	σ_{vL}	σ_{wL}	$\sigma_{\Delta uRL}$	$\sigma_{\Delta vRL}$	$\sigma_{\Delta wRL}$
1	1.74	2.05	2.58	1.20	1.10	0.77
2	3.20	2.09	1.17	0.94	0.77	0.87
3	3.19	5.31	2.31	1.29	1.23	1.37
4	3.75	4.04	2.79	1.59	1.39	1.62
5	2.56	4.10	2.85	1.41	1.38	1.42
6	3.54	3.42	3.12	1.74	1.68	1.92
7	3.07	3.06	2.22	0.85	0.80	0.89
8	3.89	5.20	2.42	1.22	1.08	1.31
9	4.18	5.12	2.34	1.35	1.16	1.45
10	2.02	4.61	2.33	0.41	0.31	0.38
11	3.77	2.18	2.13	1.12	1.01	1.26
12	1.70	1.42	1.59	0.90	0.74	0.91
13	2.59	5.56	2.41	1.53	1.39	1.59
14	2.52	3.42	2.28	1.29	1.12	1.37
15	7.32	2.87	3.35	1.45	1.24	1.49
16	5.74	3.29	3.14	1.75	1.61	2.00

is always larger than the standard deviation of the gust velocity difference between probes.

Table 2.5 lists the integral scales L for 16 runs of Flight 31. The turbulence integral length scale is usually estimated by integrating a normalized one-point auto-correlation function from zero to infinity with respect to temporal or spatial lag. The normalized correlation function (also called the correlation coefficient), $B_x(\tau)$, is given by

$$B_x(\tau) = \overline{x(t)x(t+\tau)}/\sigma_x\sigma_x$$

where x is any of the velocity components. Due to noise in the measured data, the auto-correlation coefficient, however, nearly always oscillates about zero due to either real physical effects but most probably due to aliasing and other digitizing effects. Therefore, in this report the integral length scale is obtained by integrating the normalized auto-correlation function to the point where it first crosses zero ($\ell = S = \overline{V}T$ or $\tau = T$):

$$L = \int_0^S B_x(\ell)d\ell = \overline{V}\int_0^T B_x(\tau)d\tau \qquad (2.1)$$

Detailed study of different definitions of the integral length scales is given in Frost and Lin (1983) (also see Houbolt, et al. (1964)). Frost and Lin (1983) suggest that using the L as defined in Equation 2.1 in theoretical models gives best agreement with experimental results. This length scale is therefore used throughout this report.

In addition to the integral scales calculated from the normalized values of one-point auto-correlation functions, $\overline{u_R u_R}$, $\overline{v_R v_R}$, and $\overline{w_R w_R}$, the integral length scales are also estimated with Equation 2.1 using the normalized values of the two-point correlation functions, $\overline{u_R u_L}$, $\overline{v_R v_L}$, and $\overline{w_R w_L}$. These two integral scales have the same order of magnitude for each corresponding

TABLE 2.5. Turbulence Length Scales for Flight 31.

Run Number	Integral Length Scale (m)					
	L_{uR}	L_{vR}	L_{wR}	L_{uRL}	L_{vRL}	L_{wRL}
1	297.7	149.7	255.1	248.4	35.3	254.5
2	325.9	250.1	79.1	322.4	251.8	89.3
3	234.0	425.6	116.9	258.4	422.8	115.3
4	419.8	350.8	66.9	408.0	344.7	61.9
5	333.9	168.6	189.7	317.5	173.5	204.0
6	364.7	92.0	51.7	344.5	104.2	47.5
7	562.8	249.6	287.6	532.2	242.9	283.5
8	306.7	364.4	232.9	302.5	380.7	249.6
9	327.8	338.0	93.9	341.5	338.0	83.9
10	641.8	729.7	832.2	638.3	742.9	863.8
11	370.0	246.1	203.3	375.6	241.7	193.1
12	127.7	252.6	202.4	137.5	250.1	190.8
13	156.0	428.8	83.7	148.6	424.4	82.6
14	174.9	204.4	66.8	161.3	205.4	64.5
15	540.0	225.8	526.1	526.5	225.3	494.0
16	348.1	362.2	95.0	347.5	336.5	115.3

turbulence velocity component (see Table 2.5). The individual velocity component characteristics do not vary appreciably across the wing span which is in agreement with the fact that the calculated length scales are much larger than the 19.5 m wing span of the aircraft. This implies that the energy-containing turbulence fluctuations essentially engulf the total airfoil.

Finally, Table 2.6 shows the two-point correlation coefficients of the gust velocities computed for 16 runs of Flight 31. The symbols $\overline{u_R u_L}$, $\overline{v_R v_L}$, and $\overline{w_R w_L}$ represent the two-point common velocity component correlation functions for longitudinal, lateral, and vertical components, respectively, whereas $\overline{u_R v_R}$, $\overline{v_R w_R}$, and $\overline{w_R u_R}$ represent the one-point cross-correlation functions, and $\overline{u_R v_L}$, $\overline{v_R w_L}$, and $\overline{w_R u_L}$ represent the two-point cross-correlation functions. Although several other correlations of the gust velocities could

TABLE 2.6. Two-Point Correlation Coefficient of Gust Velocity for Flight 31.

Run Number	$\frac{\overline{u_R u_L}}{\sigma_{v_R}\sigma_{v_L}}$	$\frac{\overline{v_R v_L}}{\sigma_{w_R}\sigma_{w_L}}$	$\frac{\overline{w_R w_L}}{\sigma_{u_R}\sigma_{v_L}}$	$\frac{\overline{u_R v_R}}{\sigma_{v_R}\sigma_{w_R}}$	$\frac{\overline{v_R w_R}}{\sigma_{w_R}\sigma_{u_R}}$	$\frac{\overline{w_R u_R}}{\sigma_{u_R}\sigma_{v_R}}$	$\frac{\overline{u_R v_L}}{\sigma_{v_R}\sigma_{w_L}}$	$\frac{\overline{v_R w_L}}{\sigma_{w_R}\sigma_{u_L}}$	$\frac{\overline{w_R u_L}}{\sigma_{w_R}\sigma_{u_L}}$
1	0.75	0.34	0.80	0.08	0.14	0.52	-0.40	0.11	0.45
2	0.80	0.81	0.82	0.00	-0.05	0.11	-0.02	-0.03	0.10
3	0.80	0.91	0.75	0.09	-0.19	0.06	0.04	-0.19	0.05
4	0.88	0.91	0.80	-0.19	0.20	0.09	-0.19	0.20	0.06
5	0.87	0.90	0.90	-0.09	-0.10	-0.17	-0.08	-0.09	-0.20
6	0.82	0.90	0.81	-0.18	0.60	-0.10	-0.18	0.61	0.00
7	0.92	0.90	0.90	0.02	-0.21	0.39	0.01	-0.21	0.32
8	0.89	0.81	0.80	-0.20	0.15	0.00	-0.19	0.10	0.03
9	0.80	0.90	0.80	0.30	0.20	0.19	0.30	0.20	0.18
10	0.98	0.99	0.98	0.08	0.00	-0.47	0.09	-0.01	-0.45
11	0.83	0.81	0.78	-0.21	-0.09	0.48	-0.28	-0.10	0.40
12	0.66	0.81	0.78	0.00	0.30	-0.22	0.01	0.31	-0.20
13	0.80	0.91	0.79	-0.18	-0.32	0.25	-0.19	-0.32	0.22
14	0.79	0.90	0.77	0.18	0.19	0.10	0.13	0.27	0.07
15	0.90	0.88	0.88	0.32	0.06	0.02	0.30	0.01	0.00
16	0.85	0.86	0.85	0.49	0.05	-0.10	0.49	0.02	-0.10

be estimated, the combinations shown in Table 2.6 are sufficient to detect any trends or physical effects associated with the normalized spatial correlation computed from these data. Note that the appreciable difference in value between the one-point auto-correlation evaluated at zero lag, (shown in Table 2.4) and the two-point correlations evaluated at zero lag (shown in Table 2.6) is that correlation coefficients (i.e., normalized values) are tabulated in Table 2.6 whereas non-normalized correlations are given in Table 2.4. It is clear from inspection of Table 2.6 that the correlation between like components of turbulence has a roughly uniform decrease in value of 20 percent over the wing span of the aircraft.

All of the two-point correlation coefficients between common velocity components are larger than 0.75 except the value of $\overline{v_R v_L}/\sigma_{v_R}\sigma_{v_L}$ for Run 1 and

$\overline{u_R u_L}/\sigma_{u_R}\sigma_{u_L}$ for Run 12. The former may be associated with Run 1 being a take-off flight path (see Figure A.1). No explanation is evident for Run 12. The one-point cross-correlation coefficients are the Reynolds stresses (Frost and Moulden, 1977; Hinze, 1975) and are thus a measure of momentum transfer. For isotropic turbulence the cross-correlation terms theoretically are zero. The very low values shown in Table 2.6 suggest that the atmospheric turbulence is indeed nearly isotropic. It is believed that the large value of $\overline{v_R w_R}/\sigma_{v_R}\sigma_{w_R}$ and $\overline{v_R w_L}/\sigma_{v_R}\sigma_{w_L}$ for Run 6 is caused by the very short averaging time of 63 seconds associated with the run. It therefore does not represent a meaningful statistical average. Similar arguments can be made for other unjustifiably large values of the cross-correlation coefficient.

2.4 Probability Density Function for Gust Velocities and Gust Velocity Differences

The fourth part of the analysis for each run in Appendix A contains the probability density function of the turbulent wind velocities. Data measured by the B-57B aircraft for all three different probe positions and for all three velocity components (longitudinal, lateral, and vertical) are plotted. The degree of or lack of normality of the turbulent wind velocities is illustrated by comparing the experimental probability density distributions with the theoretical normal distribution and the theoretical non-Gaussian probability density model (modified Bessel function distribution see Reeves, et al. (1974)).

The probability density function for the turbulence wind velocities is defined as:

$$p(x) = \lim_{\Delta x \to 0} \frac{\text{Prob}[x < x(t) < x + \Delta x]}{\Delta x} \qquad (2.2)$$

where x(t) may be u, v, w, Δu, Δv, or Δw and where Prob[$x < x(t) \leq x + \Delta x$] is the probability that the turbulence wind velocity at time t lies within a specified speed interval. The Gaussian probability density function is given by:

$$p(x) = \frac{1}{\sigma\sqrt{2\pi}} \, e^{-\frac{(x-\bar{x})^2}{2\sigma^2}} \tag{2.3}$$

where $\bar{x}$ is the mean value of x(t) and σ is the standard deviation of x(t). In calculating the probability density distributions in Appendix A, the gust velocity and the gust velocity differences are normalized with their standard deviations.

The non-Gaussian probability density distribution is given by Reeves, et al. (1974) as:

$$p\left(\frac{x}{\sigma}\right) = \frac{1}{\sigma} \frac{(1 + r^2)^{1/2}}{\pi} \int_0^\infty \left[\frac{2}{1 + 2\ell^2 r^2}\right]^{1/2} \exp\left[-\ell^2 - \frac{1}{2}\left(\frac{x}{\sigma}\right)^2 \frac{(1 + r^2)}{(1 + 2\ell^2 r^2)}\right] d\ell \tag{2.4}$$

where r is an adjustable parameter which is a measure of the degree to which the distribution is non-Gaussian and ℓ is the dummy variable of integration. If r = 0, the function is exactly the Gaussian function; however, as r increases, the distribution departs from the Gaussian probability density function and approaches a modified Bessel function distribution as $r \to \infty$.

Figure 2.6 shows typical probability density distributions for Run 3 of Flight 31. The upper half of the figure shows the probability density distributions of the three individual gust velocity components and the bottom half of the figure shows the probability density distributions of the gust velocity differences between the right and left probes. These probability density calculations for the measured turbulence do not fit the normalized Gaussian distribution very well. Fitting the individual probability

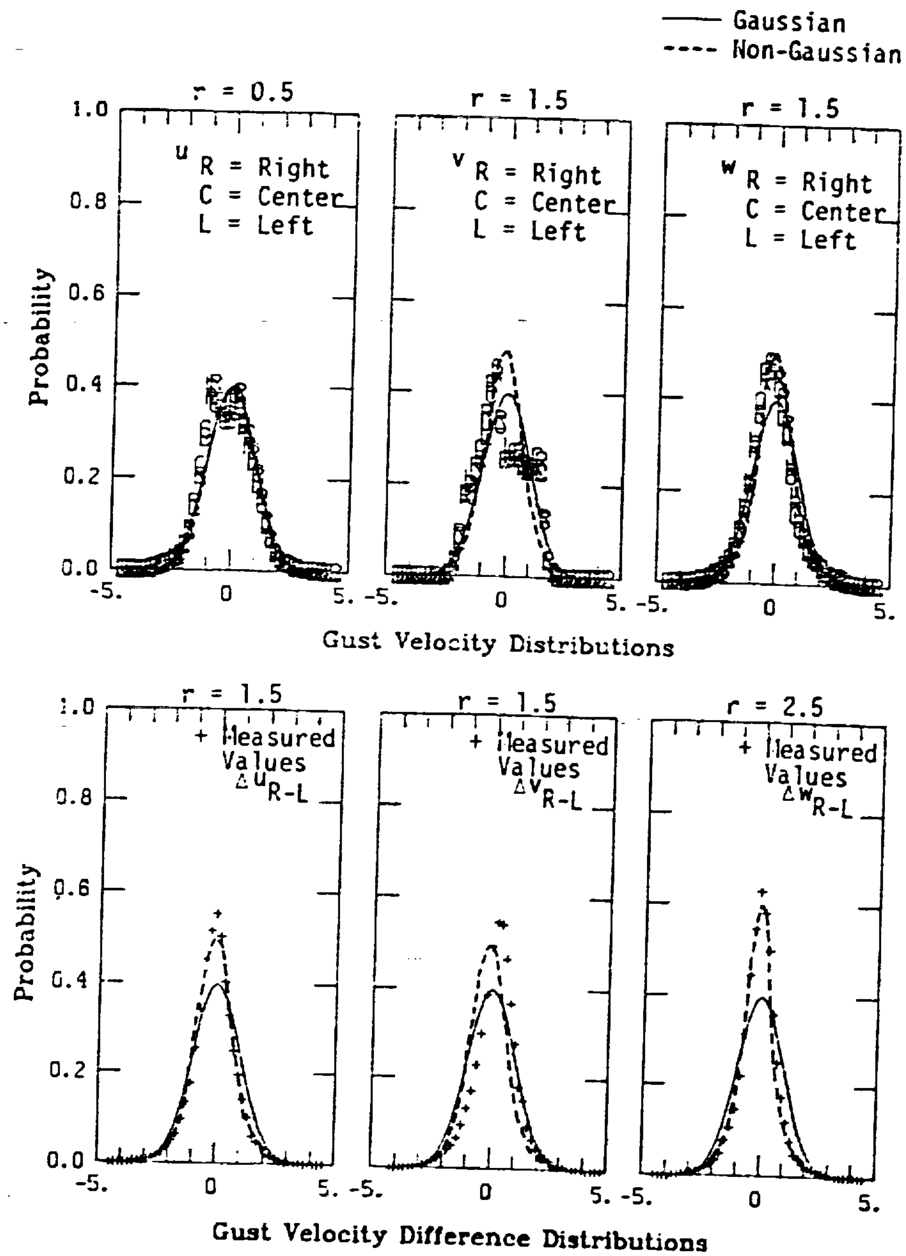

Figure 2.6. Comparison of probability density functions for gust velocities and gust velocity differences (normalized with the standard deviation) with theoretical models, Flight 31, Run 3 (r = degree of non-Gaussian).

distributions to Equation 2.4 by adjusting r, a non-Gaussian form which provides a closer fit to the experimental data is found. Inspection of Figure 2.6 and similar figures in Appendix A shows the non-Gaussian distribution gives a very good fit of the gust velocity difference probability distribution. The individual gust velocity probability distribution however, in many cases, appears to be bimodal. This is associated with trends in the mean velocity that have not been removed from the data.

Runs 1 and 9 are clear examples of the effects of trends in the mean wind on the probability distribution. For Run 1 during climb-out, the longitudinal mean wind which is essentially a headwind (see Figure A.1, Appendix A) will increase from zero at the surface to the value aloft. This vertical variation in the mean wind will typically vary logarithmically (Panofsky and Dutton, 1984). By simply assuming the mean wind speed is uniform and removing a constant value from the data (as was done in this study) causes the velocity fluctuations about the mean at low levels to be mainly negative and at higher levels mainly positive fluctuations (see Figure A.2, Appendix A). Thus, there is a bimodal distribution in the probability density function of the velocity fluctuations. This bimodal effect can probably be eliminated by removing a logarithmic velocity profile* trend. However, this was not done.

Now consider Run 9. The quasi-steady horizontal wind speed along the flight path is shown in Figure A.41. For the initial part of this flight, the winds were partially headwinds with a dominate northward direction. During the latter part, the winds became partially tailwinds with a westerly

*Note vertical variation of horizontal wind with height is typically logarithmic (Panofsky and Dutton, 1984).

direction. Again, removing a uniform average wind speed from the data results in the longitudinal velocity fluctuations being mainly negative during the initial part of the flight and positive during the latter part (see Figure A.42). Again, this results in a strong bimodal distribution in both the longitudinal and lateral wind speed gust distributions as shown in Figure A.43.

Returning to the discussion of the analytical models which best fit the data, it is clear that Equation 2.4 fits the experimental data considerably better than the Gaussian distribution. The value of r which gives the best fit of the data changes for different velocity components and from run to run. Table 2.7 lists values of r determined from "eye-ball" fits of the data for the three components of the gust velocity and gust velocity differences. The variation in r might be expected to be a result of the underlying surface roughness. Inspecting of the terrain features beneath each flight path, however, suggests no apparent relationship between surface roughness and the value of r, nor is there an obvious correlation between r and altitude. Further work is required to associate the degree of non-Gaussianness of the atmospheric turbulence with physical causes.

2.5 Normalized One- and Two-Point Correlation Functions of Gust Velocities

The fifth part of the analysis for a given run in Appendix A is the normalized one- and two-point correlation functions of the turbulent wind velocities at the right and left wing tips. The correlation function between the same velocity components at two different positions separated by a vector distance $\vec{\zeta}$ is defined as (Panchev, 1971; Hinze, 1975):

$$R_x(\vec{\zeta},\tau) = \lim_{T\to\infty} \frac{1}{T} \int_0^T x(\vec{\xi},t)\ x'(\vec{\xi}+\vec{\zeta},\ t+\tau)dt \qquad (2.5)$$

where τ is the lag time, x and x' designate any one of the velocity components u, v, and w, and $\vec{\xi}$ is the position vector at which the velocity x is measured.

TABLE 2.7. Values of r (Equation 2.4) Which Represent a Measure of the Degree of Departure from a Gaussian Probability Distribution of the Gust Velocities.

Run Number	u_R, u_C, u_L	v_R, v_C, v_L	w_R, w_C, w_L	Δu_{R-L}	Δv_{R-L}	Δw_{R-L}
1	1.5	1.5	1.5	3.5	3.5	0.5
2	2.5	1.0	1.0	1.5	1.5	1.5
3	0.5	1.5	1.5	1.5	1.5	2.5
4	2.5	1.0	2.5	2.5	2.5	3.5
5	3.5	3.5	3.5	4.5	7.5	6.5
6	3.5	4.5	4.5	4.5	6.5	7.5
7	2.5	2.5	2.5	4.5	6.5	6.5
8	4.5	1.5	1.5	2.5	2.5	3.5
9	2.5	1.0	1.0	2.5	2.5	2.5
10	1.5	3.5	2.5	2.5	4.5	2.5
11	2.5	1.5	1.5	2.5	2.5	2.5
12	1.5	1.0	1.0	1.5	1.5	1.5
13	1.5	2.5	1.0	1.5	1.5	2.5
14	3.5	3.5	3.5	4.5	4.5	4.5
15	4.5	4.5	1.5	7.5	7.5	7.5
16	1.5	1.5	1.5	1.5	1.5	1.5

The normalized correlation function:

$$B_x(\vec{\zeta},\tau) = \frac{R_x(\vec{\zeta},\tau)}{\sigma_x \sigma_{x'}} \qquad (2.6)$$

is called the correlation coefficient, σ_x and $\sigma_{x'}$ are the standard deviations of $x(\vec{\xi},t)$ and $x'(\vec{\xi}+\vec{\zeta},t)$, respectively. If $\vec{\zeta}$ is not equal to zero, and x and x' are the same velocity component, the correlation function is called the two-point common component correlation function in this report. The absolute value of $B_x(\vec{\zeta},\tau)$ is always less than one. At $\vec{\zeta} = 0$, $R_x(\vec{\zeta},\tau)$ reduces to the one-point auto-correlation function given by:

$$R_x(\tau) = \lim_{T\to\infty} \frac{1}{T} \int_0^T x(t)\, x(t+\tau)dt \tag{2.7}$$

The correlation function may be evaluated using a time history summation technique or by using the direct Fourier transformation method for computing spectra. Steely and Frost (1981) and Frost and Lin (1983) have compared the direct method with the summation technique and found they give identical results. The direct method is therefore used throughout this report unless otherwise stated.

Theoretical models of the one-point auto-correlation and of the two-point correlation are the von Karman model (Hinze, 1975) and the Houbolt and Sen (1972) extension of the von Karman model, respectively. The von Karman theoretical model for the normalized one-point auto-correlation functions for longitudinal and transverse velocity components is expressed as:

$$B_L(\zeta) = c\left[\frac{\zeta}{aL_L}\right]^{1/3} K_{1/3}\left[\frac{\zeta}{aL_L}\right]$$

$$B_T(\zeta) = c\left[\frac{\zeta}{aL_T}\right]^{1/3} \left[K_{1/3}\left[\frac{\zeta}{aL_T}\right] - \left[\frac{\zeta}{2aL_T}\right] K_{2/3}\left[\frac{\zeta}{aL_T}\right]\right] \tag{2.8}$$

where $c = 2^{2/3}/\Gamma(1/3)$, $a = 1.339$, K is a modified Bessel function of the second kind, Γ is the gamma function, L is the integral length scale, and ζ is the spatial lag distance. The subscripts L and T refer to longitudinal and transverse, respectively. The longitudinal and transverse velocity correlation are defined as shown in Figure 2.7.

The von Karman correlation is in principle only valid for isotropic turbulence. The more general non-isotropic velocity correlation is a second order tensor given by (Hinze, 1975) as:

$$R_{ij}(\xi,\zeta) = \overline{u_i(\xi)\, u_j(\xi+\zeta)}\, e_i(\xi)\, e_j(\xi+\zeta) \tag{2.9}$$

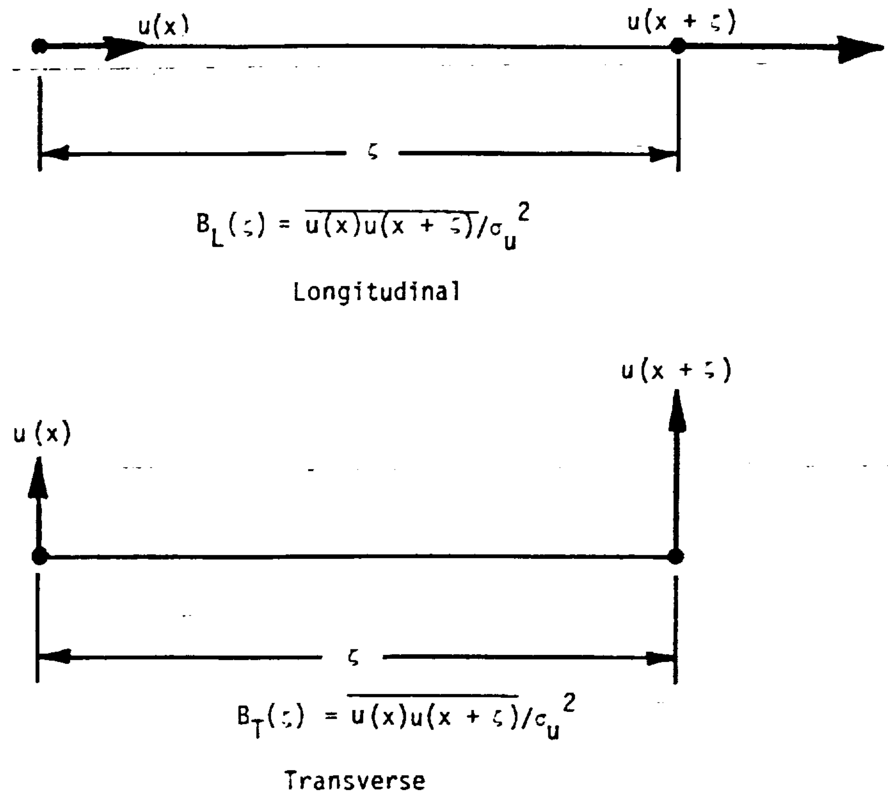

Figure 2.7. Definition of the longitudinal and transverse velocity correlation coefficients.

where $e_i(\xi)$ represents the direction cosines of the velocity vector at the position ξ with respect to the ith axis and $e_j(\xi + \zeta)$ is similarly defined at a distance ζ from the position ξ. The symbol $u_i(\xi)$ is the instantaneous component of the velocity fluctuation with respect to the mean at the position ξ and $u_j(\xi + \zeta)$ is similarily defined. The general correlation, $R_{ij}(\xi,\zeta)$, is thus described in terms of nine components. When the turbulence is isotropic and homogeneous it can be shown that the correlation can be expressed solely in terms of the longitudinal and transverse correlations shown in Figure 2.7.

In the present investigation the velocity components are expressed relative to the axis of the aircraft (the assumption of small angles is evoked (see Appendix B)). For the longitudinal and transverse correlations the velocity components must be resolved parallel and perpendicular to the line between the two measuring points as illustrated in Figure 2.8. Therefore, to transform the longitudinal and transverse correlations to the aircraft frame of reference, the cosines in Equation 2.9 must be taken into account.

Frost, et al. (1985a) have shown following Hinze (1975) that for isotropic turbulence (see Figure 2.8):

$$R_u(\zeta) = \frac{s^2}{\xi^2 + s^2}\,\sigma_T{}^2 B_T(\zeta) + \frac{\xi^2}{\xi^2 + s^2}\,\sigma_L{}^2 B_L(\zeta) \qquad (2.10)$$

$$R_v(\zeta) = \frac{s^2}{\xi^2 + s^2}\,\sigma_L{}^2 B_L(\zeta) + \frac{\xi^2}{\xi^2 + s^2}\,\sigma_T{}^2 B_T(\zeta) \qquad (2.11)$$

The vertical velocity correlation is, of course:

$$R_w(\zeta) = \sigma_T{}^2 B_T(\zeta) \qquad (2.12)$$

This model is referred to as the Houbolt and Sen model since Houbolt and Sen (1972) utilized it with Equations 2.7 and 2.8 early on to develop a two-point spectrum for use in design analyses. (It should be noted that in actual fact, Houbolt and Sen did not account for the direction cosines and hence their

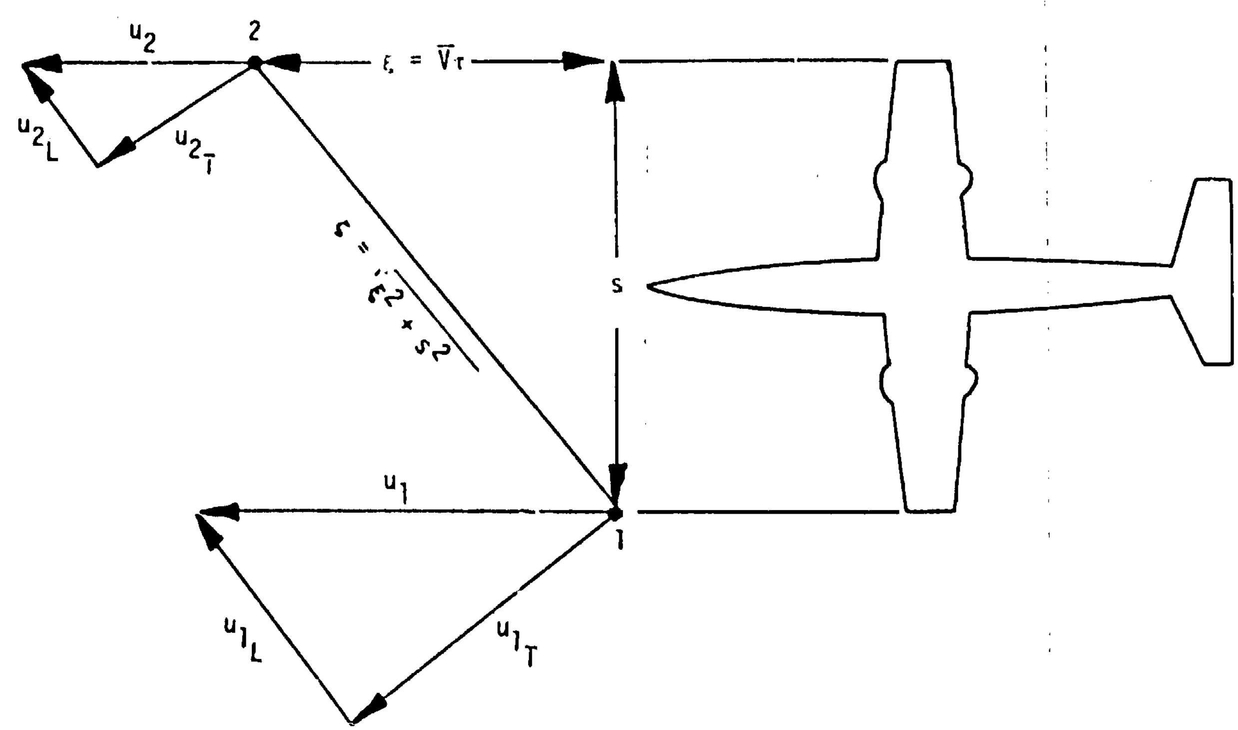

Figure 2.8. Terminology of the two-point auto-correlation relationship (the lateral velocity components are similarly resolved).

longitudinal spectrum is incorrect.) For isotropic turbulence, $\sigma_T = \sigma_L = \sigma$ which is not the case for the experimental data as is apparent from Table 2.4.

Figure 2.9 shows normalized one- and two-point correlation functions. The correlations are from Run 3, Flight 31. All correlation coefficients are plotted versus the spatial lag distance, $\zeta = V\tau$, in the direction of flight. The normalized one-point auto-correlation functions are plotted in the upper part of the figure, and the normalized two-point correlation functions in the lower part. The two-point correlations have both negative and positive time lags. Only the positive lag is given in the figure. Negative lags behave similarly but are not symmetric. The influence of negative lag appear in the phase angle of the two-point spectrum which is discussed in a later section of this report. The area obtained by integrating the one-point auto-correlation coefficient from zero spatial lag to the point where the correlation coefficient first crosses zero is defined as the integral length scale (see Table 2.5). Comparisons of the experimental data with the von Karman theoretical one-point auto-correlation coefficient and with the Houbolt and Sen (1972) theoretical two-point correlation function are shown in the figure. The integral length scale, L, used in the theoretical models was that determined as described above. Using length scales determined from other definitions (see Frost and Lin, 1983) gave no better and, in most cases, poorer agreement with the experimental data.

In general, auto-correlations are expected to decay faster for the vertical and lateral components than for the longitudinal component. Results of Run 3 shown in Figure 2.9 appear to be an exception to this rule since similar plots of correlations for other runs given in Appendix A behave as expected. However, employing the length scales, computed as described in the theoretical model, results in the one-point auto-correlation coefficient

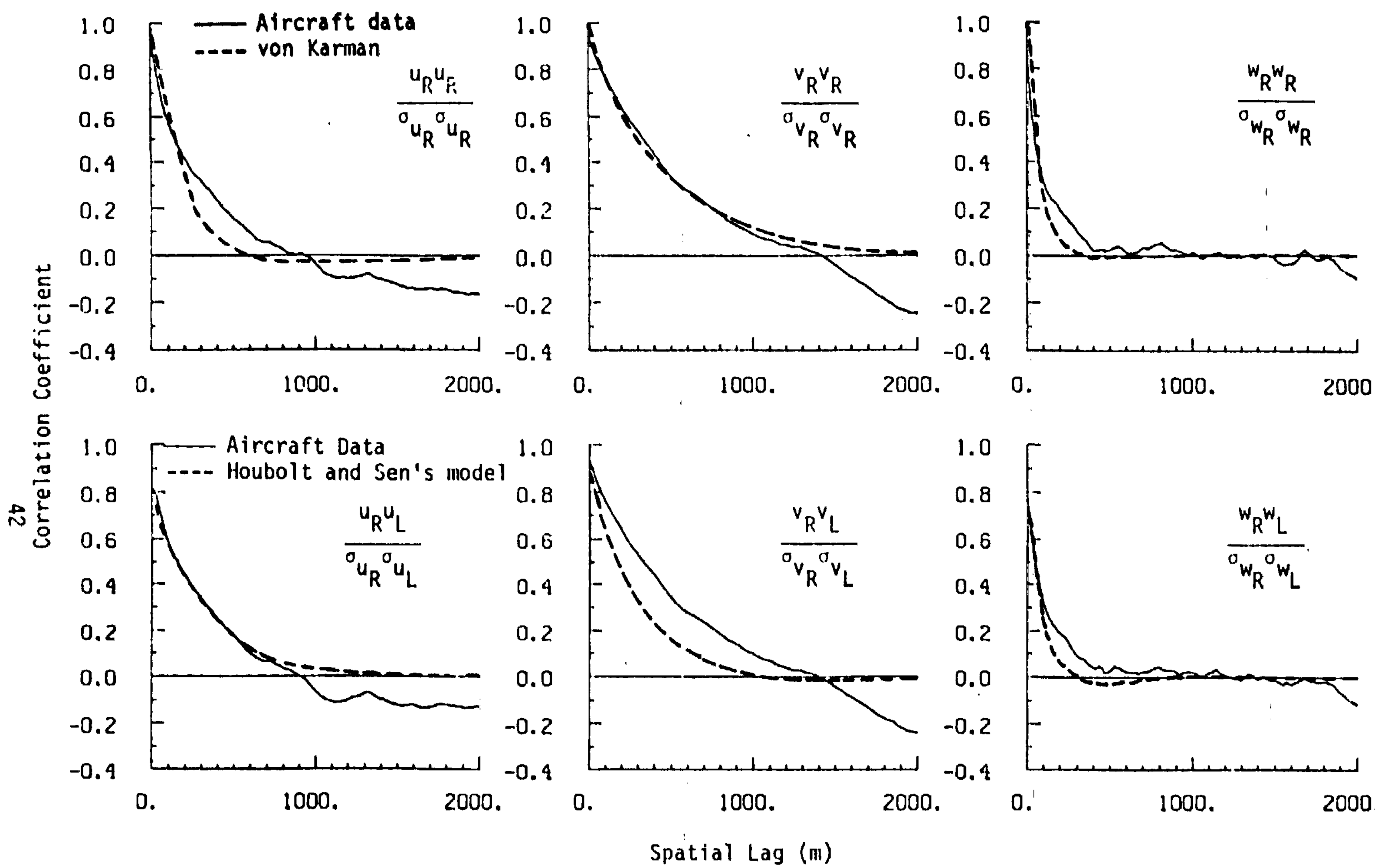

Figure 2.9. Comparison of normalized one- and two-point correlation functions for gust velocities with theoretical models, Flight 31, Run 3.

fitting the measured data quite well (see for example Runs 6, 14). The experimental correlation coefficient does depart, however, from the theory. It is higher than the value predicted by the von Karman model at the larger spatial lags.

It is interesting that poorer agreement with von Karman's theoretical models occurs for the high altitude flight Run 10 than for the others. This is surprising since it is generally assumed that turbulence at higher altitudes is isotropic. The wind at the higher level, however, may have been stratified with embedded gravity waves. This is suggested by the high degree of correlation shown in Figure A.49 and inspection of the time history in Figure A.47 which suggests Run 10 encountered a wave pattern.

Consideration of Figures 2.7 and 2.8 shows that $R_u(\zeta)$ defined by Equation 2.10 converges to $\sigma_T{}^2 B_T(\zeta)$ at $\xi = 0$. Inspection of the correlation coefficients plotted in Appendix A shows this to be approximately true in most cases. In turn, as ξ becomes large $R_u(\zeta)$ approaches the longitudinal correlation $\sigma_L{}^2 B_L(\zeta)$. This is also approximately true based on inspection of the experimental results. The above observation suggests that the turbulence is reasonably isotropic for all runs except Run 10. Run 10 at high altitude as noted appears to be associated with wave motion. This is even more apparent in the cross-correlation coefficients described next.

The cross-correlation function of two sets of random data describes a general dependence between the variations of the sets. The two-point cross-correlation function is given by:

$$R_{xy}(\vec{\zeta},\tau) = \lim_{T\to\infty} \frac{1}{T} \int_0^T x(\vec{\xi},t)\; y(\vec{\xi}+\vec{\zeta},\; t+\tau)dt \qquad (2.13)$$

where x and y are time histories of any two of the turbulence velocity components u, v, and w, τ represents the lag time, and $\vec{\xi}$ indicates the position vector. For a given $\vec{\zeta}$, the function $R_{xy}(\vec{\zeta},\tau)$ is always a real-valued function which may be either positive or negative. Furthermore, $R_{xy}(\vec{\zeta},\tau)$ does not necessarily have a maximum at $\tau = 0$, nor is $R_{xy}(\vec{\zeta},\tau)$ an even function as was true for the one-point auto-correlation functions. However, $R_{xy}(\vec{\zeta},\tau)$ does display the symmetric relation (Bendat and Piersol, 1971):

$$R_{xy}(\vec{\zeta},-\tau) = R_{yx}(\vec{\zeta},\tau) \tag{2.14}$$

where x and y are interchanged.

The normalized cross-correlation function is then defined as:

$$B_{xy}(\vec{\zeta},\tau) = \frac{R_{xy}(\vec{\zeta},\tau)}{\sigma_x\sigma_y} \tag{2.15}$$

where σ_x and σ_y are the standard deviations of $x(\vec{\xi},t)$ and $y(\vec{\xi}+\vec{\zeta},t)$, respectively. At $\vec{\zeta} = 0$, $R_{xy}(\tau)$ and $B_{xy}(\tau)$ are called the one-point cross-correlation and the normalized one-point cross-correlation functions, respectively.

Figure 2.10 shows typical normalized one- and two-point cross-correlation functions for Run 3 in Flight 31. The upper half of the figure shows the one-point cross-correlation coefficients for three combinations of the turbulent velocity components measured with respect to the right wing tip of the aircraft. The lower half of the figure shows the two-point cross-correlation coefficients for three corresponding combinations of the turbulent velocity components measured from the right and left wing tips. Since the wing span is much smaller than the characteristic length scale of the turbulence, the two-point cross-correlation coefficients are quite similar to those of the one-point cross-correlation for all runs.

The cross-correlation coefficients, shown in Appendix A, are, with the exception of Run 10, generally small and almost constant with spatial lags.

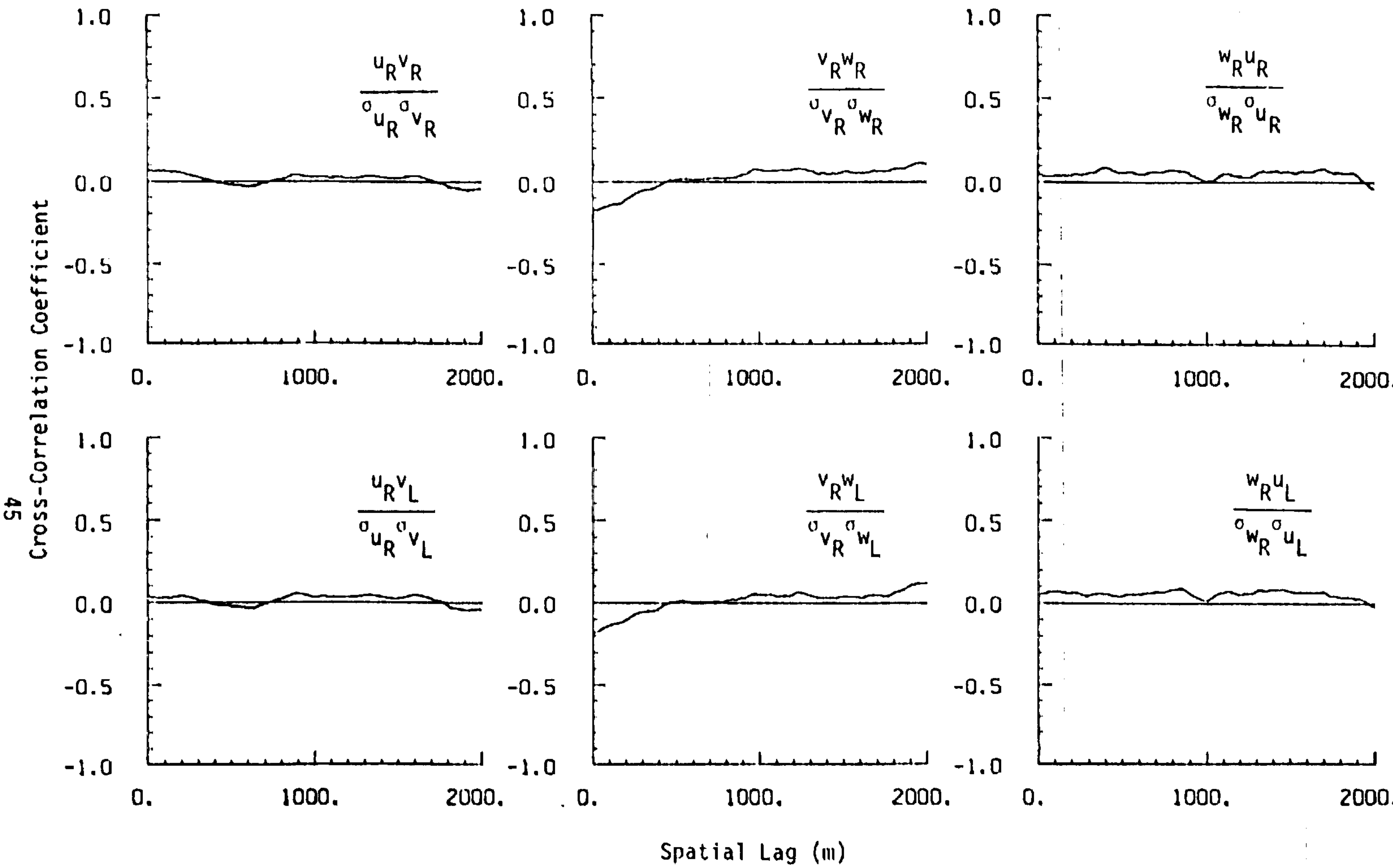

Figure 2.10. Normalized one- and two-point cross-correlation functions of gust velocities, Flight 31, Run 3.

The cross-correlations for Run 10 increases with spatial lag having a maximum at $\zeta = 1500$ m. Inspection of the time histories suggests a wave phenomenon at the high altitude at which Run 10 was made. The first wave occurs at roughly 17 seconds which corresponds to $\zeta = V\tau$ of approximately 1700 m. The u and v components are approximately 180° out of phase resulting in a strong cross-correlation at $\zeta = 1500$ m.

In contrast to Run 10, the cross-correlations for the other runs have values on the order of 0.5 or less but show no pronounced peak. The value of these correlations (i.e., approximately 0.5) are higher than expected but the high values may be due to the short time records. For best results, the cross-correlation function of Equation 2.13, requires the sample record length to approach infinity. However, this is not well approximated for several of the runs. The cross-correlation coefficient for Run 3, which has the longest sample record is very small and is expected to be the best representative of the true cross-correlation coefficients.

2.6 Normalized One- and Two-Point Spectral Density Functions of Gust Velocities

The sixth part of the analysis for each run in Appendix A is the spectral analyses of the turbulence velocity components. The spectral analysis includes the normalized one- and two-point spectral density functions of the gust velocity components measured with respect to the right and left wing tips of the aircraft. In addition, the auto-spectrum and the one-point cross-spectrum are compared with predictions from theoretical models. The spectra presented in this report are one-sided spectra (see Bendat and Piersol, 1971).

The definition of spectral density functions in terms of Fourier transforms of the correlation functions yields two-sided spectral density functions which are defined for both positive and negative frequencies $(-\infty,\infty)$ and are denoted by $S(f)$. Assume that the auto- and cross-correlation functions $R_x(\vec{\zeta},\tau)$ and $R_{xy}(\vec{\zeta},\tau)$ exist, as defined in Equations 2.5 and 2.13. At $\vec{\zeta}$ = zero, $R_x(\tau)$ and $R_{xy}(\tau)$ represent the one-point auto- and cross-correlation functions, respectively. The two-sided auto- and cross-spectral density functions are given by:

$$S_x(\vec{\zeta},f) = \int_{-\infty}^{\infty} R_x(\vec{\zeta},\tau)e^{-j2\pi f\tau}\, d\tau \tag{2.16}$$

and

$$S_{xy}(\vec{\zeta},f) = \int_{-\infty}^{\infty} R_{xy}(\vec{\zeta},\tau)e^{-j2\pi f\tau}\, d\tau \tag{2.17}$$

respectively. The letter j denotes the imaginary number $j = \sqrt{-1}$ and f is the frequency.

From the symmetry properties of the correlation functions, it follows that:

$$\begin{aligned} &S_x(-f) = S_x(f); \quad \vec{\zeta} = 0 \\ &S_x(\vec{\zeta},-f) = S_x^*(\vec{\zeta},f); \quad \vec{\zeta} \neq 0 \\ &S_{xy}(\vec{\zeta},-f) = S_{xy}^*(\vec{\zeta},f) = S_{yx}(\vec{\zeta},f) \end{aligned} \tag{2.18}$$

where "*" designates the complex conjugate. These equations state that the two-sided one-point auto-spectral density functions are real, non-negative, and even functions of f, whereas the two-sided two-point spectral density functions and the one- and two-point cross-spectral density functions are complex-valued functions of f.

The one-sided spectral density functions, $\Phi_x(\vec{\zeta},f)$ and $\Phi_{xy}(\vec{\zeta},f)$ where f varies only over the frequency range $(0,\infty)$ are defined by:

$$\Phi_x(\vec{\zeta},f) = 2S_x(\vec{\zeta},f) \qquad 0 \leq f < \infty \qquad \text{otherwise zero}$$

$$\Phi_{xy}(\vec{\zeta},f) = 2S_{xy}(\vec{\zeta},f) \qquad 0 \leq f < \infty \qquad \text{otherwise zero} \tag{2.19}$$

In terms of the correlation function, the one-sided one-point auto-spectral density function becomes:

$$\Phi_x(f) = 4\int_0^{\infty} R_x(\tau)\cos 2\pi f\tau \, d\tau \qquad 0 \leq f < \infty \tag{2.20}$$

The one-sided two-point spectral density function is:

$$\Phi_x(\vec{\zeta},f) = 2\int_{-\infty}^{\infty} R_x(\vec{\zeta},\tau)e^{-j2\pi f\tau}\, d\tau$$

$$= C_x(\vec{\zeta},f) - jQ_x(\vec{\zeta},f) \tag{2.21}$$

and the one-sided one- and two-point cross-spectral density function is:

$$\Phi_{xy}(\vec{\zeta},f) = 2\int_{-\infty}^{\infty} R_{xy}(\vec{\zeta},\tau)e^{-j2\pi f\tau}\, d\tau$$

$$= C_{xy}(\vec{\zeta},f) - jQ_{xy}(\vec{\zeta},f) \tag{2.22}$$

where $C_x(\vec{\zeta},f)$ and $C_{xy}(\vec{\zeta},f)$ are called the coincident spectral density functions (co-spectrum) and are even functions of f, and where $Q_x(\vec{\zeta},f)$ and $Q_{xy}(\vec{\zeta},f)$ are called the quadrature spectral density functions (quad-spectrum) and are odd functions of f. An alternative way to describe the complex-valued spectral density functions is with the polar form, $\Phi(\vec{\zeta},f) = |\Phi(\vec{\zeta},f)|e^{\theta(\vec{\zeta},f)}$, defined in terms of an absolute magnitude and a phase angle:

$$\left|\Phi_x(\vec{\zeta},f)\right| = \sqrt{C_x^2(\vec{\zeta},f) + Q_x^2(\vec{\zeta},f)}\,, \qquad \theta_x(\vec{\zeta},f) = \tan^{-1}\frac{Q_x(\vec{\zeta},f)}{C_x(\vec{\zeta},f)} \tag{2.23}$$

and

$$\left|\Phi_{xy}(\vec{\zeta},f)\right| = \sqrt{C_{xy}{}^2(\vec{\zeta},f) + Q_{xy}{}^2(\vec{\zeta},f)}\ , \quad \theta_{xy}(\vec{\zeta},f) = \tan^{-1} \frac{Q_{xy}(\vec{\zeta},f)}{C_{xy}(\vec{\zeta},f)} \qquad (2.24)$$

The magnitude of the complex-valued spectral density functions represents the energy associated with fluctuations at specific frequencies within the turbulent flow. For each run of Flight 31, only the magnitude of the normalized spectral density functions are presented in Appendix A. A segment-averaging technique was used to compute and smooth the raw spectral estimates obtained from the direct Fourier transform of the individual data segments. Data smoothing procedures for two-point spectra are discussed in Section 3.

Figure 2.11 shows a typical plot of the normalized spectral density functions for Run 3 in Flight 31. The upper half of Figure 2.11 shows the normalized one-sided one-point auto-spectral density functions for the three respective turbulence velocity components measured at the right wing tip. The theoretical von Karman spectral density functions are also plotted for comparisons. The comparisons show good agreement between the experimental results and those predicted by the theoretical models. The integral length scales, L_u, L_v, and L_w, which were computed from the longitudinal, lateral, and vertical correlation functions, respectively, were used in the theoretical models. The experimental data is higher than the von Karman predictions at high frequencies. The spectra have been corrected for variance error but not for aliasing nor bias error. These effects are discussed in Section 3.

The lower half of Figure 2.11 shows the normalized one-sided two-point spectral density functions for three respective turbulence velocity components measured at the right and left wing tips of Run 3. Also plotted for comparison are the Houbolt and Sen theoretical models. This two-point spectrum model is derived from the Fourier transform of Equations 2.10 and

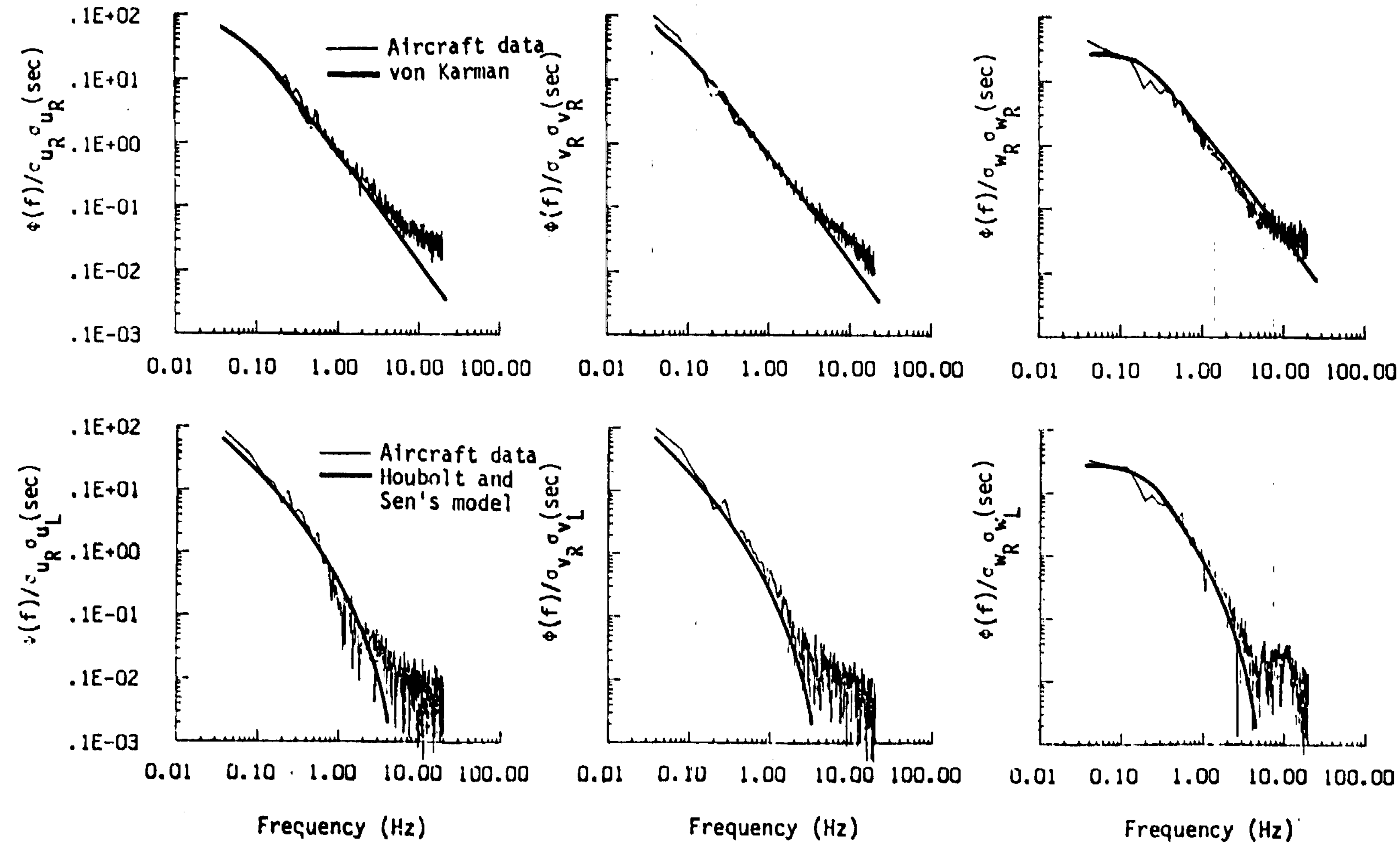

Figure 2.11. Comparison of normalized one- and two-point spectral density functions for gust velocities with theoretical models, Flight 31, Run 3.

2.11 where $B_L(\zeta)$ and $B_T(\zeta)$ are the von Karman longitudinal and transverse correlations (Equation 2.8), respectively. The form of the theoretical spectra is:

$$\Phi_u(s,f) = C\sigma_u^2 \left(\frac{L_u}{\overline{V}}\right)\left[2\,\frac{\left(\frac{s}{L_u}\right)^{5/3}}{Z^{5/6}}\,K_{5/6}(Z) - (s/L_u)^{5/3}\,Z^{1/6}\,K_{1/6}(Z)\right] \qquad (2.25)$$

for the longitudinal component, and

$$\Phi_v(s,f) = C\sigma_v^2\left(\frac{L_v}{\overline{V}}\right)\left[\frac{8}{3}\,\frac{\left(\frac{s}{L_v}\right)^{5/3}}{Z^{5/6}}\,K_{5/6}(Z) - \frac{\left(\frac{s}{L_v}\right)^{11/3}}{a^2Z^{11/6}}\,K_{11/6}(Z) + (s/L_v)^{5/3}Z^{1/6}K_{1/6}(Z)\right] \qquad (2.26)$$

for the lateral component. For the vertical component, the spectrum is given by:

$$\Phi_w(s,f) = C\sigma_w^2\left(\frac{L_w}{\overline{V}}\right)\left[\frac{8}{3}\,\frac{\left(\frac{s}{L_w}\right)^{5/3}}{Z^{5/6}}\,K_{5/6}(Z) - \frac{\left(\frac{s}{L_w}\right)^{11/3}}{a^2Z^{11/6}}\,K_{11/6}(Z)\right] \qquad (2.27)$$

where

$$C = \frac{\sqrt{2\pi}}{\Gamma(1/3)}\left(\frac{2}{a}\right)^{2/3},$$

$$Z = \frac{s}{La}\sqrt{1 + \left(a\,\frac{2\pi fL}{\overline{V}}\right)^2}, \quad a = 1.339$$

where L is any integral length scale of L_u, L_v, and L_w, $\overline{V}$ is the mean airspeed, and K is a modified Bessel function of the second kind.

Equations 2.25, 2.26, and 2.27 are plotted in Figures 2.12, 2.13, and 2.14 for different s/L values, respectively. The termination of the curves in Figure 2.12 for the two-point spectra for the longitudinal velocity component are not arbitrary. At this point, the spectra based on Equation 2.25 takes on negative values. Negative values occur when the last term in the brackets of

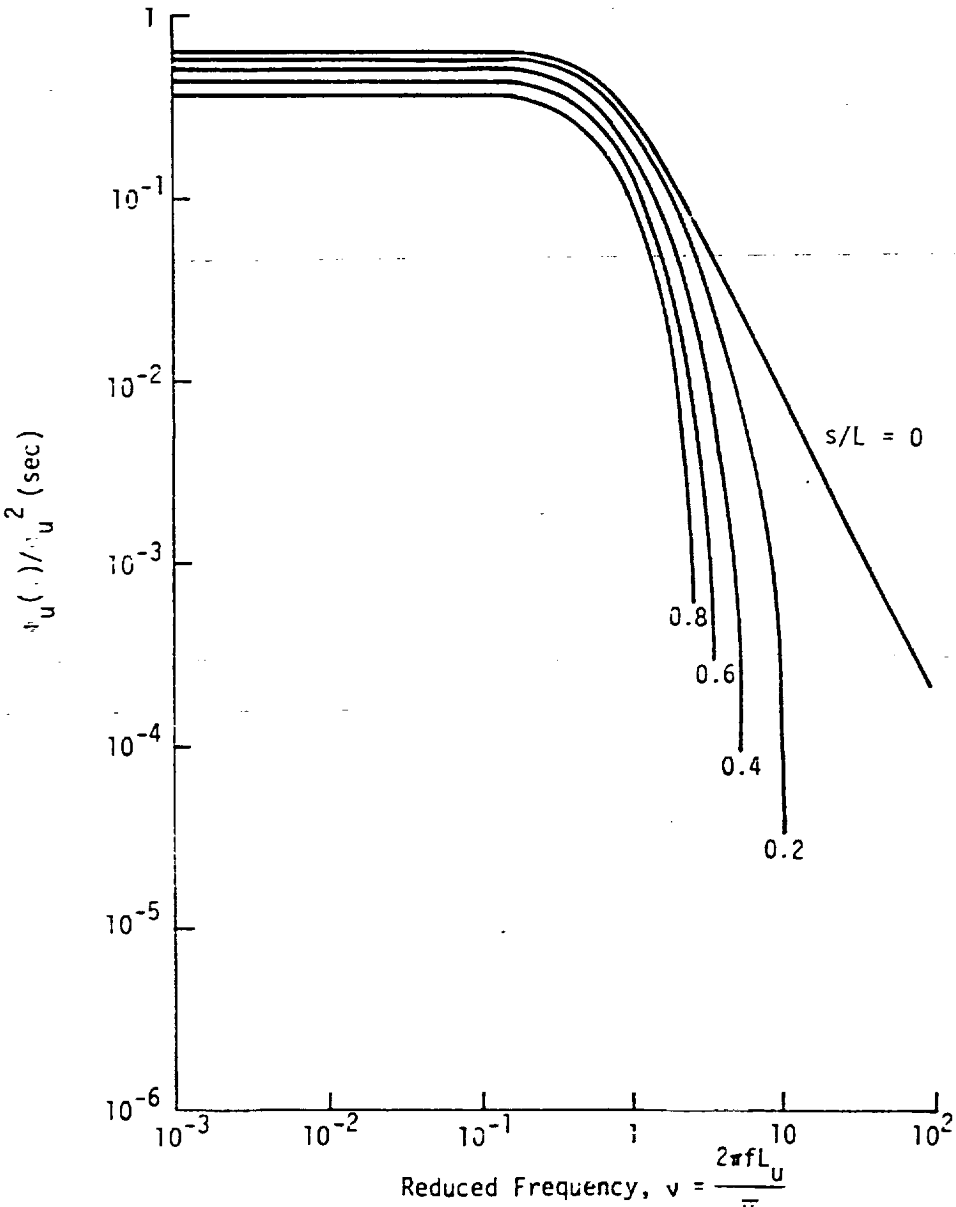

Figure 2.12. Two-point spectra for the longitudinal velocity component.

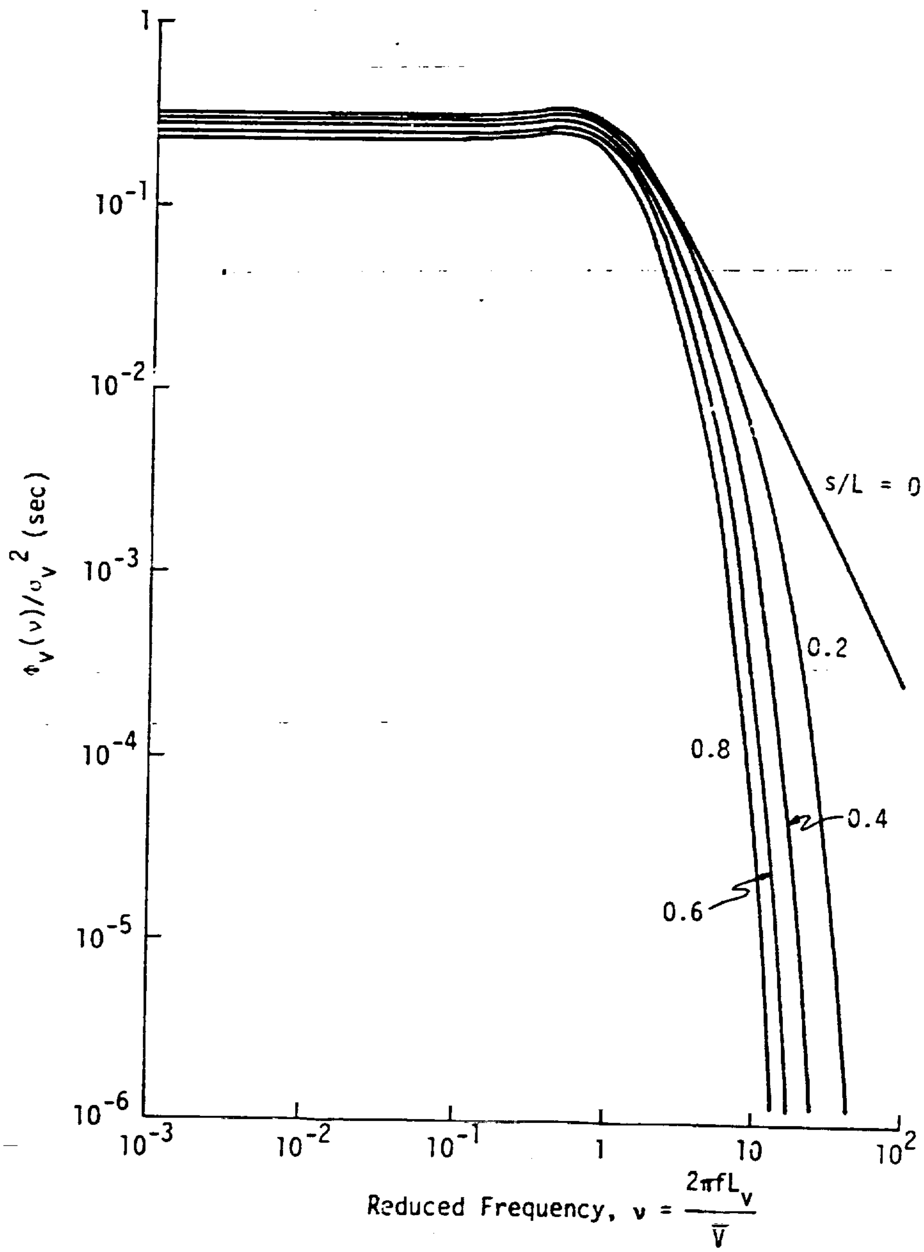

Figure 2.13. Two-point auto-spectra for the lateral velocity component.

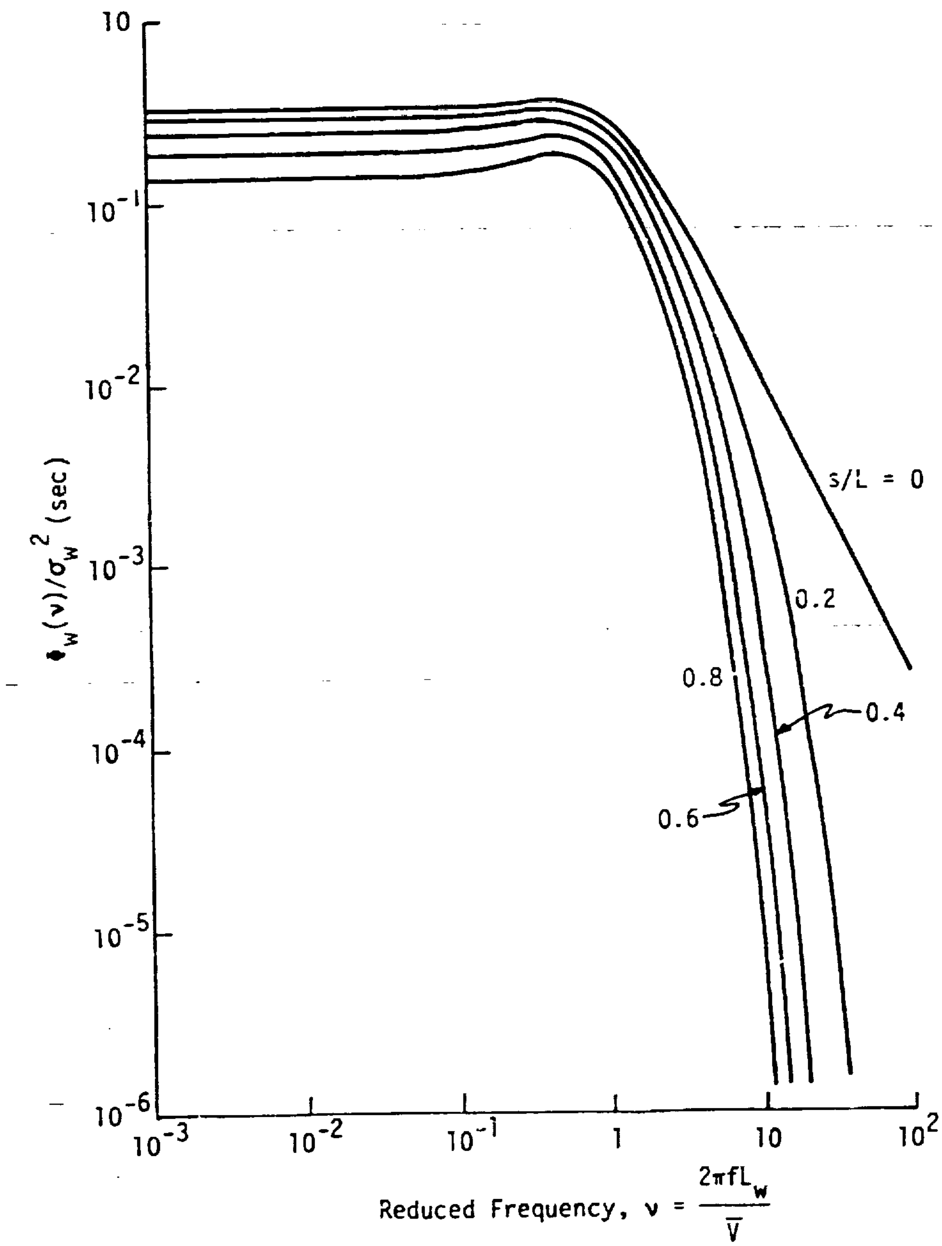

Figure 2.14. Two-point auto-spectra for vertical velocity component.

Equation 2.25 becomes negative. This corresponds to the ratio $2K_{5/6}(Z)/(Z K_{1/6}(Z))$ becoming unity. A plot of this ratio versus wave number for different values of s/L is shown in Figure 2.15. The value of wave number for which the ratio becomes unity is indicated by the solid circles. Inspection of this figure shows that these values of wave number correspond to wavelengths of approximately one half the separation distance s.

The idea of a negative spectrum is initially inconsistent with one's normal thinking. However, after further consideration, it is totally consistent with physical reasoning that the energy contained in fluctuations of wavelengths smaller than one-half the separation distance s would be zero or even negative. It is also very likely that values of the lateral and vertical spectrum shown in Figures 2.13 and 2.14 should be truncated at corresponding values of reduced frequency for which the longitudinal spectrum is truncated. The energy contained in eddies of size smaller than the separation distance predicted by the model for the lateral and vertical spectra is not likely meaningful.

Equations 2.25 through 2.27 were derived analytically in this study. Campbell (1984) obtained results consistent with those shown in Figures 2.12, 2.13, and 2.14 by numerically integrating equations similar to Equations 2.10 and 2.11. Campbell obtained negative values for the longitudinal spectrum, however, he erroneously contributed them to round-off errors in his numerical integration (Campbell, 1986). Further work is needed to fully resolve the meaning of the two-point spectrum at high frequencies for which it becomes negative. However, it is believed that it is consistent with physical principles to simply truncate the two-point spectrum at these negative values.

Returning to a consideration of Figure 2.11, the two-point spectral density functions, calculated from the experimental data, are consistent with

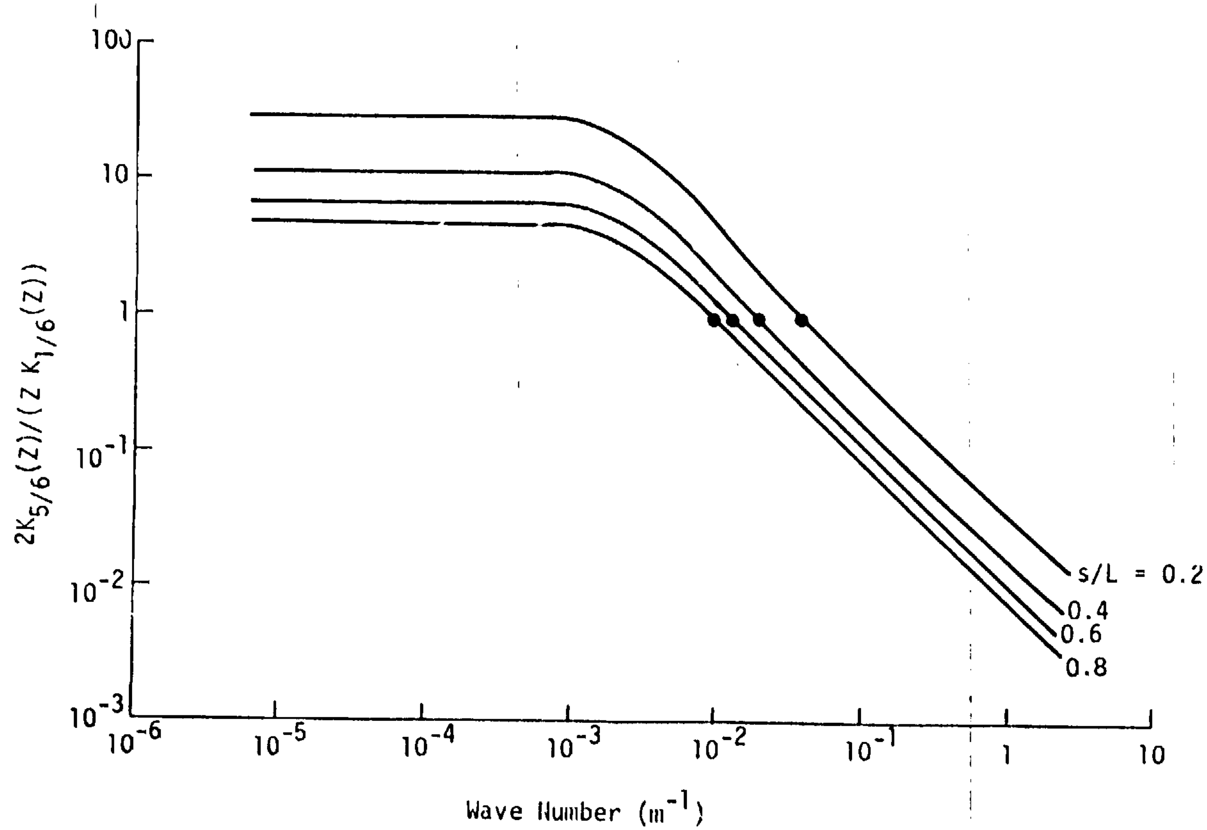

Figure 2.15. Ratio $2K_{5/6}(Z)/(Z\ K_{1/6}(Z))$ versus wave number. The solid circles are the values of wave number consistent with values of reduced frequency for which the longitudinal two-point spectral model (Equation 2.25) becomes negative.

the theoretical model until a mid-range frequency value. Above that frequency, the theoretical model drops off rapidly compared with the experimental data. Since the spectral estimate is calculated from a digitized turbulence time history with a finite record length, the departure of the data from the theory is due to aliasing and truncation error. This will be discussed further in Section 3.

The normalized one- and two-point cross-spectral density functions for three combinations of the three respective turbulence velocity components measured at the right and left wing tips in Run 3 are shown in Figure 2.16. As mentioned earlier, the spectral density functions plotted in this report are magnitude only. The shape of the normalized magnitude of the spectral density functions are observed to be very similar for both the auto-spectral density functions and the cross-spectral density functions. This would not intuitively be expected because the normalized auto-correlation and cross-correlation functions, Figures 2.9 and 2.10 respectively, are very different. However, the non-normalized or absolute value of the auto-spectral density function (i.e., ϕ as contrasted to ϕ/σ^2) is about one order of magnitude larger than the value of the cross-spectral density function. The above observations suggest that the eddies of a given frequency contain cross-component energy proportionate to the distribution of common component energy; however, the cross-components are out of phase and have little correlation. Phase relationships for the spectra are dictated by the magnitude of quadspectra (see Equations 2.23 and 2.24). The quadspectra for the two-point common component spectra are very small; however, for the cross-spectra, both one-point and two-point, the quadspectra are of the same magnitude as the co-spectra. The former result indicates little phase shift between common-components displaced spatially whereas the latter result

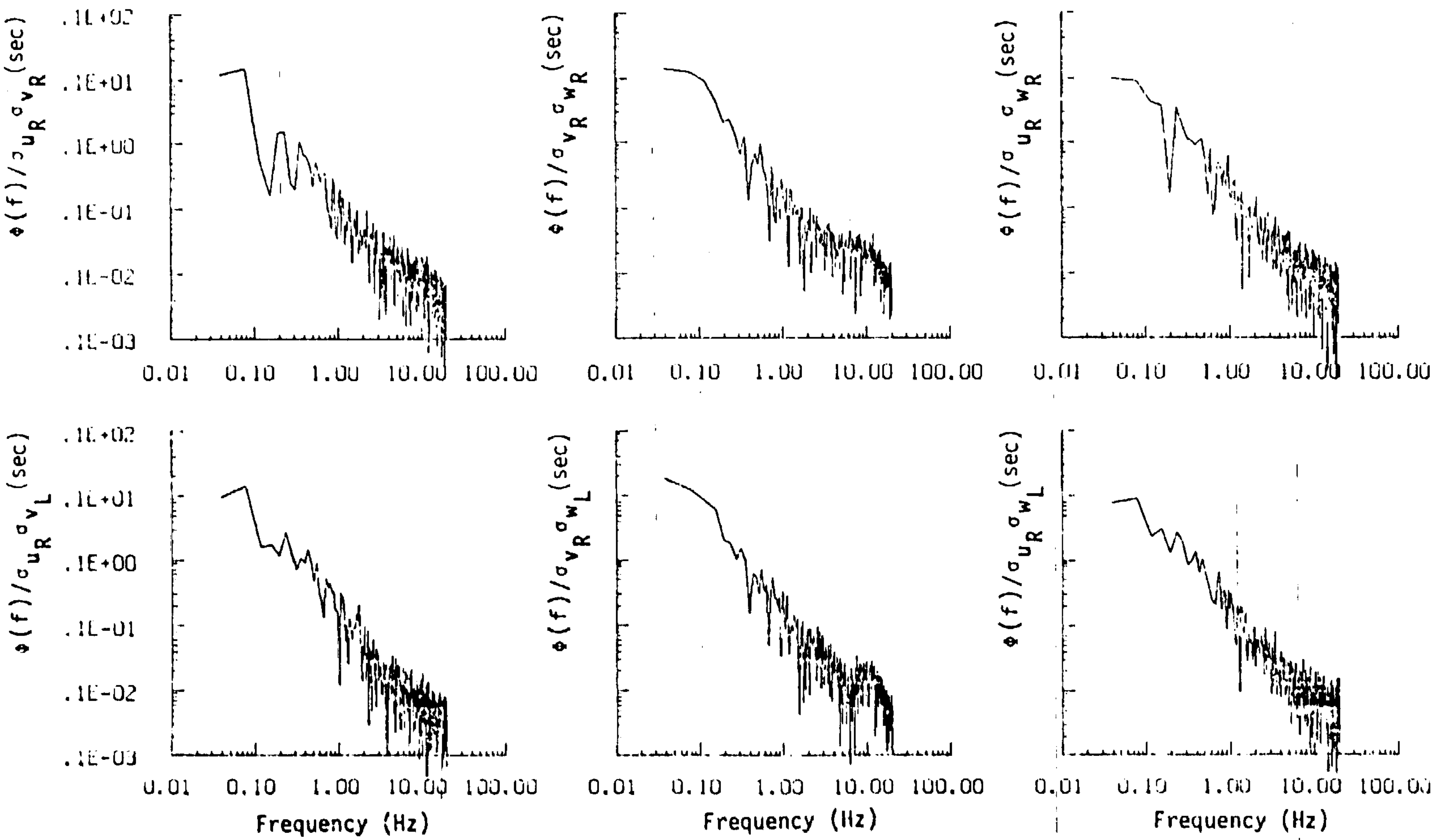

Figure 2.16. Normalized one- and two-point cross-spectral density functions of gust velocities, Flight 31, Run 3.

indicates significant phase shift between uncommon components regardless of spatial displacement.

Similar analyses on the turbulence velocities gathered by the NASA B-57B aircraft (Frost, et al., 1985a) for the two-point common component spectra have shown that the quadrature spectra have values near zero (<0.1) for all frequencies. Emphasizing that the phase shift between the same turbulence components measured at the different probes are negligible. Again, this is probably because the wing span of the airplane is much smaller than a characteristic length scale and significant phase shift would not occur for most of the turbulent eddy sizes involved. Therefore, the shapes of the one-point and two-point correlation functions will be similar to each other. However, as noted for the one- and two-point cross-spectra, the quadrature spectra are comparable with the corresponding coincident spectra, which means the phase angles are significant. Thus, when utilizing turbulence cross-spectral functions to assess the influence of the gust gradient on an aircraft's response, the phase angle of the spectral function is an important parameter.

There is little information on theoretical or empirical models for one-point cross-spectra and virtually no information on two-point cross-spectra in the literature. Reeves, et al. (1974) suggests the following two-sided one-point cross-spectral density function to relate the u and w gust components at low altitudes:

$$S_{xy}(f) = \frac{\sigma_u \sigma_w \sqrt{2}}{r^2 + 1} \left\{ \frac{2r^2}{A^2} \left(\frac{L_w}{V}\right)^2 \left(\frac{L_u}{V}\right) \left[\frac{[1 + 3(\pi A f)^2] - j(2\pi A f)}{[1 + (\pi A f)^2]^2} \right] \right.$$

$$+ \sqrt{\frac{L_u L_w}{\overline{V}^2}} \left[\frac{\left[1 + j\sqrt{3}\left(2\pi \frac{L_w}{\overline{V}}\right) f\right]}{\left\{1 + j\left(2\pi \frac{L_w}{\overline{V}} f\right)\right\} [1 + (2\pi B f)^2]} \right] \Bigg\} \quad (2.28)$$

where r, A, and B are arbitrary parameters satisfying the inequalities:

$r > 0,$

$A > \frac{2L_w}{\overline{V}}, \quad A > \frac{2L_u}{\overline{V}},$

$B > \frac{L_w}{\overline{V}}, \quad B > \frac{L_u}{\overline{V}}$

In this equation, r is the parameter defined in Equation 2.4. The model developed by Reeves, et al. (1974) is basically for low-altitude applications. Therefore, the lowest flight level was chosen for comparison of the experiment with the theory. Inspection of the flight altitude of all runs of Flight 31 shows that Run 12 was flown at the lowest average altitude of approximately 400 ft above the ground. The normalized one-point cross-spectral density function, $\Phi_{uw}(f)/\sigma_u\sigma_w$, for the turbulence velocity components u and w at the right wing tip in Run 12 was calculated from Equation 2.28 and the results are shown in Figure 2.17.

The parameters A and B for Run 12 are chosen to best fit the experimental data. The value of r is taken as 1.25 the average value for u and w tabulated in Table 2.7. Figure 2.17 shows good agreement between the experimental results (symbol "x") and the results predicted by the Reeves model (solid line) except in the high-frequency regions. As discussed earlier for the one-point auto-spectrum, the higher experimental values in the high-frequency region are probably due to aliasing and truncation error.

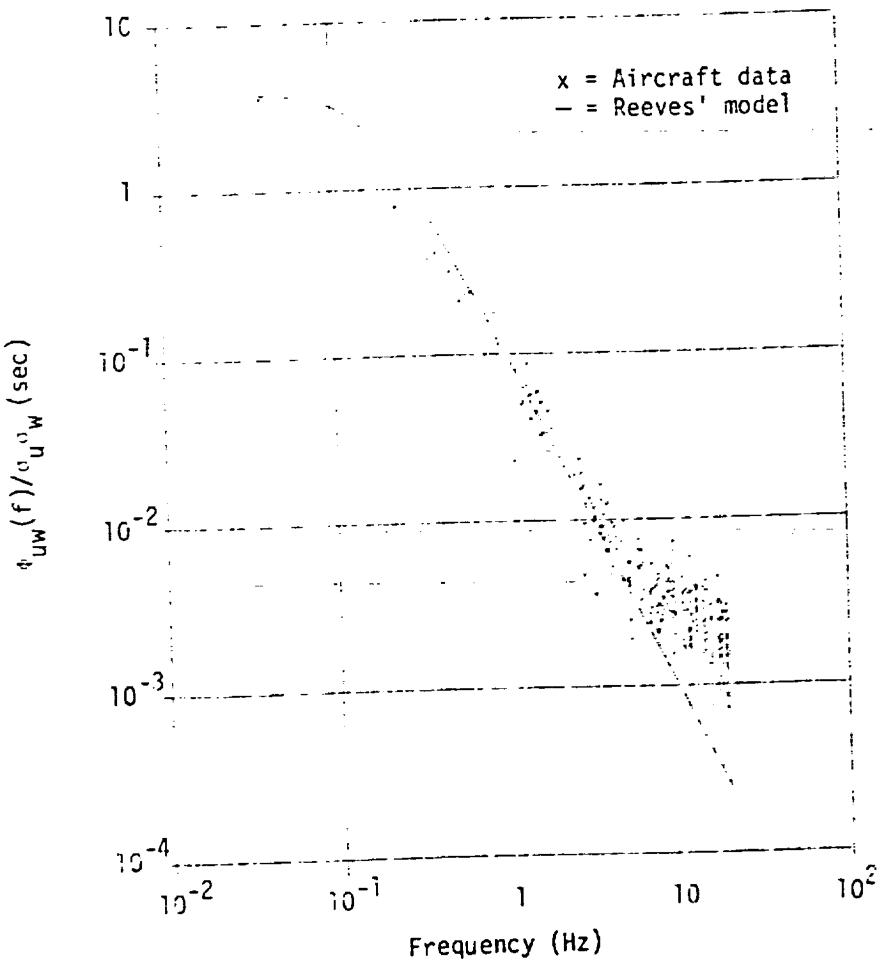

Figure 2.17. Comparison of cross-spectral density function for u and w components with theoretical model, Flight 31, Run 12 ($A = 1.25\ L_u/\overline{V}$; $B = L_u/\overline{V}$; and $r = 1.25$).

2.7 List of All Parameters Measured and the Range of Their Extreme and Average Values

Finally in Appendix A, a table is presented for each run which lists all parameters recorded during a flight: the units, the maximum and minimum values, the mean value, the root mean square value, and the number of data points for each parameter. These parameters are stored on magnetic tapes in the following order (the symbols used to represent the variable are appended in brackets):

1. Mountain Daylight Time (MDT) in seconds for each record [t].
2. Roll rate measured by body-mounted roll-rate transducer (positive with right wing going down), rad/s [$d\phi/dt$].
3. Normal acceleration at c.g. (positive up) g units [a_n].
4. Pitch rate measured by body-mounted pitch-rate transducer (positive with nose going up), rad/s [$d\theta/dt$].
5. Pitch attitude measured in the vertical plane (positive with nose up), rad [θ].
6. Roll attitude of airplane with reference to horizontal (positive with right wing down), rad [ϕ].
7. Airplane heading measured in a horizontal plane clockwise from true north (always positive), 0 to 360° range [ψ_1].
8. Sensitive airplane heading obtained from ψ_1 with arbitrary zero at the instant the data switch is turned on (positive with nose right) ±15° range [ψ_1].
9. Airplane heading measured in a horizontal plane clockwise from true north (always positive) 240° to 600° range [ψ_2].
10. Sensitive airplane heading obtained from ψ_2, with arbitrary zero at the instant the data switch is turned on (positive with nose right) ±15° range [$\Delta\psi_2$].
11. Normal acceleration at the left wing tip (positive up), g units [a_{nL}].
12. Normal acceleration at the right wing tip (positive up), g units [a_{nR}].

13. Longitudinal acceleration at the c.g. (positive forward), g units [a_x].

14. Lateral acceleration at the c.g. (positive toward right wing), g units [a_y].

15. Angle of attack measured at the airplane nose boom (positive with flow vane trailing edge up), rad [α_C].

16. Angle of sideslip measured at the airplane nose boom (positive with flow vane trailing edge toward right as viewed from the aircraft), rad [β_C].

17. Temperature of the INS pallet, °F [T_I].

18. Temperature of the instrument pallet, °F [T_p].

19. Vertical acceleration of the INS stable element (positive up), g units [a_z].

20. Angle of attack measured at the right wing tip boom (positive with flow vane trailing edge up), rad [α_R].

21. Angle of sideslip measured at right wing tip boom (positive with flow vane trailing edge toward right as viewed from the aircraft), rad [β_R].

22. Angle of attack measured at the left wing tip boom (positive with flow vane trailing edge up), rad [α_L].

23. Angle of sideslip measured at the left wing tip boom (positive with flow vane trailing edge toward right as viewed from the aircraft), rad [β_L].

24. Yaw rate measured by a body-mounted yaw-rate transducer (positive with nose going right), rad/s [$d\psi/dt$].

25. Total temperature, °C [T_o].

26. Impact pressure measured at the left wing tip boom, P_a [q_{CL}].

27. Impact pressure measured at the airplane nose boom, P_a [q_{CC}].

28. Impact pressure measured at the right wing tip boom, P_a [q_{CR}].

29. Free-stream static pressure measured at the airplane nose boom, KP_a [p].

30. Temperature of IRT, °C [T_{IRT}].

31. Wet-bulb temperature, °C [T_{wb}].

32. Turbulent fluctuation of impact pressure at the left wing tip boom, Pa [q_{ctL}].

33. Turbulent fluctuation of impact pressure at the airplane nose boom, Pa [q_{ctC}].

34. Turbulent fluctuation of impact pressure at the right wing tip boom, Pa [q_{ctR}].

35. Deflection angle of the right aileron, deg [δ_{aR}].

36. Deflection angle of the left aileron, deg [δ_{aL}].

37. Deflection angle of the elevator, deg [δ_e].

38. Deflection angle of the stabilizer, deg [δ_s].

39. Deflection angle of the rudder, deg [δ_r].

40. Thrust ratio of the right engine to the maximum thrust, percent [T_R].

41. Thrust ratio of the left engine to the maximum thrust, percent [T_L].

42. Deflection position of the flap system [δ_f].

43. Deflection position of the speed brake system [δ_{sb}].

44. Distance to go from the present position of the aircraft to the next waypoint set on the INS (always positive), m [$\Delta \ell$].

45. Bearing to destination, i.e., bearing from the aircraft's present position to the next waypoint set on the INS, measured in a horizontal plane clockwise from true north (always positive), deg [γ_B].

46. Longitude of aircraft as measured by INS, deg [LONG].

47. Latitude of aircraft as measured by INS, deg [LAT].

48. Track angle of airplane measured in a horizontal plane clockwise from true north (always positive), deg [γ_T].

49. Airplane heading, measured in a horizontal plane clockwise from true north, rad [ψ].

50. East-west component of the airplane inertial velocity as measured by INS (positive toward east), m/s [V_E].

51. North-south component of the airplane inertial velocity as measured by the INS (positive toward north), m/s [V_N].

52. Pressure-derived altitude based on standard atmosphere tables, km [h_p].

53. Computed free-stream temperature, °C [T_C].

54. Computed east-west wind component (positive toward east), knots [W_E].

55. Computed north-south wind component (positive toward north), knots [W_N].

56. Computed magnitude of wind vector, knots [W].

57-60. Computed direction of wind vector, deg [ψ_W].

61. True airspeed computed from impact pressure measurement at right wind tip boom, m/s [V_R].

62. True airspeed computed from impact pressure measurement at the airplane nose boom, m/s [V_C].

63. True airspeed computed from the impact pressure measurement at left wing tip boom, m/s [V_L].

64. Incremental pressure-derived altitude with reference to value at beginning of run (positive when altitude increases), m [Δh_p].

65. Computed corrected inertial displacement, m [Δh_C].

66. Computed longitudinal component of gust velocity at right wing tip boom (positive in direction of flight path), m/s [u_R].

67. Computed longitudinal component of gust velocity at airplane centerline nose boom (positive in direction of flight path), m/s [u_C].

68. Computed longitudinal component of gust velocity at left wing tip boom (positive in direction of flight path), m/s [u_L].

69. Computed lateral component of gust velocity at right wing tip (positive toward right), m/s [v_R].

70. Computed lateral component of gust velocity at airplane centerline nose boom (positive toward right), m/s [v_C].

71. Computed lateral component of gust velocity at left wing tip boom (positive toward right), m/s [v_L].

72. Computed vertical component of gust velocity at right wing tip boom (positive up), m/s [w_R].

73. Computed vertical component of gust velocity at airplane centerline nose boom (positive up), m/s [w_C].

74. Computed vertical component of gust velocity at left wing tip boom (positive up), m/s [w_L].

3.0 SPECTRAL ESTIMATION

Spectral analysis of atmospheric turbulence generally involves the Fourier transform of a digitized finite-duration velocity fluctuation time history. The digitization process and the truncation associated with the finite time increment of the time history result in both aliasing and bias errors; while the random nature of turbulence results in variance errors. Although these errors cannot be totally eliminated, appropriate filtering will reduce their magnitudes. It was found that the magnitudes of the respective errors and the effects of the filtering process are quite different for two-point spectra than they are for one-point spectra. Because of the significance of the difference, a detailed discussion of the effect of aliasing, bias, and variance errors on the one-point and two-point spectra is given in this section. The magnitude of the errors are also estimated for typical data such as that reported in Appendix A.

To illustrate the magnitude and nature of the errors, an analytical von Karman one-point correlation and the Houbolt and Sen (1972) two-point correlation are used to investigate aliasing and the bias error (also called truncation error or spectral leakage) associated with discrete Fourier transforms. Spectrum for each of these correlations has been computed analytically. The analytical spectra is then compared graphically with the spectrum estimate calculated from the discrete Fourier transform (DFT) of the digitized analytical correlation functions. This comparison, based on analytical models, illustrates the aliasing and bias errors occurring simply from the digitization and truncation process.

The DFT of the actual turbulence data is then computed. The resulting spectra which are now based on a random signal are then compared with the spectra calculated analytically from the digitized continuous correlations functions. It is shown that the spectra calculated from the random data contain not only aliasing and bias errors but also variance errors. The use of segment- averaging (Bendat and Piersol, 1971) to reduce the variance error of the spectra computed from the random turbulence data time histories is then discussed.

3.1 Graphical Illustration of the Discrete Fourier Transform

The generation of errors associated with the Fourier transform of a digitized function can be conceptually explained by a graphical illustration. Following closely the development of Brigham (1974), consider some function $h(\tau)$ and its Fourier transform $H(f)$ illustrated in Figure 3.1a. To determine the Fourier transform of $h(\tau)$ by means of digital analysis techniques, it is necessary to digitize $h(\tau)$ at discrete increments in time.

Digitizing $h(\tau)$ in increments of $\Delta\tau$ is equivalent to multiplying it by the comb function shown in Figure 3.1b. The comb function, $\Delta_0(\tau)$, has the Fourier transform, $\Delta_0(f)$, shown in the corresponding figure. The Fourier transform of the product $h(\tau)\Delta_0(\tau)$ is given by the convolution integral of $H(f)$ and $\Delta_0(f)$ designated by $H(f)*\Delta_0(f)$, i.e.

$$H(f)*\Delta_0(f) = \int_{-\infty}^{\infty} H(f')\Delta_0(f - f')df' \qquad (3.1)$$

Figure 3.1c illustrates $H(f)*\Delta_0(f)$.

Note that the transform $H(f)*\Delta_0(f)$ differs from the analytical transform by the appearance of images of the analytical spectrum $H(f)$ displaced along the frequency axis at a spacing of $\pm|1/\Delta\tau|$. Each of the images contribute some energy to the true spectrum centered about $f = 0$. This effect is called aliasing which occurs due to working with a digitized function.

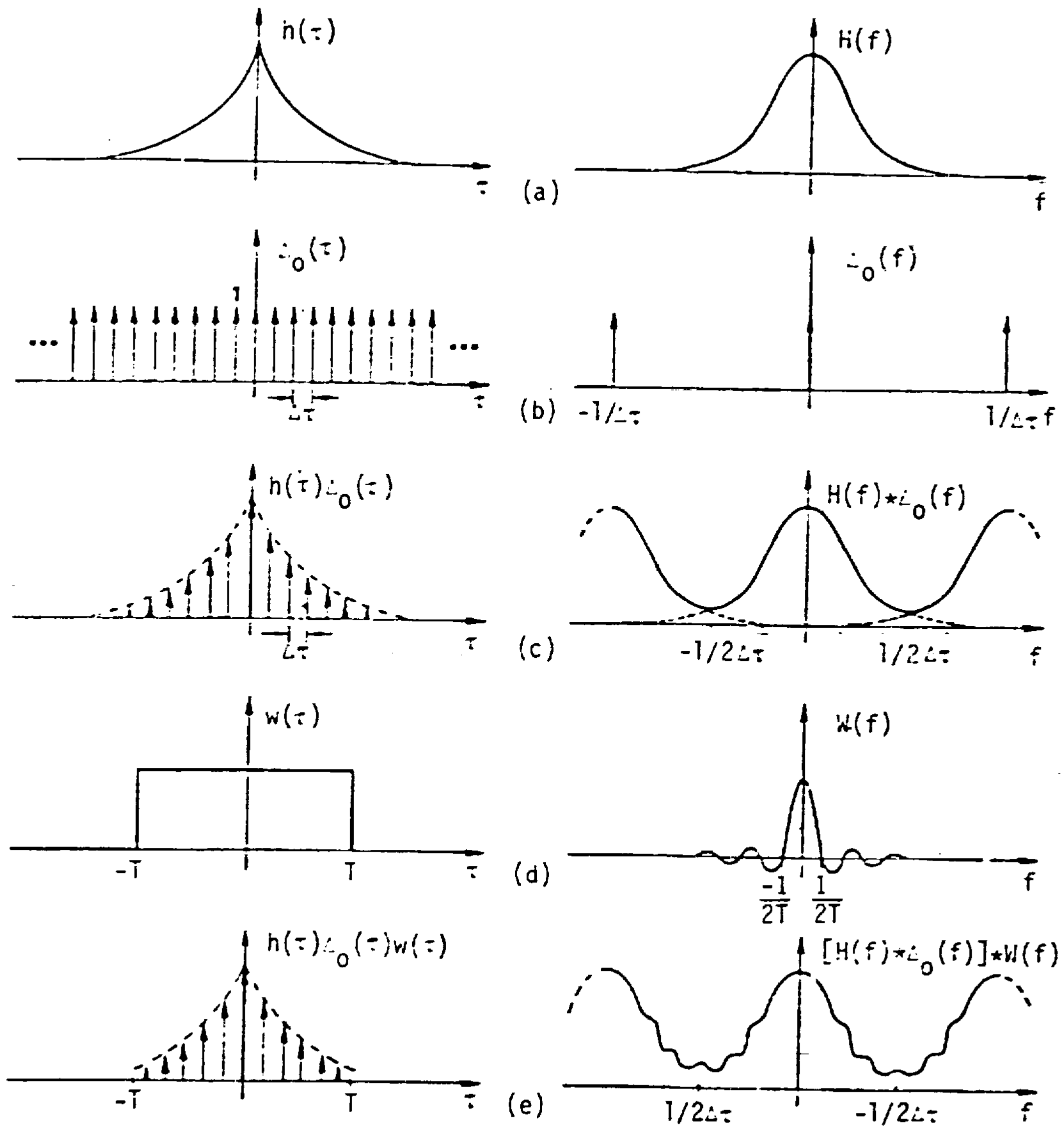

Figure 3.1. Graphical development of the discrete Fourier transform (Brigham, 1974).

The Fourier transform pair in Figure 3.1c is still not suitable for machine computation, however, because an infinity of digitized values of $h(\tau)$ is considered; it is necessary to truncate the sampled function $h(\tau)$ so that only a finite number of points, say N, are considered. The rectangular or truncation function, $w(\tau)$, and its Fourier transform, $W(f)$, are illustrated in Figure 3.1d. The product of the infinite sequence of impulse functions representing $h(\tau)$ and the truncation function (i.e., $h(\tau)\Delta_0(\tau)w(\tau)$) yields the finite length time function illustrated in Figure 3.1e. The Fourier transform of the truncated, digitized function is given by the convolution of $H(f)*\Delta_0(f)$ with $W(f)$ or $[H(f)*\Delta_0(f)]*W(f)$.

As illustrated in Figure 3.1e, the frequency transform now has a ripple to it; this effect has been accentuated in the illustration for emphasis. The form of $W(f)$ for the rectangular function of unit magnitude is:

$$W(f) = 2T \sin(2\pi Tf)/2\pi Tf \tag{3.2}$$

Hence, if the truncation (rectangular) function is increased in length, then the $\sin(f)/f$ function will approach an impulse; the more closely the $\sin(f)/f$ function approximates an impulse, the less ripple or error due to truncation will be introduced by the convolution. Therefore, it is desirable to choose the length of the truncation function as long as possible.

The effect of digitization and truncation on typical turbulence correlation/spectrum Fourier transform pairs is discussed in the following sections. The discussion is presented in terms of an example for the one- and two-point correlations and spectra, respectively. For the one-point correlation, assume the function $h(t)$ in Figure 3.1 represents the theoretical von Karman transverse correlation function given by Equation 2.8 and repeated here in lag time domain ($\zeta = \overline{V}\tau$) for convenience:

$$R_w(\tau) = \sigma_w^2 \frac{2^{2/3}}{\Gamma\left(\frac{1}{3}\right)} \left(\frac{\overline{V}\tau}{aL_w}\right)^{1/3} \left[K_{1/3}\left(\frac{\overline{V}\tau}{aL_w}\right) - \frac{1}{2}\left(\frac{\overline{V}\tau}{aL_w}\right) K_{2/3}\left(\frac{\overline{V}\tau}{aL_w}\right)\right] , \quad a = 1.339 \qquad (3.3)$$

and the function H(f) corresponds to the spectrum given by an analytical Fourier transform of Equation 3.3, i.e.:

$$\Phi_w(f) = \sigma_w^2 \frac{2L_w}{\overline{V}} \frac{1 + \frac{8}{3}\left(\frac{2\pi aL_w}{\overline{V}}\right)^2 f^2}{\left[1 + \left(\frac{2\pi aL_w}{\overline{V}}\right)^2 f^2\right]^{11/6}} \qquad (3.4)$$

For the theoretical two-point correlation, the Houbolt and Sen (1972) model is used, i.e.:

$$R_w(s,\zeta) = \sigma_w^2 \frac{2^{2/3}}{\Gamma\left(\frac{1}{3}\right)} \left(\frac{\zeta}{aL_w}\right)^{1/3} \left[K_{1/3}\left(\frac{\zeta}{aL_w}\right) - \frac{1}{2}\left(\frac{\zeta}{aL_w}\right)\right] , \quad a = 1.339 \qquad (3.5)$$

where

$$\zeta = \sqrt{s^2 + (\overline{V}\tau)^2}$$

and the theoretical spectrum is given by:

$$\Phi_w(f) = \sqrt{2\pi}\, \sigma_w^2 \frac{2^{2/3}}{\Gamma\left(\frac{1}{3}\right)} \frac{L_w}{\overline{V}} \frac{1}{a^{8/3}} \left[\frac{8}{3} a^2 \frac{\left(\frac{s}{L_w}\right)^{5/3}}{Z^{5/6}} K_{5/6}(Z) - \frac{\left(\frac{s}{L_w}\right)^{11/3}}{Z^{11/6}} K_{11/6}(Z)\right] \qquad (3.6)$$

$$Z = \frac{s}{L_w a} \sqrt{1 + \left(a \frac{2\pi f L_w}{\sigma}\right)^2}$$

3.2 Aliasing

Consider first the problem of aliasing. Aliasing can be described by considering a continuous record which is sampled such that the time interval between sample values is $\Delta\tau$ seconds. The sampling rate is then $1/\Delta\tau$ samples per second. However, at least two samples per cycle are required to define a frequency component in the original data as illustrated by the sketch in

Figure 3.2. Hence, the highest frequency which can be defined by sampling at a rate of $1/\Delta\tau$ samples per second is $1/2\Delta\tau$ Hz. Frequencies in the original data above $1/2\Delta\tau$ Hz will be folded back into the frequency range from 0 to $1/2\Delta\tau$ Hz, and be confused with data in this lower range, as illustrated in Figure 3.1. The cutoff frequency $f_c = 1/2\Delta\tau$ is called the Nyquist frequency or folding frequency. For any frequency f in the range $0 \leq f \leq f_c$, the higher frequencies which are aliased with f are given by (see Bendat and Piersol, 1971):

$$(2f_c \pm f),\ (4f_c \pm f),\ \ldots,\ (2nf_c \pm f),\ \ldots \qquad (3.7)$$

To demonstrate the magnitude of aliasing, we have digitized Equation 3.3 representing $h(\tau)$ in Figure 3.1 for values of L = 300 m and $\overline{V}$ = 100 m/s and we have used a discrete Fourier transform (DFT) to compute H(f). The resulting value, $H(f)_{DFT}$, is plotted along with the analytical H(f) in Figure 3.3. The analytical function can be computed to as high a value of frequency as desired by integrating Equation 3.3 mathematically to give Equation 3.4 (i.e., mathematically f can approach infinity). However, to employ a DFT method to compute the spectra from Equation 3.3 a finite record length, T, must be used. Spectra computed for two different values of T = 12.8 sec and T = 51.2 sec as contrasted to infinity for the theoretical model are shown in Figure 3.3. Considerable departure of the theoretical spectrum curve from the DFT determined spectrum curve is observed. The reason for this departure is associated with both aliasing and truncation errors as discussed in the following.

Since the theoretical value of H(f) is known, the turbulence energy aliased into a given frequency f can be computed by inputting the values from Equation 3.7 into Equation 3.4, i.e.:

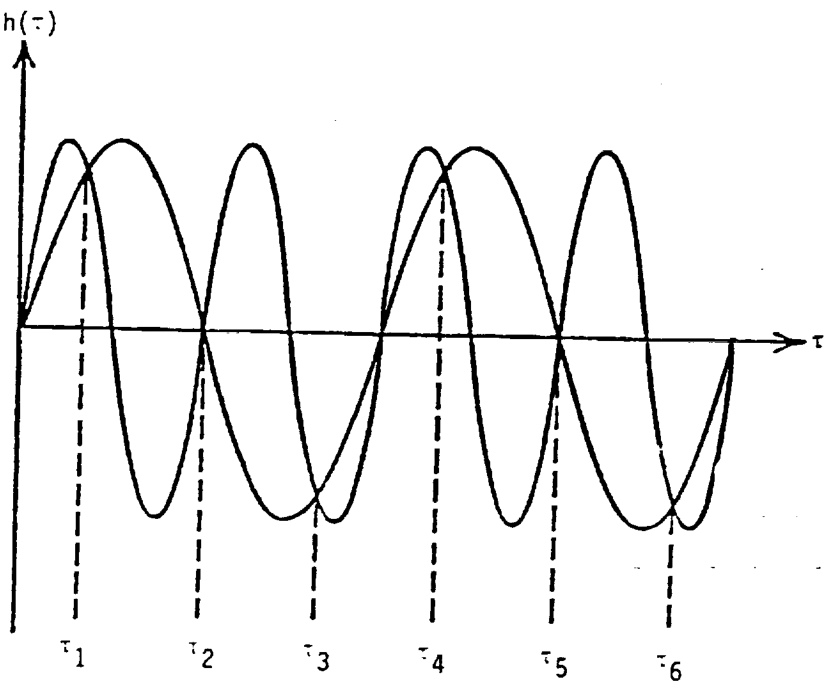

Figure 3.2. Illustration of aliasing problem.

$$\text{Aliased energy at frequency } f = \sum_{n=0}^{\infty} H(2nf_c \pm f) \qquad (3.8)$$

Table 3.1 illustrates the magnitude of aliasing for the case f = 15 Hz and 20 Hz, respectively. The values in the table are obtained by summing Equation 3.8 for $0 \leq n \leq 20$ with H(f) given by $\Phi_w(f)$ from Equation 3.4.

TABLE 3.1. Comparison of Aliased Spectrum Values with True Analytical Values at f = 15 Hz and 20 Hz (see Figure 3.4).

	f = 15 Hz	f = 20 Hz
True theoretical value	0.8075×10^{-3}	0.5000×10^{-3}
Aliased value	1.579×10^{-3}	1.424×10^{-3}

Figure 3.4 is an enlargement of Figure 3.3 for the 1 to 100 Hz frequency range. (The variance error bars shown on the figure are described later.) The aliased values for the 15 and 20 Hz frequencies in Table 3.1 are plotted on the figure. The plot clearly shows that the major portion of the difference between the theoretical curve and the DFT curves is due to aliasing. This is evident from the fact that when the aliased energy is added to the theoretical curve, the results almost coincided with the $H(f)_{DFT}$ functions. There remains a small difference which is attributed to bias error. Note that this small difference decreases with increasing record length.

Table 3.2 shows a similar aliasing calculation for the two-point spectra (Equation 3.6). The energy aliased into the 15 Hz frequency is almost zero and in the 20 Hz frequency is only doubled.

Figure 3.5 is a comparison of the two-point spectrum computed from a DFT of Equation 3.5 digitized at $\Delta\tau = 0.025$ sec with the analytical value from Equation 3.6. (The solid circles and variance bars are described later.)

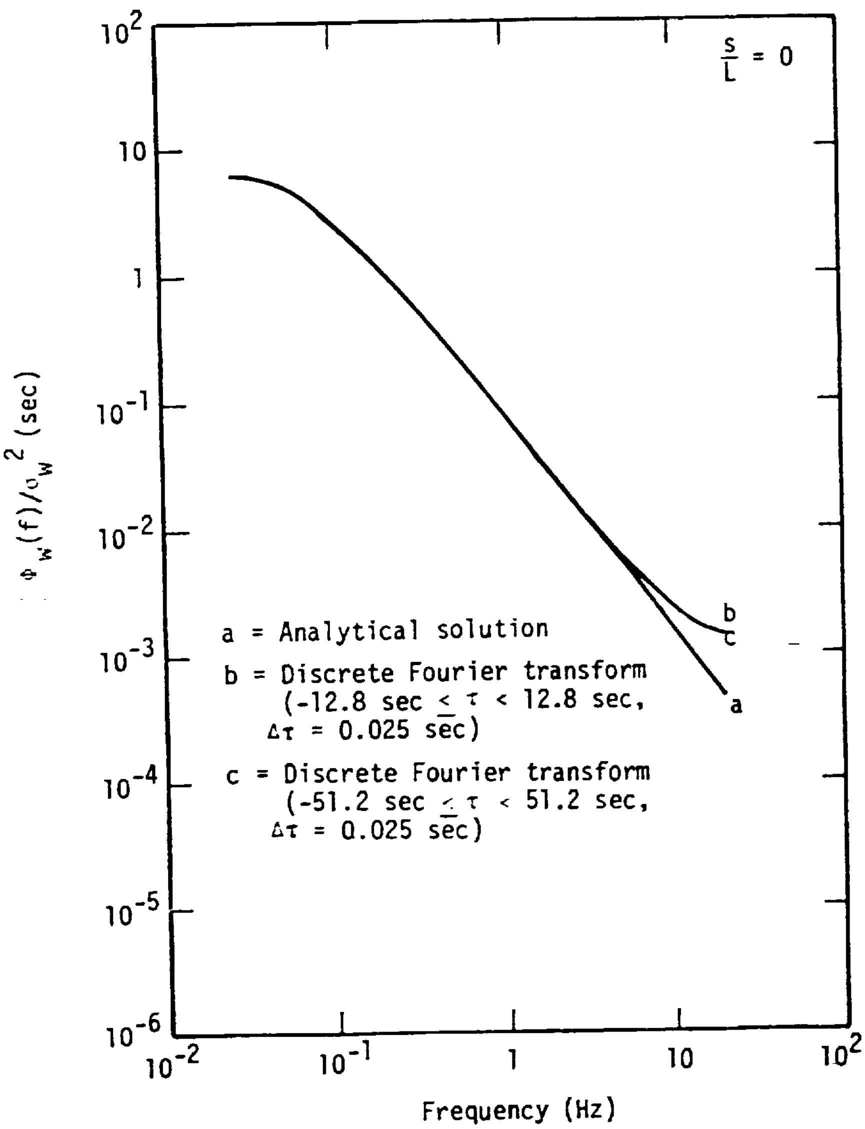

Figure 3.3. The theoretical von Karman one-point auto spectrum compared with the DFT computed values (triangular spectrum window).

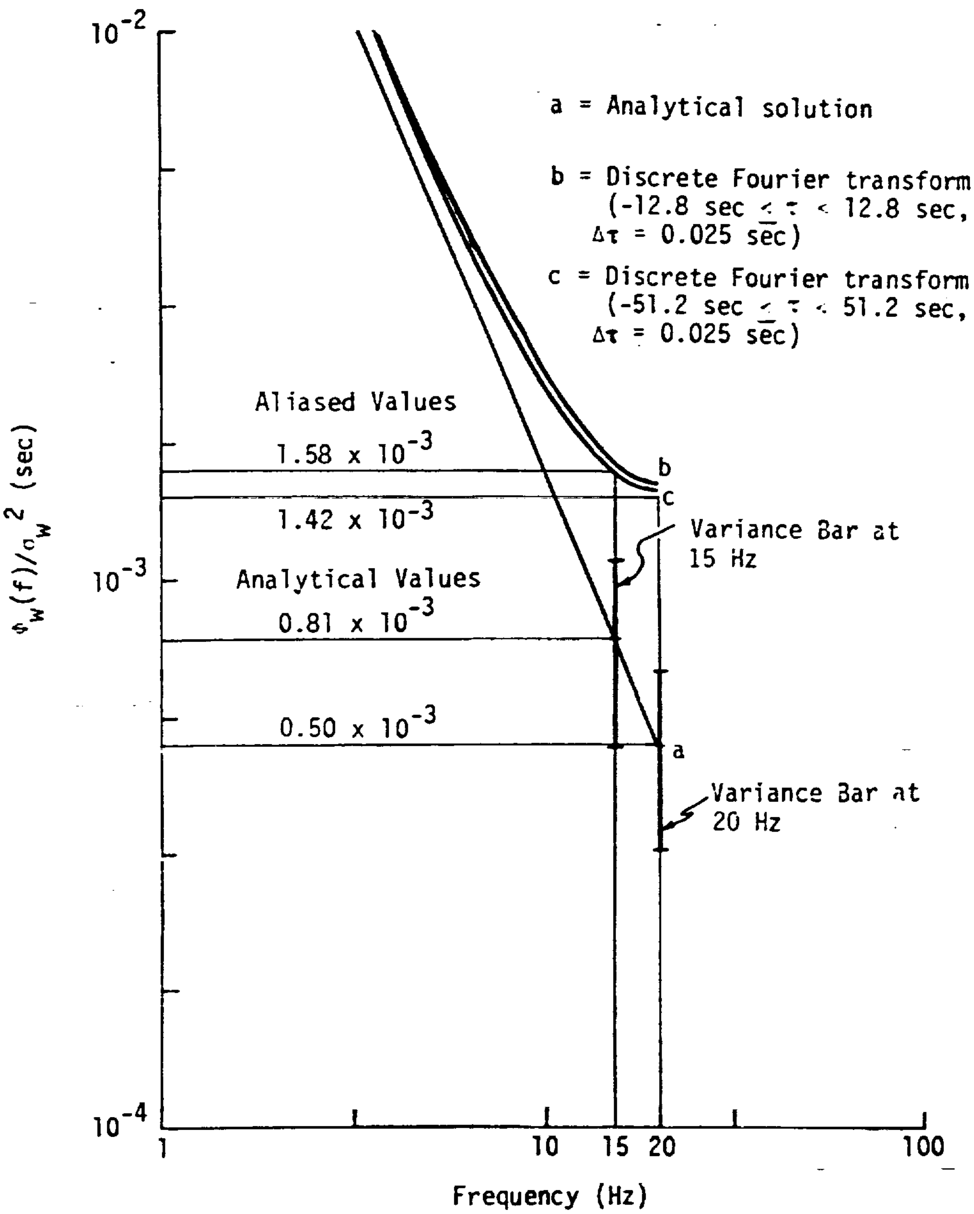

Figure 3.4. Comparison of aliased one-point auto-spectrum with true analytical values.

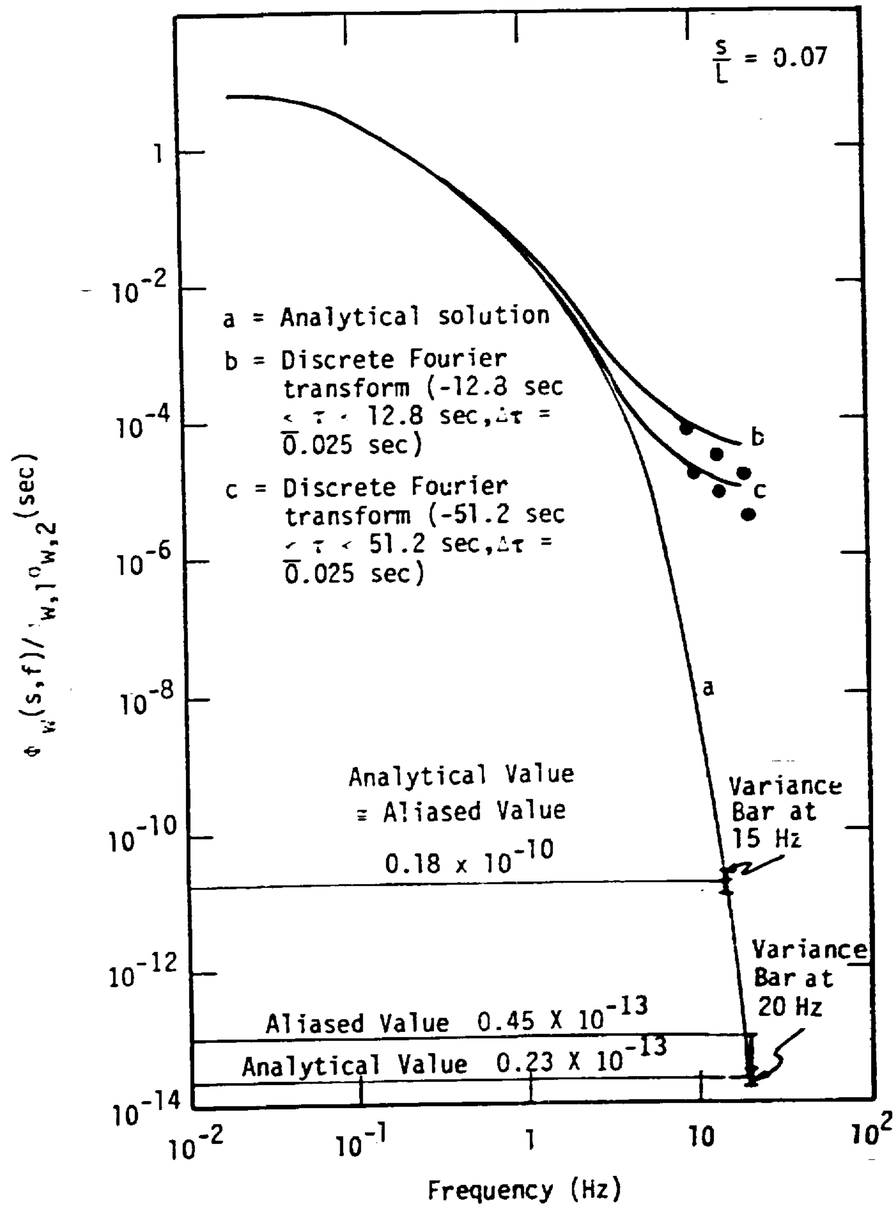

Figure 3.5. Comparison of theoretical two-point spectrum (Equation 3.6) with the DFT of the correlation function (Equation 3.5).

Significant difference between the analytical H(f) and the DFT, $H(f)_{DFT}$, is observed. The difference in this case, however, is not due to aliasing as is evident from the aliased values plotted on the figure. The significant departure of the DFT value from the analytical value is due to bias error.

TABLE 3.2. Comparison of Aliased Values for Two-Point Spectra with True Analytical Value.

	f = 15 Hz	f = 20 Hz
True analytical value	0.1764×10^{-10}	0.2239×10^{-13}
Aliased value	0.1764×10^{-10}	0.4478×10^{-13}

3.3 Truncation Error

Bias error occurs due to truncation of the time history and appears as ripples in the DFT curve as illustrated in Figure 3.1e. Bias error and truncation error are in effect the same thing and are referred to interchangeably throughout the remainder of this Chapter. Bias error is influenced by the use of the lag window $w(\tau)$. In Figure 3.1d the function $w(\tau)$ is a rectangular lag window.

The spectra shown in Figures 3.3 and 3.5 have been corrected for bias errors with a triangular or Bartlett lag window, $w(\tau)$, defined as:

$$w(\tau) = 1 - \frac{|\tau|}{2T}, \quad |\tau| < 2T \tag{3.9}$$

The Fourier transform of $w(\tau)$ is called the spectral window, $W(\omega)$. The Bartlett spectral window is given by:

$$W(\omega) = \frac{\sin^2 T\omega}{\pi T\omega^2} \tag{3.10}$$

Bias or truncation errors occur when attempting to compute the power spectrum $S(\omega)$ of a real, stationary process, $x(t)$, from a single realization of $x(t)$

available only over a finite interval (-T,T). To demonstrate the generation of bias error when computing turbulence spectra, consider first the calculation of the spectrum from the Fourier transform of the $R(\tau)$ function. This development closely follows the excellent presentation in Papoulis, 1977.

We will use as an estimate of $R(\tau)$ the time average:

$$\tilde{R}(\tau) = \frac{1}{2T} \int_{-T+|\tau|/2}^{T-|\tau|/2} x\left[t + \frac{\tau}{2}\right] x\left[t - \frac{\tau}{2}\right] dt \tag{3.11}$$

where the function is defined as above for $|\tau| < 2T$; and, for $|\tau| > 2T$, it is assumed to be zero. The estimate of the spectrum, $S(\omega)$, is then given by the transform of $\tilde{R}(\tau)$:

$$\tilde{S}(\omega) = \int_{-2T}^{2T} \tilde{R}(\tau) e^{-j\omega\tau} \, d\tau \tag{3.12}$$

It follows from Equation 3.11 that the expected value of $\tilde{R}(\tau)$ in terms of the true $R(\tau)$ is:

$$E\{\tilde{R}(\tau)\} = R(\tau)\left[1 - \frac{|\tau|}{2T}\right] p_{2T}(\tau) = R(\tau) q_{2T}(\tau) \tag{3.13}$$

where $p_{2T}(\tau)$ and $q_{2T}(\tau)$ are a pulse and a triangle lag window, respectively (see Figure 3.6). Thus the estimated autocorrelation function is biased, because its mean is not the true autocorrelation function at lag τ. We can say, however, that this $R(\tau)$ is asymptotically unbiased because the $|\tau|/2T$ term vanishes at $T \to \infty$. We could easily get unbiased estimates by using $2T - |\tau|$ to divide the integral in Equation 3.11 rather than 2T. The form used here is preferred for the reason that $\tilde{R}(\tau)$ in this form can be expressed in terms of the given x(t) as a convolution.

$$\tilde{R}(\tau) = \frac{1}{2T} X(\tau) * X(-\tau)$$

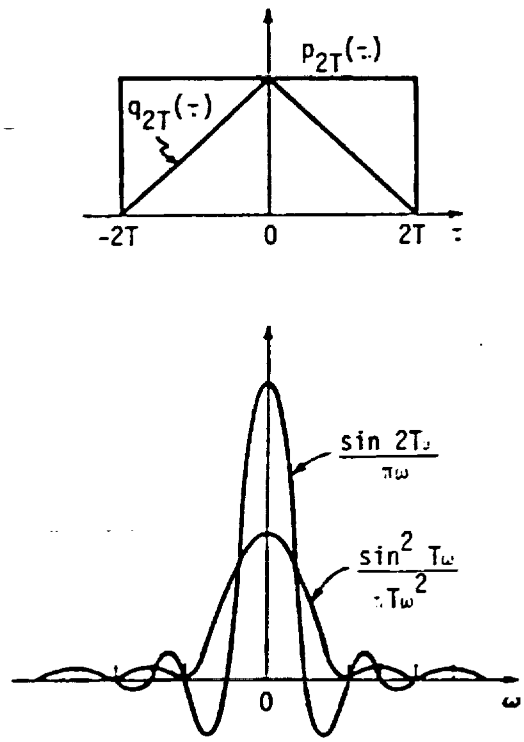

Figure 3.6. Rectangular and triangular lag window and their respective Fourier transform.

From Equation 3.12 the expected value of the spectrum is:

$$E\{\tilde{S}(\omega)\} = \int_{-2T}^{2T} R(\tau)q_{2T}(\tau)e^{-j\omega\tau}\, d\tau = S(\omega) * \frac{\sin^2 T\omega}{\pi T\omega^2} \quad (3.14)$$

where "$*$" designates the convolution integration as defined in Equation 3.1. Thus, the estimate $\tilde{S}(\omega)$ equals the convolution of $S(\omega)$ with the kernel $\sin^2(T\omega)/\pi T\omega^2$ (i.e., Bartlett window). The estimator is therefore biased. However,

$$E\{\tilde{S}(\omega)\} \xrightarrow[T\to\infty]{} S(\omega) \quad (3.15)$$

The effect of a rectangular versus triangular lag window is illustrated in the following. Figure 3.7 shows the spectrum computed from a discrete Fourier transform of Equation 3.3 without a lag window (or in other words with a rectangular lag window, see Figure 3.6). Figure 3.7 should be compared with the spectrum in Figure 3.3 which was computed with a triangular lag window. The two curves are not appreciably different in terms of departure from the analytical spectrum except they do show some dissimilarity in shape near the cutoff frequency.

It should be observed that the magnitude of aliasing for the spectrum in Figure 3.7 is of the same magnitude as that given in Table 3.1, for Figure 3.3. One may conclude then for the one-point spectrum the primary source of error is due to aliasing and that the bias errors are negligible.

For the two-point spectrum, however, one cannot draw this conclusion. Figure 3.8 shows the spectrum computed from Equation 3.6 by the DFT using a rectangular lag window. This figure should be compared with Figure 3.5 which shows the two-point spectrum computed with a triangular window. Notice that the curves behave considerably different in Figure 3.8 than they do in Figure 3.5. A ripple in the spectrum curve at high frequencies appears in Figure

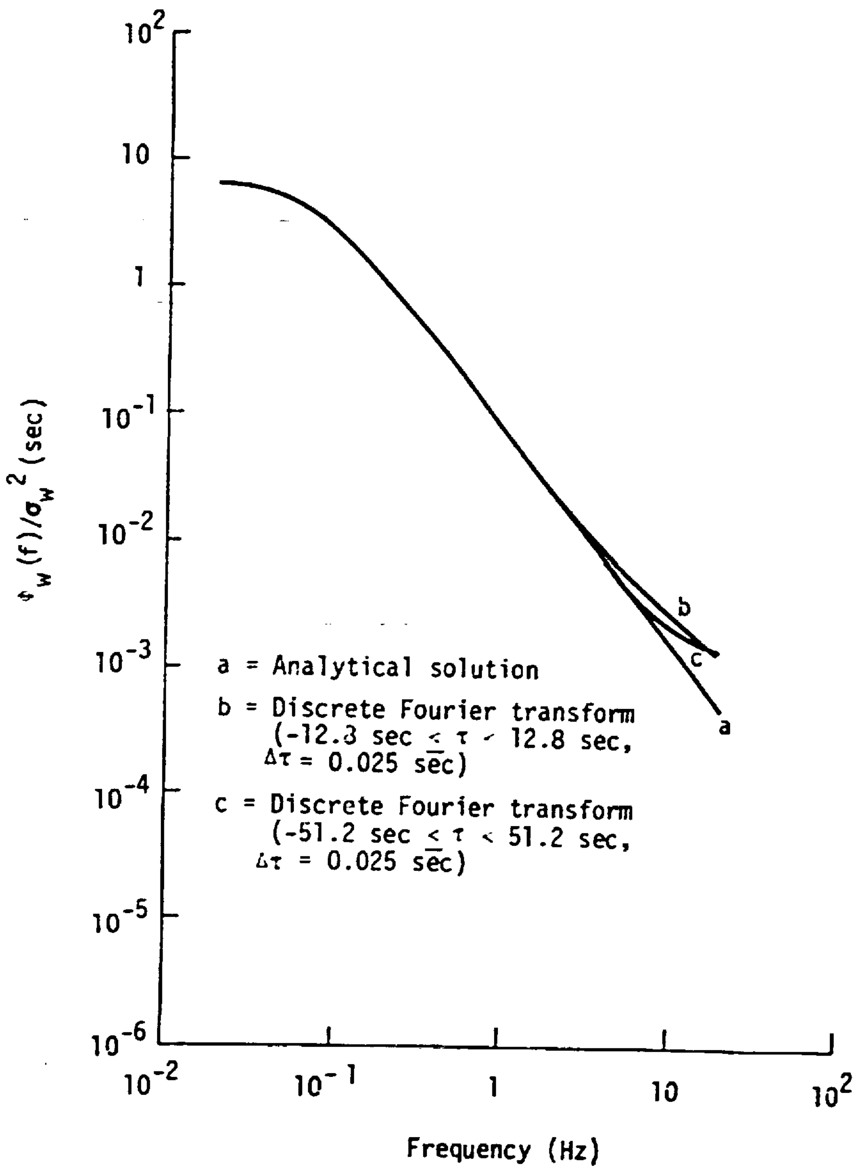

Figure 3.7. Comparison of the theoretical von Karman one-point auto-spectrum with the DFT computed values (square lag window).

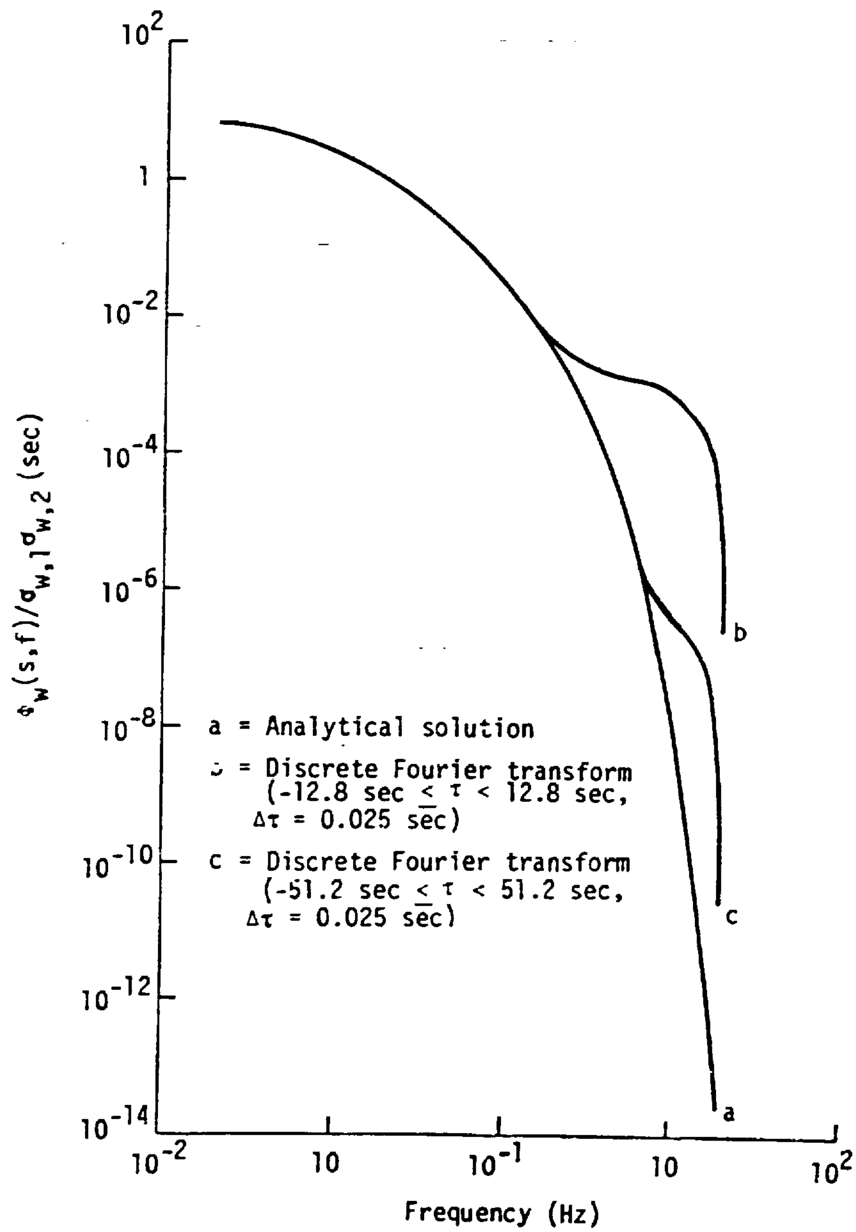

Figure 3.8. Comparison of the analytical two-point spectrum (Equation 3.6) with the DFT values computed from truncating Equation 3.5 with a rectangular lag window.

3.8. This is the same ripple as indicated in Figure 3.1e due to the truncation or application of the rectangular lag window to h(t). Thus the graphical illustration in Figure 3.1e clearly reveals how the rectangular spectrum window W(ω) convolved with the theoretical spectrum results in a truncation or bias error shown in Figure 3.8. Employing the triangular lag window results in a much smoother spectral curve (Figure 3.5) but there is still appreciable error between the DFT and the theoretically computed spectra.

The order of magnitude of aliasing associated with digitization of Equation 3.5 is the same as given in Table 3.2. The aliasing error is very small. It can, therefore, be concluded that the bias error contributes significantly to the error produced from computing two-point spectra with discrete Fourier transforms. The fact that the bias error for the one-point spectrum is small compared to aliasing whereas the bias error for the two-point spectra is very large compared to aliasing is a very striking observation when one considers that the correlations functions from which these two spectrum are computed differ only by just a miniscule amount near the zero lag value (see Figure 3.9).

Figure 3.9 illustrates the very small difference between the one-point correlation function and the two-point correlation function from which the spectra in Figures 3.3, 3.5, 3.7, and 3.8 were computed. A very small change in the correlation near zero lag causes the very large differences observed in the spectra. The effects of bias error generally not significant for autospectra must, however, be carefully considered when computing or interpreting two-point spectra.

In addition to abiasing and bias error, there is a third form of error called variance error. Variance error occurs when computing spectra and

C-2

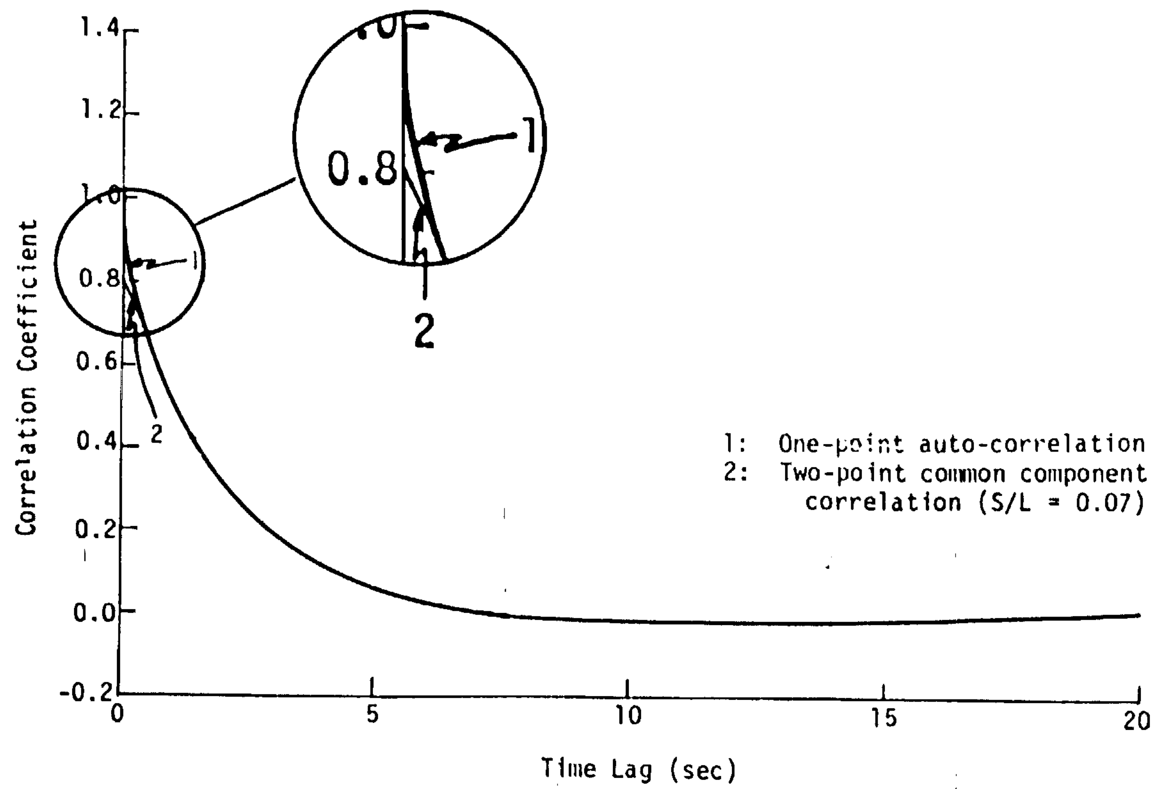

Figure 3.9. Comparison of one-point and two-point analytical correlations for vertical turbulence fluctuations (Equations 3.3 and 3.5).

correlations from random data. The analyses described to this point have dealt with deterministic correlation functions which do not cause any variance error in the spectral calculation. The aliasing and truncation error discussed occur because of the digitization of the function and because of the finite length of the record required for application of the DFT. The variance error occur because of the random nature of the gust velocities. In attempting to minimize both the bias and variance error, there are conflicting requirements on record length. These requirements result in accepting certain tradeoffs between resolution and accuracy. A more detailed look at the bias and variance errors will shed some light on these tradeoffs.

Consider initially the method of computing the spectrum by first calculating the correlation $R(\tau)$ and then Fourier transforming $R(\tau)$ to obtain $\Phi(f)$ as we have done for the deterministic functions in the previous discussions. It follows from Equation 3.14 and 3.15 that if T is sufficiently large, then:

$$\tilde{E}\{S(\omega)\} \approx S(\omega) \tag{3.16}$$

for analytical functions.

However, even for analytical functions with large T the variance of $\tilde{S}(\omega)$ will not be small for random data. In fact, for any T,

$$\mathrm{var}[\tilde{S}(\omega)] \geq E^2\{\tilde{S}(\omega)\} \tag{3.17}$$

Therefore, $\tilde{S}(\omega)$ is not a good estimator of $S(\omega)$, no matter how large T is. The reason is that with random data the values of the integrand, $\tilde{R}(\tau)$, in Equation 3.12 are not reliable (have large variance) for τ close to $\pm 2T$. Thus, the power spectrum $S(\omega)$ of a process $x(t)$ cannot be determined from a single sample, no matter how large the sample is. To reduce the variance of the estimate, we must accept only a smoothed version of $S(\omega)$; that is, we must sacrifice resolution.

3.4 Smoothing the Spectrum

The variance of the integral in Equation 3.12 can be reduced by deemphasizing the contribution of $\tilde{R}(\tau)$ for τ near $\pm 2T$. For this purpose, the estimator:

$$\tilde{S}_w(\omega) = \int_{-2T}^{2T} \tilde{R}(\tau)w(\tau)e^{-j\omega\tau}\, d\tau \tag{3.18}$$

is formed where $w(\tau)$ is a lag window vanishing for $|\tau| > 2T$. In this section, we examine the properties of $\tilde{S}_w(\omega)$ and the factors affecting the selection of the window $w(\tau)$.

The estimator $\tilde{S}_w(\omega)$ is the Fourier transform of the product $\tilde{R}(\tau)w(\tau)$; hence,

$$\tilde{S}_w(\omega) = \frac{1}{2\pi} \int_{-\infty}^{\infty} \tilde{S}(\omega - y)W(y)dy = \frac{1}{2\pi} \tilde{S}(\omega) * W(\omega) \tag{3.19}$$

From the above and Equation 3.14, it follows that:

$$E\{\tilde{S}_w(\omega)\} = \frac{1}{2\pi} E\{\tilde{S}(\omega)\} * W(\omega) = \frac{1}{2\pi} S(\omega) * \frac{\sin^2 T\omega}{\pi T\omega^2} * W(\omega) \tag{3.20}$$

For a reliable estimation, the duration of $W(\omega)$ must be large compared to $1/T$. This leads to the approximation:

$$\frac{\sin^2 T\omega}{\pi T\omega^2} * W(\omega) \simeq W(\omega) \tag{3.21}$$

Inserting this approximate expression into Equation 3.20 gives:

$$E\{\tilde{S}_w(\omega)\} \simeq \frac{1}{2\pi} S(\omega) * W(\omega) \tag{3.22}$$

It can be shown that under certain general conditions (Papoulis, 1977) the variance of $\tilde{S}_w(\omega)$ is given by:

$$\mathrm{var}[\tilde{S}_w(\omega)] \approx \frac{E_w}{2T} S^2(\omega) \qquad \omega \neq 0 \tag{3.23}$$

where

$$E_w = \int_{-2T}^{2T} w^2(\tau)d\tau = \frac{1}{2\pi} \int_{-\infty}^{\infty} W^2(\omega)d\omega \tag{3.24}$$

Equations 3.22 and 3.23 dictate the factors affecting the selection of the window pair $w(\tau)$ and $W(\omega)$. For the bias error,

$$b = E\{\tilde{S}_w(\omega)\} - S(\omega) \tag{3.25}$$

to be small, $W(\omega)$ must be of short duration. For the variance to be small, E_w must be small. We shall presently see that if T is sufficiently large, then both requirements can be reasonably satisfied.

3.5 Window Selection

For a satisfactory estimation of $S(\omega)$, the variance of the estimator $\tilde{S}_w(\omega)$ must be small compared to $S^2(\omega)$ or, equivalently, the variance ratio

$$\beta = \frac{\mathrm{var}[\tilde{S}_w(\omega)]}{S^2(\omega)} \tag{3.26}$$

must be very small compared to 1:

$$\beta \ll 1 \tag{3.27}$$

This is the case if E_w (see Equation 3.23) is very small compared to $2T$:

$$E_w \approx 2T\beta \ll 2T$$

The above requirement leads to the conclusion that $w(\tau)$ must take on significant values only in an interval $(-M,M)$ such that $M \ll 2T$. We shall assume that $|w(\tau)| \leq 1$ for all τ and that, for $|\tau| > M$, it is not just small but it vanishes:

$$w(\tau) = 0 \text{ for } |\tau| > M \tag{3.28}$$

From these assumptions, it follows that

$E_w \leqslant 2M$ so that $\beta \leqslant M/T$ (3.29)

Thus, to satisfy the variance requirement (Equation 3.27), we must choose M such that

$$M \ll T \tag{3.30}$$

With M so determined, the shape of the window is selected so as to minimize the bias

$$b = \frac{1}{2\pi} \int_{-\infty}^{\infty} S(\omega - y)W(y)dy - S(\omega) \tag{3.31}$$

The bias b depends not only on $W(\omega)$ but also on he shape of $S(\omega)$. Therefore, there is no well-defined optimum window. However, if T is sufficiently large and $W(\omega) \geqslant 0$, it can be shown (Papoulis, 1977) that:

$$b \simeq \frac{S''(\omega)}{4\pi} \int_{-\infty}^{\infty} \omega^2 W(\omega)d\omega \tag{3.32}$$

The problem is to find a positive function $W(\omega)$ for a specified value E_w (Equation 3.24) which minimizes the integral in Equation 3.31 or 3.32. We will now consider some estimates of the bias and variance errors which may be expected to occur in the computation of turbulence spectra.

3.6 Variance Error

The variance error associated with atmospheric turbulence spectra which follow Equations 3.4 and 3.6 can be estimated from Equations 3.23 and 3.24. The lag window for these figures is $w(\tau) = 1 - |\tau|/2T_m$ where $T_m = T/M$. Hence,

$$E_w = \int_{-2T_m}^{2T_m} \left[1 - \frac{|\tau|}{2T_m}\right]^2 dt$$

$$E_w = \frac{4T}{3M} \tag{3.33}$$

Substituting into Equation 3.23 gives:

$$\mathrm{var}[\tilde{S}_W(\omega)] \approx \frac{2}{3M} S^2(\omega) \qquad (3.34)$$

The magnitude of the variance errors estimated from Equation 3.34 is indicated on Figures 3.4 and 3.5 by the variance error bars. The variance is computed from Equation 3.34 at f = 15 Hz and 20 Hz and at f = 10 Hz and 15 Hz, for Figures 3.4 and 3.5, respectively, with M = 5 which is the typical number of segments used in computing the spectra shown in Appendix A. It should be noted that the spectra shown in Figures 3.3 and 3.5 have no actual variance error since they are computed from deterministic functions. However, the error bars do indicate the one standard deviation error which can be expected in analyses of random turbulence signals which physically obey the analytical Equations 3.4 and 3.6.

Now consider the magnitude of the bias error. Equation 3.31 can be used to compute the bias error. Values for the convolution of $S(\omega)$ (given by Equation 3.4 for the one-point spectrum and by Equation 3.6 for the two-point spectrum, respectively) with $W(\omega)$ for a triangular spectral window (see Figure 3.6) are given in Table 3.3 for frequency values of 10, 15, and 20 Hz. The values of the convolution integral which includes bias error given in the table for the two-point spectrum are plotted on Figure 3.5 (as marked by the solid circles). They coincide very closely with the DFT curves clearly illustrating that the departure of the DFT curves from the theoretical curve for the two-point spectral is due almost entirely to bias error.

The important conclusion from Table 3.3 is that a two-point spectrum computed with truncated digitized turbulence data with no prior knowledge of the actual form of the spectrum may show appreciable energy in the high frequency range whereas in reality there is no energy at those frequencies. The bias error in the two-point spectrum is approximately 385,400 percent at

TABLE 3.3. Values of $1/2\pi \int_{-\infty}^{\infty} S(\omega - y)W(y)dy$ for $S(\omega)$ Given by Equations 3.4 and 3.6, Respectively, and a Triangular Spectral Window ($N = 512$, $\Delta\tau = 0.025$).

	One-Point Spectrum		Two-Point Spectrum	
f	Bias Error	True	Bias Error	True
10	0.8000×10^{-3}	1.5731×10^{-3}	0.6286×10^{-4}	0.1631×10^{-7}
15	0.4011×10^{-3}	0.8075×10^{-3}	0.1789×10^{-4}	0.1764×10^{-10}
20	0.2460×10^{-3}	0.5000×10^{-3}	0.1568×10^{-4}	0.2218×10^{-13}

10 Hz as contrasted to only about 50 percent for one-point spectrum. The remarkable phenomenon, however, is that the two spectra are computed from correlations which are almost identical except for a very small difference at zero lag (see Figure 3.9). These factors have strong implication when computing spectra from turbulence time histories where the true spectrum is not known *a priori*. With this in mind, improved windows for reducing bias errors in two-point spectra were investigated.

Considerable study of computing spectra for random data has been carried out in the communication engineering field. Several alternate windows for smoothing the spectra estimates have been proposed. Papoulis (1977) gives the expression:

$$w(\tau) = \frac{1}{\pi}\left|\sin \frac{\pi}{T}\tau\right| + \left[1 - \frac{|\tau|}{T}\right]\cos\frac{\pi}{T}\tau\ ,\ 0 \leq |\tau| \leq T \tag{3.35}$$

and

$$W(\omega) = 4T\pi^2 \frac{(1 + \cos T\omega)}{(\pi^2 - T^2\omega^2)^2} \tag{3.36}$$

This spectral window is called the minimum-bias window because it minimizes the value of the integral in Equation 3.32. When this window is applied to the two-point correlation, the results shown in Figure 3.10 are achieved. The

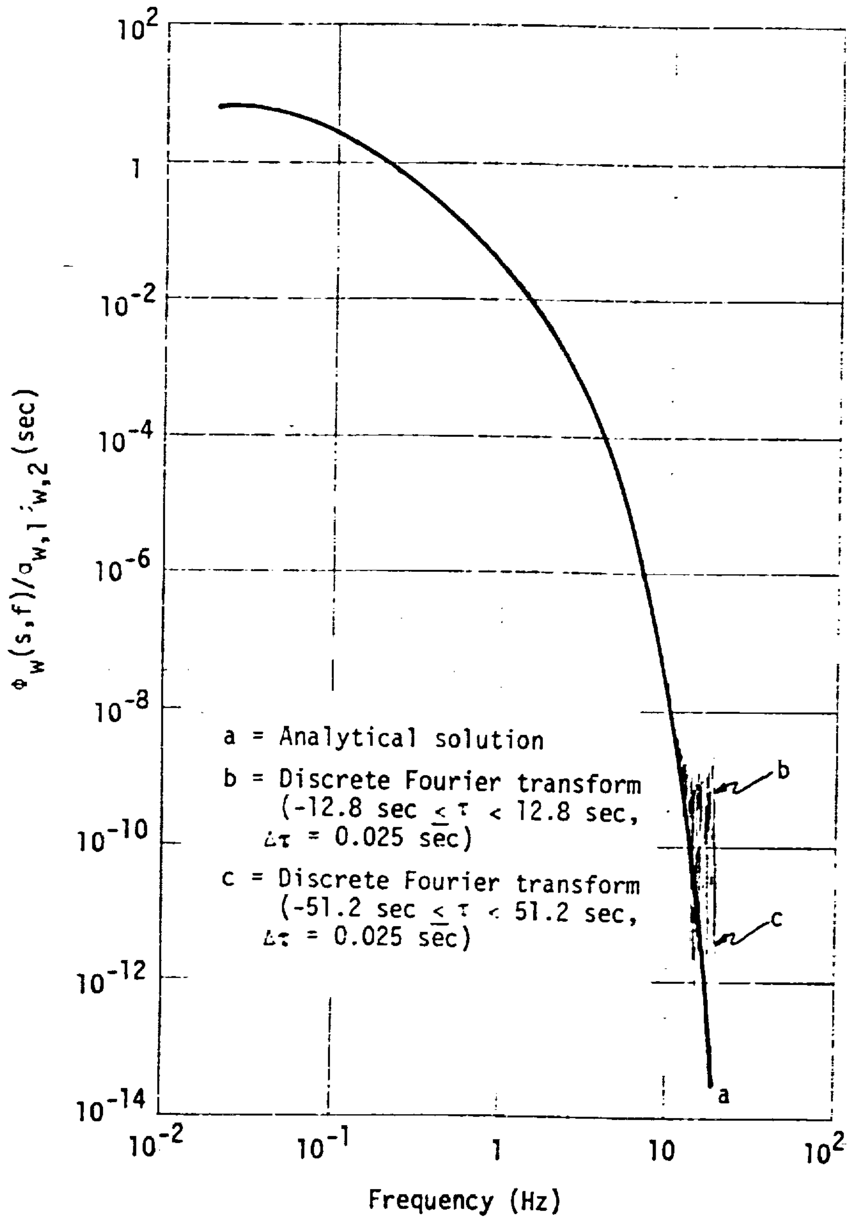

Figure 3.10. Results of applying minimum-bias window (Equation 3.34) to the DFT computation of the two-point spectrum from Equation 3.5 as compared with the analytical value.

bias error is almost completely eliminated to frequencies as high as 15 Hz. The fluctuation in the curve at higher frequencies is believed to be a computer-generated numerical roundoff error. Although this window has not been used in computing the turbulence spectra in this report further consideration of its use is recommended.

Attention is now directed toward calculation of spectra from the turbulence time histories. The spectra discussed will now not only contain aliasing and bias error but also variance error.

3.7 Spectrum Calculation from a Finite Turbulence Time History

Consider the variable x(t) as a velocity fluctuation in the interval (-T,T). The correlation estimator is then given by:

$$\tilde{R}(\tau) = \frac{1}{2T} \int_{-T+|\tau|/2}^{T-|\tau|/2} x\left(t + \frac{\tau}{2}\right) x\left(t - \frac{\tau}{2}\right) dt , \qquad |\tau| < 2T \tag{3.37}$$

The integral in Equation 3.37 is the convolution

$$\tilde{R}(\tau) = a\frac{1}{2T} \; x'(\tau) * x'(-\tau) \tag{3.38}$$

where

$$x'(\tau) = x(\tau) p_{2T}(\tau) = \begin{cases} x(\tau) & |\tau| \leq T \\ 0 & |\tau| > T \end{cases} \tag{3.39}$$

equals the truncated time record of x(t).

It follows from Equation 3.39 and the convolution theorem that the Fourier transform of $\tilde{R}(\tau)$ gives the estimate of the spectrum:

$$\tilde{S}(\omega) = \int_{-2T}^{2T} \tilde{R}(\tau) e^{-j\omega\tau} \, d\tau = \frac{1}{2T} \left| \int_{-T}^{T} x(t) e^{-j\omega t} \, dt \right|^2 \tag{3.40}$$

Thus, $\tilde{S}(\omega)$ can be determined directly from the given sample or turbulence time history x(t). This approach was used in computing all spectra in Appendix A and those discussed in Section 2.

It is interesting to consider now three numerical methods for estimating the power spectrum $S(\omega)$ in terms of the given segment, $x'(\tau) = x(\tau)p_{2T}(\tau)$. All three methods are statistically identical but differ only in the computational procedures.

1. Determine the sample auto-correlation $\tilde{R}(\tau)$ by convolving $x'(\tau)$ with $x'(-\tau)$ as in Equation 3.36:

$$\tilde{R}(\tau) = \frac{1}{2T} x'(\tau) * x'(-\tau) \tag{3.41}$$

Multiply $R(\tau)$ by the window $w(\tau)$ and compute the Fourier transform of the product as in Equation 3.18 to get $\tilde{S}_w(\omega)$. The required operations are one convolution, one multiplication, and one Fourier transform.

2. Compute the Fourier transform of $x'(\tau)$ to get $X'(\omega)$. Multiply $X'(\omega)$ by its conjugate and form the sample spectrum $\tilde{S}(\omega)$:

$$\tilde{S}(\omega) = \frac{1}{2T} \left|X'(\omega)\right|^2 \tag{3.42}$$

Convolve $\tilde{S}(\omega)$ with the window $W(\omega)$ to get:

$$\tilde{S}_w(\omega) = \frac{1}{2\pi} \tilde{S}(\omega) * W(\omega) \tag{3.43}$$

The required operations are one Fourier transform, one multiplication, and one convolution.

3. Compute $X'(\omega)$ and $\tilde{S}(\omega)$ as in method 2. Find the inverse Fourier transform $\tilde{R}(\tau)$ of $\tilde{S}(\omega)$. Form the product $\tilde{R}(\tau)w(\tau)$ and compute its Fourier transform $\tilde{S}_w(\omega)$ as in method 1. The required operations are two multiplications, two Fourier transforms, and one inverse Fourier transform.

Method 3 has been used for computing spectra from the turbulence time histories discussed in this report. In most cases, however, the lag window operation has not been performed for reasons described later. The variance error for spectrum estimates obtained by a direct Fourier transform operation on the digitized time history (Method 3) may be determined differently from that given by Equation 3.23.

Consider the spectrum function of a stationary (ergodic) Gaussian random process $x'(\tau)$. An estimate of $\tilde{S}(\omega)$ can be obtained from Equation 3.42. The narrowest possible bandwidth resolution from Equation 3.42 is $B_e = (1/T)$. To determine the variance of the estimate of $\tilde{S}(\omega)$, observe that the Fourier transform $X(\omega)$ is defined by a series of components at frequencies $f = k/T$; $k = 1,2,3$, etc. Further observe that $X'(\omega)$ is a complex number where the real and imaginary parts, $X'_R(\omega)$ and $X'_I(\omega)$, can be shown to be uncorrelated random variables with zero means and equal variances (Bendat and Piersol, 1971). Since a Fourier transformation is a linear operation, $X'_R(\omega)$ and $X'_I(\omega)$ will be Gaussian random variables if $x(t)$ is Gaussian. The random variable $x(t)$ is not strictly Gaussian as discussed in Section 2; however, the variance error to be described is expected to be representative of the error associated with atmospheric turbulence. It follows then that the quantity

$$|X'(\omega)|^2 = X'^2_R(\omega) + X'^2_I(\omega) \tag{3.44}$$

is the sum of the squares of two independent Gaussian variables. It can be shown that each frequency component of the estimate $\tilde{S}(\omega)$ will have a sampling distribution given by

$$\frac{\tilde{S}(\omega)}{S(\omega)} = \frac{\chi_2^2}{2} \tag{3.45}$$

where χ_2^2 is the chi-square variable with $n = 2$ degrees of freedom.

Note that the result in Equation 3.45 is independent of the record length T, that is, increasing the record length does not alter the distribution function defining the random error of the estimate. It only increases the number of spectral components in the estimate. The variance error of the estimate is substantial. The mean and variance of the chi-square variable are n and 2n, respectively. Thus the normalized standard error, which defines the variance error of the estimate is:

$$\beta = \frac{\text{var}^2[\tilde{S}(\omega)]}{S^2(\omega)} = \frac{2}{n} \tag{3.46}$$

For the case at hand, n = 2 so $\beta = 1$, which means that the standard deviation of the estimate is as great as the quantity being estimated. This is an unacceptable error for most applications.

In practice, the variance error of an estimate , duced by Equation 3.42 is reduced by smoothing the estimate in one of two ways. The first way is to smooth over an ensemble of estimates. This can be done by computing individual estimates from M independent sample records, $x_i(t)$; $i = 1,2,3,\ldots M$, and then averaging the M estimates at each frequency of a spectral component as illustrated in Figure 3.11a from Bendat and Piersol (1971). The second way is to smooth over frequency. This can be done by averaging together the results for ℓ contiguous spectral components in the estimate from a single sample record as illustrated in Figure 3.11b. In either case, the smoothing technique approximates the expectation operation in Equation 3.42.

For smoothing the spectra presented in Appendix A, ensemble averaging has been used throughout this study. Care must be used when ensemble averaging, however. Each spectrum from the M segments of the total time history is generally complex. To estimate the mean (or magnitude) of the spectrum from the segments some authors imply ensemble-averaging of the absolute values:

$$\left|\Phi_{xy}(s,f)\right| = \frac{1}{N_m} \sum_{i=1}^{N_m} \left|C_{xy,i}(s,f) - jQ_{xy,i}(s,f)\right| \tag{3.47}$$

where N_m is the number of segments. However, few authors deal with two-point spectra. Jenkins and Watts (1969) correctly defined the mean of the complex two-point spectral function as:

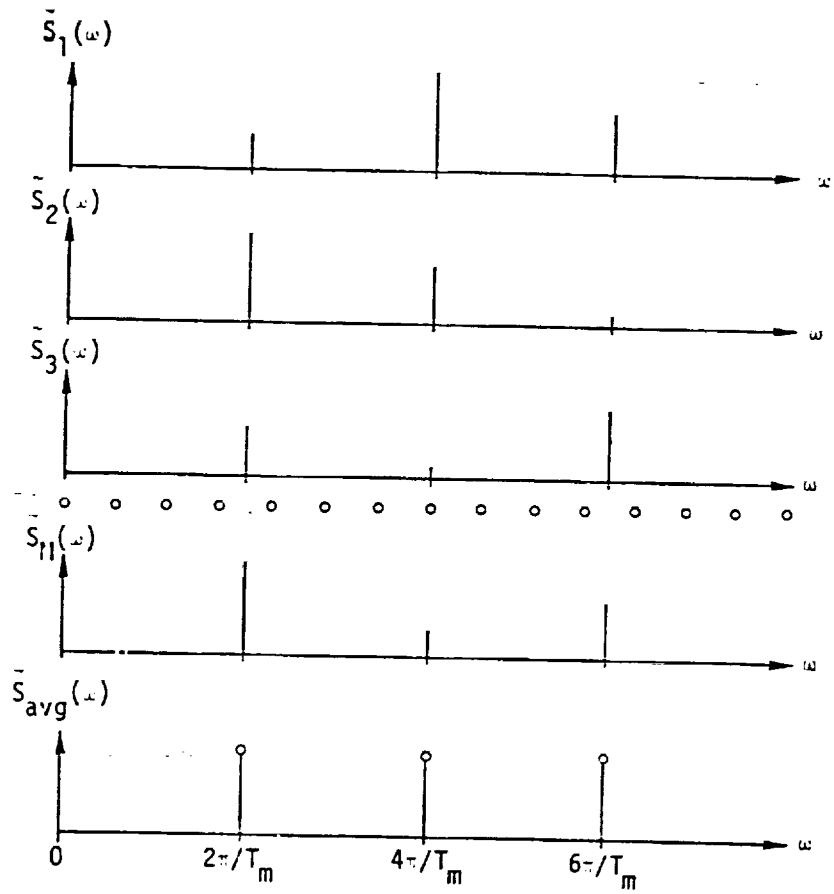

(a) Ensemble smoothing procedure

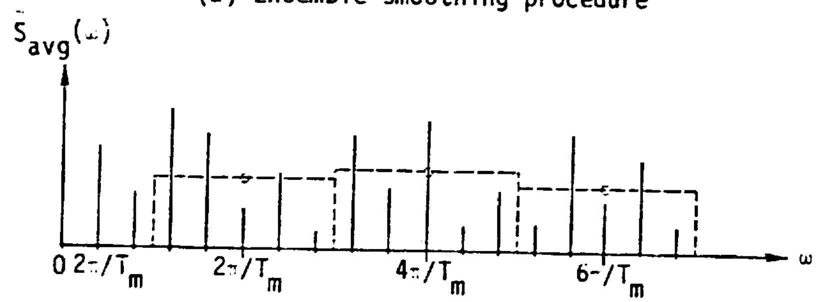

(b) Frequency smoothing procedure

Figure 3.11. Smoothing procedures for spectrum estimates. (Bendat and Piersol, 1971).

$$|\Phi_{xy}(s,f)| = \left| \frac{1}{N_m} \sum_{i=1}^{N_m} C_{xy,i}(s,f) - j \frac{1}{N_m} \sum_{i=1}^{N_m} Q_{xy,i}(s,f) \right| \tag{3.48}$$

wherein the real and imaginary parts of the spectral function are segment-averaged separately.

Figures 3.12 and 3.13 demonstrate the difference between the two-point spectrum estimations from Equations 3.47 and 3.48, respectively. Both cases are compared with the Houbolt and Sen theoretical model. Equation 3.48 gives better agreement with the theoretical model. It is also important to note that when smoothed by the Equation 3.47 technique, the two-point spectrum in Figure 3.12 is almost indistinguishable from the one-point spectra as shown in Figure 2.11. Notice the variance is larger for a two-point spectrum than for a one-point spectrum. Also, one- and two-point cross-spectra have apparent higher variance levels. The increase in variance is due to the fact that variability is introduced by two separate processes rather than one (i.e., averaging C_{xy} and Q_{xy} separately as contrasted to averaging C_{xy} itself which is the only contribution to the one-point auto-spectrum).

3.8 Lag Windows for Reducing Bias Error

A number of data windows for reducing bias errors are described in the literature. No single window has been identified as most appropriate for an atmospheric turbulence signal. A cosine tapered data window to smooth the data at each end of the record is commonly used in the literature but was found to have no effect on spectra calculated and was not used in this report.

Lag windows (as contrasted to data windows) are applied to the correlation function as defined in Case 3, page 94. Figure 3.14 shows the two-point spectrum for a turbulence measurement and a digitized deterministic model with a rectangular lag window. The shape of the spectrum from the data deviates

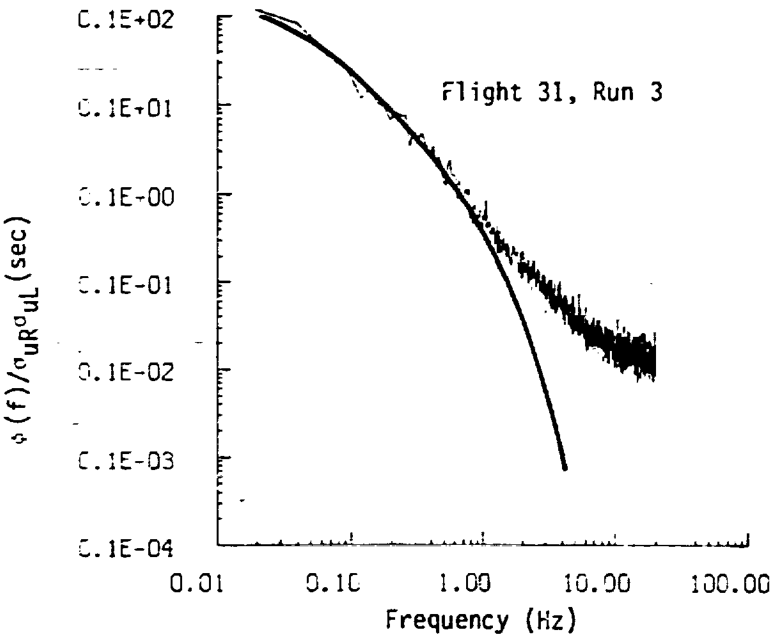

Figure 3.12. Segment-averaged two-point auto-spectrum using Equation 3.47. (Heavy solid line designates Houbolt and Sen's theoretical model.)

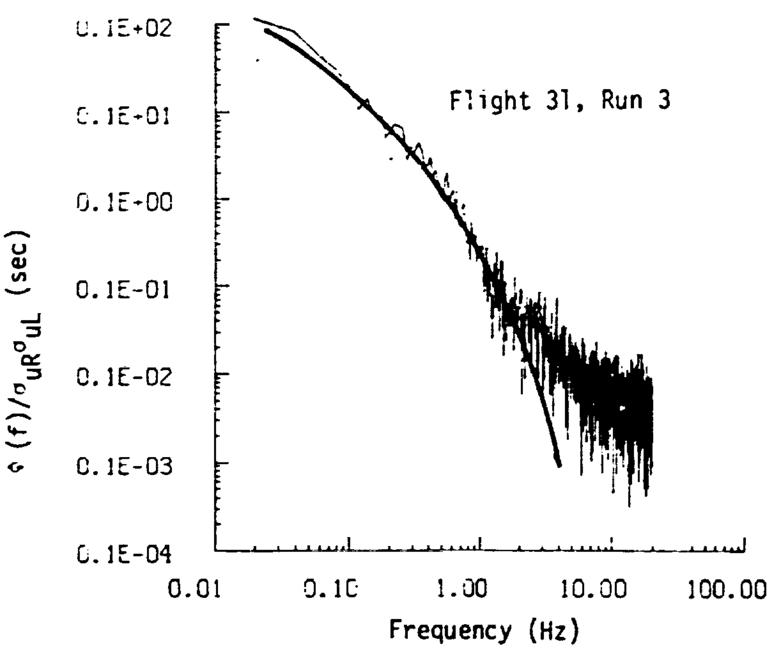

Figure 3.13. Segment-averaged two-point auto-spectrum using Equation 3.48. (Heavy solid line designates Houbolt and Sen's theoretical model.)

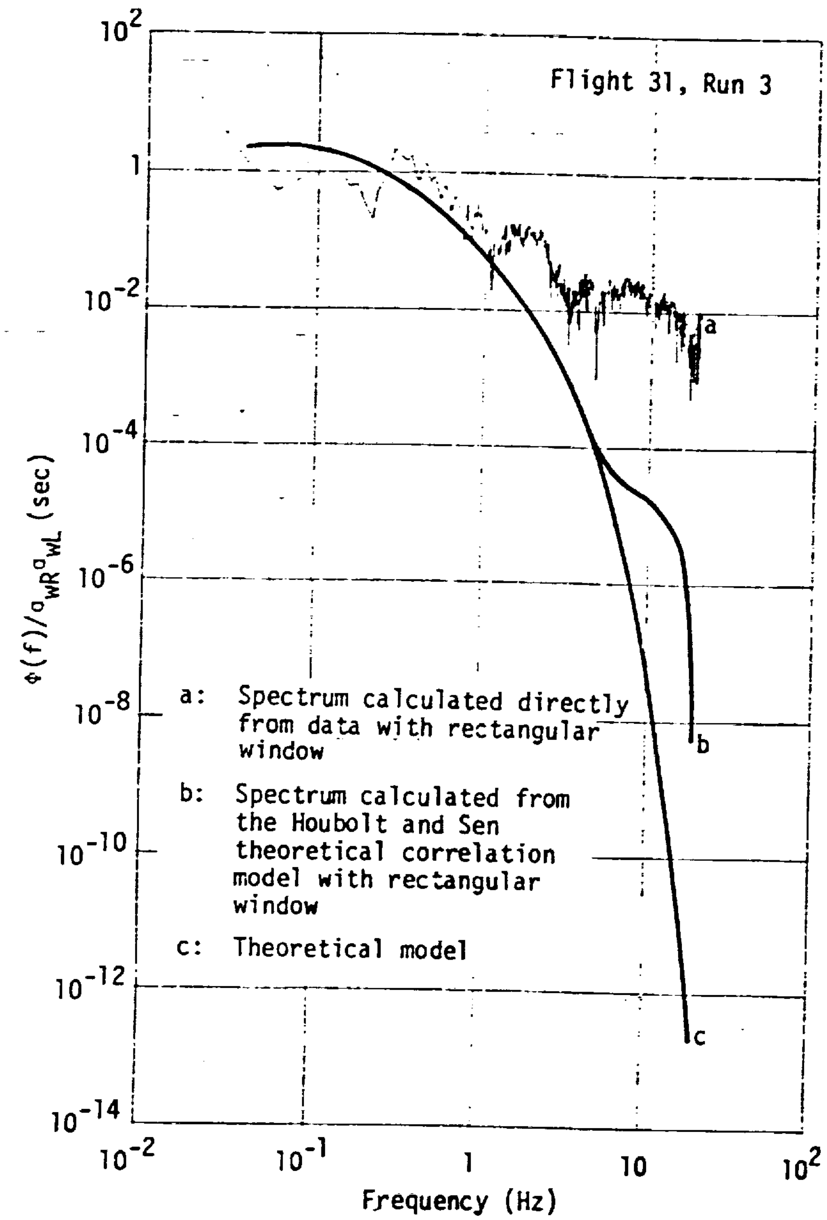

Figure 3.14. Two-point spectrum computed directly from data with a rectangular lag window.

significantly from the values predicted by the model even at low frequencies. The minimum amplitude window Equation 3.35 was also used with the direct FFT of the turbulence time history as shown in Figure 3.15. The window does not correct the random data input to the same degree it corrects the deterministic input. It does, however, give a better correction of the bias error than any of the other windows used in this study. Further investigation of the effect of lag windows on two-point spectra computed directly from the turbulence is recommended.

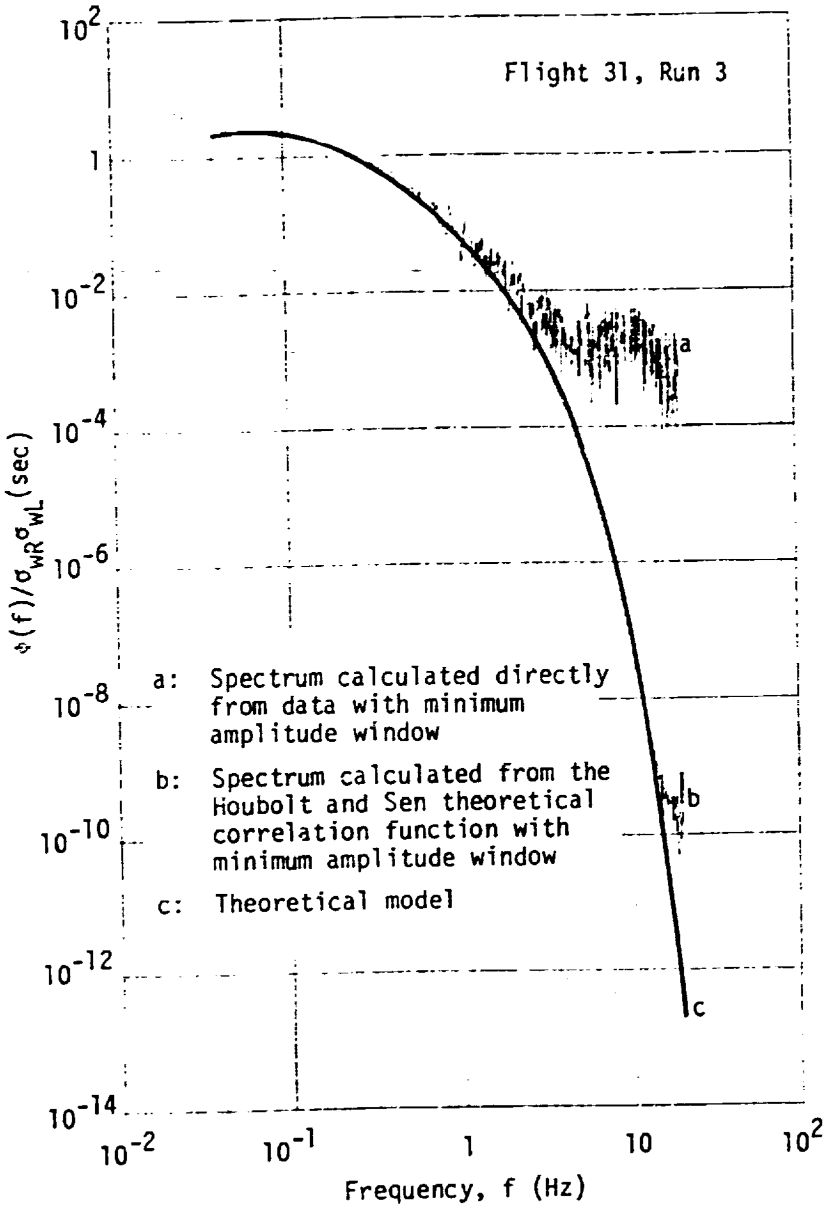

Figure 3.15. Two-point spectrum with minimum amplitude window, Equation 3.35.

4.0 INSTRUMENTATION ERROR ANALYSIS

4.1 Instrumentation Problems

The instrumentation platform is the B-57B aircraft. This aircraft is a U.S. Air Force (USAF) version of the English Electric Canberra and was built under license by the Martin Company. The B-57B, designed as a tactical bomber, first flew in 1954 but is no longer in use by the USAF. NASA uses the aircraft as a flight research tool to measure wind velocity, turbulence, temperature, and other properties of the atmosphere. The aircraft is equipped to gather data on gust gradients across the 19.5 m (64 ft) wing span. Characteristics and dimensions of the B-57B are given in Figure 4.1. Additional information about aerodynamic coefficients and stability derivatives can be obtained from Ringnes and Frost (1985). The instrumentation on the B-57B include three airspeed probes located at the nose section and at each wing tip. The flight angles, sideslip angle, and angle-of-attack are measured at the same three locations. Also, accelerometers are placed at both wing tips and at the center of gravity (c.g.) for use in studying wing vibrations. Ground speed, Euler angles and angular rates, acceleration components, and geographical location are provided by the Inertial Navigation System (INS).* Details on the instrumentation and its accuracy is given in Meissner (1976), Rhyne (1980), and Murrow and Rhyne (1981).**

---

*Carousel IV made by AC Electronics, Division of General Motors Corporation.

**The INS and pressure transducers used in the flights are different from reported in these references.

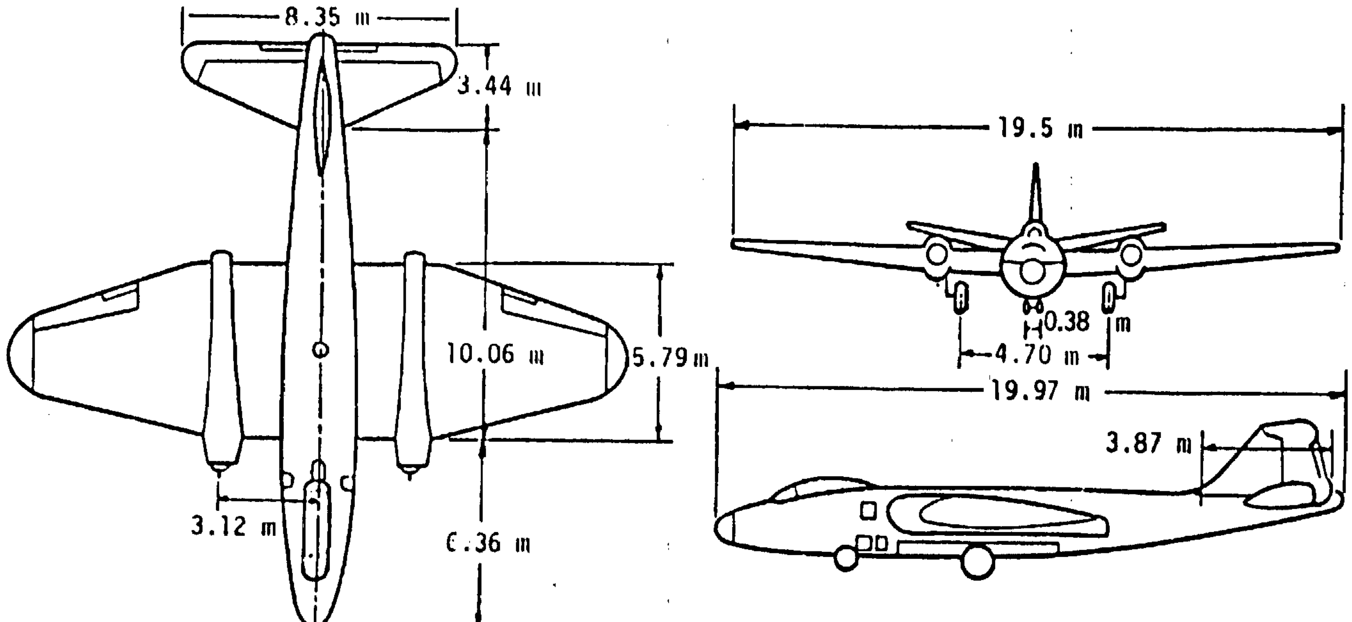

Wing span	19.50 m	Fin and rudder chord,		Main plane incidence	2°
Mean aerodynamic chord	4.57 m	Root	3.87 m	Dihedral, inner plane	2°
Root chord	5.79 m	Tip	1.54 m	Outer plane	4°21'
Tip chord	2.34 m	Fuselage ground		Tail plane and elevator	
Length, fuselage	19.97 m	clearance, normal	0.61 m	Area, cross	15.90 m^2
Length, overall	20.20 m	Wing area, gross	89.10 m^2	Incidence, normal	+1°
Height	4.75 m	Aspect ratio	4.3	Maximum	+1°52'
Track	4.70 m	Thickness/chord ratio,		Minimum	-3°52'
Tail plane span	8.35 m	Root	12%	Fin and rudder area, gross	6.60 m^2
Root chord	3.44 m	Tip	9%		
Tip chord	1.23 m				

Figure 4.1. Characteristics of the B-57B.

During previous research (Chang and Frost, 1985; Frost, et al., 1985a; Ringnes and Frost, 1985) using data gathered with the B-57B aircraft, various uncertainties in the measured wind velocities and turbulence measurements were traced to instrumentation characteristics. Frost, et al. (1985a) have pointed out irregularities in the total pressure measurements and postulated that water droplets may have occasionally been ingested in the pitot tubes. These caused spikes in the turbulence spectrum at approximately 15 Hz. No similar spikes were observed for the data from Run 31 which is analyzed in this report. Chang and Frost (1985) and Frost and Huang (1983) also noted that there are, in some cases, discrepancies in the calculation of the total wind vectors. These were attributed to problems with boom alignment and with the INS. In this section, the data reduction procedures of the quasi-steady wind vector and of the turbulence are reviewed in detail to pinpoint how instrumentation errors might affect the wind measurements. The magnitude of the errors are estimated and methods of correcting for them suggested.

4.2 Wind and Gust Velocity Equations

The velocity of a moving airmass with respect to earth, in this study, is obtained by vectorially subtracting aircraft velocity with respect to the air mass from aircraft velocity with respect to earth. These velocities are referred to as airspeed and ground speed, respectively. Since airspeed is measured in a body-axis (airplane fixed) reference system, it is necessary to rotate the airspeed vector into the inertial (earth fixed) frame of reference. The governing equations are derived in detail in Appendix B (see also Frost (1981); Crooks, et al. (1967); Houbolt, et al. (1964); Lenschow (1972); and Axford (1968)). The present assumptions used in the equations for removing the aircraft motions from the wind vector are straight and level flight without large perturbations. Therefore, small angle assumptions are made for the roll, pitch and yaw angles, and for the angle of attack and sideslip angle. Furthermore, it is assumed that the product of sines of any of the small angles mentioned above vanishes and the cosines of small angles are unity. The application of these linearized equations to computing gust velocities for touch-and-go flights and during excursions from level flight during a run (e.g., Run 9 at 7 to 11 miles, see Figure A.41) is discussed later. Based on the small angle, level flight assumptions, the following expressions are used for computing the horizontal wind velocity components from the measured parameters:

$$W_E = V_E - V_C \sin\left(\psi - \beta_C - \frac{\ell_{xC}\dot{\psi}}{V_C}\right) \qquad (4.1)$$

$$W_N = V_N - V_C \cos\left(\psi - \beta_C - \frac{\ell_{xC}\dot{\psi}}{V_C}\right) \qquad (4.2)$$

where ψ is aircraft heading and β_C is sideslip angle. V_C is the true airspeed of the aircraft, V_E and V_N are east-west and north-south components of the airplane inertial velocity, and ℓ_{xC} is the longitudinal distance measured parallel to the x-axis of the airplane from the INS to the centerline measuring station. The higher order term containing $\dot{\psi}$ arise because the airspeed and ground speed are measured at different locations.

Wind speed and direction are derived directly from two independent components and are given by:

$$W = (W_E{}^2 + W_N{}^2)^{1/2} \qquad (4.3)$$

$$\psi_W = \tan^{-1}\left(\frac{W_E}{W_N}\right) + \pi \quad \text{for } \pi/2 > \tan^{-1}\left(\frac{W_E}{W_N}\right) > -\pi/2 \qquad (4.4)$$

Positive wind is defined as a wind blowing towards the east, W_E, and north, W_N, which in meteorology is referred to as west and south winds, respectively.

The turbulence components are calculated in the aircraft-fixed coordinate system. A complete derivation of the equations has been carried out both by NASA Langley Research Center and by FWG Associates in the past. The FWG derivation is also restated in Appendix B. The linearized equations for the center probe are:

$$u_C = \hat{V}_E \sin \overline{\psi} + \hat{V}_N \cos \overline{\psi} - \hat{V}_C \tag{4.5}$$

$$v_C = V_C\hat{\beta}_C - V_C\hat{\psi} + \hat{V}_E \cos \overline{\psi} - \hat{V}_N \sin \overline{\psi} + \ell_{xC}\hat{\dot{\psi}} + V_C\hat{\alpha}_C\phi \tag{4.6}$$

$$w_C = V_C\hat{\alpha}_C - V_C\hat{\theta} + \hat{V}_{az} + \ell_{xC}\hat{\dot{\theta}} - V_C\hat{\beta}_C\phi \tag{4.7}$$

where ϕ, θ, and ψ are roll, pitch, and yaw angles of the aircraft. Those for the wing tip probes are straightforward modifications of those for the center probe. It is assumed that the average pitch angle of the average pitch angle of the average flight path, $\overline{\theta}$, is zero. The caret (^) symbol indicates deviation from the mean value and the overbar (¯) indicates average value.

4.3 Sources of Inaccuracy in Data Reduction

Instrumentation errors influence the quantities appearing on the right-hand side of Equations 4.1 and 4.2 and thus the accuracy of the computed wind velocities. Instrumentation errors in the INS ground speed components, the airspeed, and the sideslip angle have been identified and studied. Errors in the yaw rate are negligible, and the yaw angle is believed to be accurate. A test to verify yaw angle accuracy is suggested since yaw angle errors could significantly contribute to errors in the calculation of horizontal wind.

Of these sources of instrumentation errors, the most difficult to correct is the dynamic error in the velocity inherent in the INS, termed the Schuler error to which aircraft motions contribute. All other errors can be removed by careful calibration. The effects on the magnitude of the measured wind and also turbulence calculations due to the sources of error in the instrumentation are presented next.

4.4 Inertial Velocity and Position Errors

The accuracy of the calculations of horizontal winds depends upon the performance of the INS and its capability to provide correct measurements of the inertial (ground) speed of the aircraft. In recent years mechanical and electronic advances have greatly improved INS accuracy. However, a cumulative oscillation in the INS stable platform element called the Schuler drift effect, first pointed out in the famous paper by Schuler (1923), can be quite significant. Inertial navigation theory including derivation of the Schuler pendulum effects is explained in many textbooks (see for example, Boxmeyer, 1964). The Schuler error is essentially periodic with a period near that of an earth radius pendulum, 84.4 minutes.* The error behaves sinusoidally and

---

*Huber and Bogers (1983) point out that a platform used in an airplane cannot strictly be kept tuned to T_0 = 84.4 minutes after takeoff since R (distance between the airplane and center of the earth) and g (gravitational acceleration) change with altitude. They propose to define T_0 = 84.4 minutes as the Schuler constant (for the earth). The actual period of oscillation proposed by these authors for a specific Schuler-adjusted system takes into account the gravity gradient, the mass distribution in the system, and the centrifugal forces due to the velocity of the carrying vehicle. This is called the actual oscillation period. The actual oscillation period of a specific Schuler-adjusted system (acceleration insensitive system) under specific circumstances is given by them as:

$$T = k \cdot 2\pi \sqrt{R/g}$$

where k will always have a value between 0.5 and ∞.

will thus change polarity. The error caused by a slow oscillation of the INS stable platform causes the two horizontal accelerometers to detect a part of the gravity vector. This false indication of acceleration is carried through the integration for velocity and produces errors in the W_E and W_N values. Distance traveled or geographical position is obtained from a second integration of the measured accelerations. Thus the Schuler oscillations will create errors in acceleration, velocity, and position. The following procedures were used to estimate the velocity errors associated with Schuler drift.

Position error can be computed from aircraft data during overflight of landmarks where exact geographical locations are known. Since acceleration, velocity, and position errors are all interrelated the Schuler error can experimentally be investigated by obtaining data on either one of the three parameters having a Schuler oscillation induced error. The velocity error is generally small but increases with time, e.g., after several hours of operation it can be on the order of 3 to 5 m/s (Rhyne, 1980; Lenschow, 1983). The magnitude of the position errors for the IV INS used in B-747 airacraft reported by Weber (1975) normally are on the order of 10 nautical miles or less even after transatlantic flights. These errors are not critical for pure navigation purposes. But, when the objective is to calculate wind velocity, the Schuler error can be quite important.

In an attempt to model in-flight Schuler error, data from Flight 63 have been analyzed. Specifics about the flight can be found in Table 1.1. A box pattern flight plan as shown in Figure 4.2 was flown sequentially at 1000 ft levels over Boulder, Colorado, in February 1984. Details of the flight and results are given in Chang and Frost (1985). Each time the B-57B flew the leg

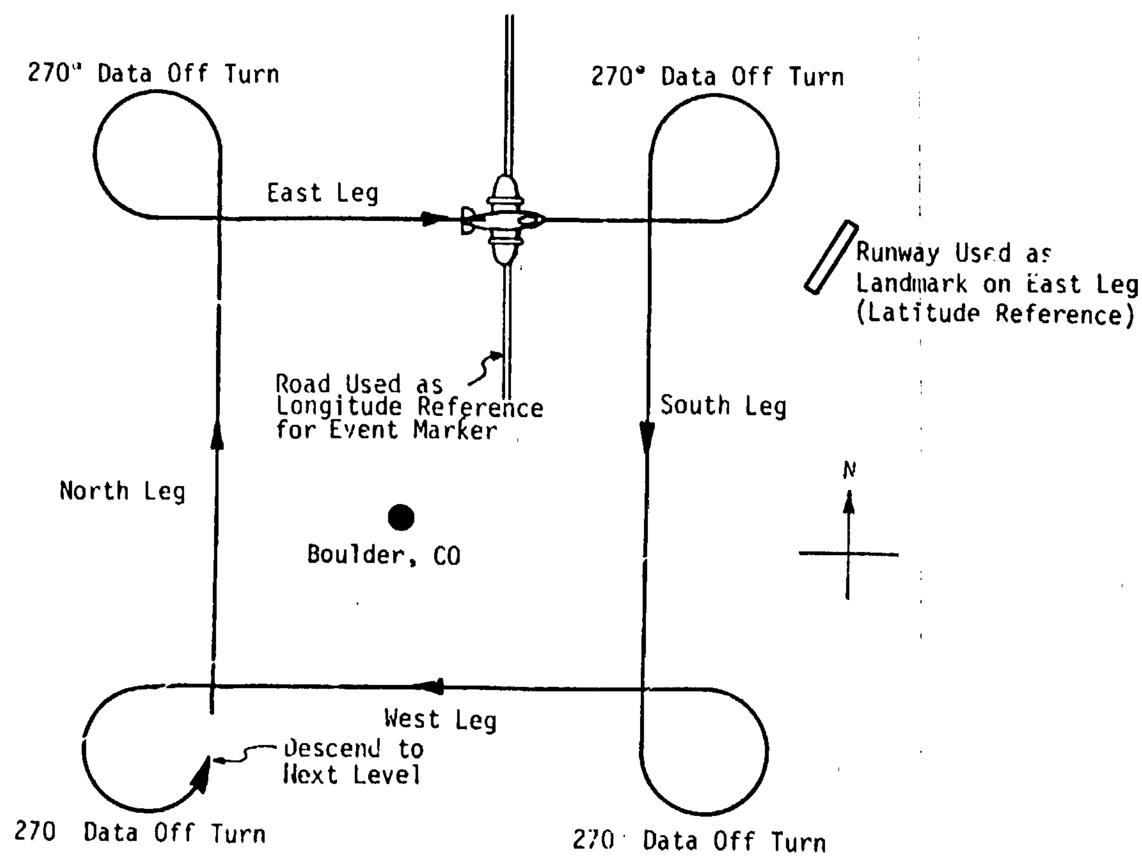

Figure 4.2. Event marker location of B-57B on box pattern flights.

heading east, an event marker on the ground was activated to record the moment a north-south running road lined up perpendicular to the flight path (see Figure 4.2). INS recorded longitude at the time of the event marker can thus be compared with the known longitude of the road to construct the Schuler position error (see Figure 4.3a). The exact latitude of the aircraft at the time of the event markers is less certain. In fact, it depends upon the ability of the pilot to fly the intended flight path. But, since the flight paths were flown toward a fixed landmark, only small deviations in the latitude position of the east test runs are expected. A similar indication of position errors has also been plotted for the latitude, Figure 4.3b. In both cases, the error appears to have a sinusoidal behavior. Curve fits by simple trial and error techniques are also plotted on the two figures. The curve fits suggest the latitude error has a 77-minute period of oscillation, and the longitude has an 111-minute period. The latitudinal period is reasonably close to the Schuler constant of 84 minutes, but the longitudinal period does not conform to that for the latitude. Since longitude and latitude errors are two components derived from the same stable platform oscillation, equal period lengths differing only by a phase angle would be expected. Thus, additional investigation of the discrepancy is needed.

Flight 66 (see Table 1.1) followed the same flight pattern as Flight 63, and the same technique for marking geographical position by event markers was used. Figure 4.4 has been constructed similarly to Figure 4.3. The dashed lines outline sinusoidal trends but are not represented by mathematical equations. The latitude oscillation in Flight 66 seems to have a period of approximately 110 minutes which is similar to the longitude oscillation of Flight 63. The longitude error of Flight 66 contains more scatter in the

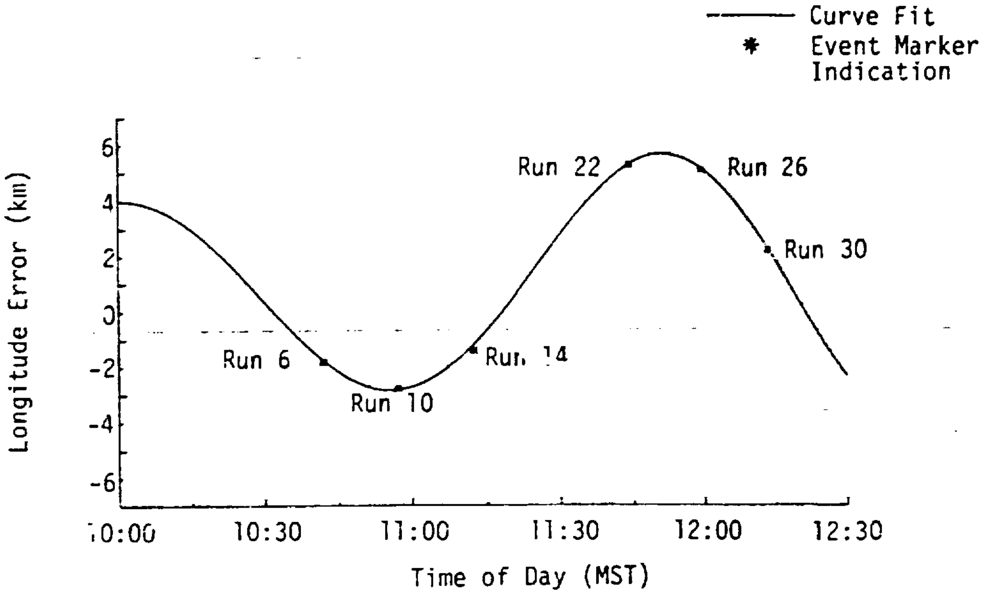

(a) Error in INS longitude indication

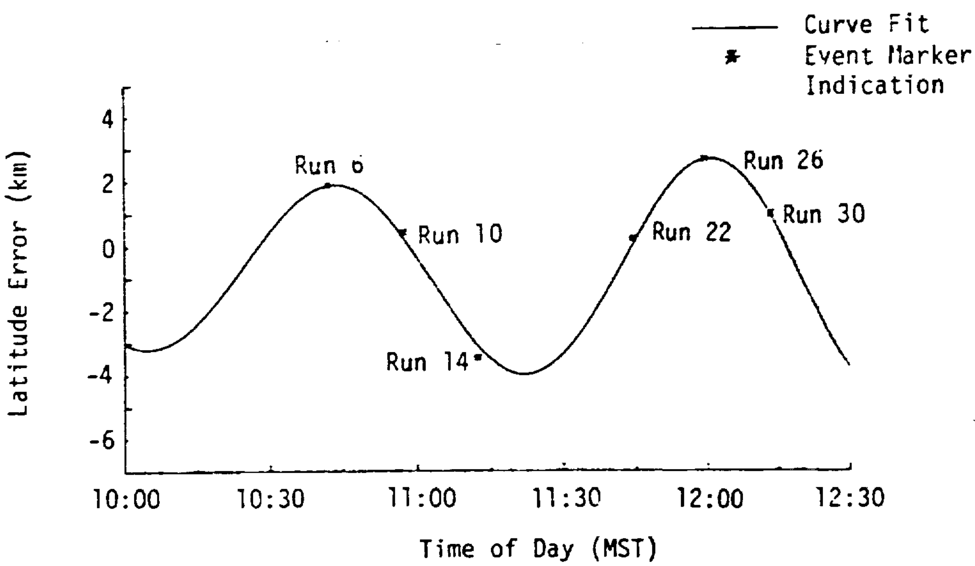

(b) Error in INS latitude indication

Figure 4.3. In-flight Schuler position error, Flight 63.

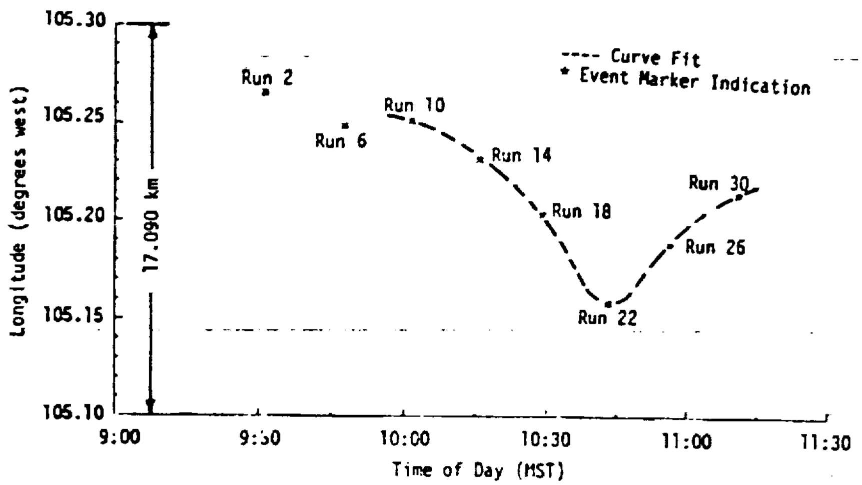

(a) Drift in INS longitude indication

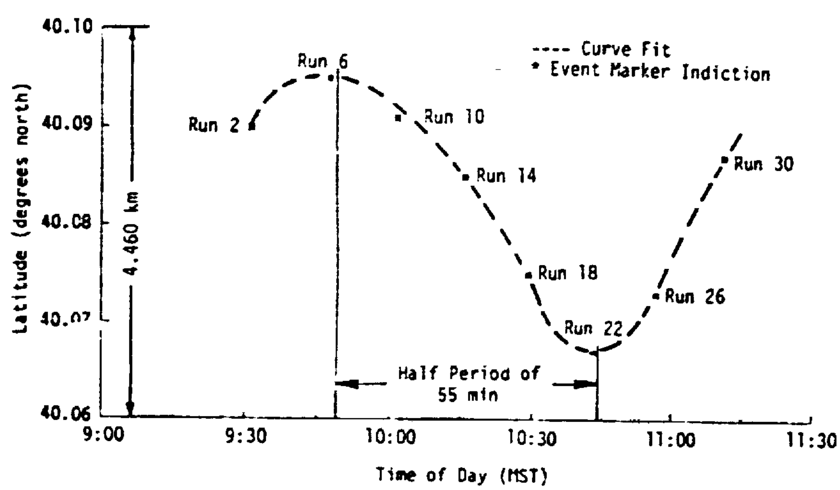

(b) Drift in INS latitude indication

Figure 4.4. In-flight Schuler position error, Flight 66.

data, although the period seems to be of roughly the same length as the latitude oscillation on this flight.

The magnitude INS position errors identified are within a range of less than 15 km or 10 nautical miles. From a commercial aircraft operation standpoint, these errors are not a large problem, particularly in the proximity of an airport where other means of navigation are available in the proximity of an airport. However, Schuler position errors are of significance for wind measurements. Exact ground tracks are needed to determine terrain effects on turbulence such as wake regions behind mountains, etc. An error on the order of several kilometers can drastically distort the picture.

The INS velocity errors are especially important in the wind measurements. Horizontal wind components are calculated based on Equations 4.1 and 4.2. As will be demonstrated, the velocity errors can be of the same order of magnitude as the wind speed, which will greatly alter the calculation of the wind vector. An estimate of these errors is presented in Figure 4.5. The velocity error curves are calculated by taking the derivative of the position error curve fits illustrated in Figure 4.3. The magnitude of the velocity errors determined is within the range of that quoted in the literature (Rhyne, 1980; Lenschow, 1983). The influence of these errors is demonstrated in Sections 4.7 and 4.8.

To further investigate the Schuler error Flights 73 and 74 were carried out where the aircraft was tracked by the NASA EPS-16 #34 tracking radar. The radar track provided the location and the ground speed of the aircraft throughout the flight. The investigation of Schuler velocity errors for Flight 73 and 74 has not been completed due to the late reception of flight data for Flight 73 and of the need to correct the radar tracking. However,

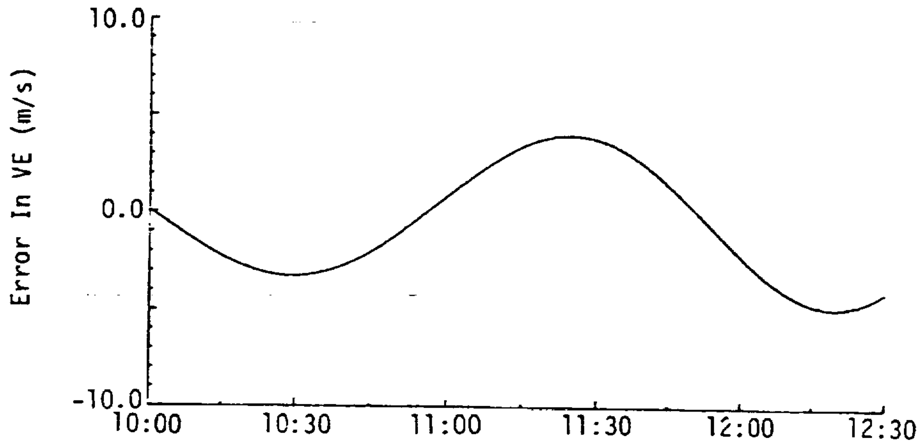

(a) East inertial speed error

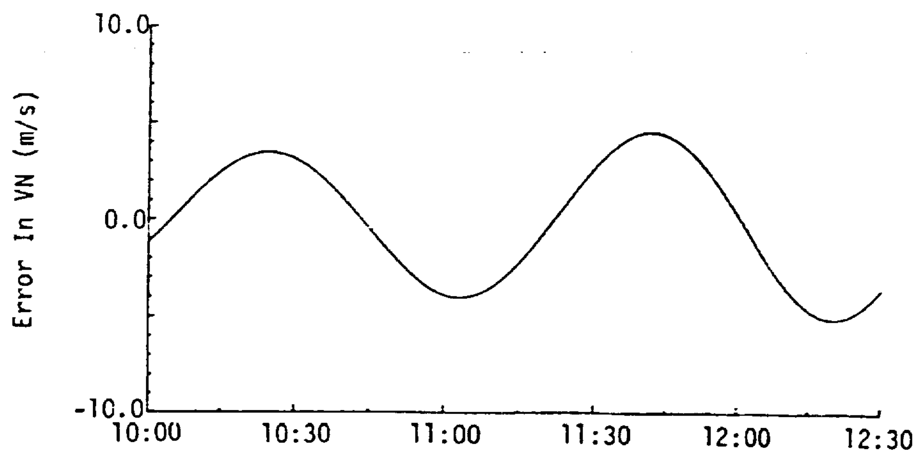

(b) North inertial speed error

Figure 4.5. In-flight Schuler inertial speed error, Flight 63.

data on post-flight Schuler velocity errors recorded on the ground have been received from NASA/LaRC along with data from Flight 74. The north-south and east-west velocity errors of Flight 74 and the ensuing post-flight velocity measurements are plotted in Figures 4.6 and 4.7. The in-flight velocity errors are obtained by comparing aircraft and radar data assuming the radar indications are free of error. The data recorded on the ground is a direct measure of the indicated velocity from the INS while the aircraft was parked and hence not moving. This velocity fluctuation is attributed to the Schuler error. The INS was left on during the entire time span covered in the plots. The magnitude of the errors are within expected limits. Both figures show one complete cycle of a near perfect 84-minute Schuler oscillation in the post-flight data in the latter part of the test period. This is in keeping with Huber and Bogers (1983) who noted that near the ground without accelerations involved the Schuler oscillations will have an 84.4-minute period. But, in the first half of Flight 74 the errors are more random in their behavior and the oscillation is an irregular period. This complicates attempts to model or predict the error in advance. Lenschow (1972) suggests that post-flight data recorded with a stationary aircraft be used to back out the error. He proposed to simply trace back a recorded post-flight error oscillation with an 84-minute period constant amplitude sinusoidal curve. The present study shows, however, that both the period and the amplitude of the velocity error are altered substantially during flight and thus the Lenschow (1972) approach would not be successful here. This observation is in keeping with Huber and Bogers (1983) physical description of the Schuler effects. Additional investigation of Flight 74 is needed to determine if the INS errors are accurately described in Figures 4.6 and 4.7. While the inertial velocity

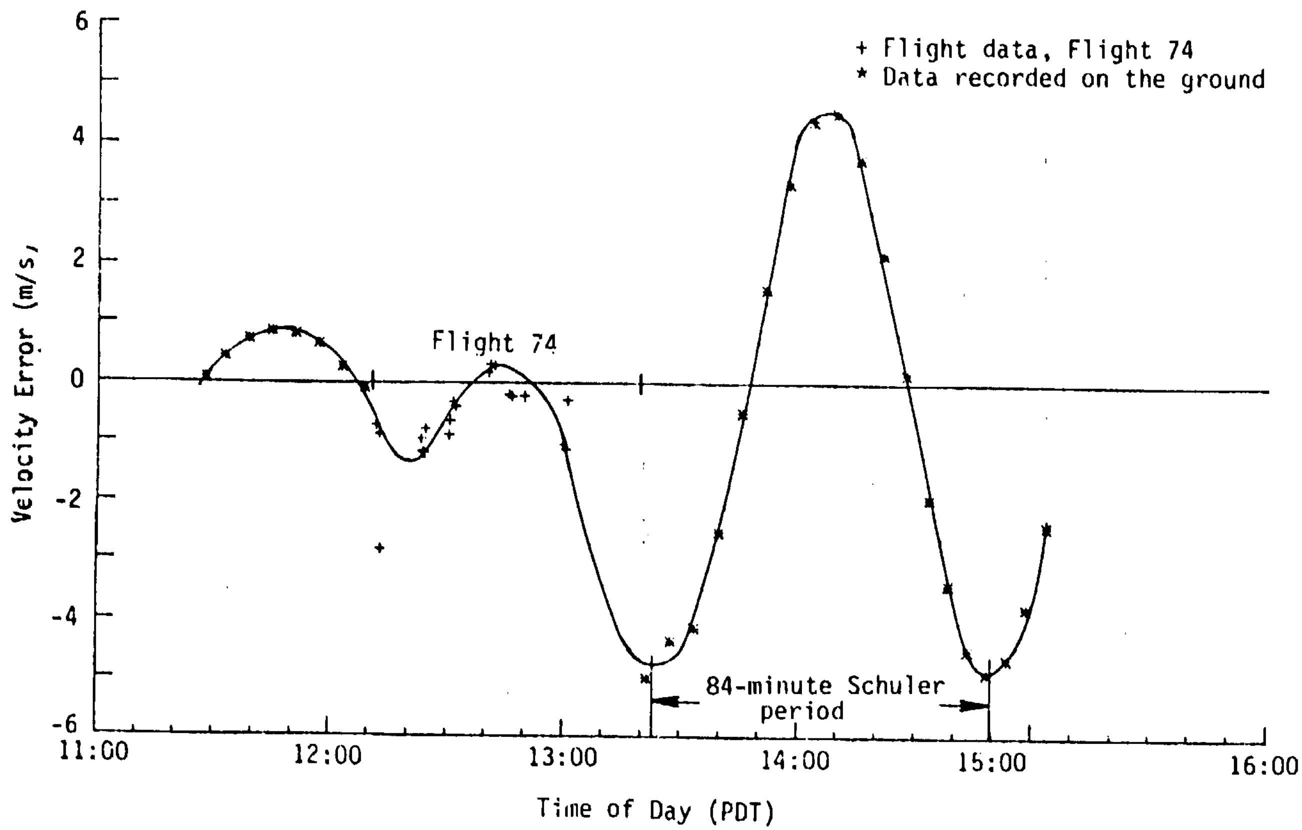

Figure 4.6. Error in east inertial speed on Flight 74.

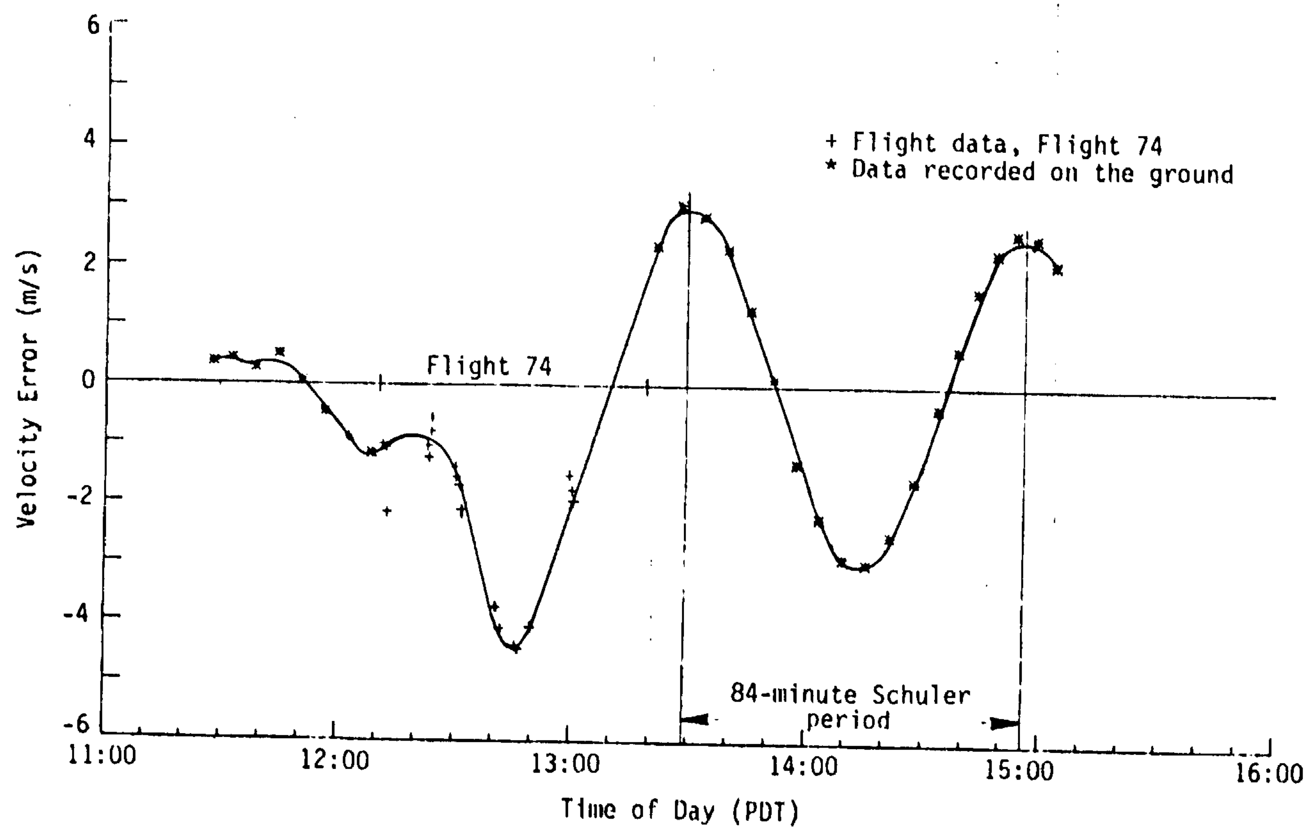

Figure 4.7. Error in north inertial speed on Flight 74.

measurement errors strongly influence the horizontal wind vector calculations, they generally have little effect on the gust velocity computations because the effect of the slow variations in velocity is greatly diminished or eliminated when the average velocity is removed.

4.5 Flow Vane Errors

Ringnes and Frost (1985) observed in analyzing the B-57B data that constant differences existed between the angles of attack measured at the three different stations along the wing. The constant offset from the true value again has little influence on the computed turbulence since the mean value is removed during the computation. The angle of attack terms have negligibly small effect on the computed values and therefore the inaccuracies cause no problems of the total horizontal wind vector. The cause of the angle of attack difference, however, were attributed to misalignment of the wing tip booms.

The average sideslip angles were also found to be different from the expected value. All aircraft are designed directionally stable and will fly with zero average sideslip angle unless forcefully kept in a sideslip flight condition. The average sideslip angle of 2.23 degrees, for example, recorded at the centerboom on Flight 63 is therefore attributed to error. The source of the error is not clear but boom misalignment or problems with the data acquisition system are suspected causes. Again, the average sideslip error is removed in the turbulence calculations, but it does affect the computed value of the horizontal wind vector noticeably as will be demonstrated.

4.6 Airspeed Errors

Frost, et al. (1985a) observed a difference in airspeed measured by the three separate wing probes. They compared average values for all runs on

Flight 21 and reported an average difference between the right and center boom measured velocites of 1.82 m/s. The difference between the right and left wing tip measured airspeed was 0.79 m/s. The overall averaged airspeed was about 105 m/s. In Flight 31, the airspeed difference between the right and left probes is 0.3 m/s at an average airspeed of 102 m/s. The accuracy of the horizontal wind vector calculations depends upon the quality of airspeed measurements. Possible instrument calibration, position errors, or conversion from indicated to true airspeed can cause these inaccuracies. Also, the lack of separate static pressure transducers at the wind tips could have contributed to the inconsistances. A test flight conducted with the B-57B also revealed a value of horizontal wind speed of 2.5 m/s lower at the center boom than at the wing tip booms at a relative airspeed of roughly 122 m/s (Ehernberger, 1987). An approximate analysis based on a potential flow solution for a Rankine body (Karamcheti, 1966) predicted a 6 percent error. This is expected to be high because the B-57B is a more streamlined body than a Rankine body, but the results do support the hypothesis that the airspeed may be retarded sufficiently by the aircraft body to produce the relative airspeed difference a boom's length from the nose. This 2 percent error is accounted for in the following investigation of the influence of instrumentation errors on horizontal wind calculations.

4.7 Gust Velocity Corrections

The only instrumentation errors of those reported above which would noticeably effects the gust velocity calculation based on inspection of Equations 4.5, 4.6, and 4.7 is airspeed. The magnitude of correction to the gust velocities due to airspeed corrections is illustrated in Figure 4.8. Uncorrected turbulence is plotted directly from the tapes received from NASA

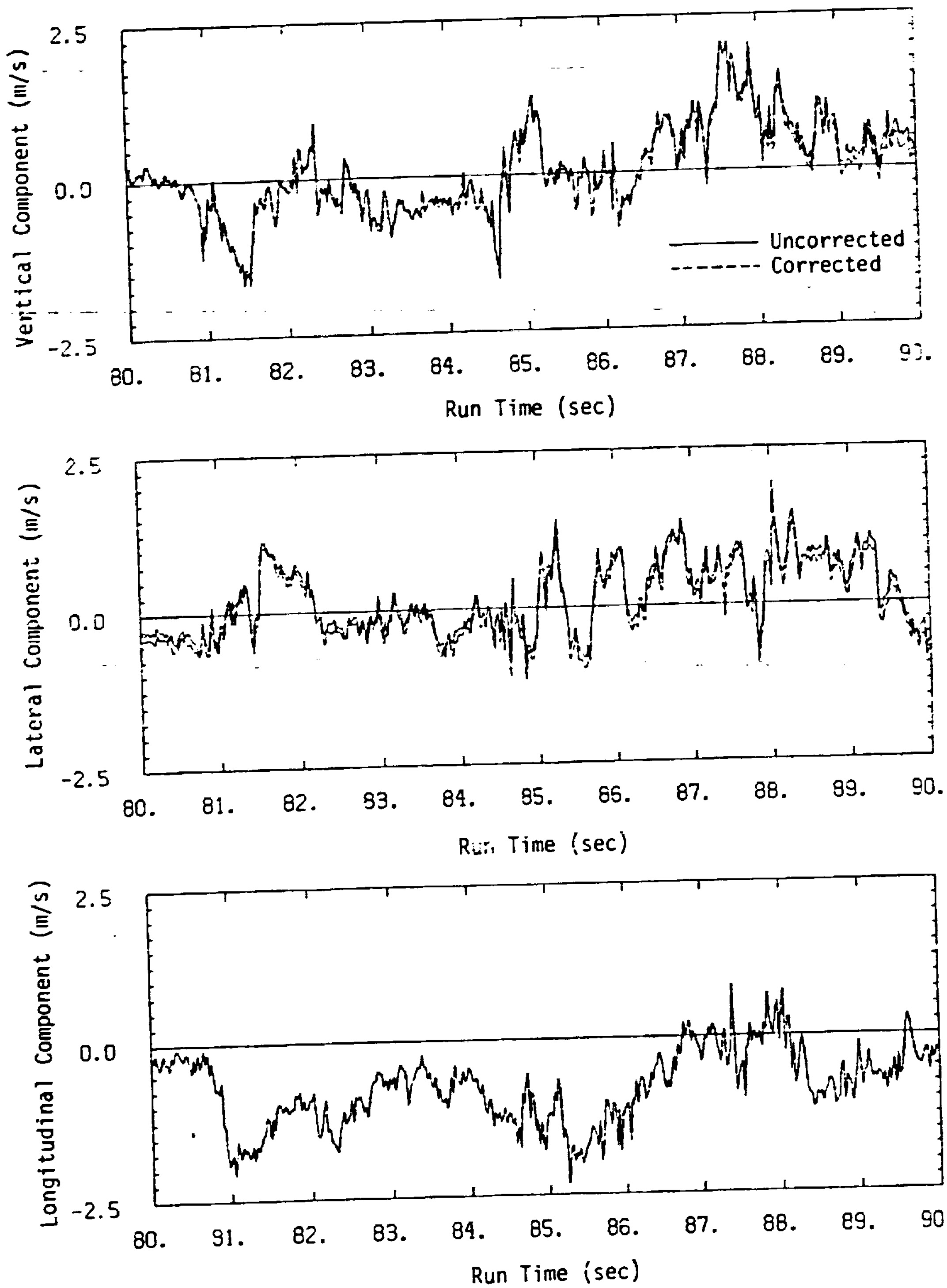

Figure 4.8. Effect of instrumentation errors on the three turbulence components on Flight 63, Run 16.

Langley Research Center. The "corrected" turbulence has been computed with the predicted inertial velocity, airspeed, and sideslip angle errors removed. The differences between the two computations are small and only detectable for the lateral and vertical components where total airspeed enters the Equations 4.5 and 4.7. It is apparent that even the airspeed error is of little significance in gust velocity calculations.

4.8 Horizontal Wind Vector Correction

The INS velocity and position indication, sideslip angle, and airspeed errors identified as described above have been removed from the recorded data on some runs of Flight 63. The influence these errors have on the calculation of horizontal winds are demonstrated in this subsection. A series of wind vectors are plotted before and after corrections have been made along the flight path recorded by the INS. Each vector represents a one-second average from the 40 samples per second data tapes.

In Figure 4.9 one of the box patterns flown on Flight 63 is plotted. In this figure, no corrections have been made. There are some obvious inconsistencies in the wind vectors, particularly, at the corners where it is expected that the wind would agree closer between the two runs. The aircraft made 270-degree turns between runs which take less than two minutes. The wind direction is not expected to change significantly during that short of an interval. Instrumentation errors are, therefore, the probable cause for the discontinuities in wind direction. Figure 4.10 differs from Figure 4.11 only by removal of the 2.23-degree sideslip error in the calculation of the wind vectors. It is debatable whether this correction alone has improved the wind vectors but it clearly demonstrates that seemingly small errors have significant effect on the wind vectors. In Figure 4.11 corrections have been

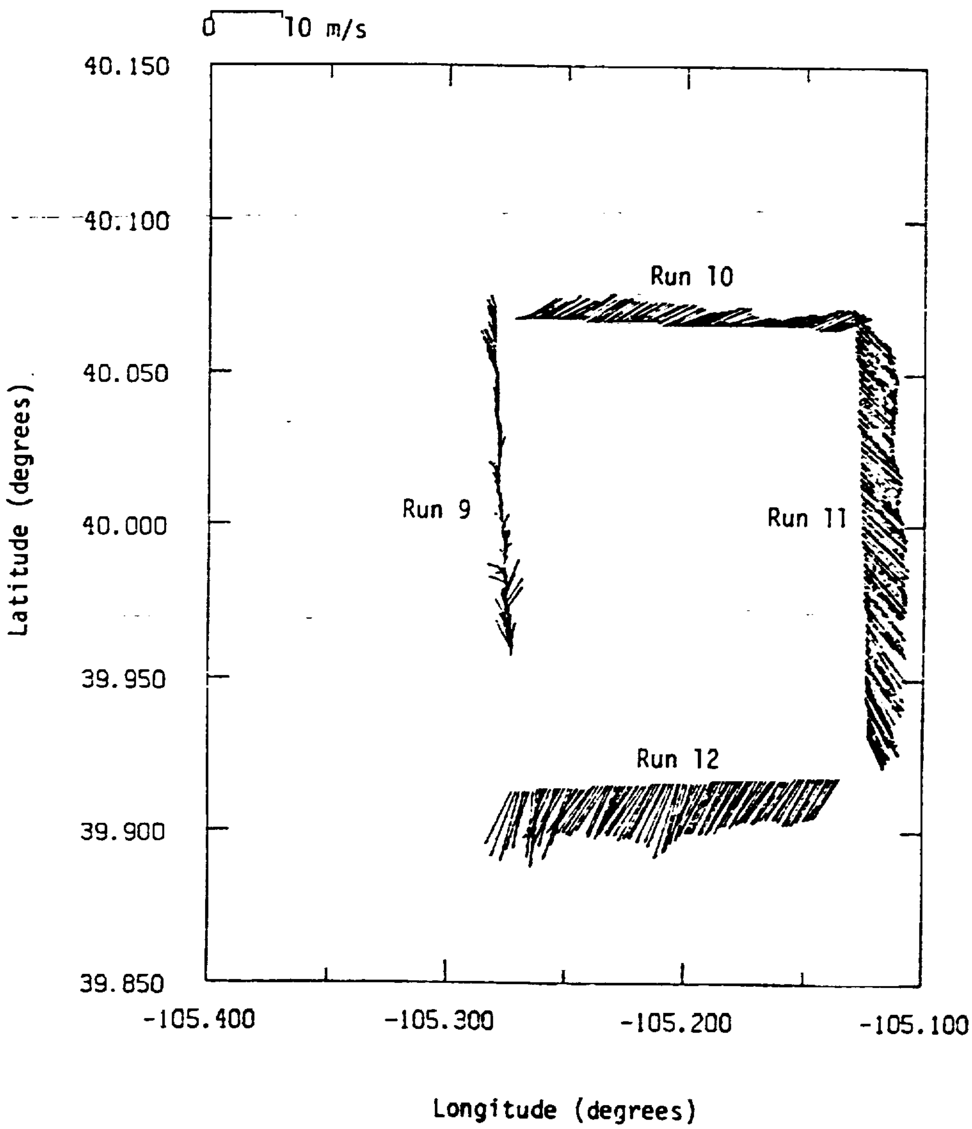

Figure 4.9. Horizontal wind vectors on Flight 63 without corrections (Runs 9 through 12).

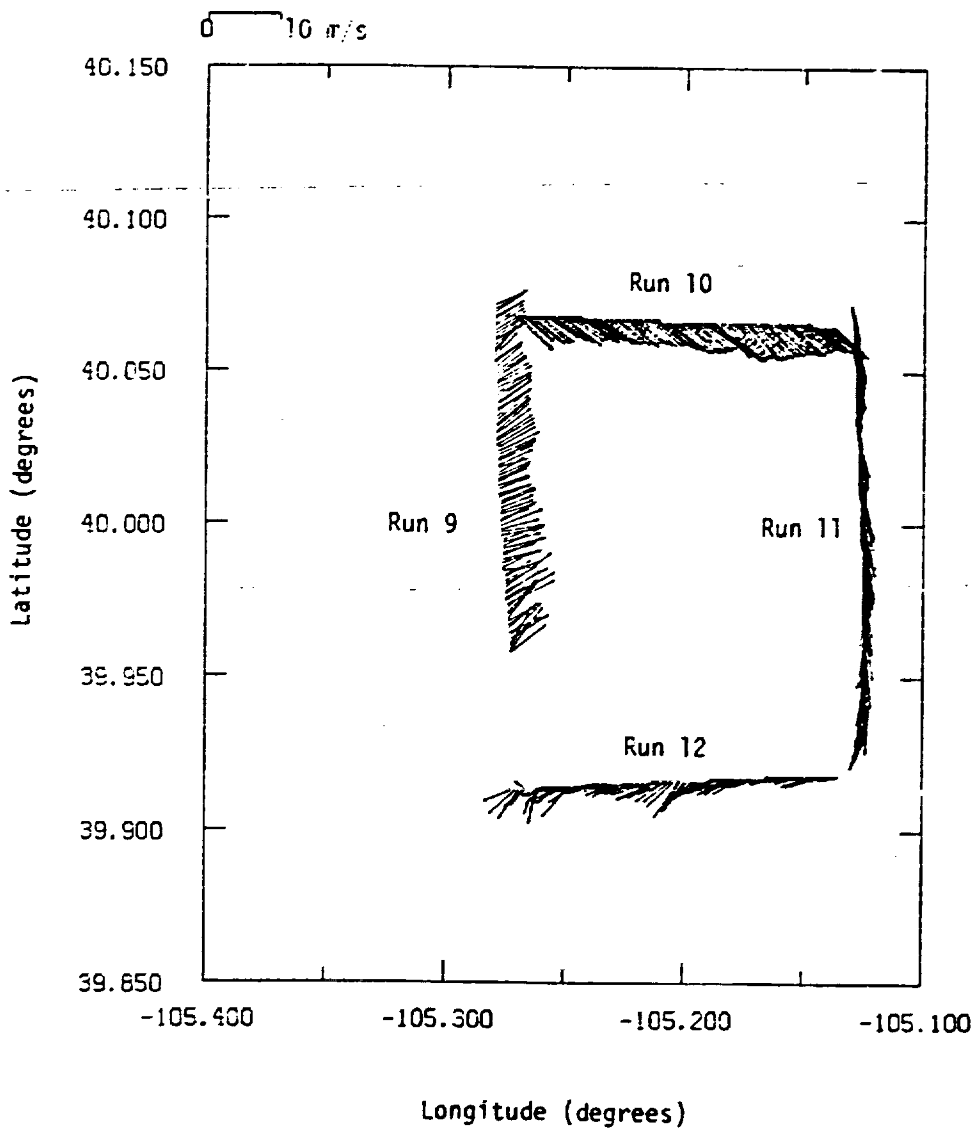

Figure 4.10. Horizontal wind vectors on Flight 63 with beta corrections (Runs 9 through 12).

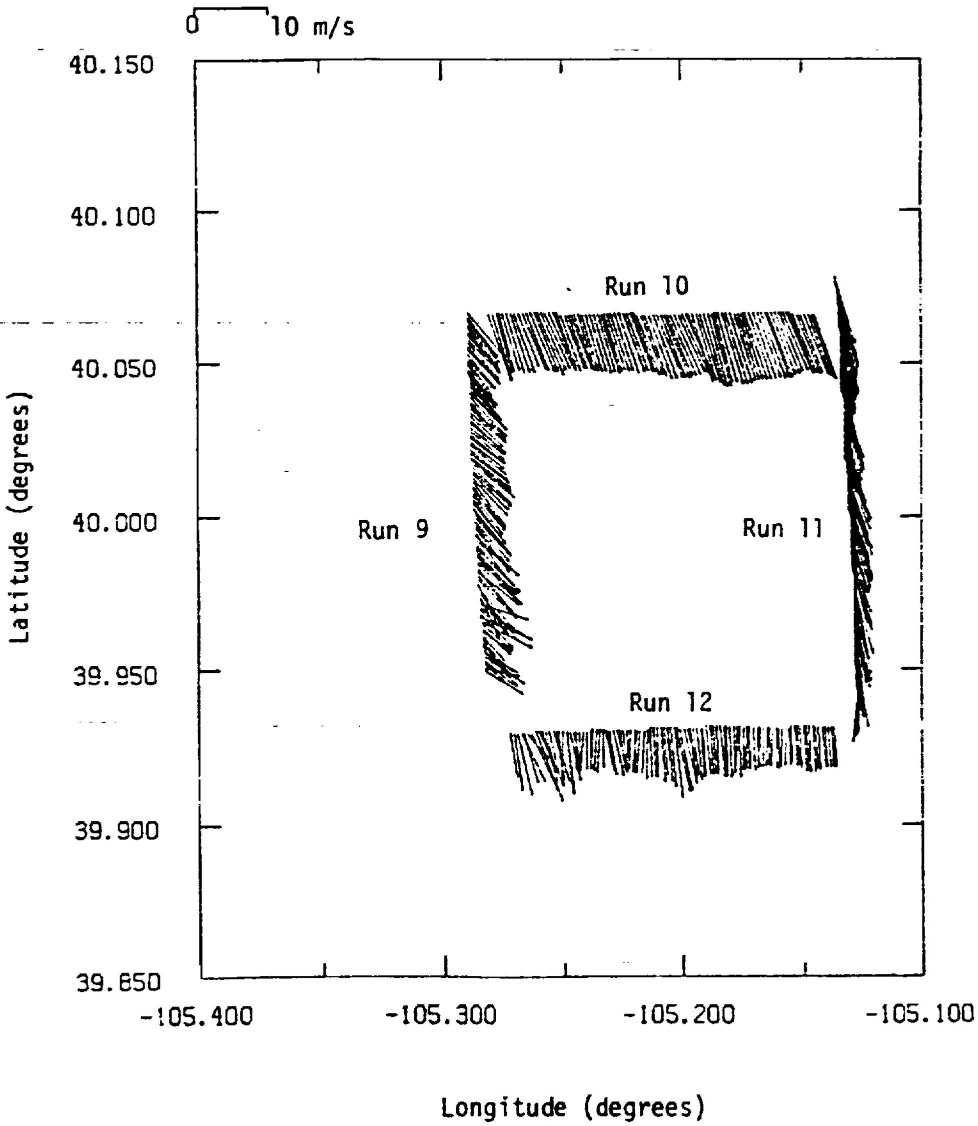

Figure 4.11. Horizontal wind vectors on Flight 63 after airspeed, beta, and inertial velocity and position corrections (Runs 9 through 12).

made for the known errors. The discontinuities in the wind vectors at the corners have all but vanished except for the bottom left-hand corner. However, as the numerical order of the runs indicates the box pattern was flown in a clockwise direction; thus, the beginning of Run 9 and the end of Run 12 are separated in time by approximately 15 minutes. Therefore, it is conceivable that the wind could have changed in that time span. The position errors are not severe for this box pattern but still noticeable.

Figure 4.12 is similar to Figure 4.9 except Runs 13 through 16 on Flight 63 have been plotted. No corrections have been made. Only the discontinuities in the direction of the wind in the upper left-hand corner and in the magnitude of the wind in the upper right-hand corner appear questionable. Figure 4.13 illustrates the effect of removing the errors on wind vectors and INS indicated locations. The horizontal wind vectors are more consistent and also the location of the runs are in better agreement with the flight plan.

A third box pattern on Flight 63 (Runs 17 through 20) does not show the same improvement with corrections. Figure 4.14 shows the uncorrected wind vector and Figure 4.15 the corrected version. The INS indicated location is improved but not the wind vectors. After correction, the wind directions on Runs 18 and 20 are in sharp contrast to each other and additional or better corrections are needed.

4.9 Effects of Non-Level Flight

The algorithms used by NASA Langley computer facility to compute the turbulent gust velocities from the measured aircraft data are based on the assumption of straight, level flight. The more complete generalized system of equations which will allow for departure from level flight are derived in Appendix B. Questions arose during the study as to whether those portions of

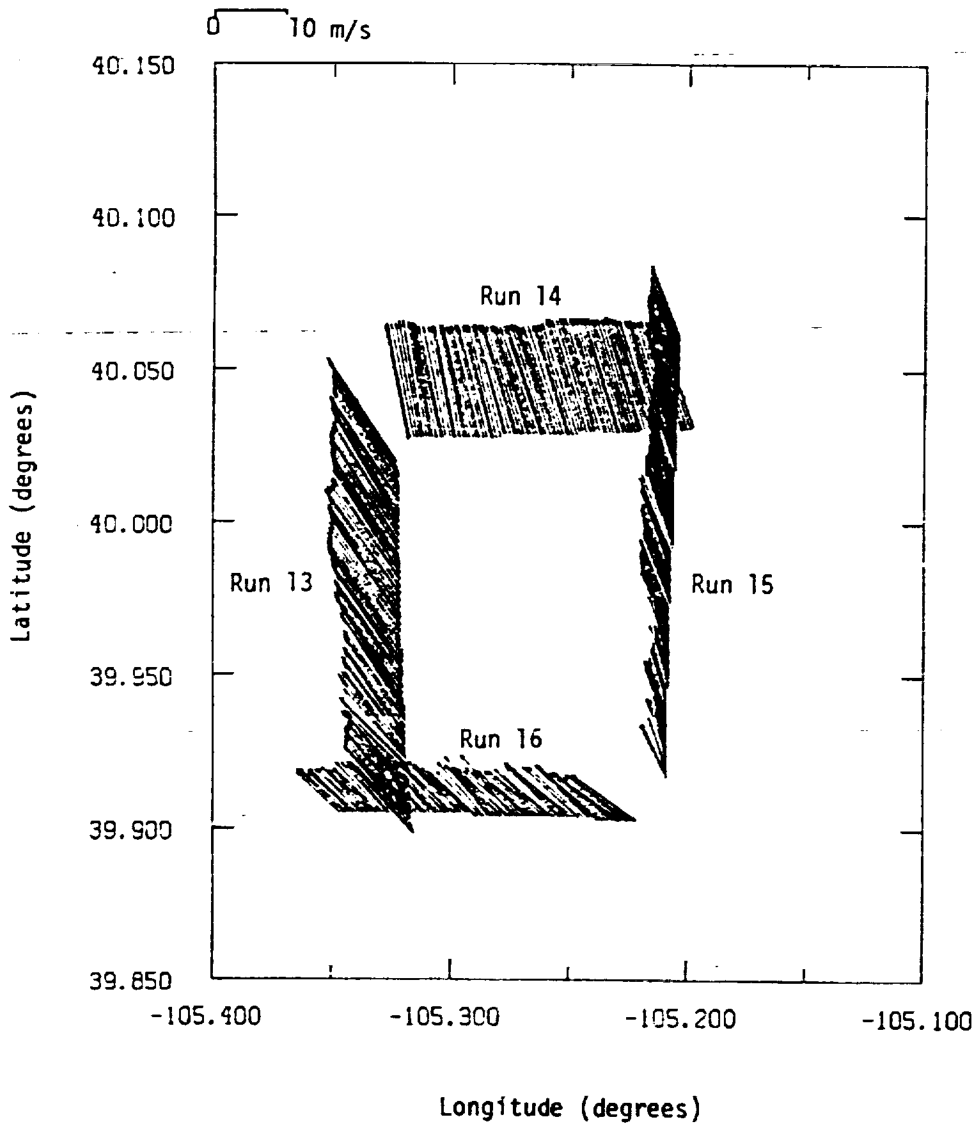

Figure 4.12. Horizontal wind vectors on Flight 63 without corrections (Runs 13 through 16).

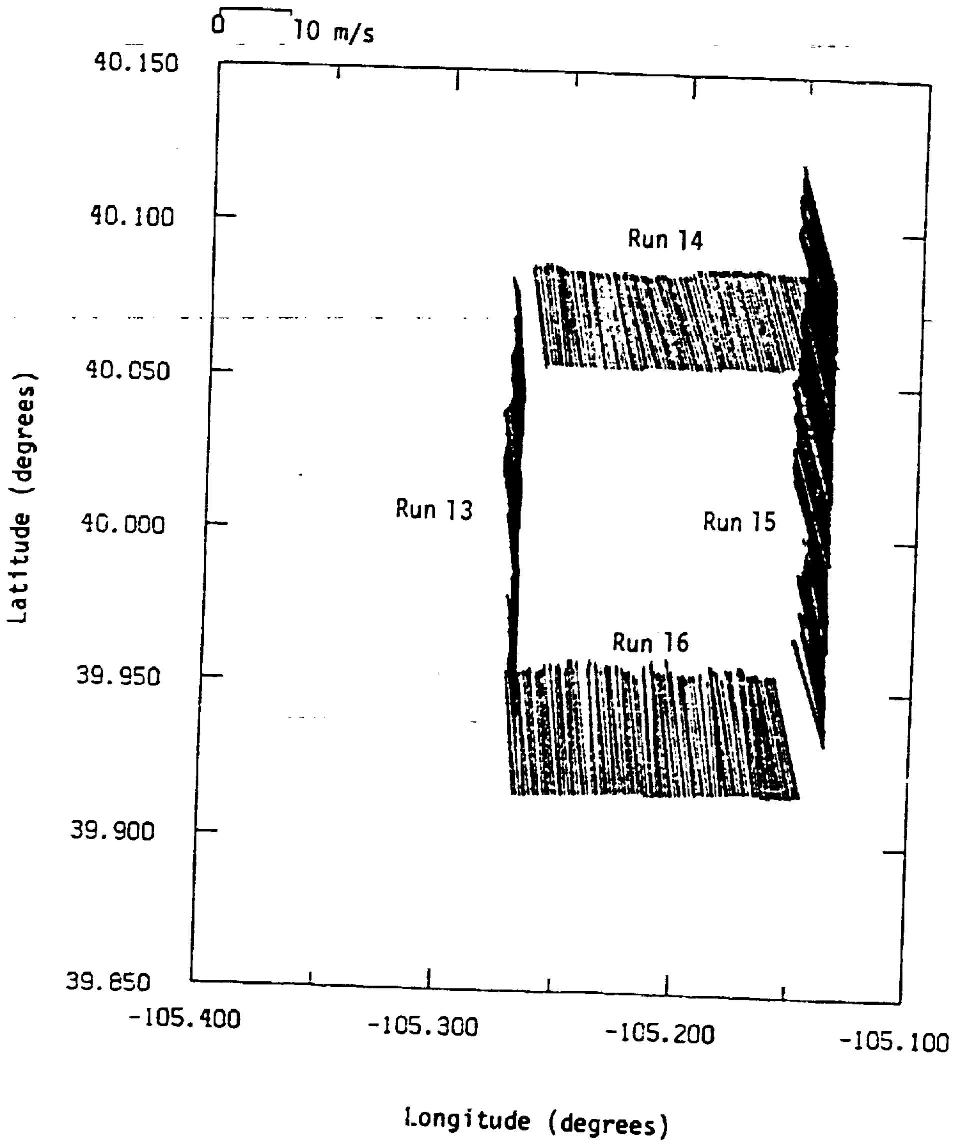

Figure 4.13. Horizontal wind vectors on Flight 63 after airspeed, beta, and inertial velocity and position corrections (Runs 13 through 16).

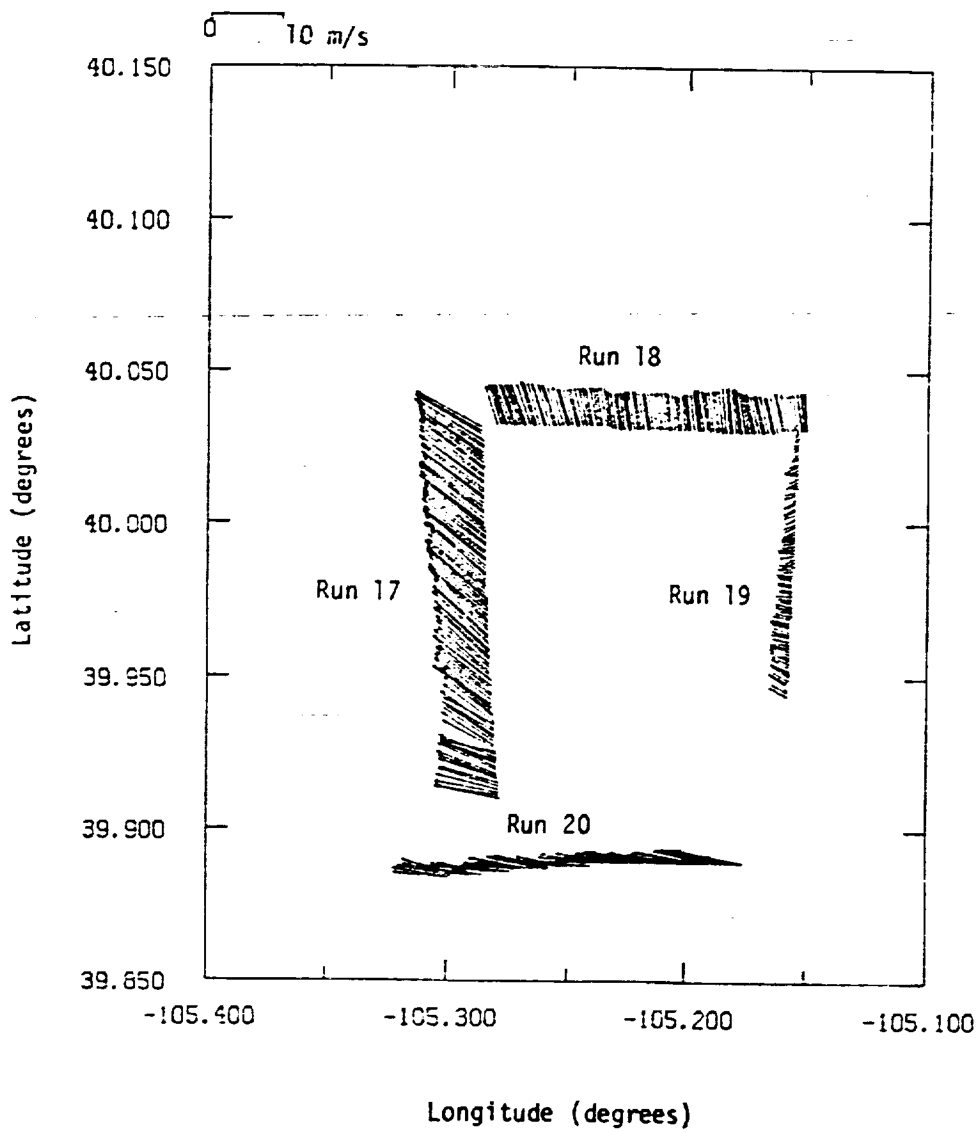

Figure 4.14. Horizontal wind vectors on Flight 63 without corrections (Runs 17 through 20).

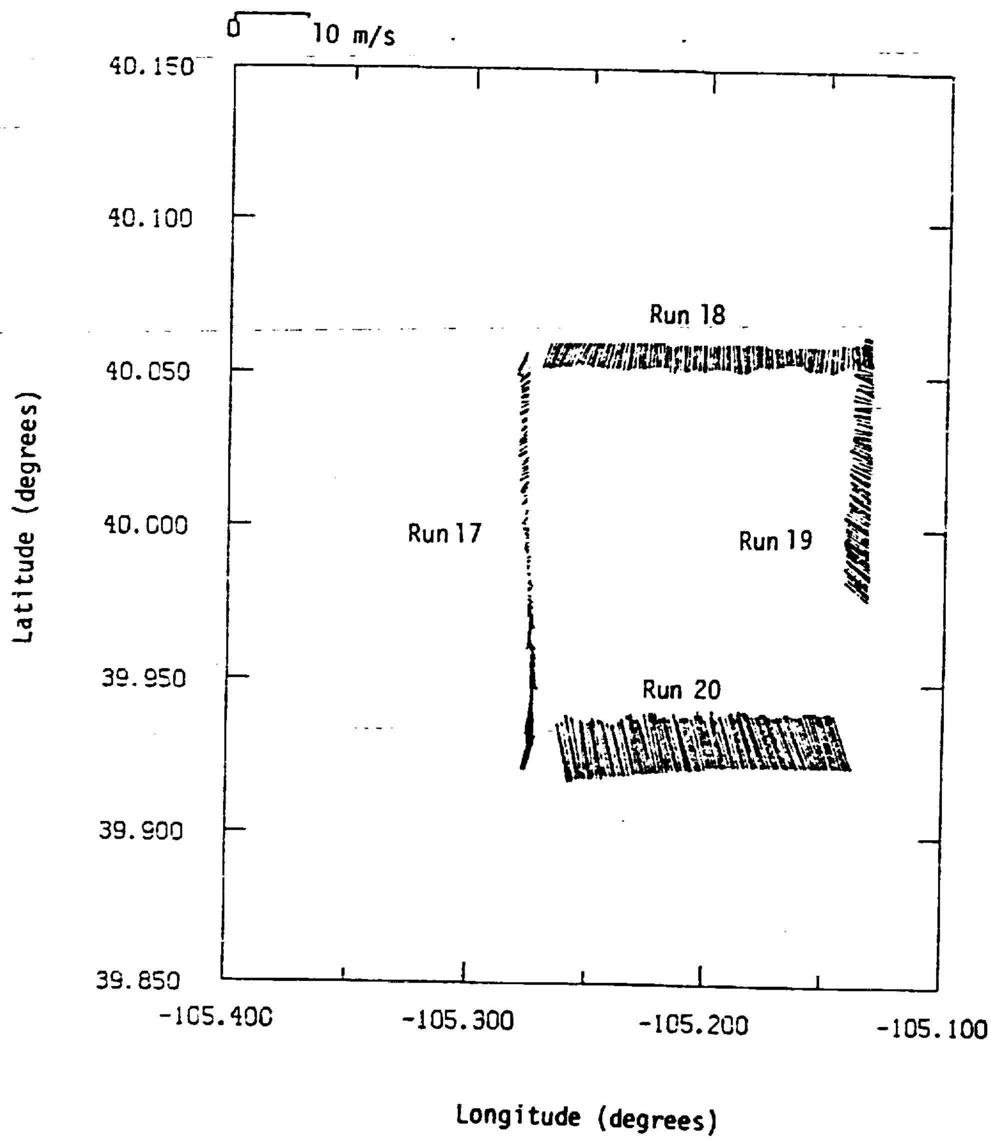

Figure 4.15. Horizontal wind vectors on Flight 63 after airspeed, beta, and inertial velocity and position corrections (Runs 17 through 20).

flights for which the aircraft climbed or descended should be removed from the data. For example, during Run 3 at approximately 536 seconds (34 miles) into the flight the aircraft climbed approximately 1000 ft (see Figure A.11). In turn, during Flight 9 the aircraft climbed roughly 1000 ft beginning at t = 80 seconds (7 miles) and descended again at t = 135 seconds (8.4 miles), see Figure A.41. Also, Runs 1 and 2 where the aircraft took off or made touch-and-go's. This section shows that algorithms to reduce the data based on small angles and perturbations have no significant effect on the computed turbulence for runs where departures from straight and level flight occur.

First it should be noted that because of the exaggerated vertical scale in, say for example, Figures A.11, A.41, and all other plots of this nature given in Appendix A, the departure from level flight appears to be severe. It should be noted, however, that in no cases is the climb or descent angle greater than 7°. This size angle adequately satisfies the small angle requirement defined in the algorithms presently used in the data reduction process. However, this statement is further supported by quantitative analyses in the following.

To investigate the effects of climb and descent angles on the computed gust velocities, Equation B.27, which are used in the NASA Langley algorithms and Equation B.15 which FWG has derived and programmed to investigate the effect of "large angles" where compared. The FWG equation still assumes the mean roll angles, $\bar{\phi}$, is zero. Equation B.27 was programmed and the turbulence time histories at central probe for the descending ($\bar{\theta}$ = -2.83°) and climbing ($\bar{\theta}$ = 2.9°) segments of Run 2 were computed separately. Figure 4.16 shows the comparison of the descending segment. Figures 4.16a, 4.16b, and 4.16c are for the longitudinal (u), lateral (v), and vertical (w) components, respectively.

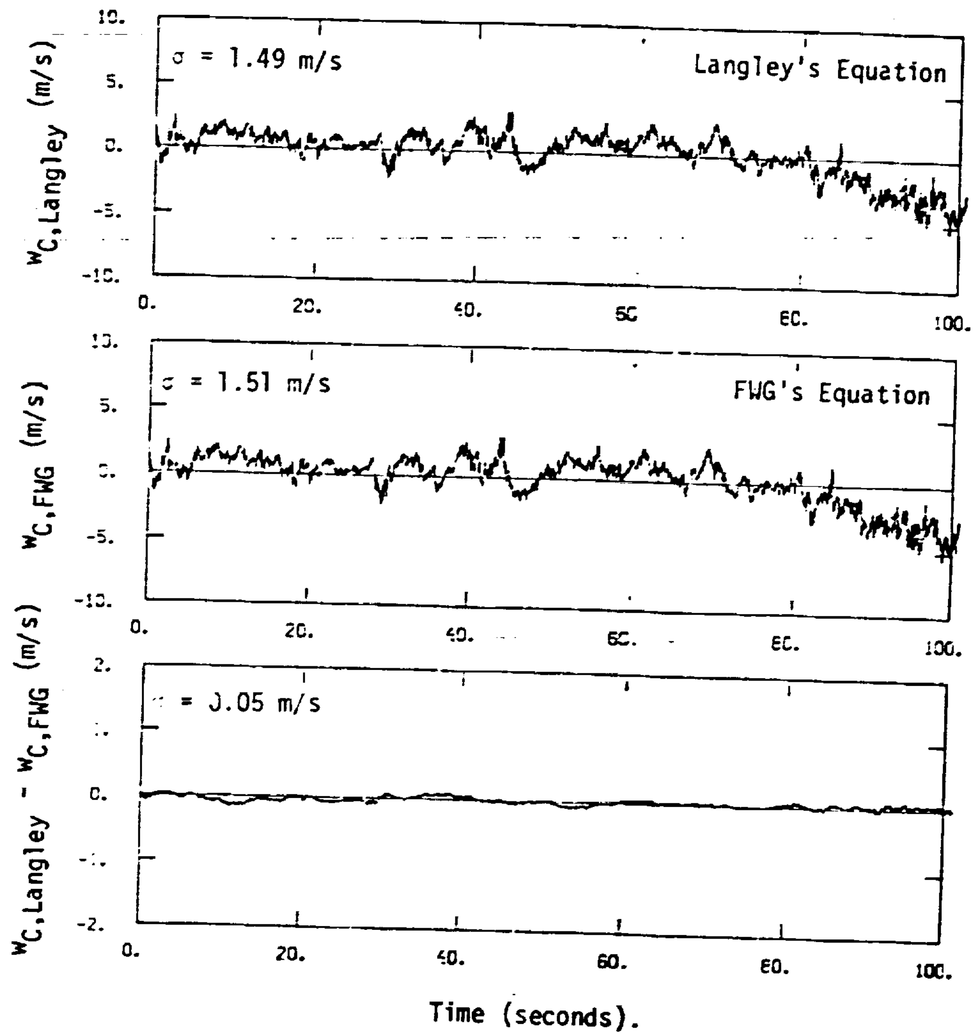

(a) Longitudinal Component

Figure 4.16. Comparison of turbulence time histories calculated from NASA Langley's equation and FWG's equation (descending segment of Run 2; Flight 31).

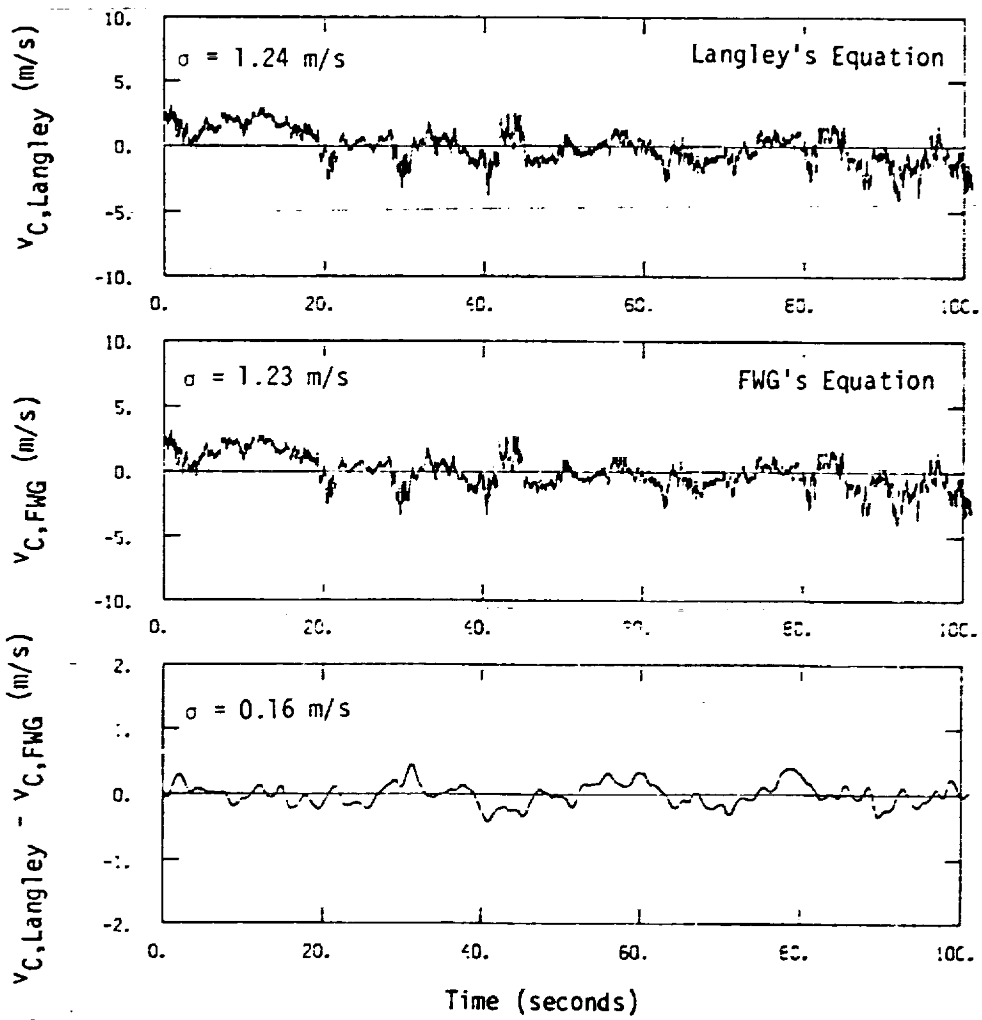

(b) Lateral Component

Figure 4.16. (cont'd).

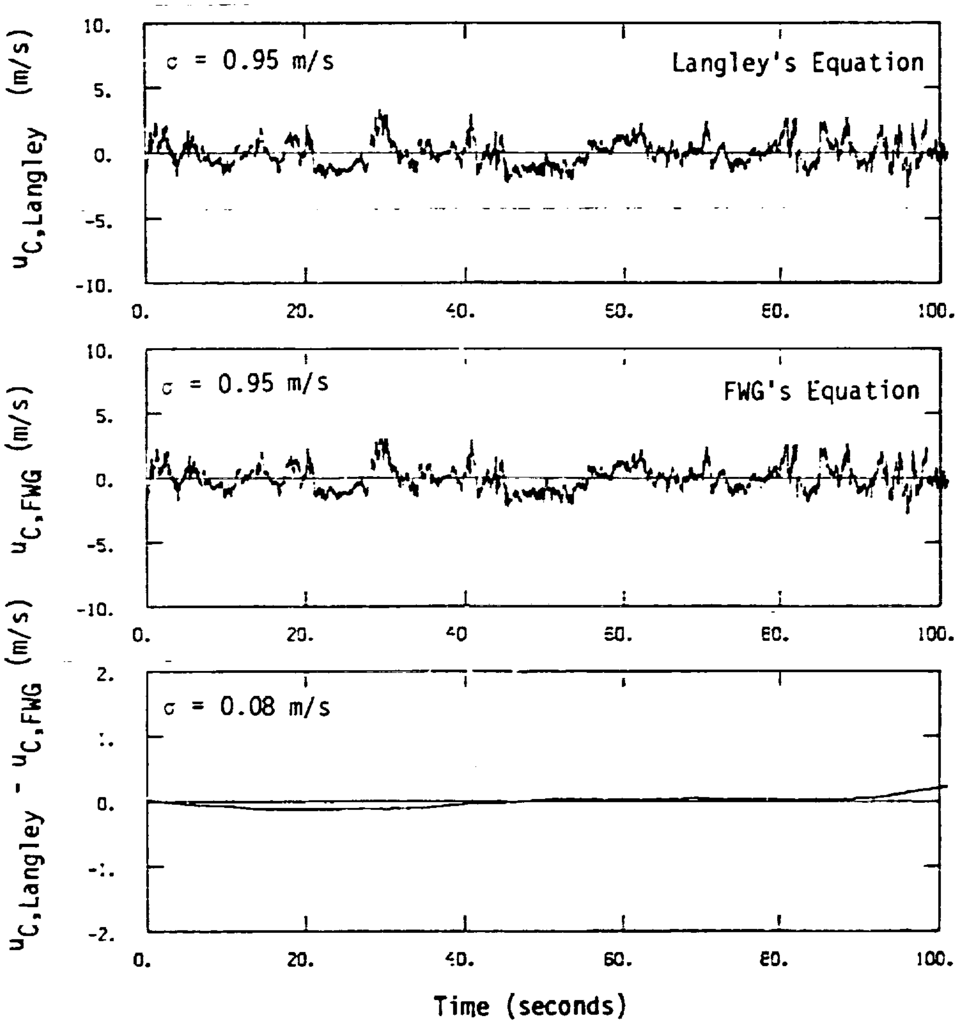

(c) Vertical component

Figure 4.16. (cont'd).

The standard deviation of each time history is also shown in the figure. Similar comparison for the climbing segment is shown in Figure 4.17. An abnormal spike occurs in the lateral turbulence component at t = 201 seconds. It is believed that the attitude of the aircraft at this moment probably deviated from the small angle assumptions significantly. Therefore, the maximum difference of the turbulence calculations from Equations B.15 and B.27 occurs at this point. Although the complete equation (Equation B.15) calculates turbulence more accurately, Equation 3.27 saves a lot of computer time and still holds an acceptable accuracy for small angles considered here. For all practical purposes, the two calculations will introduce only negligible difference in the turbulence analyses presented in this report.

To further investigate the departure from level flight, the turbulence time history for Flight 3 was divided into two segments. Segment 1 is from 0 to 512 seconds (0 to 32 miles) and segment 2 from 512 to 691 seconds (32 to 44 miles). The turbulence statistics were computed for the total run and for each segment individually. The spectra for the two individual legs of the flight are compared with the total run in Figure 4.18; no apparent difference is observed. The turbulence intensity for each segment of the flight are listed in Table 4.1. Difference in turbulence intensity for each leg of the flight are apparent. These differences, however, are not attributable to departure from level flight but rather due to patchiness of the turbulence associated with terrain features beneath the flight path. Figure 4.19 shows the turbulence time history and the approximate location relative to the underlying terrain at which the measurement was made. This figure, in view of the fact that the mean wind is essentially out of the plane of the paper at approximately 15°, clearly suggests that strong turbulence is associated with

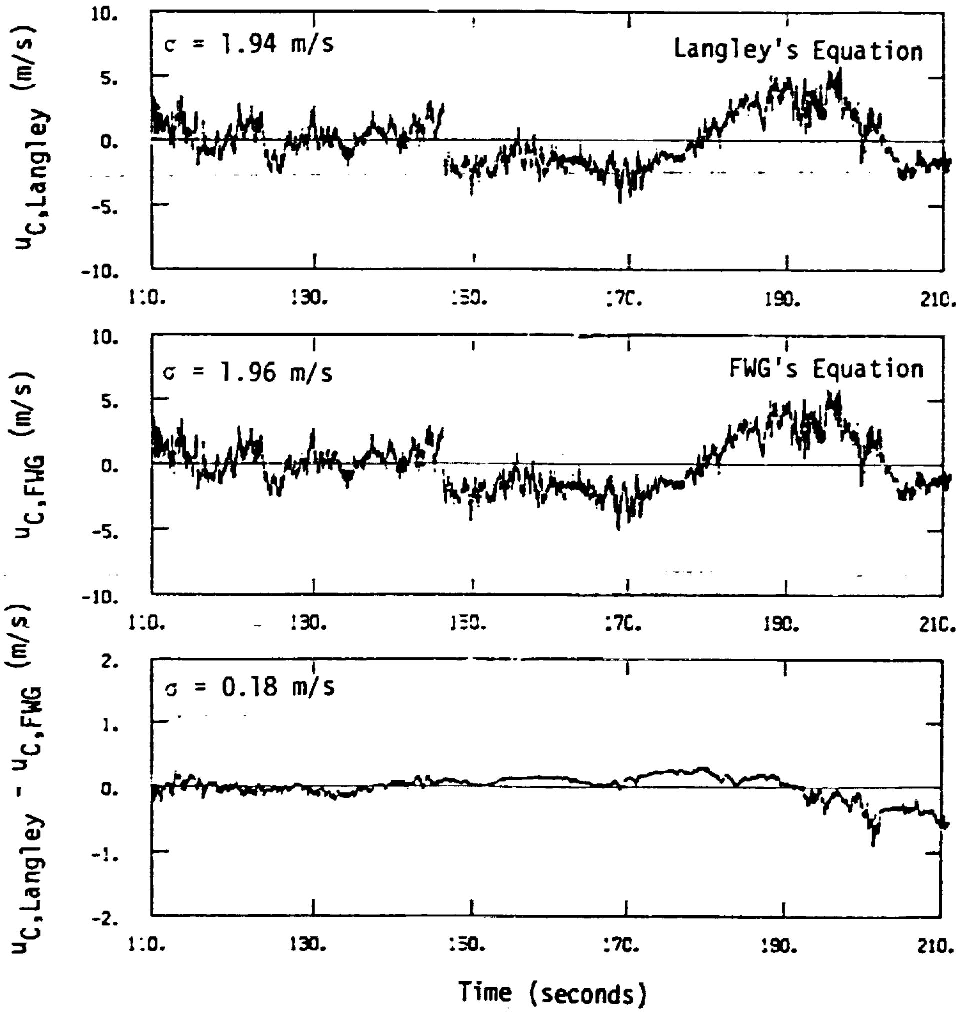

(a) Longitudinal Component

Figure 4.17. Comparison of turbulence time histories calculated from NASA Langley's equation and FWG's equation (climbing segment of Run 2; Flight 31).

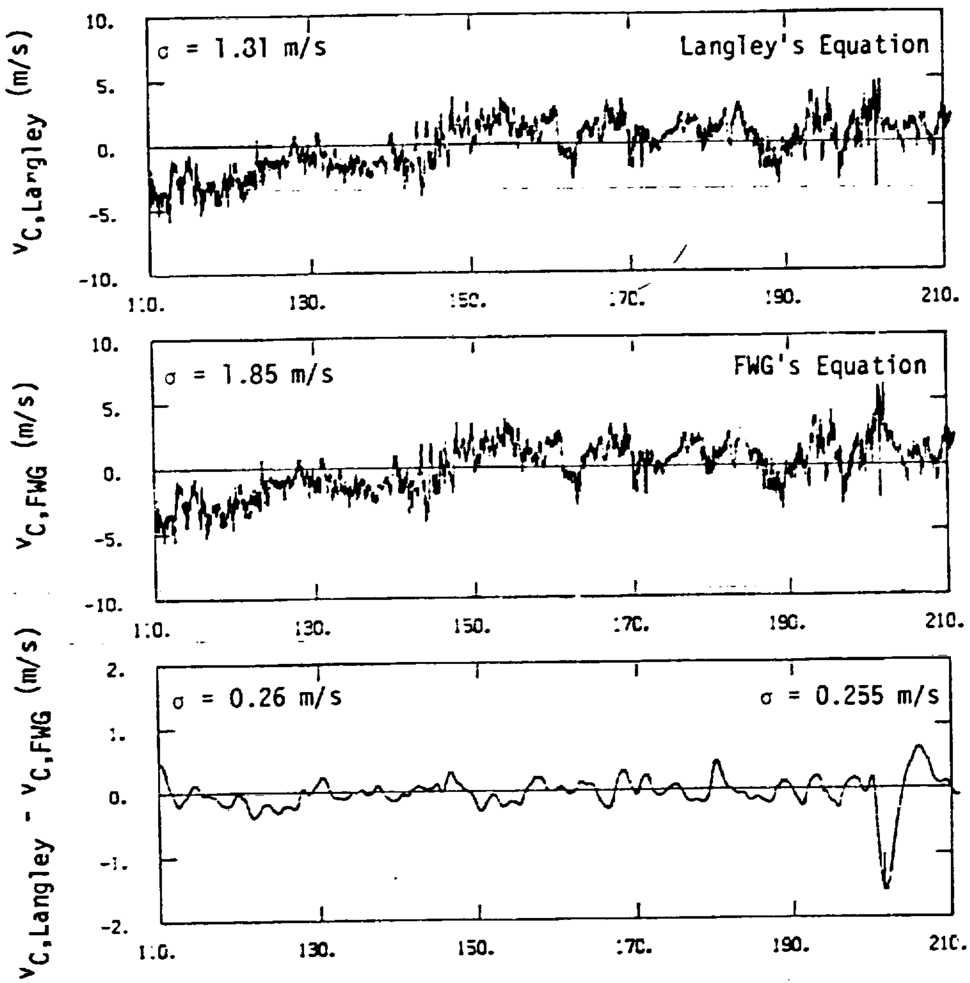

(b) Lateral Component

Figure 4.17. (cont'd).

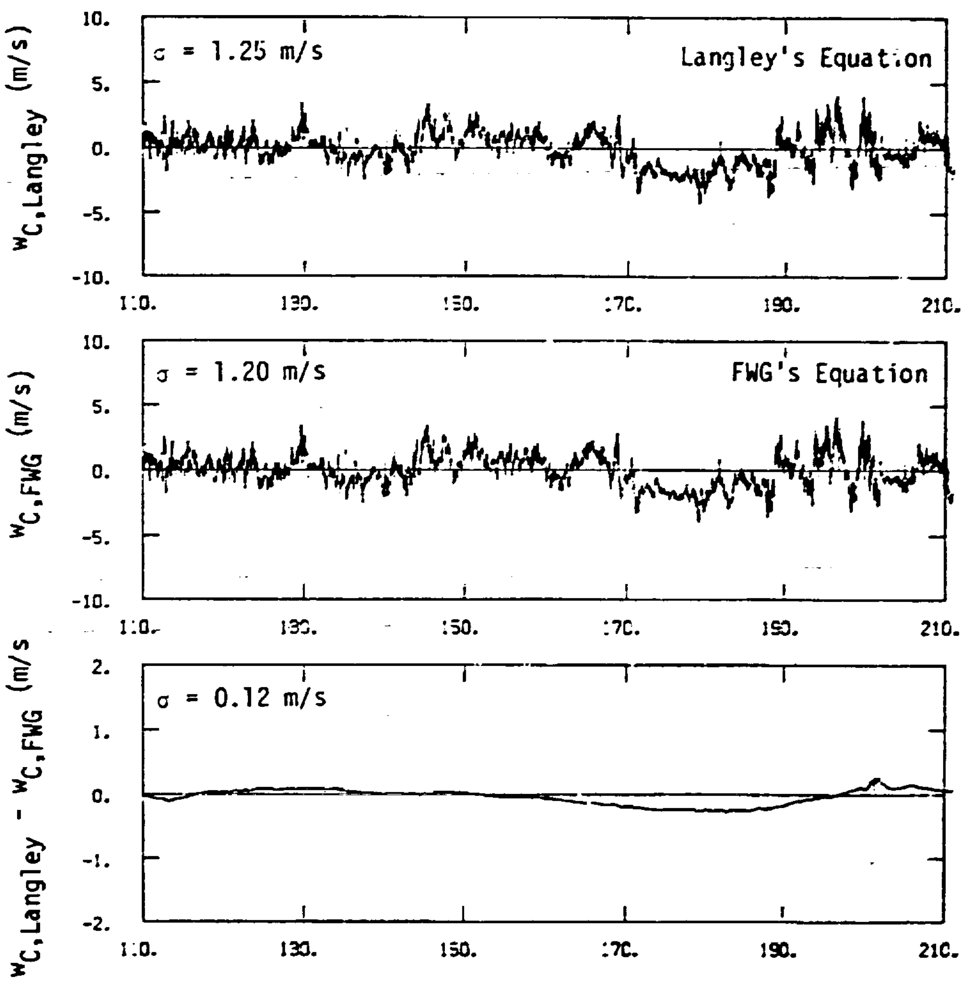

(c) Vertical Component

Figure 4.17. (cont'd).

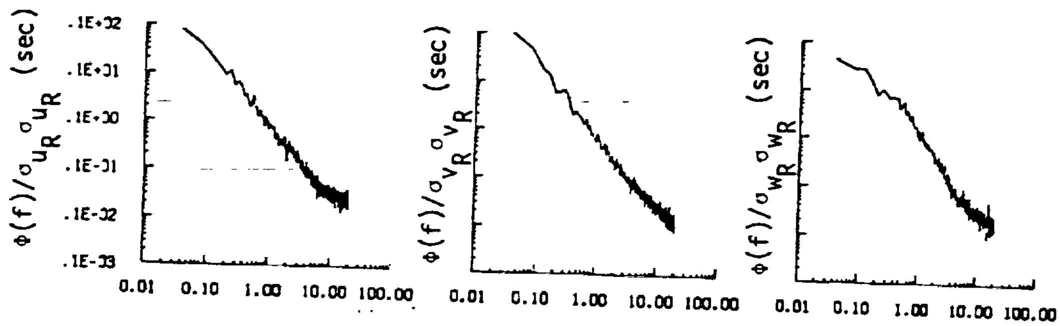

(a) Total time history, 0-691 sec

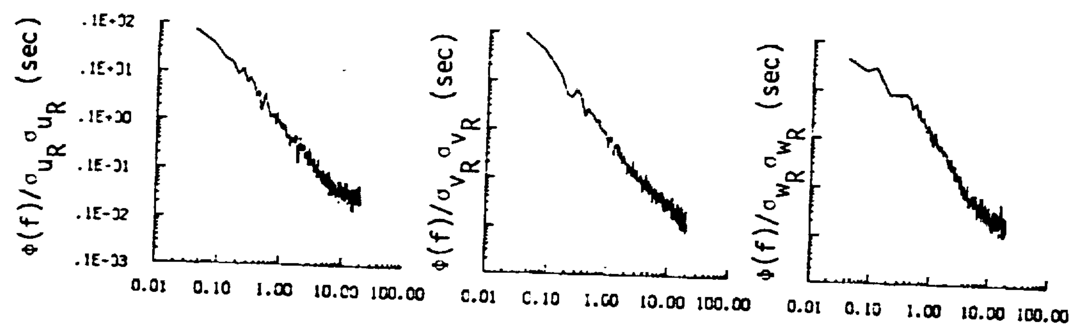

(b) Segment 1, 0-512 sec

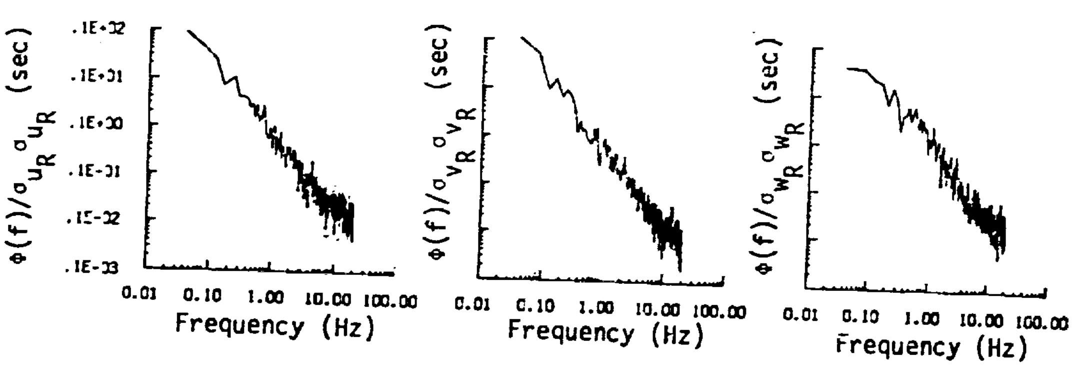

(c) Segment 2, 512-691 sec

Figure 4.18. Comparison of turbulence spectra computed for individual segments of Run 3. Segment 2 contains an approximate 7° climb during a 536 to 555 second interval.

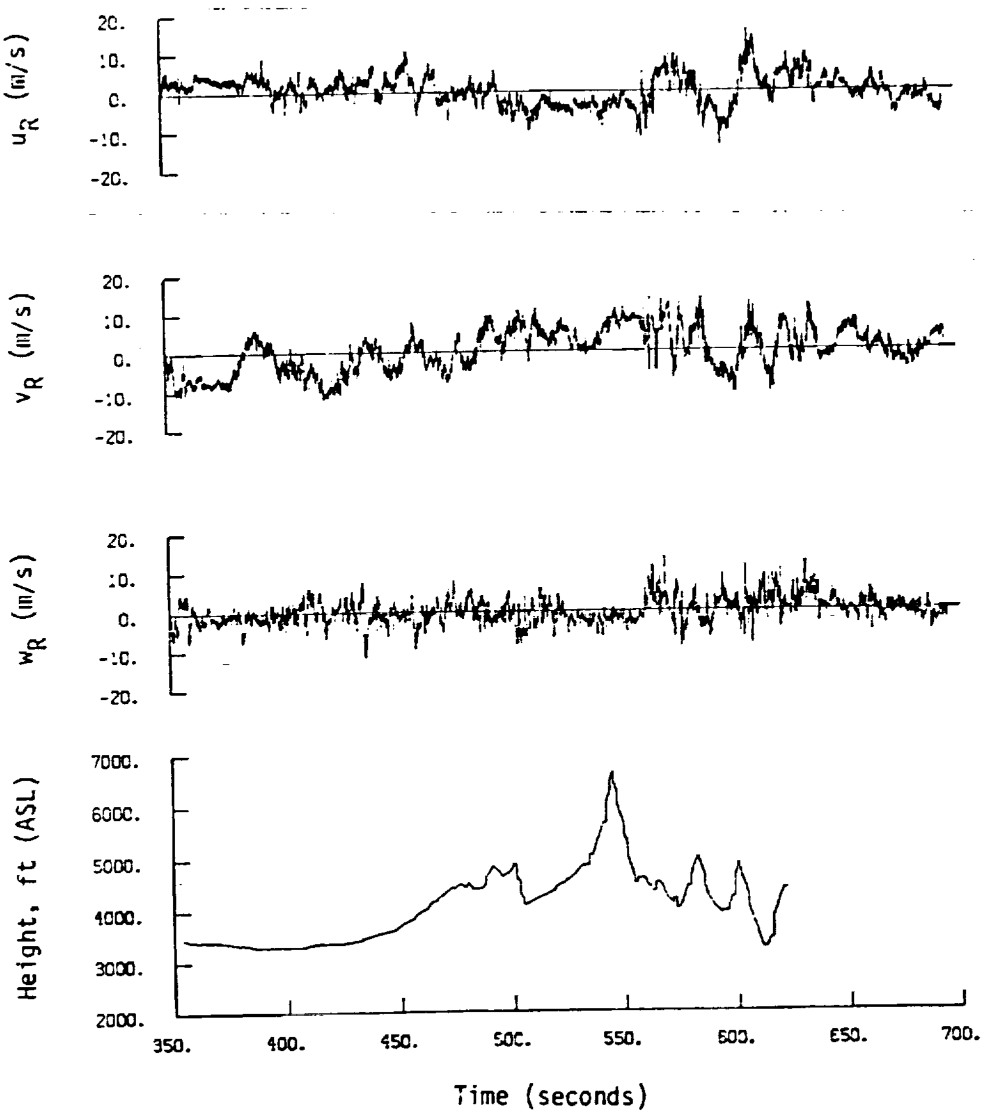

Figure 4.19. Illustration of terrain-induced turbulence.

TABLE 4.1. Turbulence Intensities for Total Time History and Each Segment Individually for Run 3.

Component	Total	Segment 1	Segment 2
σ_{UR}	3.17	2.64	2.87
σ_{VR}	5.25	5.29	4.27
σ_{WR}	2.36	2.10	4.55

flow over the mountain peaks. Thus, it is concluded that the patchiness of the turbulence is due to terrain effects and not associated with any departure of the aircraft from straight and level flight.

5.0 CONCLUSIONS

The results of the analysis of Flight 31 coupled with experience from previous analysis of flight data from the NASA B-57 aircraft gust gradient program, lead to the following conclusions and recommendations:

1. The probability density distribution of gust velocities in the atmosphere are not Gaussian. The distribution of velocity differences across the airfoil which filters out trends in the quasi-steady wind have a definite modified Bessel function type distribution, i.e., a higher percentage of small and large velocity differences and lower percentage of intermediate values than is predicted by a Gaussian distribution. The parameter r of the modified Bessel function distribution however could not be related to the existing meteorology or to specific terrain features. It is recommended that additional work to establish a physical meaning of the parameter r be carried out. The probability density distribution of the gust components themselves, i.e., not the difference, were rather ill behaved in this study and in many cases showed bimodal distributions. This is believed to be due to the fact that a trend due to spatially varying mean wind along the flight path, caused by terrain features or other factors, were not removed from the gust velocities when computing the probability density functions.
2. The theoretical von Karman spectrum fits the turbulence data well over the frequency range investigated in this study (0.04 to 20 Hz). The theoretical models were computed with length scales determined from integration of the correlation coefficient from zero lag to the point where the correlation first becomes zero.

The results of the study strongly suggest that the turbulence behaves relatively consistent with the assumption of isotropic, homogeneous turbulence despite the fact that flights were made over mountainous terrain and during touch-and-go's through the atmospheric boundary layer.

3. The two-point common component theoretical spectra (that is, the spectra for the same velocity component for spatially separated positions) proposed by Houbolt and Sen (1972) for the vertical fluctuations and the spectra for longitudinal and lateral velocity fluctuations derived in this report, agree with the experimental flight data provided the care described in Chapter 3 is exercised in computing the two-point spectra from the truncated, digitized gust velocity time histories.

4. In calculating one-point auto-spectra and two-point common component spectra from a direct Fourier transform of the data can result in large errors due to aliasing and truncation estimator bias. Aliasing is the major source of error in the auto-spectrum whereas bias is the major source of error in the two-point common component spectra. This is physically evident since the energy contained at high frequencies in two-point spectra vanishes significantly faster than that in one-point spectra. What is not evident is that a very small departure of two-point correlation coefficient from unity at zero lag can cause high bias errors. To remove bias error from two-point spectra it is recommended that the minimum-bias lag window be utilized.

5. To reduce the variance error associated with a two-point common component as well as all cross-spectra it is important to carry

out segment averaging of the co- and quad-spectra C(s,f) and Q(s,f) separately as contrasted to averaging the absolute value, i.e., $\sqrt{C^2(s,f) + Q^2(s,f)}$.

6. The small values (0.07) of the ratio of the spanwidth separation distance of 20 m to the typical turbulence integral length scale was found to have a relatively significant effect on the two-point spectra in terms of spectrum dropoff at high frequencies. However, for other statistical parameters; ie, cross correlations, there were indications that the separation distance of 20 m is too small to resolve some of the statistical issues of interest. It is recommended that experiments be carried out with larger separation distances than 20 m for a firmer understanding of two-point statistical pamameters.

7. The one-point and two-point cross-correlations between uncommon velocity components shows almost zero correlation (further supporting the assumption of isotropic turbulence). However, close examination of the complex phase angle associated with the cross-spectra indicate there is significant phase difference between various frequencies. The one-point cross-spectrum appears to agree well with the model proposed by Reeves, et al. (1974). No empirical expression or analytical model of two-point cross-spectra is available. Further work is required in this area.

8. The instrumentation system and data processing algorithms for the NASA B-57B aircraft provides highly accurate measurements of turbulent gust velocities. The measurements of the total instantaneous wind speed, however, may contain certain errors induced by some of the present characteristics of the measuring

system. In particular the INS Schuler drift problem causes significant uncertainty in the position of the flight path and of the magnitude of the mean wind speed (i.e., ±2 to 5 m/s). This uncertainty in velocity coupled with small inaccuracies in the flow vane measurements (possibly due to boom misalignment or other factors), while having insignificant effect on the gust velocity measurement, can result in major errors in the wind field. These errors can be corrected if appropriate data other than that measured by the on-board instrumentation system is gathered during the flight. For example, visual observed position recorded with a designation marker utilized can be used to estimate INS Schuler position drift from post-analysis of the data. Since the Schuler drift does not appear to have a constant amplitude nor period of oscillation, procedures to correct for this error by backing cut the inertial winds and position from measurements made with the aircraft stationary on the runways are not feasible.

REFERENCES

Akkari, S. H., and W. Frost (1982): "Analysis of Vibration Induced Error in Turbulence Velocity Measurements from an Aircraft Wing Tip Boom," NASA CR 3571.

Axford, D. N. (1968): "On the Accuracy of Wind Measurements Using an Inertial Platform in an Aircraft, and an Example of a Measurement of the Vertical Mesostructure of the Atmosphere," J. of Applied Met., 7:645-666.

Bendat, J. S., and A. G. Piersol (1971): Random Data: Analysis and Measurement Procedures. New York: John Wiley & Sons, Inc.

Bisplinghoff, R. L., and H. Ashley (1957): Aeroelasticity. Menlo Park, Calif.: Addison-Wesley Pub. Co.

Brigham, E. O. (1974): Tne Fast Fourier Transform. Englewood Cliffs, N. J.: Prentice-Hall, Inc.

Boxmeyer, C. (1964): Inertial Navigation Systems. New York: McGraw-Hill Book Co.

Brook, R. R. (1975): "A Note on Vertical Coherence of Wind Measured in an Urban Boundary Layer," Boundary-Layer Met., 9:11-20.

Camp, D. W., W. Campbell, C. Dow, M. Phillips, R. Gregory, and W. Frost (1984): "Visualization of Gust Gradients and Aircraft Response as Measured by the NASA B-57B Aircraft," Paper presented at the AIAA 22nd Aerospace Sciences Meeting, Reno, Nev., Jan. 9-12.

Campbell, W., D. W. Camp, and W. Frost (1983): "An Analysis of Spanwise Gust Gradient Data," Paper presented at the Ninth Conference on Aerospace and Aeronautical Meteorology of the AMS, Omaha, Neb., June 6-9.

Campbell, W. C. (1984): "A Spatial Model of Wind Shear and Turbulence for Flight Simulation," NASA TP 2313.

Campbell, W. (1986): Private communication.

Chang, H. P., and W. Frost (1985): "NASA B-57B Orographic Data Reduction and Analysis Relative to PBL Parameterization Models," Final report for NASA Goddard Space Flight Center under Contract NAS5-28558.

Chang, H. P., D. W. Camp, and W. Frost (1986): "Analysis of Aircraft Data Measured Near Microbursts," Interim report under Contract NAS5-29302 for NASA Goddard Space Flight Center, Dec.

Crooks, W. M., F. M. Hoblit, D. T. Prophet, et al. (1967): "Project Hicat an Investigatioin of High Altitude Clear Air Turbulence," Technical Report AFFDL-TR-67-123, Vol. I, Wright-Patterson Air Force Base, OH, Nov.

Davenport, A. G. (1961): "The Spectrum of Horizontal Gustiness Near the Ground in High Winds," Quarterly Journal of the Royal Met. Soc., 87:194-211.

Diederich, F. W. (1957): "The Response of an Airplane to Random Turbulence," NACA TN 3910.

Diederich, F. W., and J. A. Drischler (1957): "Effect of Spanwise Variation in Gust Intensity on the Lift Due to Atmospheric Turbulence," NACA TN 3920.

Eggleston, J. M., and F. W. Diederich (1956): "Theoretical Calculation of the Power Spectra of the Rolling and Yawing Moments on a Wing in Random Turbulence," NACA TN 3864.

Ehernberger, L. J. (1987): NASA Dryden Flight Test Facility; Personnel Communications

Eichenbaum, F. D. (1972): "Response of Aircraft to Three-Dimensional Random Turbulence," AFFDL-TR-72-28.

Etkin, B. (1972): Dynamics of Atmospheric Flight. New York: John Wiley & Sons, Inc.

Frost, W., and T. H. Moulden (1977): Handbook on Turbulence. New York: Plenum Press.

Frost, W. (1981): FWG Associates, Inc. Internal Memo.

Frost, W. (1983): "Spanwise Turbulence Modeling," Paper presented at the Ninth Conference on Aerospace and Aeronautical Meteorology of the AMS, Omaha, Neb., June 6-9.

Frost, W., and K. H. Huang (1983): "Doppler Lidar Signal and Turbulence Study," Final Report for NASA/MSFC under Contract NAS8-35185, by FWG Associates, Inc., Tullahoma, Tenn.

Frost, W., and M. C. Lin (1983): "Statistical Analysis of Turbulence Data from the NASA Marshall Space Flight Center Atmospheric Boundary Layer Tower Array Facility," NASA CR 3737.

Frost, W., M. C. Lin, and H. P. Chang (1983): FWG Associates, Inc. Internal Memo.

Frost, W., M. C. Lin, H. P. Chang, and E. A. Ringnes (1985a): "Analysis of Data from NASA B-57B Gust Gradient Program," Final report for NASA Marshall Space Flight Center under Contracts NAS8-36177 and NAS8-35347.

Frost, W., K. H. Huang, and J. S. Theon (1985b): "Comparison of Winds and Turbulence Measurements from Doppler Lidar and Instrumented Aircraft," Paper presented at the 3rd Topical Meeting on Coherent Laser Radar: Technology and Applications, Worchestershire, England, July 7-11.

Frost, W., J. S. Theon, K. H. Huang, and R. E. Turner (1985c): "Field Study of the Effects of Orographic Features on Planetary Boundary Layer Models," Paper presented at the WMO/ICSU/IAMAP Scientific Conference on the Results of the Alpine Experiment (ALPEX), Venice, Italy, Oct. 29-Nov. 2.

Haugen, D. A., ed. (1973): Workshop on Micrometeorology. Boston, American Meteorological Society.

Hinze, J. O. (1975): Turbulence. New York: McGraw-Hill.

Houbolt, J. C., R. Steiner, and K. G. Pratt (1964): "Dynamic Response of Airplanes to Atmospheric Turbulence Including Flight Data on Input and Response," NASA TR R-199.

Houbolt, J. C., and A. Sen (1972): "Cross-Spectral Functions Based on von Karman's Spectral Equation," NASA CR 2011.

Houbolt, J. C. (1973): "Atmospheric Turbulence," AIAA Journal, 4:421-437.

Huang, K. H., W. Frost, and E. A. Ringnes (1985): "Comparison of Wind and Turbulence Measurements from Doppler Lidar and Instrumented Aircraft," Final report under NASA Marshall Contract NAS8-36188.

Huber, C., and W. J. Bogers (1983): "The Schuler Principle: A Discussion of Some Facts and Misconceptions," EUT Research Report 83-E-136 (ISBN 90-6144-136-6), Eindhoven University of Technology, Dept. of Electrical Engineering, Eindhoven, The Netherlands, May.

Jenkins, G. M., and D. G. Watts (1969): Spectral Analysis and Its Applications. San Francisco: Holden-Day.

Karamcheti, K. (1966): Principles of Ideal-Fluid Aerodynamics. New York: John Wiley and Sons, Inc.

Kordes, E. E., and J. C. Houbolt (1953): "Evaluation of Gust Response Characteristics of Some Existing Aircraft with Wing Bending," NACA TN 2897.

Kristensen, L., and N. O. Jensen (1979): "Lateral Coherence in Isotropic Turbulence and in the Natural Wind," Boundary-Layer Met., 17:353-373.

Lenschow, D. H. (1972): "The Measurement of Air Velocity and Temperature Using the NCAR Buffalo Aircraft Measuring System," NCAR-TN/EDD-74.

Lenschow, D. H. (1983): "Aircraft Measurements in the Boundary Layer," in Probing the Atmospheric Boundary Layer originally prepared for the AMS short-course, Aug. 8-12, 1983, Boulder, Colorado.

Lichtenstein, J. H. (1978): "Comparison of Wing-Span Averaging Effects Rolling Moment, and Bending Moment for Two Span Load Distributions and for Two Turbulence Representatives," NASA TM-78699.

Meissner, C. W., Jr. (1976): "A Flight Instrumentation System for Acquisition of Atmospheric Turbulence Data," NASA TN D-8314.

Murrow, H. N. and R. H. Rhyne (1981): "Flight Instrumentation for Turbulence Measurements in the Atmosphere," Presentation at The University of Tenn. Space Institute Short Course on Turbulence Measurements.

Panchev, S. (1971): Random Functions and Turbulence. New York: Pergamon Press.

Panofsky, H. A., D. W. Thomson, D. A. Sullivan, and D. E. Moravek (1974): "Two-Point Velocity Statistics Over Lake Ontario," Boundary-Layer Met., 7:301-321.

Panofsky, H. A., and T. Mizuno (1975): "Horizontal Coherence and Pasquill's Beta," Boundary-Layer Met., 9:247-256.

Panofsky, H. A., and J. A. Dutton (1984): Atmospheric Turbulence. Models and Methods for Engineering Applications. New York: John Wiley and Sons, Inc.

Papoulis, A. (1977): Signal Analysis. New York: McGraw-Hill Book Co.

Pastel, R. L., J. E. Caruthers, and W. Frost (1981): "Airplane Wing Vibrations Due to Atmospheric Turbulence," NASA CR 3431.

Pielke, R. A., and H. A. Panofsky (1970): "Turbulence Characteristics Along Several Towers," Boundary-Layer Met., 1:115-130.

Reeves, P. M., G. S. Campbell, V. M. Ganzer, and R. G. Joppa (1974): "Development and Application of a Non-Gaussian Atmospheric Turbulence Model for Use in Flight Simulators," NASA CR-2451.

Ringnes, E. A., and W. Frost (1985): "Analysis of Aerodynamic Coefficients Using Gust Gradient Data: Spanwise Turbulence Effects on Airplane Response," NASA CR 3961.

Rhyne, R. H. (1980): "Accuracy of Aircraft Velocities Obtained from Inertial Navigation Systems for Application to Airborne Wind Meaurements," NASA TM-81826.

Schuler, M. (1923): "Die Störung von Pendelund Kreiselapparaten durch die Beschleunigung des Fahrzeuges, Physik Z., Vol. 24, July. A translation appears in Inertial Guidance (G. R. Pittman, Jr., ed.). New York: John Wiley & Sons, Inc., 1962.

Steely, S. L., and W. Frost (1981): "Statistical Analysis of Atmospheric Turbulence About a Simulated Block Building," NASA CR 3366.

Theon, J. S., W. Frost, K. H. Huang, and R. E. Turner (1986): "Field Study of the Effect of Orographic Features on Planetary Boundary Layer Models," to be published in the Journal of Atmospheric and Oceanic Technology.

Wang, S. T., and W. Frost (1982): "Data Cataloging and Analysis Plan for B-57b Flight Facility Turbulence Measurement Program," Final report for NASA Marshall under Contract NAS8-33458 by FWG Associates, Inc.

Weber, O. (1975): "Statistical Studies on the Accuracy of Carousel IV Inertial Navigation System after Flight over the North Atlantic," European Space Research Organization (ESRO) Technical Translation (TT) ESRO TT-136.

APPENDICES

APPENDIX A

RESULTS OF STATISTICAL ANALYSIS OF FLIGHT 31

General information, ground track terrain features, and statistical values for all runs (except landing operation, Run 17) of Flight 31 on November 29, 1982, are presented in this appendix. The analysis of each run is given in two tables and five figures. The first table shows the turbulence average parameters, integral length scales, and correlation coefficients and the second one lists all parameters measured and their range of values. Five figures show the flight altitude, time history, probability density function, normalized correlation function, and normalized spectral density function of gust velocities, respectively.

Flight 31, Run 1 (Take-off)
Date: Nov. 29, 1982
Start Time: 10:32:46 (PST)
Duration: 135.9 seconds

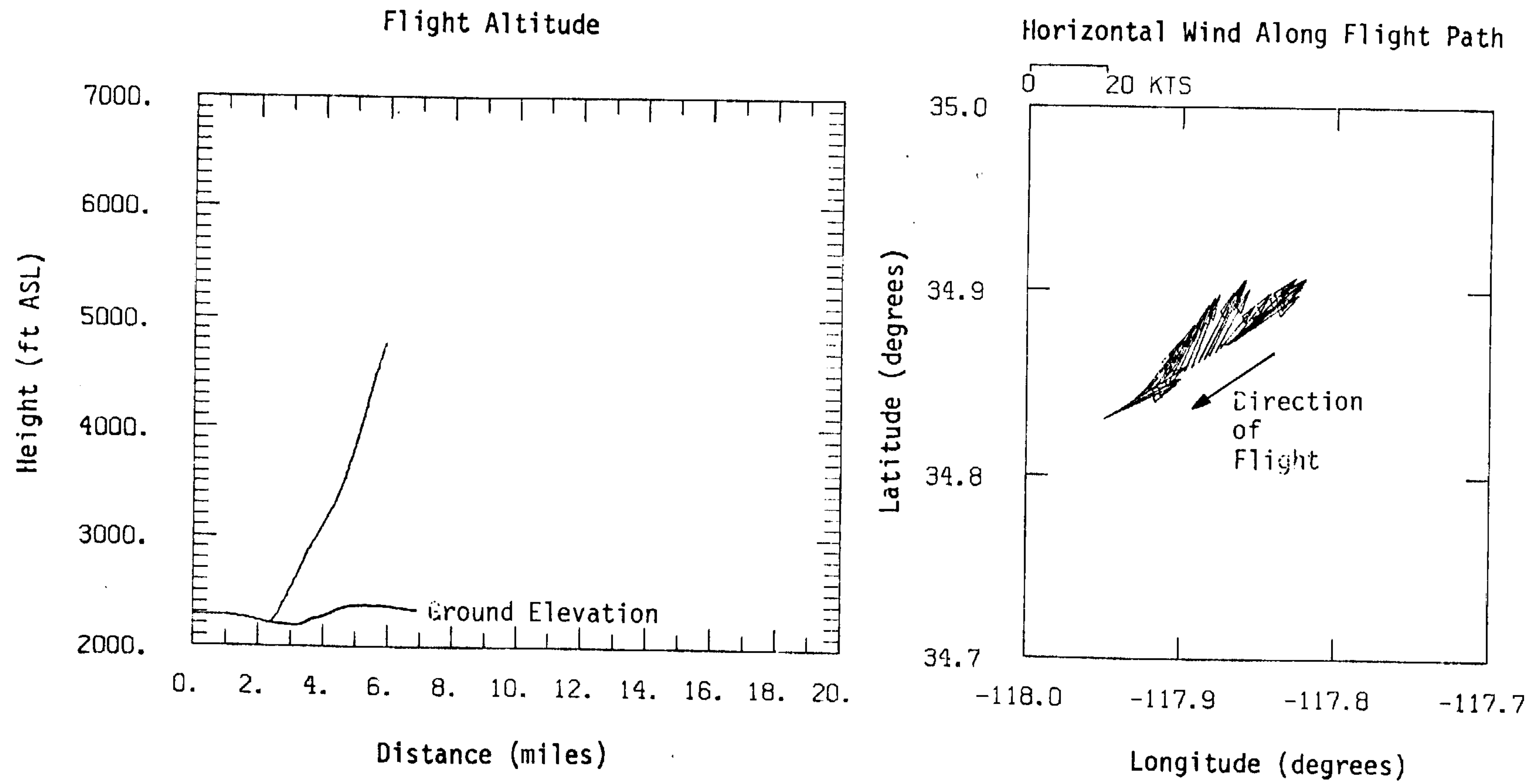

Figure A.1. Flight altitude and horizontal wind along flight path, Flight 31, Run 1.

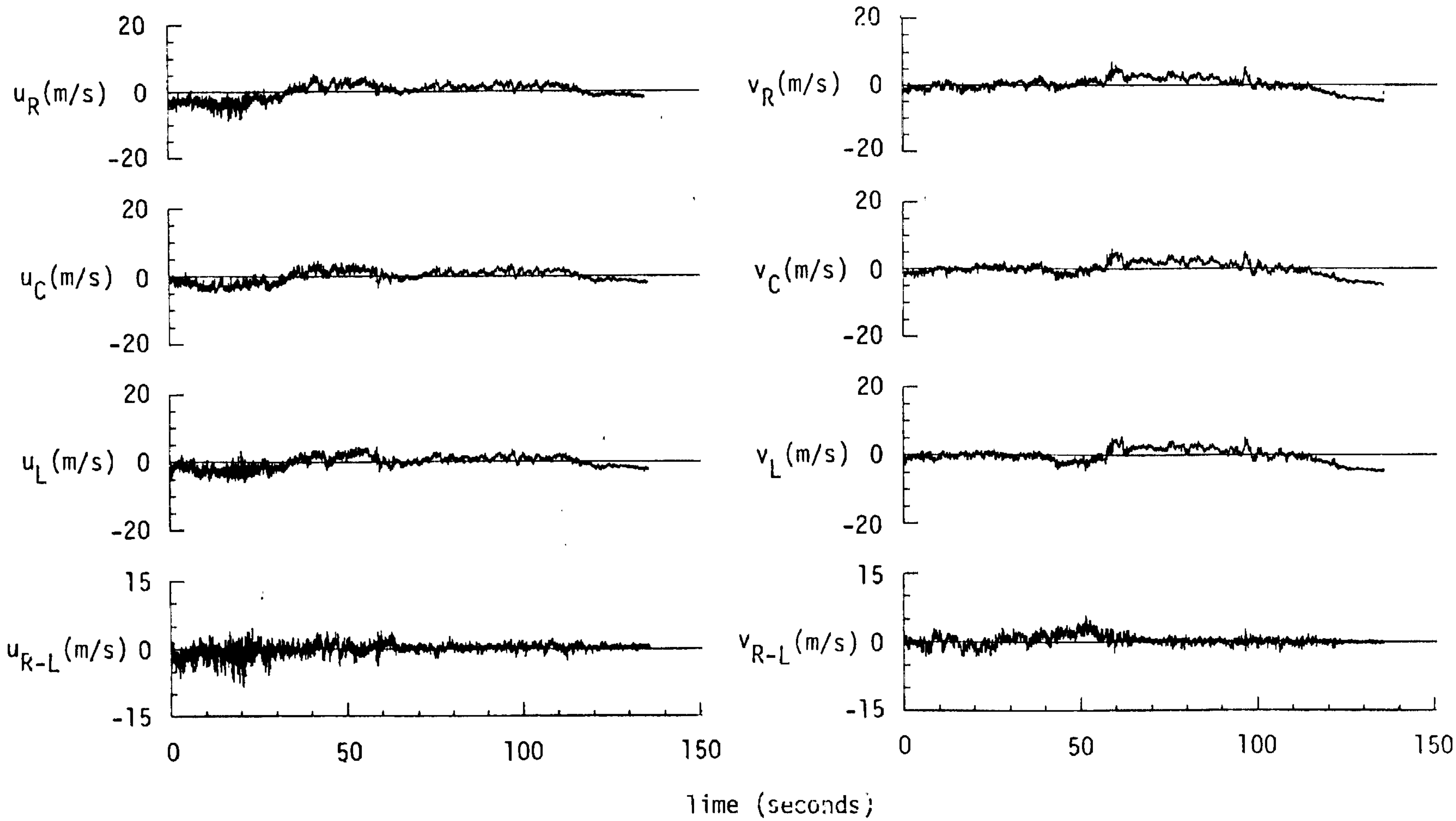

Figure A.2. Time histories of gust velocities, gust velocity differences, and aircraft's normal accelerations, Flight 31, Run 1.

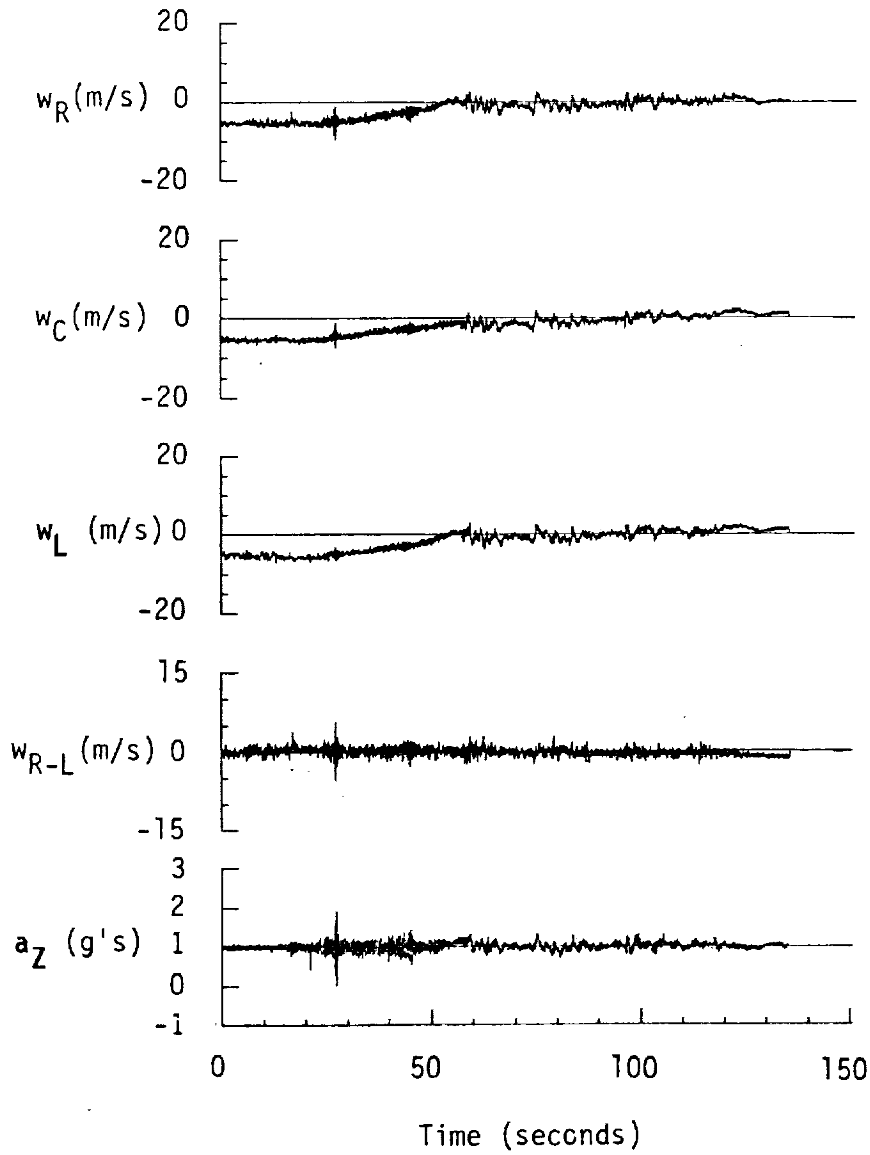

Figure A.2. (continued).

TABLE A.1. Average Turbulence Parameters, Integral Length Scales, and Correlation Coefficients of Gust Velocities, Flight 31, Run 1.

1. Mean Airspeed (m/s):

$\overline{V}_L$	$\overline{V}_C$	$\overline{V}_R$
81.13	78.92	81.21

2. Standard Deviation of Gust Velocities (m/s):

σ_{uR}	σ_{vR}	σ_{wR}
2.12	2.11	2.31

σ_{uC}	σ_{vC}	σ_{wC}
1.69	1.99	2.33

σ_{uL}	σ_{vL}	σ_{wL}
1.74	2.05	2.58

3. Standard Deviation of Gust Velocity Differences (m/s):

$\sigma_{\Delta uRL}$	$\sigma_{\Delta vRL}$	$\sigma_{\Delta wRL}$
1.20	1.10	0.77

4. Integral Length Scale (m):

L_{uR}	L_{vR}	L_{wR}
297.7	149.7	255.1

L_{uRL}	L_{vRL}	L_{wRL}
248.4	35.3	254.5

5. Correlation Coefficient of Gust Velocities:

$\overline{u_R u_L}/\sigma_{u_R}\sigma_{u_L}$	$\overline{v_R v_L}/\sigma_{v_R}\sigma_{v_L}$	$\overline{w_R w_L}/\sigma_{w_R}\sigma_{w_L}$
0.75	0.34	0.80

$\overline{u_R v_R}/\sigma_{u_R}\sigma_{v_R}$	$\overline{v_R w_R}/\sigma_{v_R}\sigma_{w_R}$	$\overline{w_R u_R}/\sigma_{w_R}\sigma_{u_R}$
0.08	0.14	0.52

$\overline{u_R v_L}/\sigma_{u_R}\sigma_{v_L}$	$\overline{v_R w_L}/\sigma_{v_R}\sigma_{w_L}$	$\overline{w_R u_L}/\sigma_{w_R}\sigma_{u_L}$
-0.40	0.11	0.45

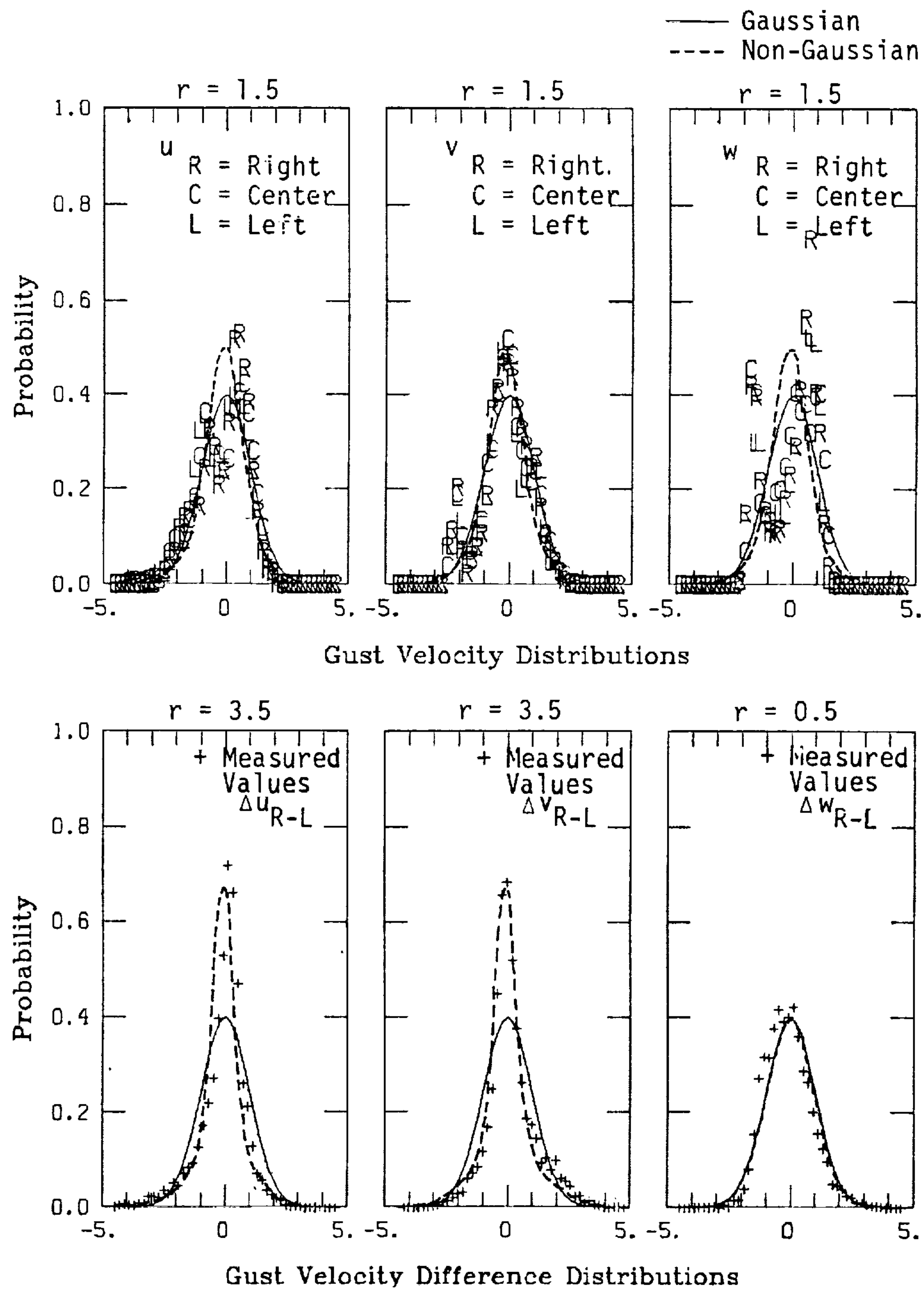

Figure A.3. Probability density functions for gust velocities and gust velocity differences (normalized with the standard deviation), Flight 31, Run 1 (r = degree of non-Gaussian).

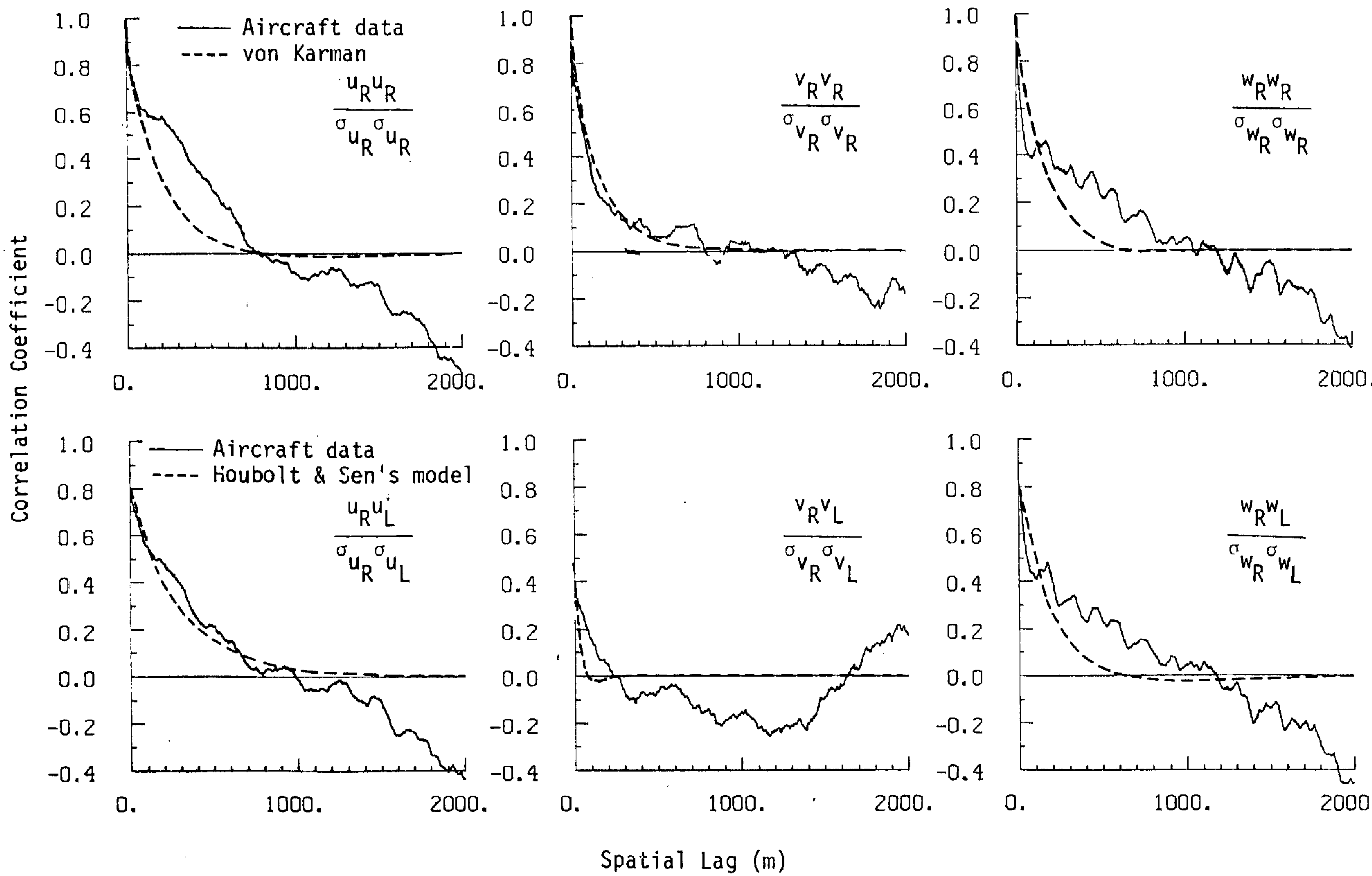

a. One- and two-point common component correlations.

Figure A.4. Comparison of normalized one- and two-point correlation functions for gust velocities with theoretical models, Flight 31, Run 1.

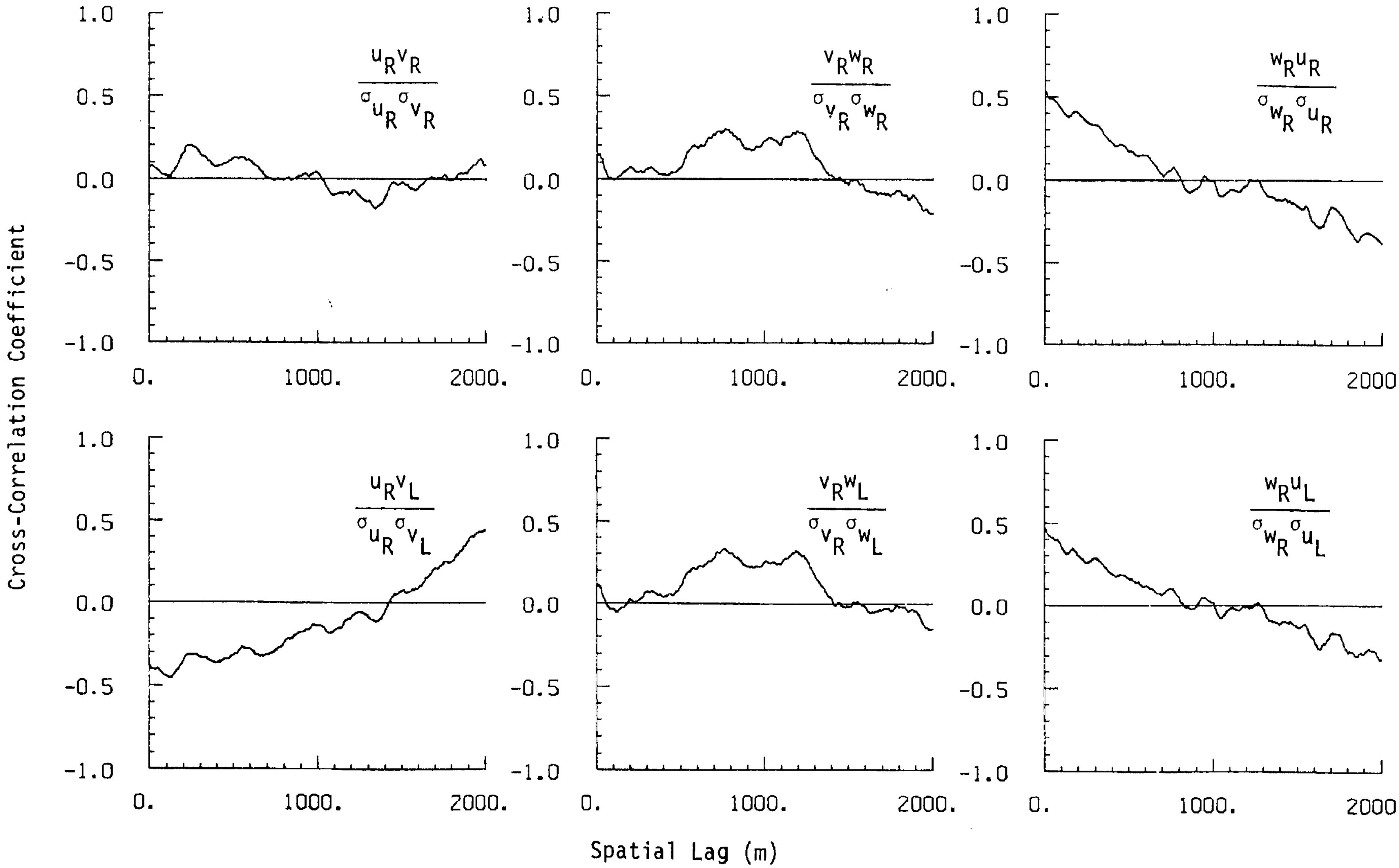

b. One- and two-point cross-correlations.

Figure A.4. (continued).

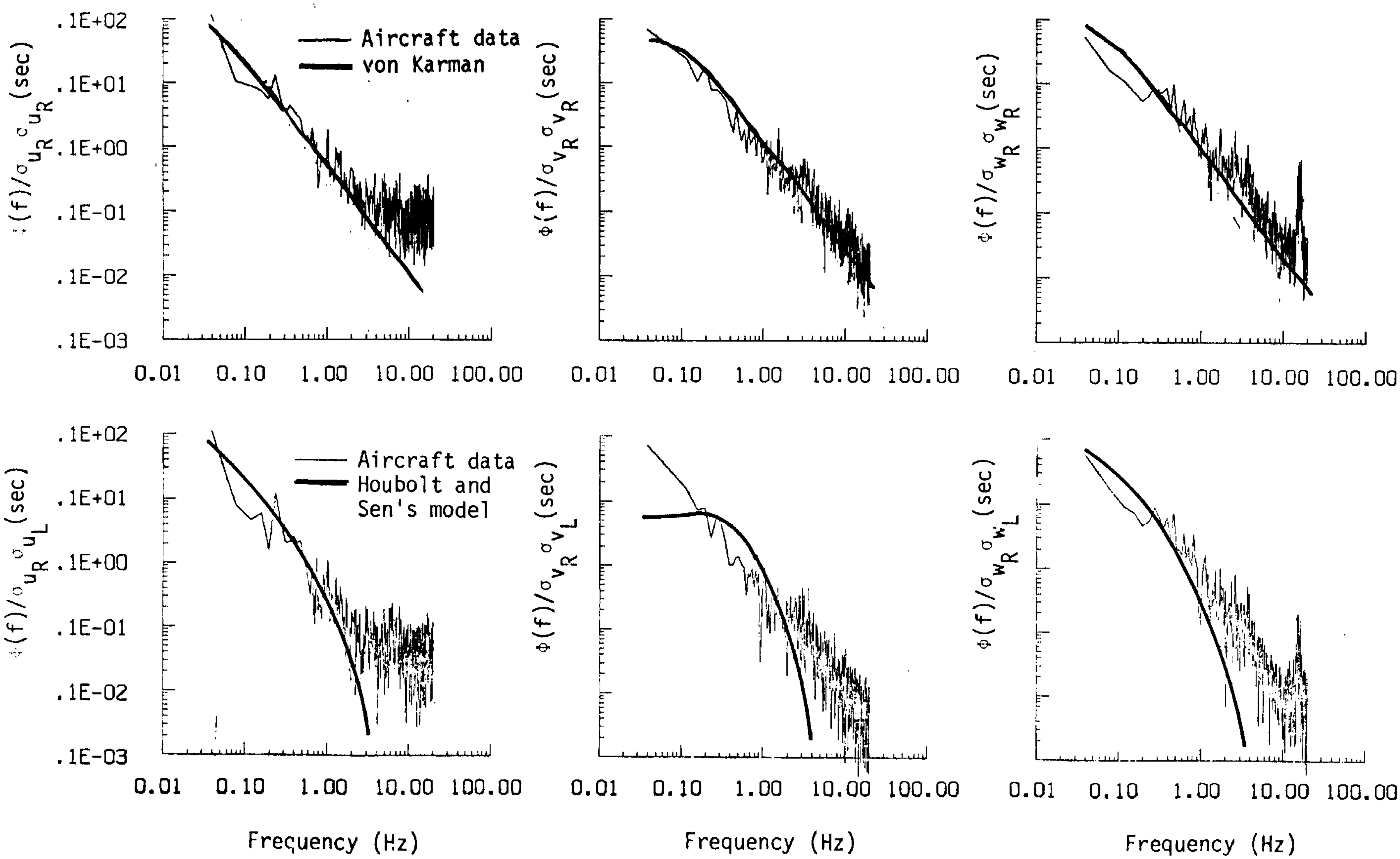

a. One and two-point common component spectra.

Figure A.5. Comparison of normalized one- and two-point spectral density functions for gust velocities with theoretical models, Flight 31, Run 1.

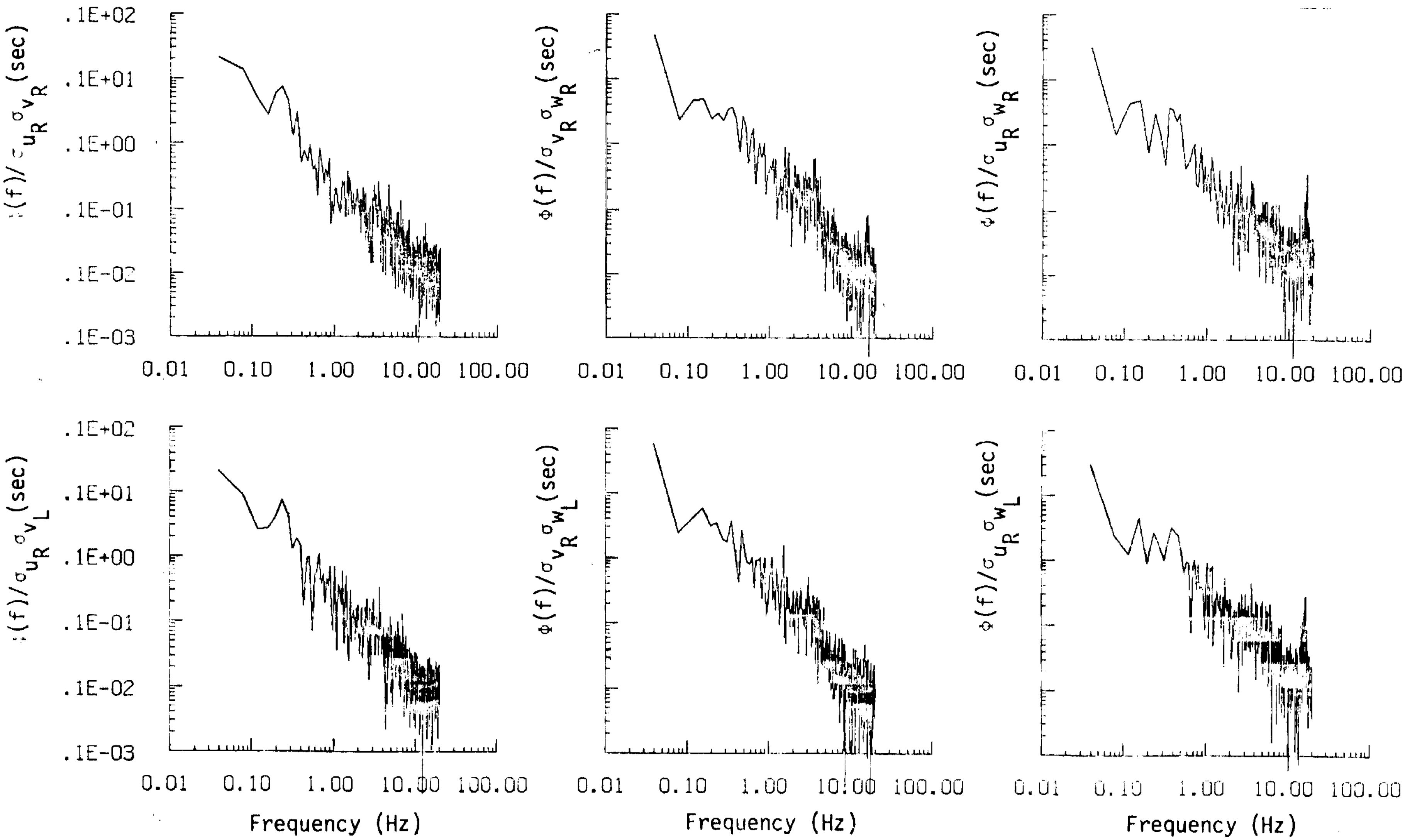

b. One- and two-point cross-spectra.

Figure A.5. (continued).

ORIGINAL PAGE IS
OF POOR QUALITY

TABLE A. 2. List of All Parameters Measured and Their Range of Values, Flight 31, Run 1.

	CHANNEL	UNITS	HIGH	LOW	MEAN	RMS	STD	POINTS
1	TIME	SECONDS	38101.502	37965.627	38033.56410	38033.58433	39.23456	5436
2	PHI DOT	RAD/SEC	.278	-.270	-.00227	.02115	.02102	5436
3	ACCL N CG	G UNITS	1.337	.734	1.00067	1.00266	.06626	5436
4	THETA DOT	RAD/SEC	.545	-.562	.00424	.03273	.03246	5436
5	THETA	RAD	.190	-.036	.08658	.11174	.07065	5436
6	PHI	RAD	.051	-.061	.00050	.01779	.01779	5436
7	PSI 1	RAD	240.065	232.668	237.35125	237.35382	1.10419	5436
8	DEL PSI 1	DEG	2.140	-15.081	-.45010	1.46304	1.39221	5436
9	PSI 2	RAD	599.075	239.651	595.15164	595.53185	21.27894	5436
10	DEL PSI 2	DEG	2.667	-4.448	.03810	1.09320	1.09264	5436
11	ACCL N LT	G UNITS	1.973	.009	1.01136	1.02141	.14298	5436
12	ACCL N RT	G UNITS	2.204	-.269	1.01246	1.02615	.16705	5436
13	ACCL X CG	G UNITS	.332	-.061	.17096	.19540	.09464	5436
14	ACCL Y CG	G UNITS	.215	-.165	.00019	.02839	.02839	5436
15	ALPHA CTR	RAD	.061	-.216	-.04731	.06159	.03943	5436
16	BETA CTR	RAD	.198	-.177	.01564	.03842	.03510	5436
17	TEMP T	DEG F	82.059	55.511	81.72687	81.72778	.38591	5436
18	TEMP P	DEG F	58.365	13.442	58.29338	58.29661	.61436	5436
19	ACCL Z INS	G UNITS	1.899	.031	1.01470	1.01844	.08723	5436
20	ALPHA RT	RAD	.081	-.160	-.03694	.05834	.04516	5436
21	BETA RT	RAD	.169	-.163	.02222	.03814	.03100	5436
22	ALPHA LT	RAD	.110	-.186	-.01399	.05100	.04905	5436
23	BETA LT	RAD	.150	-.146	.01825	.03544	.03038	5436
24	PSI DOT	RAD/SEC	.041	-.406	.00282	.01255	.01223	5436
25	TEMP TOT	DEG C	17.902	14.458	16.52312	16.55116	.96314	5436
26	QC LT	PSID	1.342	.005	.68927	.85341	.50325	5436
27	QC CTR	PSID	1.286	.005	.65867	.81831	.48562	5436
28	QC RT	PSID	1.334	.009	.68673	.84952	.50014	5436
29	PS	PSIA	13.561	12.303	13.22214	13.22750	.37638	5436
30	TEMP IRT	VOLTS	11.453	4.557	7.72675	7.84881	1.37893	5436
31	HYGROM	DEG C	6.860	-5.262	5.10541	5.80571	2.76451	5436
32	QC2 LT	PSID	-.022	-.113	-.04365	.04581	.01565	5436
33	QC2 CTR	PSID	.144	-.039	.10623	.10990	.02815	5436
34	QC2 RT	PSID	.065	-.010	.04434	.05010	.02333	5436
35	DAR	DEG	-.047	-.428	-.18086	.20153	.08891	5436
36	DAL	DEG	5.997	.193	.25455	.26718	.08117	5436
37	DELEV	DEG	-4.171	-11.012	-4.22889	4.23001	.09730	5436
38	DSTAB	DEG	.541	.170	.17220	.17228	.00521	5436
39	DRUD	DEG	-2.861	-12.545	-2.86356	2.86658	.13148	5436
40	DTHRR	PCT MAX	44.141	28.305	44.04595	44.04648	.21452	5436
41	DTHRL	PCT MAX	44.824	27.173	44.74639	44.74704	.24173	5436
42	DFLP	POSITION	1.180	.433	1.17618	1.17623	.01015	5436
43	DSB	POSITION	.245	-.345	-.11524	.11538	.00580	5436
44	D TO G	METERS	7510442.688	7501274.304	***********	***********	2908.20914	5436
45	B TO D	DEGREES	73.210	73.170	73.19680	73.19680	.01295	5436
46	LONG	DEGREES	-117.864	-117.952	-117.89282	117.89282	.02789	5436
47	LAT	DEGREES	34.875	34.829	34.86008	34.86008	.01440	5436
48	TRK ANG	DEGREES	240.331	2[illegible].367	237.86041	237.86162	.75862	5436
49	HDG	RADIANS	4.188	4.061	4.14165	4.14170	.01960	5436
50	VE	M/SEC	-.092	-96.318	-59.45499	69.82182	36.61198	5436
51	VN	M/SEC	.063	-63.674	-37.54033	44.31629	23.55332	5436
52	ALTITUDE	KM	1.474	.673	.88519	.91663	.23803	5436
53	TEMPC	DEGREES C	15.801	8.283	12.51436	12.71989	2.27754	5436
54	EW WND SPD	KNOTS	21.769	2.013	12.20800	12.89115	4.14119	5436
55	NS WND SPD	KNOTS	22.473	3.537	11.85215	12.23842	3.05078	5436
56	WIND SPEED	KNOTS	25.701	8.226	17.50985	17.77528	3.06062	5436
57	WIND DIREC	DEGREES	252.838	187.065	225.22768	225.63187	13.49727	5436
58	WIND DIR2	DEGREES	72.838	7.065	45.22768	47.19856	13.49727	5436
59	WIND DIR3	DEGREES	252.838	187.065	225.22768	225.63187	13.49727	5436
60	WIND DIR4	DEGREES	252.638	187.065	225.22768	225.63187	13.49727	5436
61	AIRSPEED R	M/SEC	130.060	10.417	81.21330	91.59170	42.35290	5436
62	AIRSPEED C	M/SEC	127.753	7.500	76.91686	89.74769	42.74518	5436
63	AIRSPEED L	M/SEC	130.357	7.647	81.13083	91.74510	42.86170	5436
64	DELTA ALT	METERS	776.557	-22.915	169.47034	304.21726	238.03268	5436
65	INRTL DISP	METERS	778.398	-14.796	189.76276	305.09925	238.92708	5436
66	UG RIGHT	M/SEC	5.108	-8.446	.00000	2.11541	2.11561	5436
67	UG CENTER	M/SEC	4.496	-4.458	.00060	1.68975	1.68990	5436
68	UG LEFT	M/SEC	4.412	-5.742	.00000	1.73837	1.73853	5436
69	VG RIGHT	M/SEC	6.790	-5.126	.11583	2.11639	2.11341	5436
70	VG CENTER	M/SEC	6.007	-4.856	-.03314	1.99438	1.99429	5436
71	VG LEFT	M/SEC	5.578	-4.972	-.12248	2.05717	2.05371	5436
72	WG RIGHT	M/SEC	2.516	-9.562	-1.71229	2.87291	2.30686	5436
73	WG CENTER	M/SEC	2.510	-7.344	-1.81065	2.45271	2.33245	5436
74	WG LEFT	M/SEC	2.887	-6.705	-1.51645	2.99012	2.57700	5436

Flight 31, Run 2
Date: Nov. 29, 1982
Start Time: 10:39:15 (PST)
Duration: 213.8 seconds

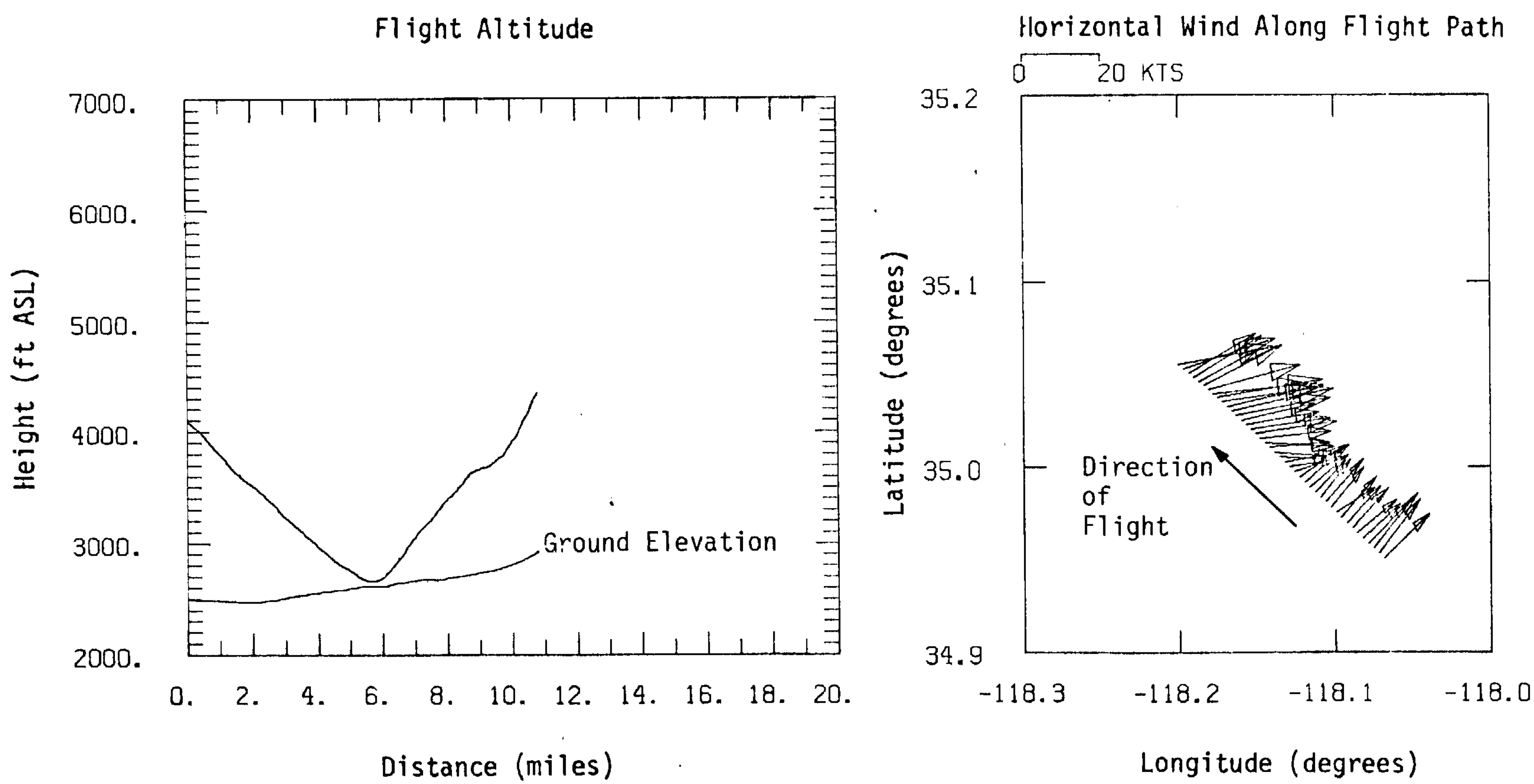

Figure A.6. Flight altitude and horizontal wind along flight path, Flight 31, Run 2.

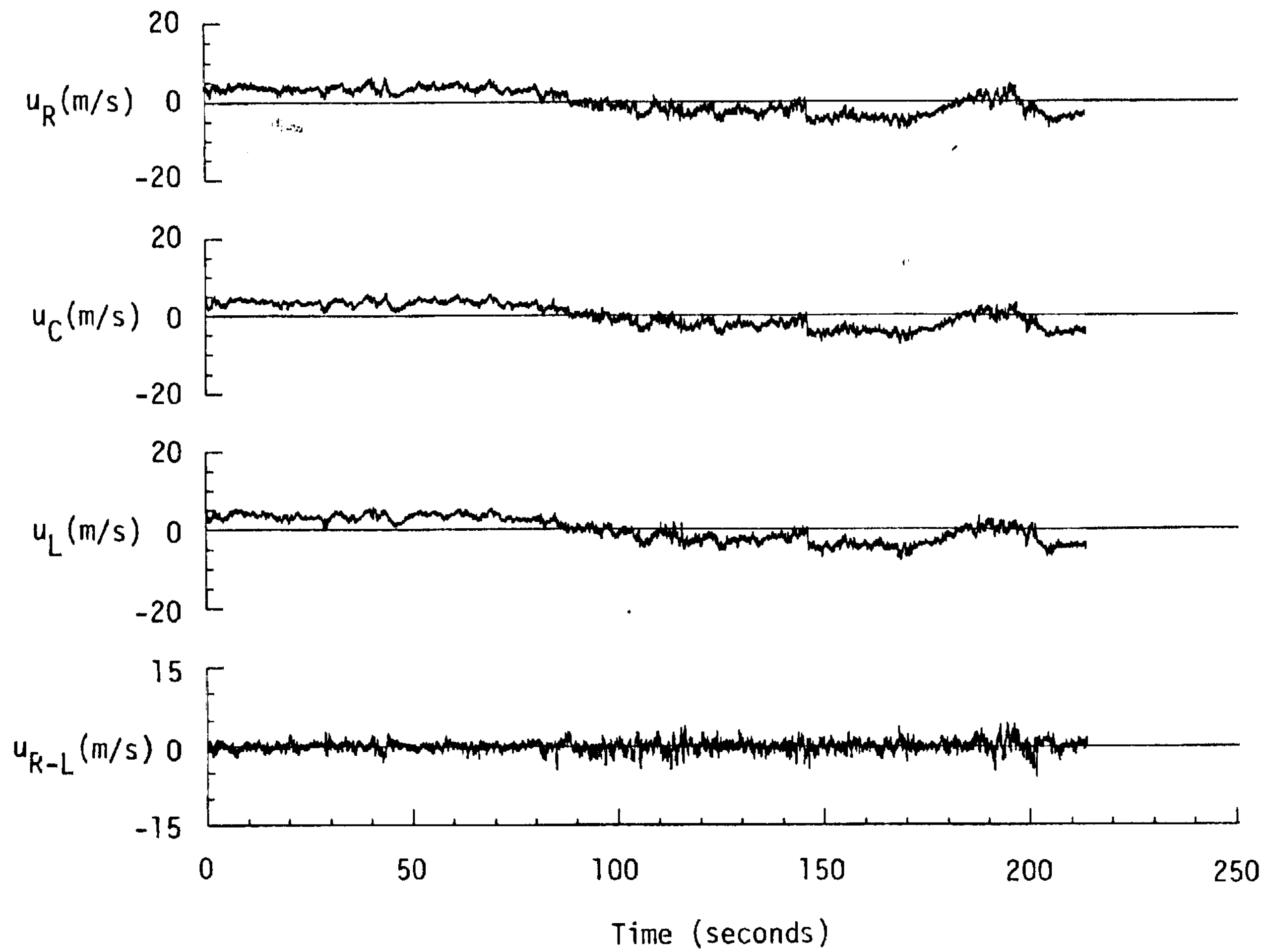

Figure A.7. Time histories of gust velocities, gust velocity differences, and aircraft's normal accelerations, Flight 31, Run 2.

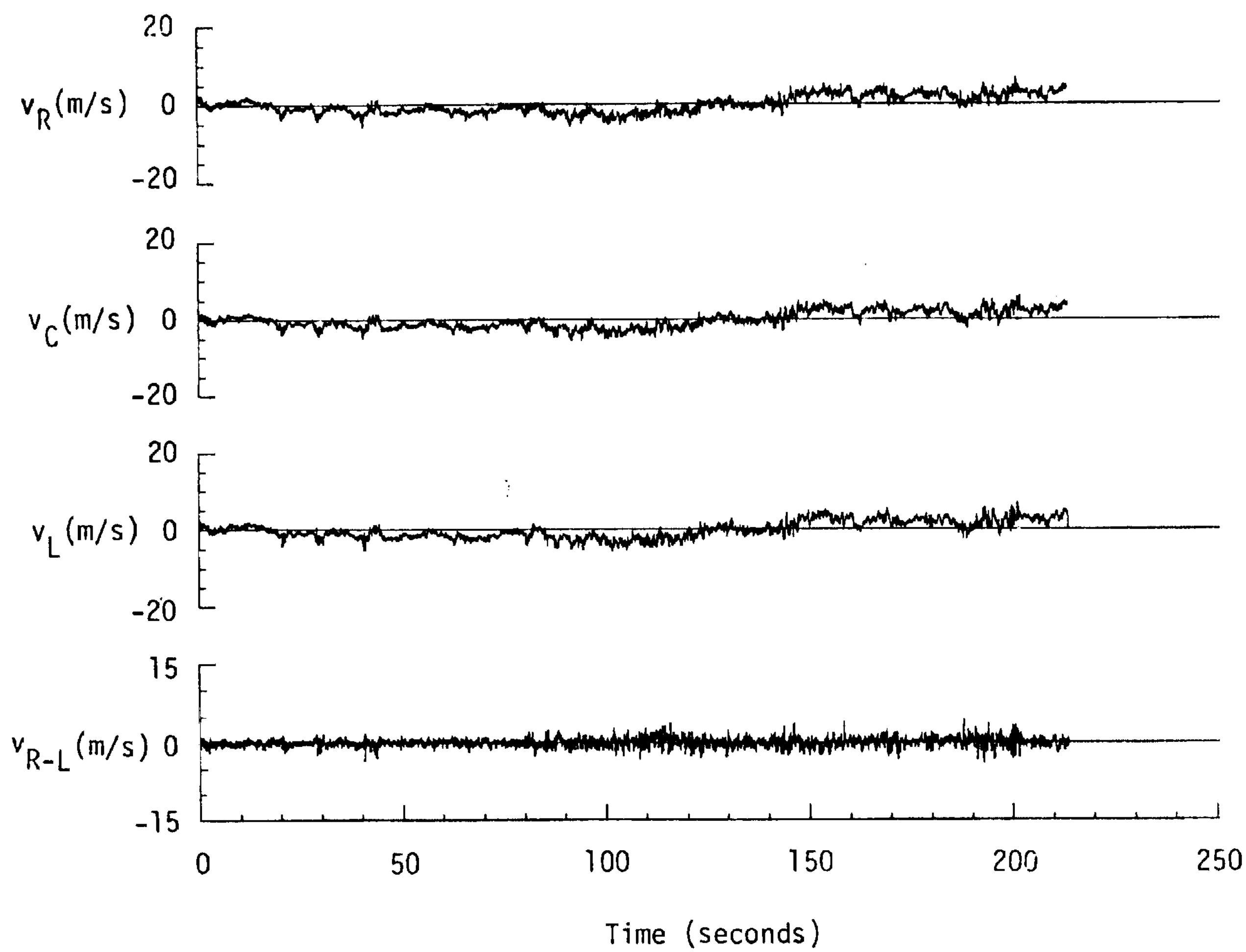

Figure A.7. (continued).

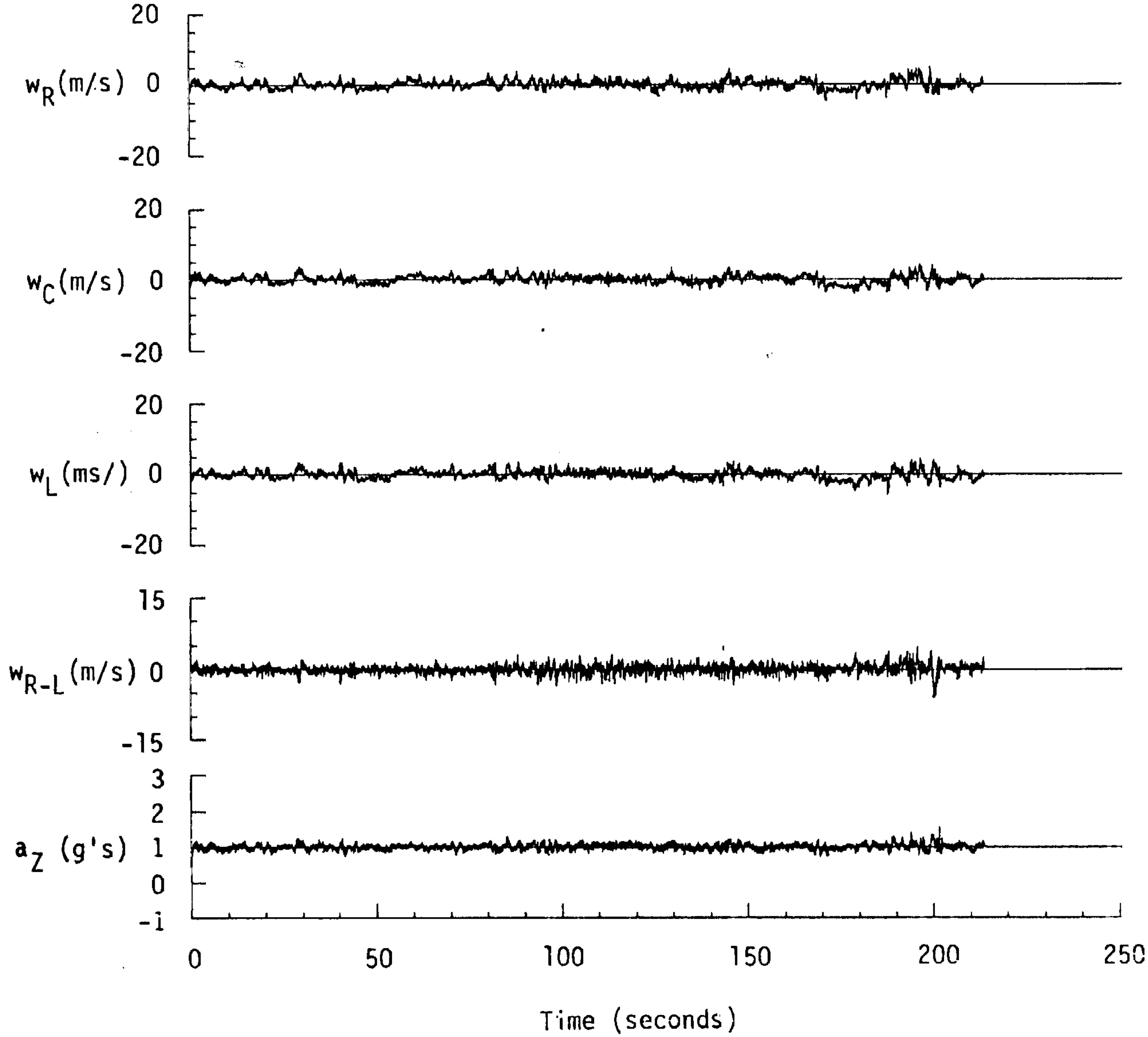

Figure A.7. (continued).

TABLE A.3. Average Turbulence Parameters, Integral Length Scales, and Correlation Coefficients of Gust Velocities, Flight 31, Run 2.

1. Mean Airspeed (m/s):

$\overline{V}_L$	$\overline{V}_C$	$\overline{V}_R$
87.82	85.79	87.51

2. Standard Deviation of Gust Velocities (m/s):

σ_{uR}	σ_{vR}	σ_{wR}
3.23	2.03	1.16

σ_{uC}	σ_{vC}	σ_{wC}
3.20	2.01	1.08

σ_{uL}	σ_{vL}	σ_{wL}
3.20	2.09	1.17

3. Standard Deviation of Gust Velocity Differences (m/s):

$\sigma_{\Delta uRL}$	$\sigma_{\Delta vRL}$	$\sigma_{\Delta wRL}$
0.94	0.77	0.87

4. Integral Length Scale (m):

L_{uR}	L_{vR}	L_{wR}
325.9	250.1	79.1

L_{uRL}	L_{vRL}	L_{wRL}
322.4	251.8	89.3

5. Correlation Coefficient of Gust Velocities:

$\overline{u_R u_L}/\sigma_{u_R}\sigma_{u_L}$	$\overline{v_R v_L}/\sigma_{v_R}\sigma_{v_L}$	$\overline{w_R w_L}/\sigma_{w_R}\sigma_{w_L}$
0.80	0.81	0.82

$\overline{u_R v_R}/\sigma_{u_R}\sigma_{v_R}$	$\overline{v_R w_R}/\sigma_{v_R}\sigma_{w_R}$	$\overline{w_R u_R}/\sigma_{w_R}\sigma_{u_R}$
0.00	-0.05	0.11

$\overline{u_R v_L}/\sigma_{u_R}\sigma_{v_L}$	$\overline{v_R w_L}/\sigma_{v_R}\sigma_{w_L}$	$\overline{w_R u_L}/\sigma_{w_R}\sigma_{u_L}$
-0.02	-0.03	0.10

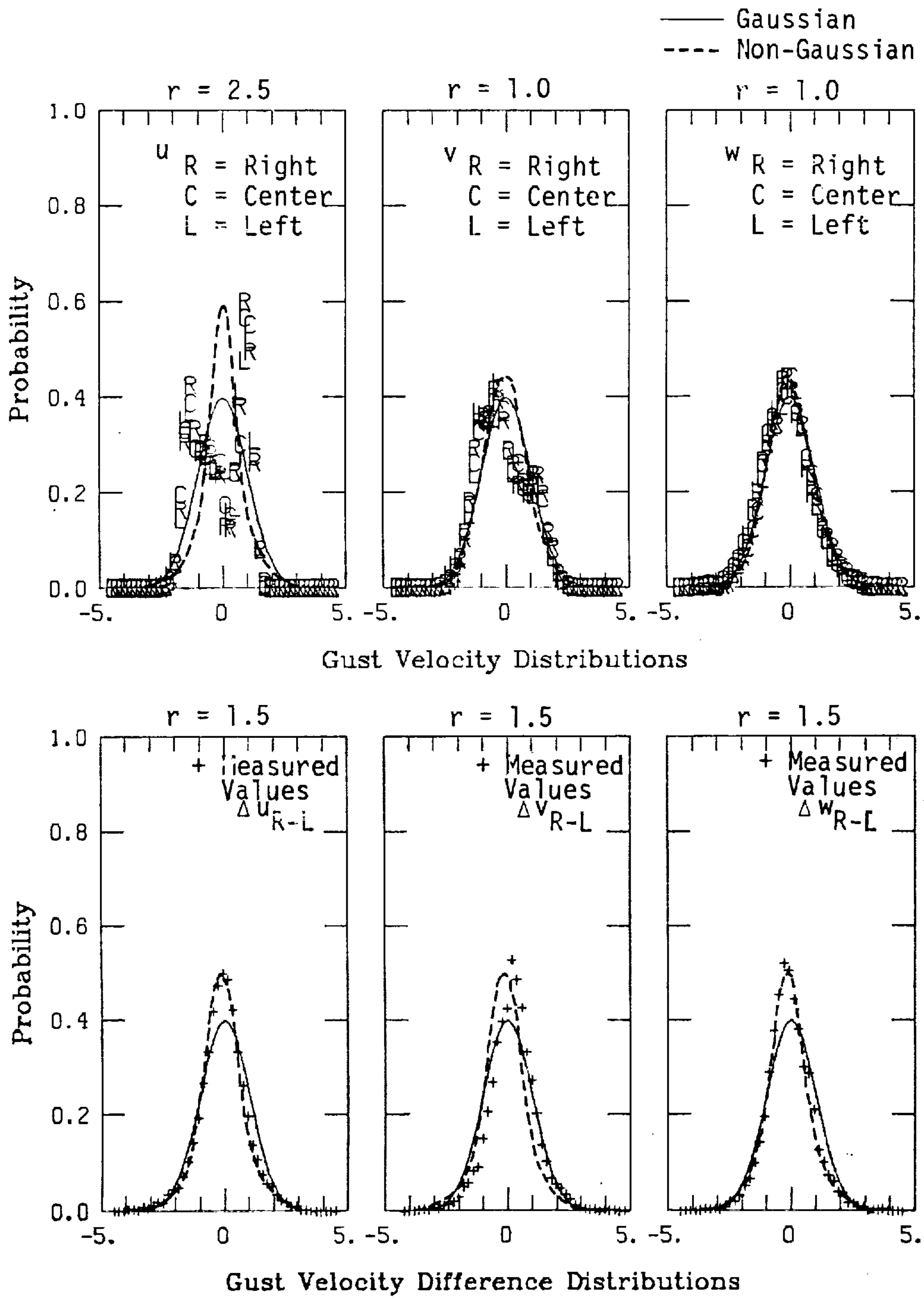

Figure A.8. Probability density functions for gust velocities and gust velocity differences (normalized with the standard deviation), Flight 31, Run 2 (r = degree of non-Gaussian).

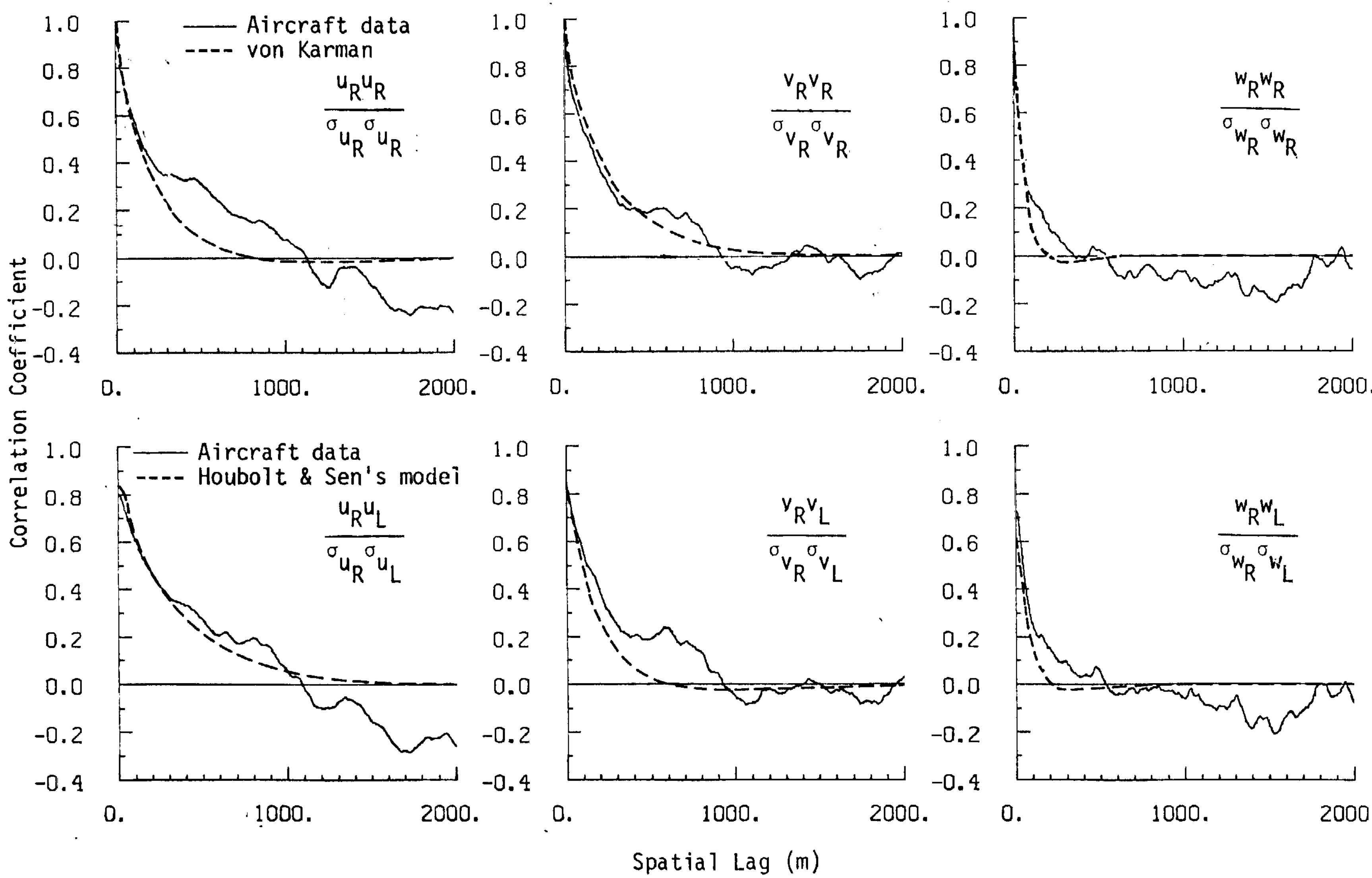

a. One- and two-point common component correlations.

Figure A.9. Comparison of normalized one- and two-point correlation functions for gust velocities with theoretical models, Flight 31, Run 2.

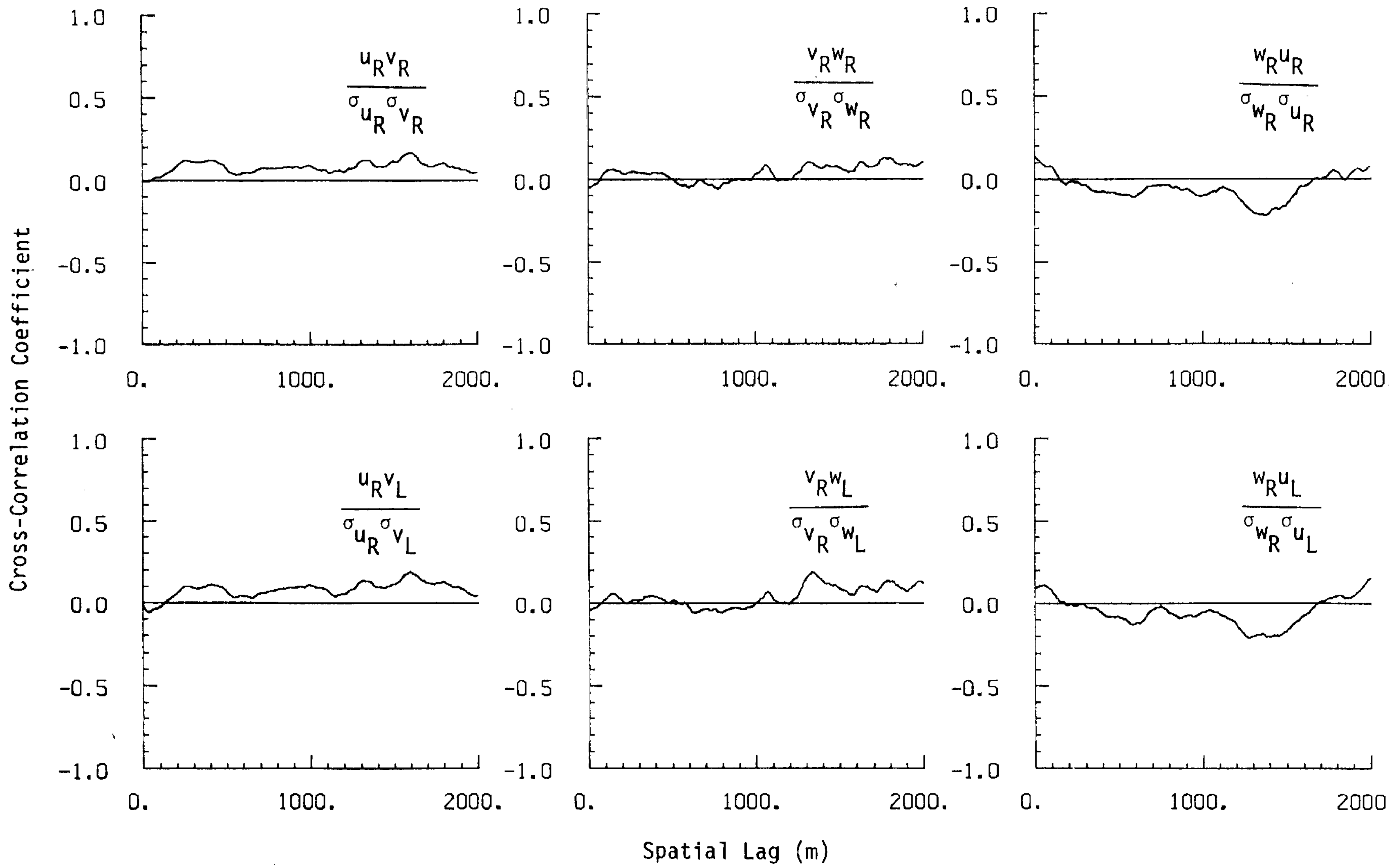

b. One- and two-point cross-correlations.

Figure A.9. (continued).

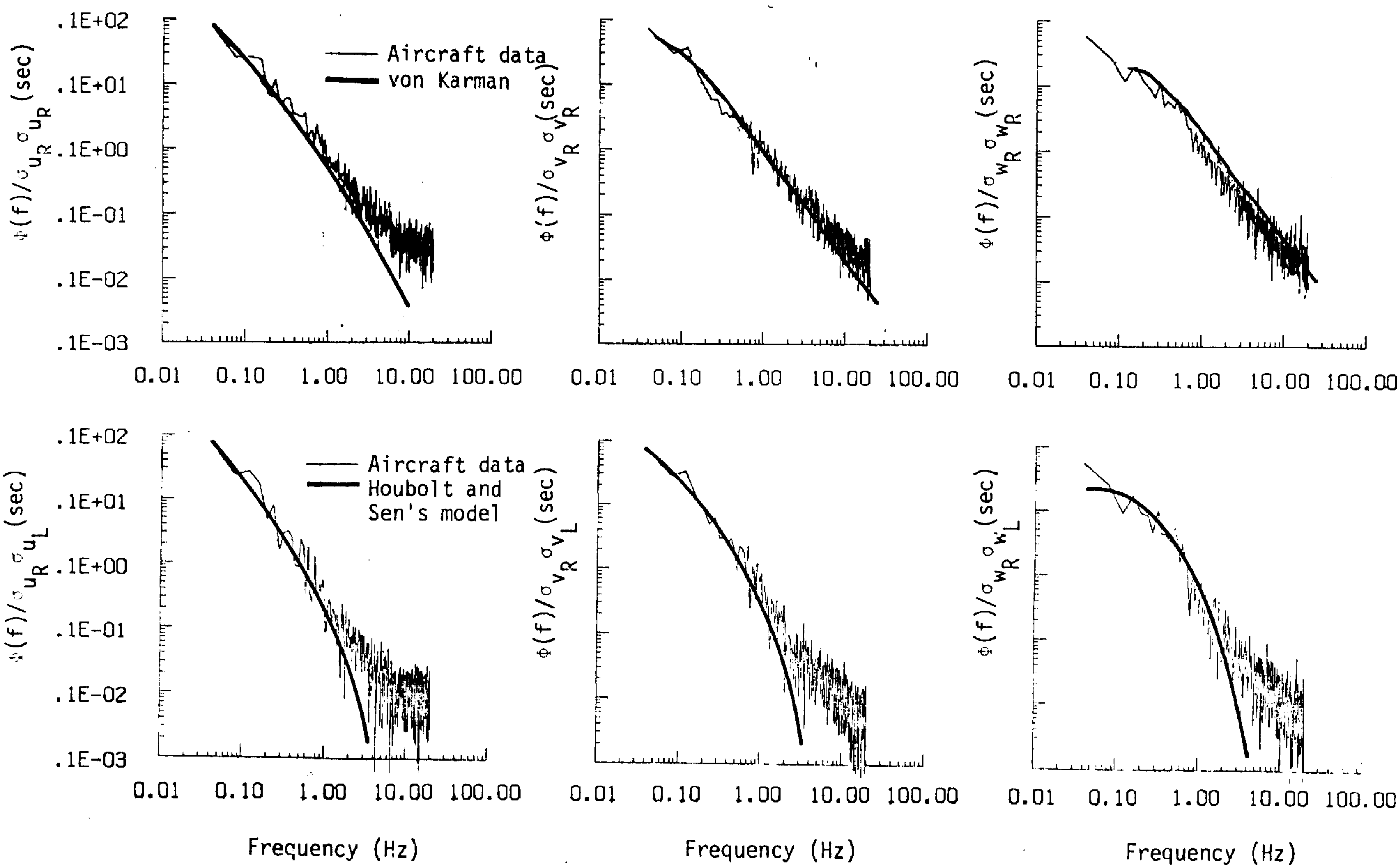

a. One- and two-point common component spectra.

Figure A.10. Comparison of normalized one- and two-point spectral density functions for gust velocities with theoretical models, Flight 31, Run 2.

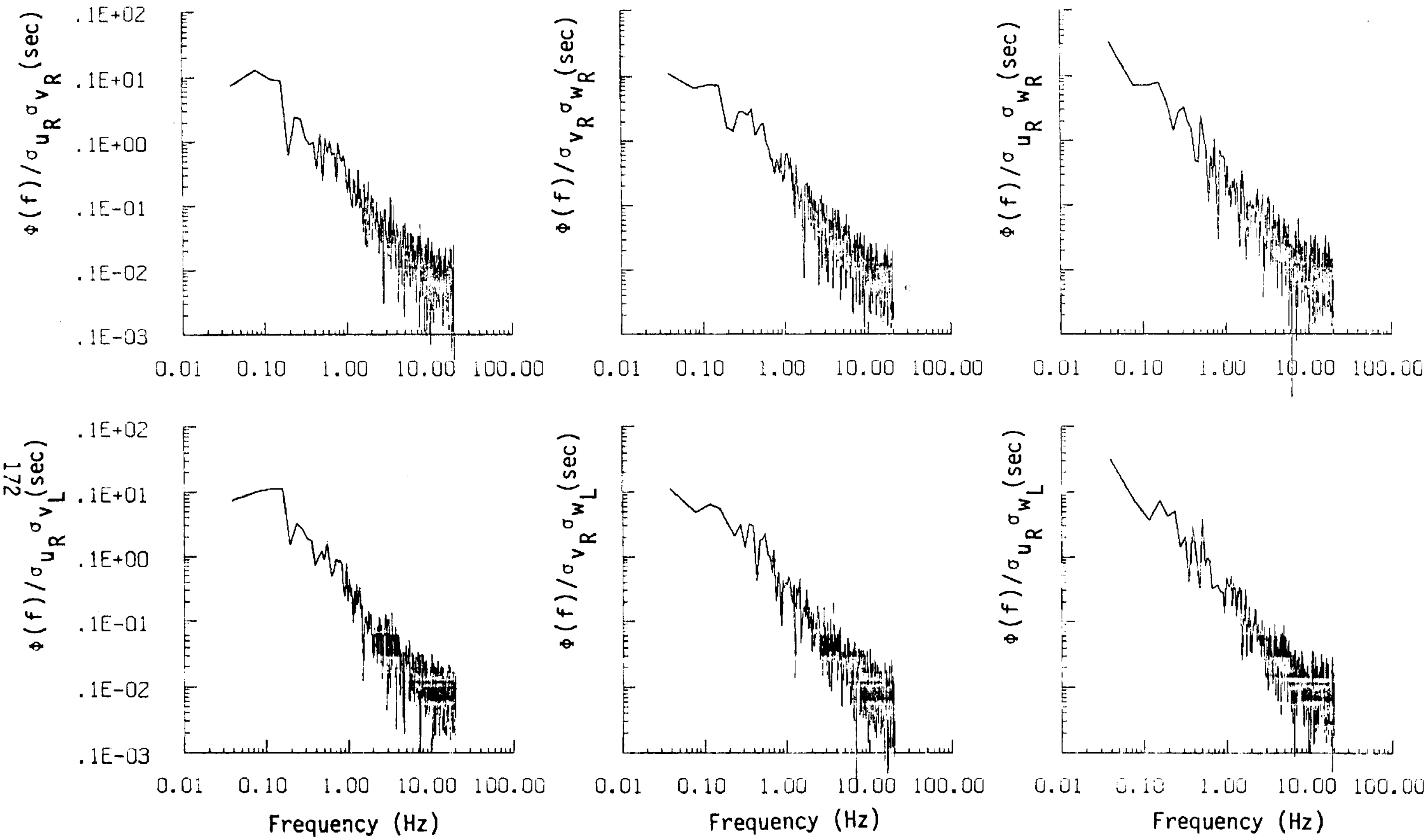

b. One- and two-point cruss-spectra.

Figure A.10. (continued).

ORIGINAL PAGE IS
OF POOR QUALITY

TABLE A. 4. List of All Parameters Measured and Their Range of Values, Flight 31, Run 2.

CHANNEL	UNITS	HIGH	LOW	MEAN	RMS	STD	POINTS
1 TIME	SECONDS	38569.480	38355.680	38462.57960	38462.62913	61.72956	8553
2 PHI DOT	RAD/SEC	.227	-.115	-.00251	.02860	.02849	8553
3 ACCL N CG	G UNITS	1.346	.714	1.00315	1.00549	.06859	8553
4 THETA DOT	RAD/SEC	.057	-.300	.00363	.01359	.01304	8553
5 THETA	RAD	.205	.017	.09551	.11383	.06192	8553
6 PHI	RAD	.199	-.070	.00359	.02820	.02798	8553
7 PSI 1	RAD	311.567	285.776	307.23980	307.25309	2.85796	8553
8 DEL PSI 1	DEG	3.551	-8.175	-.66239	2.92770	2.85196	8553
9 PSI 2	RAD	326.559	301.611	309.00041	309.01289	2.77760	8553
10 DEL PSI 2	DEG	4.020	-7.585	-.17968	2.82493	2.81938	8553
11 ACCL N LT	G UNITS	2.139	.265	1.01329	1.02488	.15371	8553
12 ACCL N RT	G UNITS	1.994	.105	1.01543	1.02855	.16375	8553
13 ACCL X CG	G UNITS	.255	-.057	.08842	.10989	.06526	8553
14 ACCL Y CG	G UNITS	.118	-.274	-.00606	.02688	.02619	8553
15 ALPHA CTR	RAD	.083	-.076	.01408	.01966	.01372	8553
16 BETA CTR	RAD	.070	-.080	.00193	.02184	.02176	8553
17 TEMP I	DEG F	84.053	63.854	82.19946	82.22031	1.85189	8553
18 TEMP P	DEG F	59.566	38.378	59.27732	59.27793	.27067	8553
19 ACCL Z INS	G UNITS	1.556	.730	1.01160	1.01433	.07439	8553
20 ALPHA RT	RAD	.112	-.042	.03470	.03832	.01626	8553
21 BETA RT	RAD	.082	-.057	.01527	.02497	.01977	8553
22 ALPHA LT	RAD	.132	-.012	.05993	.06183	.01522	8553
23 BETA LT	RAD	.075	-.075	.00168	.02052	.02044	8553
24 PSI DOT	RAD/SEC	.301	-.047	.00204	.01240	.01223	8553
25 TEMP TOT	DEG C	18.135	11.404	15.12241	15.21165	1.64534	8553
26 QC LT	PSID	.724	.483	.62462	.62593	.04048	8553
27 QC CTR	PSID	.679	.468	.59555	.59683	.03901	8553
28 QC RT	PSID	.702	.467	.62016	.62152	.04106	8553
29 PS	PSIA	13.338	12.507	12.99476	12.99661	.21950	8553
30 TEMP IRT	VOLTS	15.153	-41.227	7.60538	7.77961	1.63734	8553
31 HYGROM	DEG C	5.492	-9.750	3.67597	3.83721	1.10070	8553
32 QC2 LT	PSID	.038	-.039	.01222	.01318	.00494	8553
33 QC2 CTR	PSID	.158	.033	.11891	.12401	.03520	8553
34 QC2 RT	PSID	.119	.041	.07745	.08160	.02570	8553
35 DAR	DEG	-.971	-4.247	-3.92706	3.93044	.16260	8553
36 DAL	DEG	.008	-3.416	-2.84371	2.87181	.40082	8553
37 DELEV	DEG	3.838	-4.120	-2.95363	2.97594	.36371	8553
38 DSTAB	DEG	.192	-.257	.12607	.12749	.01897	8553
39 DRUD	DEG	6.952	-2.690	-2.24098	2.26445	.32518	8553
40 DTHRR	PCT MAX	59.561	37.110	44.56779	44.56930	.36684	8553
41 DTHRL	PCT MAX	59.561	42.225	44.88212	44.88266	.22100	8553
42 DFLP	POSITION	1.469	.583	1.17359	1.17361	.00757	8553
43 DSB	POSITION	.167	-.170	-.11579	.11583	.00325	8553
44 D TO G	METERS	7495236.826	7486780.454	***********	***********	2394.01216	8553
45 B TO D	DEGREES	73.045	72.908	72.97481	72.97482	.03913	8553
46 LONG	DEGREES	-118.066	-118.204	-118.13623	118.13623	.03929	8553
47 LAT	DEGREES	35.058	34.949	35.00627	35.00628	.03163	8553
48 TRK ANG	DEGREES	315.901	309.369	313.81002	313.81420	1.62051	8553
49 HDG	RADIANS	5.465	5.255	5.38919	5.38944	.05112	8553
50 VE	M/SEC	-54.059	-63.700	-58.69607	58.77770	3.09695	8553
51 VN	M/SEC	62.297	48.391	56.40953	56.58154	4.40878	8553
52 ALTITUDE	KM	1.340	.810	1.02655	1.03596	.13928	8553
53 TEMPC	DEGREES C	14.679	7.695	11.45527	11.56612	1.59760	8553
54 EW WND SPD	KNOTS	31.953	3.859	15.89623	17.09024	6.27620	8553
55 NS WND SPD	KNOTS	16.271	-4.922	5.48742	6.62977	3.72072	8553
56 WIND SPEED	KNOTS	32.250	5.089	17.51617	18.33112	5.40529	8553
57 WIND DIREC	DEGREES	287.974	208.321	248.07574	248.67848	17.30453	8553
58 WIND DIR2	DEGREES	107.974	28.321	68.07575	70.24044	17.30454	8553
59 WIND DIR3	DEGREES	287.974	208.321	248.07575	248.67848	17.30454	8553
60 WIND DIR4	DEGREES	287.974	208.321	248.07575	248.67848	17.30454	8553
61 AIRSPEED R	M/SEC	93.378	78.052	87.51776	87.56476	2.86895	8553
62 AIRSPEED C	M/SEC	91.900	76.506	85.79319	85.83874	2.79627	8553
63 AIRSPEED L	M/SEC	94.811	77.718	87.82903	87.87441	2.82402	8553
64 DELTA ALT	METERS	90.600	-438.875	-222.37870	262.39315	139.28442	8553
65 INRTL DISP	METERS	90.093	-438.569	-224.03475	263.75437	139.20152	8553
66 UG RIGHT	M/SEC	6.320	-7.157	.00000	3.23504	3.23523	8553
67 UG CENTER	M/SEC	6.010	-7.558	.00000	3.20694	3.20713	8553
68 UG LEFT	M/SEC	5.846	-7.891	.00000	3.20447	3.20466	8553
69 VG RIGHT	M/SEC	6.663	-6.974	-.07647	2.03826	2.03694	8553
70 VG CENTER	M/SEC	6.018	-5.251	-.07065	2.01446	2.01333	8553
71 VG LEFT	M/SEC	6.679	-5.562	-.06860	2.09369	2.09269	8553
72 WG RIGHT	M/SEC	4.941	-4.561	.06738	1.16498	1.16310	8553
73 WG CENTER	M/SEC	4.405	-3.997	.07158	1.08901	1.08672	8553
74 WG LEFT	M/SEC	4.705	-5.577	.06846	1.17453	1.17258	8553

Flight 31, Run 3
Date: Nov. 29, 1982
Start Time: 10:44:29 (PST)
Duration: 694.8 seconds

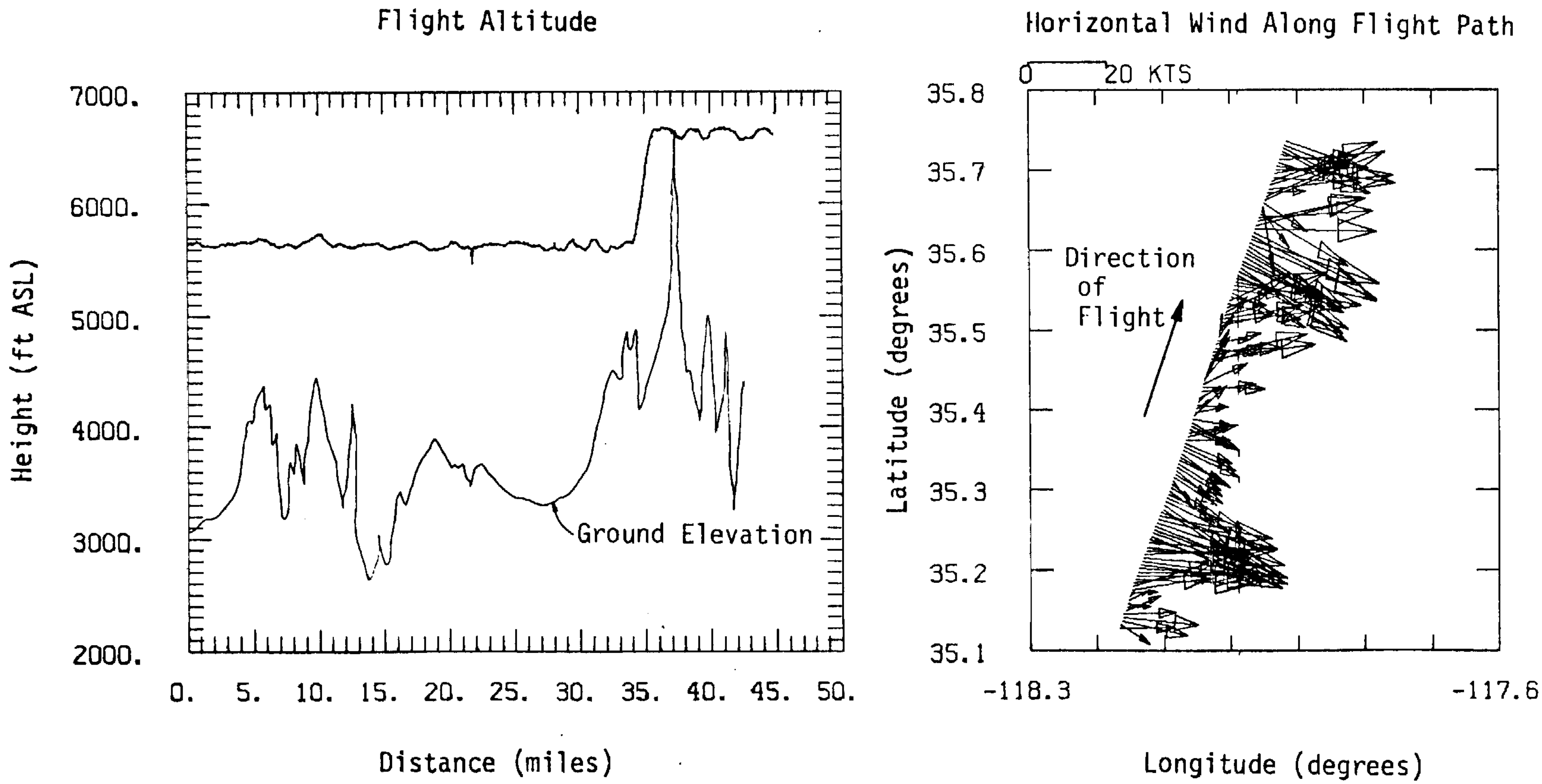

Figure A.11. Flight altitude and horizontal wind along flight path, Flight 31, Run 3.

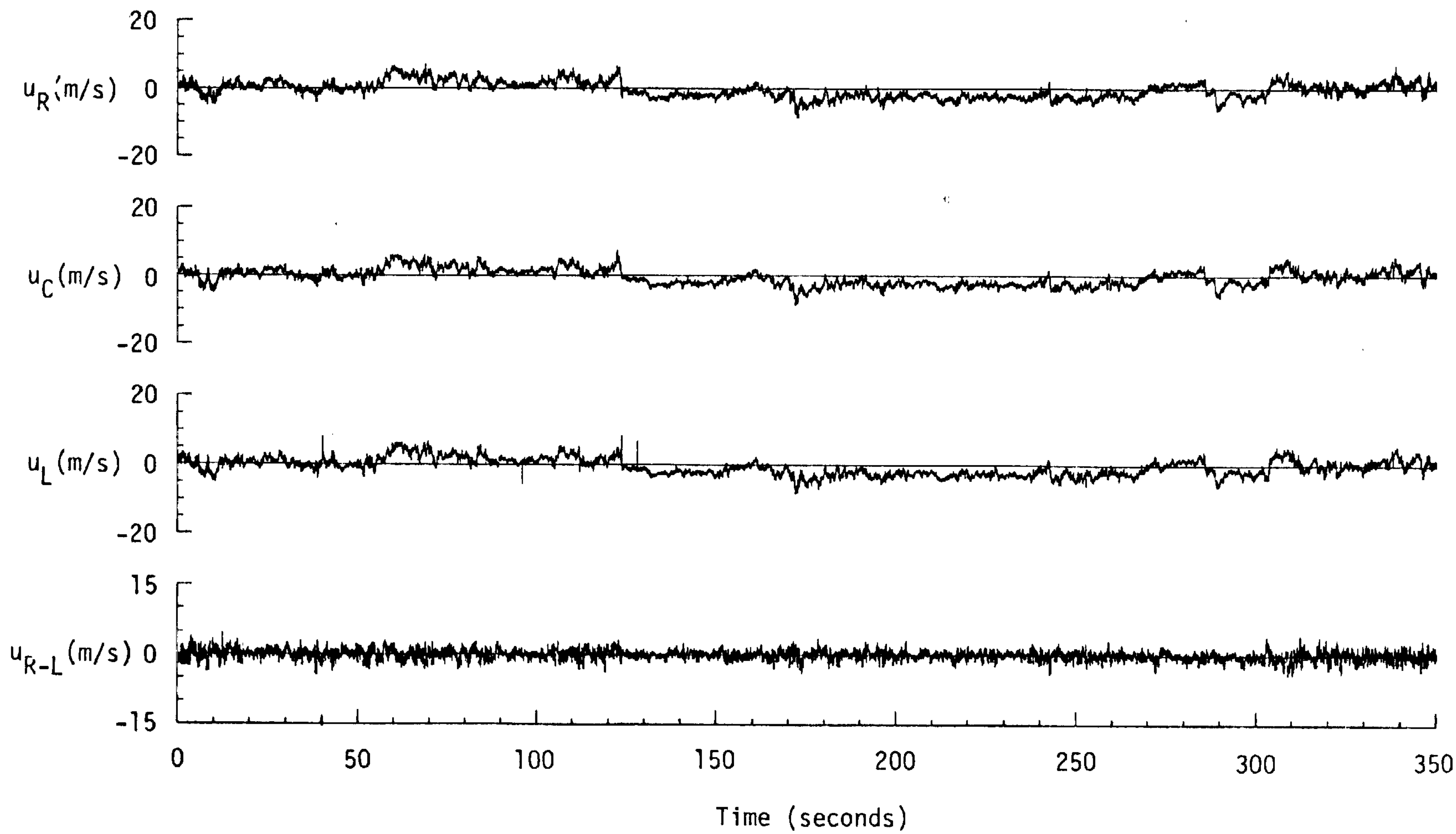

Figure A.12. Time histories of gust velocities, gust velocity differences, and aircraft's normal accelerations, Flight 31, Run 3.

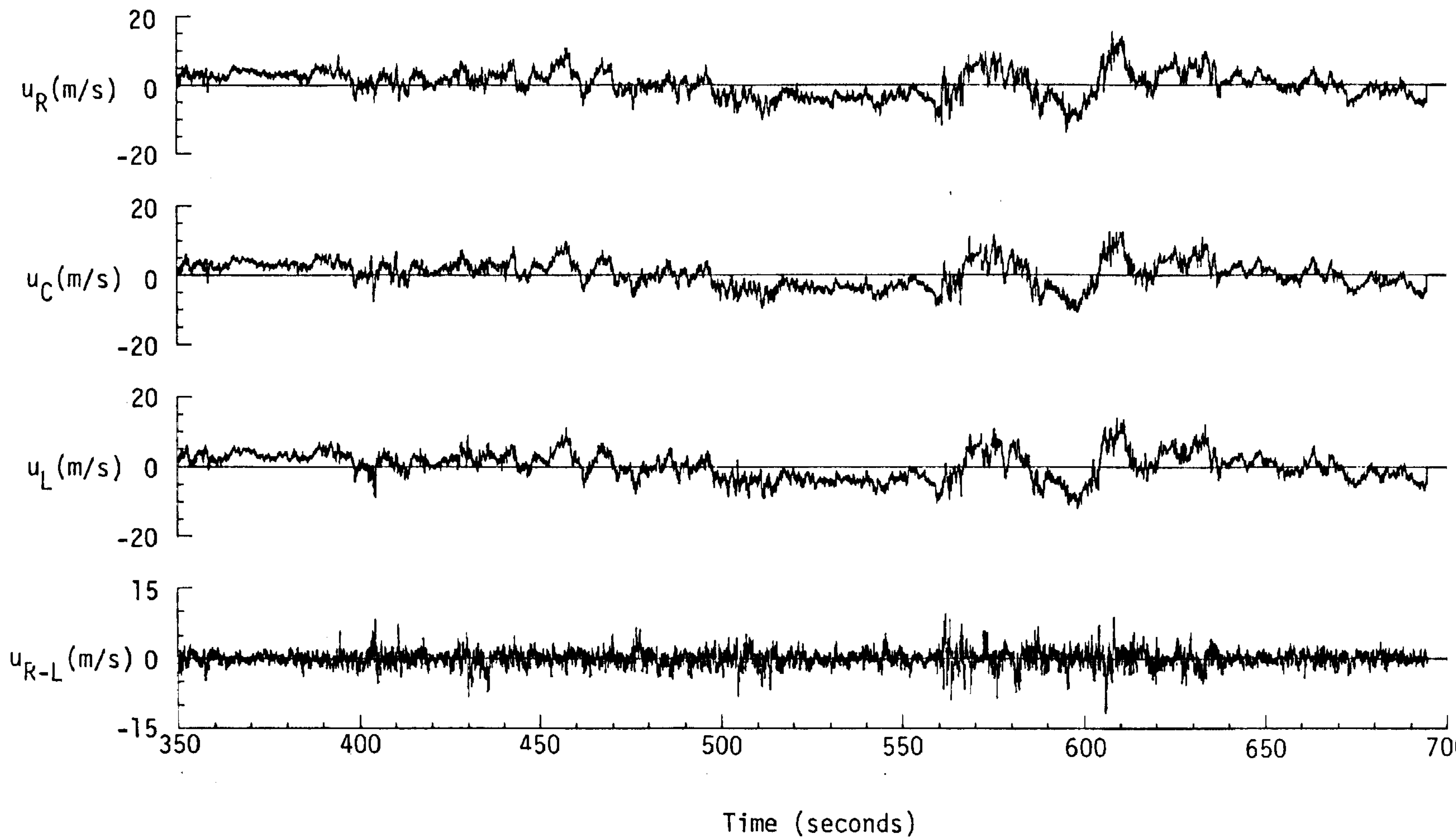

Figure A.12. (continued).

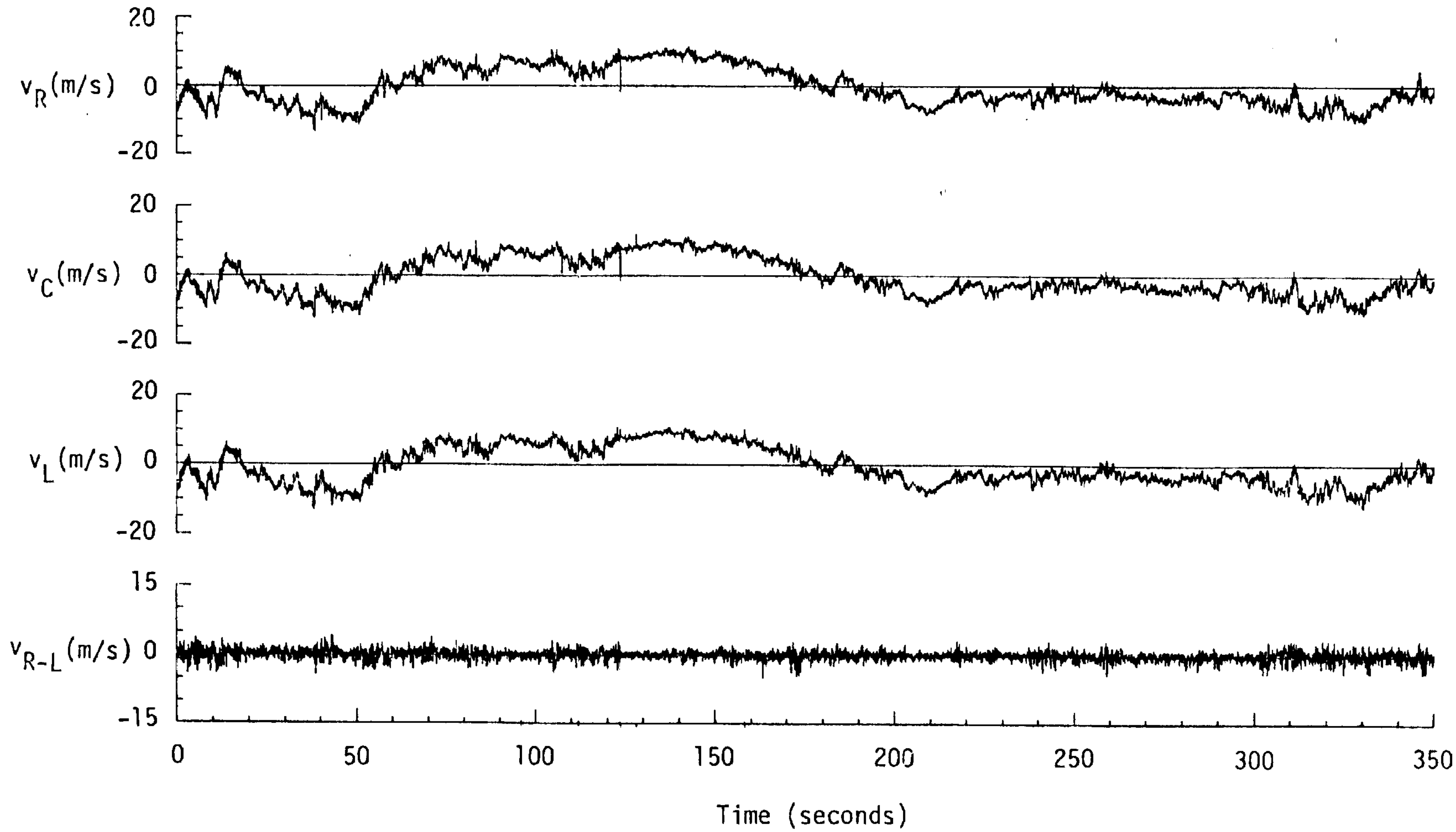

Figure A.12. (continued).

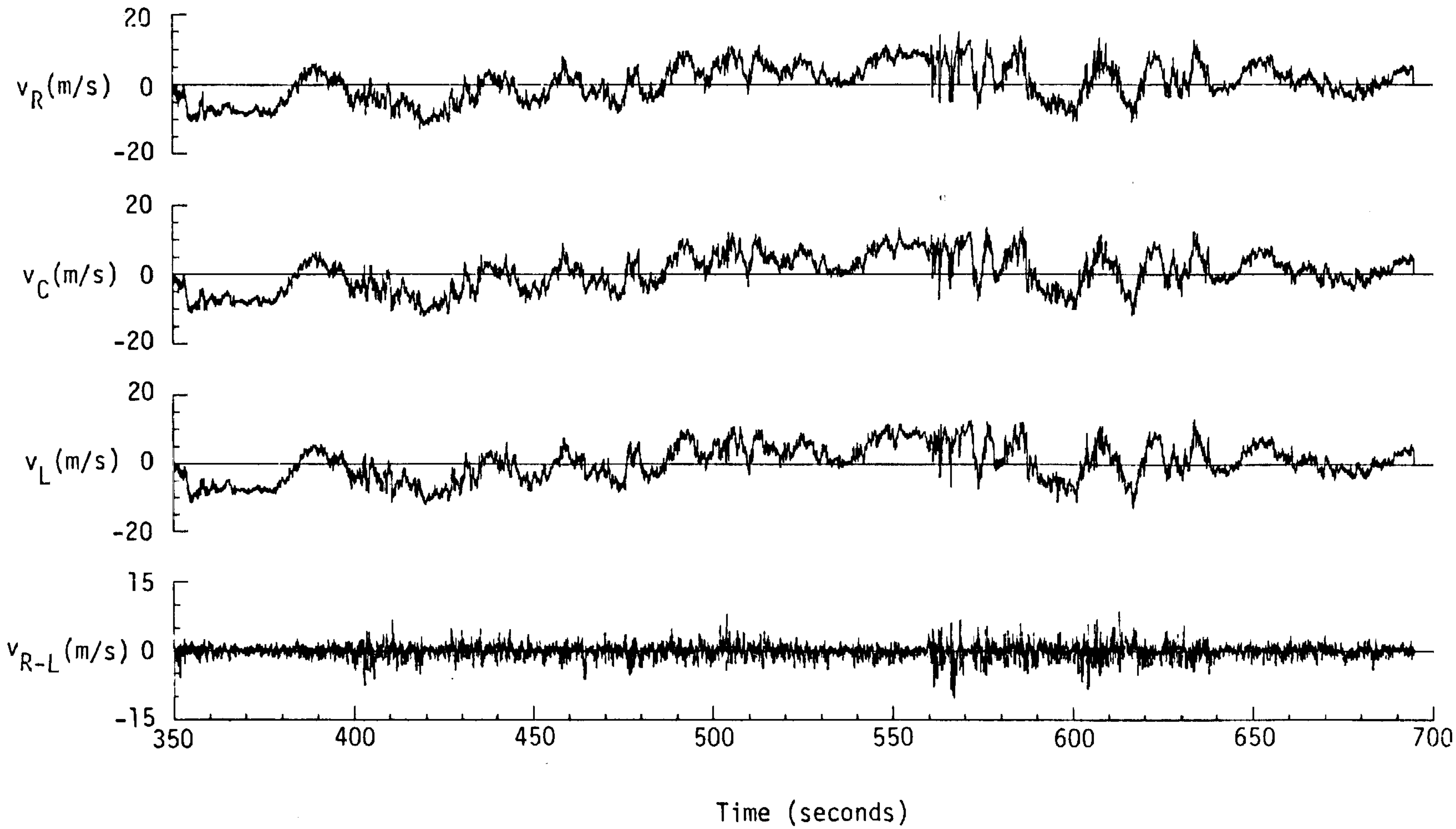

Figure A.12. (continued).

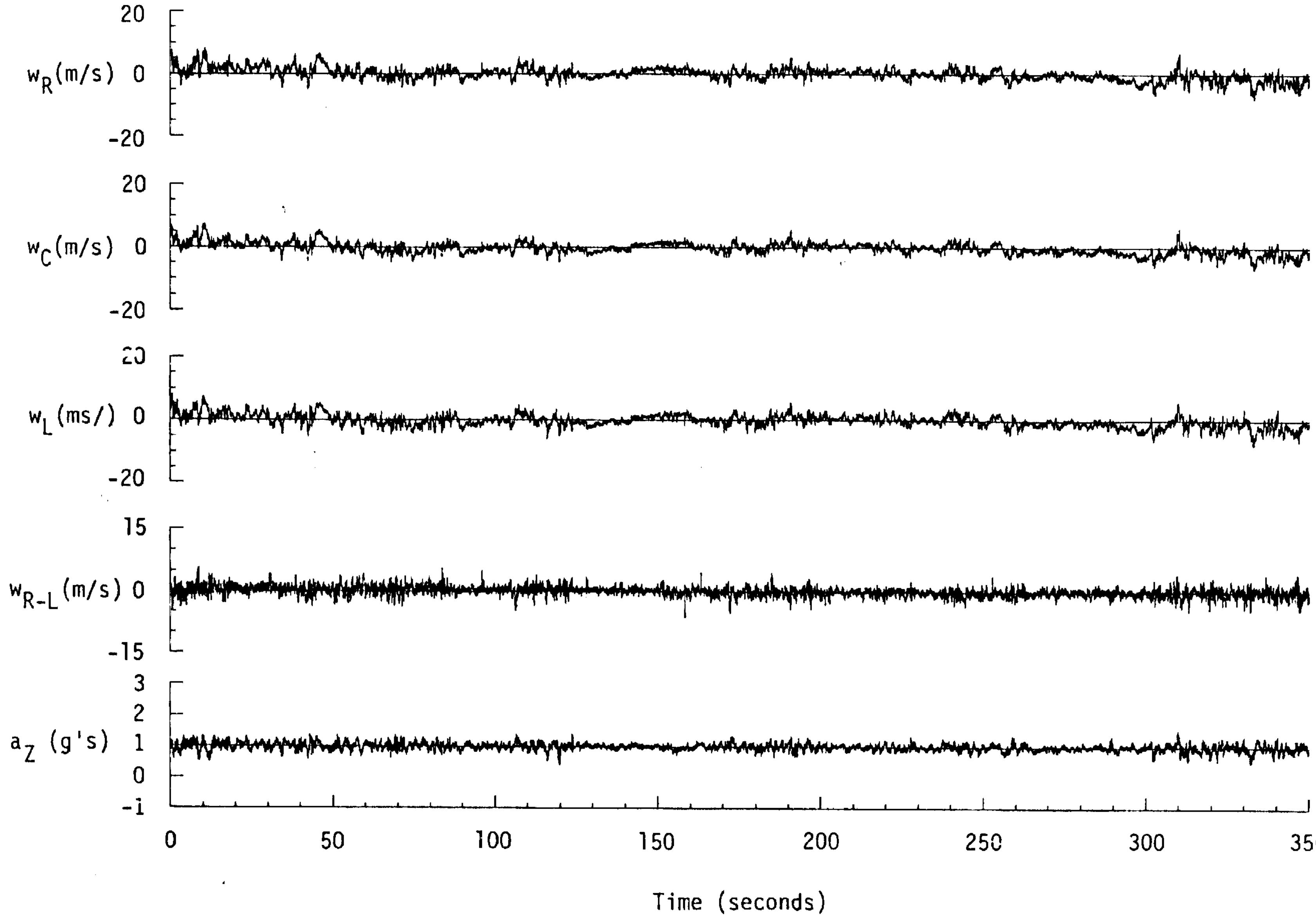

Figure A.12. (continued).

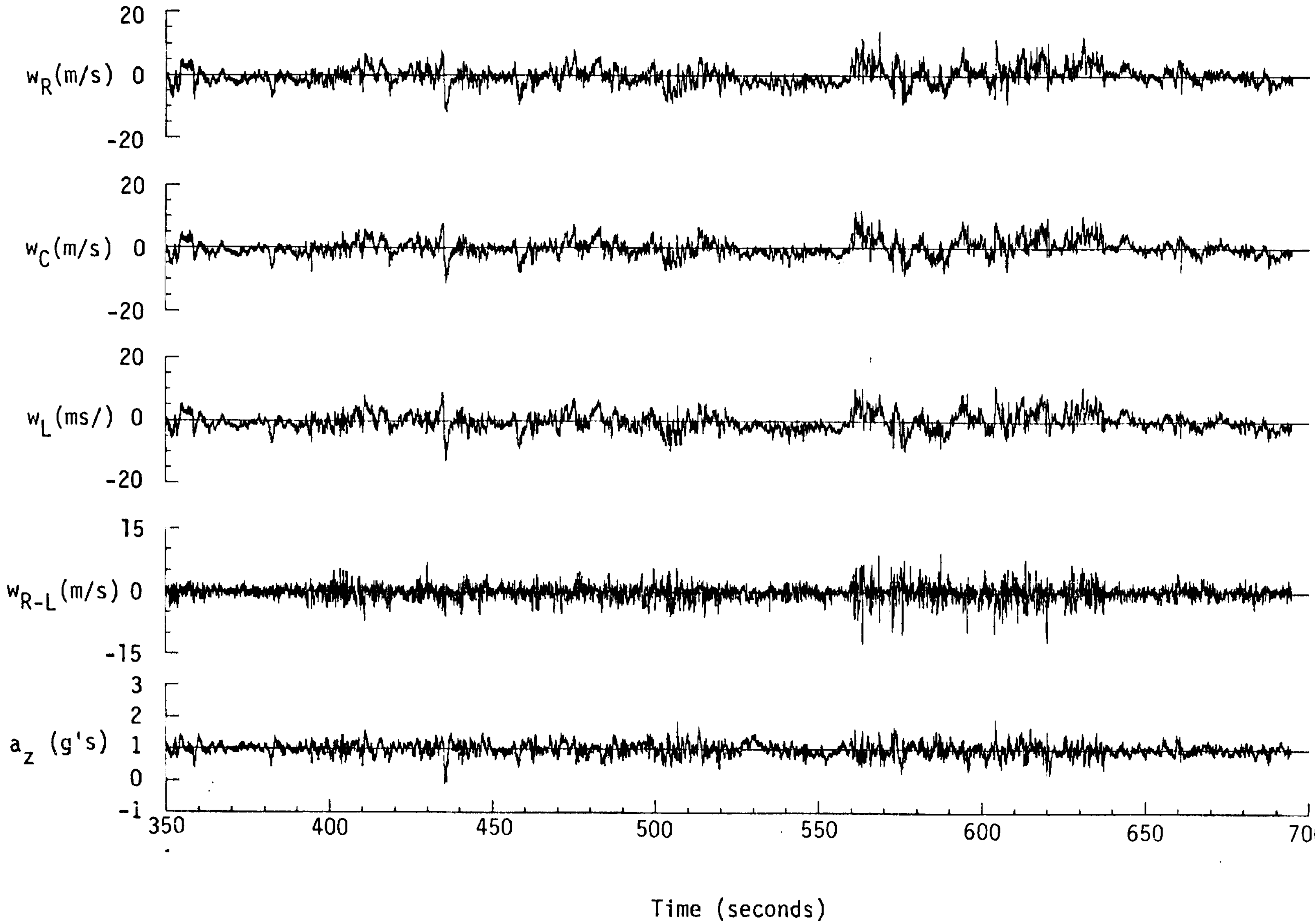

Figure A.12. (continued).

TABLE A.5. Average Turbulence Parameters, Integral Length Scales, and Correlation Coefficients of Gust Velocities, Flight 31, Run 3.

1. Mean Airspeed (m/s):

$\overline{V}_L$	$\overline{V}_C$	$\overline{V}_R$
104.21	102.52	104.60

2. Standard Deviation of Gust Velocities (m/s):

σ_{uR}	σ_{vR}	σ_{wR}
3.17	5.25	2.36

σ_{uC}	σ_{vC}	σ_{wC}
3.15	5.29	2.18

σ_{uL}	σ_{vL}	σ_{wL}
3.19	5.31	2.31

3. Standard Deviation of Gust Velocity Differences (m/s):

$\sigma_{\Delta uRL}$	$\sigma_{\Delta vRL}$	$\sigma_{\Delta wRL}$
1.29	1.23	1.37

4. Integral Length Scale (m):

L_{uR}	L_{vR}	L_{wR}
234.0	425.6	116.9

L_{uRL}	L_{vRL}	L_{wRL}
238.4	422.8	115.3

5. Correlation Coefficient of Gust Velocities:

$\overline{u_R u_L}/\sigma_{u_R}\sigma_{u_L}$	$\overline{v_R v_L}/\sigma_{v_R}\sigma_{v_L}$	$\overline{w_R w_L}/\sigma_{w_R}\sigma_{w_L}$
0.80	0.91	0.75

$\overline{u_R v_R}/\sigma_{u_R}\sigma_{v_R}$	$\overline{v_R w_R}/\sigma_{v_R}\sigma_{w_R}$	$\overline{w_R u_R}/\sigma_{w_R}\sigma_{u_R}$
0.09	-0.19	0.06

$\overline{u_R v_L}/\sigma_{u_R}\sigma_{v_L}$	$\overline{v_R w_L}/\sigma_{v_R}\sigma_{w_L}$	$\overline{w_R u_L}/\sigma_{w_R}\sigma_{u_L}$
0.04	-0.19	0.05

C-3

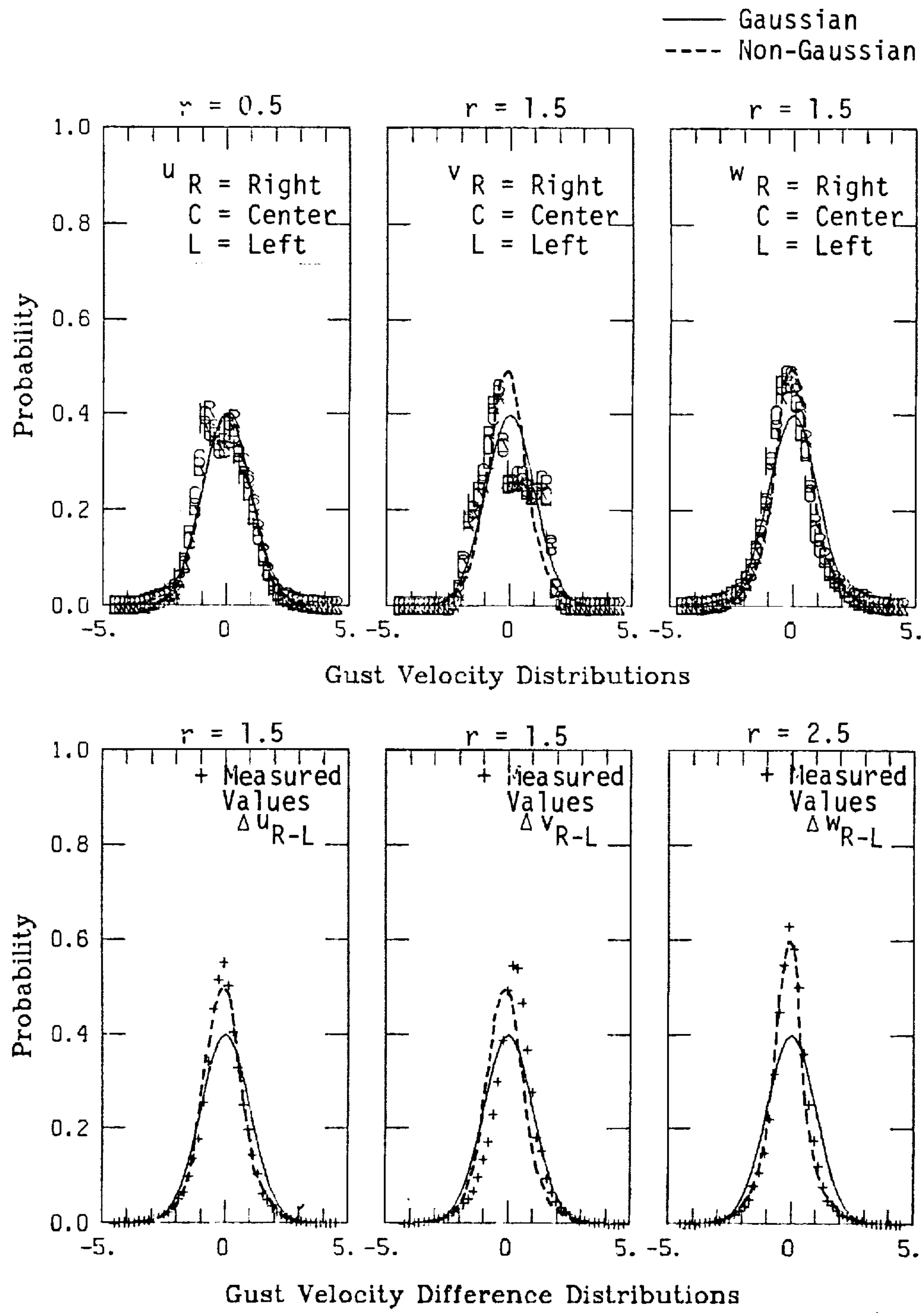

Figure A.13. Probability density functions for gust velocities and gust velocity differences (normalized with the standard deviation), Flight 31, Run 3 (r = degree of non-Gaussian).

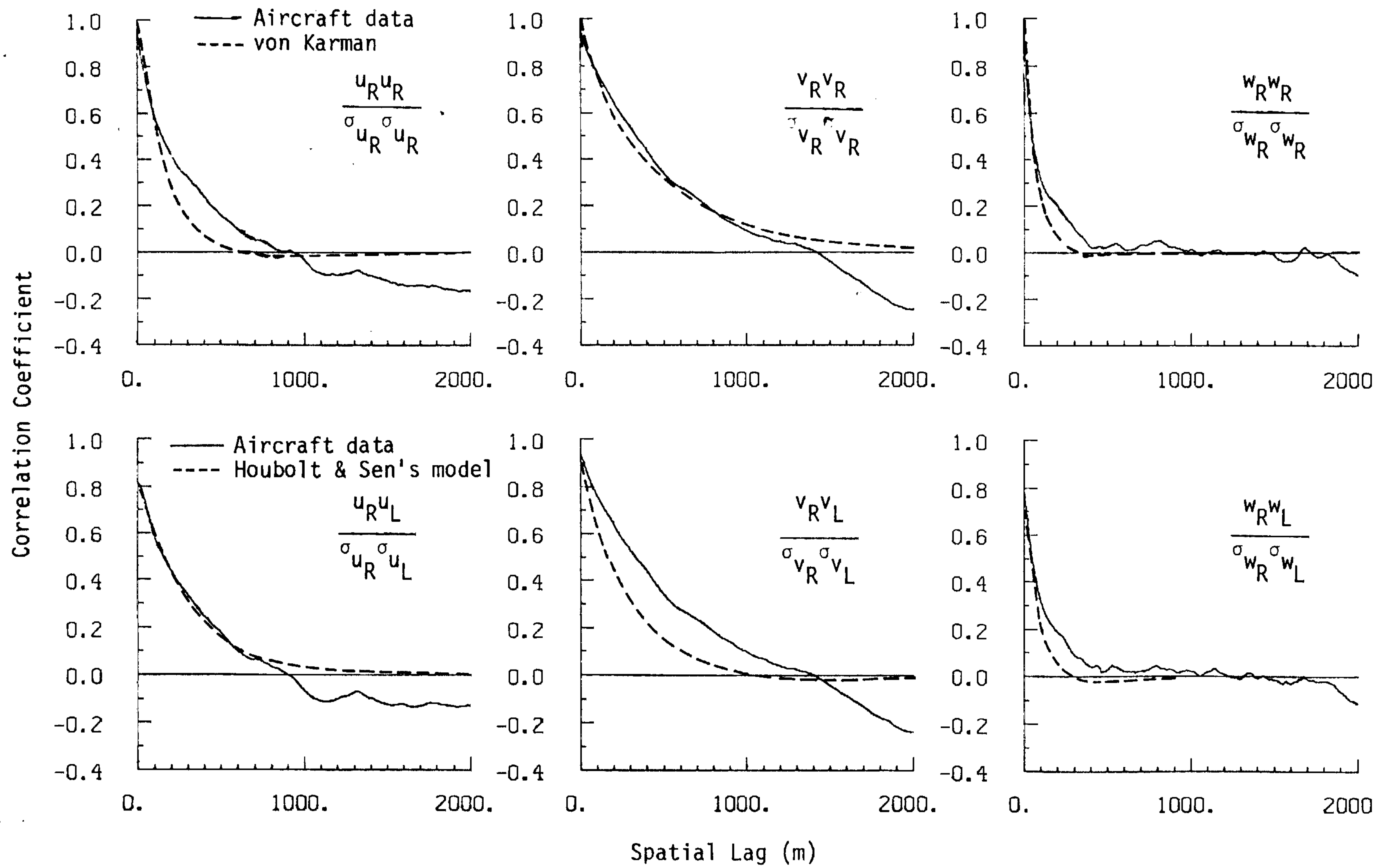

a. One- and two-point common component correlations.

Figure A.14. Comparison of normalized one- and two-point correlation functions for gust velocities with theoretical models, Flight 31, Run 3.

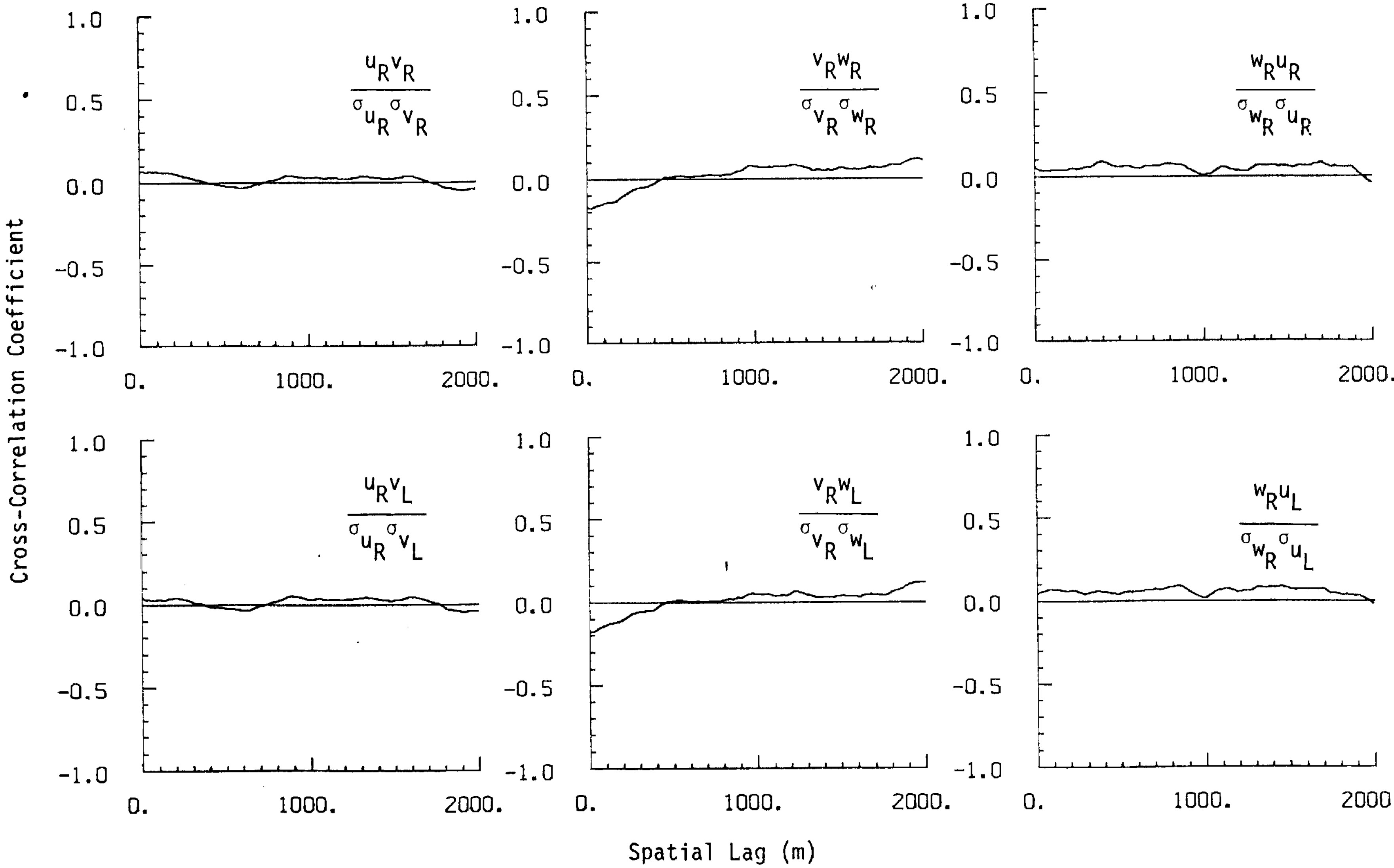

b. One- and two-point cross-correlations.

Figure A.14. (continued).

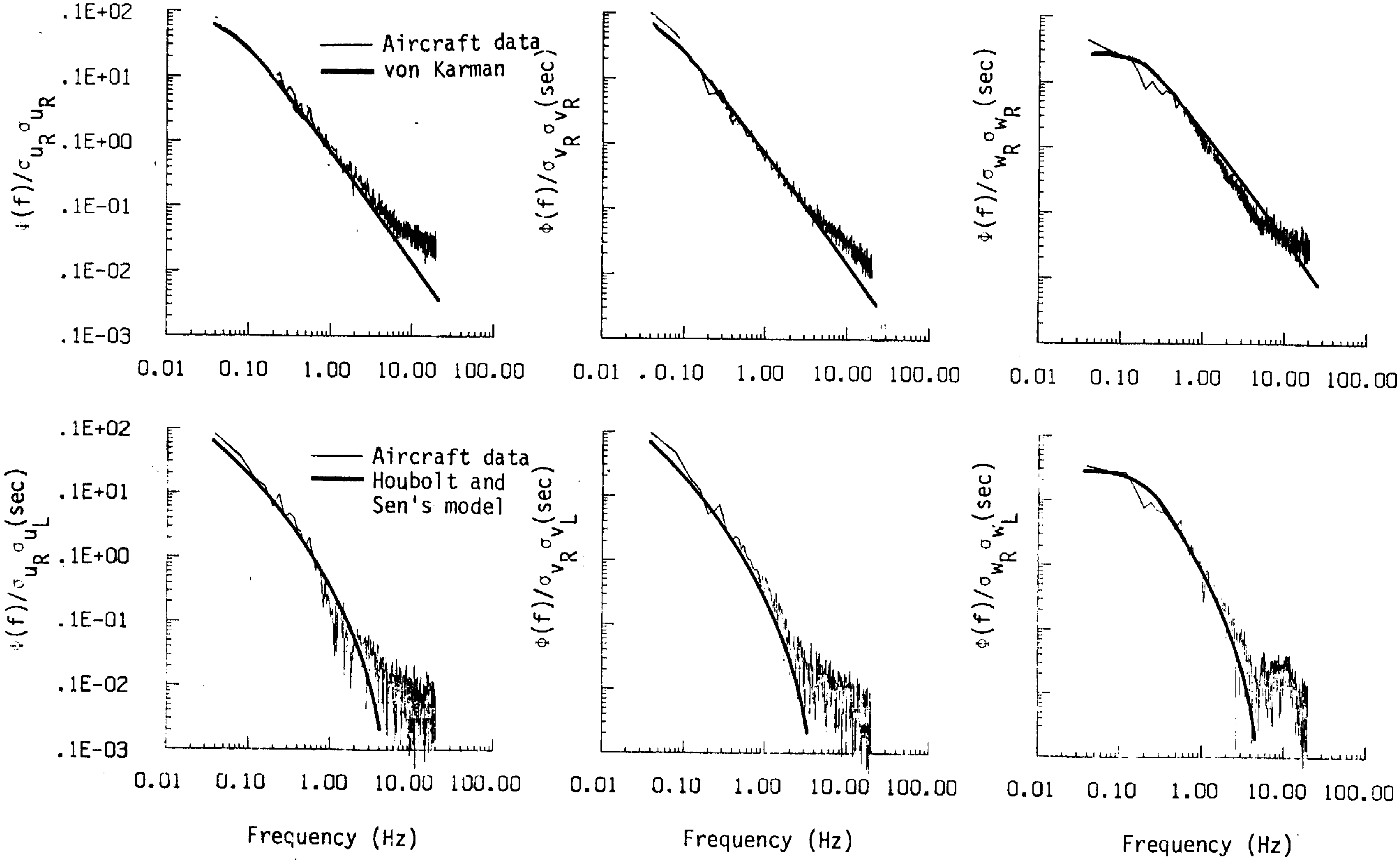

a. One- and two-point common component spectra.

Figure A.15. Comparison of normalized one- and two-point spectral density functions for gust velocities with theoretical models, Flight 31, Run 3.

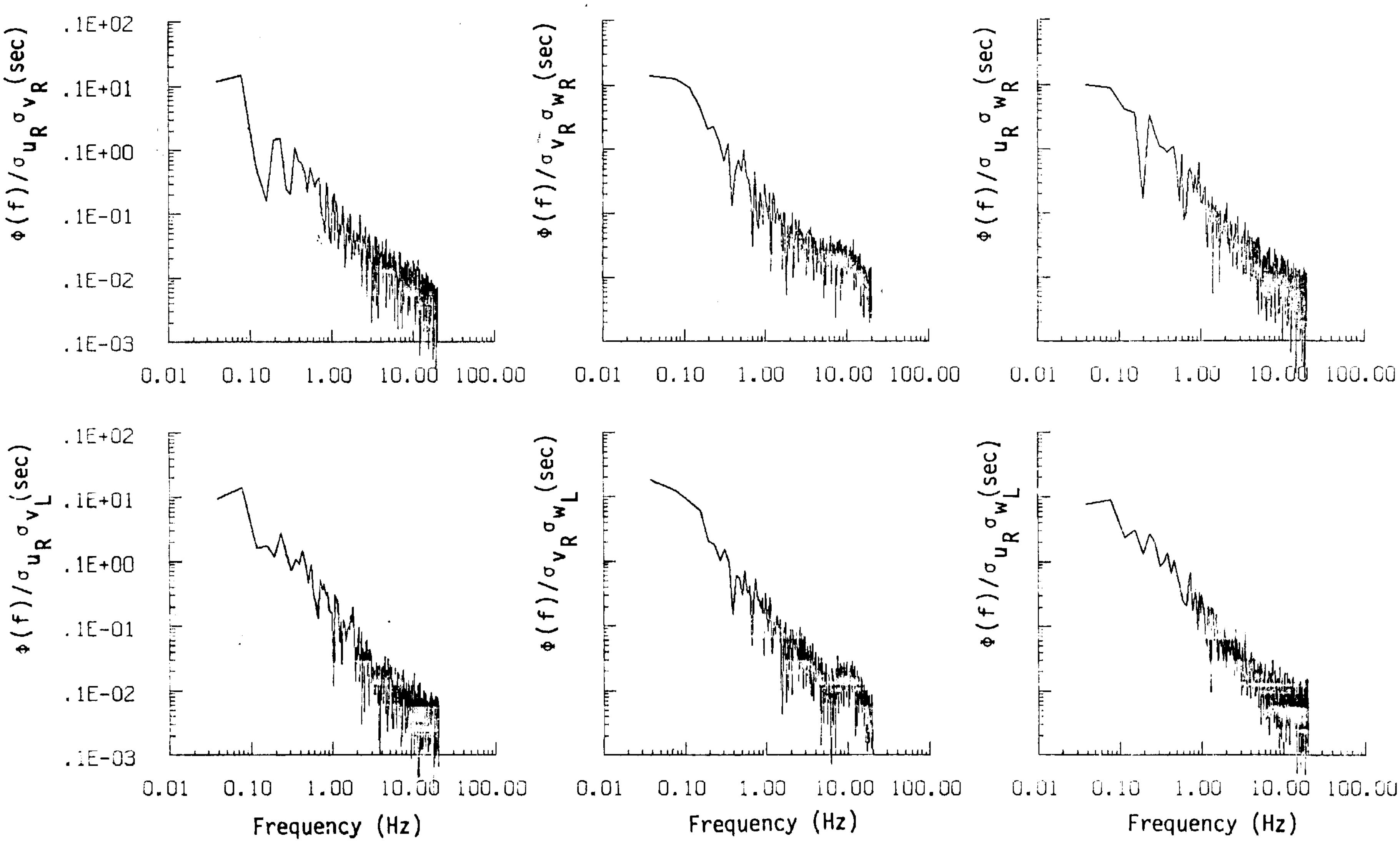

b. One- and two-point cross-spectra.

Figure A.15. (continued).

ORIGINAL PAGE IS
OF POOR QUALITY

TABLE A. 6. List of All Parameters Measured and Their Range of Values, Flight 31, Run 3.

CHANNEL	UNITS	HIGH	LOW	MEAN	RMS	STD	POINTS
1 TIME	SECONDS	39006.672	38668.647	38837.65950	38837.75210	97.59023	13522
2 PHI DOT	RAD/SEC	.147	-.121	-.00234	.03028	.03019	13522
3 ACCL N CG	G UNITS	1.455	-.310	.99556	1.00384	.10494	13522
4 THETA DOT	RAD/SEC	.066	-.549	.00305	.01522	.01491	13522
5 THETA	RAD	.242	.308	.06317	.06523	.01627	13522
6 PHI	RAD	.263	-.067	.00490	.03189	.03151	13522
7 PSI 1	RAD	338.337	7.242	12.75567	13.62139	5.32219	13522
8 DEL PSI 1	DEG	13.249	-15.081	-10.97857	11.53739	3.54728	13522
9 PSI 2	RAD	410.597	239.519	371.91518	371.93505	4.12562	13522
10 DEL PSI 2	DEG	1.021	-12.534	-7.06116	7.30434	1.78397	13522
11 ACCL N LT	G UNITS	2.977	-2.266	1.01165	1.03651	.22471	13522
12 ACCL N RT	G UNITS	3.935	-2.196	1.01148	1.04075	.24511	13522
13 ACCL X CG	G UNITS	.205	-.735	.05973	.06555	.02700	13522
14 ACCL Y CG	G UNITS	.198	-.718	-.00630	.02150	.02055	13522
15 ALPHA CTR	RAD	.123	-.228	-.01568	.02070	.01351	13522
16 BETA CTR	RAD	.100	-.184	-.00170	.02353	.02352	13522
17 TEMP T	DEG F	81.714	-34.557	76.52095	76.60347	3.46752	13522
18 TEMP P	DEG F	60.522	-33.065	60.00250	60.03757	2.05203	13522
19 ACCL Z INS	G UNITS	2.599	-.550	1.00273	1.00908	.11297	13522
20 ALPHA RT	RAD	.157	-.215	-.00157	.01544	.01538	13522
21 BETA RT	RAD	.076	-.191	.00467	.02117	.02105	13522
22 ALPHA LT	RAD	.188	-.162	.02626	.03022	.01496	13522
23 BETA LT	RAD	.210	-.153	.00275	.02205	.02187	13522
24 PSI DOT	RAD/SEC	.648	-.609	.00249	.02377	.02364	13522
25 TEMP TOT	DEG C	14.356	9.337	11.74237	11.80331	1.19794	13522
26 QC LT	PSID	.974	.684	.81248	.81390	.04801	13522
27 QC CTR	PSID	.950	.601	.77934	.78070	.04616	13522
28 QC RT	PSID	.952	.665	.80607	.80747	.04753	13522
29 PS	PSIA	11.961	11.891	11.93477	11.93478	.01232	13522
30 TEMP IRT	VOLTS	33.192	-169.190	5.41467	6.27501	3.17141	13522
31 HYGROM	DEG C	1.972	-145.447	-2.99353	4.45976	3.30591	13522
32 QC2 LT	PSID	.043	-.130	.03416	.03477	.00650	13522
33 QC2 CTR	PSID	.171	-.097	.14963	.15159	.02246	13522
34 QC2 RT	PSID	.149	-.130	.12670	.12769	.01544	13522
35 DAR	DEG	8.513	-7.396	-6.33695	6.37121	.66373	13522
36 DAL	DEG	9.001	-6.337	-5.19844	5.24761	.71675	13522
37 DELEV	DEG	2.742	-18.430	-1.39958	1.50754	.56025	13522
38 DSTAB	DEG	.792	-.965	.03159	.04394	.03054	13522
39 DRUD	DEG	24.418	-18.306	-.05020	.72530	.72359	13522
40 DTHPR	PCT MAX	50.412	16.474	47.81367	47.82911	1.21505	13522
41 DTHRL	PCT MAX	67.501	26.099	47.34052	47.35410	1.13408	13522
42 DFLP	POSITION	1.955	-.504	1.10647	1.10726	.04164	13522
43 DSB	POSITION	.676	-.317	-.09434	.09626	.01918	13522
44 D TO G	METERS	7512401.683	7492216.008	***********	***********	5939.39681	13522
45 B TO D	DEGREES	72.907	72.872	72.89001	72.89001	.00911	13522
46 LONG	DEGREES	-118.044	-118.166	-118.10429	118.10429	.03642	13522
47 LAT	DEGREES	35.419	35.126	35.27307	35.27318	.08476	13522
48 TRK ANG	DEGREES	23.476	14.131	18.74730	18.86030	2.06153	13522
49 HDG	RADIANS	.320	.141	.23966	.24201	.03216	13522
50 VF	M/SEC	41.095	26.877	32.83017	33.05258	3.82850	13522
51 VN	M/SEC	101.437	90.312	96.67615	96.71767	2.83348	13522
52 ALTITUDE	KM	1.751	1.704	1.72164	1.72166	.00836	13522
53 TEMPC	DEGREES C	8.658	4.074	6.65058	6.74679	1.19249	13522
54 EW WND SPD	KNOTS	55.635	-17.154	16.79962	19.71630	10.32021	13522
55 NS WND SPD	KNOTS	10.843	-14.524	-2.99624	5.56724	4.69237	13522
56 WIND SPEED	KNOTS	55.596	.049	17.62851	20.48723	10.09349	13522
57 WIND DIREC	DEGREES	357.550	.499	276.24866	277.96924	30.88118	13522
58 WIND DIR2	DEGREES	177.556	-179.501	96.24871	101.09111	30.88120	13522
59 WIND DIR3	DEGREES	357.558	.499	276.24871	277.96929	30.88120	13522
60 WIND DIR4	DEGREES	410.778	-1576.567	-664.45237	766.62365	349.73794	13522
61 AIRSPEED R	M/SEC	113.555	95.346	102.80778	102.92912	2.91696	13522
62 AIRSPEED C	M/SEC	111.759	93.505	101.20556	101.24664	2.88388	13522
63 AIRSPEED L	M/SEC	113.145	95.111	103.28648	103.32823	2.93690	13522
64 DELTA ALT	METERS	33.820	-13.132	4.33768	9.42958	8.37557	13522
65 INRTL DISP	METERS	107.477	-3.544	45.39428	53.01185	27.38013	13522
66 UG RIGHT	M/SEC	7.418	-6.760	-.43924	2.32914	2.28743	13522
67 UG CENTER	M/SEC	7.261	-8.434	-.44608	2.32752	2.28434	13522
68 UG LEFT	M/SEC	6.381	-7.075	-.44876	2.34676	2.30354	13522
69 VG RIGHT	M/SEC	11.305	-20.932	-.31620	5.35914	5.35000	13522
70 VG CENTER	M/SEC	19.627	-22.265	-.39496	5.38642	5.37212	13522
71 VG LEFT	M/SEC	24.487	-21.909	-.37312	5.41140	5.39872	13522
72 WG RIGHT	M/SEC	24.393	-35.377	.12772	1.86715	1.86284	13522
73 WG CENTER	M/SEC	7.373	-35.726	-.05366	1.69161	1.69081	13522
74 WG LEFT	M/SEC	17.432	-39.047	.04533	1.83675	1.83626	13522

ORIGINAL PAGE IS
OF POOR QUALITY

(TABLE A. 6. continued)

CHANNEL	UNITS	HIGH	LOW	MEAN	RMS	STD	POINTS
1 TIME	SECONDS	39363.447	39006.697	39165.07200	39195.20735	102.99568	14271
2 PHI DOT	RAD/SEC	.242	-.219	-.00262	.04781	.04774	14271
3 ACCL N CG	G UNITS	1.927	-.056	.99868	1.01381	.17449	14271
4 THETA DOT	RAD/SEC	.087	-.190	.00294	.01861	.01837	14271
5 THETA	RAD	.216	-.012	.06597	.07620	.03814	14271
6 PHI	RAD	.182	-.161	.00429	.04772	.04753	14271
7 PSI 1	RAD	74.206	4.776	12.24660	12.48124	2.35745	14271
8 DEL PSI 1	DEG	-2.899	-15.061	-11.19235	11.81779	3.79374	14271
9 PSI 2	RAD	379.765	344.407	371.59721	371.61766	3.91779	14271
10 DEL PSI 2	DEG	-2.406	-14.916	-7.40715	7.79945	2.27761	14271
11 ACCL N LT	G UNITS	3.063	-.993	1.01294	1.07117	.34839	14271
12 ACCL N RT	G UNITS	3.160	-1.486	1.01129	1.07993	.37890	14271
13 ACCL X CG	G UNITS	.251	-.032	.06314	.07243	.03549	14271
14 ACCL Y CG	G UNITS	.104	-.250	-.00268	.02354	.02336	14271
15 ALPHA CTR	RAD	.079	-.137	-.02042	.02839	.01972	14271
16 BETA CTR	RAD	.185	-.171	.00138	.03421	.03419	14271
17 TEMP I	DEG F	63.153	31.094	52.37248	87.37535	.62386	14271
18 TEMP P	DEG F	61.062	34.725	60.71895	60.71987	.33493	14271
19 ACCL Z INS	G UNITS	1.937	-.071	1.00364	1.01892	.17762	14271
20 ALPHA RT	RAD	.121	-.142	-.00947	.02405	.02211	14271
21 BETA RT	RAD	.164	-.150	.01111	.03257	.03061	14271
22 ALPHA LT	RAD	.125	-.106	.01977	.02933	.02167	14271
23 BETA LT	RAD	.166	-.156	.00524	.03192	.03149	14271
24 PSI DOT	RAD/SEC	.169	-.374	.00248	.02759	.02748	14271
25 TEMP TOT	DEG C	14.358	9.153	11.67404	11.73217	1.16651	14271
26 QC LT	PSID	1.025	.603	.84357	.84587	.06233	14271
27 QC CTR	PSID	.982	.502	.81005	.81229	.06017	14271
28 QC RT	PSID	1.038	.573	.83740	.83970	.06217	14271
29 PS	PSIA	11.969	11.459	11.74802	11.74992	.21547	14271
30 TEMP IRT	VOLTS	6.675	-84.221	5.63551	5.79809	1.36342	14271
31 HYGROM	DEG C	-.176	-31.593	-4.63734	4.94175	1.70768	14271
32 QC2 LT	PSID	.061	.022	.05256	.05282	.00507	14271
33 QC2 CTR	PSID	.178	.139	.17532	.17533	.00209	14271
34 QC2 RT	PSID	.169	.098	.16064	.16074	.00570	14271
35 DAR	DEG	.035	-9.358	-9.41225	9.43202	.57712	14271
36 DAL	DEG	-6.337	-9.310	-7.24662	7.26303	.48790	14271
37 DELEV	DEG	.936	-6.148	.16314	.47460	.44569	14271
38 DSTAB	DEG	.369	-.104	-.05830	.06417	.02681	14271
39 DRUD	DEG	3.284	-9.024	2.11294	2.21615	.66857	14271
40 DTHRR	PCT MAX	53.320	30.269	51.41193	51.42439	1.13162	14271
41 DTHRL	PCT MAX	66.951	42.710	50.73657	50.74610	1.08203	14271
42 DFLP	POSITION	1.307	.266	.98162	.98250	.04168	14271
43 DSB	POSITION	.261	-.145	-.03961	.04433	.01951	14271
44 D TO G	METERS	7534421.914	7512461.663	***********	***********	6396.54532	14271
45 B TO D	DEGREES	72.877	72.835	72.85201	72.85201	.01048	14271
46 LONG	DEGREES	-117.913	-118.044	-117.98051	117.98052	.03860	14271
47 LAT	DEGREES	35.742	35.419	35.58132	35.59144	.09313	14271
48 TRK ANG	DEGREES	21.374	14.027	18.45445	18.52902	1.66075	14271
49 HDG	RADIANS	.323	.097	.23297	.23660	.04130	14271
50 VE	M/SEC	39.642	25.560	33.42048	33.56105	3.06846	14271
51 VN	M/SEC	105.239	93.886	100.14604	100.17122	2.24572	14271
52 ALTITUDE	KM	2.050	1.698	1.84961	1.85577	.14855	14271
53 TEMPC	DEGREES C	8.594	3.665	6.30066	6.40066	1.13042	14271
54 EW WND SPD	KNOTS	46.350	-4.720	18.66167	21.04250	9.72295	14271
55 NS WND SPD	KNOTS	20.140	-24.146	-1.62659	7.90308	7.73415	14271
56 WIND SPEED	KNOTS	46.513	.925	20.51785	22.47767	9.17983	14271
57 WIND DIREC	DEGREES	359.816	.019	267.70529	270.10718	35.94241	14271
58 WIND DIR2	DEGREES	179.816	-179.961	87.70553	94.78392	35.94243	14271
59 WIND DIR3	DEGREES	359.816	.019	267.70553	270.10722	35.94243	14271
60 WIND DIR4	DEGREES	-691.176	-1261.930	-884.26963	898.73956	160.51931	14271
61 AIRSPEED R	M/SEC	118.420	88.606	105.54417	105.61017	3.73326	14271
62 AIRSPEED C	M/SEC	113.484	89.314	103.84731	103.91240	3.67774	14271
63 AIRSPEED L	M/SEC	116.331	90.850	105.92402	105.98986	3.73542	14271
64 DELTA ALT	METERS	333.039	-19.041	133.10607	199.45480	148.54738	14271
65 INRTL DISP	METERS	311.725	-59.516	109.06179	164.15849	148.39615	14271
66 UG RIGHT	M/SEC	15.707	-13.600	.41619	3.79886	3.77613	14271
67 UG CENTER	M/SEC	17.666	-10.773	.42324	3.76874	3.74503	14271
68 UG LEFT	M/SEC	14.139	-11.774	.42521	3.81579	3.79216	14271
69 VG RIGHT	M/SEC	14.901	-12.700	.29665	5.14715	5.13877	14271
70 VG CENTER	M/SEC	13.648	-11.944	.37467	5.19851	5.18523	14271
71 VG LEFT	M/SEC	13.056	-12.744	.35260	5.21987	5.20811	14271
72 WG RIGHT	M/SEC	13.623	-11.574	-.19605	2.75694	2.75000	14271
73 WG CENTER	M/SEC	11.865	-11.073	-.01730	2.55812	2.55815	14271
74 WG LEFT	M/SEC	11.415	-12.667	-.11385	2.68582	2.68350	14271

Flight 31, Run 4
Date: Nov. 29, 1982
Start Time: 10:58:26 (PST)
Duration: 283.8 seconds

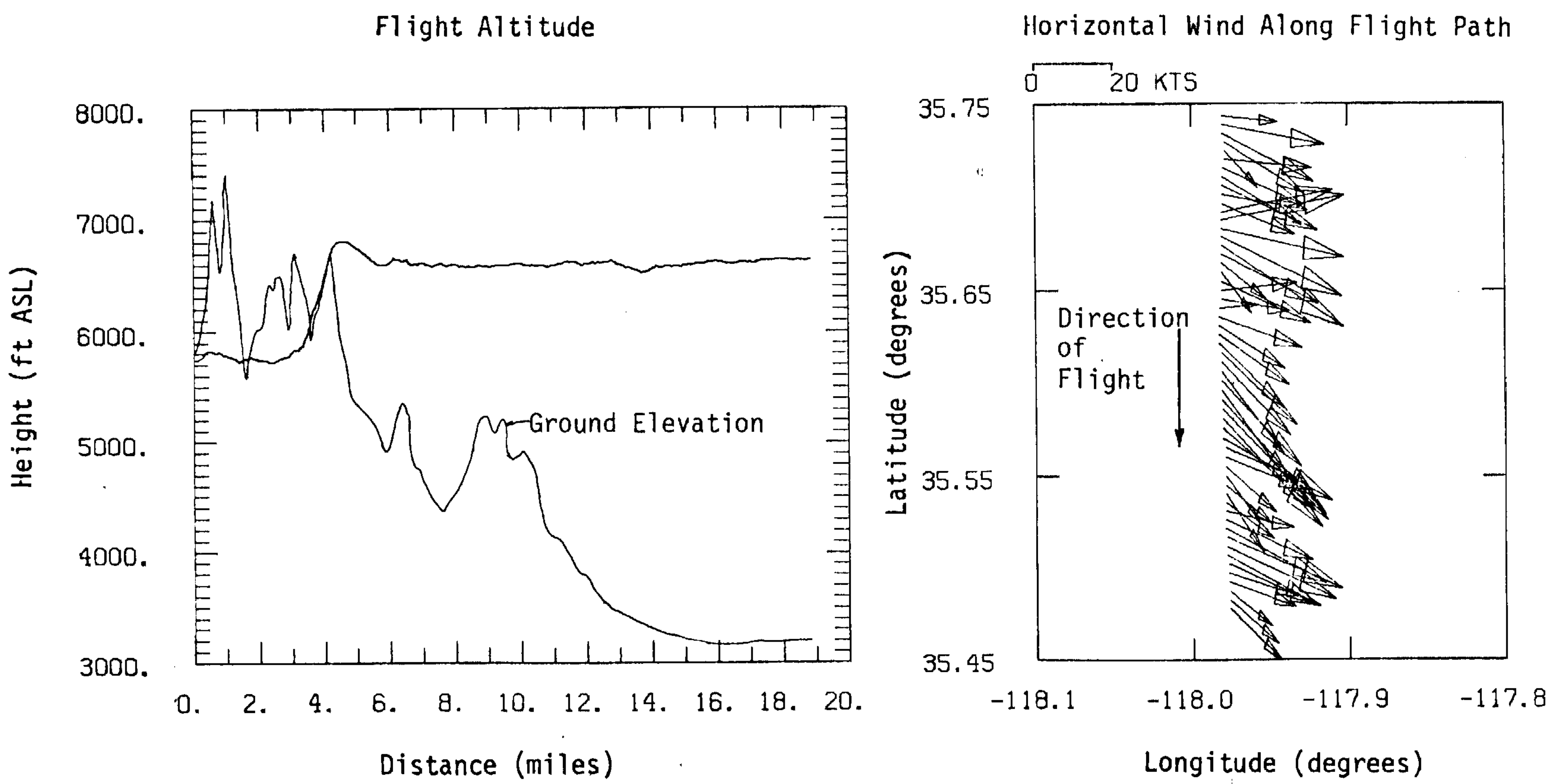

Figure A.16. Flight altitude and horizontal wind along flight path, Flight 31, Run 4.

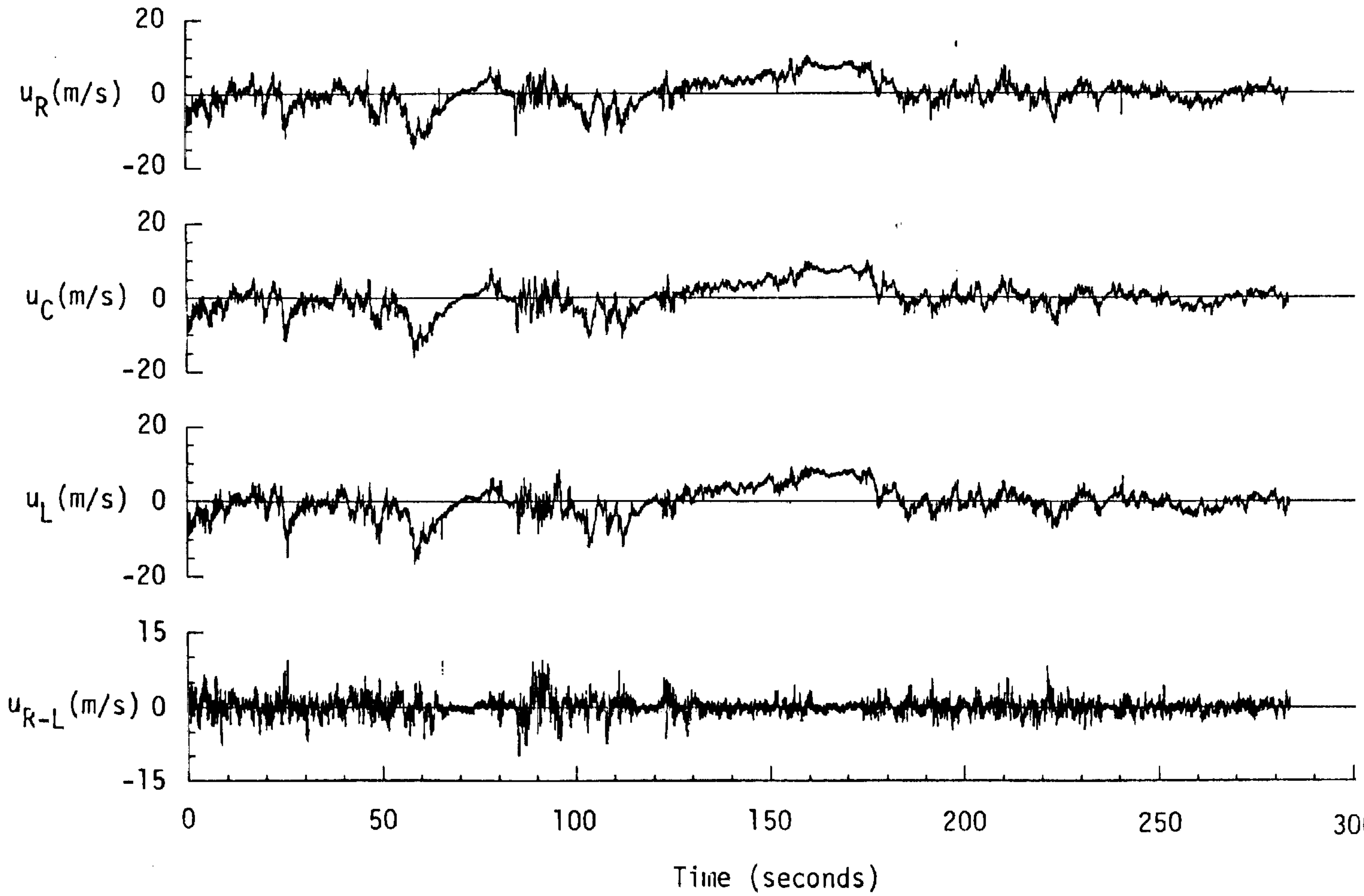

Figure A.17. Time histories of gust velocities, gust velocity differences, and aircraft's normal accelerations, Flight 31, Run 4.

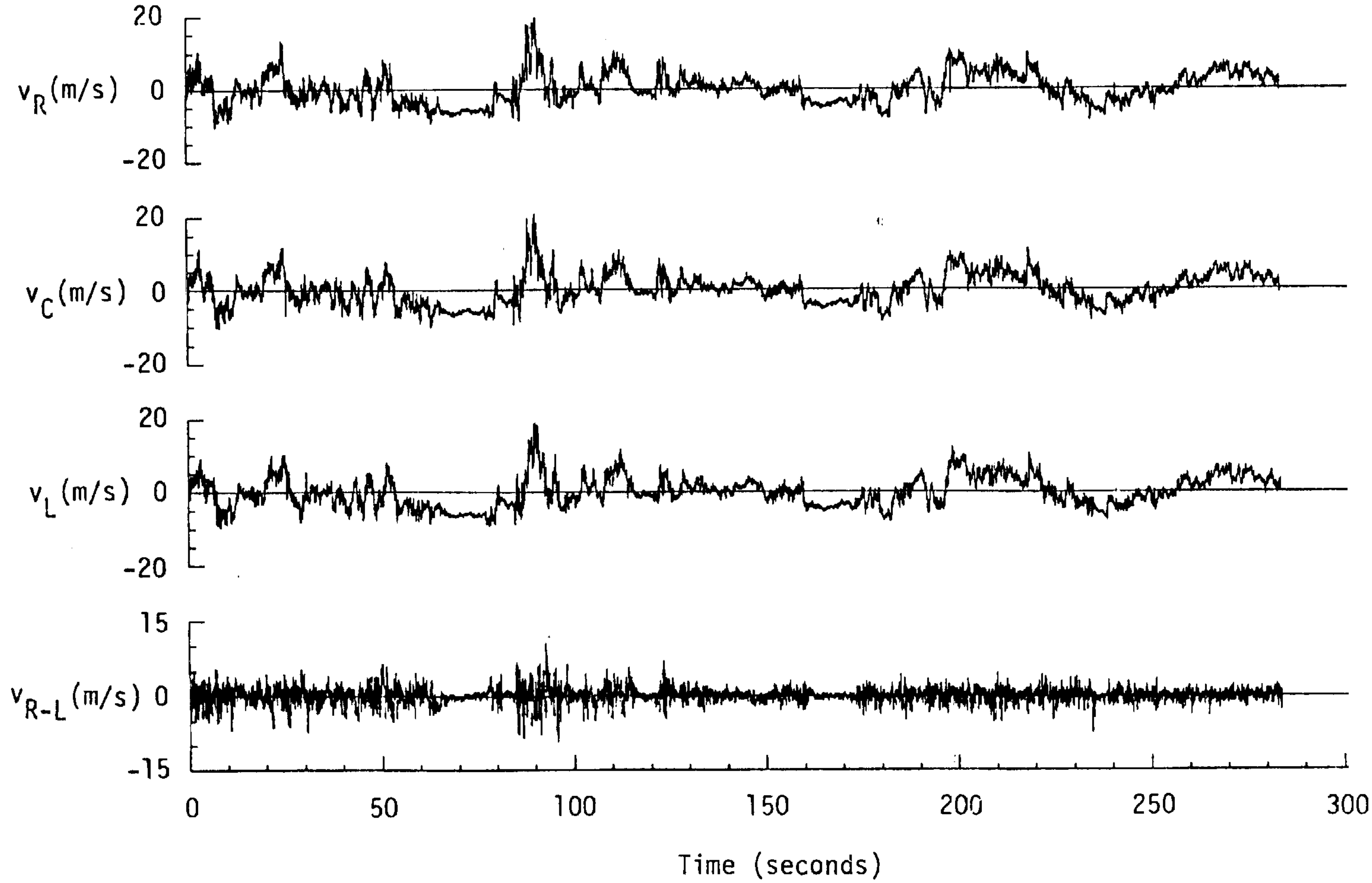

Figure A.17. (continued).

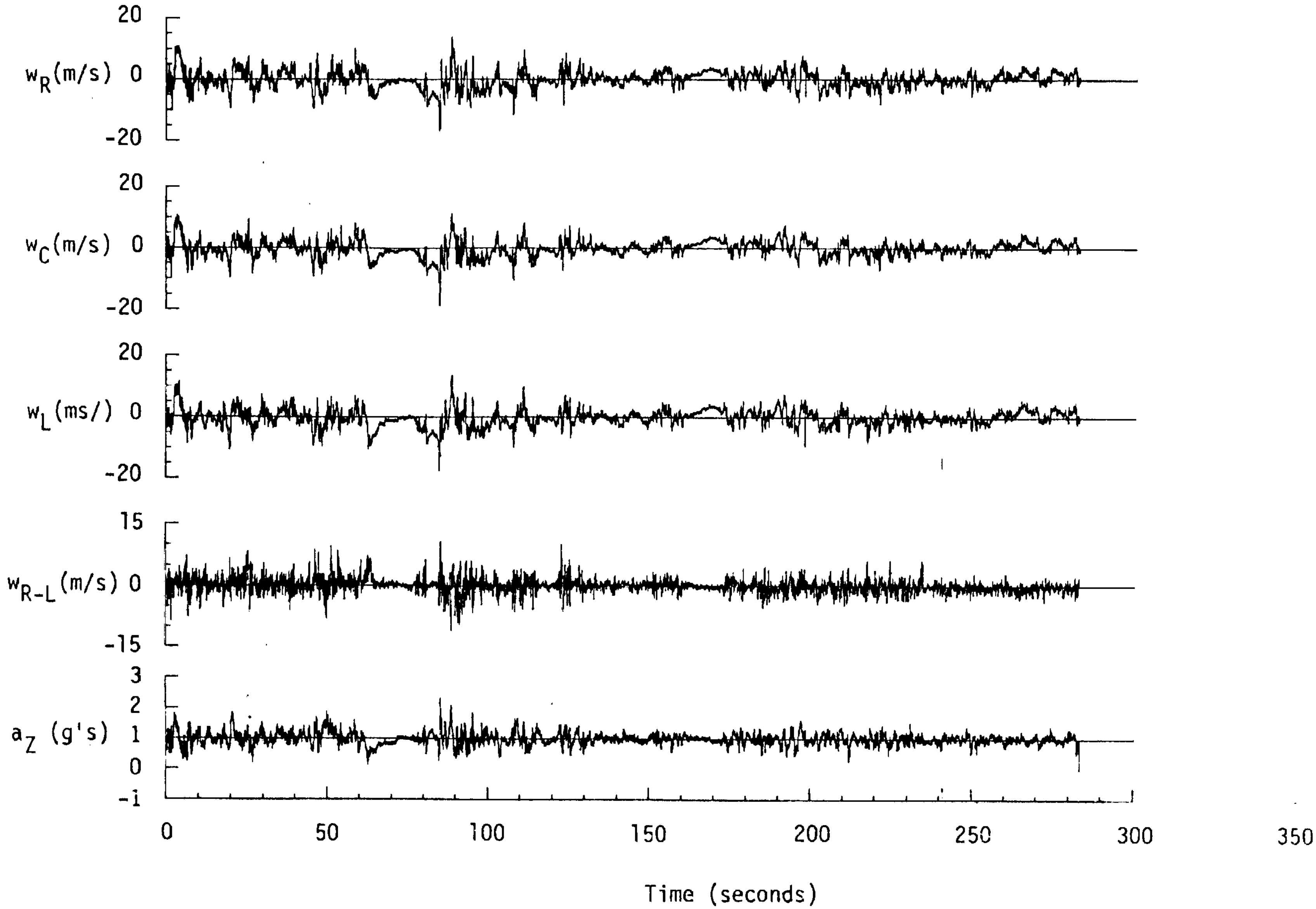

Figure A.17. (continued).

TABLE A.7. Average Turbulence Parameters, Integral Length Scales, and Correlation Coefficients of Gust Velocities, Flight 31, Run 4.

1. Mean Airspeed (m/s):

$\overline{V}_L$	$\overline{V}_C$	$\overline{V}_R$
104.78	102.62	104.32

2. Standard Deviation of Gust Velocities (m/s):

σ_{uR}	σ_{vR}	σ_{wR}

σ_{uC}	σ_{vC}	σ_{wC}

σ_{uL}	σ_{vL}	σ_{wL}

3. Standard Deviation of Gust Velocity Differences (m/s):

$\sigma_{\Delta uRL}$	$\sigma_{\Delta vRL}$	$\sigma_{\Delta wRL}$

4. Integral Length Scale (m):

L_{uR}	L_{vR}	L_{wR}
419.8	350.8	66.9

L_{uRL}	L_{vRL}	L_{wRL}
408.0	344.7	61.9

5. Correlation Coefficient of Gust Velocities:

$\overline{u_R u_L}/\sigma_{u_R}\sigma_{u_L}$	$\overline{v_R v_L}/\sigma_{v_R}\sigma_{v_L}$	$\overline{w_R w_L}/\sigma_{w_R}\sigma_{w_L}$
0.88	0.91	0.80

$\overline{u_R v_R}/\sigma_{u_R}\sigma_{v_R}$	$\overline{v_R w_R}/\sigma_{v_R}\sigma_{w_R}$	$\overline{w_R u_R}/\sigma_{w_R}\sigma_{u_R}$
-0.19	0.20	0.09

$\overline{u_R v_L}/\sigma_{u_R}\sigma_{v_L}$	$\overline{v_R w_L}/\sigma_{v_R}\sigma_{w_L}$	$\overline{w_R u_L}/\sigma_{w_R}\sigma_{u_L}$
-0.19	0.20	0.06

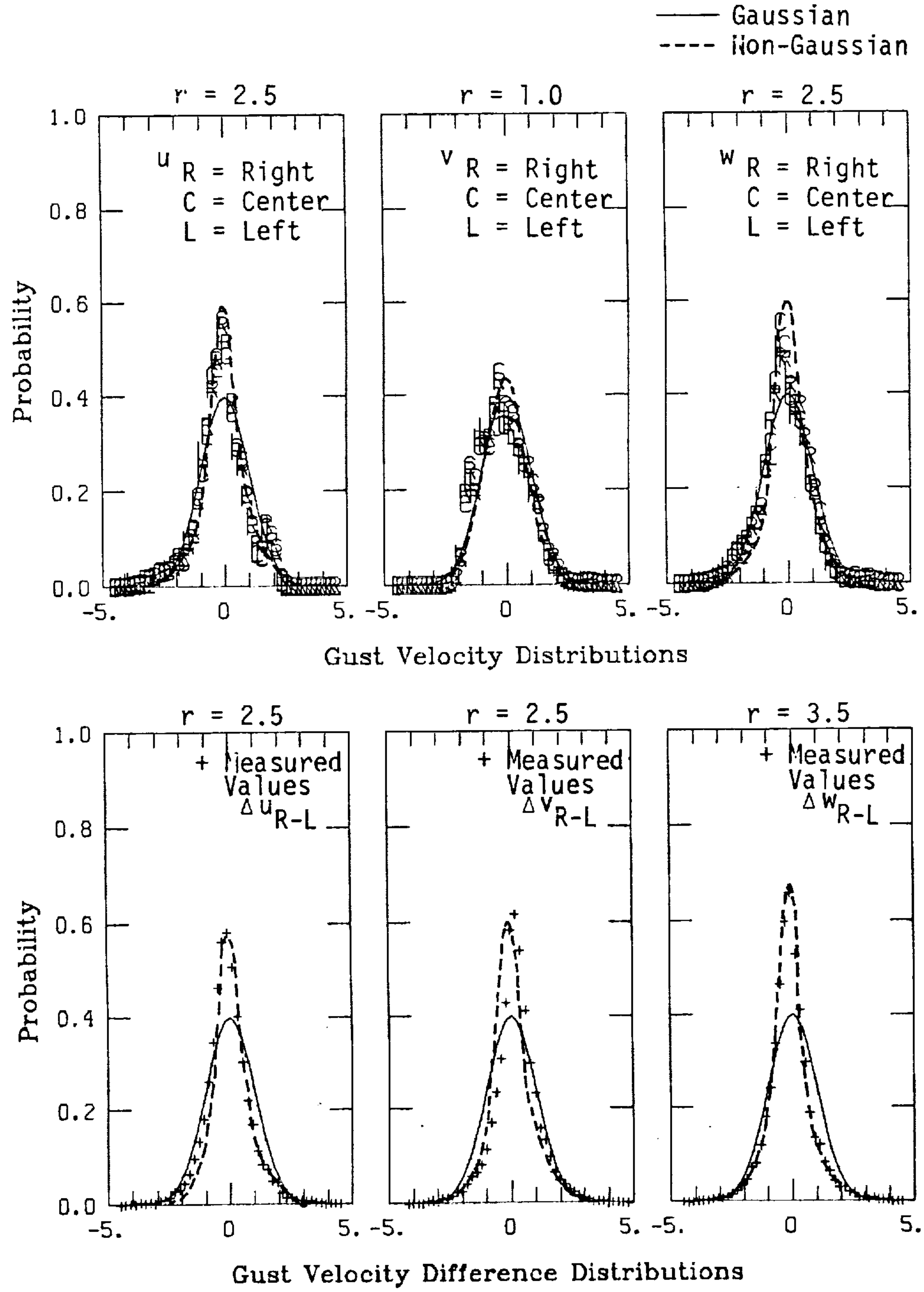

Figure A.18. Probability density functions for gust velocities and gust velocity differences (normalized with the standard deviation), Flight 31, Run 4 (r = degree of non-Gaussian).

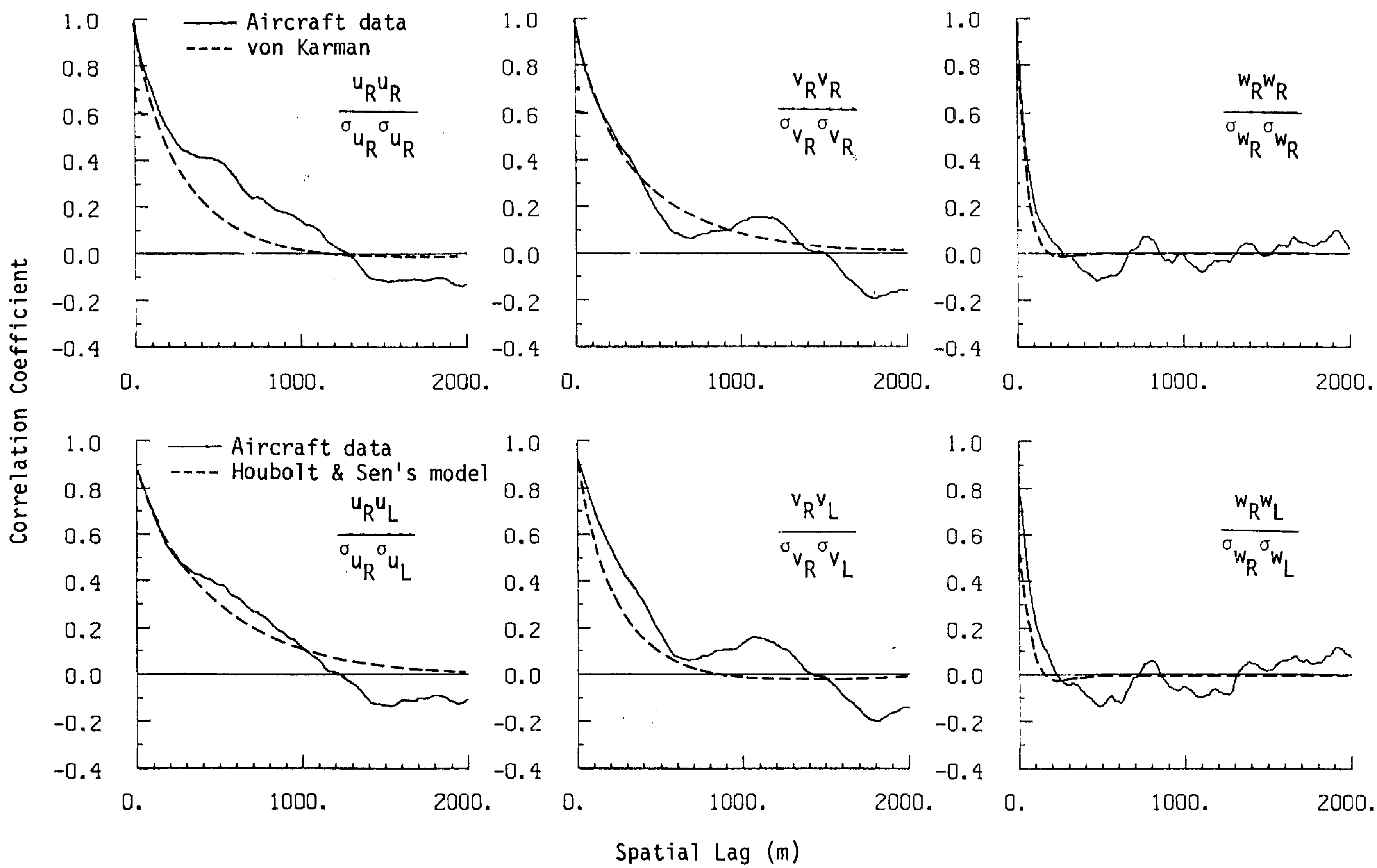

a. One- and two-point common component correlations.

Figure A.19. Comparison of normalized one- and two-point correlation functions for gust velocities with theoretical models, Flight 31, Run 4.

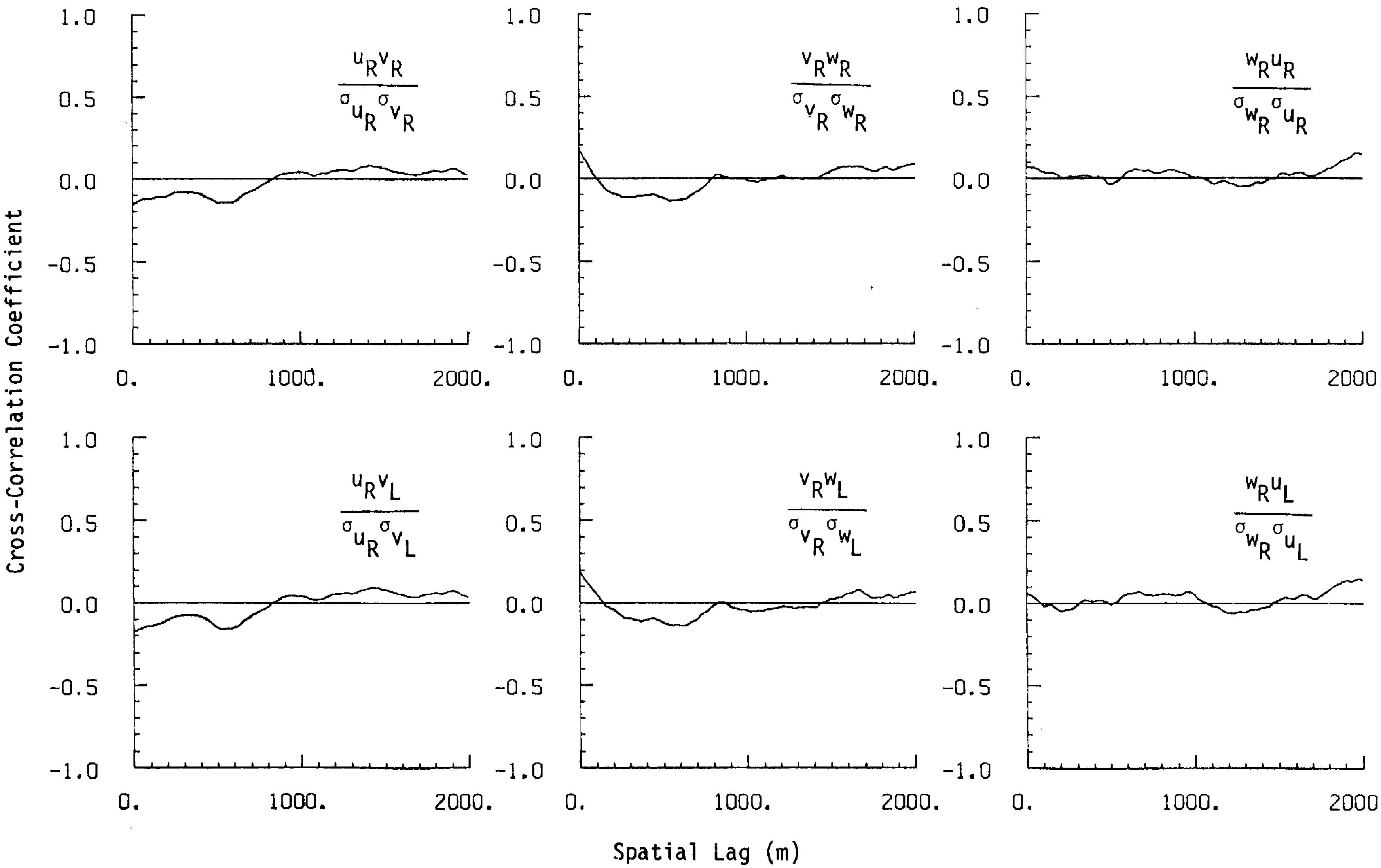

b. One- and two-point cross-correlations.

Figure A.19. (continued).

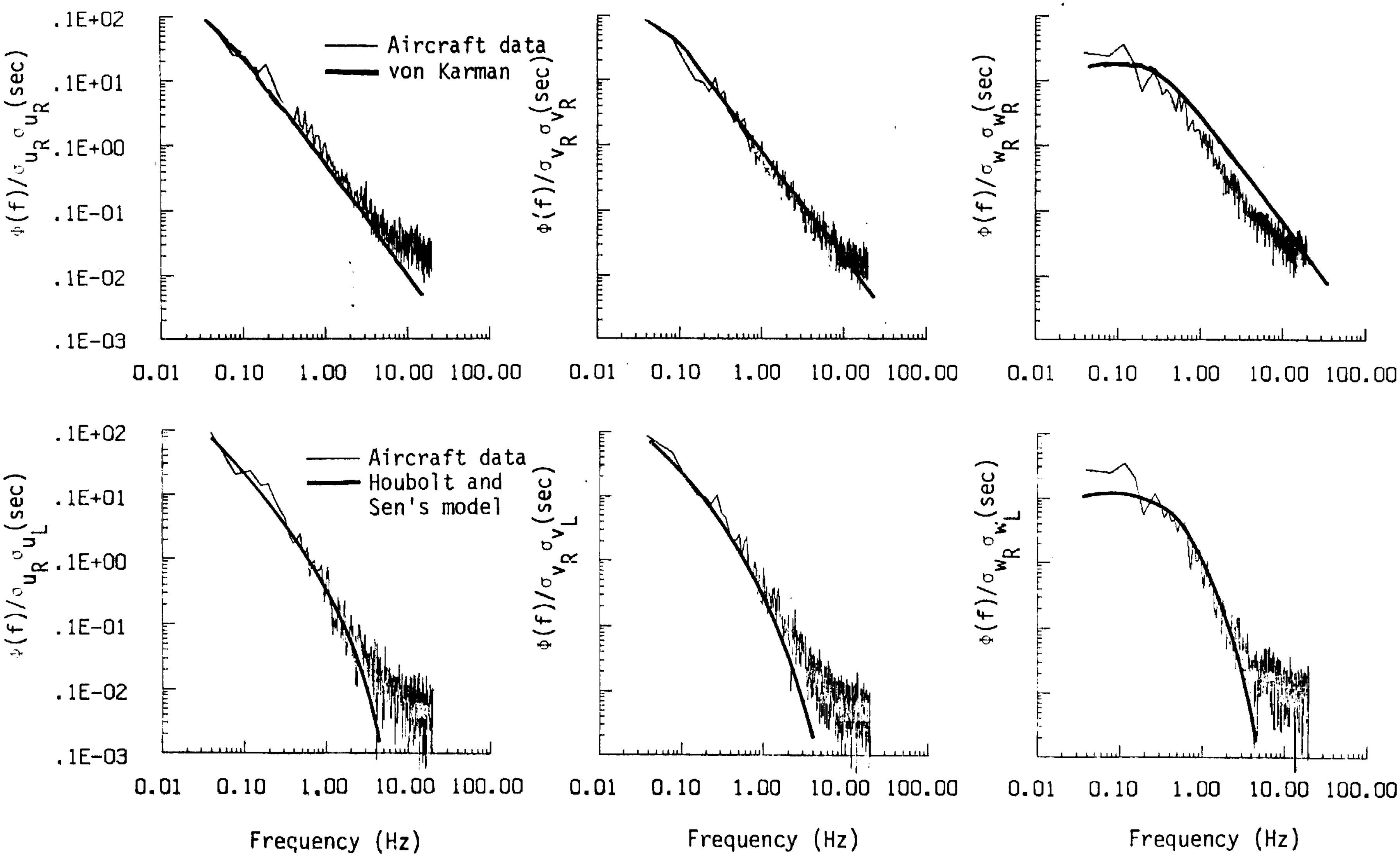

a. One- and two-point common component spectra.

Figure A.20. Comparison of normalized one- and two-point spectral density functions for gust velocities with theoretical models, Flight 31, Run 4.

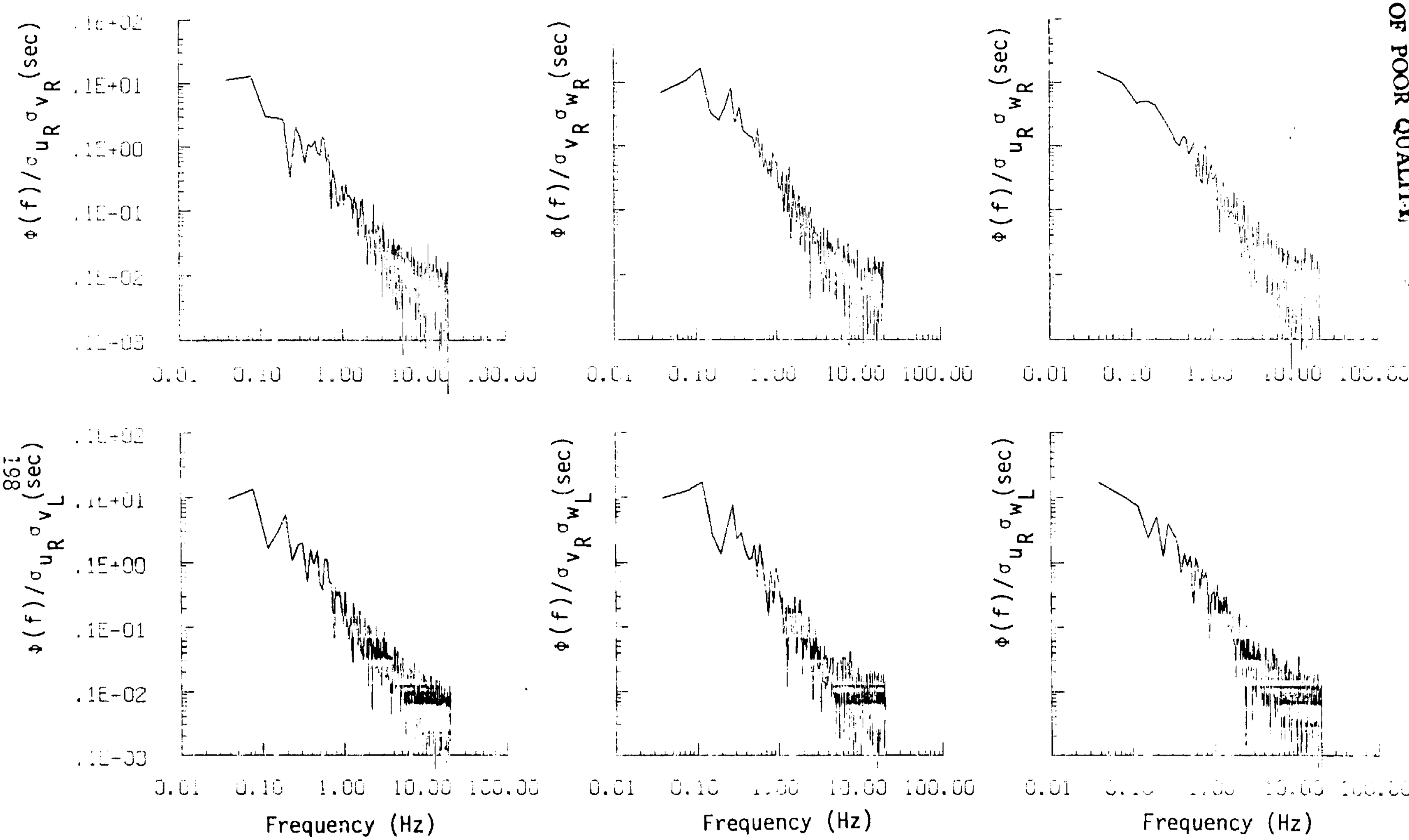

b. One- and two-point cross-spectra.

Figure A.20. (continued).

TABLE A. 8. List of All Parameters Measured and Their Range of Values, Flight 31, Run 4.

CHANNEL	UNITS	HIGH	LOW	MEAN	RMS	STD	POINTS
1 TIME	SECONDS	39780.418	39505.593	39647.50580	39647.59047	81.54404	11354
2 PHI DOT	RAD/SEC	.279	-.275	-.00304	.05429	.05420	11354
3 ACCL N CG	G UNITS	2.172	.144	.95774	1.01726	.19636	11354
4 THETA DOT	RAD/SEC	.126	-.113	.00285	.02114	.02095	11354
5 THETA	RAD	.259	-.004	.07938	.09178	.04609	11354
6 PHI	RAD	.234	-.250	-.00088	.04564	.04563	11354
7 PSI 1	RAD	193.193	175.959	184.56962	184.59307	2.94239	11354
8 DEL PSI 1	DEG	11.103	-5.677	2.79683	4.02734	2.89792	11354
9 PSI 2	RAD	550.959	534.313	542.59293	542.60027	2.82186	11354
10 DEL PSI 2	DEG	11.398	-5.389	3.05738	4.21552	2.90876	11354
11 ACCL N LT	G UNITS	4.152	-1.527	1.00919	1.07557	.37201	11354
12 ACCL N RT	G UNITS	4.093	-1.429	1.00824	1.08234	.35360	11354
13 ACCL X CG	G UNITS	.493	-.051	.08036	.09458	.05063	11354
14 ACCL Y CG	G UNITS	.113	-.941	-.00111	.02697	.02695	11354
15 ALPHA CTR	RAD	.086	-.244	-.01908	.02978	.02221	11354
16 BETA CTR	RAD	.153	-.186	.00562	.03745	.03702	11354
17 TEMP T	DEG F	82.074	-49.332	78.68240	78.70902	2.04713	11354
18 TEMP R	DEG F	61.601	-39.510	61.31623	61.32387	.96613	11354
19 ACCL Z THS	G UNITS	2.322	-.860	1.00311	1.02282	.19985	11354
20 ALPHA RT	RAD	.127	-.241	-.00527	.02615	.02559	11354
21 BETA RT	RAD	.183	-.141	.01571	.03697	.03347	11354
22 ALPHA LT	RAD	.127	-.219	.02124	.03173	.02357	11354
23 BETA LT	RAD	.154	-.154	.00790	.03429	.03347	11354
24 PSI DOT	RAD/SEC	.856	-.716	.00250	.03159	.03149	11354
25 TEMP TOT	DEG C	14.161	-42.333	10.47860	10.52522	1.02136	11354
26 QC LT	PSID	1.065	.666	.81651	.81927	.06713	11354
27 QC CTR	PSID	1.015	.529	.78235	.79453	.06360	11354
28 QC RT	PSID	1.061	.643	.80910	.81177	.06584	11354
29 PS	PSIA	11.901	11.416	11.57613	11.57703	.14469	11354
30 TEMP TOT	VOLTS	5.739	-104.176	4.50116	4.77006	1.57859	11354
31 HYGROM	DEG C	1.396	-137.277	-4.82625	5.65941	2.95585	11354
32 QC2 LT	PSID	.072	-.119	.07004	.07008	.00239	11354
33 QC2 CTR	PSID	.174	-.122	.14300	.14601	.02950	11354
34 QC2 RT	PSID	.155	-.105	.12510	.12637	.01791	11354
35 DAR	DEG	9.433	-9.910	-9.43358	9.44278	.41677	11354
36 DAL	DEG	9.749	-9.899	-8.79618	8.79965	.24692	11354
37 DELEV	DEG	2.443	-13.434	2.03011	2.06003	.34988	11354
38 DSTAB	DEG	.709	-.202	-.17106	.17259	.02294	11354
39 DRUD	DEG	5.791	-16.569	4.95214	4.98444	.56662	11354
40 DTHRR	PCT MAX	57.913	17.913	56.27779	56.28640	.98428	11354
41 DTHRL	PCT MAX	57.031	16.488	55.54684	55.55530	.96939	11354
42 DSLR	POSITION	2.367	.730	.78921	.79012	.03758	11354
43 DSB	POSITION	.092	-.759	.05243	.05554	.01951	11354
44 R TO G	METERS	7528798.963	7520147.520	***********	***********	2533.38458	11354
45 B TO R	DEGREES	72.399	72.788	72.84144	72.84145	.03212	11354
46 LONG	DEGREES	-117.975	-117.981	-117.97512	117.97512	.00154	11354
47 LAT	DEGREES	35.746	35.472	35.61076	35.61055	.07574	11354
48 TRK ANG	DEGREES	183.022	176.145	179.36238	179.37015	1.67003	11354
49 HDG	RADIANS	3.387	3.082	3.23525	3.23568	.05276	11354
50 VE	M/SEC	7.400	-5.589	1.27726	3.43376	3.18751	11354
51 VN	M/SEC	-92.928	-117.325	-107.04515	107.16110	4.98391	11354
52 ALTITUDE	KM	2.080	1.744	1.96818	1.97072	.10000	11354
53 TEMPC	DEGREES C	9.497	-47.030	5.22871	5.33251	1.04710	11354
54 EW WND SPD	KNOTS	47.403	-19.718	19.83073	21.34131	7.88662	11354
55 NS WND SPD	KNOTS	21.471	-28.306	-9.01551	12.06588	7.28915	11354
56 WIND SPEED	KNOTS	50.149	.090	23.25414	24.51604	7.64360	11354
57 WIND DIREC	DEGREES	358.950	1.460	293.39173	295.01759	30.93613	11354
58 WIND DIR2	DEGREES	171.950	-178.540	113.39129	117.53530	30.93615	11354
59 WIND DIR3	DEGREES	358.950	1.460	293.39129	295.01765	30.93615	11354
60 WIND DIR4	DEGREES	-603.933	-1273.646	-1109.35311	1114.59457	107.97105	11354
61 AIRSPEED R	M/SEC	119.534	92.737	104.32261	104.40646	4.15876	11354
62 AIRSPEED C	M/SEC	116.949	91.773	102.62456	102.70582	4.07925	11354
63 AIRSPEED L	M/SEC	119.777	94.515	104.78721	104.87175	4.20778	11354
64 DELTA ALT	METERS	329.384	-6.099	217.77329	239.63276	99.95760	11354
65 INRTL DISP	METERS	325.336	-12.602	215.68011	243.19419	104.33129	11354
66 UG RIGHT	M/SEC	15.927	-14.701	.00000	3.73038	3.73054	11354
67 UG CENTER	M/SEC	13.472	-15.957	.00000	3.73026	3.73042	11354
68 UG LEFT	M/SEC	9.780	-16.640	.00000	3.75282	3.75299	11354
69 VG RIGHT	M/SEC	19.408	-10.231	.07438	4.07350	4.07331	11354
70 VG CENTER	M/SEC	20.693	-14.408	.06136	4.05427	4.05364	11354
71 VG LEFT	M/SEC	18.027	-25.507	.06604	4.04472	4.04358	11354
72 WG RIGHT	M/SEC	13.744	-24.117	-.02445	2.80154	2.80156	11354
73 WG CENTER	M/SEC	11.266	-23.169	-.02337	2.61648	2.61649	11354
74 WG LEFT	M/SEC	13.564	-26.116	-.01777	2.79854	2.75901	11354

Flight 31, Run 5
Date: Nov. 29, 1982
Start Time: 11:08:55 (PST)
Duration: 145.0 seconds

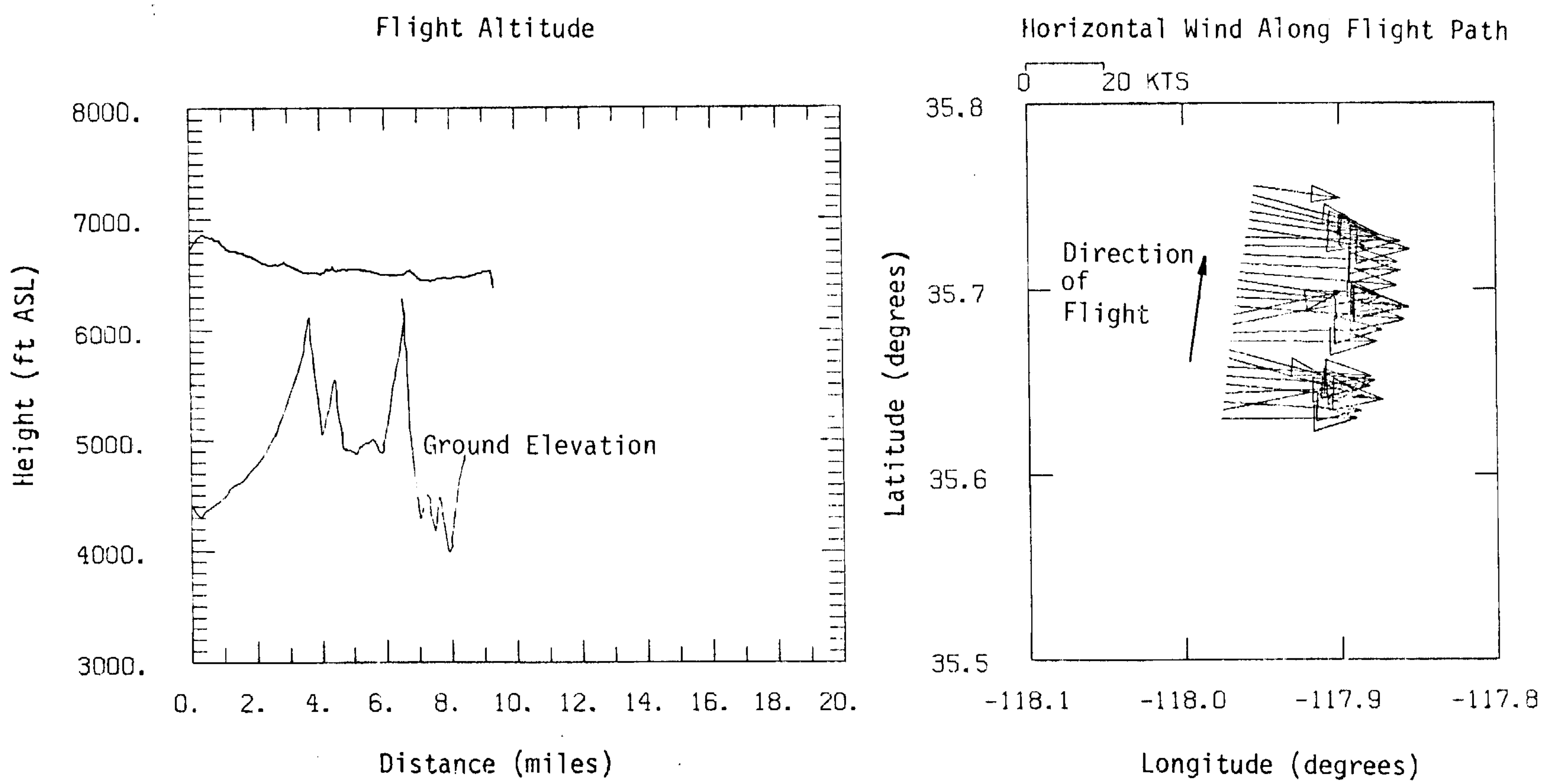

Figure A.21. Flight altitude and horizontal wind along flight path, Flight 31, Run 5.

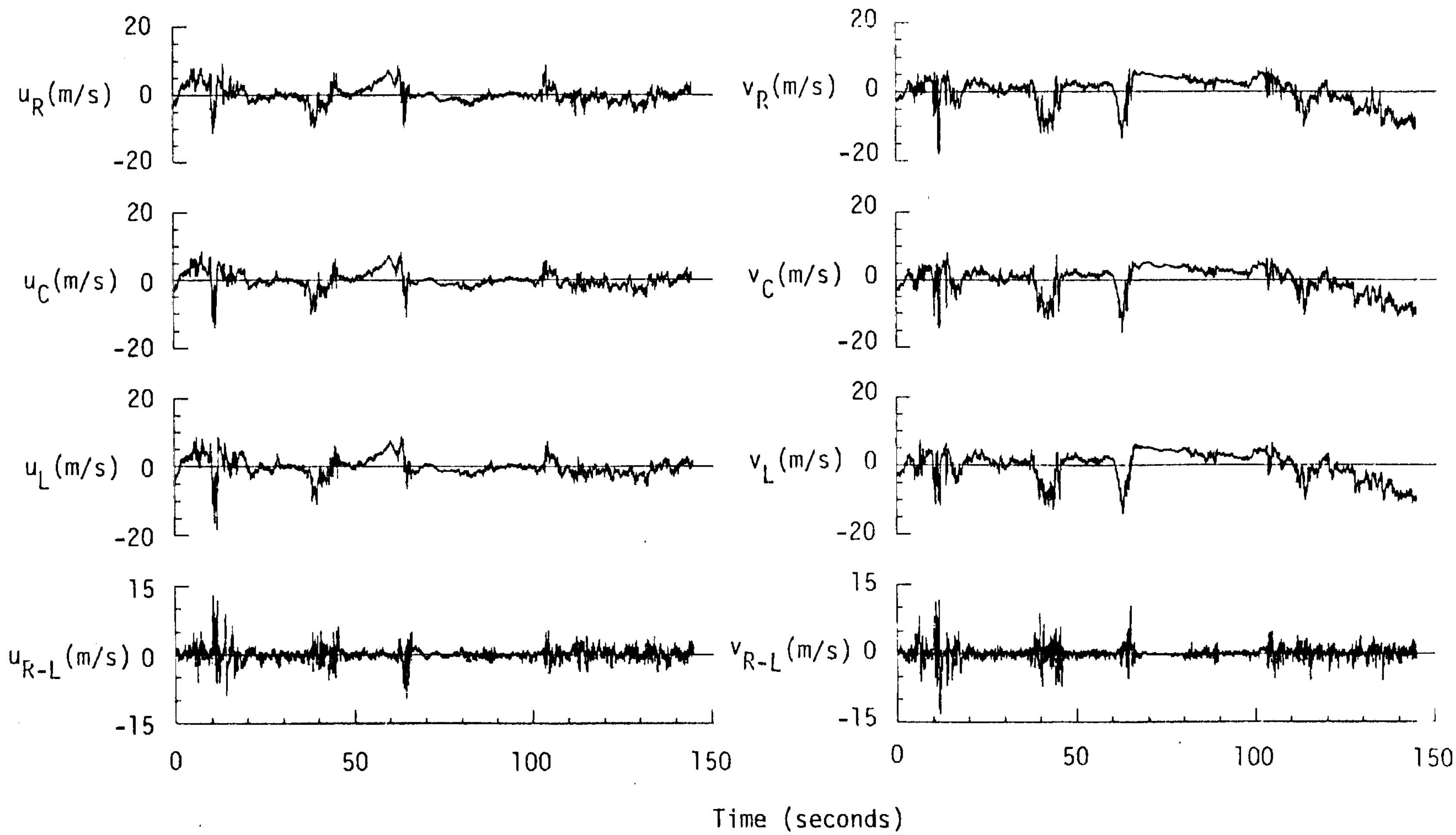

Figure A.22. Time histories of gust velocities, gust velocity differences, and aircraft's normal accelerations, Flight 31, Run 5.

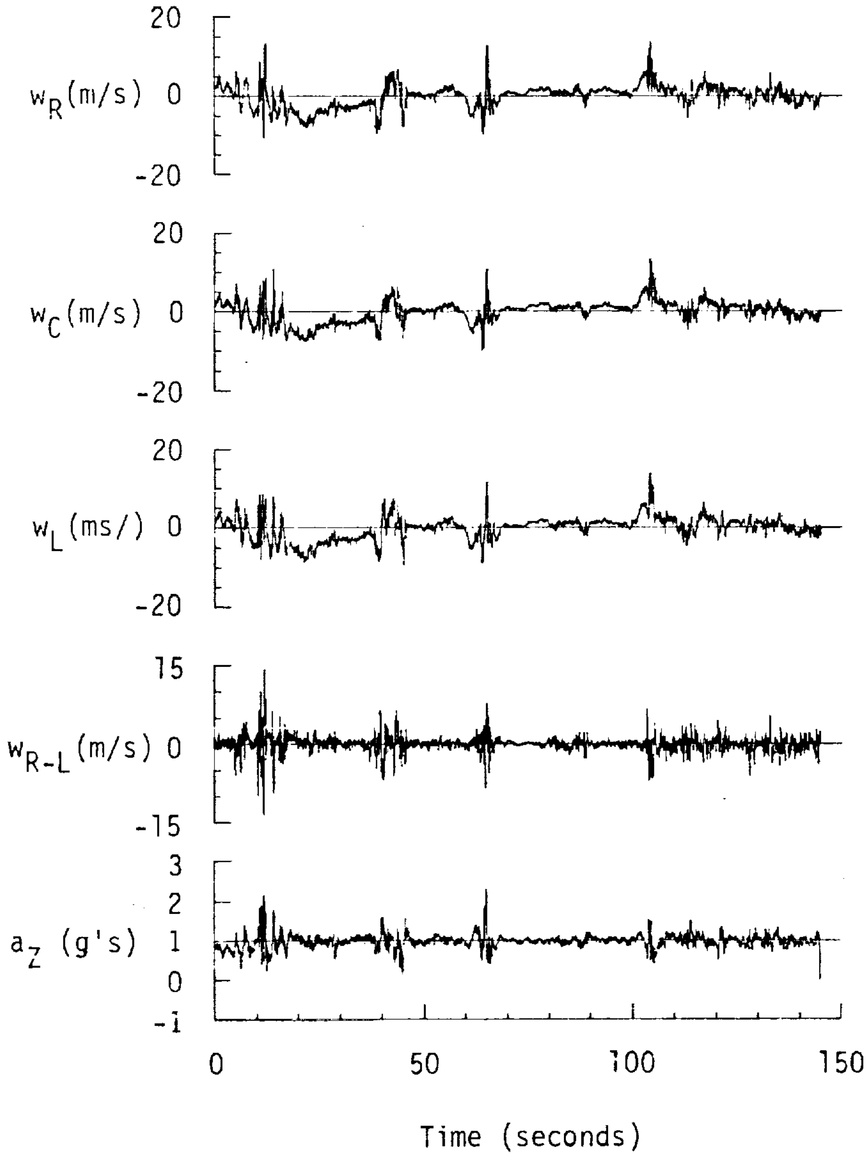

Figure A.22. (continued).

TABLE A.9. Average Turbulence Parameters, Integral Length Scales, and Correlation Coefficients of Gust Velocities, Flight 31, Run 5.

1. Mean Airspeed (m/s):

$\overline{V}_L$	$\overline{V}_C$	$\overline{V}_R$
105.79	103.53	105.33

2. Standard Deviation of Gust Velocities (m/s):

σ_{uR}	σ_{vR}	σ_{wR}
2.49	4.06	2.76

σ_{uC}	σ_{vC}	σ_{wC}
2.47	4.04	2.66

σ_{uL}	σ_{vL}	σ_{wL}
2.56	4.10	2.85

3. Standard Deviation of Gust Velocity Differences (m/s):

$\sigma_{\Delta uRL}$	$\sigma_{\Delta vRL}$	$\sigma_{\Delta wRL}$
1.41	1.38	1.42

4. Integral Length Scale (m):

L_{uR}	L_{vR}	L_{wR}
333.9	168.6	189.7

L_{uRL}	L_{vRL}	L_{wRL}
317.5	173.5	204.0

5. Correlation Coefficient of Gust Velocities:

$\overline{u_R u_L}/\sigma_{u_R}\sigma_{u_L}$	$\overline{v_R v_L}/\sigma_{v_R}\sigma_{v_L}$	$\overline{w_R w_L}/\sigma_{w_R}\sigma_{w_L}$
0.87	0.90	0.90

$\overline{u_R v_R}/\sigma_{u_R}\sigma_{v_R}$	$\overline{v_R w_R}/\sigma_{v_R}\sigma_{w_R}$	$\overline{w_R u_R}/\sigma_{w_R}\sigma_{u_R}$
-0.09	-0.10	-0.17

$\overline{u_R v_L}/\sigma_{u_R}\sigma_{v_L}$	$\overline{v_R w_L}/\sigma_{v_R}\sigma_{w_L}$	$\overline{w_R u_L}/\sigma_{w_R}\sigma_{u_L}$
-0.08	-0.09	-0.20

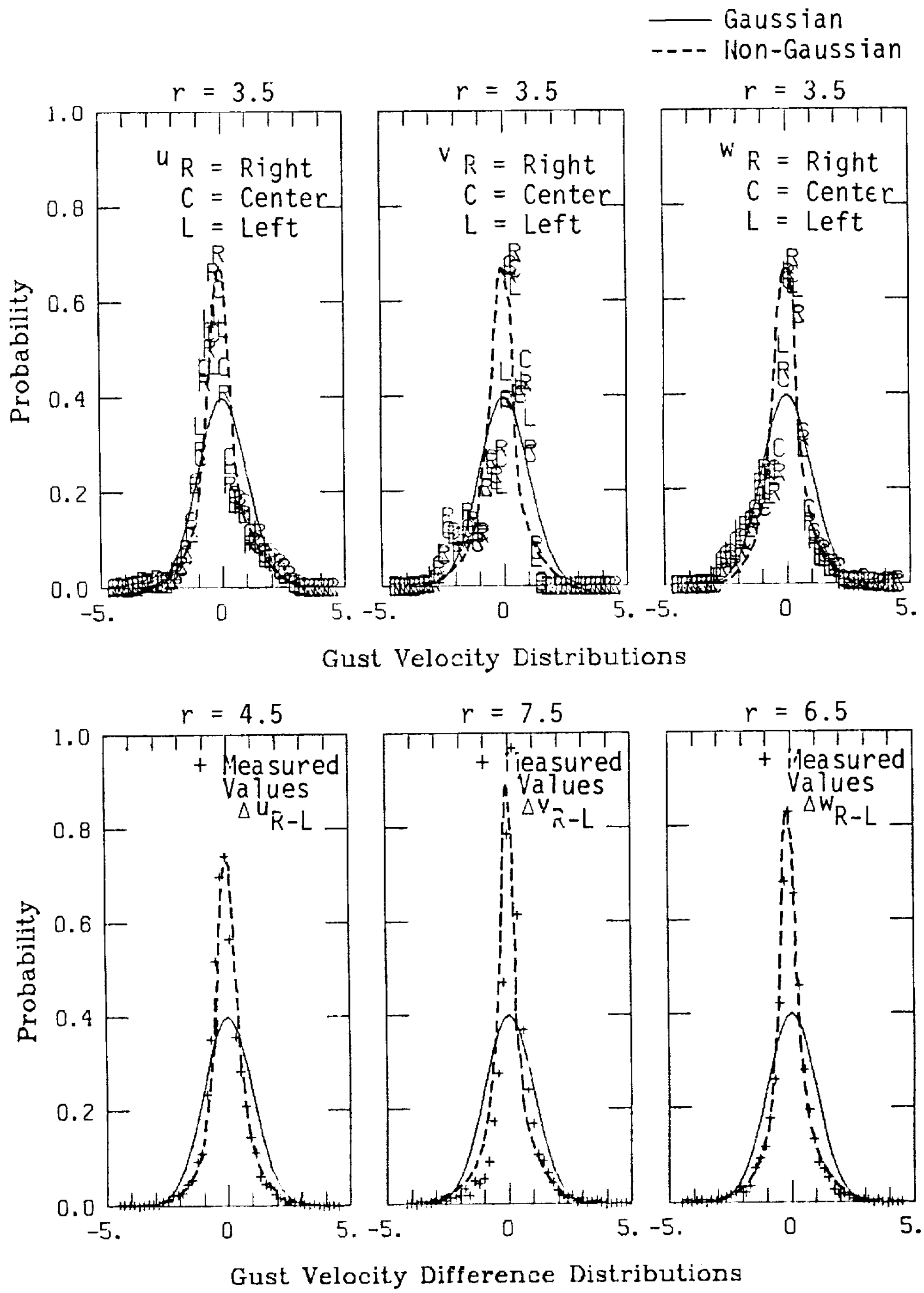

Figure A.23. Probability density functions for gust velocities and gust velocity differences (normalized with the standard deviation), Flight 31, Run 5 (r = degree of non-Gaussian).

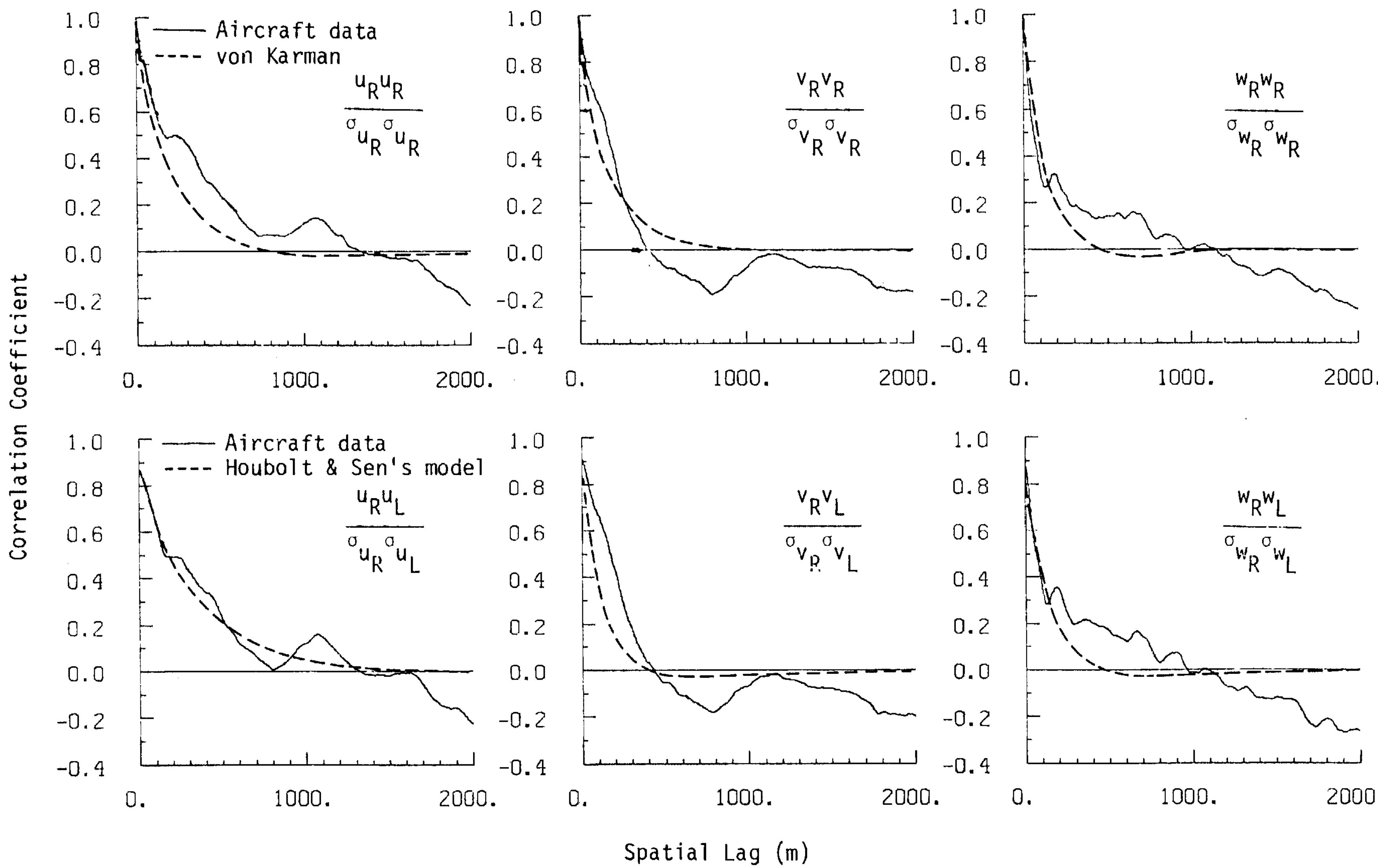

a. One- and two-point common component correlations.

Figure A.24. Comparison of normalized one- and two-point correlation functions for gust velocities with theoretical models, Flight 31, Run 5.

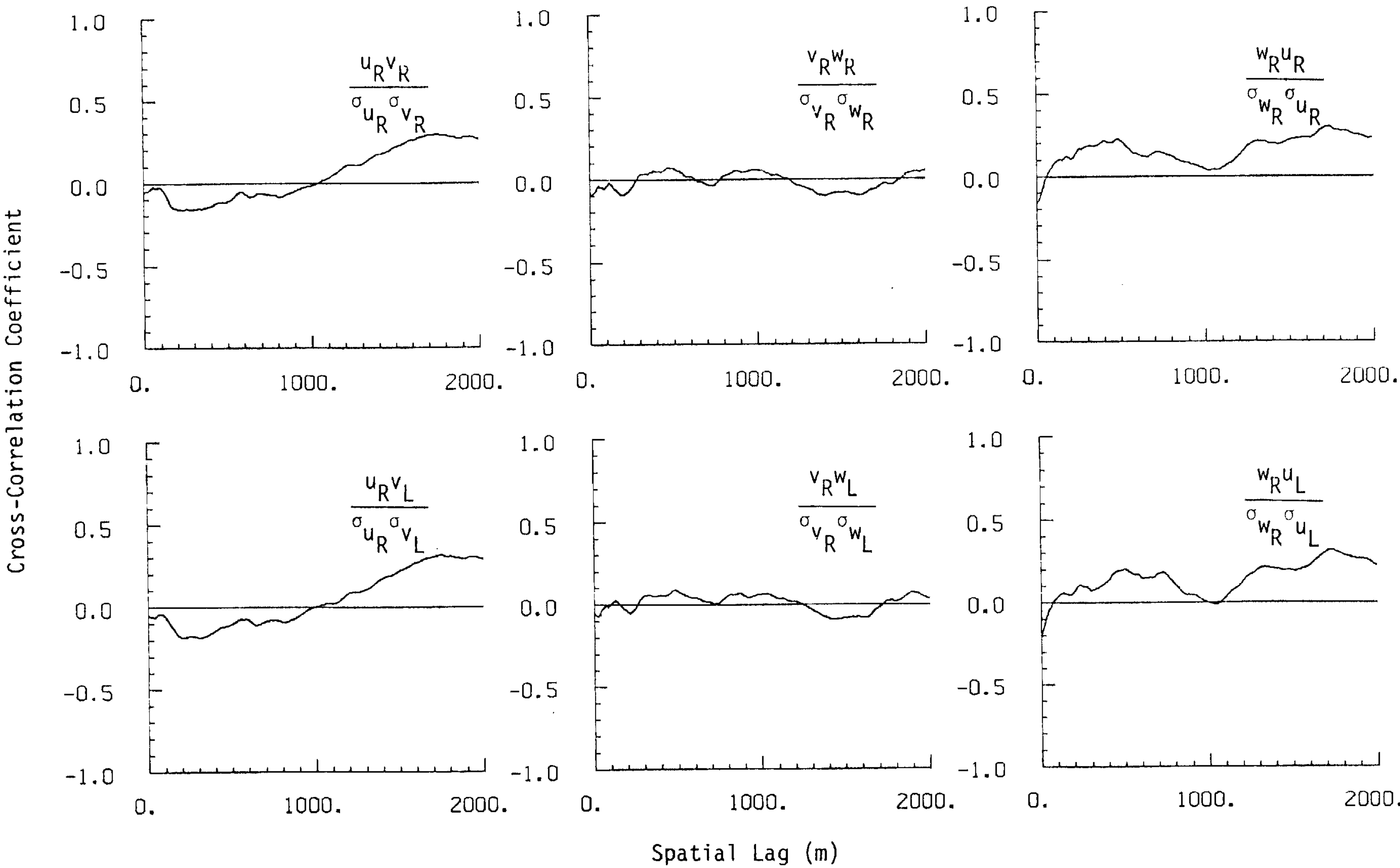

b. One- and two-point cross-correlations.

Figure A.24. (continued).

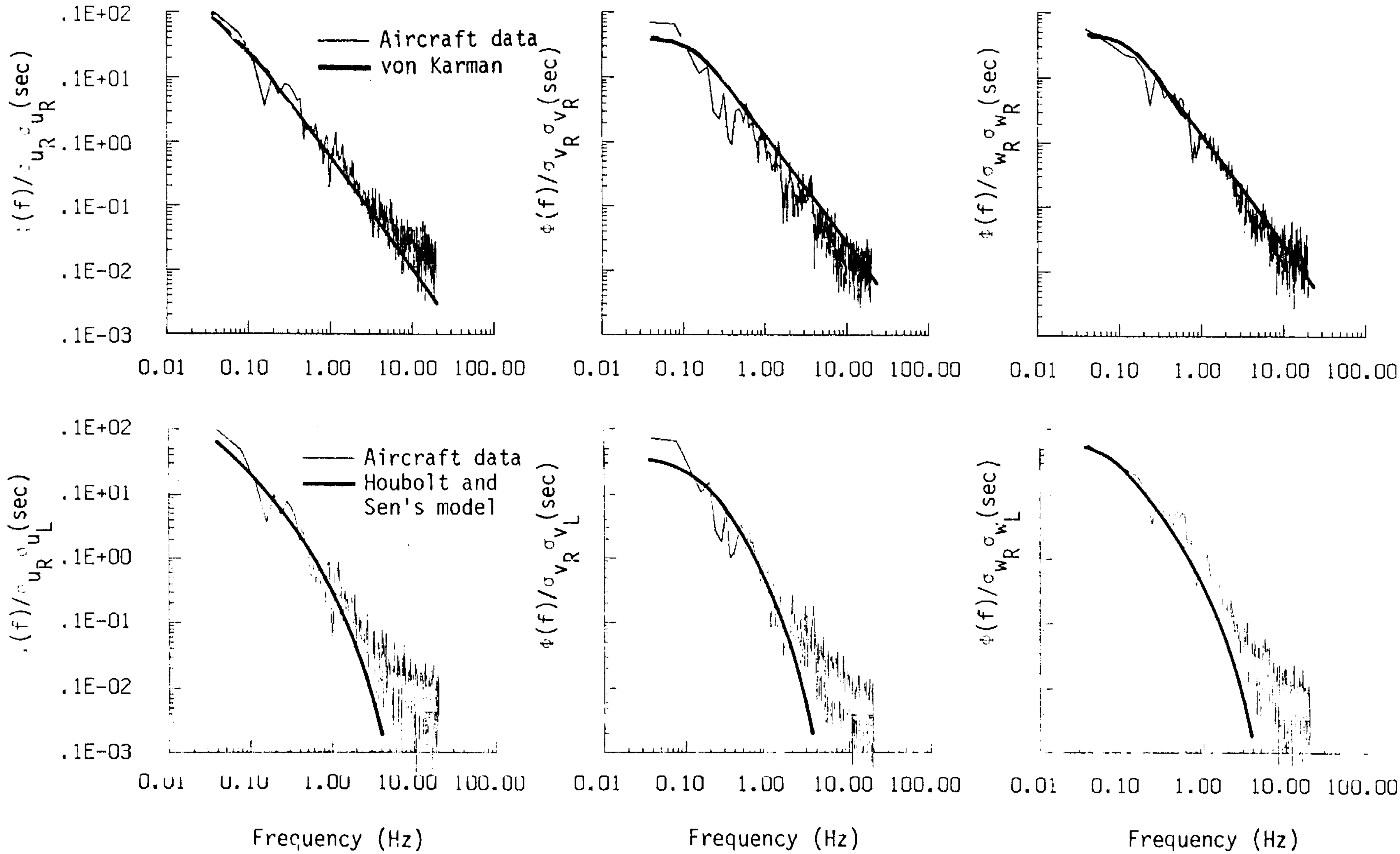

a. One- and two-point common component spectra.

Figure A.25. Comparison of normalized one- and two-point spectral density functions for gust velocities with theoretical models, Flight 31, Run 5.

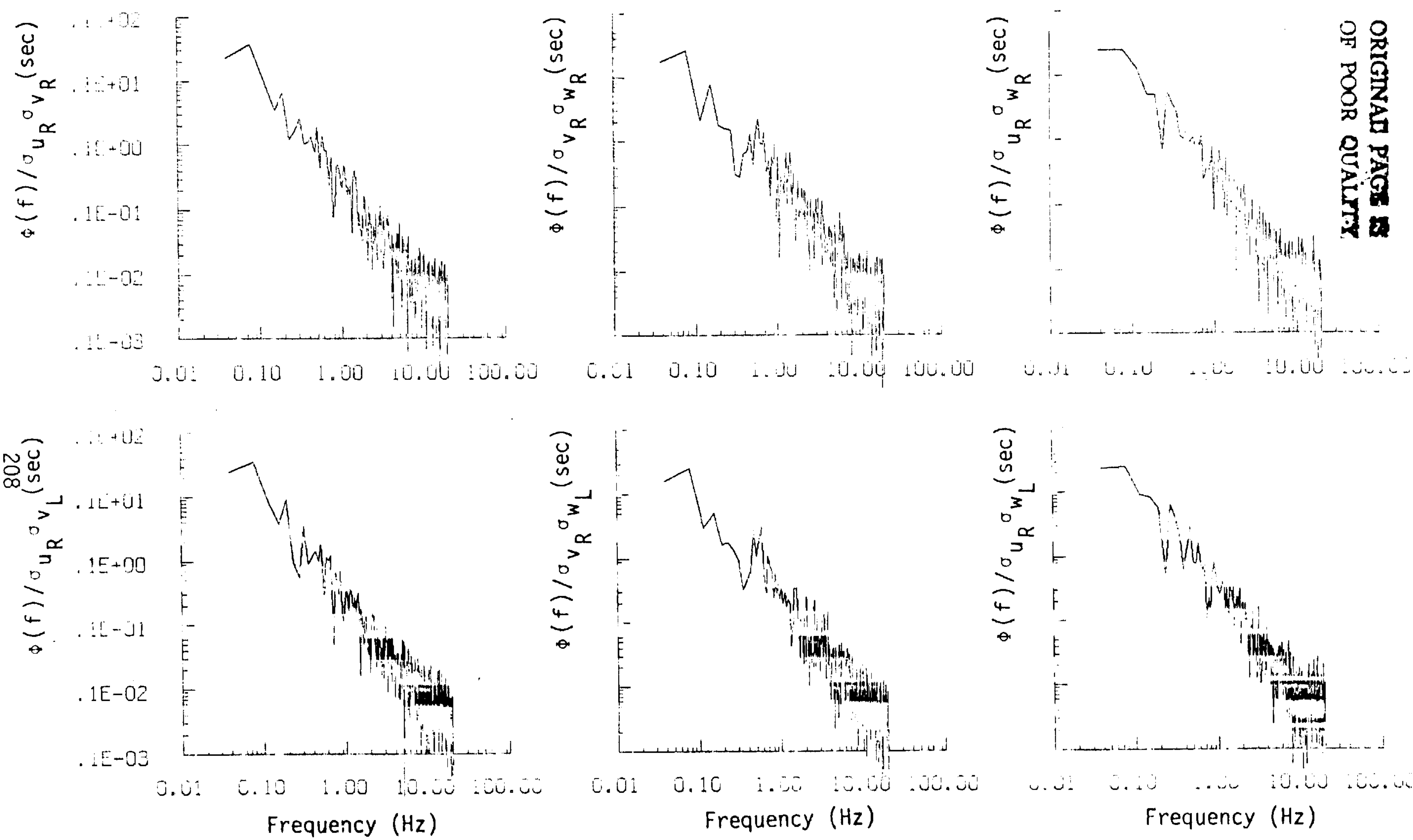

b. One- and two-point cross-spectra.

Figure A.25. (continued).

ORIGINAL PAGE IS
OF POOR QUALITY

ORIGINAL PAGE IS
OF POOR QUALITY

TABLE A.10. List of All Parameters Measured and Their Range of Values, Flight 31, Run 5.

CHANNEL	UNITS	HIGH	LOW	MEAN	RMS	STD	POINTS
1 TIME	SECONDS	40279.553	40134.578	40207.06540	40207.08719	41.86150	5800
2 PHI DOT	RAD/SEC	.208	-.195	-.00218	.04443	.04438	5800
3 ACCL N CG	G UNITS	2.327	.230	.99249	1.00515	.15907	5800
4 THETA DOT	RAD/SEC	.153	-.151	.00264	.01892	.01873	5800
5 THETA	RAD	.154	-.033	.04342	.05090	.02655	5800
6 PHI	RAD	.133	-.184	.00088	.04024	.04023	5800
7 PSI 1	RAD	359.118	-.155	299.64552	326.65102	130.06294	5800
8 DEL PSI 1	DEG	7.929	-9.556	-.29595	2.35956	2.34113	5800
9 PSI 2	RAD	363.571	346.672	355.57109	355.57842	2.28427	5800
10 DEL PSI 2	DEG	2.138	-15.092	-2.84581	6.26277	5.57933	5800
11 ACCL N LT	G UNITS	4.881	-2.620	1.00522	1.06613	.35524	5600
12 ACCL N RT	G UNITS	4.993	-2.651	1.00395	1.07230	.37674	5800
13 ACCL X CG	G UNITS	.202	-.013	.04563	.05809	.03595	5800
14 ACCL Y CG	G UNITS	.143	-.109	-.00165	.02553	.02548	5800
15 ALPHA CTR	RAD	.128	-.106	-.02076	.02707	.01739	5800
16 BETA CTR	RAD	.178	-.168	.00413	.03557	.03533	5800
17 TEMP I	DEG F	76.497	74.878	75.76997	75.77078	.35062	5800
18 TEMP P	DEG F	61.781	61.425	61.61107	61.61108	.03676	5800
19 ACCL Z INS	G UNITS	2.272	.202	.99627	1.00934	.16193	5800
20 ALPHA RT	RAD	.140	-.105	-.01016	.02160	.01906	5800
21 BETA RT	RAD	.190	-.165	.01321	.03486	.03227	5800
22 ALPHA LT	RAD	.133	-.086	.01899	.02656	.01857	5800
23 BETA LT	RAD	.142	-.161	.00764	.03341	.03253	5800
24 PSI DOT	RAD/SEC	.105	-.204	.00271	.03135	.03123	5800
25 TEMP TOT	DEG C	14.259	8.057	11.50946	11.58680	1.33665	5800
26 QC LT	PSID	1.121	.604	.82579	.82801	.06055	5800
27 QC CTR	PSID	1.003	.578	.78997	.79214	.05861	5800
28 QC RT	PSID	1.023	.588	.81840	.82065	.06070	5800
29 PS	PSIA	11.581	11.376	11.52128	11.52138	.04622	5800
30 TEMP IRT	VOLTS	7.371	2.638	6.51844	6.54426	.58078	5800
31 HYGROM	DEG C	-1.547	-9.759	-5.86794	6.15471	1.85697	5800
32 QC2 LT	PSID	.070	.068	.06965	.06965	.00042	5800
33 QC2 CTR	PSID	.177	.167	.17330	.17333	.00303	5800
34 QC2 RT	PSID	.163	-.035	.15347	.15364	.00727	5800
35 DAR	DEG	1.169	-8.916	-8.76417	8.76534	.14316	5800
36 DAL	DEG	1.513	-8.596	-8.47692	8.47811	.14203	5800
37 DELEV	DEG	3.395	-15.431	3.27645	3.28624	.25345	5800
38 DSTAB	DEG	.764	-.267	-.25796	.25836	.01427	5800
39 DRUD	DEG	7.612	-14.981	7.36917	7.37639	.32644	5800
40 DTHRR	PCT MAX	61.328	23.376	60.84641	60.84900	.56216	5800
41 DTHRL	PCT MAX	60.938	23.288	60.44540	60.44805	.56558	5800
42 DFLP	POSITION	1.968	.559	.57880	.57922	.02204	5800
43 DSB	POSITION	.174	.058	.16219	.16234	.00704	5800
44 D TO G	METERS	7531608.000	7525273.037	***********	***********	1870.13318	5800
45 B TO D	DEGREES	72.836	72.799	72.81743	72.81743	.01070	5800
46 LONG	DEGREES	-117.953	-117.976	-117.96500	117.96500	.00681	5800
47 LAT	DEGREES	35.763	35.629	35.69585	35.69587	.03898	5800
48 TRK ANG	DEGREES	10.653	5.074	7.73819	7.87254	1.44833	5800
49 HDG	RADIANS	.112	-.204	-.03712	.05631	.04235	5800
50 VE	M/SEC	19.468	8.599	13.92588	14.19503	2.75239	5800
51 VN	M/SEC	105.408	91.895	102.33217	102.37126	2.82896	5800
52 ALTITUDE	KM	2.108	1.964	2.00600	2.00626	.03237	5800
53 TEMPC	DEGREES C	8.949	3.293	6.16740	6.27054	1.13273	5800
54 EW WND SPD	KNOTS	50.684	5.746	35.36690	36.22351	7.83171	5800
55 NS WND SPD	KNOTS	14.845	-29.404	-2.01583	5.26183	4.86080	5800
56 WIND SPEED	KNOTS	51.566	7.565	35.81271	36.60369	7.56906	5800
57 WIND DIREC	DEGREES	334.159	218.077	273.71739	273.87670	9.34098	5800
58 WIND DIR2	DEGREES	154.159	38.077	93.71744	94.18172	9.34099	5800
59 WIND DIR3	DEGREES	334.159	218.077	273.71744	273.87675	9.34099	5800
60 WIND DIR4	DEGREES	334.159	218.077	273.71744	273.87675	9.34099	5800
61 AIRSPEED R	M/SEC	117.187	89.826	105.33378	105.40679	3.92291	5800
62 AIRSPEED C	M/SEC	115.996	89.111	103.53182	103.60331	3.84857	5800
63 AIRSPEED L	M/SEC	122.810	90.975	105.79945	105.87052	3.87892	5800
64 DELTA ALT	METERS	59.411	-84.477	-42.43732	53.37152	32.36932	5800
65 INRTL DISP	METERS	37.737	-82.204	-41.49497	52.29241	31.82511	5800
66 UG RIGHT	M/SEC	9.156	-11.101	.00000	2.49780	2.49801	5800
67 UG CENTER	M/SEC	8.546	-14.081	.00000	2.47382	2.47403	5800
68 UG LEFT	M/SEC	8.844	-18.166	.00000	2.56178	2.56200	5800
69 VG RIGHT	M/SEC	6.832	-17.989	-.01423	4.06130	4.06163	5800
70 VG CENTER	M/SEC	8.216	-15.520	-.01413	4.04630	4.04662	5800
71 VG LEFT	M/SEC	7.272	-13.953	-.01740	4.10718	4.10750	5800
72 WG RIGHT	M/SEC	13.841	-10.461	.01471	2.76238	2.76258	5800
73 WG CENTER	M/SEC	13.351	-9.627	.02009	2.66078	2.66093	5800
74 WG LEFT	M/SEC	13.921	-9.047	.02031	2.85228	2.85245	5800

Flight 31, Run 6
Date: Nov. 29, 1982
Start Time: 11:14:12 (PST)
Duration: 62.8 seconds

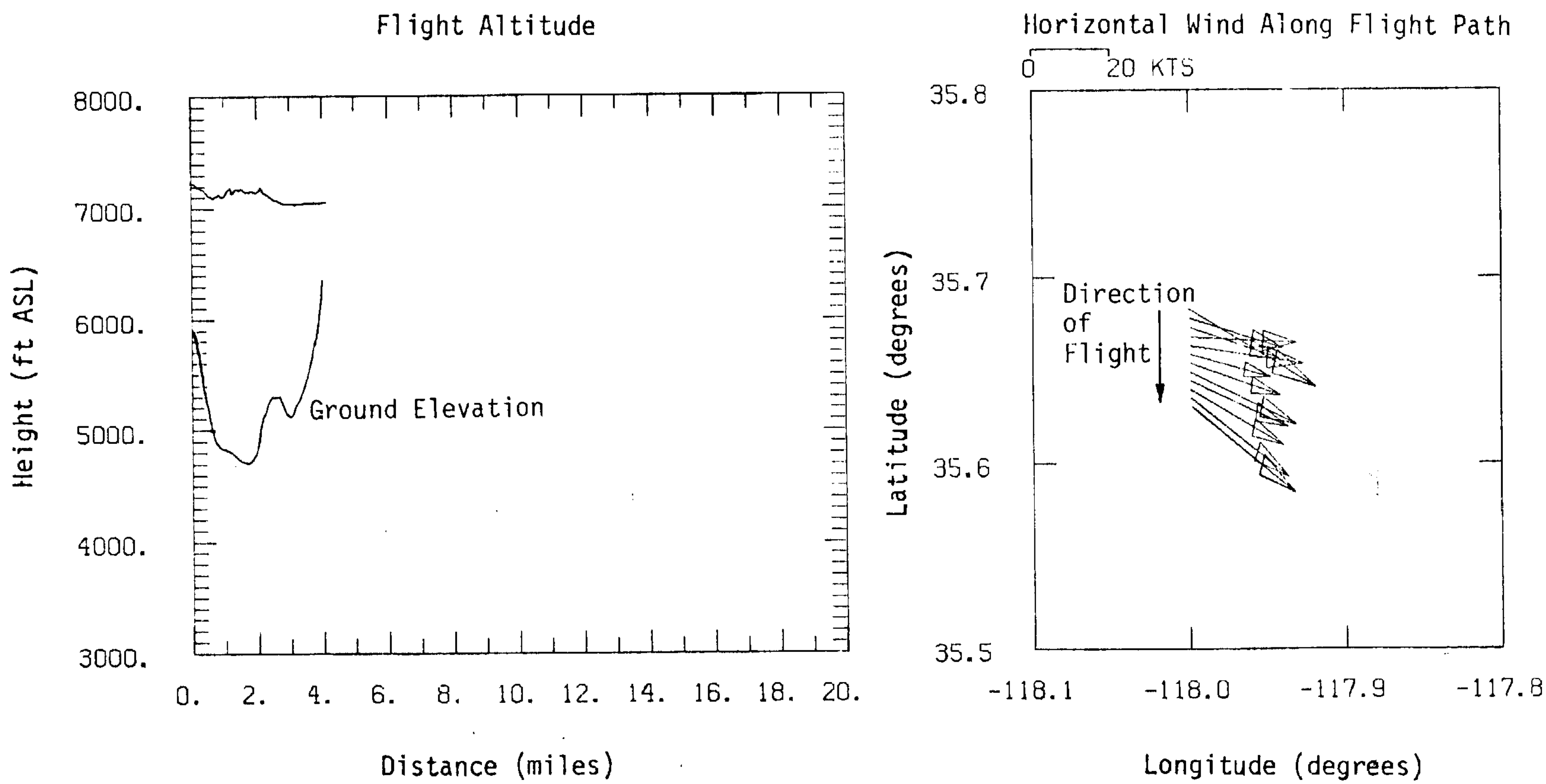

Figure A.26. Flight altitude and horizontal wind along flight path, Flight 31, Run 6.

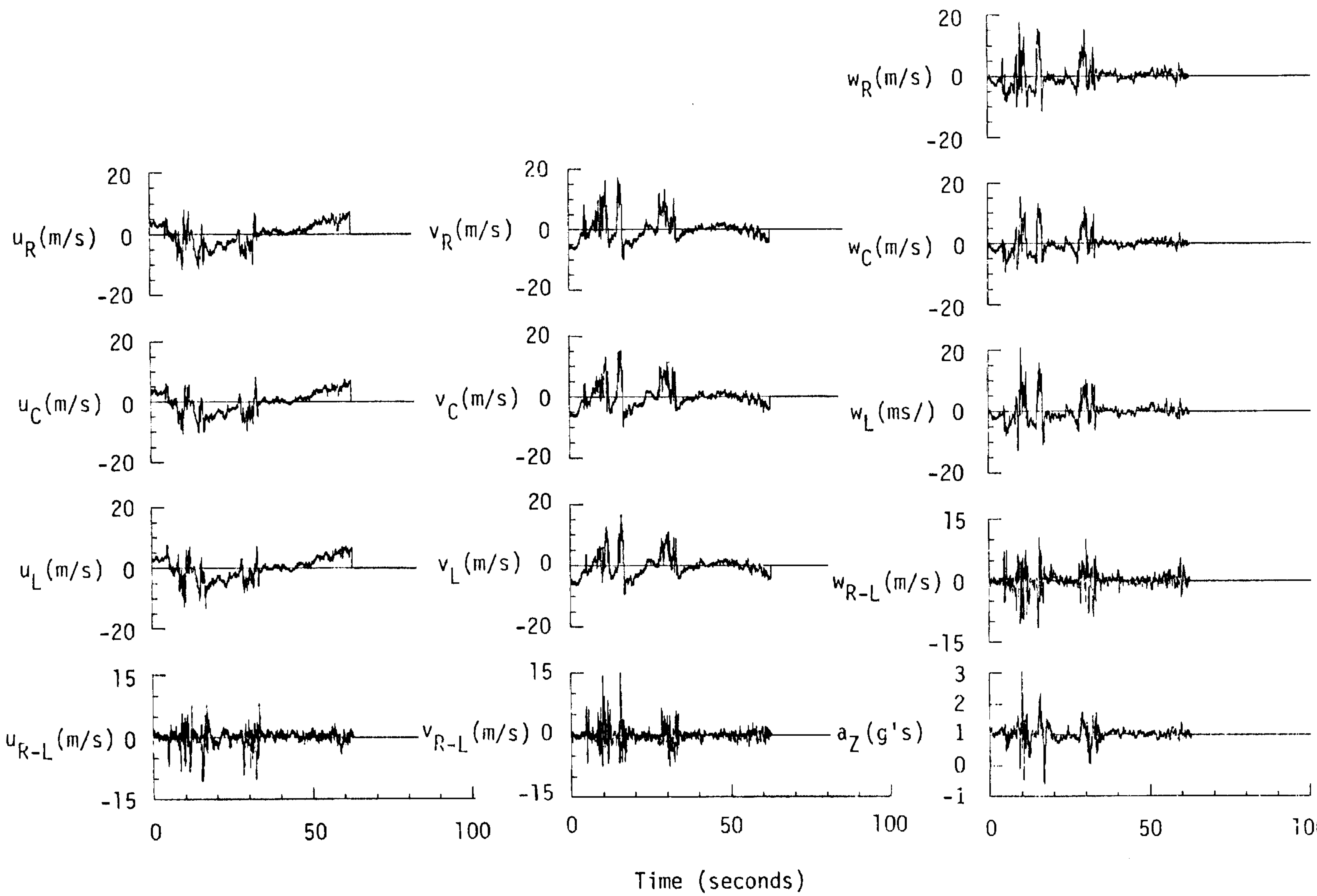

Figure A.27. Time histories of gust velocities, gust velocity differences, and aircraft's normal accelerations, Flight 31, Run 6.

TABLE A.11. Average Turbulence Parameters, Integral Length Scales, and Correlation Coefficients of Gust Velocities, Flight 31, Run 6.

1. Mean Airspeed (m/s):

$\overline{V}_L$	$\overline{V}_C$	$\overline{V}_R$
104.31	102.19	104.01

2. Standard Deviation of Gust Velocities (m/s):

σ_{uR}	σ_{vR}	σ_{wR}
3.64	3.67	3.41

σ_{uC}	σ_{vC}	σ_{wC}
3.54	3.65	3.00

σ_{uL}	σ_{vL}	σ_{wL}
3.54	3.42	3.12

3. Standard Deviation of Gust Velocity Differences (m/s):

$\sigma_{\Delta uRL}$	$\sigma_{\Delta vRL}$	$\sigma_{\Delta wRL}$
1.74	1.68	1.92

4. Integral Length Scale (m):

L_{uR}	L_{vR}	L_{wR}
364.7	92.0	51.7

L_{uRL}	L_{vRL}	L_{wRL}
344.5	104.2	47.5

5. Correlation Coefficient of Gust Velocities:

$\overline{u_R u_L}/\sigma_{u_R}\sigma_{u_L}$	$\overline{v_R v_L}/\sigma_{v_R}\sigma_{v_L}$	$\overline{w_R w_L}/\sigma_{w_R}\sigma_{w_L}$
0.82	0.90	0.81

$\overline{u_R v_R}/\sigma_{u_R}\sigma_{v_R}$	$\overline{v_R w_R}/\sigma_{v_R}\sigma_{w_R}$	$\overline{w_R u_R}/\sigma_{w_R}\sigma_{u_R}$
-0.18	0.60	-0.10

$\overline{u_R v_L}/\sigma_{u_R}\sigma_{v_L}$	$\overline{v_R w_L}/\sigma_{v_R}\sigma_{w_L}$	$\overline{w_R u_L}/\sigma_{w_R}\sigma_{u_L}$
-0.18	0.61	0.00

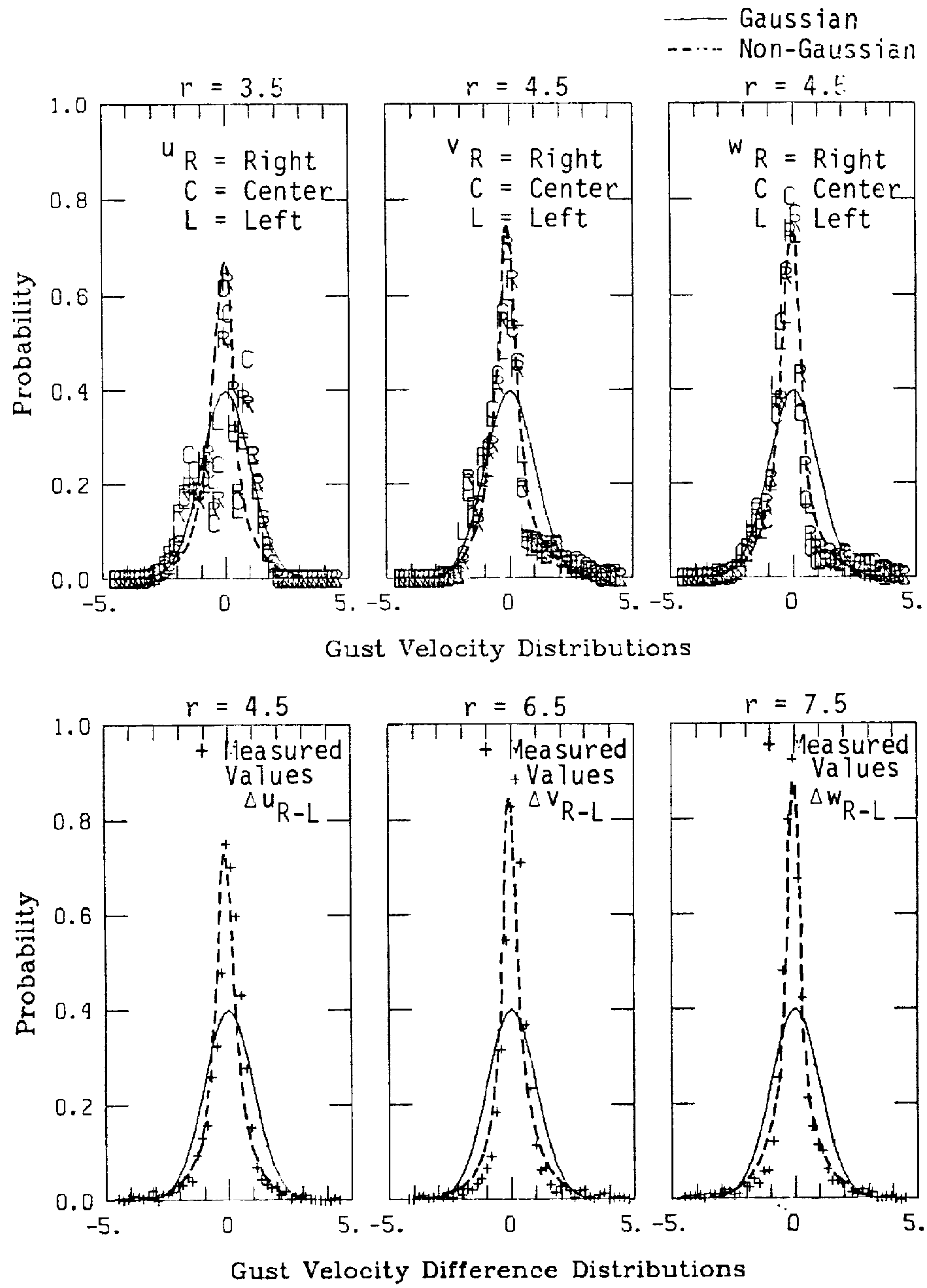

Figure A.28. Probability density functions for gust velocities and gust velocity differences (normalized with the standard deviation), Flight 31, Run 6 (r = degree of non-Gaussian).

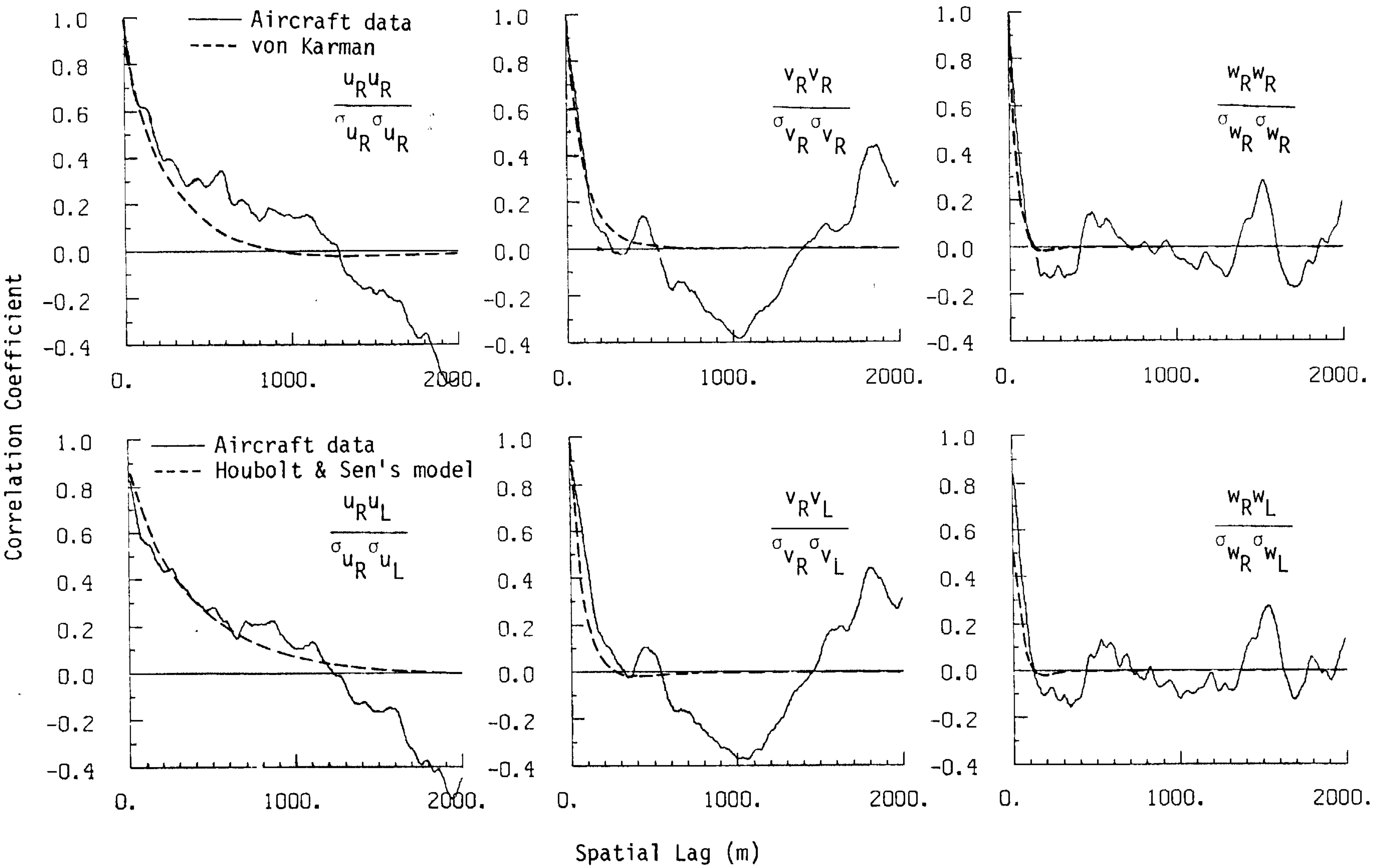

a. One- and two-point common component correlations.

Figure A.29. Comparison of normalized one- and two-point correlation functions for gust velocities with theoretical models, Flight 31, Run 6.

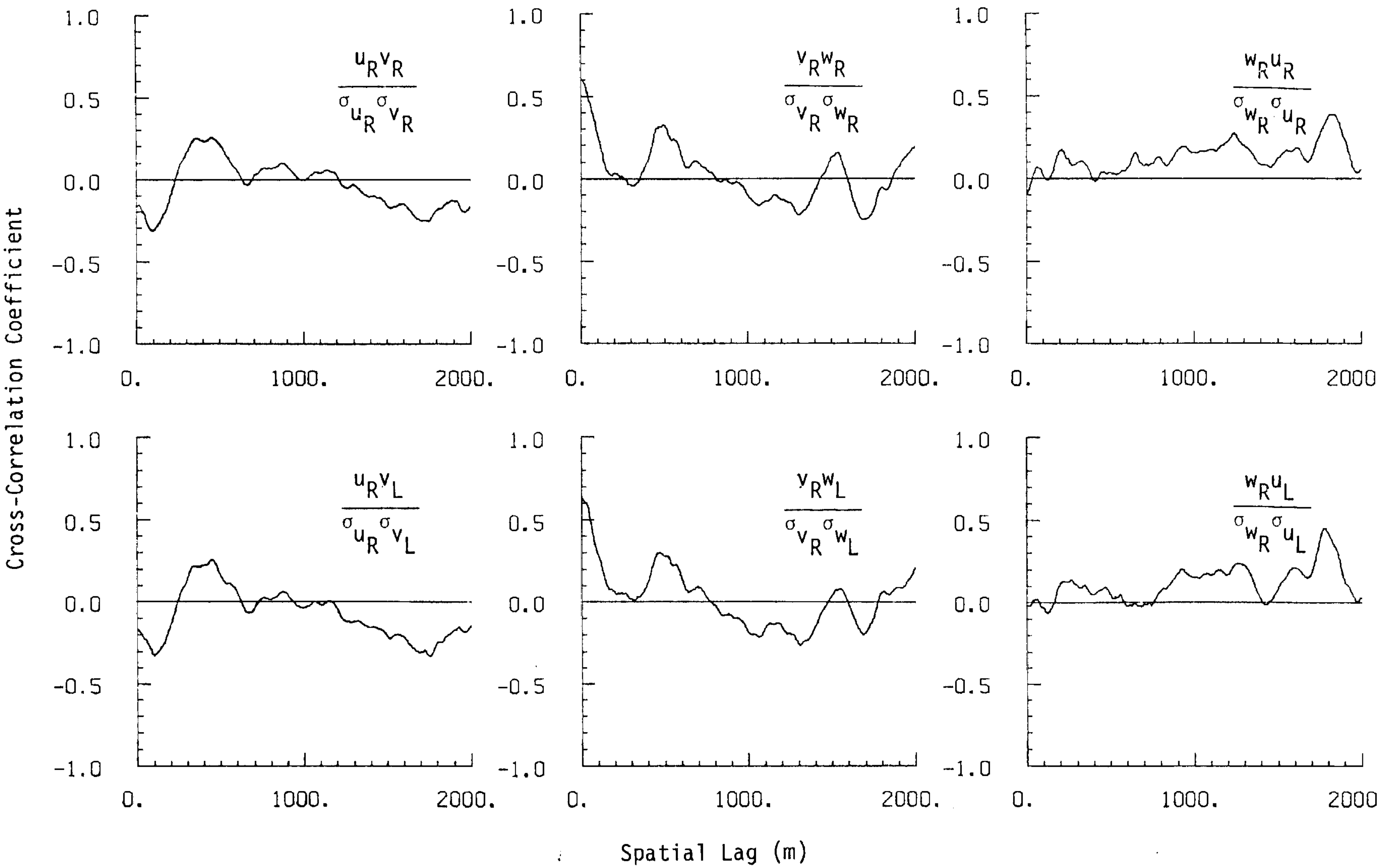

b. One- and two-point cross-correlations.

Figure A.29. (continued).

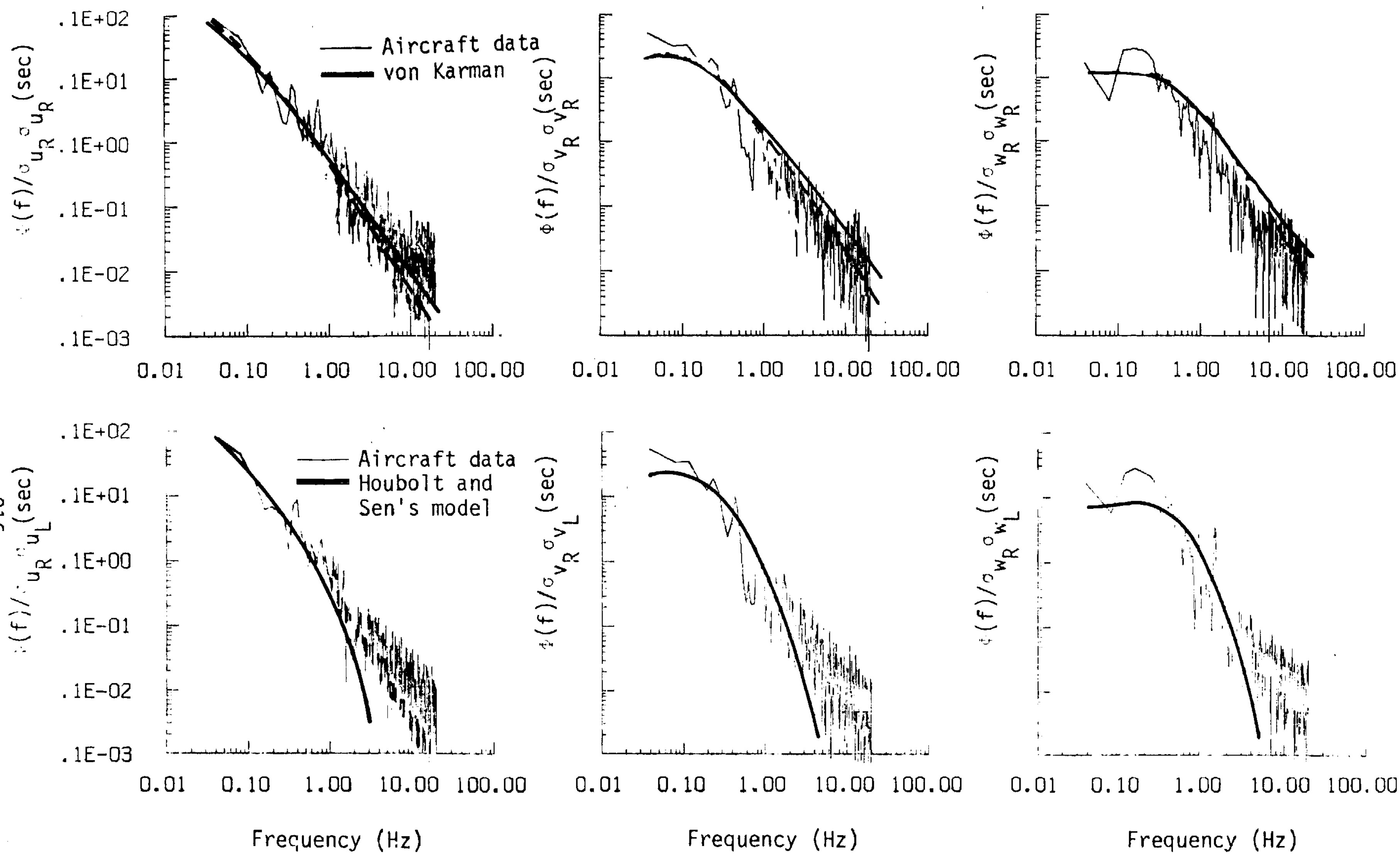

a. One- and two-point common component spectra.

Figure A.30. Comparison of normalized one- and two-point spectral density functions for gust velocities with theoretical models, Flight 31, Run 6.

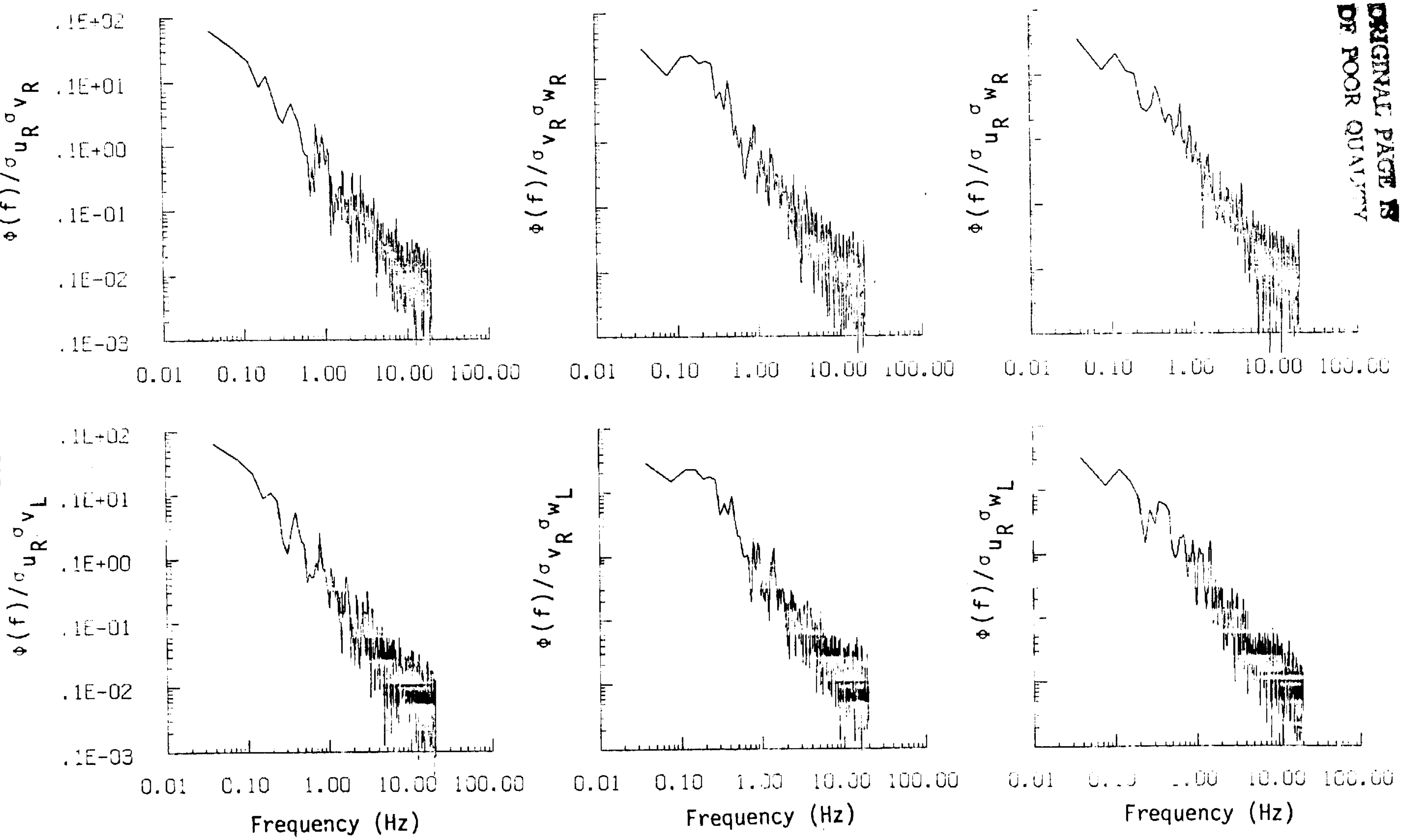

b. One- and two-point cross-spectra.

Figure A.30. (continued).

ORIGINAL PAGE IS
OF POOR QUALITY

TABLE A.12. List of All Parameters Measured and Their Range of Values, Flight 31, Run 6.

CHANNEL	UNITS	HIGH	LOW	MEAN	RMS	STD	POINTS
1 TIME	SECONDS	40514.445	40451.620	40483.03270	40483.03677	18.14684	2514
2 PHI DOT	RAD/SEC	.456	-.235	-.00310	.06217	.06210	2514
3 ACCL N CG	G UNITS	2.781	-.523	1.01158	1.04299	.25412	2514
4 THETA DOT	RAD/SEC	.184	-.196	.00335	.02708	.02688	2514
5 THETA	RAD	.146	.020	.08762	.09017	.02131	2514
6 PHI	RAD	.263	-.107	-.00172	.05970	.05969	2514
7 PSI 1	RAD	196.388	179.129	184.51265	184.53591	2.93071	2514
8 DEL PSI 1	DEG	14.983	-2.562	2.80766	4.09430	2.98058	2514
9 PSI 2	RAD	558.604	537.481	542.62956	542.63938	3.26409	2514
10 DEL PSI 2	DEG	14.841	-2.213	3.10556	4.24230	2.89066	2514
11 ACCL N LT	G UNITS	5.024	-2.819	1.02459	1.16053	.54511	2514
12 ACCL N RT	G UNITS	4.993	-2.960	1.01898	1.17818	.59156	2514
13 ACCL X CG	G UNITS	.233	-.020	.08353	.09368	.04240	2514
14 ACCL Y CG	G UNITS	.135	-.164	-.00087	.03531	.03530	2514
15 ALPHA CTR	RAD	.118	-.160	-.01681	.03148	.02663	2514
16 BETA CTR	RAD	.208	-.165	.00400	.04819	.04803	2514
17 TEMP I	DEG F	78.476	77.397	77.96893	77.96927	.22974	2514
18 TEMP P	DEG F	61.781	61.601	61.74117	61.74122	.07356	2514
19 ACCL Z INS	G UNITS	3.045	-.562	1.01599	1.04685	.25236	2514
20 ALPHA RT	RAD	.150	-.194	-.00244	.03131	.03122	2514
21 BETA RT	RAD	.203	-.167	.01407	.04765	.04553	2514
22 ALPHA LT	RAD	.155	-.151	.02282	.03582	.02761	2514
23 BETA LT	RAD	.174	-.164	.00548	.04307	.04273	2514
24 PSI DOT	RAD/SEC	.159	-.128	.00198	.04015	.04011	2514
25 TEMP TOT	DEG C	10.715	7.072	8.67362	8.70365	.72253	2514
26 QC LT	PSID	1.110	.641	.79533	.80003	.08656	2514
27 QC CTR	PSID	1.037	.585	.76269	.76735	.08445	2514
28 QC RT	PSID	1.081	.618	.79085	.79568	.08761	2514
29 PS	PSIA	11.324	11.237	11.29206	11.29209	.02389	2514
30 TEMP IRT	VOLTS	5.503	3.121	4.81438	4.83667	.46390	2514
31 HYGROM	DEG C	-1.942	-8.194	-5.40948	5.63043	1.56212	2514
32 QC2 LT	PSID	.072	.072	.07180	.07180	.00025	2514
33 QC2 CTR	PSID	.158	.137	.14859	.14870	.00588	2514
34 QC2 RT	PSID	.137	.126	.13074	.13078	.00301	2514
35 DAR	DEG	-9.689	-9.717	-9.68945	9.68946	.00261	2514
36 DAL	DEG	-8.899	-9.037	-8.98630	8.98639	.04009	2514
37 DELEV	DEG	4.058	3.785	3.92190	3.92248	.06743	2514
38 DSTAB	DEG	-.283	-.294	-.28861	.28863	.00328	2514
39 DRUD	DEG	8.295	8.068	8.15400	8.15421	.05977	2514
40 DTHRR	PCT MAX	62.590	62.207	62.38175	62.38182	.09379	2514
41 DTHRL	PCT MAX	62.305	62.012	62.16127	62.16136	.10322	2514
42 DFLP	POSITION	.512	.496	.50417	.50418	.00443	2514
43 DSB	POSITION	.207	.197	.20250	.20252	.00251	2514
44 D TO G	METERS	7525058.458	7523312.563	***********	***********	524.55013	2514
45 B TO D	DEGREES	72.824	72.798	72.81079	72.81079	.00720	2514
46 LONG	DEGREES	-117.997	-118.000	-117.99856	117.99856	.00061	2514
47 LAT	DEGREES	35.686	35.625	35.65489	35.65489	.01733	2514
48 TRK ANG	DEGREES	182.249	174.899	177.83402	177.84529	2.00259	2514
49 HDG	RADIANS	3.447	3.138	3.23368	3.23411	.05251	2514
50 VE	M/SEC	9.799	-4.430	4.09913	5.61498	3.83809	2514
51 VN	M/SEC	-102.169	-112.961	-106.90144	106.96891	3.79957	2514
52 ALTITUDE	KM	2.206	2.145	2.16746	2.16753	.01698	2514
53 TEMPC	DEGREES C	4.802	2.085	3.46107	3.51936	.63802	2514
54 EW WND SPD	KNOTS	42.305	-1.321	25.54551	26.42022	6.74336	2514
55 NS WND SPD	KNOTS	11.402	-25.054	-10.14093	12.26832	6.90596	2514
56 WIND SPEED	KNOTS	42.407	3.865	28.29386	29.12970	6.92939	2514
57 WIND DIREC	DEGREES	357.798	6.301	290.70819	291.23767	17.55703	2514
58 WIND DIR2	DEGREES	177.798	-173.699	110.70825	112.09123	17.55705	2514
59 WIND DIR3	DEGREES	357.798	6.301	290.70825	291.23773	17.55705	2514
60 WIND DIR4	DEGREES	368.755	181.166	290.99465	291.42208	15.78111	2514
61 AIRSPEED R	M/SEC	121.266	92.271	104.01912	104.16727	5.55470	2514
62 AIRSPEED C	M/SEC	118.709	89.929	102.19461	102.33983	5.45103	2514
63 AIRSPEED L	M/SEC	122.780	93.967	104.31353	104.45593	5.45346	2514
64 DELTA ALT	METERS	1.015	-60.608	-37.81934	41.45465	16.97942	2514
65 INRTL DISP	METERS	.000	-52.813	-30.60195	34.32676	15.55452	2514
66 UG RIGHT	M/SEC	8.054	-11.346	.00000	3.64237	3.64309	2514
67 UG CENTER	M/SEC	8.341	-10.706	.00000	3.54397	3.54467	2514
68 UG LEFT	M/SEC	7.622	-13.375	.00000	3.54621	3.54692	2514
69 VG RIGHT	M/SEC	17.341	-9.962	-.08764	3.67656	3.67624	2514
70 VG CENTER	M/SEC	15.198	-9.738	-.08299	3.65269	3.65247	2514
71 VG LEFT	M/SEC	16.523	-9.308	-.10410	3.42577	3.42487	2514
72 WG RIGHT	M/SEC	17.793	-11.422	-.10907	3.42058	3.41952	2514
73 WG CENTER	M/SEC	15.330	-9.243	-.09851	3.00378	3.00277	2514
74 WG LEFT	M/SEC	20.597	-12.616	-.09179	3.12148	3.12075	2514

Flight 31, Run 7
Date Nov. 29, 1982
Start Time: 11:17:36 (PST)
Duration: 203.9 seconds

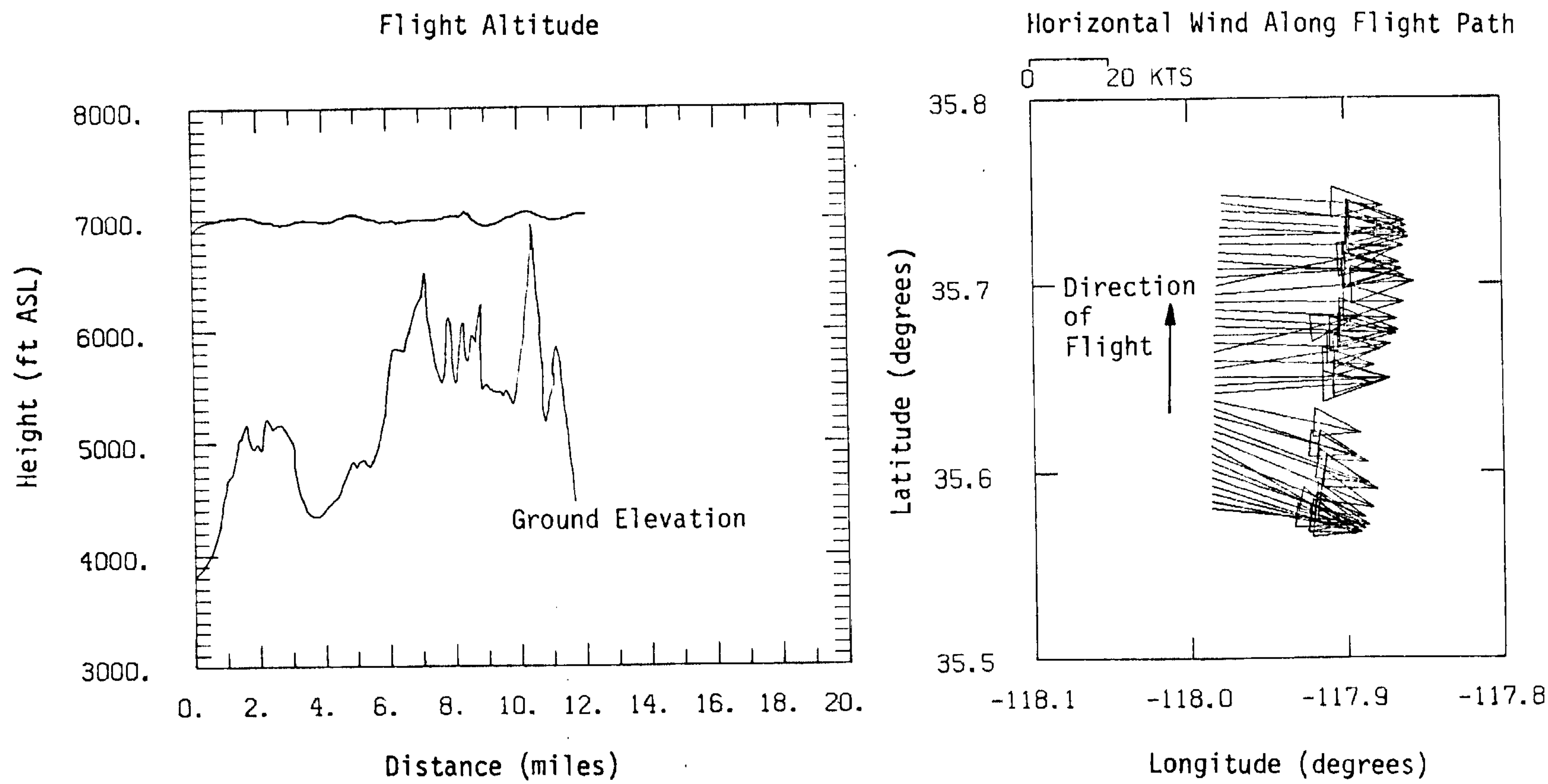

Figure A.31. Flight altitude and horizontal wind along flight path, Flight 31, Run 7.

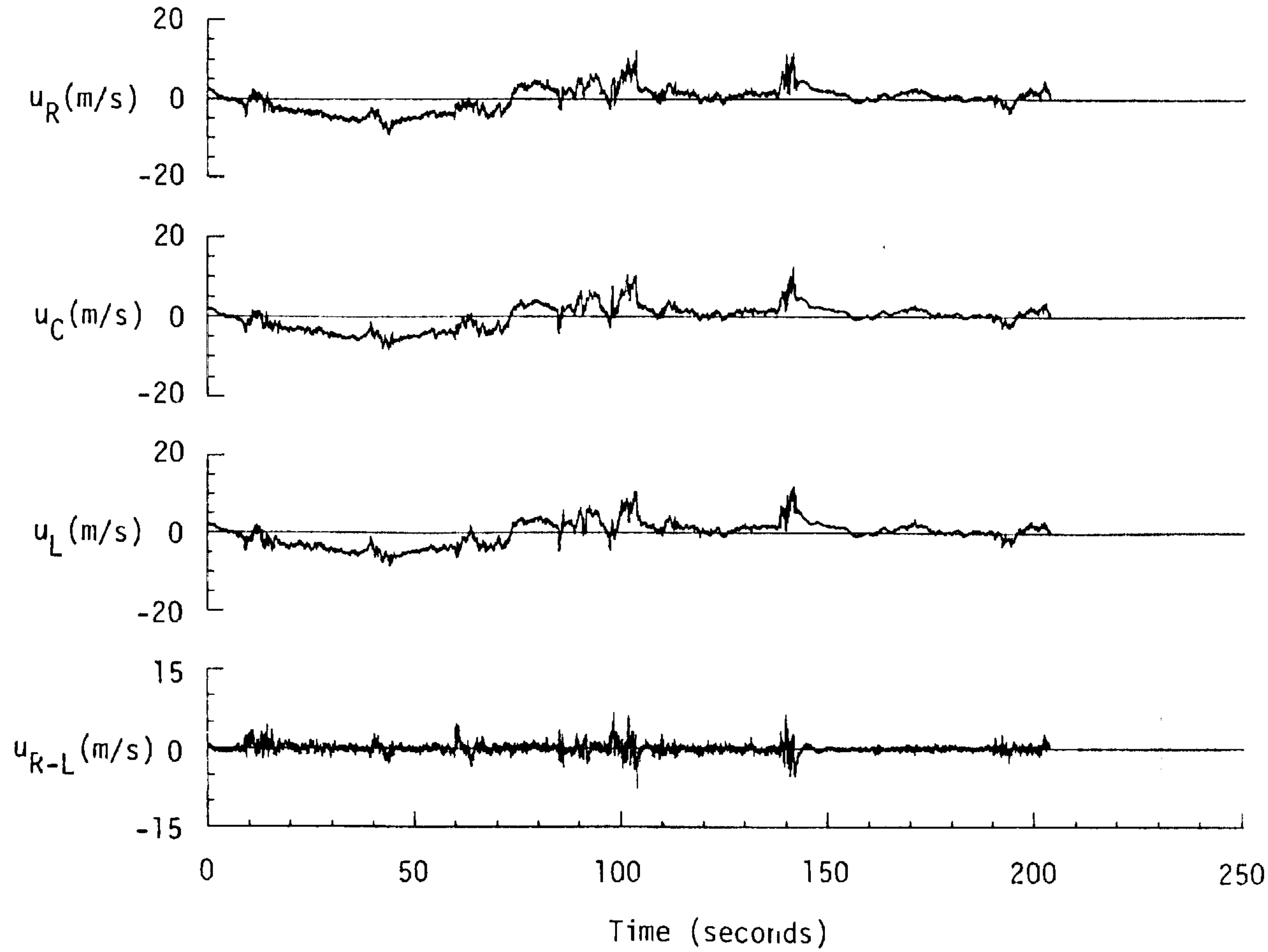

Figure A.32. Time histories of gust velocities, gust velocity differences, and aircraft's normal accelerations, Flight 31, Run 7.

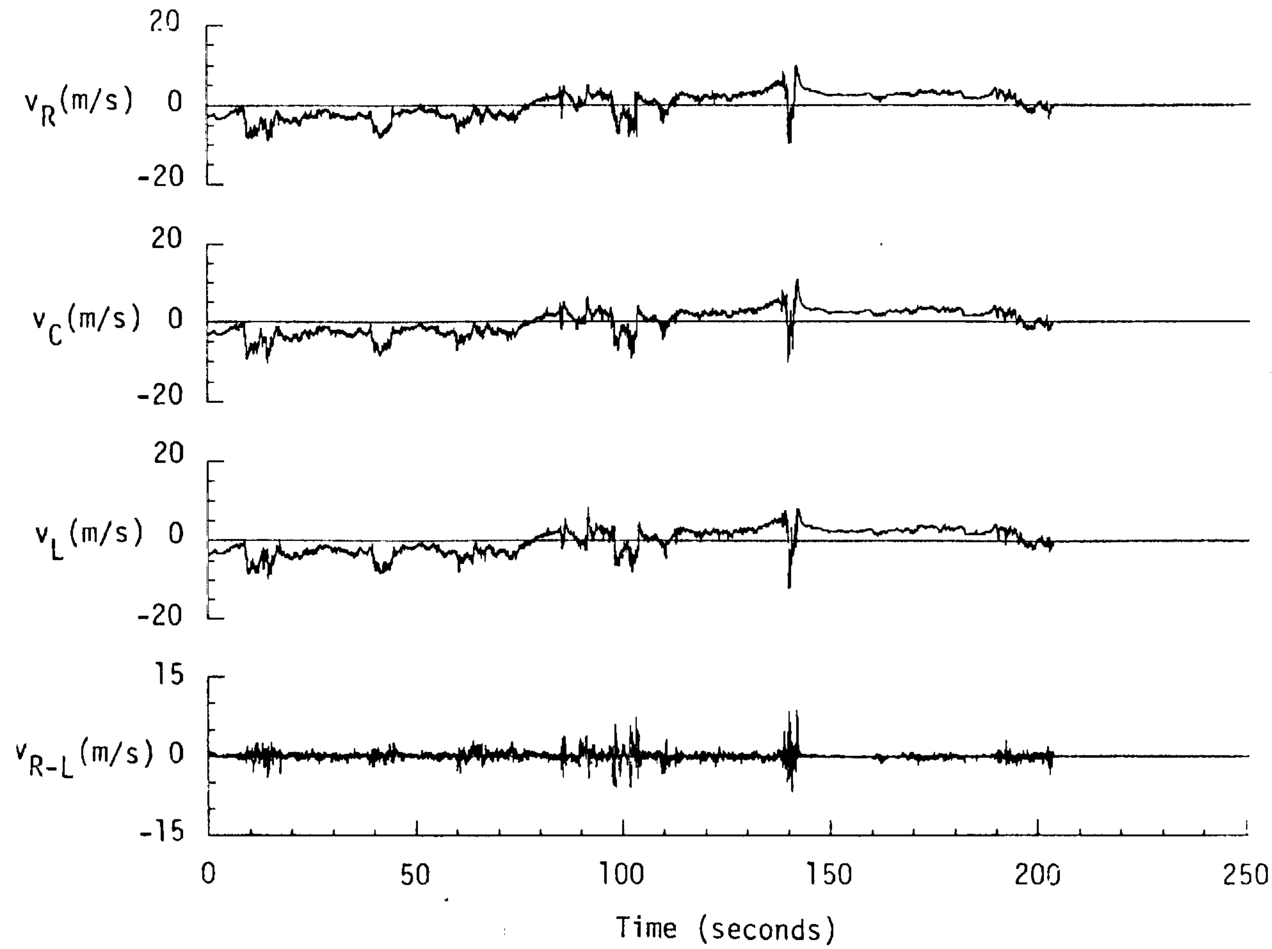

Figure A.32. (continued).

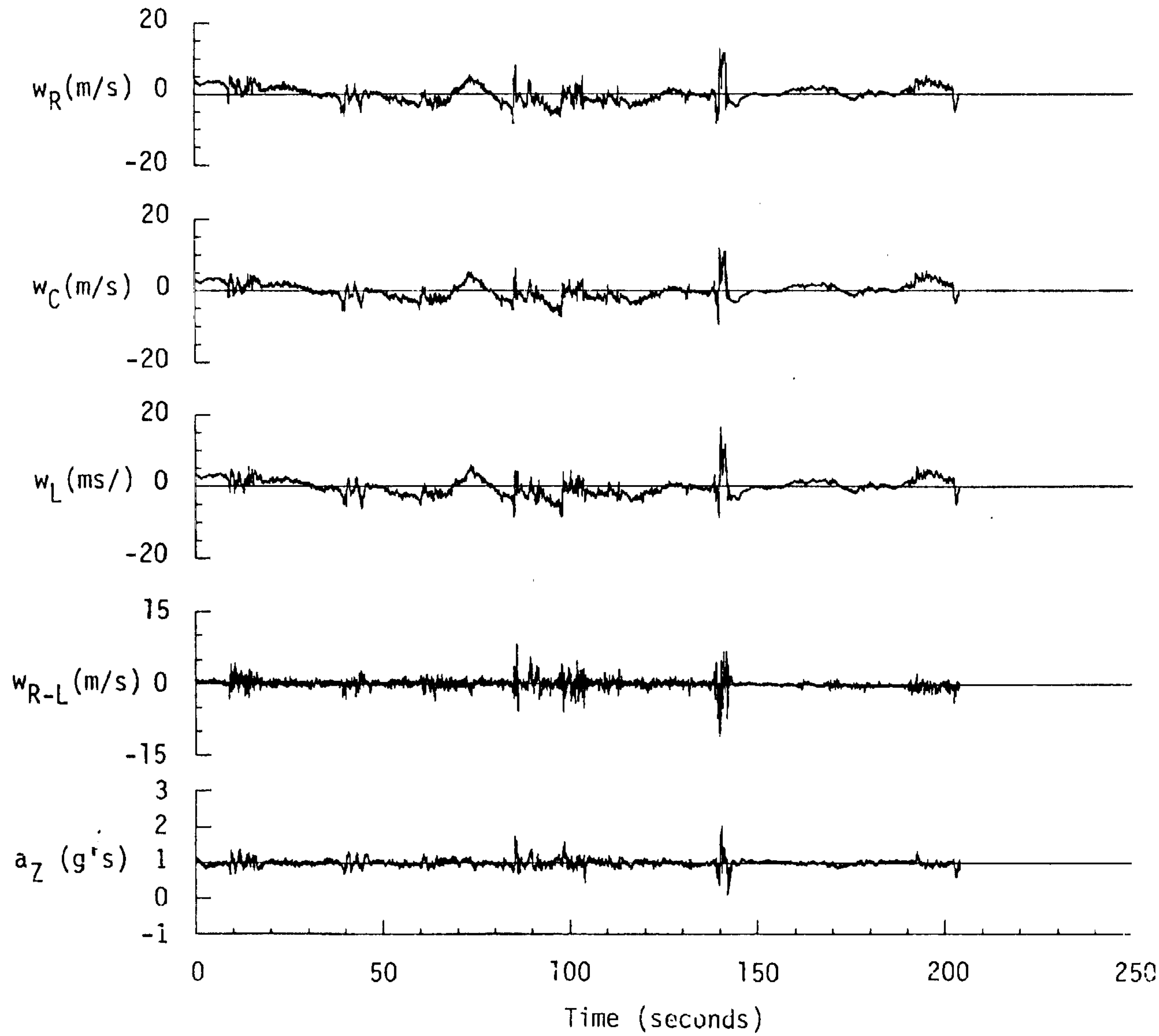

Figure A.32. (continued).

TABLE A.13. Average Turbulence Parameters, Integral Length Scales, and Correlation Coefficients of Gust Velocities, Flight 31, Run 7.

1. Mean Airspeed (m/s):

$\overline{V}_L$	$\overline{V}_C$	$\overline{V}_R$
101.47	99.23	100.93

2. Standard Deviation of Gust Velocities (m/s):

σ_{uR}	σ_{vR}	σ_{wR}
3.03	3.00	2.23

σ_{uC}	σ_{vC}	σ_{wC}
3.03	3.03	2.15

σ_{uL}	σ_{vL}	σ_{wL}
3.07	3.06	2.22

3. Standard Deviation of Gust Velocity Differences (m/s):

$\sigma_{\Delta uRL}$	$\sigma_{\Delta vRL}$	$\sigma_{\Delta wRL}$
0.85	0.80	0.89

4. Integral Length Scale (m):

L_{uR}	L_{vR}	L_{wR}
562.8	249.6	287.6

L_{uRL}	L_{vRL}	L_{wRL}
532.2	242.9	283.5

5. Correlation Coefficient of Gust Velocities:

$\overline{u_R u_L}/\sigma_{u_R}\sigma_{u_L}$	$\overline{v_R v_L}/\sigma_{v_R}\sigma_{v_L}$	$\overline{w_R w_L}/\sigma_{w_R}\sigma_{w_L}$
0.92	0.90	0.90

$\overline{u_R v_R}/\sigma_{u_R}\sigma_{v_R}$	$\overline{v_R w_R}/\sigma_{v_R}\sigma_{w_R}$	$\overline{w_R u_R}/\sigma_{w_R}\sigma_{u_R}$
0.02	-0.21	0.39

$\overline{u_R v_L}/\sigma_{u_R}\sigma_{v_L}$	$\overline{v_R w_L}/\sigma_{v_R}\sigma_{w_L}$	$\overline{w_R u_L}/\sigma_{w_R}\sigma_{u_L}$
0.01	-0.21	0.32

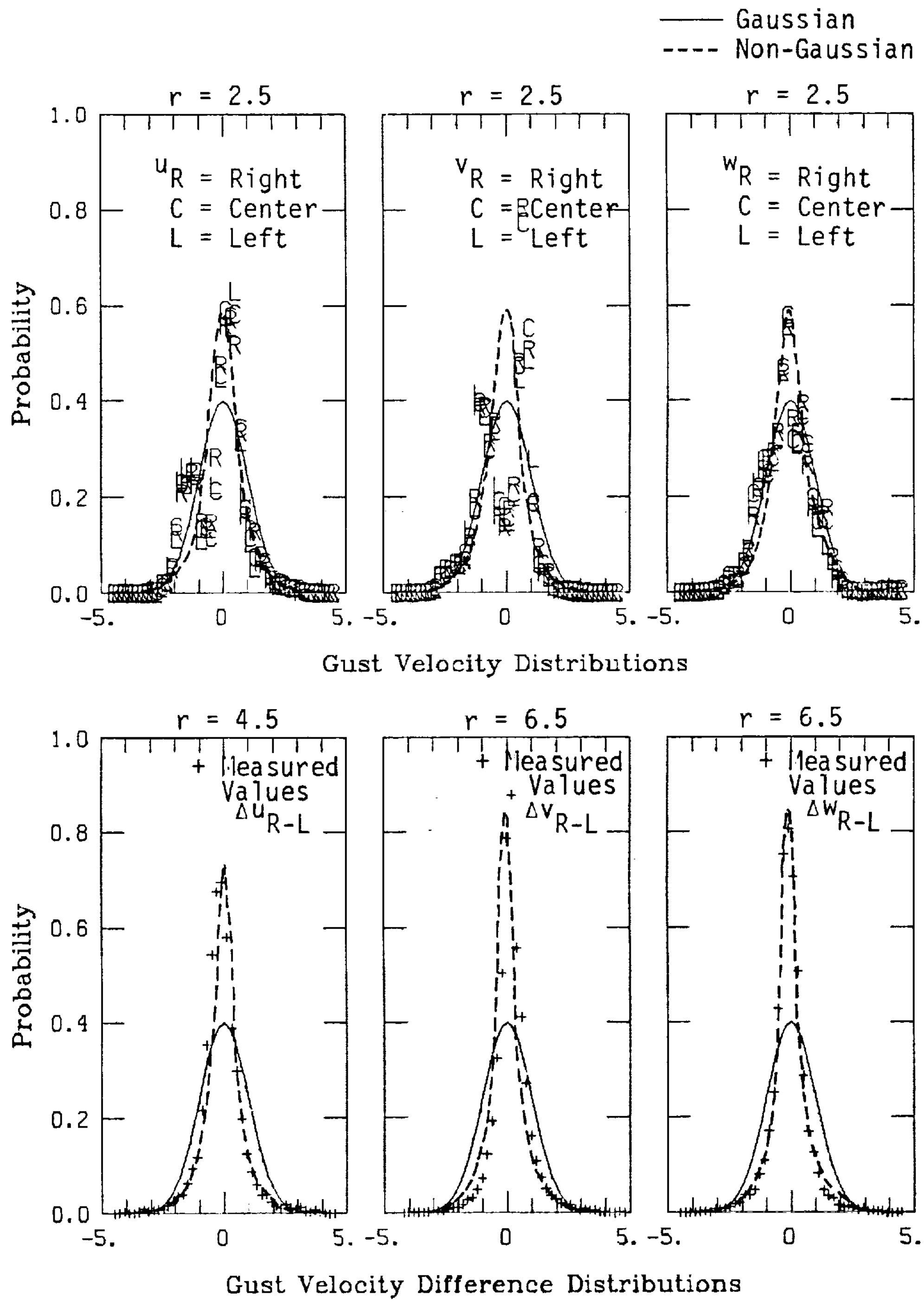

Figure A.33. Probability density functions for gust velocities and gust velocity differences (normalized with the standard deviation), Flight 31, Run 7 (r = degree of non-Gaussian).

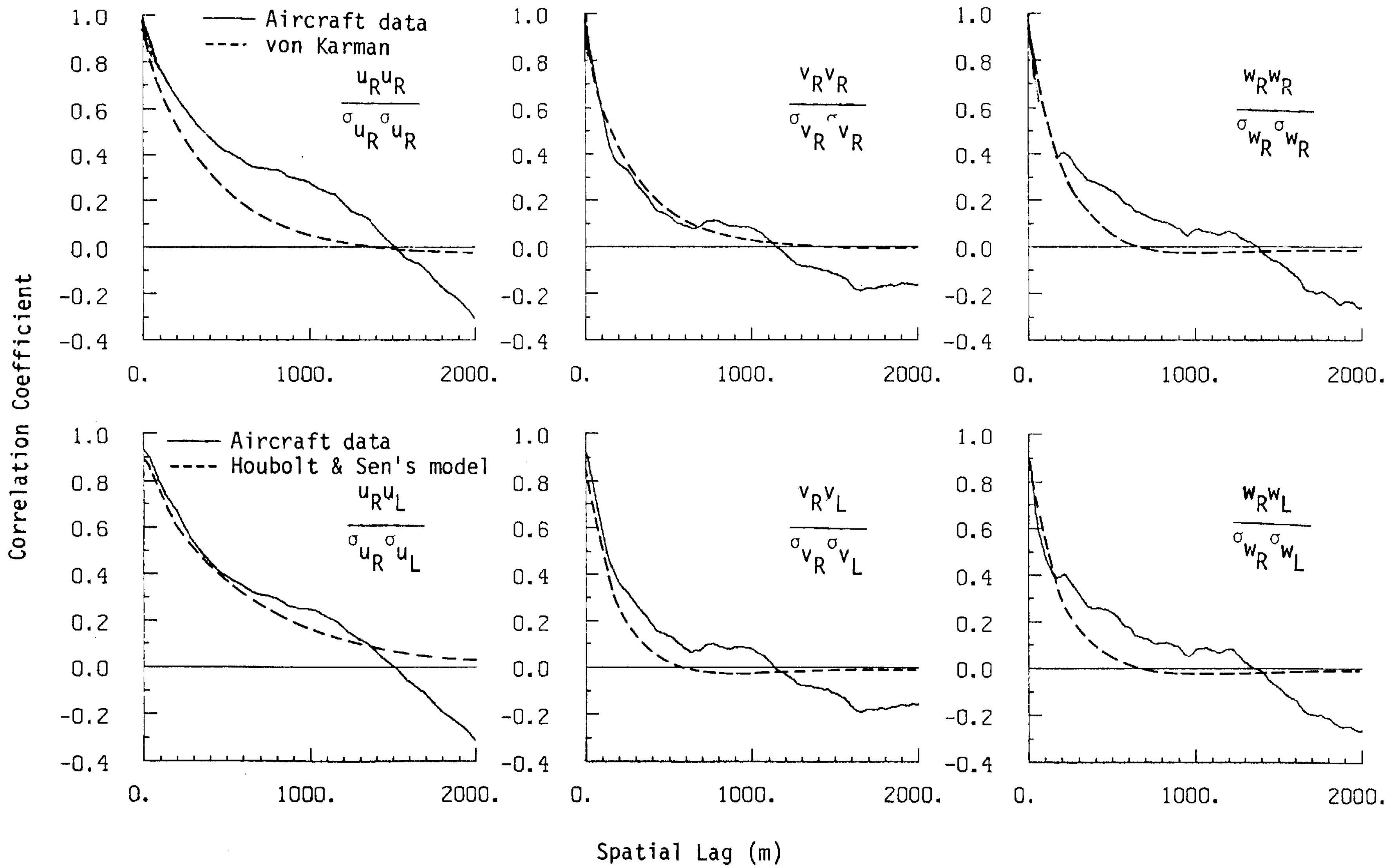

a. One- and two-point common component correlations.

Figure A.34. Comparison of normalized one- and two-point correlation functions for gust velocities with theoretical models, Flight 31, Run 7.

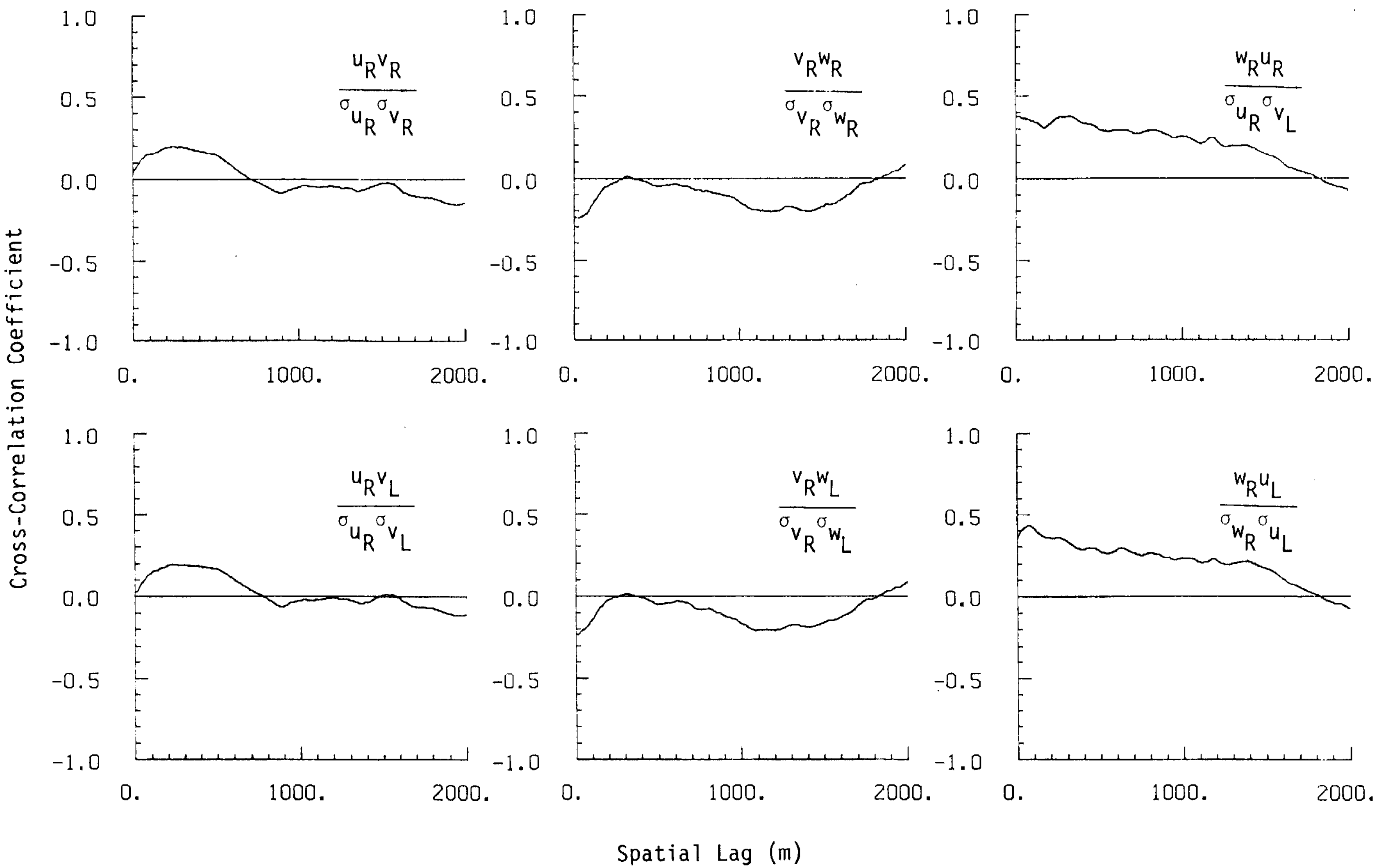

b. One- and two-point cross-correlations.

Figure A.34. (continued).

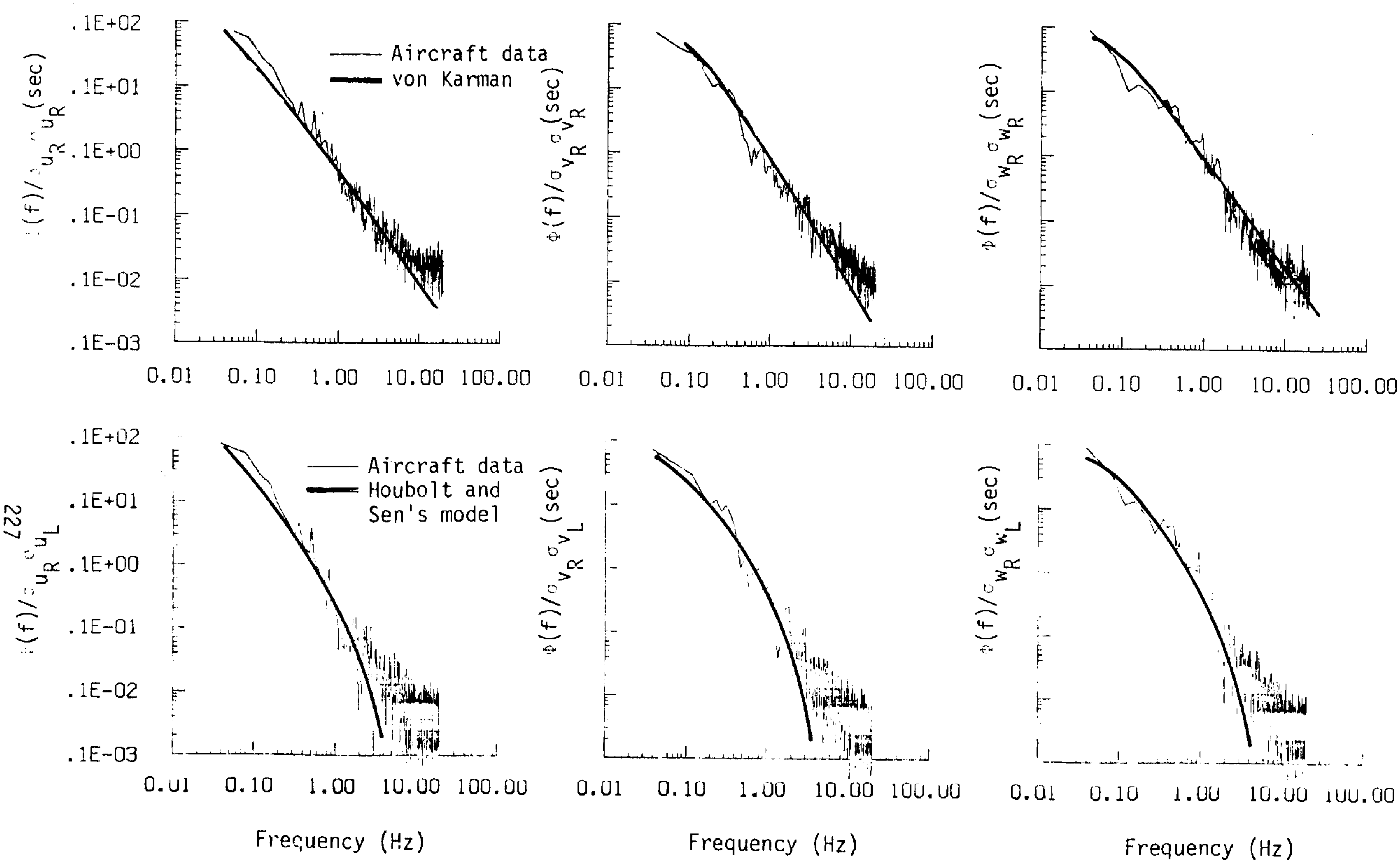

a. One- and two-point common component spectra.

Figure A.35. Comparison of normalized one- and two-point spectral density functions for gust velocities with theoretical models, Flight 31, Run 7.

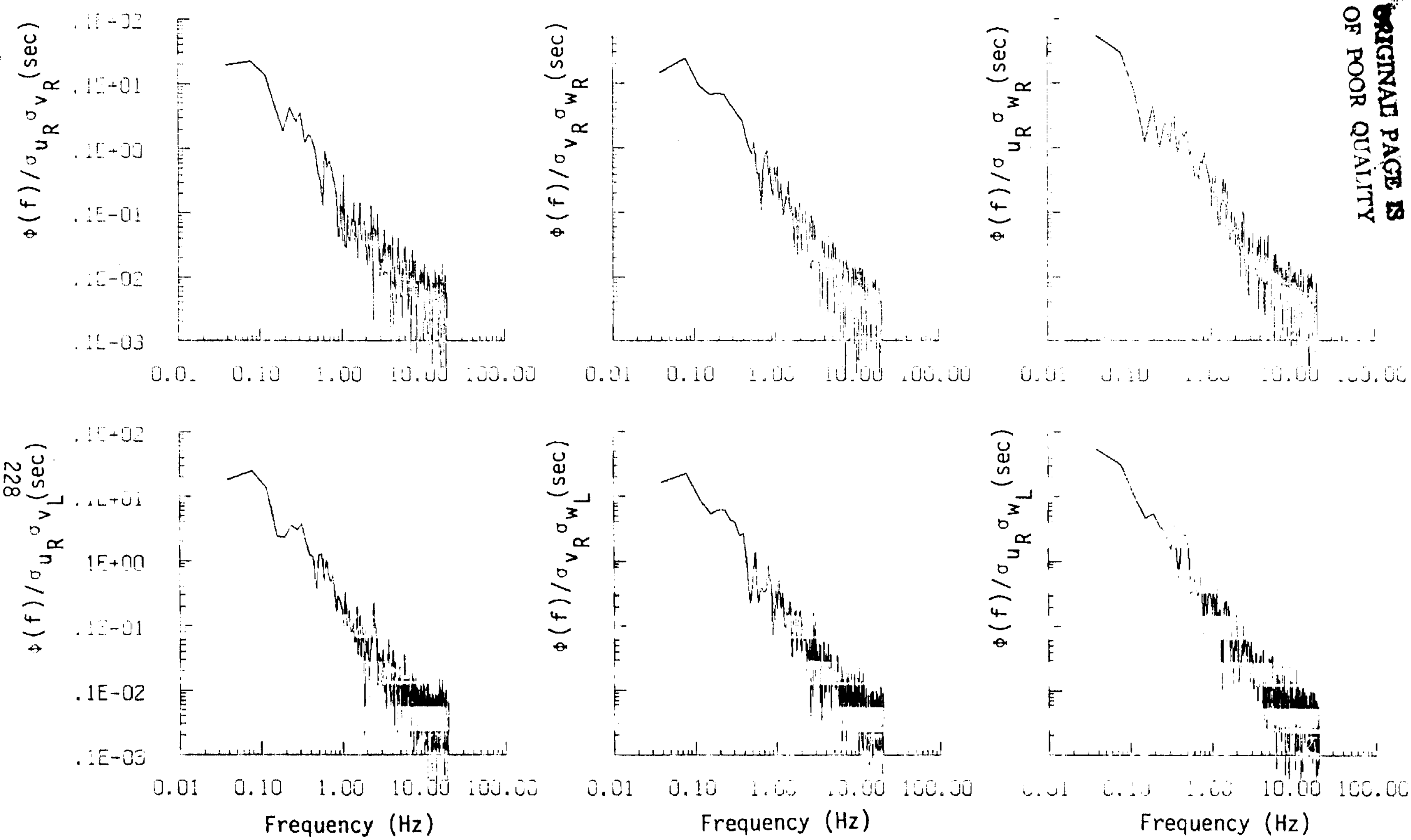

b. One- and two-point cross-spectra.

Figure A.35. (continued).

ORIGINAL PAGE IS
OF POOR QUALITY

TABLE A.14. List of All Parameters Measured and Their Range of Values, Flight 31, Run 7.

	CHANNEL	UNITS	HIGH	LOW	MEAN	RMS	STD	POINTS
1	TIME	SECONDS	40859.502	40655.627	40757.56410	40757.60660	58.86447	8156
2	PHI DOT	RAD/SEC	.160	-.143	-.00271	.02918	.02906	8156
3	ACCL N CG	G UNITS	2.067	.159	.99544	1.00084	.10381	8156
4	THETA DOT	RAD/SEC	.099	-.110	.00306	.01370	.01336	8156
5	THETA	RAD	.119	-.009	.06305	.06569	.01843	8156
6	PHI	RAD	.140	-.084	.00142	.02966	.02963	8156
7	PSI 1	RAD	354.891	275.719	349.38821	349.39191	1.60740	8156
8	DEL PSI 1	DEG	3.057	-5.942	-2.21736	2.61189	1.38040	8156
9	PSI 2	RAD	353.009	344.286	347.99832	348.00093	1.34844	8156
10	DEL PSI 2	DEG	3.638	-5.376	-1.64475	2.14194	1.37220	8156
11	ACCL N LT	G UNITS	3.249	-.680	1.00864	1.02644	.19034	8156
12	ACCL N RT	G UNITS	3.891	-1.336	1.00569	1.03030	.22385	8156
13	ACCL X CG	G UNITS	.230	.011	.06404	.07038	.02920	8156
14	ACCL Y CG	G UNITS	.124	-.079	.00096	.01789	.01787	8156
15	ALPHA CTR	RAD	.133	-.110	-.01274	.01818	.01297	8156
16	BETA CTR	RAD	.175	-.149	.00689	.02546	.02452	8156
17	TEMP I	DEG F	79.016	77.576	78.47828	78.47957	.45001	8156
18	TEMP P	DEG F	61.961	61.605	61.77957	61.77957	.01328	8156
19	ACCL Z INS	G UNITS	2.062	.133	1.00037	1.00562	.10264	8156
20	ALPHA RT	RAD	.160	-.128	.00055	.01438	.01437	8156
21	BETA RT	RAD	.174	-.129	.01674	.02806	.02252	8156
22	ALPHA LT	RAD	.217	-.078	.02815	.03163	.01442	8156
23	BETA LT	RAD	.151	-.153	.01000	.02465	.02253	8156
24	PSI DOT	RAD/SEC	.085	-.095	.00266	.01892	.01873	8156
25	TEMP TOT	DEG C	13.570	7.170	10.29486	10.40512	1.51067	8156
26	QC LT	PSID	.903	.627	.74751	.74855	.03939	8156
27	QC CTR	PSID	.846	.591	.71422	.71521	.03759	8156
28	QC_RT	PSID	.870	.612	.73949	.74053	.03936	8156
29	PS	PSIA	11.383	11.282	11.33648	11.33649	.01311	8156
30	TEMP IRT	VOLTS	7.140	4.794	5.91822	5.94657	.57999	8156
31	HYGROM	DFG C	-1.938	-9.759	-7.46488	7.60921	1.47513	8156
32	QC2 LT	PSID	.076	.073	.07456	.07457	.00065	8156
33	QC2 CTR	PSID	.166	.069	.13343	.13618	.02722	8156
34	QC2_RT	PSID	.140	.101	.11580	.11646	.01235	8156
35	DAR	DEG	-8.750	-9.551	-9.17613	9.17961	.25281	8156
36	DAL	DEG	-8.678	-9.092	-8.94551	8.94639	.12566	8156
37	DELEV	DEG	4.710	3.306	4.55243	4.55381	.11232	8156
38	DSTAB	DEG	.022	-.350	-.33087	.33099	.00895	8156
39	DRUD	DEG	9.548	.705	9.16363	9.16672	.23797	8156
40	DTHRR	PCT MAX	64.551	49.841	63.89992	63.90119	.40372	8156
41	DTHPL	PCT MAX	64.348	49.825	63.61769	63.61871	.36006	8156
42	DILP	POSITION	1.182	.418	.44116	.44144	.01591	8156
43	DSB	POSITION	.408	.006	.23535	.23548	.00781	8156
44	D TO G	METERS	7529228.122	7522746.854	***********	***********	1883.47666	8156
45	B TO D	DEGREES	72.849	72.786	72.81735	72.81736	.01834	8156
46	LONG	DEGREES	-117.978	-117.986	-117.98276	117.98276	.00249	8156
47	LAT	DEGREES	35.754	35.579	35.66524	35.66528	.05080	8156
48	TRK ANG	DEGREES	359.961	.028	5.78841	36.00202	35.53582	8156
49	HDG	RADIANS	6.200	6.039	6.10577	6.10582	.02499	8156
50	VE	M/SEC	7.474	-.876	3.66628	4.16317	1.97253	8156
51	VN	M/SEC	101.162	87.945	95.43015	95.51802	4.09644	8156
52	ALTITUDE	KM	2.175	2.103	2.13595	2.13597	.00929	8156
53	TEMPC	DEGREES C	8.464	2.357	5.39005	5.56526	1.38553	8156
54	EW WND SPD	KNOTS	60.593	19.506	42.50833	42.84876	5.39092	8156
55	NS WND SPD	KNOTS	20.659	-21.728	-4.07377	7.57962	6.39219	8156
56	WIND SPEED	KNOTS	61.124	19.863	43.23778	43.51399	4.89530	8156
57	WIND DIREC	DEGREES	303.845	245.044	275.89681	276.05272	9.27708	8156
58	WIND DIR2	DEGREES	123.845	65.044	95.89686	96.34450	9.27710	8156
59	WIND DIR3	DEGREES	303.845	245.044	275.89686	276.05277	9.27710	8156
60	WIND DIR4	DEGREES	303.845	245.044	275.89686	276.05277	9.27710	8156
61	AIRSPEED R	M/SEC	109.065	91.750	100.93810	100.97547	2.74714	8156
62	AIRSPEED C	M/SEC	107.536	90.222	99.23685	99.27276	2.67007	8156
63	AIRSPEED L	M/SEC	111.063	92.927	101.47274	101.50925	2.72263	8156
64	DELTA ALT	METERS	71.366	-.779	32.43872	33.74127	9.28512	8156
65	INRTL DISP	METERS	56.331	.000	34.34776	35.50321	8.98441	8156
66	UG RIGHT	M/SEC	12.332	-9.102	.00000	3.03782	3.03801	8156
67	UG CENTER	M/SEC	12.289	-8.184	.00000	3.03101	3.03120	8156
68	UG LEFT	M/SEC	11.994	-8.519	.00000	3.07700	3.07718	8156
69	VG RIGHT	M/SEC	9.833	-9.468	.00968	3.00277	3.00294	8156
70	VG CENTER	M/SEC	10.724	-10.387	.00890	3.03892	3.03910	8156
71	VG LEFT	M/SEC	8.489	-11.962	.00956	3.06967	3.06984	8156
72	WG RIGHT	M/SEC	12.808	-8.420	.00545	2.23956	2.23969	8156
73	WG CENTER	M/SEC	11.798	-9.297	.00860	2.15312	2.15323	8156
74	WG LEFT	M/SEC	16.661	-8.046	.00692	2.22691	2.22704	8156

Flight 31, Run 8
Date: Nov. 29, 1982
Start Time: 11:22:59 (PST)
Duration: 225.9 seconds

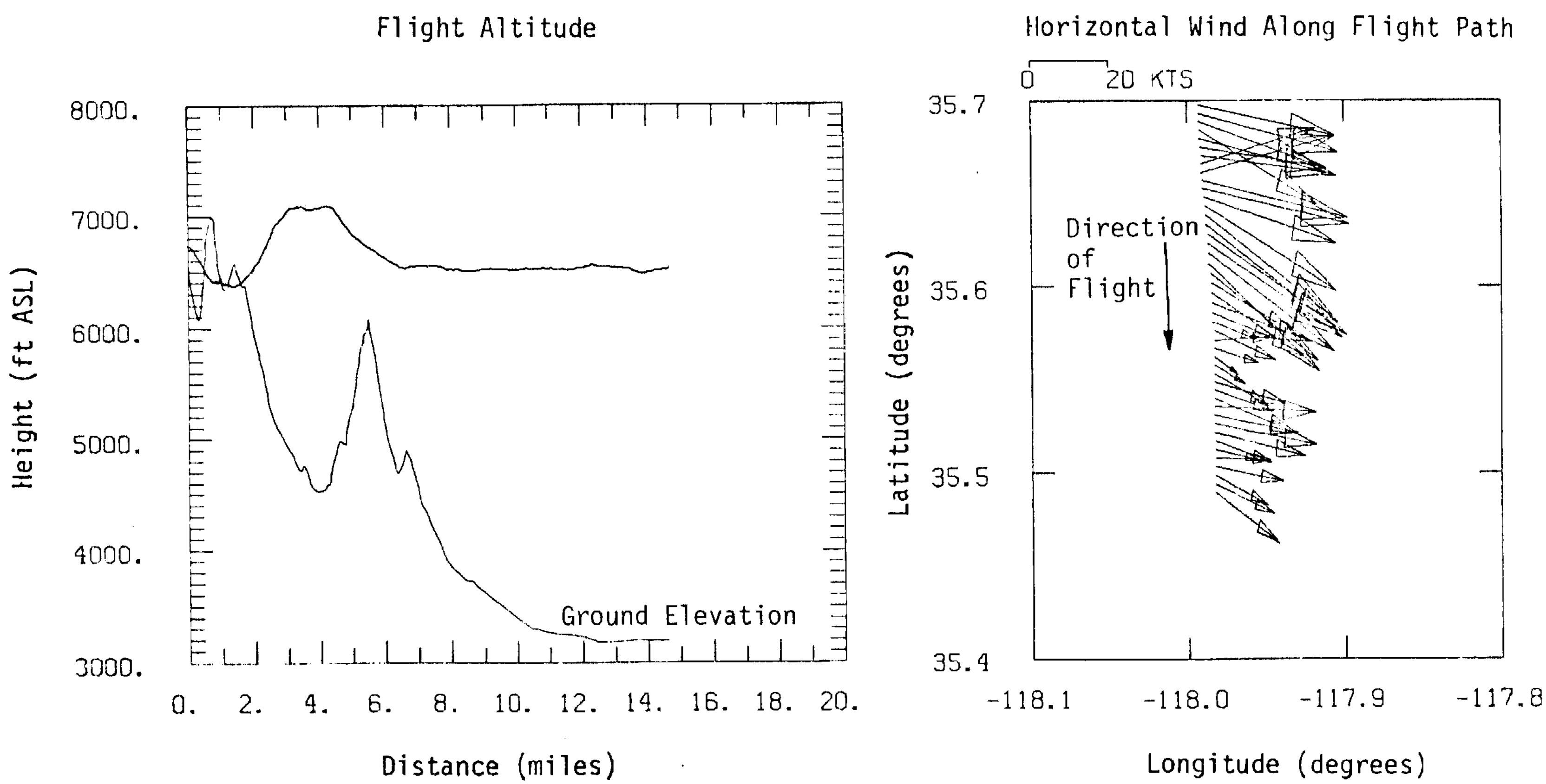

Figure A.36. Flight altitude and horizontal wind along flight path, Flight 31, Run 8.

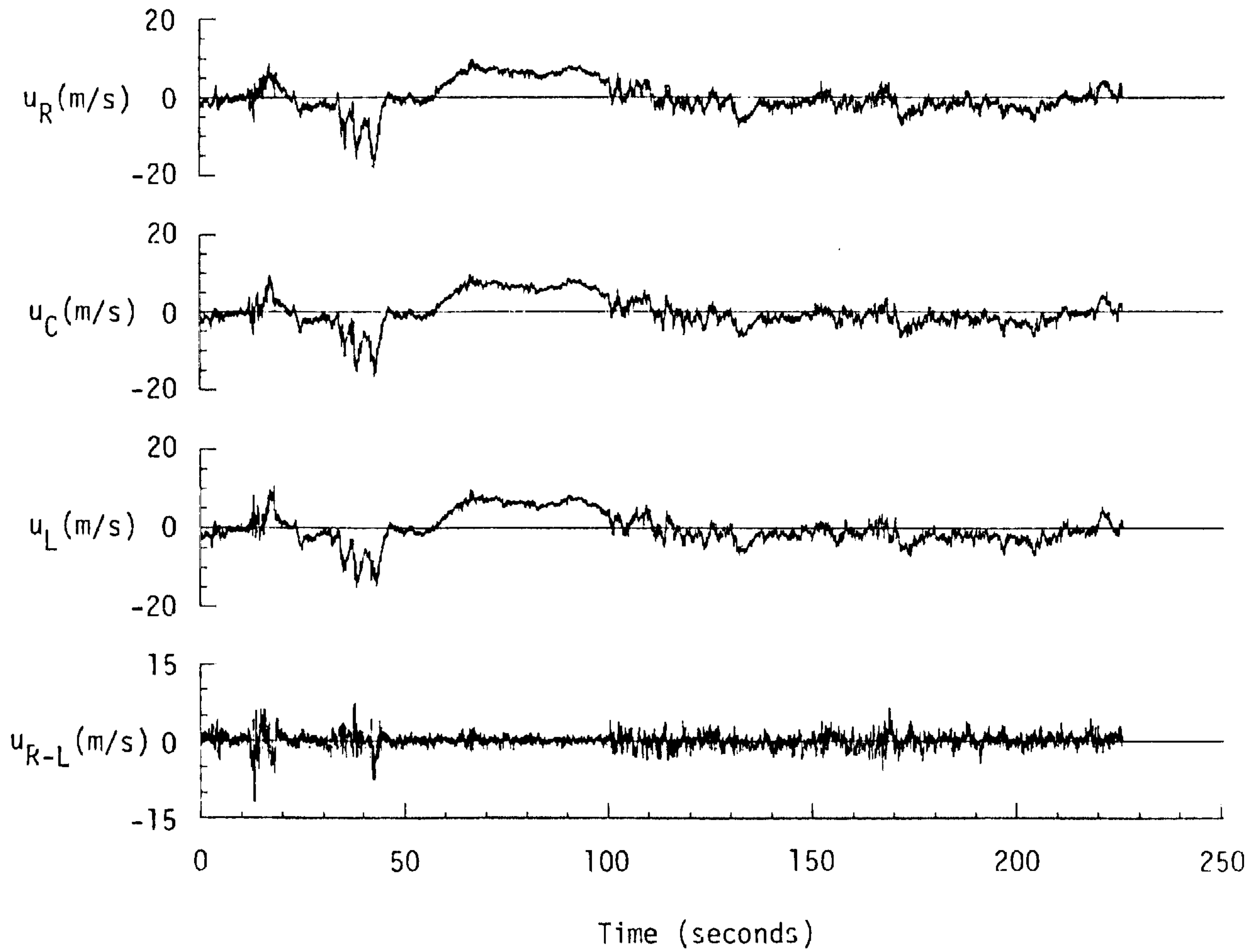

Figure A.37. Time histories of gust velocities, gust velocity differences, and aircraft's normal accelerations, Flight 31, Run 8.

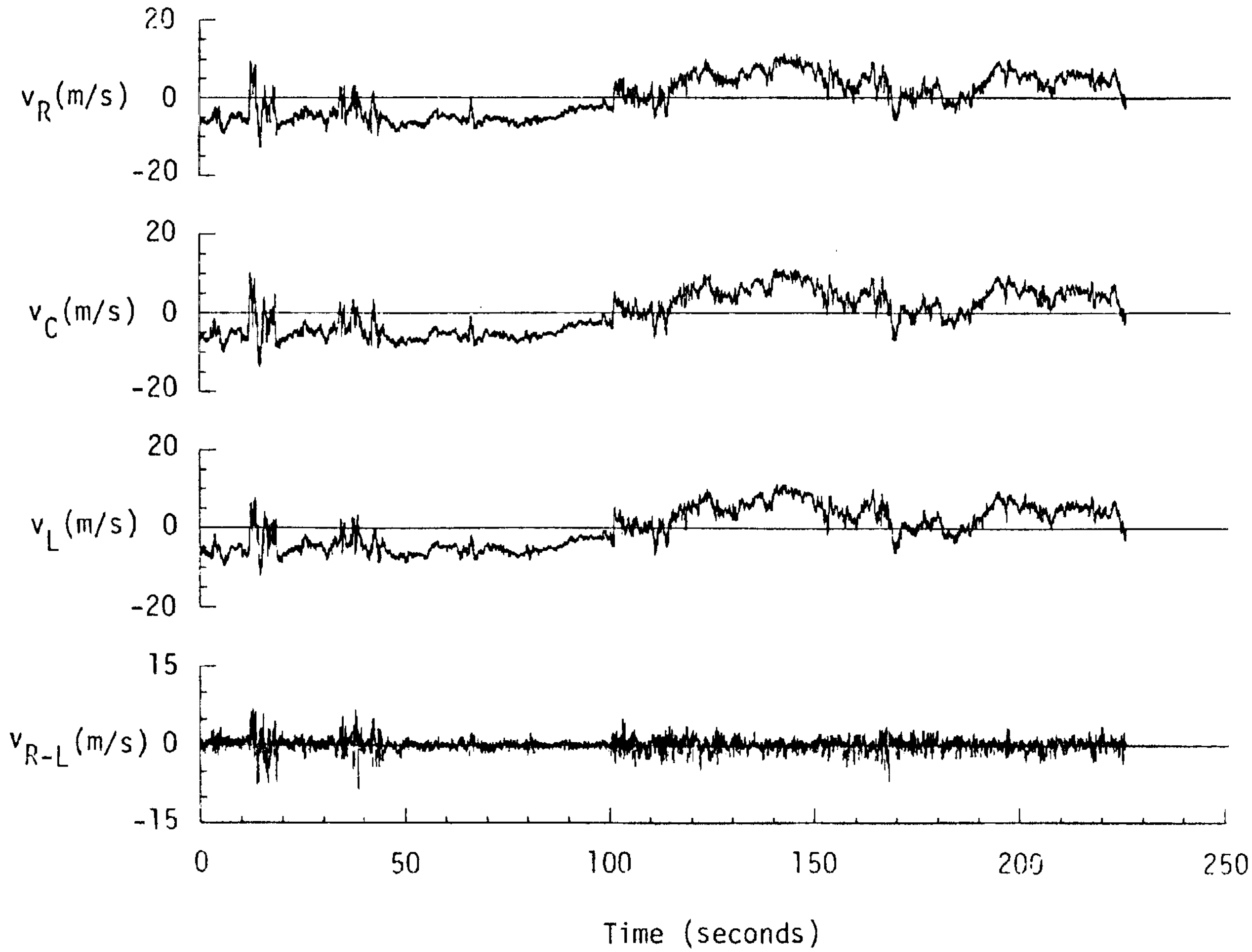

Figure A.37. (continued).

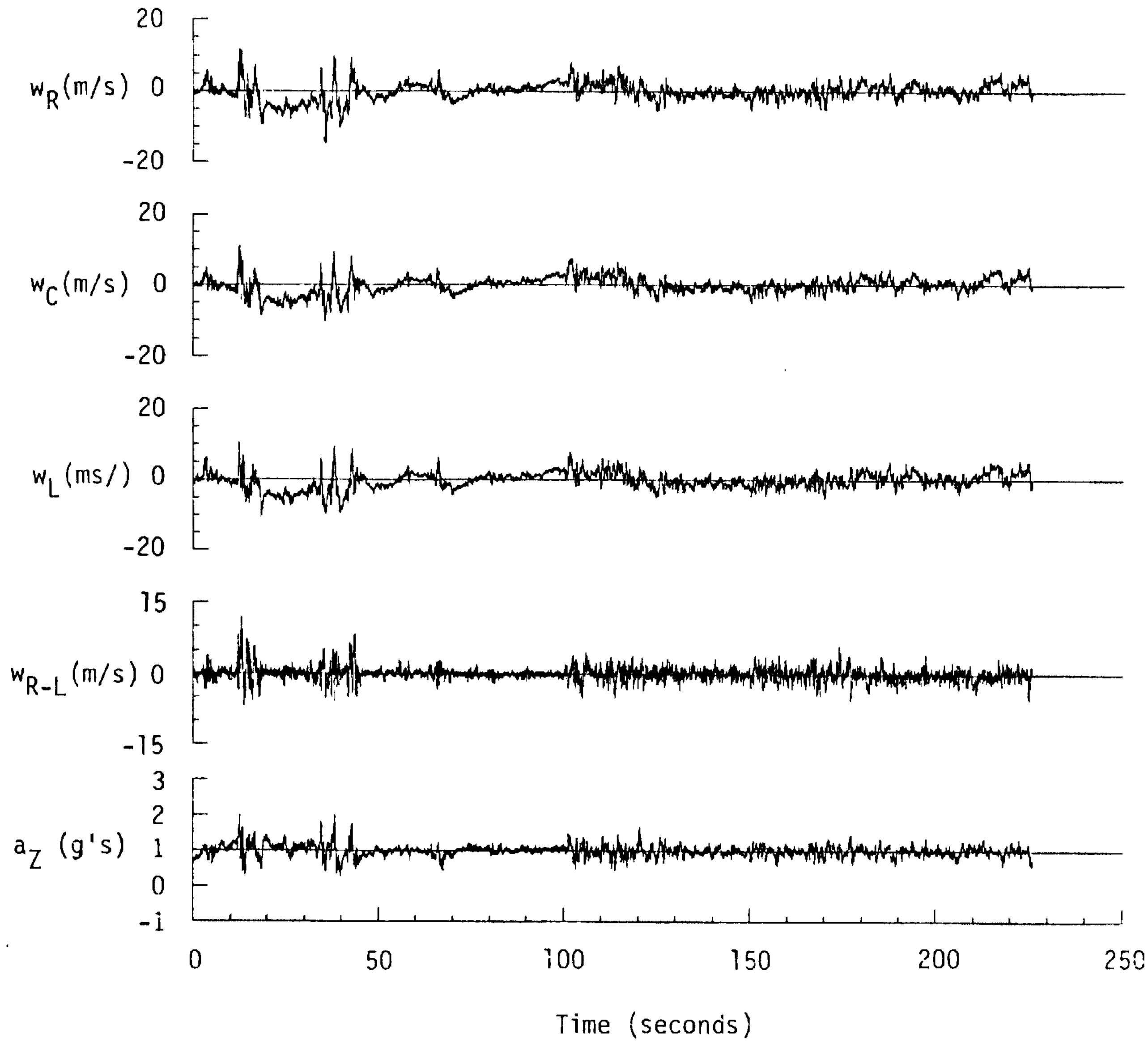

Figure A.37. (continued).

TABLE A.15. Average Turbulence Parameters, Integral Length Scales, and Correlation Coefficients of Gust Velocities, Flight 31, Run 8.

1. Mean Airspeed (m/s):

$\overline{V}_L$	$\overline{V}_C$	$\overline{V}_R$
103.22	101.05	102.86

2. Standard Deviation of Gust Velocities (m/s):

σ_{uR}	σ_{vR}	σ_{wR}
3.93	5.17	2.52
σ_{uC}	σ_{vC}	σ_{wC}
3.89	5.18	2.36
σ_{uL}	σ_{vL}	σ_{wL}
3.89	5.20	2.42

3. Standard Deviation of Gust Velocity Differences (m/s):

$\sigma_{\Delta uRL}$	$\sigma_{\Delta vRL}$	$\sigma_{\Delta wRL}$
1.22	1.08	1.31

4. Integral Length Scale (m):

L_{uR}	L_{vR}	L_{wR}
306.7	364.4	232.9
L_{uRL}	L_{vRL}	L_{wRL}
302.5	380.7	249.6

5. Correlation Coefficient of Gust Velocities:

$\overline{u_R u_L}/\sigma_{u_R}\sigma_{u_L}$	$\overline{v_R v_L}/\sigma_{v_R}\sigma_{v_L}$	$\overline{w_R w_L}/\sigma_{w_R}\sigma_{w_L}$
0.89	0.81	0.80
$\overline{u_R v_R}/\sigma_{u_R}\sigma_{v_R}$	$\overline{v_R w_R}/\sigma_{v_R}\sigma_{w_R}$	$\overline{w_R u_R}/\sigma_{w_R}\sigma_{u_R}$
-0.20	0.15	0.00
$\overline{u_R v_L}/\sigma_{u_R}\sigma_{v_L}$	$\overline{v_R w_L}/\sigma_{v_R}\sigma_{w_L}$	$\overline{w_R u_L}/\sigma_{w_R}\sigma_{u_L}$
-0.19	0.10	0.03

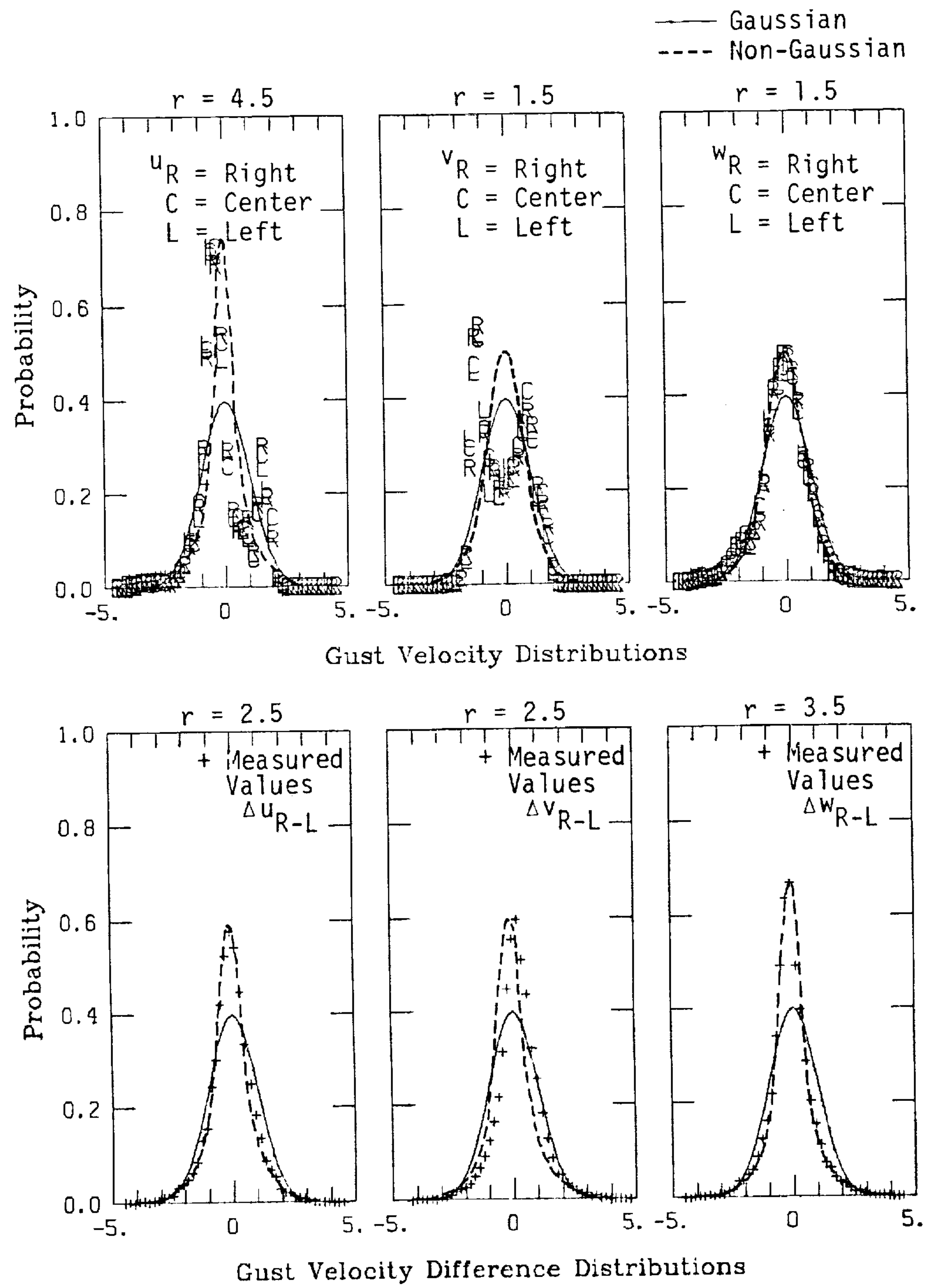

Figure A.38. Probability density functions for gust velocities and gust velocity differences (normalized with the standard deviation), Flight 31, Run 8 (r = degree of non-Gaussian).

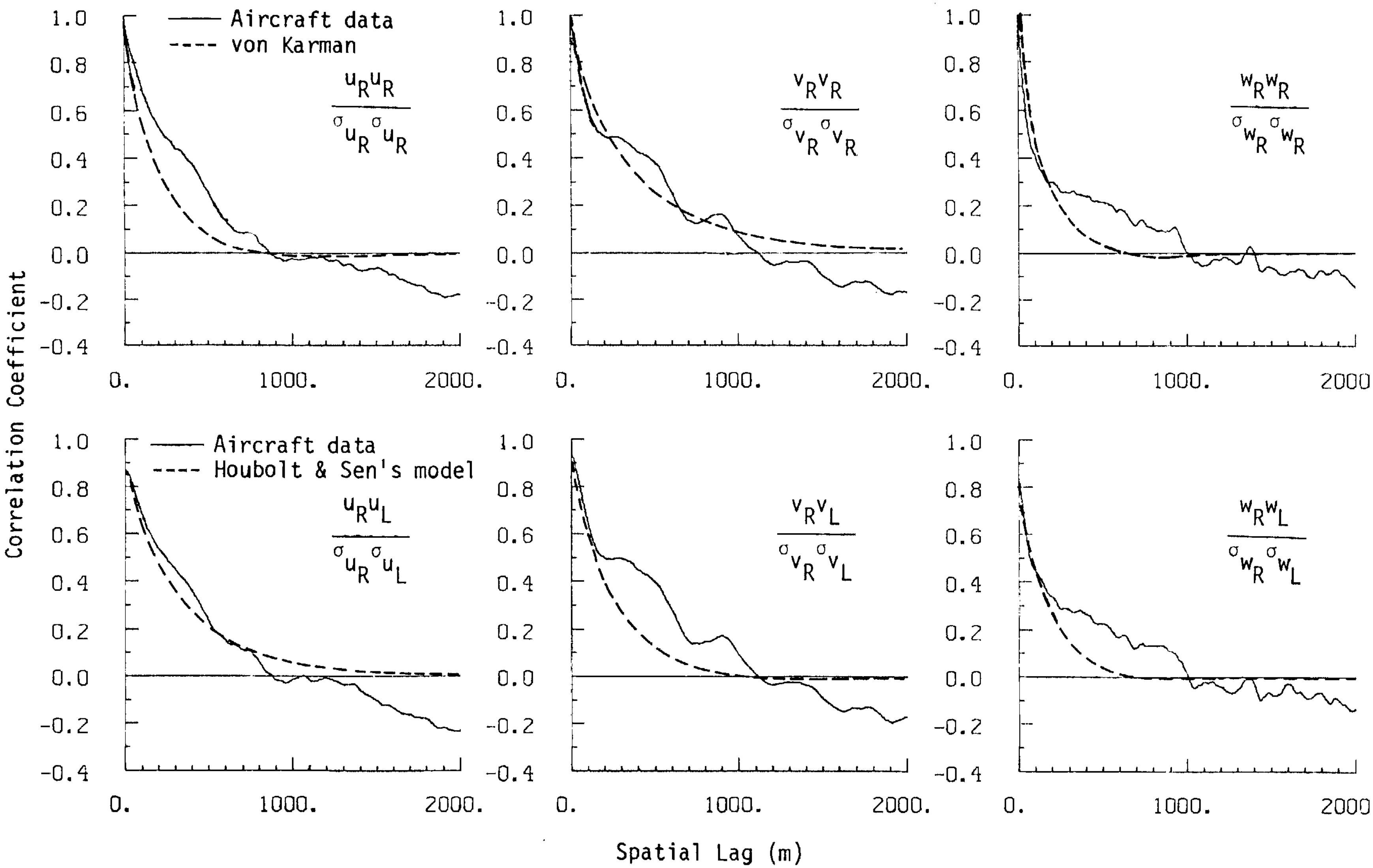

a. One- and two-point common component correlations.

Figure A.39. Comparison of normalized one- and two-point correlation functions for gust velocities with theoretical models, Flight 31, Run 8.

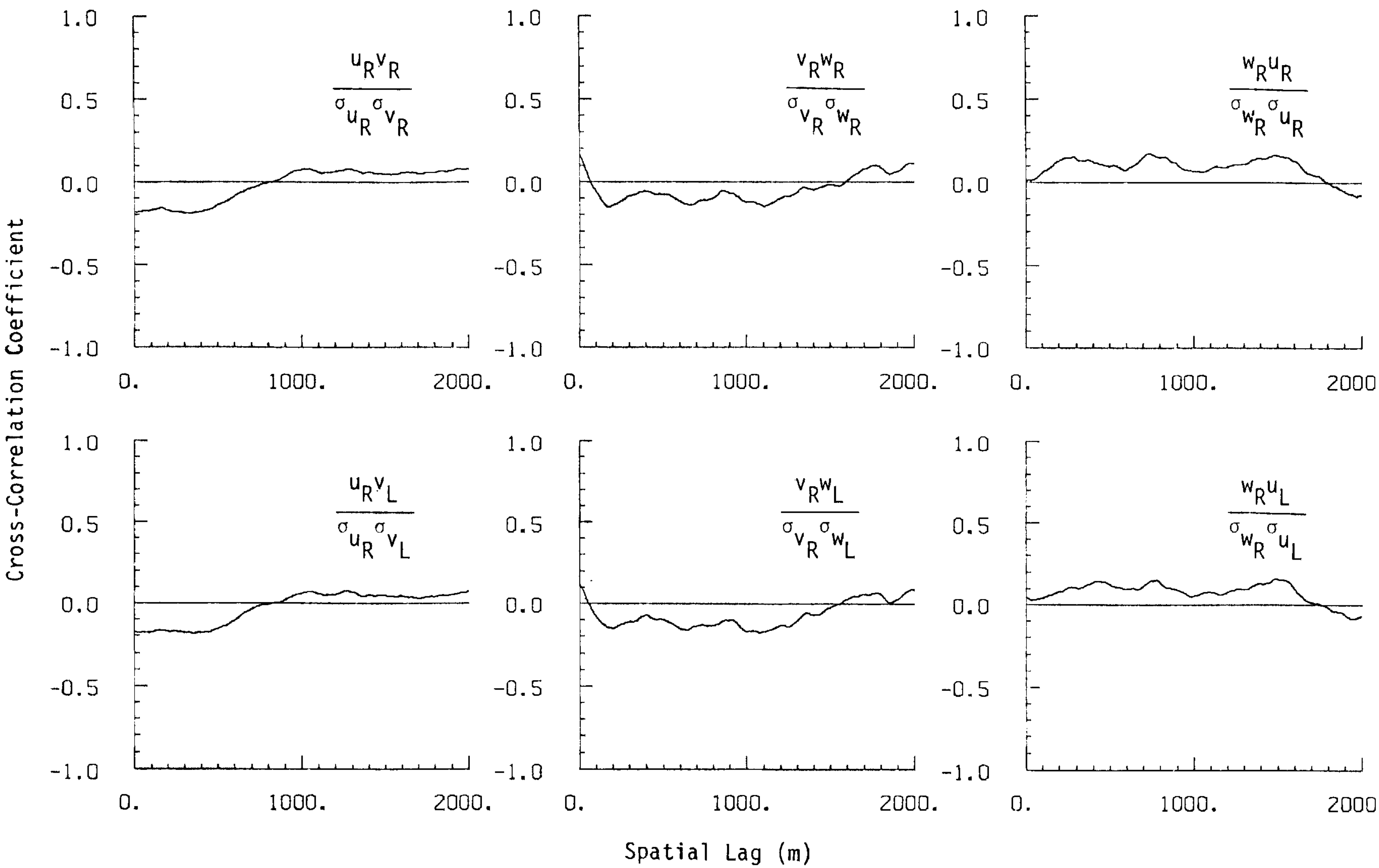

b. One- and two-point cross-correlations.

Figure A.39. (continued).

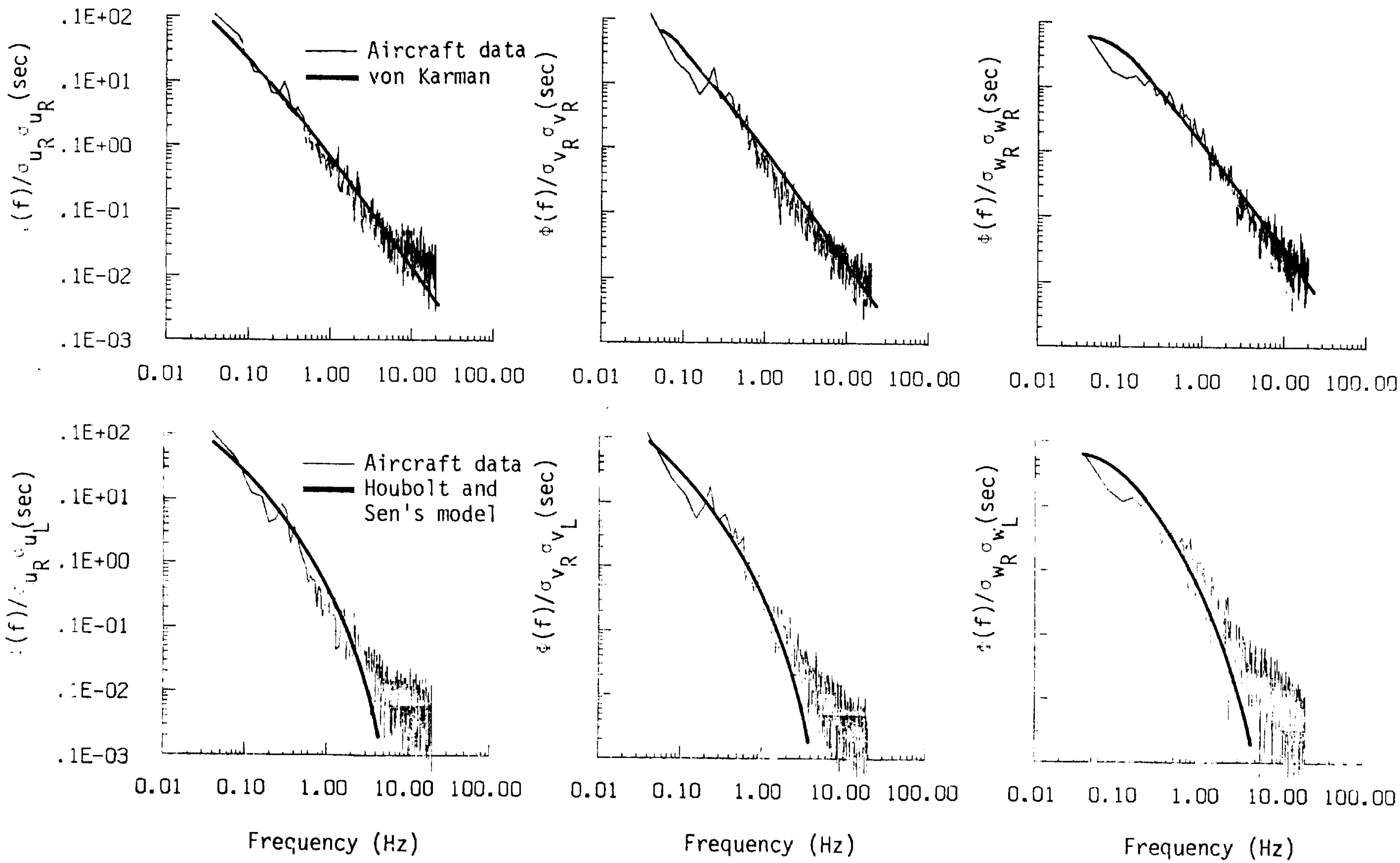

a. One- and two-point common component spectra.

Figure A.40. Comparison of normalized one- and two-point spectral density functions for gust velocities with theoretical models, Flight 31, Run 8.

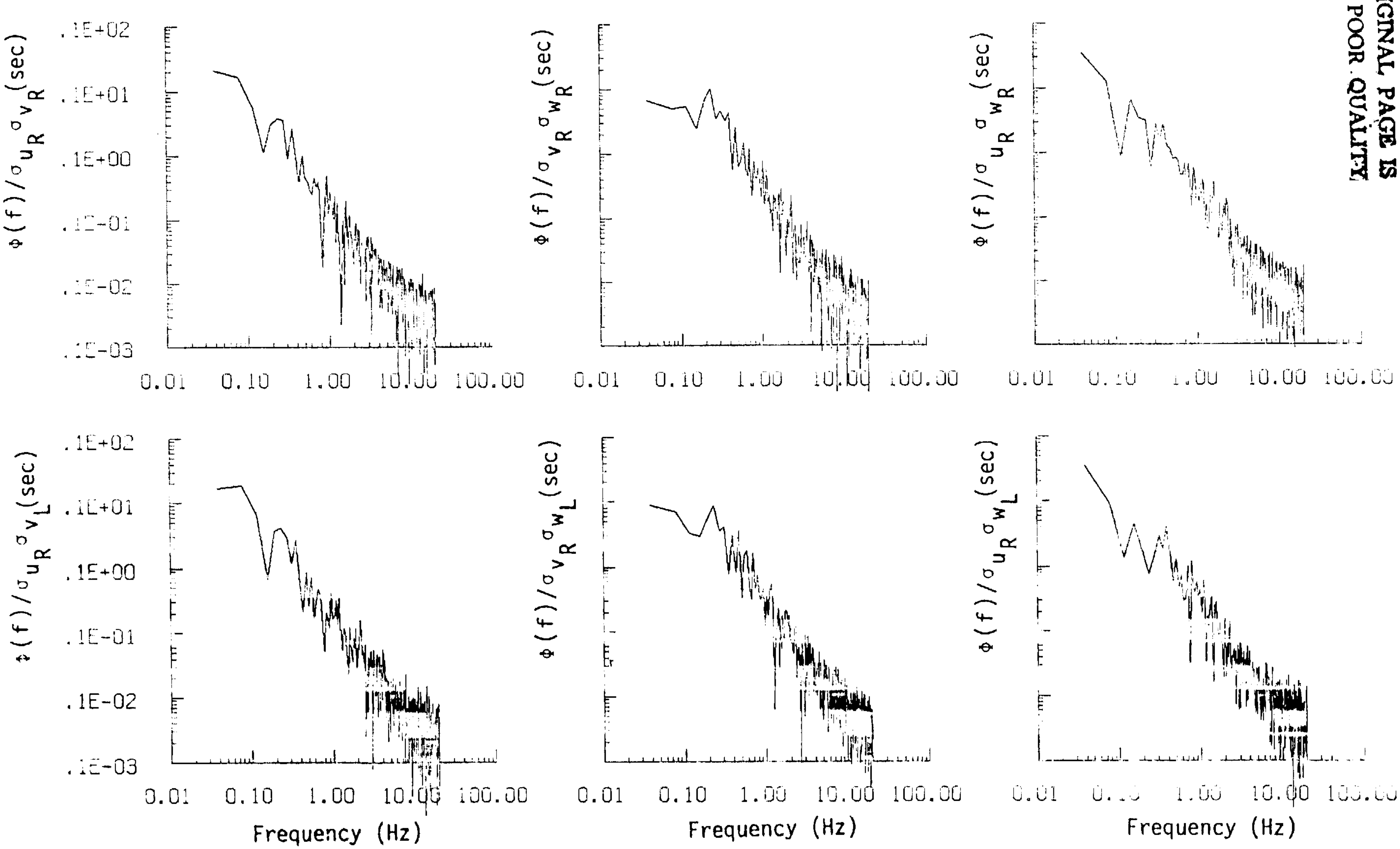

b. One- and two-point cross-spectra.

Figure A.40. (continued).

ORIGINAL PAGE IS
OF POOR QUALITY

TABLE A.16. List of All Parameters Measured and Their Range of Values, Flight 31, Run 8.

CHANNEL	UNITS	HIGH	LOW	MEAN	RMS	STD	POINTS
1 TIME	SECONDS	41204.439	40978.539	41091.48890	41091.54066	65.22255	9037
2 PHI DOT	RAD/SEC	.311	-.284	-.00291	.04454	.04444	9037
3 ACCL N CG	G UNITS	1.965	.336	1.00164	1.01212	.14526	9037
4 THETA DOT	RAD/SEC	.105	-.101	.00347	.01625	.01588	9037
5 THETA	RAD	.245	-.059	.06134	.08022	.05170	9037
6 PHI	RAD	.115	-.190	.00356	.03967	.03951	9037
7 PSI 1	RAD	190.048	179.129	183.98462	183.99642	2.08406	9037
8 DEL PSI 1	DEG	5.931	-4.779	.07258	2.05172	2.05055	9037
9 PSI 2	RAD	547.691	537.383	542.02722	542.03089	1.99686	9037
10 DEL_PSI 2	DEG	6.284	-4.448	.40391	2.09569	2.05651	9037
11 ACCL N LT	G UNITS	3.488	-2.048	1.01449	1.05546	.29122	9037
12 ACCL_N RT	G UNITS	4.347	-1.631	1.01139	1.05700	.30717	9037
13 ACCL_X_CG	G UNITS	.234	-.072	.06389	.08153	.05066	9037
14 ACCL Y CG	G UNITS	.110	-.129	-.00294	.02241	.02222	9037
15 ALPHA CTR	RAD	.103	-.106	-.01855	.02582	.01795	9037
16 BETA CTR	RAD	.187	-.190	.00385	.03193	.03170	9037
17 TEMP I	DEG F	76.497	75.418	76.06562	76.06602	.24603	9037
18 TEMP P	DEG F	61.961	61.615	61.78658	61.78659	.02734	9037
19 ACCL Z INS	G UNITS	2.004	.288	1.00677	1.01739	.14657	9037
20 ALPHA RT	RAD	.124	-.108	-.00610	.02196	.02109	9037
21 BETA RT	RAD	.192	-.175	.01325	.03237	.02954	9037
22 ALPHA LT	RAD	.131	-.064	.02118	.02815	.01855	9037
23 BETA LT	RAD	.161	-.168	.00708	.02982	.02897	9037
24 PSI DOT	RAD/SEC	.089	-.103	.00229	.02379	.02368	9037
25 TEMP TOT	DEG C	12.192	8.057	10.24093	10.28370	.93706	9037
26 QC LT	PSID	1.033	.619	.78896	.79234	.07306	9037
27 QC CTR	PSID	.988	.601	.75379	.75707	.07038	9037
28 QC_RT	PSID	1.019	.622	.78172	.78518	.07360	9037
29 PS	PSIA	11.613	11.297	11.50153	11.50185	.08570	9037
30 TEMP IRT	VOLTS	6.907	1.911	5.78063	5.86605	.99750	9037
31 HYGROM	DEG C	-.178	-8.976	-6.30606	6.46187	1.41052	9037
32 QC2 LT	PSID	.071	.068	.06942	.06942	.00044	9037
33 QC2 CTR	PSID	.177	.140	.16480	.16511	.01011	9037
34 QC2 RT	PSID	.163	.132	.14798	.14830	.00973	9037
35 DAR	DEG	-8.722	-9.330	-8.97011	8.97170	.16850	9037
36 DAL	DEG	-8.403	-8.651	-8.47336	8.47367	.07261	9037
37 DELEV	DEG	4.955	4.682	4.79274	4.79341	.07993	9037
38 DSTAB	DEG	-.347	-.360	-.35328	.35330	.00331	9037
39 DRUD	DEG	10.117	9.775	9.94806	9.94844	.08681	9037
40 DTHRR	PCT MAX	66.016	65.137	65.63407	65.63445	.22374	9037
41 DTHRL	PCT MAX	65.918	64.844	65.46682	65.46751	.29866	9037
42 DFLP	POSITION	.395	.348	.36829	.36853	.01324	9037
43 DSB	POSITION	.285	.260	.27283	.27293	.00721	9037
44 D TO G	METERS	7526165.491	7520103.629	***********	***********	1751.03911	9037
45 B TO D	DEGREES	72.889	72.797	72.84398	72.84399	.02706	9037
46 LONG	DEGREES	-117.981	-117.992	-117.98549	117.98549	.00369	9037
47 LAT	DEGREES	35.700	35.487	35.59327	35.59333	.06252	9037
48 TRK ANG	DEGREES	181.966	174.296	177.68239	177.69231	1.87781	9037
49 HDG	RADIANS	3.331	3.137	3.22416	3.22437	.03732	9037
50 VE	M/SEC	10.753	-3.436	4.39655	5.68080	3.59769	9037
51 VN	M/SEC	-94.763	-118.049	-104.88967	105.09696	6.59786	9037
52 ALTITUDE	KM	2.164	1.942	2.01994	2.02084	.06023	9037
53 TEMPC	DEGREES C	6.914	3.293	5.14864	5.19791	.71407	9037
54 EW WND SPD	KNOTS	49.366	2.533	23.79845	25.75772	9.85417	9037
55 NS WND SPD	KNOTS	23.820	-27.249	-8.19980	11.33378	7.82462	9037
56 WIND_SPEED	KNOTS	51.412	3.724	25.99354	28.14098	10.78257	9037
57 WIND DIREC	DEGREES	330.181	225.791	288.65429	289.01875	14.51058	9037
58 WIND DIR2	DEGREES	150.181	45.791	108.65435	109.61890	14.51059	9037
59 WIND_DIR3	DEGREES	330.181	225.791	288.65435	289.01880	14.51059	9037
60 WIND DIR4	DEGREES	330.181	225.791	288.65435	289.01880	14.51059	9037
61 AIRSPEED R	M/SEC	116.833	92.210	102.86079	102.96626	4.65956	9037
62 AIRSPEED C	M/SEC	115.066	90.199	101.05040	101.15233	4.54017	9037
63 AIRSPEED L	M/SEC	117.624	91.603	103.32909	103.43172	4.60668	9037
64 DELTA ALT	METERS	109.099	-113.141	-35.17826	69.74513	60.22685	9037
65 INRTL_DISP	METERS	97.056	-117.254	-39.27849	70.64242	58.71910	9037
66 UG RIGHT	M/SEC	9.631	-18.056	.00000	3.93072	3.93093	9037
67 UG CENTER	M/SEC	9.630	-16.490	.00000	3.89204	3.89225	9037
68 UG LEFT	M/SEC	10.558	-15.009	.00000	3.89019	3.89041	9037
69 VG RIGHT	M/SEC	11.370	-12.709	.07236	5.17998	5.17977	9037
70 VG CENTER	M/SEC	11.207	-13.431	.07506	5.18544	5.18518	9037
71 VG_LEFT	M/SEC	11.347	-12.009	.06833	5.20477	5.20461	9037
72 WG RIGHT	M/SEC	11.509	-14.749	.00751	2.52506	2.52519	9037
73 WG CENTER	M/SEC	10.991	-10.188	.01268	2.36776	2.36786	9037
74 WG LEFT	M/SEC	10.205	-10.885	.01106	2.42446	2.42457	9037

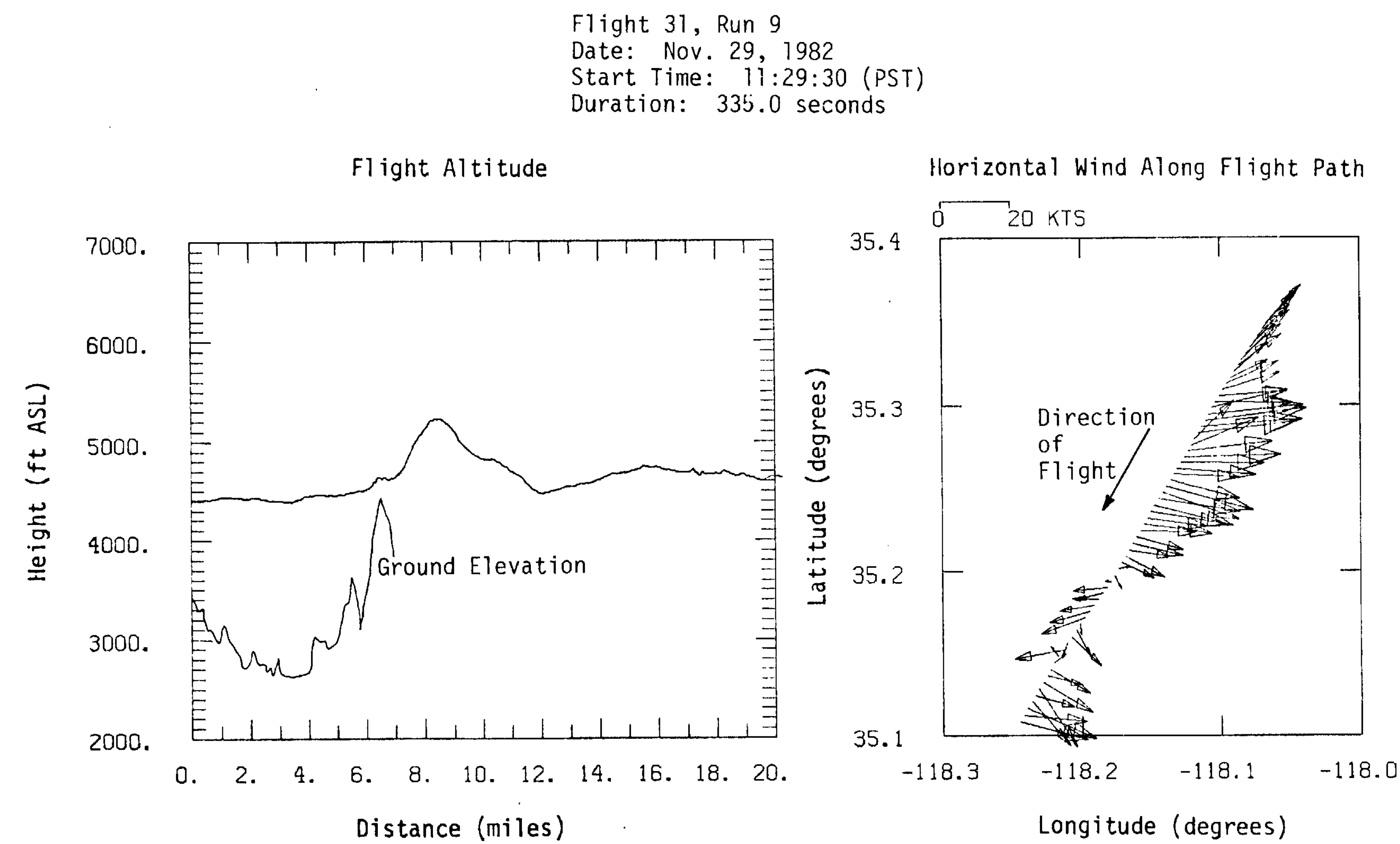

Figure A.41. Flight altitude and horizontal wind along flight path, Flight 31, Run 9.

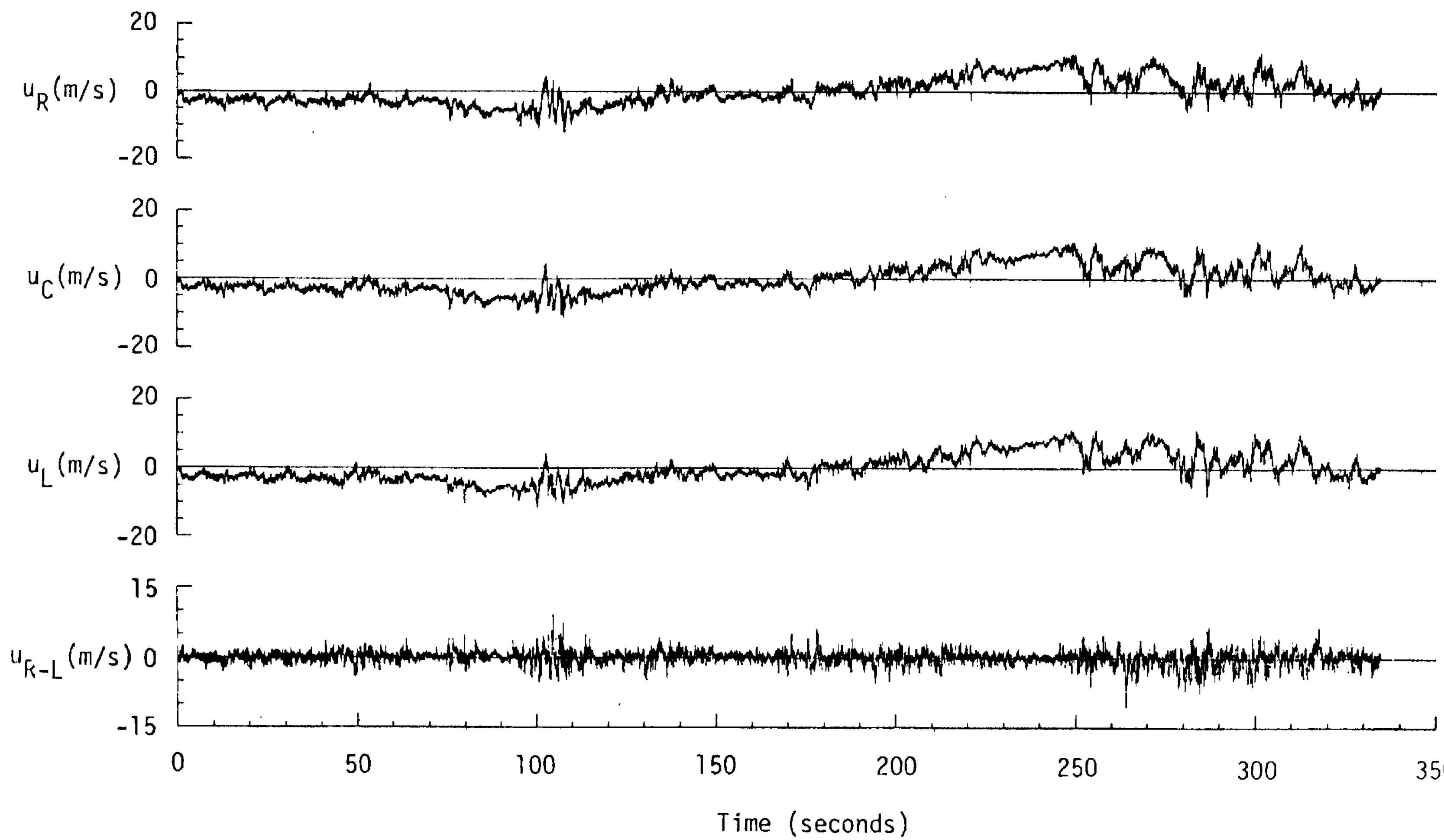

Figure A.42. Time histories of gust velocities, gust velocity differences, and aircraft's normal accelerations, Flight 31, Run 9.

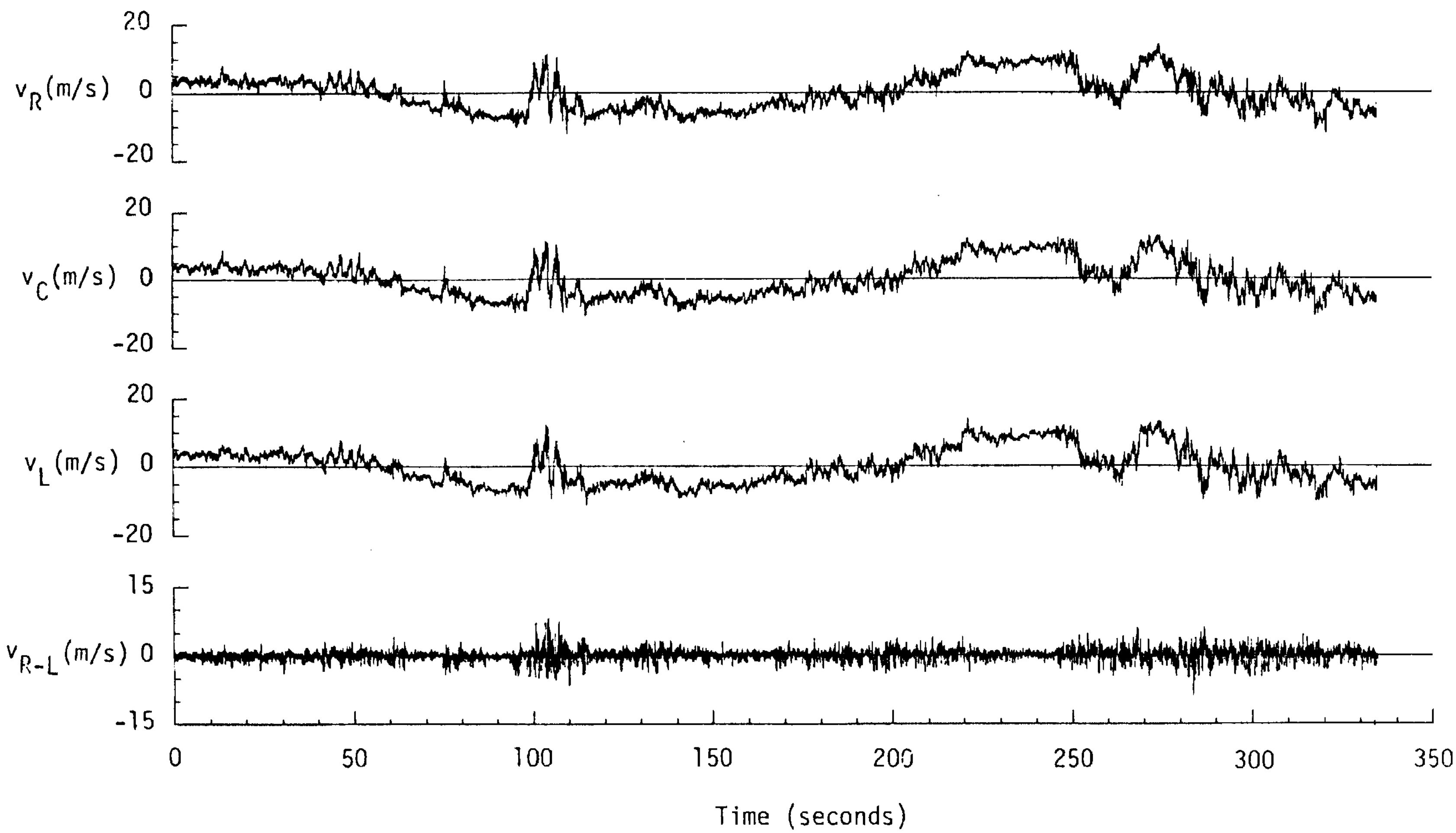

Figure A.42. (continued).

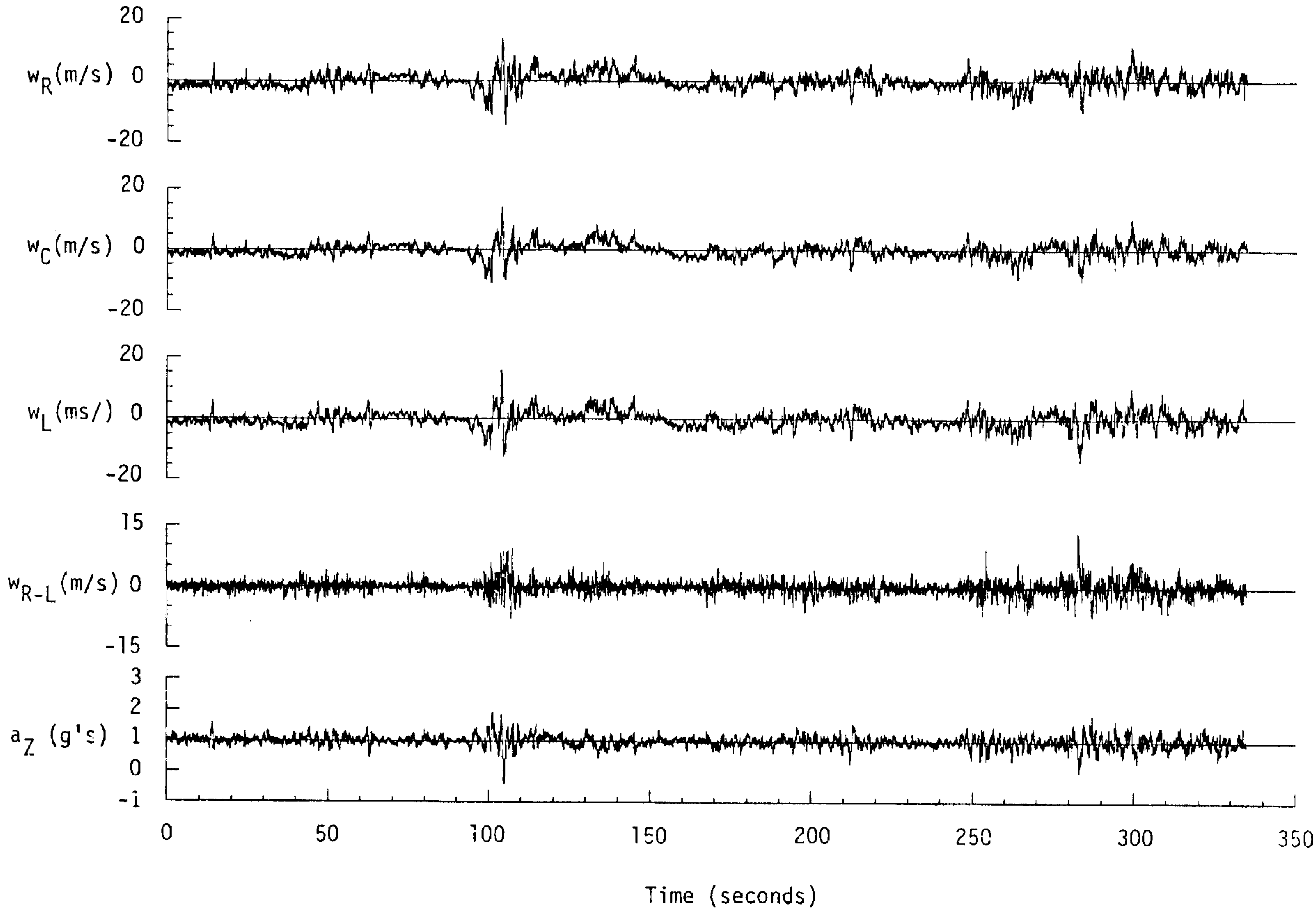

Figure A.42. (continued).

TABLE A.17. Average Turbulence Parameters, Integral Length Scales, and Correlation Coefficients of Gust Velocities, Flight 31, Run 9.

1. Mean Airspeed (m/s):

$\overline{V}_L$	$\overline{V}_C$	$\overline{V}_R$
103.15	100.84	102.84

2. Standard Deviation of Gust Velocities (m/s):

σ_{uR}	σ_{vR}	σ_{wR}
4.10	5.12	2.40

σ_{uC}	σ_{vC}	σ_{wC}
4.10	5.10	2.21

σ_{uL}	σ_{vL}	σ_{wL}
4.18	5.12	2.34

3. Standard Deviation of Gust Velocity Differences (m/s):

$\sigma_{\Delta uRL}$	$\sigma_{\Delta vRL}$	$\sigma_{\Delta wRL}$
1.35	1.16	1.45

4. Integral Length Scale (m):

L_{uR}	L_{vR}	L_{wR}
327.8	338.0	93.9

L_{uRL}	L_{vRL}	L_{wRL}
341.5	338.0	83.9

5. Correlation Coefficient of Gust Velocities:

$\overline{u_R u_L}/\sigma_{u_R}\sigma_{u_L}$	$\overline{v_R v_L}/\sigma_{v_R}\sigma_{v_L}$	$\overline{w_R w_L}/\sigma_{w_R}\sigma_{w_L}$
0.80	0.90	0.80

$\overline{u_R v_R}/\sigma_{u_R}\sigma_{v_R}$	$\overline{v_R w_R}/\sigma_{v_R}\sigma_{w_R}$	$\overline{w_R u_R}/\sigma_{w_R}\sigma_{u_R}$
0.30	0.20	0.19

$\overline{u_R v_L}/\sigma_{u_R}\sigma_{v_L}$	$\overline{v_R w_L}/\sigma_{v_R}\sigma_{w_L}$	$\overline{w_R u_L}/\sigma_{w_R}\sigma_{u_L}$
0.30	0.20	0.18

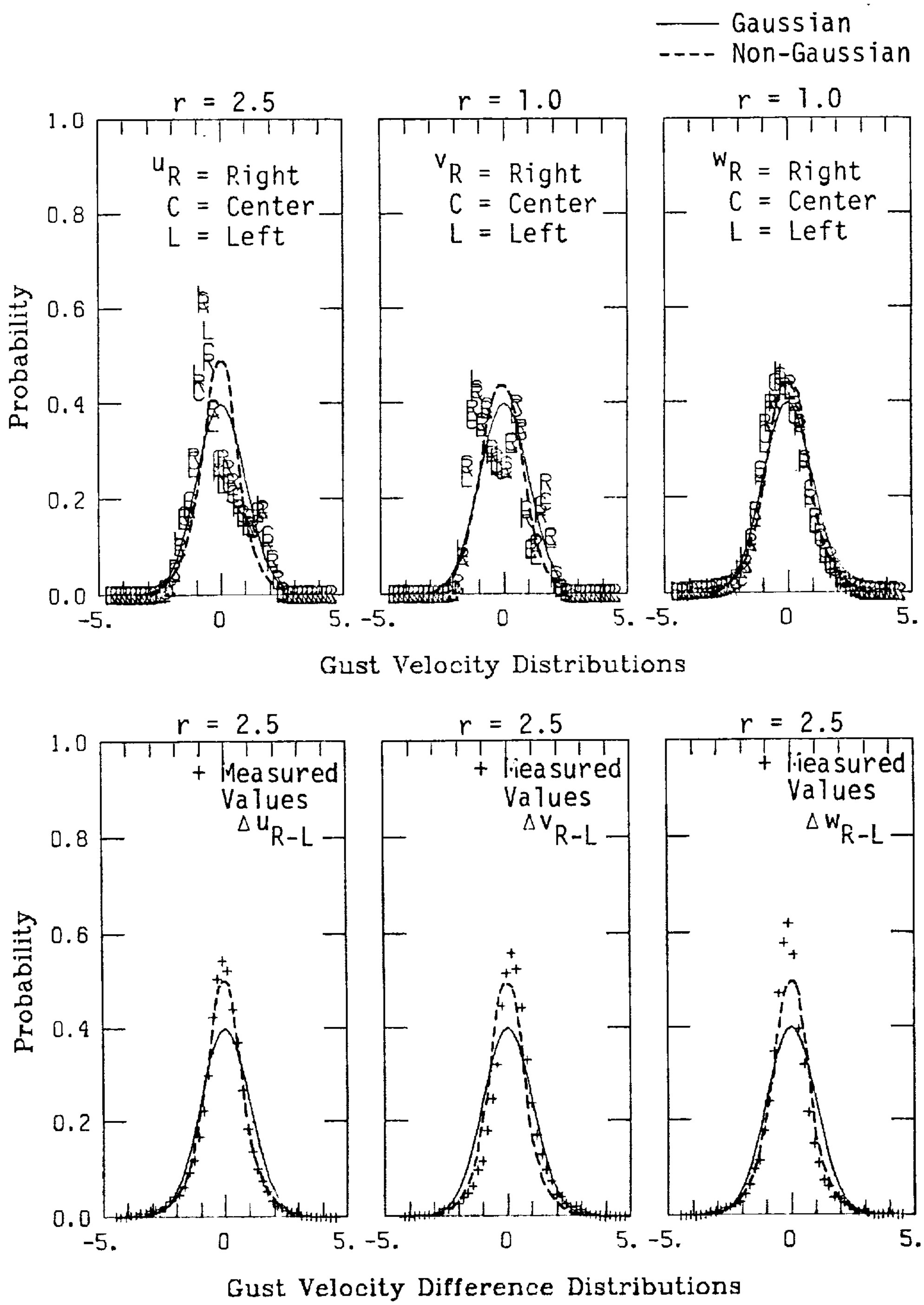

Figure A.43. Probability density functions for gust velocities and gust velocity differences (normalized with the standard deviation), Flight 31, Run 9 (r = degree of non-Gaussian).

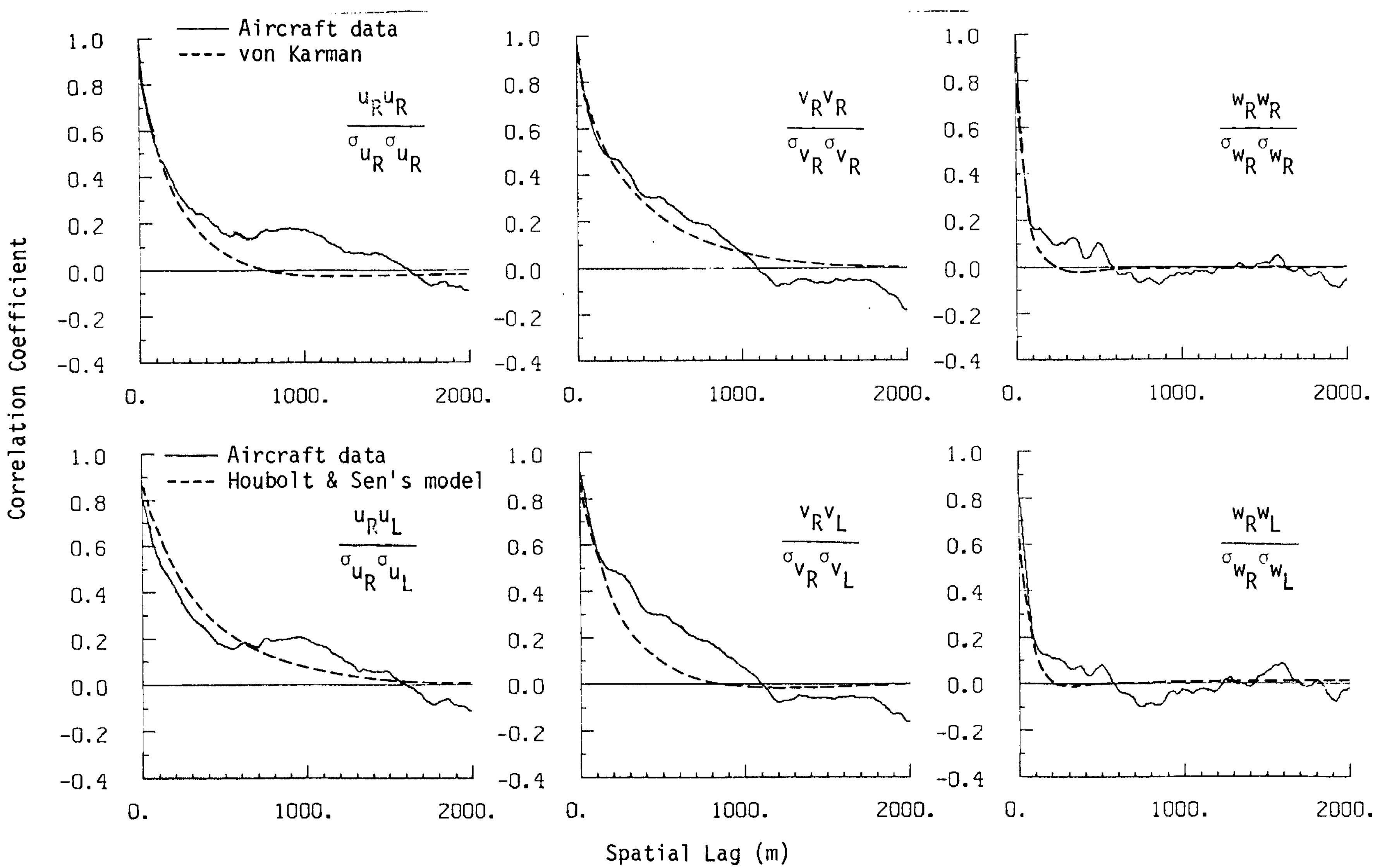

a. One- and two-point common component correlations.

Figure A.44. Comparison of normalized one- and two-point correlation functions for gust velocities with theoretical models, Flight 31, Run 9.

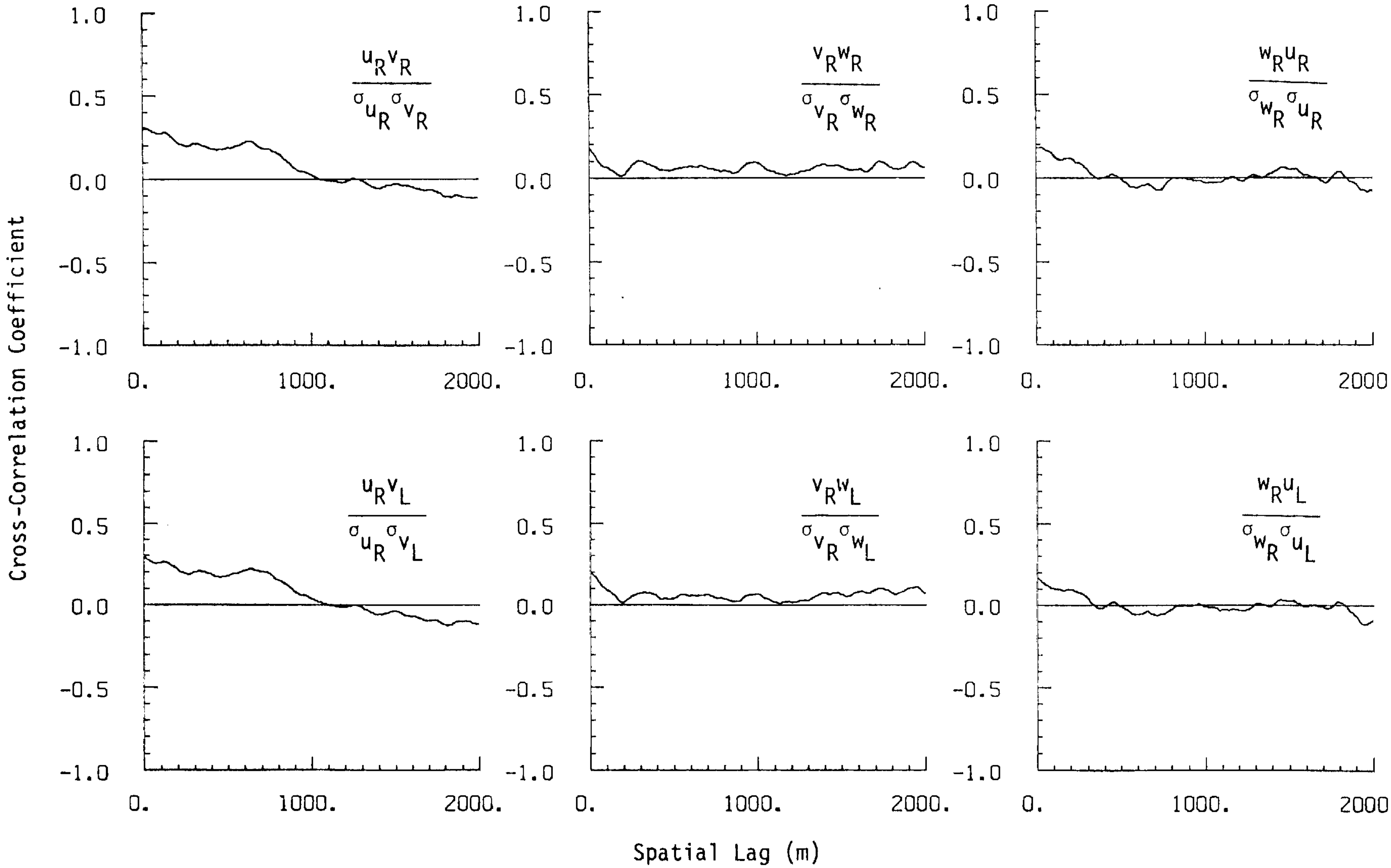

b. One- and two-point cross-correlations.

Figure A.44. (continued).

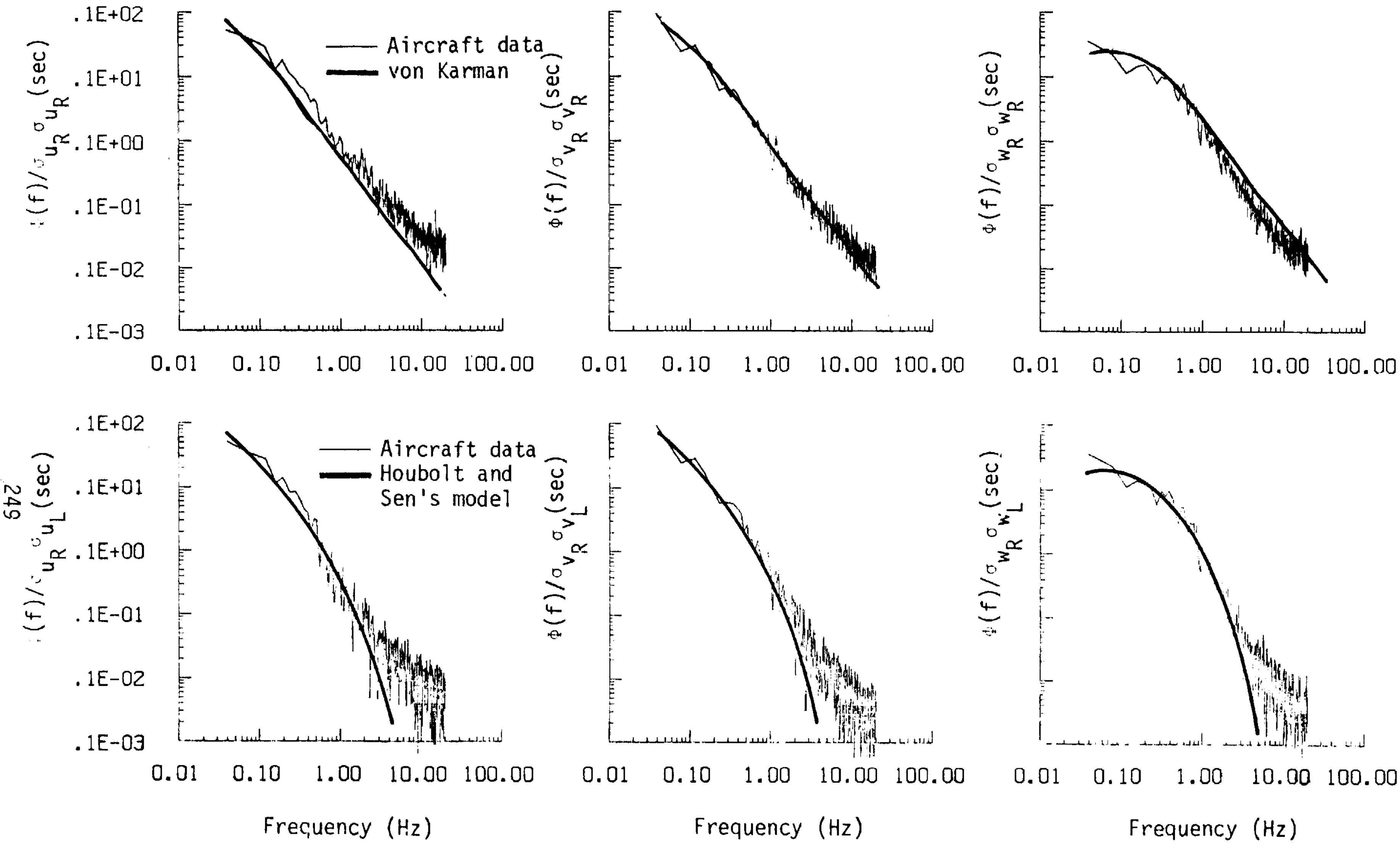

a. One- and two-point common component spectra.

Figure A.45. Comparison of normalized one- and two-point spectral density functions for gust velocities with theoretical models, Flight 31, Run 9.

ORIGINAL PAGE IS
OF POOR QUALITY

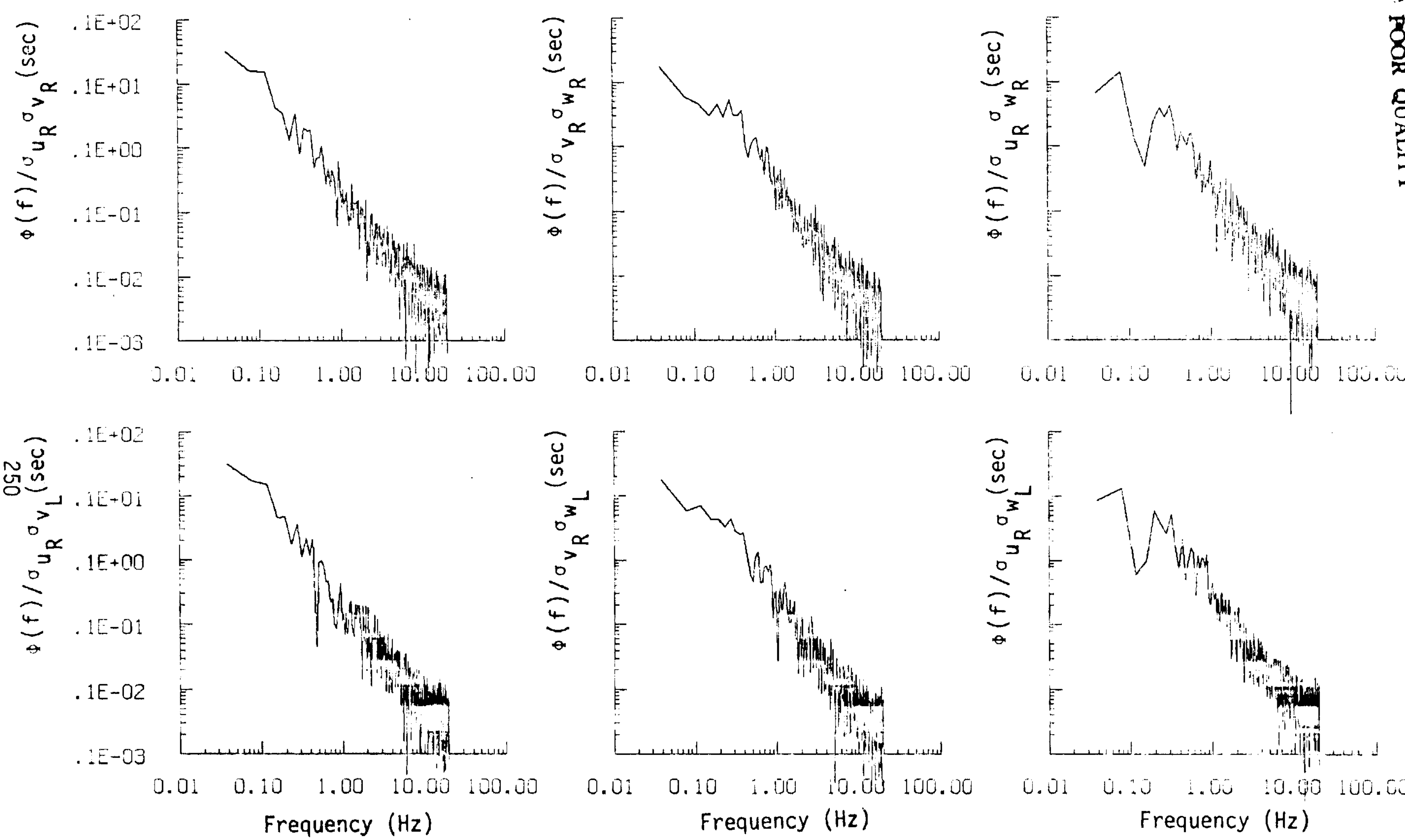

b. One- and two-point cross-spectra.

Figure A.45. (continued).

ORIGINAL PAGE IS
OF POOR QUALITY

TABLE A.18. List of All Parameters Measured and Their Range of Values, Flight 31, Run 9.

CHANNEL	UNITS	HIGH	LOW	MEAN	RMS	STD	POINTS
1 TIME	SECONDS	41704.552	41369.602	41537.07670	41537.18926	96.70255	13399
2 PHI DOT	RAD/SEC	.318	-.435	-.00239	.05126	.05120	13399
3 ACCL N CG	G UNITS	1.921	-.517	1.00123	1.01562	.17035	13399
4 THETA DOT	RAD/SEC	.112	-.089	.00301	.01688	.01661	13399
5 THETA	RAD	.188	-.036	.05660	.06526	.03248	13399
6 PHI	RAD	.152	-.260	-.00262	.04819	.04812	13399
7 PSI 1	RAD	220.340	207.660	213.51567	213.52714	2.21339	13399
8 DEL PSI 1	DEG	5.255	-7.264	-1.33276	2.55017	2.17427	13399
9 PSI 2	RAD	581.839	569.517	575.30539	575.30928	2.11580	13399
10 DEL PSI 2	DEG	5.696	-6.888	-.92423	2.37529	2.18819	13399
11 ACCL N LT	G UNITS	3.334	-1.148	1.01390	1.06483	.32540	13399
12 ACCL N RT	G UNITS	4.001	-1.443	1.01099	1.06704	.34128	13399
13 ACCL X CG	G UNITS	.178	-.012	.05691	.06568	.03279	13399
14 ACCL Y CG	G UNITS	.102	-.104	-.00127	.02394	.02391	13399
15 ALPHA CTR	RAD	.087	-.174	-.02678	.03247	.01835	13399
16 BETA CTR	RAD	.164	-.141	.01160	.03349	.03142	13399
17 TEMP I	DEG F	76.857	18.821	76.52245	76.52426	.52620	13399
18 TEMP P	DEG F	61.961	47.322	61.87709	61.87728	.15120	13399
19 ACCL Z INS	G UNITS	1.931	-.390	1.00521	1.01953	.17030	13399
20 ALPHA RT	RAD	.085	-.186	-.00918	.02266	.02072	13399
21 BETA RT	RAD	.170	-.120	.02015	.03524	.02891	13399
22 ALPHA LT	RAD	.144	-.152	.01115	.02246	.01950	13399
23 BETA LT	RAD	.143	-.123	.01432	.03243	.02910	13399
24 PSI DOT	RAD/SEC	.097	-.093	.00253	.02486	.02473	13399
25 TEMP TOT	DEG C	14.653	10.203	12.68550	12.71776	.90524	13399
26 QC LT	PSID	1.074	.651	.83864	.84041	.05450	13399
27 QC CTR	PSID	.986	.618	.80057	.80229	.05240	13399
28 QC RT	PSID	1.039	.642	.83345	.83524	.05464	13399
29 PS	PSIA	12.509	12.119	12.39236	12.39270	.09177	13399
30 TEMP IRT	VOLTS	8.063	4.319	7.15658	7.17453	.50722	13399
31 HYGROM	DEG C	4.123	-2.329	1.63444	2.15294	1.40139	13399
32 QC2 LT	PSID	.079	.074	.07689	.07691	.00150	13399
33 QC2 CTR	PSID	.179	.141	.16947	.16976	.01004	13399
34 QC2 RT	PSID	.169	.134	.15502	.15543	.01115	13399
35 DAR	DEG	-9.910	-10.242	-10.00441	10.00472	.07867	13399
36 DAL	DEG	-9.202	-9.575	-9.40686	9.40722	.08209	13399
37 DELEV	DEG	6.086	5.345	5.76381	5.76764	.21015	13399
38 DSTAB	DEG	-.374	-.422	-.40008	.40033	.01387	13399
39 DRUD	DEG	11.483	10.402	10.91013	10.91478	.31864	13399
40 DTHRR	PCT MAX	67.969	66.406	67.12432	67.12595	.46708	13399
41 DTHRL	PCT MAX	67.773	66.406	67.02022	67.02126	.37408	13399
42 DFLP	POSITION	.320	.273	.29930	.29959	.01310	13399
43 DSB	POSITION	.324	.299	.31140	.31147	.00676	13399
44 D TO G	METERS	7500823.590	7484351.808	***********	***********	7011.66724	13399
45 B TO D	DEGREES	72.886	72.861	72.87323	72.87323	.00719	13399
46 LONG	DEGREES	-118.062	-118.248	-118.15379	118.15380	.05331	13399
47 LAT	DEGREES	35.355	35.103	35.23129	35.23137	.07257	13399
48 TRK ANG	DEGREES	216.361	207.822	211.17269	211.18406	2.19175	13399
49 HDG	RADIANS	3.869	3.644	3.75054	3.75074	.03910	13399
50 VE	M/SEC	-42.984	-60.999	-50.55699	50.71865	4.04635	13399
51 VN	M/SEC	-76.290	-90.819	-83.45358	83.53606	3.71141	13399
52 ALTITUDE	KM	1.597	1.338	1.41511	1.41641	.06068	13399
53 TEMPC	DEGREES C	9.502	5.153	7.61940	7.67039	.88298	13399
54 EW WND SPD	KNOTS	39.790	-18.404	11.90551	16.43143	11.32521	13399
55 NS WND SPD	KNOTS	23.456	-24.192	-.25178	5.88026	5.87509	13399
56 WIND SPEED	KNOTS	44.252	.125	15.95477	17.45192	7.07238	13399
57 WIND DIREC	DEGREES	359.936	.142	240.11268	251.21831	73.87116	13399
58 WIND DIR2	DEGREES	179.936	-179.858	60.11270	95.23699	73.87120	13399
59 WIND DIR3	DEGREES	359.936	.142	240.11270	251.21834	73.87120	13399
60 WIND DIR4	DEGREES	843.475	-533.217	178.96187	281.19140	216.89805	13399
61 AIRSPEED R	M/SEC	114.681	90.490	102.84471	102.89615	3.25334	13399
62 AIRSPEED C	M/SEC	111.755	88.836	100.84162	100.89187	3.18411	13399
63 AIRSPEED L	M/SEC	116.498	91.024	103.15851	103.20907	3.23036	13399
64 DELTA ALT	METERS	251.146	-7.522	69.33534	92.13510	60.67753	13399
65 INRTL DISP	METERS	240.544	-10.792	65.39001	89.00817	60.38935	13399
66 UG RIGHT	M/SEC	11.496	-11.949	.00000	4.10906	4.10921	13399
67 UG CENTER	M/SEC	11.356	-11.386	.00000	4.10739	4.10755	13399
68 UG LEFT	M/SEC	11.359	-11.158	.00000	4.18736	4.18752	13399
69 VG RIGHT	M/SEC	13.853	-22.090	-.01121	5.12140	5.12158	13399
70 VG CENTER	M/SEC	12.866	-17.501	-.00555	5.10793	5.10812	13399
71 VG LEFT	M/SEC	13.763	-10.901	-.00246	5.12151	5.12170	13399
72 WG RIGHT	M/SEC	13.700	-14.128	.023F3	2.40782	2.40779	13399
73 WG CENTER	M/SEC	13.996	-10.785	.02626	2.21583	2.21576	13399
74 WG LEFT	M/SEC	15.640	-13.421	.02633	2.34881	2.34875	13399

Flight 31, Run 10
Date: Nov. 29, 1982
Start Time: 11:39:45 (PST)
Duration: 172.0 seconds

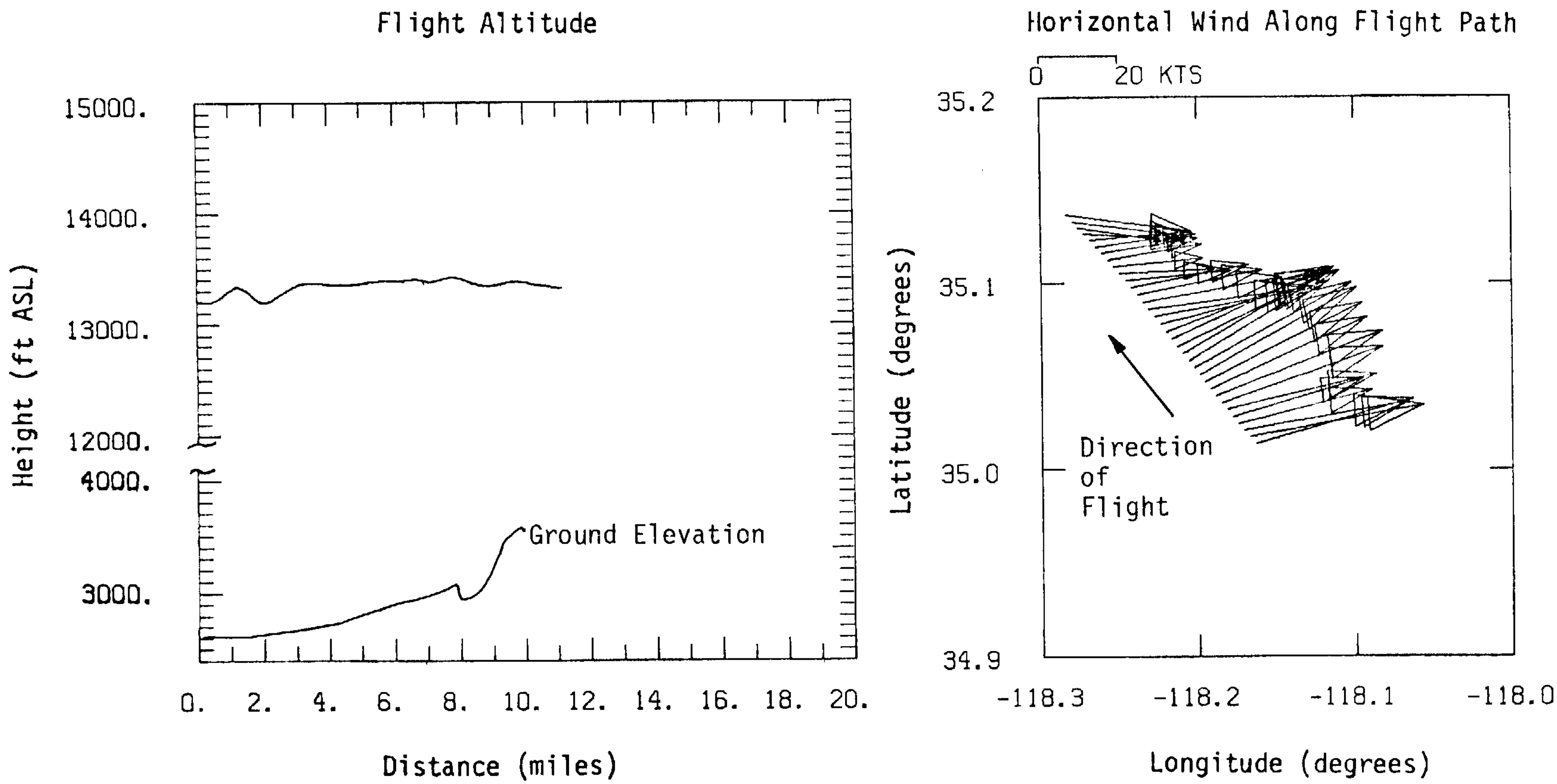

Figure A.46. Flight altitude and horizontal wind along flight path, Flight 31, Run 10.

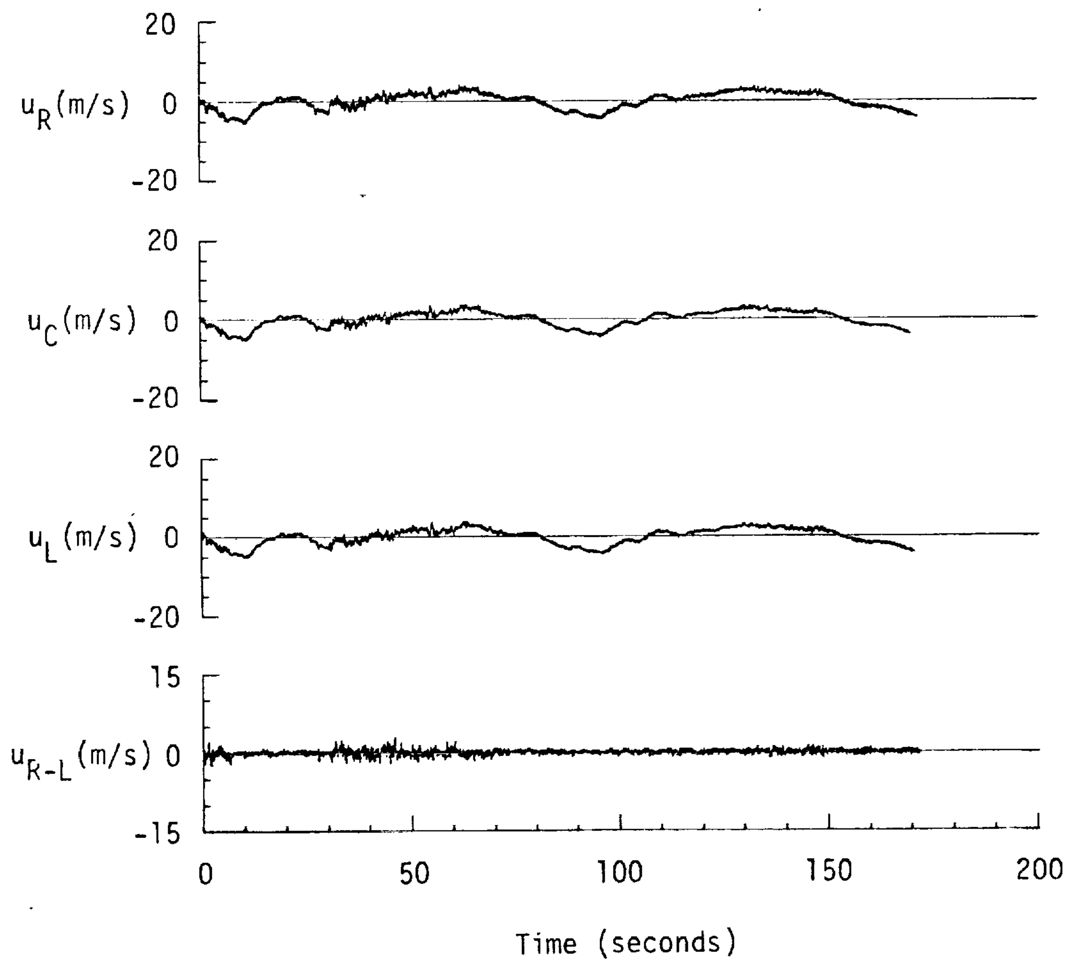

Figure A.47. Time histories of gust velocities, gust velocity differences, and aircraft's normal accelerations, Flight 31, Run 10.

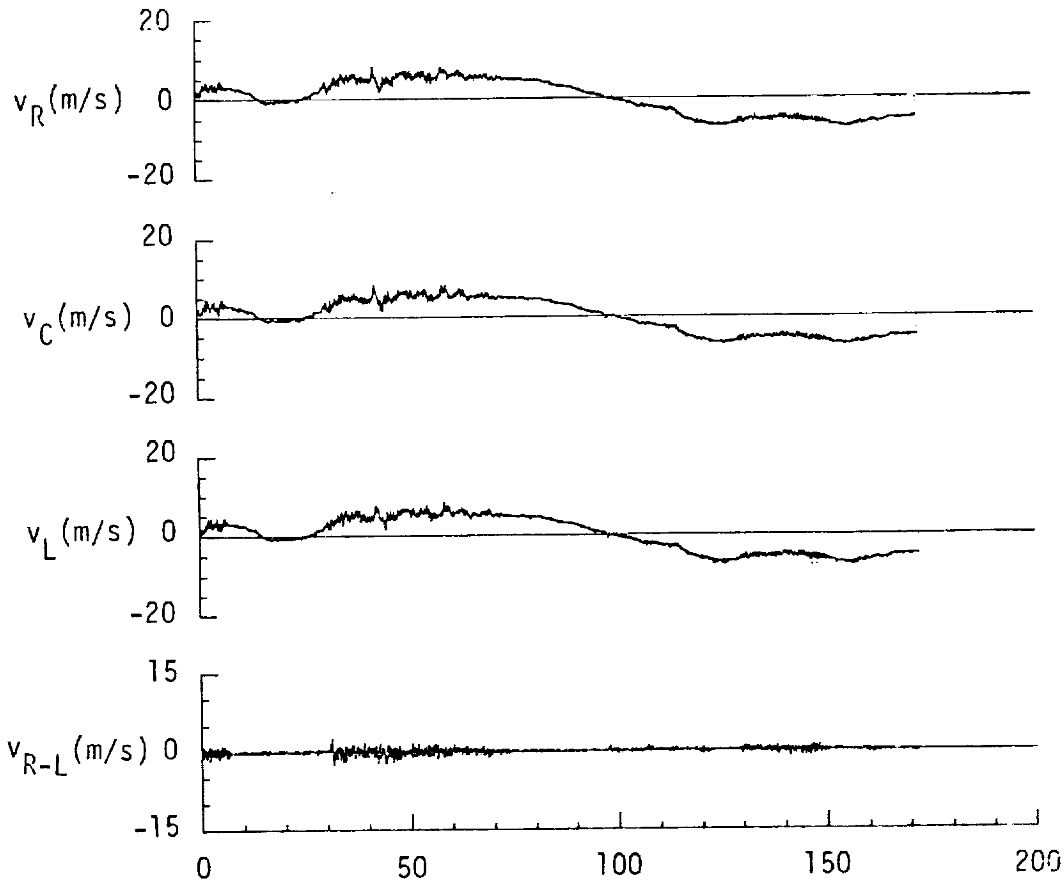

Figure A.47. (continued).

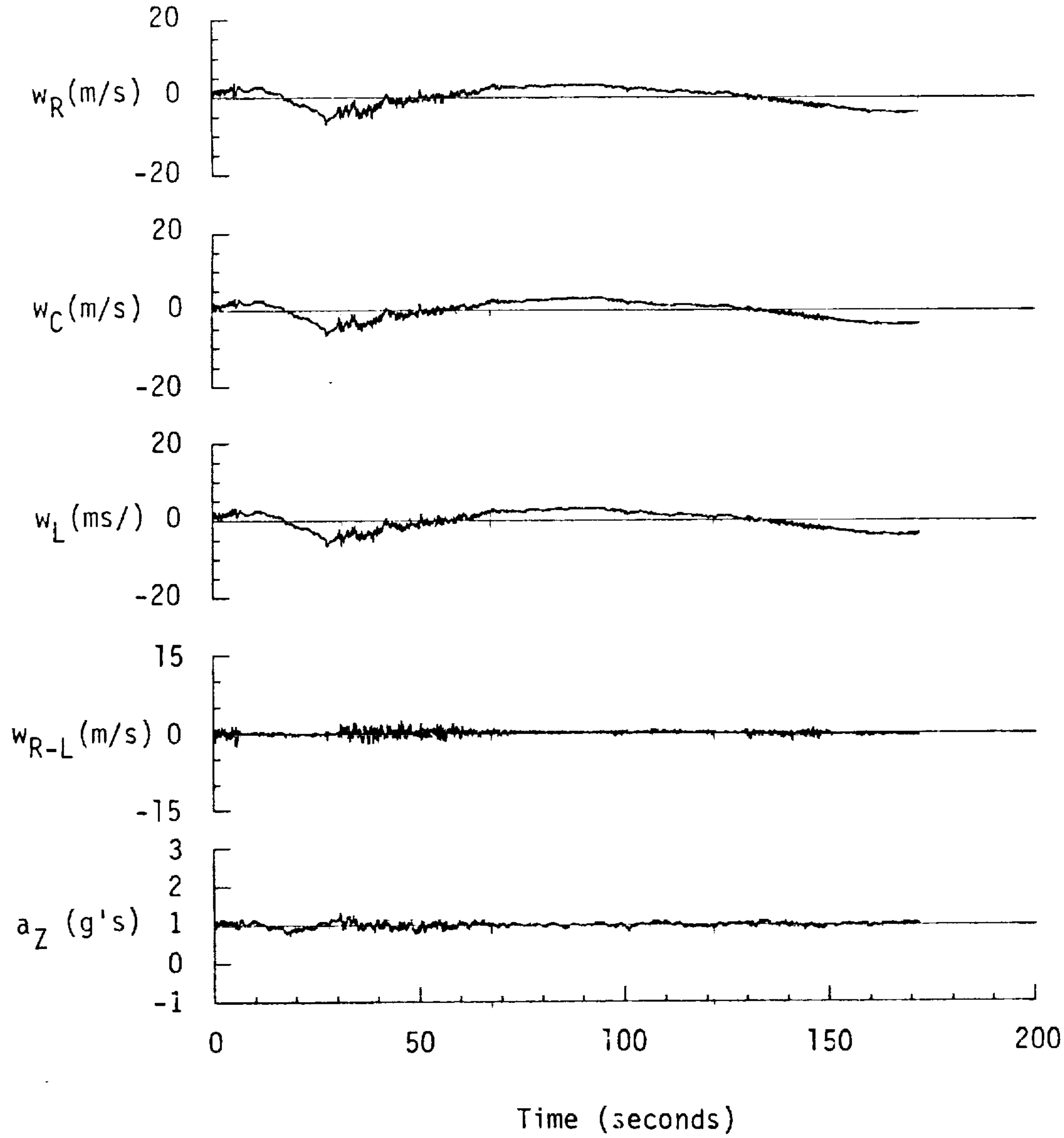

Figure A.47. (continued).

TABLE A.19. Average Turbulence Parameters, Integral Length Scales, and Correlation Coefficients of Gust Velocities, Flight 31, Run 10.

1. Mean Airspeed (m/s):

$\overline{V}_L$	$\overline{V}_C$	$\overline{V}_R$
117.27	115.20	116.70

2. Standard Deviation of Gust Velocities (m/s):

σ_{uR}	σ_{vR}	σ_{wR}
2.04	4.57	2.40
σ_{uC}	σ_{vC}	σ_{wC}
1.99	4.58	2.34
σ_{uL}	σ_{vL}	σ_{wL}
2.02	4.61	2.33

3. Standard Deviation of Gust Velocity Differences (m/s):

$\sigma_{\Delta uRL}$	$\sigma_{\Delta vRL}$	$\sigma_{\Delta wRL}$
0.41	0.31	0.38

4. Integral Length Scale (m):

L_{uR}	L_{vR}	L_{wR}
641.8	729.7	832.2
L_{uRL}	L_{vRL}	L_{wRL}
638.3	742.9	863.8

5. Correlation Coefficient of Gust Velocities:

$\overline{u_R u_L}/\sigma_{u_R}\sigma_{u_L}$	$\overline{v_R v_L}/\sigma_{v_R}\sigma_{v_L}$	$\overline{w_R w_L}/\sigma_{w_R}\sigma_{w_L}$
0.98	0.99	0.98
$\overline{u_R v_R}/\sigma_{u_R}\sigma_{v_R}$	$\overline{v_R w_R}/\sigma_{v_R}\sigma_{w_R}$	$\overline{w_R u_R}/\sigma_{w_R}\sigma_{u_R}$
0.08	0.00	-0.47
$\overline{u_R v_L}/\sigma_{u_R}\sigma_{v_L}$	$\overline{v_R w_L}/\sigma_{v_R}\sigma_{w_L}$	$\overline{w_R u_L}/\sigma_{w_R}\sigma_{u_L}$
0.09	-0.01	-0.45

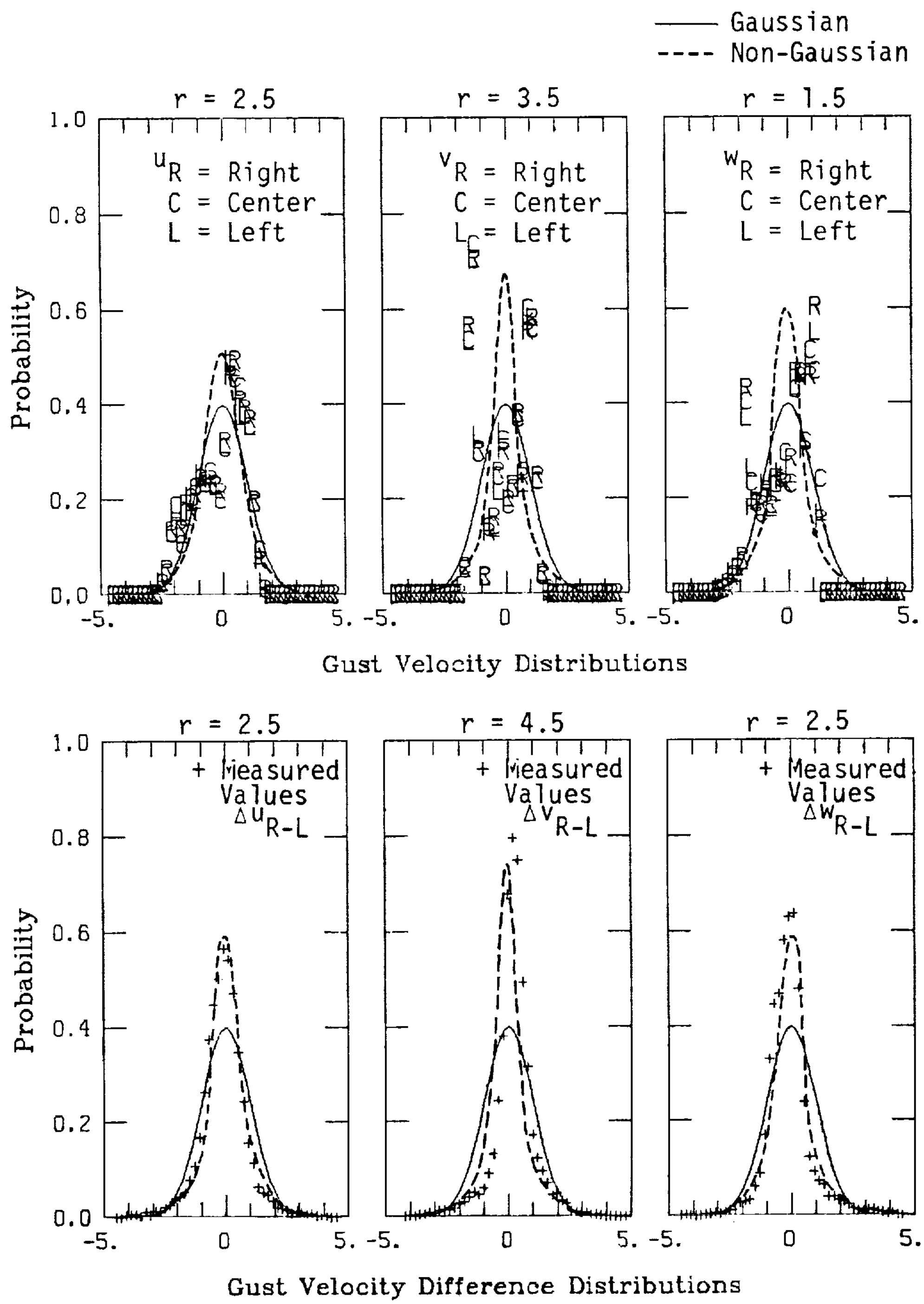

Figure A.48. Probability density functions for gust velocities and gust velocity differences (normalized with the standard deviation), Flight 31, Run 10(r = degree of non-Gaussian).

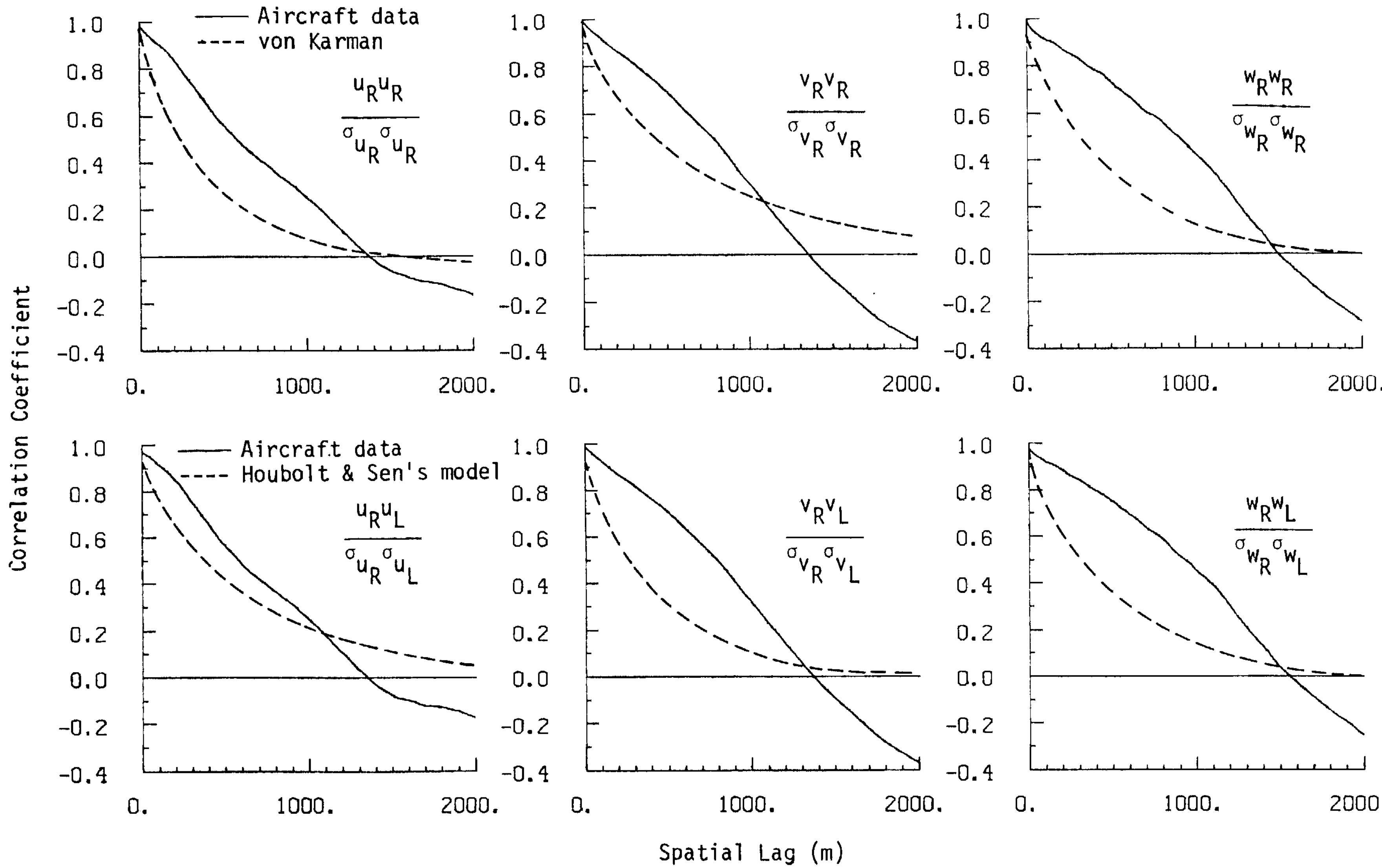

a. One- and two-point common component correlations.

Figure A.49. Comparison of normalized one- and two-point correlation functions for gust velocities with theoretical models, Flight 31, Run 10.

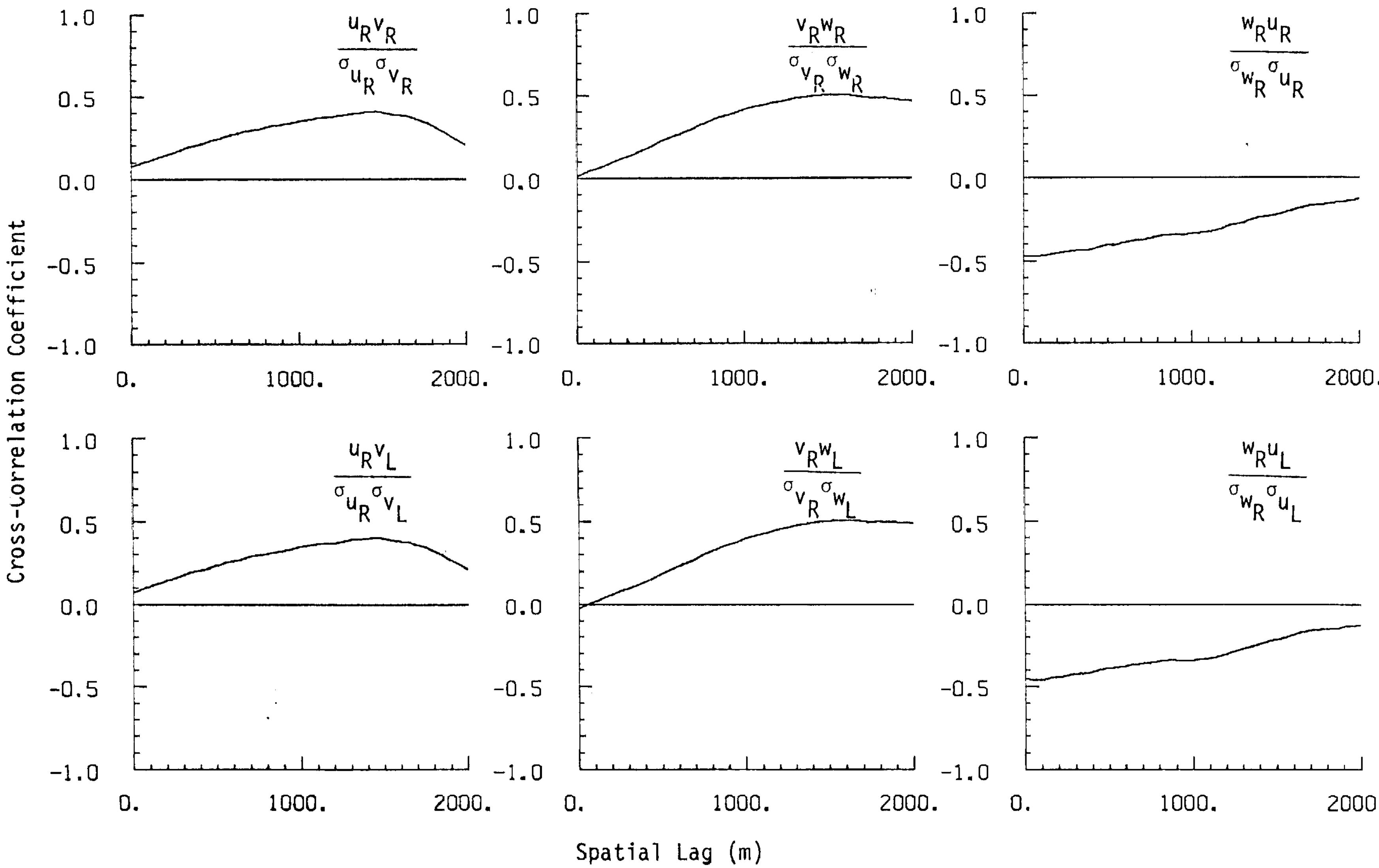

b. One- and two-point cross-correlations.

Figure A.49. (continued).

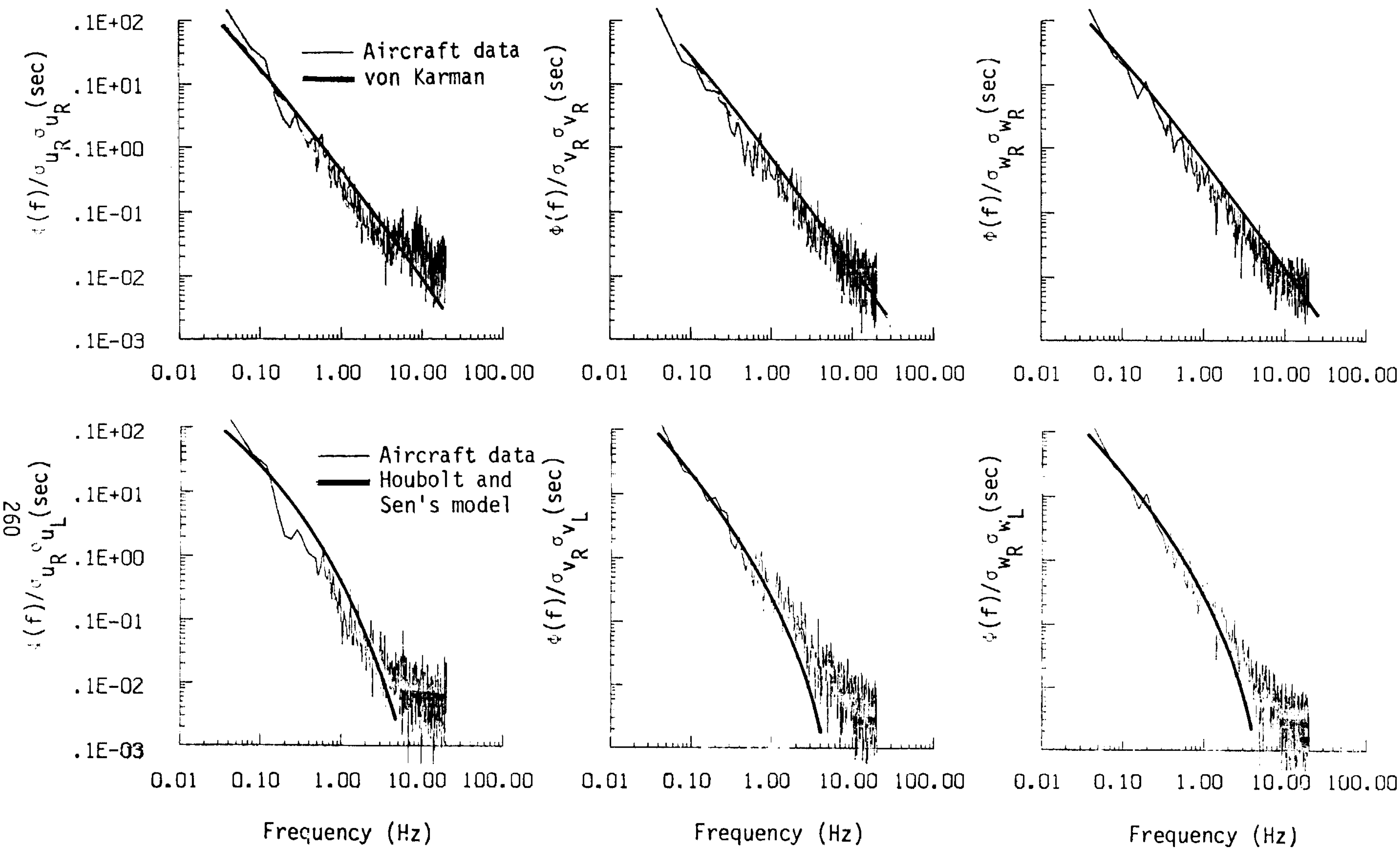

a. One- and two-point common component spectra.

Figure A.50. Comparison of normalized one- and two-point spectral density functions for gust velocities with theoretical models, Flight 31, Run 10.

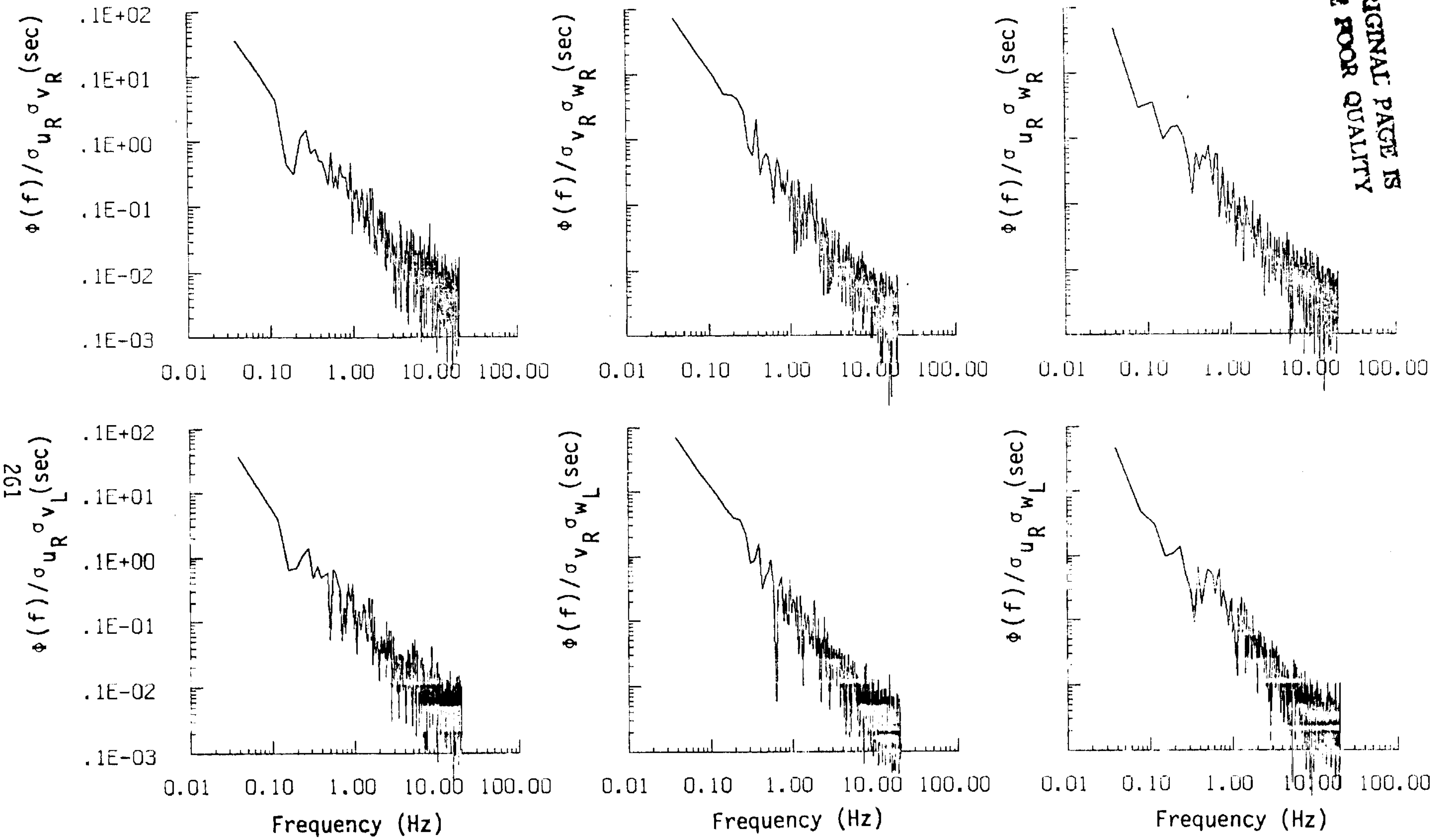

b. One- and two-point cruss-spectra.

Figure A.50. (continued).

TABLE A.20. List of All Parameters Measured and Their Range of Values, Flight 31, Run 10.

CHANNEL	UNITS	HIGH	LOW	MEAN	RMS	STD	POINTS
1 TIME	SECONDS	42157.541	41985.491	42071.51600	42071.54532	49.67740	6883
2 PHI DOT	RAD/SEC	.050	-.064	-.00242	.01224	.01200	6883
3 ACCL N CG	G UNITS	1.305	.729	1.00190	1.00349	.05664	6883
4 THETA DOT	RAD/SEC	.033	[illegible]	[illegible]	[illegible]	[illegible]	6883
5 THETA	RAD	.103	.004	.04353	[illegible]	.02608	6883
6 PHI	RAD	.062	-.046	-.00109	.01970	.01967	6883
7 PSI 1	RAD	316.794	309.102	312.00796	312.01274	1.72723	6883
8 DEL PSI 1	DEG	.906	-4.355	-1.84339	2.20519	1.21037	6883
9 PSI 2	RAD	316.045	310.764	313.42351	313.42576	1.18716	6883
10 DEL PSI 2	DEG	1.230	-6.153	-3.39606	3.80657	1.71965	6883
11 ACCL N LT	G UNITS	1.535	.412	1.01990	1.02288	.09014	6883
12 ACCL N RT	G UNITS	1.539	.450	1.01124	1.01594	.09761	6883
13 ACCL X CG	G UNITS	.098	-.004	.04012	.04533	.02109	6883
14 ACCL Y CG	G UNITS	.071	-.072	-.00168	.01545	.01536	6883
15 ALPHA CTR	RAD	.002	-.048	-.02907	.02987	.00689	6883
16 BETA CTR	RAD	.060	-.022	.00801	.01156	.00834	6883
17 TEMP I	DEG F	76.317	75.418	75.90996	75.91019	.18593	6883
18 TEMP P	DEG F	61.421	60.882	61.12074	61.12089	.13491	6883
19 ACCL Z INS	G UNITS	1.324	.767	1.00543	1.00703	.05663	6883
20 ALPHA RT	RAD	.016	-.036	-.01265	.01474	.00756	6883
21 BETA RT	RAD	.066	-.014	.01676	.01841	.00763	6883
22 ALPHA LT	RAD	.033	-.015	.01021	.01267	.00750	6883
23 BETA LT	RAD	.058	-.017	.01201	.01441	.00797	6883
24 PSI DOT	RAD/SEC	.029	-.027	.00258	.00731	.00684	6883
25 TEMP TOT	DEG C	1.657	-3.463	-.65032	1.73559	1.60926	6883
26 QC LT	PSID	.943	.735	.82538	.82694	.05077	6883
27 QC CTR	PSID	.910	.709	.79555	.79705	.04887	6883
28 QC RT	PSID	.937	.724	.81716	.81874	.05080	6883
29 PS	PSIA	8.916	8.831	8.86108	8.86111	.02153	6883
30 TEMP IRT	VOLTS	3.362	1.911	2.60482	2.61531	.23404	6883
31 HYGROM	DEG C	-12.105	-17.970	-14.51836	14.65984	2.03197	6883
32 QCZ LT	PSID	.083	.075	.07948	.07952	.00237	6883
33 QCZ CTR	PSID	.155	.034	.11109	.11613	.03387	6883
34 QCZ RT	PSID	.110	.049	.07403	.07656	.01953	6883
35 DAR	DEG	-7.230	-9.772	-8.47994	8.51409	.76181	6883
36 DAL	DEG	-8.127	-9.753	-9.05152	9.06433	.48181	6883
37 DELEV	DEG	6.476	6.242	6.41465	6.41501	.06770	6883
38 DSTAB	DEG	-.443	-.452	-.44994	.44995	.00245	6883
39 DRUD	DEG	12.394	12.109	12.27735	12.27767	.08869	6883
40 DTHRR	PCT MAX	69.898	69.141	69.53217	69.53245	.19775	6883
41 DTHRL	PCT MAX	69.629	68.945	69.29368	69.29390	.17517	6883
42 DFLP	POSITION	.219	.191	.20560	.20572	.00712	6883
43 DSB	POSITION	.363	.346	.35490	.35493	.00490	6883
44 D TO G	METERS	7489994.522	7482269.414	***********	***********	1913.22435	6883
45 B TO D	DEGREES	72.956	72.820	72.88784	72.88785	.03942	6883
46 LONG	DEGREES	-118.161	-118.286	-118.22294	118.22294	.03609	6883
47 LAT	DEGREES	35.141	35.013	35.07726	35.07728	.03752	6883
48 TRK ANG	DEGREES	323.643	317.862	321.06322	321.06890	1.91006	6883
49 HDG	RADIANS	5.518	5.425	5.46979	5.46983	.02167	6883
50 VE	M/SEC	-62.543	-71.163	-66.41174	66.44590	2.13040	6883
51 VN	M/SEC	88.517	74.356	82.31304	82.41661	4.13089	6883
52 ALTITUDE	KM	4.094	4.021	4.06812	4.06816	.01861	6883
53 TEMPC	DEGREES C	-4.817	-9.638	-7.26067	7.45198	1.67784	6883
54 EW WND SPD	KNOTS	45.717	22.132	34.78081	35.45660	6.89006	6883
55 NS WND SPD	KNOTS	22.159	-4.692	7.47755	10.15382	6.86974	6883
56 WIND SPEED	KNOTS	48.612	22.179	36.04983	36.88185	7.79030	6883
57 WIND DIREC	DEGREES	278.713	240.538	259.30237	259.47293	9.40696	6883
58 WIND DIR2	DEGREES	98.713	60.538	79.30238	79.85829	9.40697	6883
59 WIND DIR3	DEGREES	278.713	240.538	259.30238	259.47293	9.40697	6883
60 WIND DIR4	DEGREES	278.713	240.538	259.30238	259.47293	9.40697	6883
61 AIRSPEED R	M/SEC	124.637	110.705	116.70611	116.75483	3.37265	6883
62 AIRSPEED C	M/SEC	122.871	109.565	115.20051	115.24745	3.28933	6883
63 AIRSPEED L	M/SEC	125.041	111.504	117.27489	117.32274	3.35074	6883
64 DELTA ALT	METERS	65.084	-7.898	39.28590	43.47144	18.61274	6883
65 INRTL DISP	METERS	59.877	-6.515	36.30609	40.34817	17.60363	6883
66 UG RIGHT	M/SEC	3.879	-5.219	.00000	2.04380	2.04395	6883
67 UG CENTER	M/SEC	3.694	-5.032	.00000	1.99506	1.99520	6883
68 UG LEFT	M/SEC	4.199	-4.923	.00000	2.01994	2.02009	6883
69 VG RIGHT	M/SEC	8.122	-7.089	-.02885	4.57587	4.57611	6883
70 VG CENTER	M/SEC	8.388	-7.062	-.02784	4.58571	4.59596	6883
71 VG LEFT	M/SEC	8.381	-7.164	-.02897	4.61476	4.61501	6883
72 WG RIGHT	M/SEC	3.673	-6.661	.03816	2.40404	2.40391	6883
73 WG CENTER	M/SEC	3.419	-6.360	.03708	2.34800	2.34787	6883
74 WG LEFT	M/SEC	3.328	-6.552	.03587	2.33520	2.33509	6883

Flight 31, Run 11
Date: Nov. 29, 1982
Start Time: 11:46:51 (PST)
Duration: 334.0 seconds

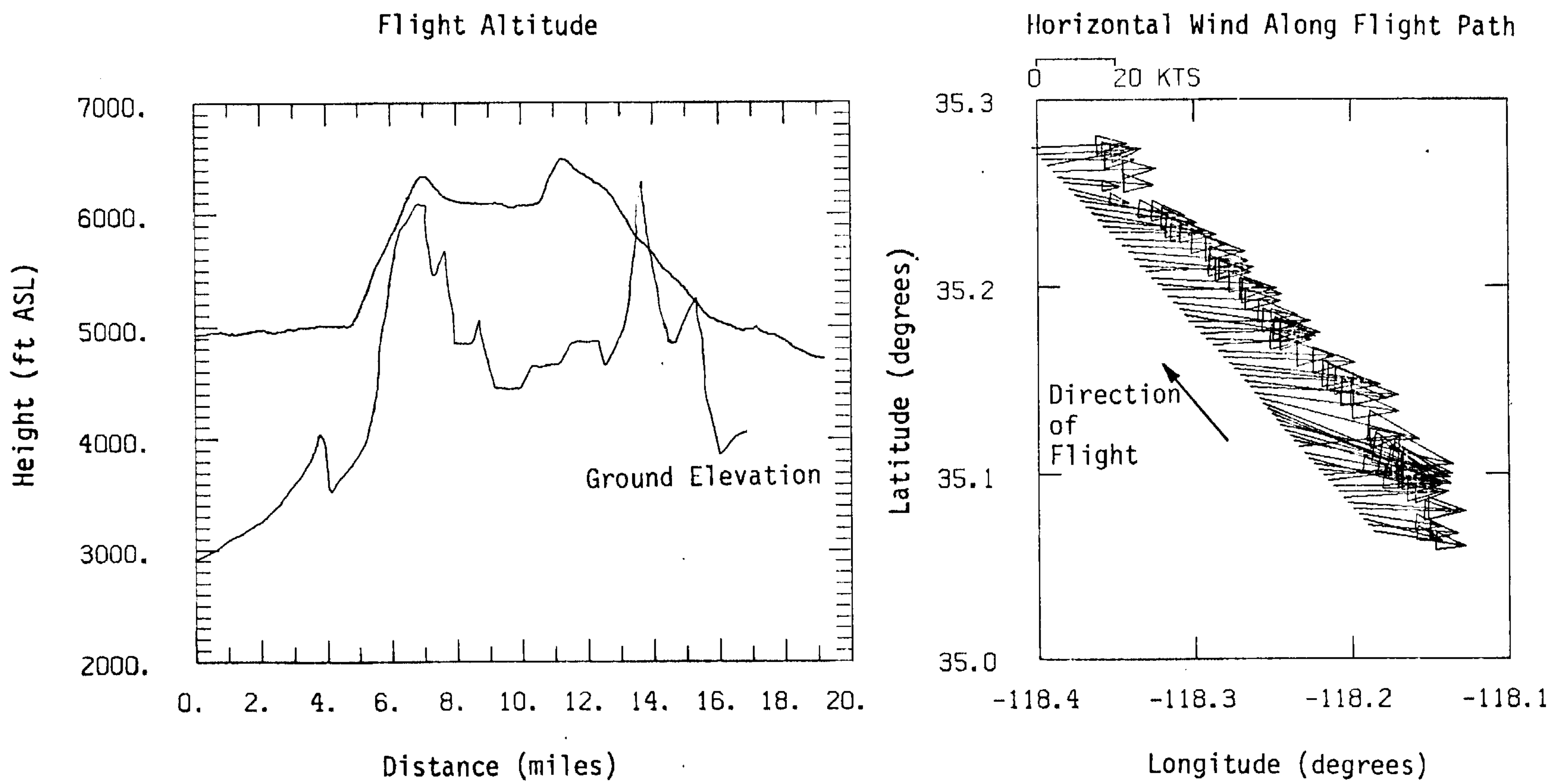

Figure A.51. Flight altitude and horizontal wind along flight path, Flight 31, Run 11.

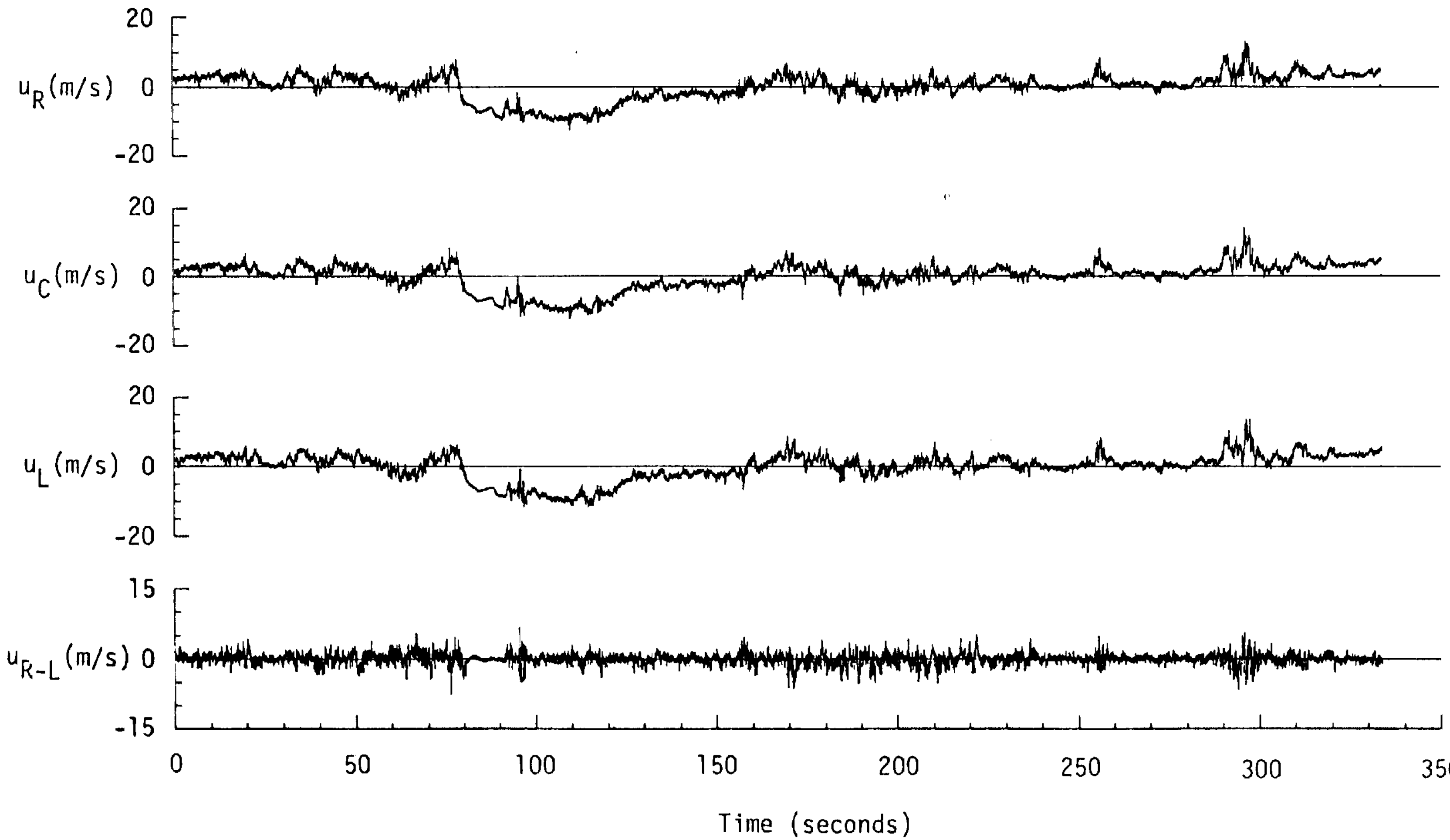

Figure A.52. Time histories of gust velocities, gust velocity differences, and aircraft's normal accelerations, Flight 31, Run 11.

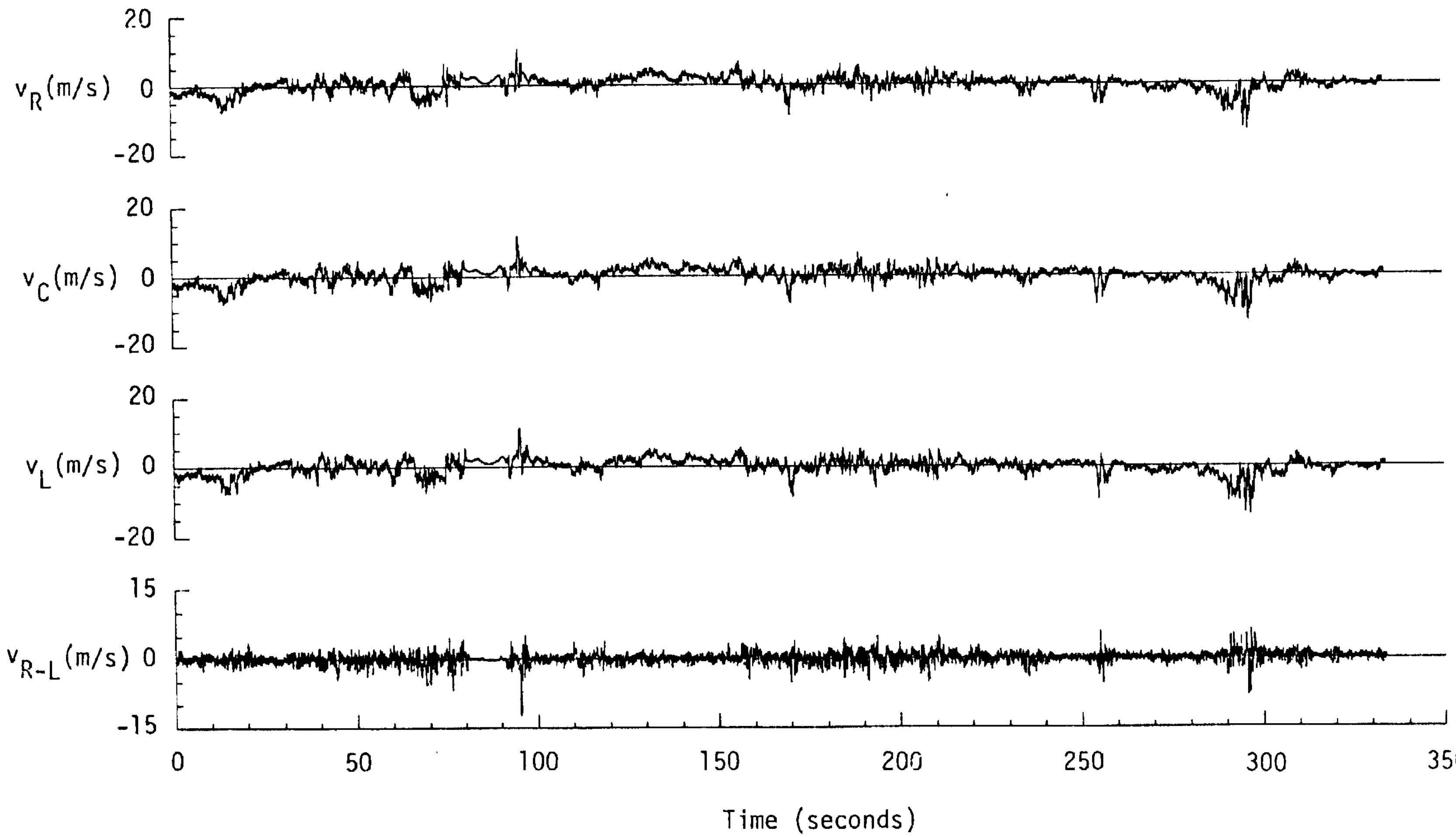

Figure A.52. (continued).

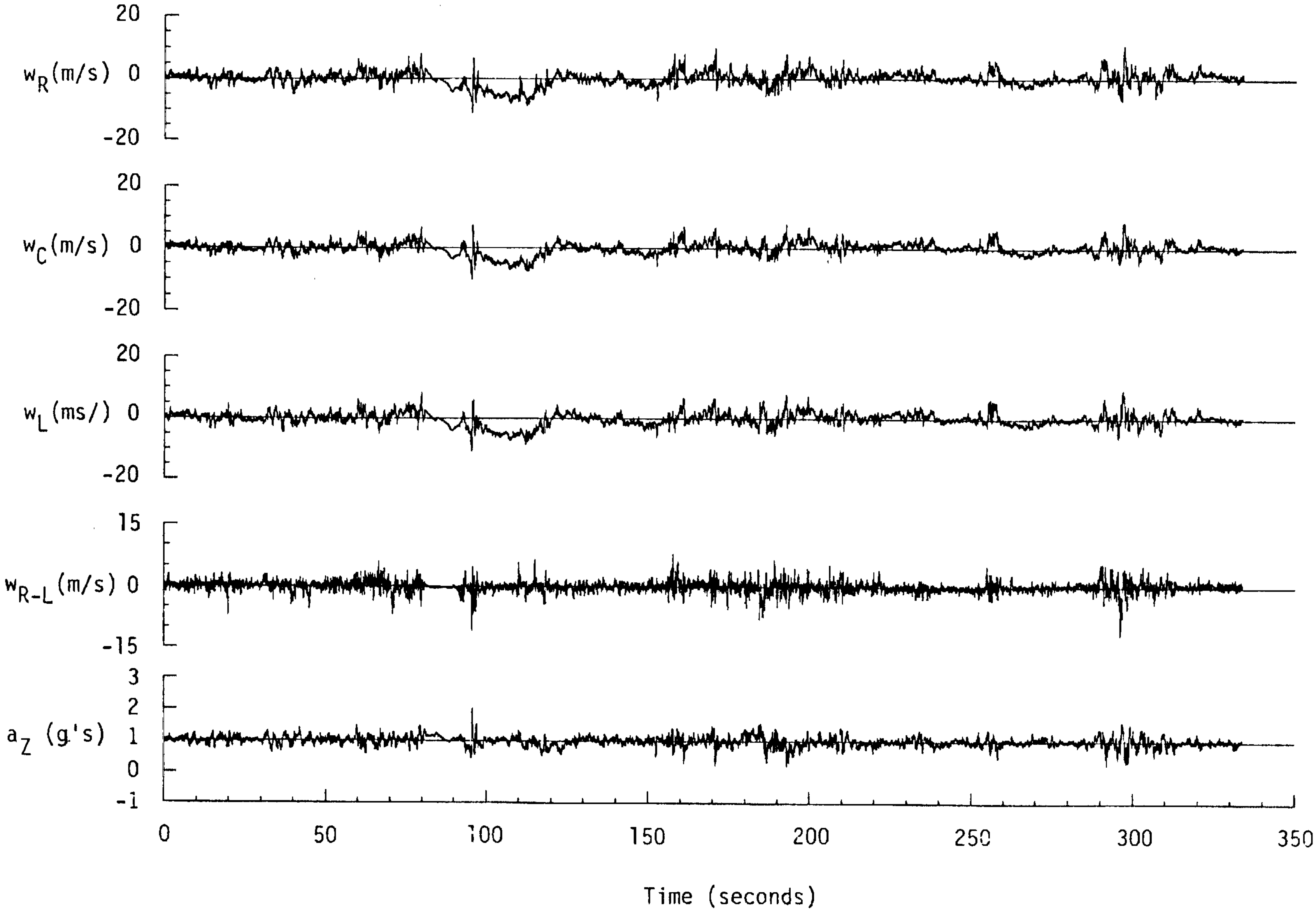

Figure A.52. (continued).

TABLE A.21. Average Turbulence Parameters, Integral Length Scales, and Correlation Coefficients of Gust Velocities, Flight 31, Run 11.

1. Mean Airspeed (m/s):

$\overline{V}_L$	$\overline{V}_C$	$\overline{V}_R$
107.01	104.47	106.49

2. Standard Deviation of Gust Velocities (m/s):

σ_{uR}	σ_{vR}	σ_{wR}
3.74	2.10	2.25

σ_{uC}	σ_{vC}	σ_{wC}
3.76	2.15	1.99

σ_{uL}	σ_{vL}	σ_{wL}
3.77	2.18	2.13

3. Standard Deviation of Gust Velocity Differences (m/s):

$\sigma_{\Delta uRL}$	$\sigma_{\Delta vRL}$	$\sigma_{\Delta wRL}$
1.12	1.01	1.26

4. Integral Length Scale (m):

L_{uR}	L_{vR}	L_{wR}
370.0	246.1	203.3

L_{uRL}	L_{vRL}	L_{wRL}
375.6	241.7	193.1

5. Correlation Coefficient of Gust Velocities:

$\overline{u_R u_L}/\sigma_{u_R}\sigma_{u_L}$	$\overline{v_R v_L}/\sigma_{v_R}\sigma_{v_L}$	$\overline{w_R w_L}/\sigma_{w_R}\sigma_{w_L}$
0.83	0.81	0.78

$\overline{u_R v_R}/\sigma_{u_R}\sigma_{v_R}$	$\overline{v_R w_R}/\sigma_{v_R}\sigma_{w_R}$	$\overline{w_R u_R}/\sigma_{w_R}\sigma_{u_R}$
-0.21	-0.09	0.48

$\overline{u_R v_L}/\sigma_{u_R}\sigma_{v_L}$	$\overline{v_R w_L}/\sigma_{v_R}\sigma_{w_L}$	$\overline{w_R u_L}/\sigma_{w_R}\sigma_{u_L}$
-0.28	-0.10	0.40

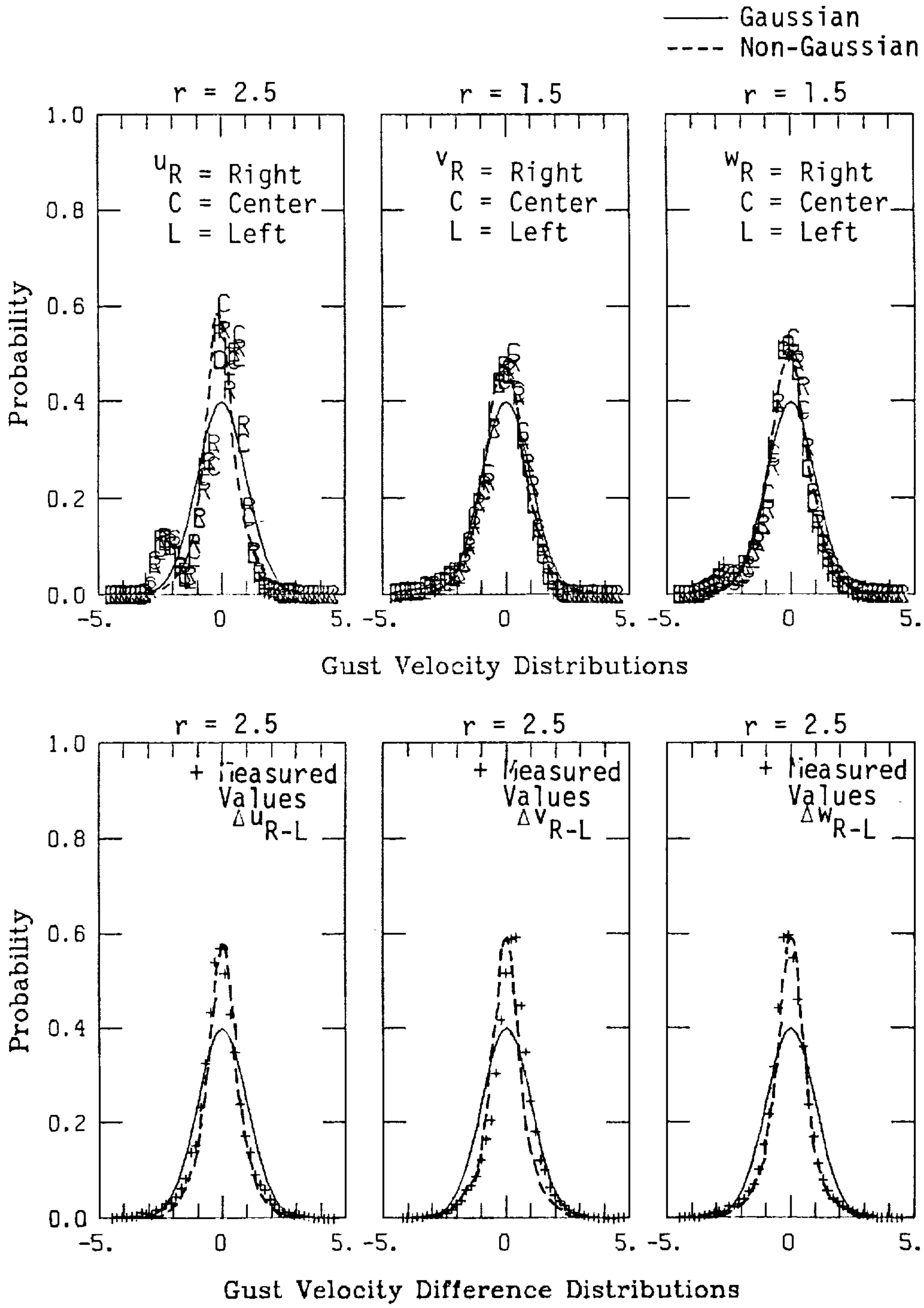

Figure A.53. Probability density functions for gust velocities and gust velocity differences (normalized with the standard deviation), Flight 31, Run 11 (r = degree of non-Gaussian).

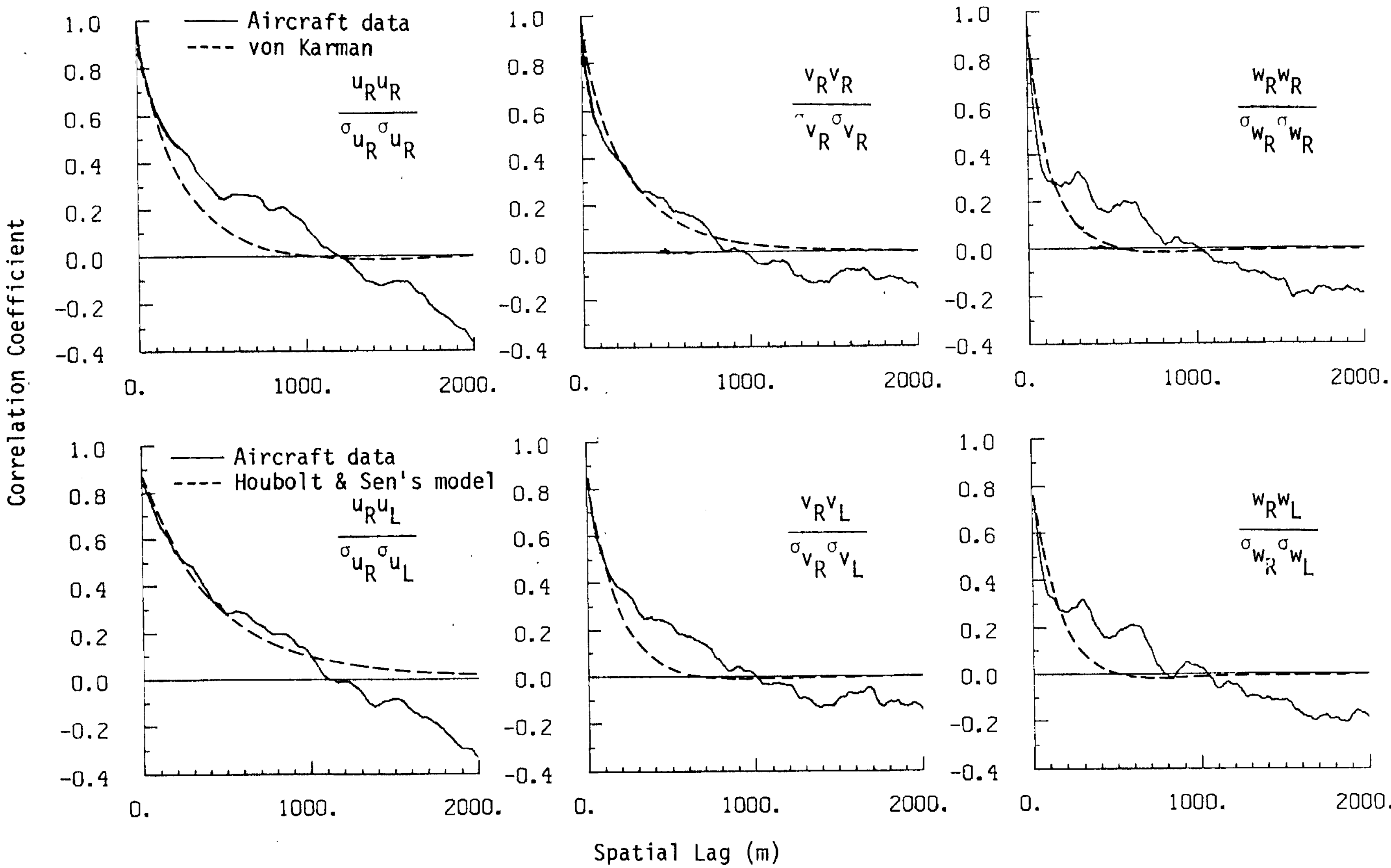

a. One- and two-point common component correlations.

Figure A.54. Comparison of normalized one- and two-point correlation functions for gust velocities with theoretical models, Flight 31, Run 11.

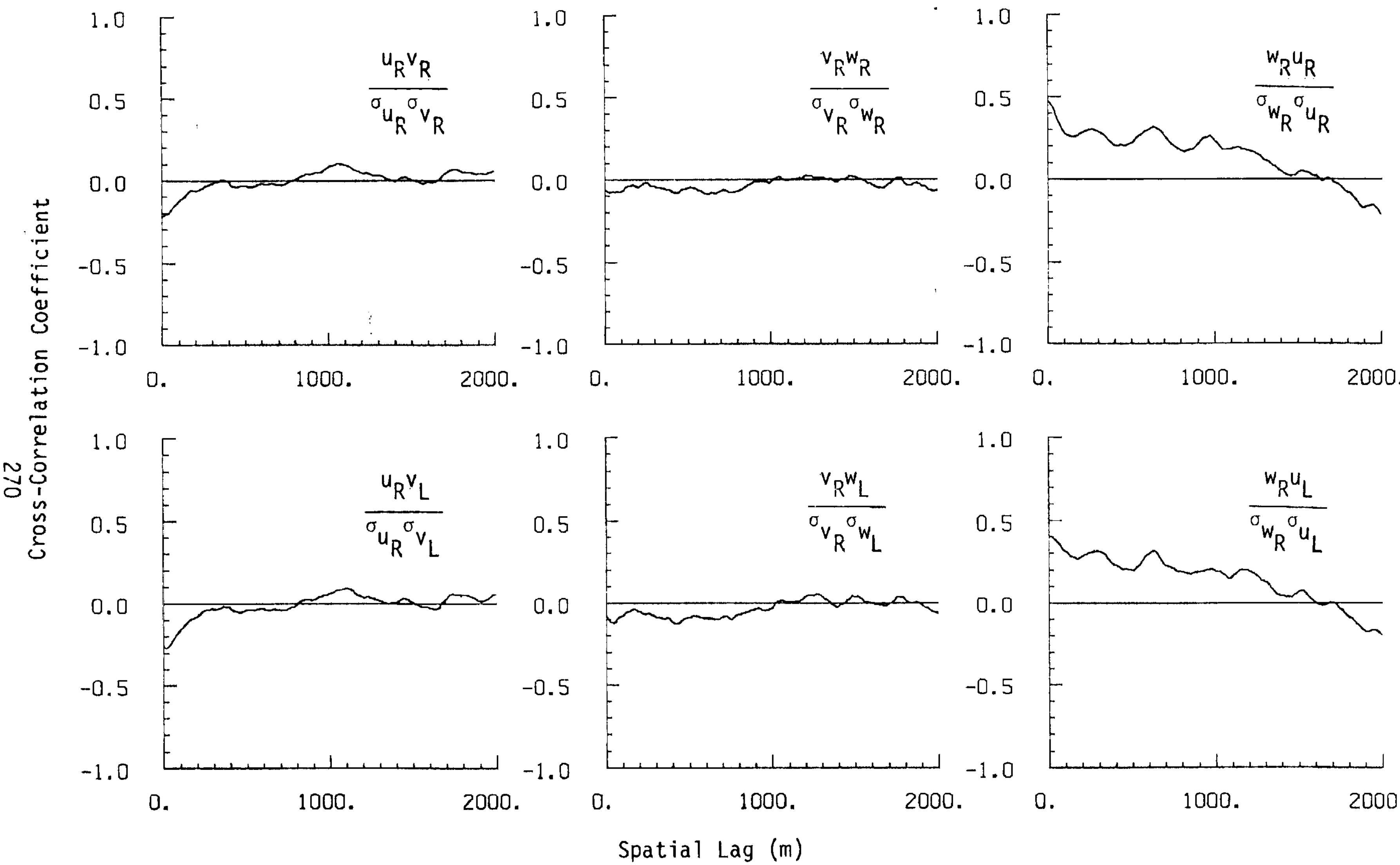

b. One- and two-point cross-correlations.

Figure A.54. (continued).

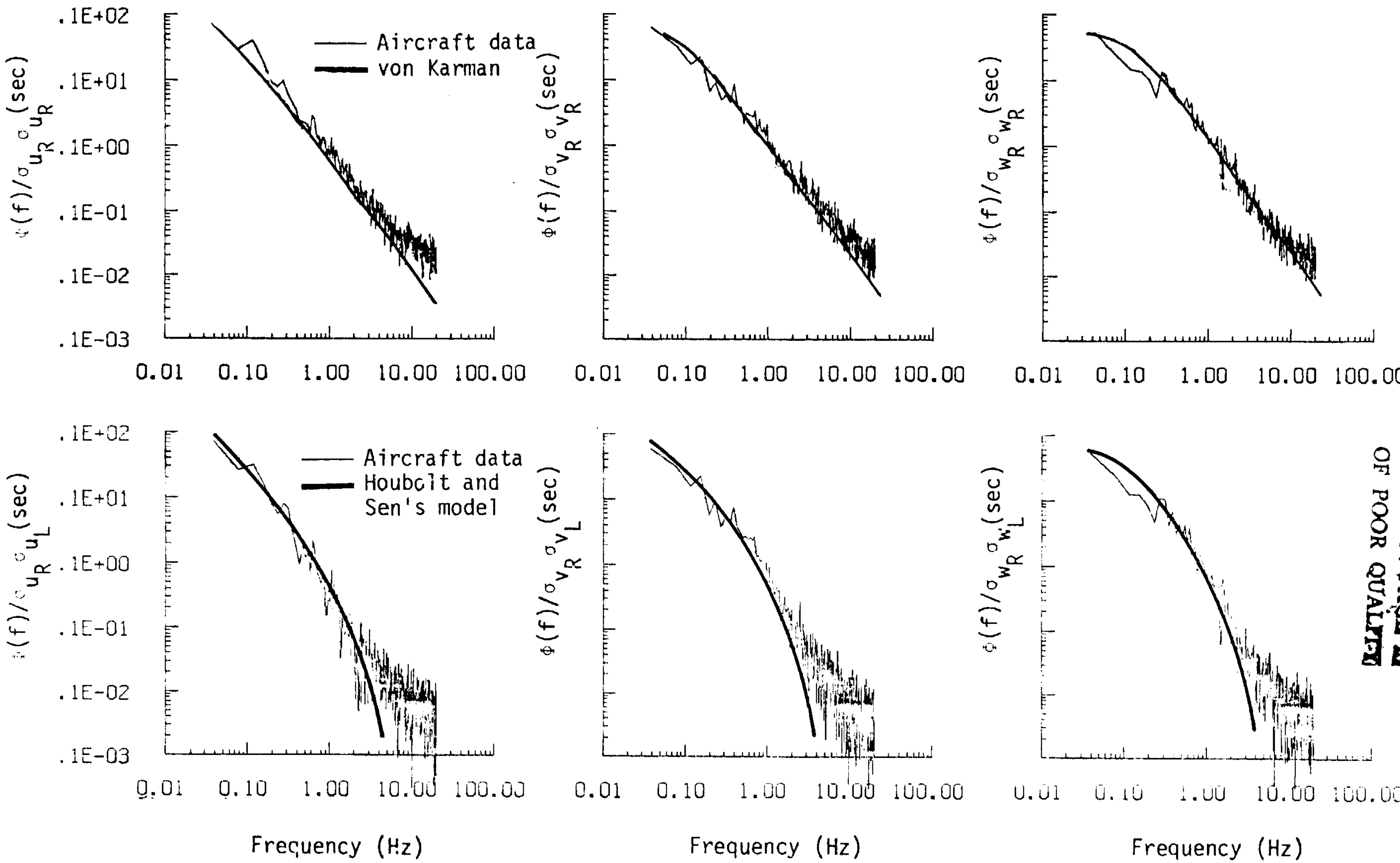

a. One- and two-point common component correlations.

Figure A.55. Comparison of normalized one- and two-point spectral density functions for gust velocities with theoretical models, Flight 31, Run 11.

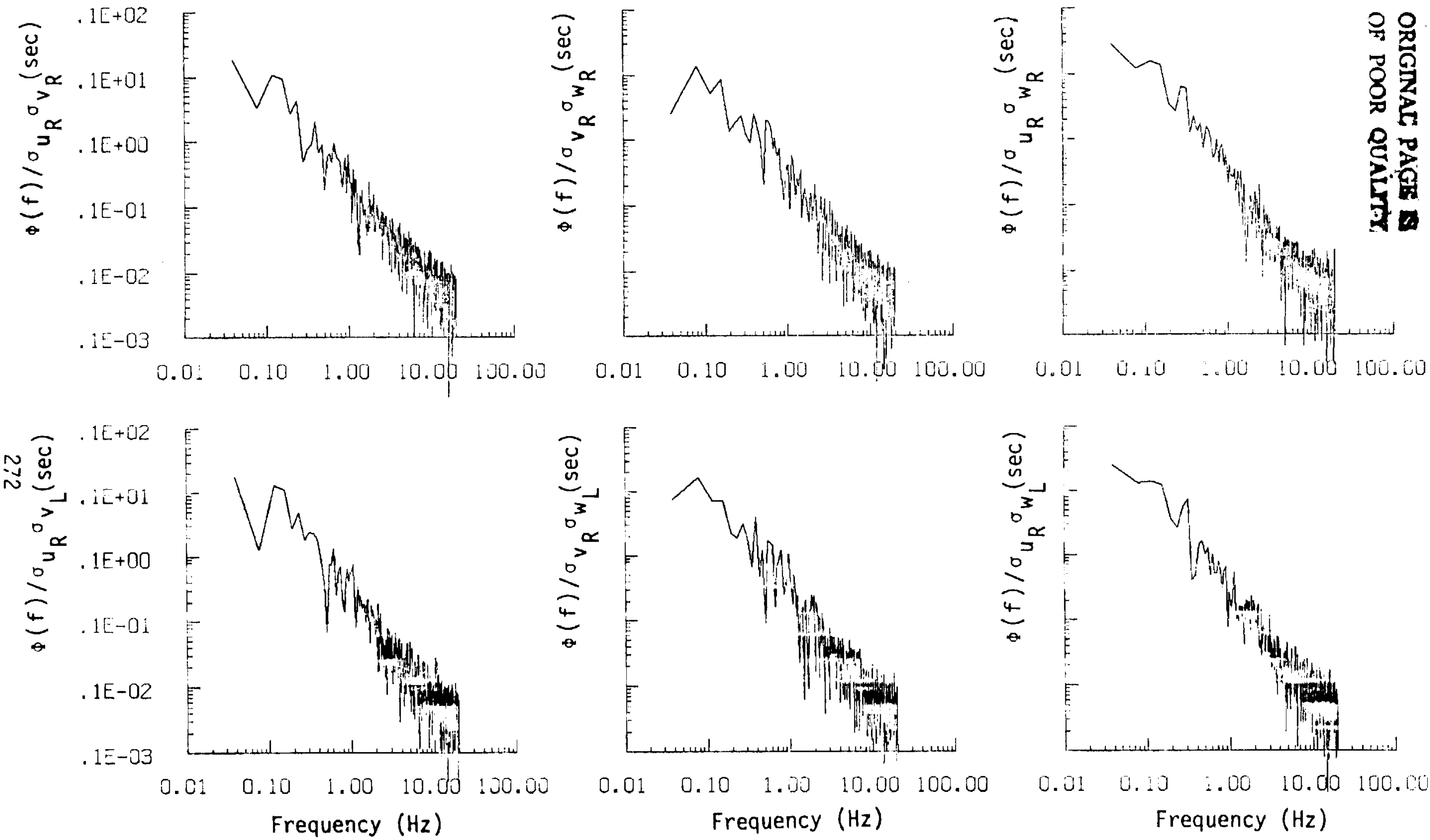

b. One- and two-point cross-spectra.

Figure A.55. (continued).

TABLE A.22. List of All Parameters Measured and Their Range of Values, Flight 31, Run 11.

CHANNEL	UNITS	HIGH	LOW	MEAN	RMS	STD	POINTS
1 TIME	SECONDS	42744.524	42410.524	42577.52400	42577.63319	96.42831	13361
2 PHI DOT	RAD/SEC	.243	-.297	-.00258	.04193	.04185	13361
3 ACCL N CG	G UNITS	1.921	.282	1.00030	1.00958	.13652	13361
4 THETA DOT	RAD/SEC	.080	-.069	.00323	.01449	.01413	13361
5 THETA	RAD	.231	-.060	.04493	.07771	.06340	13361
6 PHI	RAD	.191	-.151	.00474	.03775	.03745	13361
7 PSI 1	RAD	317.907	308.045	312.03280	312.03864	1.90874	13361
8 DEL PSI 1	DEG	1.758	-5.939	-2.20345	2.59711	1.37475	13361
9 PSI 2	RAD	317.446	309.708	313.41944	313.42230	1.33812	13361
10 DEL PSI 2	DEG	2.315	-7.474	-3.44967	3.93773	1.87889	13361
11 ACCL N LT	G UNITS	2.831	-.570	1.01478	1.04608	.25397	13361
12 ACCL N RT	G UNITS	3.031	-.992	1.00930	1.04798	.28212	13361
13 ACCL X CG	G UNITS	.277	-.048	.04825	.07276	.05447	13361
14 ACCL Y CG	G UNITS	.079	-.087	-.00582	.02027	.01942	13361
15 ALPHA CTR	RAD	.093	-.099	-.03402	.03726	.01518	13361
16 BETA CTR	RAD	.134	-.110	.00230	.02316	.02305	13361
17 TEMP I	DEG F	77.936	75.418	76.33933	76.34215	.65622	13361
18 TEMP P	DEG F	60.522	59.803	60.12133	60.12158	.17651	13361
19 ACCL Z INS	G UNITS	2.026	.212	1.00458	1.01391	.13727	13361
20 ALPHA RT	RAD	.117	-.103	-.02010	.02656	.01736	13361
21 BETA RT	RAD	.102	-.111	.01007	.02313	.02082	13361
22 ALPHA LT	RAD	.103	-.075	.00396	.01739	.01693	13361
23 BETA LT	RAD	.095	-.114	.00587	.02247	.02170	13361
24 PSI DOT	RAD/SEC	.062	-.072	.00247	.01883	.01867	13361
25 TEMP TOT	DEG C	14.838	7.761	10.42264	10.50134	1.28327	13361
26 QC LT	PSID	1.131	.697	.88530	.89059	.09692	13361
27 QC CTR	PSID	1.073	.642	.84294	.84811	.09350	13361
28 QC RT	PSID	1.111	.678	.87661	.88197	.09713	13361
29 PS	PSIA	12.360	11.555	11.99907	12.00186	.25857	13361
30 TEMP IRT	VOLTS	6.907	2.154	5.86314	5.91347	.76992	13361
31 HYGRO	DEG C	5.296	-12.105	-1.28782	3.83293	3.61024	13361
32 QC2 LT	PSID	.055	.046	.04946	.04953	.00270	13361
33 QC2 CTR	PSID	.176	.045	.14183	.14603	.03476	13361
34 QC2 RT	PSID	.157	.048	.10622	.11192	.03527	13361
35 DAR	DEG	-5.581	-6.595	-5.95484	5.96258	.30362	13361
36 DAL	DEG	-5.455	-6.474	-5.86257	5.87255	.34235	13361
37 DELEV	DEG	5.150	4.721	4.94840	4.95045	.14219	13361
38 DSTAB	DEG	-.365	-.401	-.38076	.38088	.00980	13361
39 DRUD	DEG	11.768	10.629	11.14561	11.15003	.31395	13361
40 DTHRR	PCT MAX	69.629	67.773	68.66135	68.66343	.53496	13361
41 DTHRL	PCT MAX	70.020	68.555	69.34502	69.34635	.42844	13361
42 DFLP	POSITION	.199	.160	.17571	.17610	.01173	13361
43 DSR	POSITION	.385	.377	.38130	.38130	.00195	13361
44 D TO G	METERS	7488731.174	7476295.334	***********	***********	3613.41976	13361
45 B TO D	DEGREES	72.917	72.682	72.80349	72.80352	.05844	13361
46 LONG	DEGREES	-118.145	-118.408	-118.29182	118.29183	.06476	13361
47 LAT	DEGREES	35.279	35.068	35.17133	35.17138	.06122	13361
48 TRK ANG	DEGREES	323.287	315.629	319.11203	319.11605	1.60058	13361
49 HDG	RADIANS	5.540	5.403	5.46971	5.46976	.02472	13361
50 VE	M/SEC	-48.801	-70.119	-60.83340	61.12096	5.92217	13361
51 VN	M/SEC	78.098	61.578	70.05216	70.15772	3.84730	13361
52 ALTITUDE	KM	1.982	1.436	1.67899	1.68811	.17527	13361
53 TEMPC	DEGREES C	9.358	2.050	4.97288	5.19533	1.50402	13361
54 EW WND SPD	KNOTS	50.745	-.783	29.72031	30.54943	7.06926	13361
55 NS WND SPD	KNOTS	13.282	-20.941	-2.84523	5.43256	4.62806	13361
56 WIND SPEED	KNOTS	51.255	1.561	30.15062	31.02870	7.32968	13361
57 WIND DIREC	DEGREES	351.415	.514	274.81485	274.95634	8.81949	13361
58 WIND DIR2	DEGREES	171.415	-179.486	94.81491	95.22418	8.81951	13361
59 WIND DIR3	DEGREES	351.415	.514	274.81491	274.95638	8.81951	13361
60 WIND DIR4	DEGREES	360.514	170.629	274.84186	274.97407	8.52648	13361
61 AIRSPEED R	M/SEC	119.933	93.356	106.49303	106.66015	5.95865	13361
62 AIRSPEED C	M/SEC	117.888	91.089	104.47815	104.64248	5.86239	13361
63 AIRSPEED L	M/SEC	120.976	94.575	107.01063	107.17339	5.90453	13361
64 DELTA ALT	METERS	479.601	-66.303	176.23842	248.54884	175.26792	13361
65 INRTL DISP	METERS	482.138	-65.140	176.29089	249.21271	176.15566	13361
66 UG RIGHT	M/SEC	12.725	-12.248	.00000	3.74045	3.74059	13361
67 UG CENTER	M/SEC	14.045	-11.984	.00000	3.76809	3.76823	13361
68 UG LEFT	M/SEC	13.679	-11.644	.00000	3.76992	3.77006	13361
69 VG RIGHT	M/SEC	10.493	-13.391	.06674	2.10268	2.10170	13361
70 VG CENTER	M/SEC	11.621	-12.951	.07479	2.15170	2.15048	13361
71 VG LEFT	M/SEC	11.150	-13.614	.07139	2.18210	2.18101	13361
72 WG RIGHT	M/SEC	10.645	-10.886	.12791	2.26216	2.25862	13361
73 WG CENTER	M/SEC	8.463	-9.910	.13005	2.00237	1.99822	13361
74 WG LEFT	M/SEC	9.325	-10.727	.12349	2.13430	2.13081	13361

Flight 31, Run 12
Date: Nov. 29, 1982
Start Time: 11:56:50 (PST)
Duration: 136.9 seconds

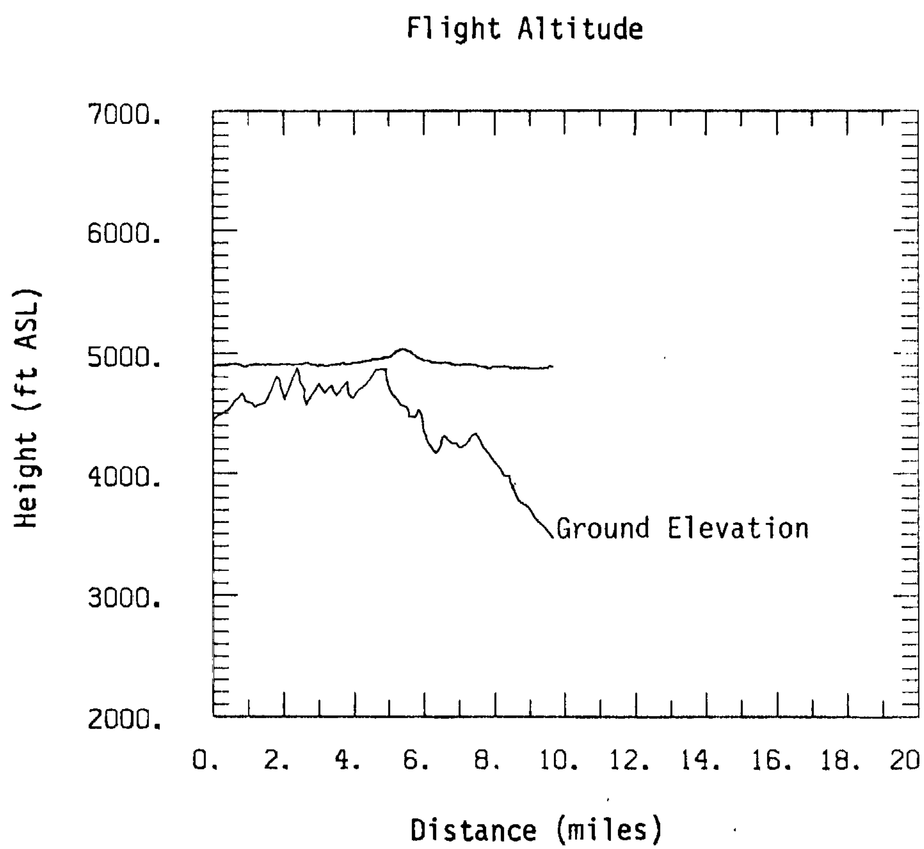

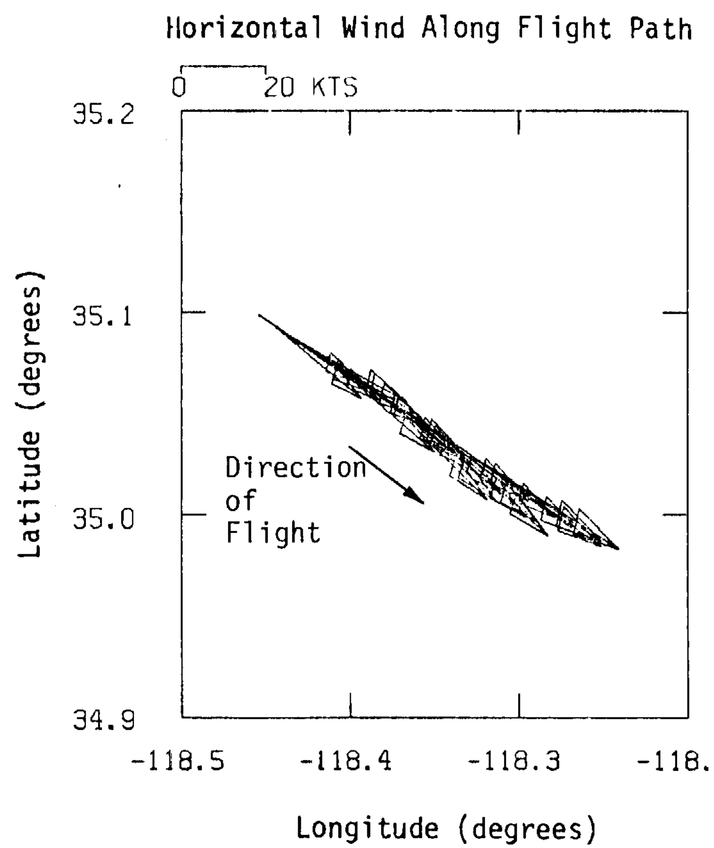

Figure A.56. Flight altitude and horizontal wind along flight path, Flight 31, Run 12.

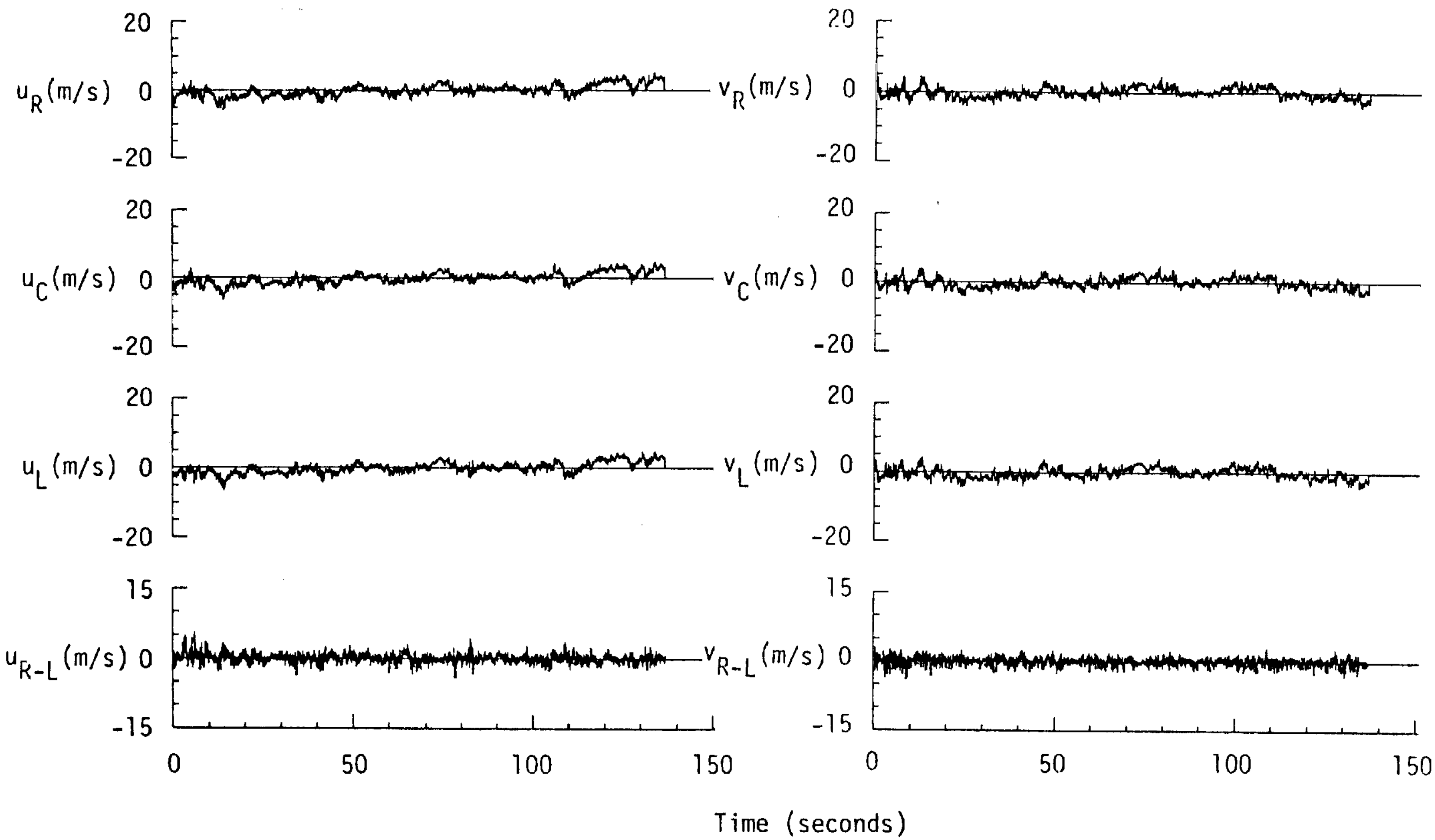

Figure A.57. Time histories of gust velocities, gust velocity differences, and aircraft's normal accelerations, Flight 31, Run 12.

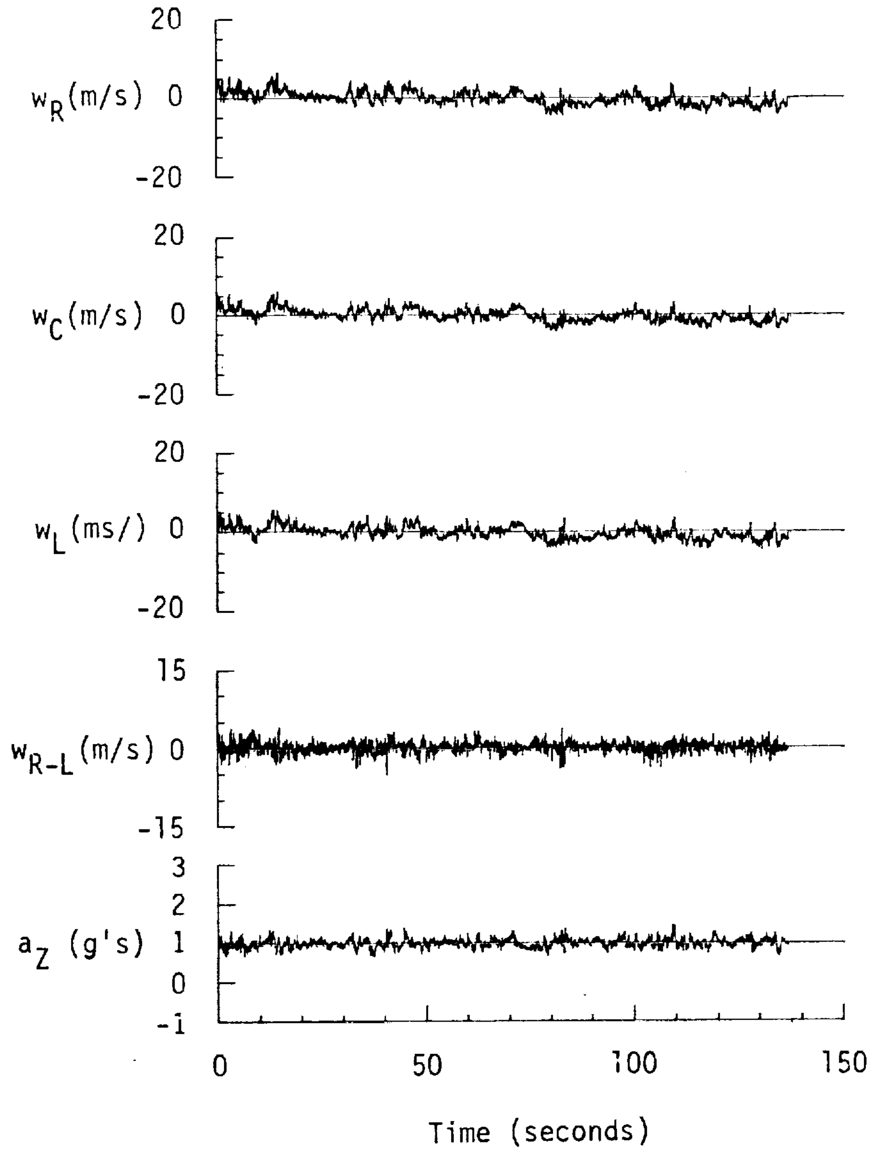

Figure A.57. (continued).

TABLE A.23. Average Turbulence Parameters, Integral Length Scales, and Correlation Coefficients of Gust Velocities, Flight 31, Run 12.

1. Mean Airspeed (m/s):

$\overline{V}_L$	$\overline{V}_C$	$\overline{V}_R$
101.03	98.55	100.56

2. Standard Deviation of Gust Velocities (m/s):

σ_{uR}	σ_{vR}	σ_{wR}
1.68	1.43	1.66

σ_{uC}	σ_{vC}	σ_{wC}
1.68	1.47	1.54

σ_{uL}	σ_{vL}	σ_{wL}
1.70	1.42	1.59

3. Standard Deviation of Gust Velocity Differences (m/s):

$\sigma_{\Delta uRL}$	$\sigma_{\Delta vRL}$	$\sigma_{\Delta wRL}$
0.90	0.74	0.91

4. Integral Length Scale #1 (m):

L_{uR}	L_{vR}	L_{wR}
127.7	252.6	202.4

L_{uRL}	L_{vRL}	L_{wRL}
137.5	250.1	190.8

5. Correlation Coefficient of Gust Velocities:

$\overline{u_R u_L}/\sigma_{u_R}\sigma_{u_L}$	$\overline{v_R v_L}/\sigma_{v_R}\sigma_{v_L}$	$\overline{w_R w_L}/\sigma_{w_R}\sigma_{w_L}$
0.66	0.81	0.78

$\overline{u_R v_R}/\sigma_{u_R}\sigma_{v_R}$	$\overline{v_R w_R}/\sigma_{v_R}\sigma_{w_R}$	$\overline{w_R u_R}/\sigma_{w_R}\sigma_{u_R}$
0.00	0.30	-0.22

$\overline{u_R v_L}/\sigma_{u_R}\sigma_{v_L}$	$\overline{v_R w_L}/\sigma_{v_R}\sigma_{w_L}$	$\overline{w_R u_L}/\sigma_{w_R}\sigma_{u_L}$
0.01	0.31	-0.20

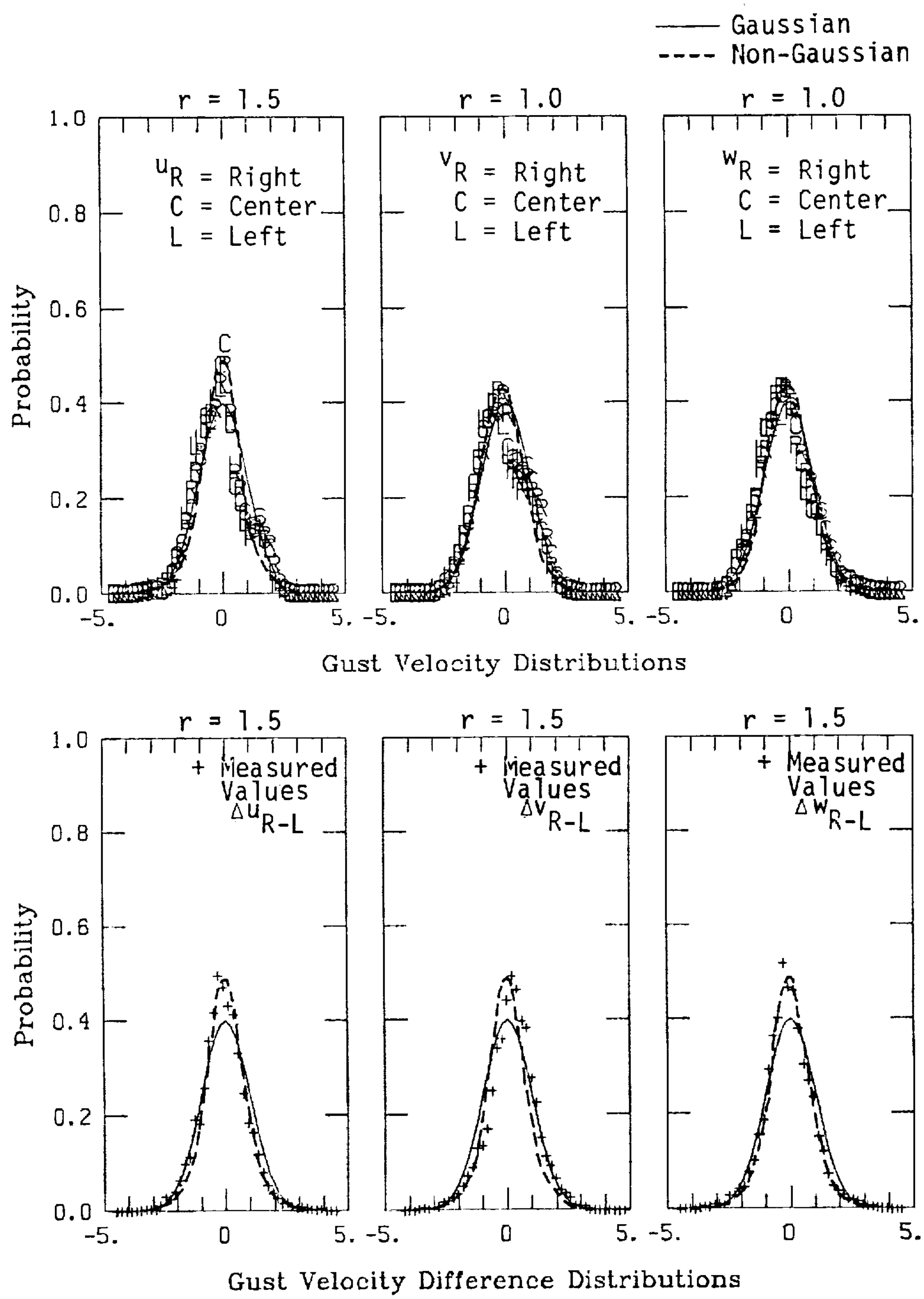

Figure A.58. Probability density functions for gust velocities and gust velocity differences (normalized with the standard deviation), Flight 31, Run 12 (r = degree of non-Gaussian).

C-4

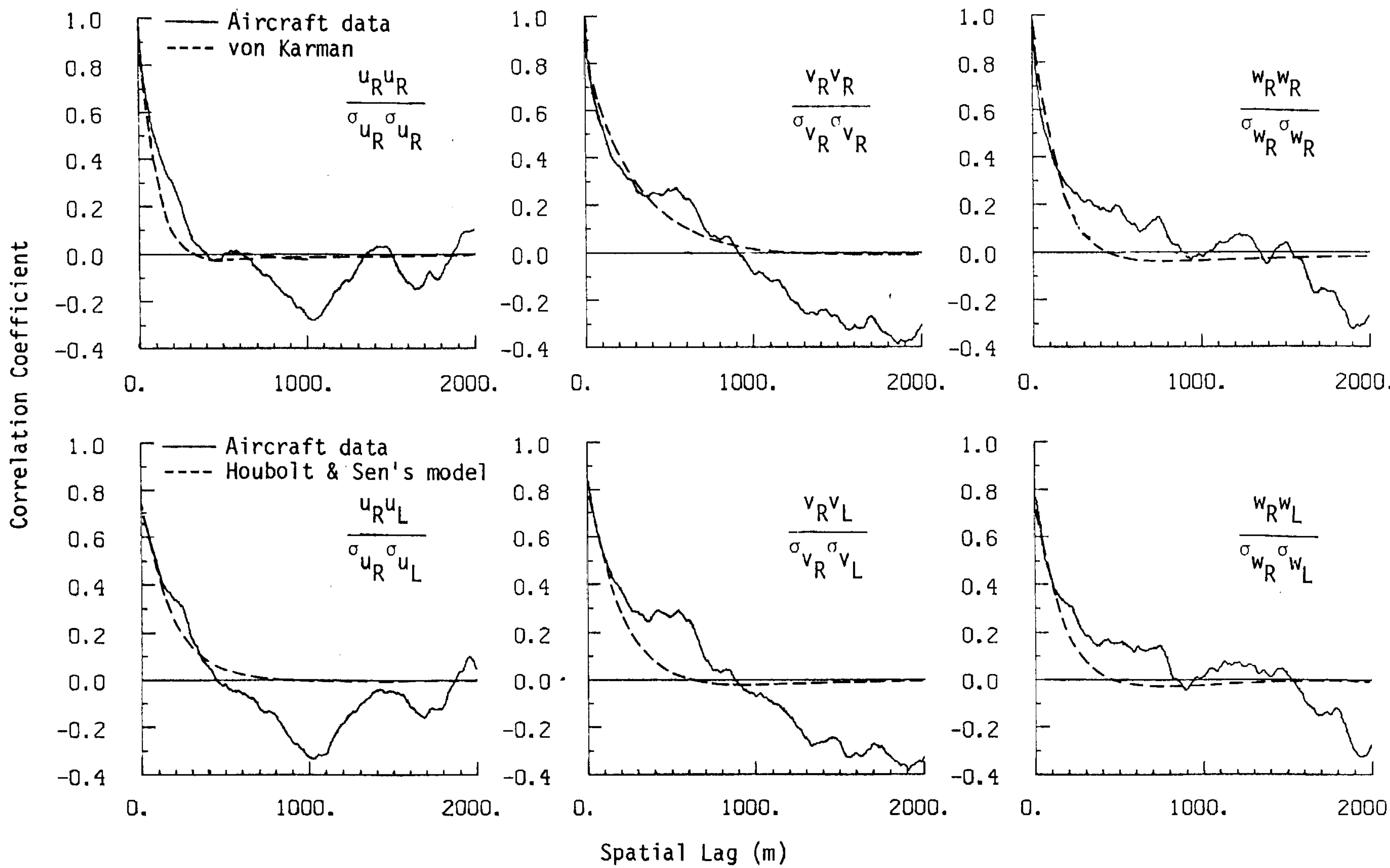

a. One- and two-point common component spectra.

Figure A.59. Comparison of normalized one- and two-point correlation functions for gust velocities with theoretical models, Flight 31, Run 12.

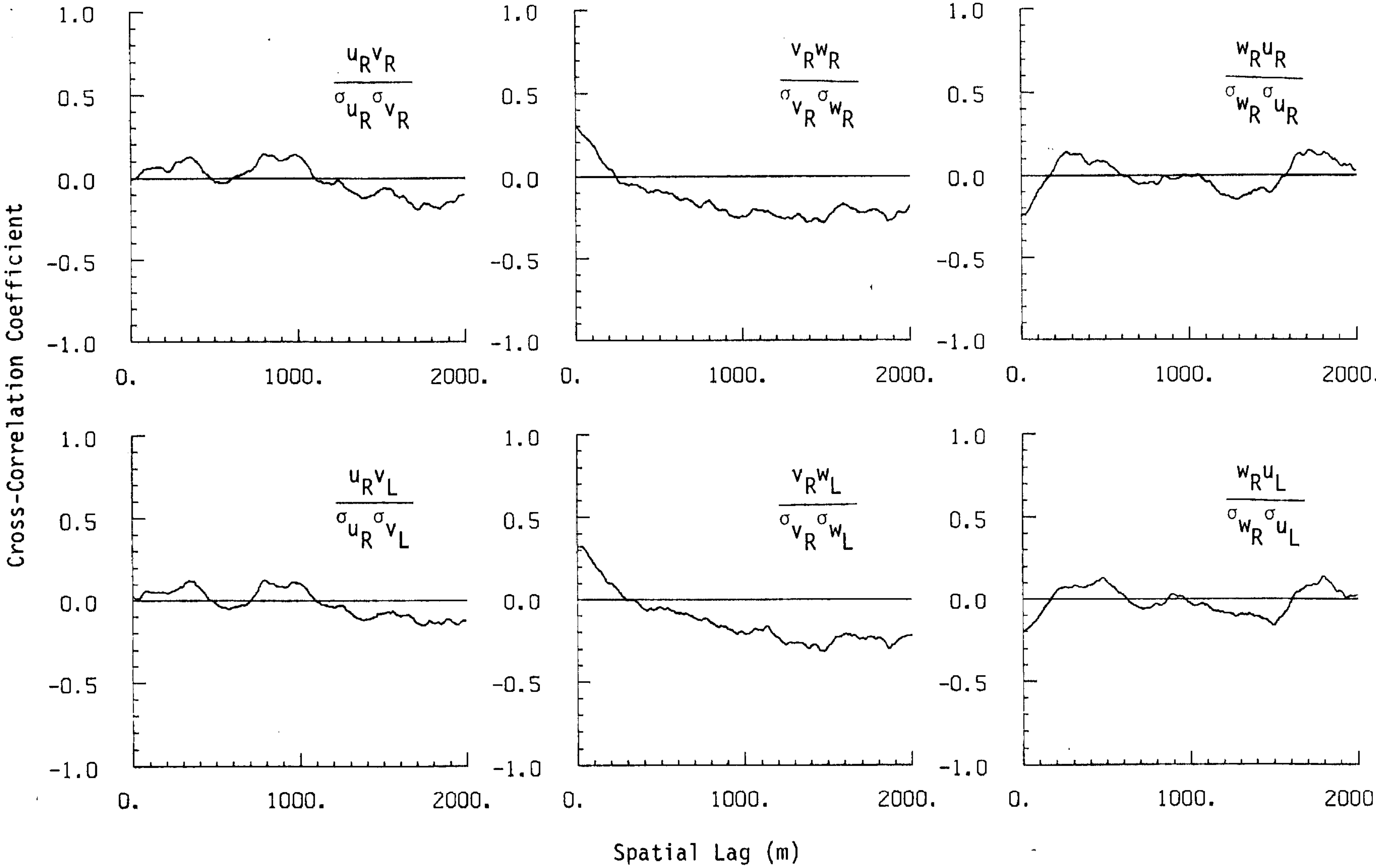

b. One- and two-point cross-correlations.

Figure A.59. (continued).

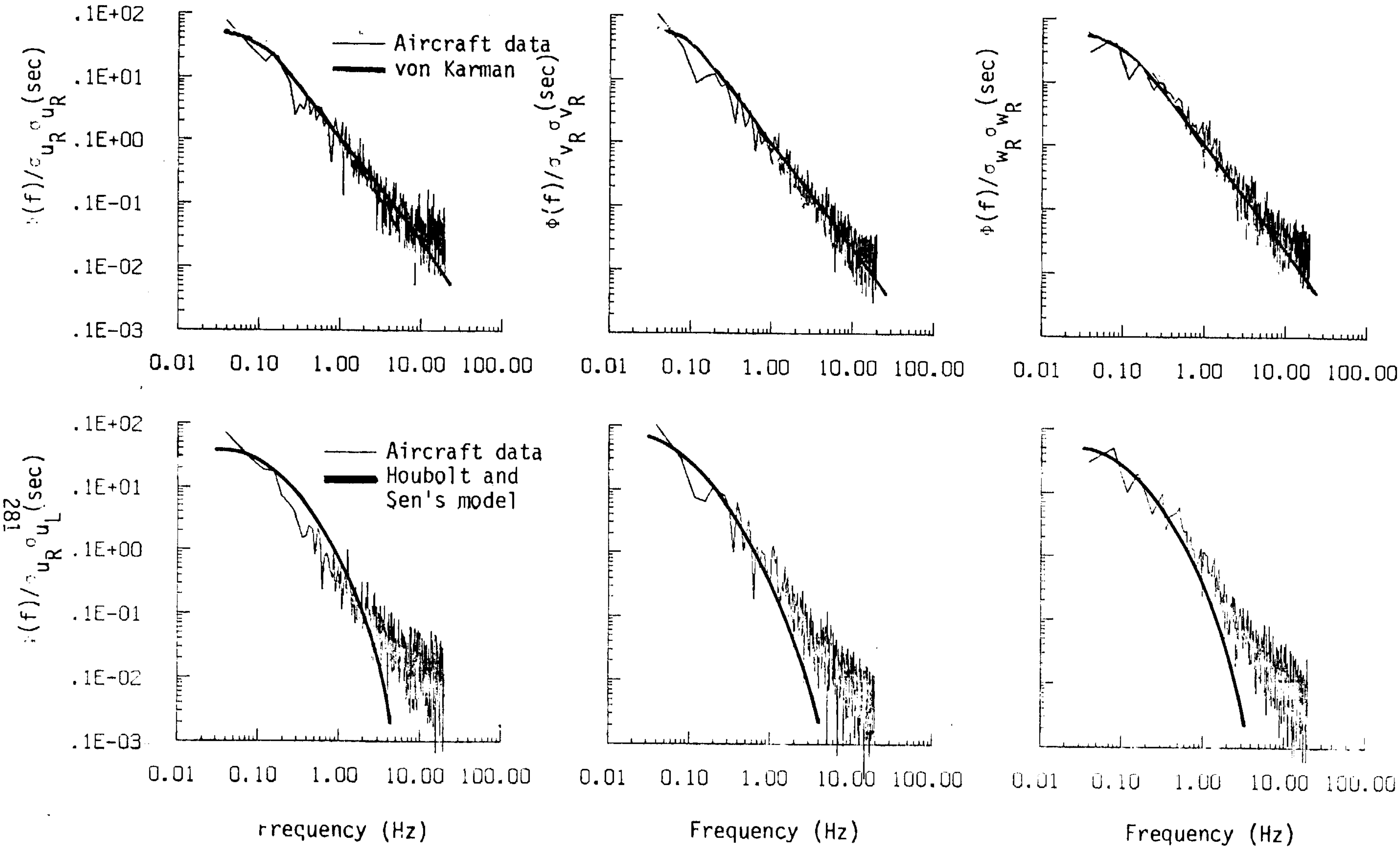

a. One- and two-point common component spectra.

Figure A.60. Comparison of normalized one- and two-point spectral density functions for gust velocities with theoretical models, Flight 31, Run 12.

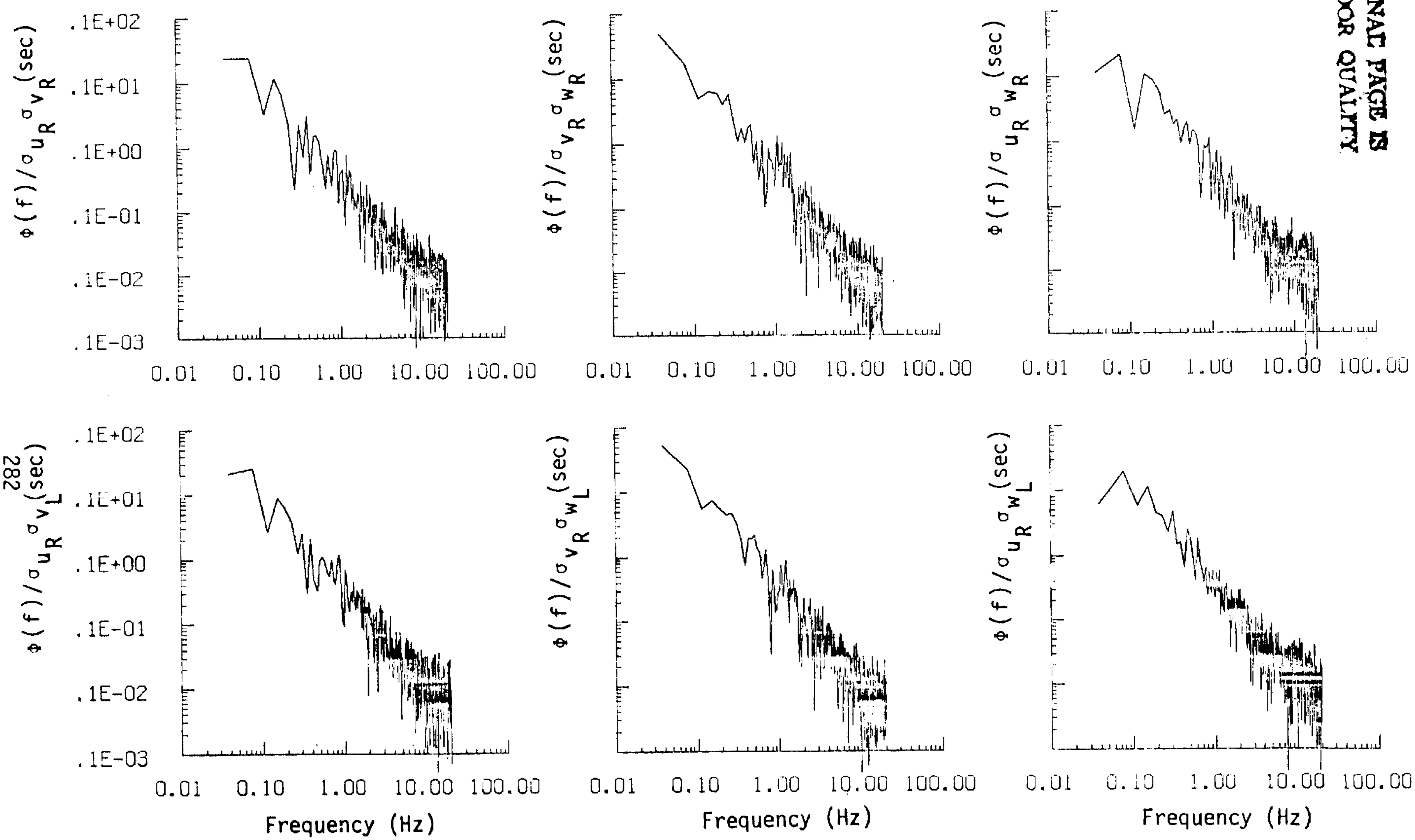

b. One- and two-point cruss-spectra.

Figure A.60. (continued).

ORIGINAL PAGE IS
OF POOR QUALITY

TABLE A.24. List of All Parameters Measured and Their Range of Values, Flight 31, Run 12.

	CHANNEL	UNITS	HIGH	LOW	MEAN	RMS	STD	POINTS
1	TIME	SECONDS	43146.508	43009.608	43078.05820	43078.07633	39.53045	5477
2	PHI DOT	RAD/SEC	.085	-.127	-.00254	.03036	.03025	5477
3	ACCL N CG	G UNITS	1.361	.659	.99898	1.00374	.09762	5477
4	THETA DOT	RAD/SEC	.048	-.045	.00352	.00997	.00933	5477
5	THETA	RAD	.080	.019	.04871	.05036	.01278	5477
6	PHI	RAD	.079	-.115	.00130	.02959	.02957	5477
7	PSI 1	RAD	125.590	118.898	123.04541	123.04938	.98859	5477
8	DEL PSI 1	DEG	-.064	-6.618	-2.50441	2.69251	.98878	5477
9	PSI 2	RAD	487.491	481.154	484.99578	484.99675	.96953	5477
10	DEL PSI 2	DEG	.253	-6.241	-2.14914	2.36268	.98165	5477
11	ACCL N LT	G UNITS	1.895	.291	1.01263	1.03064	.19181	5477
12	ACCL N RT	G UNITS	1.985	.118	1.00737	1.02931	.21142	5477
13	ACCL X CG	G UNITS	.084	.019	.05120	.05215	.00991	5477
14	ACCL Y CG	G UNITS	.077	-.089	-.00260	.01831	.01821	5477
15	ALPHA CTR	RAD	.017	-.064	-.02879	.03050	.01006	5477
16	BETA CTR	RAD	.091	-.058	.00713	.01935	.01799	5477
17	TEMP I	DEG F	76.317	75.777	75.98189	75.98198	.11839	5477
18	TEMP P	DEG F	59.623	59.264	59.37862	59.37867	.08324	5477
19	ACCL Z INS	G UNITS	1.429	.694	1.00272	1.00777	.10075	5477
20	ALPHA RT	RAD	.040	-.045	-.00789	.01387	.01141	5477
21	BETA RT	RAD	.093	-.050	.01628	.02315	.01646	5477
22	ALPHA LT	RAD	.054	-.024	.00978	.01453	.01075	5477
23	BETA LT	RAD	.089	-.057	.01092	.02021	.01701	5477
24	PSI DOT	RAD/SEC	.062	-.039	.00275	.01400	.01373	5477
25	TEMP TOT	DEG C	12.290	10.420	11.36615	11.37100	.33193	5477
26	QC LT	PSID	.890	.724	.79800	.79845	.02679	5477
27	QC CTR	PSID	.844	.657	.75843	.75888	.02617	5477
28	QC RT	PSID	.878	.691	.79030	.79079	.02775	5477
29	PS	PSIA	12.288	12.210	12.26465	12.26466	.01582	5477
30	TEMP IRT	VOLTS	7.371	6.441	6.83268	6.83772	.26243	5477
31	HYGROM	DEG C	5.492	-5.031	1.67550	2.36224	1.66535	5477
32	QC2 LT	PSID	.061	.058	.06018	.06019	.03096	5477
33	QC2 CTR	PSID	.148	.051	.11009	.11349	.02755	5477
34	QC2 RT	PSID	.102	.054	.07379	.07525	.01478	5477
35	DAR	DEG	-7.153	-8.391	-7.83437	7.84320	.37219	5477
36	DAL	DEG	-7.384	-7.685	-7.58950	7.58894	.08170	5477
37	DELEV	DEG	5.735	5.345	5.59463	5.59577	.11281	5477
38	DSTAB	DEG	-.369	-.397	-.38415	.38423	.00777	5477
39	DRUD	DEG	10.800	10.402	10.56419	10.56483	.11703	5477
40	DTHRR	PCT MAX	67.090	66.797	66.89861	66.89867	.09199	5477
41	DTHRL	PCT MAX	67.578	67.285	67.39736	67.39738	.05194	5477
42	DFLP	POSITION	.262	.242	.25280	.25286	.00574	5477
43	DSB	POSITION	.355	.346	.35014	.35015	.05260	5477
44	D TO G	METERS	7476017.357	7466219.866	***********	***********	2831.84466	5477
45	B TO D	DEGREES	72.849	72.721	72.78431	72.78432	.03700	5477
46	LONG	DEGREES	-118.314	-118.456	-118.38538	118.38538	.04115	5477
47	LAT	DEGREES	35.100	35.022	35.06193	35.06194	.02271	5477
48	TRK ANG	DEGREES	125.725	122.180	123.77760	123.78055	.85450	5477
49	HDG	RADIANS	2.215	2.099	2.17235	2.17242	.01771	5477
50	VE	M/SEC	96.407	90.972	94.81797	94.82539	1.18670	5477
51	VN	M/SEC	-59.341	-67.331	-63.38432	63.42055	2.14352	5477
52	ALTITUDE	KM	1.536	1.484	1.49943	1.49947	.01052	5477
53	TEMPC	DEGREES C	7.652	5.859	6.53056	6.53845	.32108	5477
54	EW WND SPD	KNOTS	36.236	15.498	25.60554	25.79823	3.14750	5477
55	NS WND SPD	KNOTS	-6.464	-24.517	-15.96008	16.23665	2.98432	5477
56	WIND SPEED	KNOTS	39.577	18.278	30.30926	30.48241	3.24470	5477
57	WIND DIREC	DEGREES	319.429	285.223	301.91526	301.96541	5.50373	5477
58	WIND DIR2	DEGREES	139.429	105.223	121.91532	122.03947	5.50373	5477
59	WIND DIR3	DEGREES	319.429	285.223	301.91532	301.96548	5.50373	5477
60	WIND DIR4	DEGREES	319.429	285.223	301.91532	301.96548	5.50373	5477
61	AIRSPEED R	M/SEC	105.825	94.100	100.56052	100.57521	1.71901	5477
62	AIRSPEED C	M/SEC	103.801	91.856	98.55595	98.56983	1.65438	5477
63	AIRSPEED L	M/SEC	106.555	96.417	101.03982	101.05322	1.64618	5477
64	DELTA ALT	METERS	42.685	-9.433	6.09335	12.15562	10.51905	5477
65	INRTL DISP	METERS	37.675	-6.733	6.43163	11.87560	9.98409	5477
66	UG RIGHT	M/SEC	5.091	-5.619	.00000	1.68865	1.68880	5477
67	UG CENTER	M/SEC	4.728	-6.367	.00000	1.68332	1.68347	5477
68	UG LEFT	M/SEC	4.886	-6.301	.00000	1.70633	1.70649	5477
69	VG RIGHT	M/SEC	4.507	-3.960	-.00207	1.43489	1.43502	5477
70	VG CENTER	M/SEC	4.764	-3.920	-.00122	1.47317	1.47330	5477
71	VG LEFT	M/SEC	4.193	-3.940	-.00148	1.42311	1.42324	5477
72	WG RIGHT	M/SEC	6.515	-4.363	-.00572	1.66421	1.66435	5477
73	WG CENTER	M/SEC	6.134	-4.002	-.00464	1.54289	1.54303	5477
74	WG LEFT	M/SEC	5.661	-4.071	-.00385	1.59581	1.59595	5477

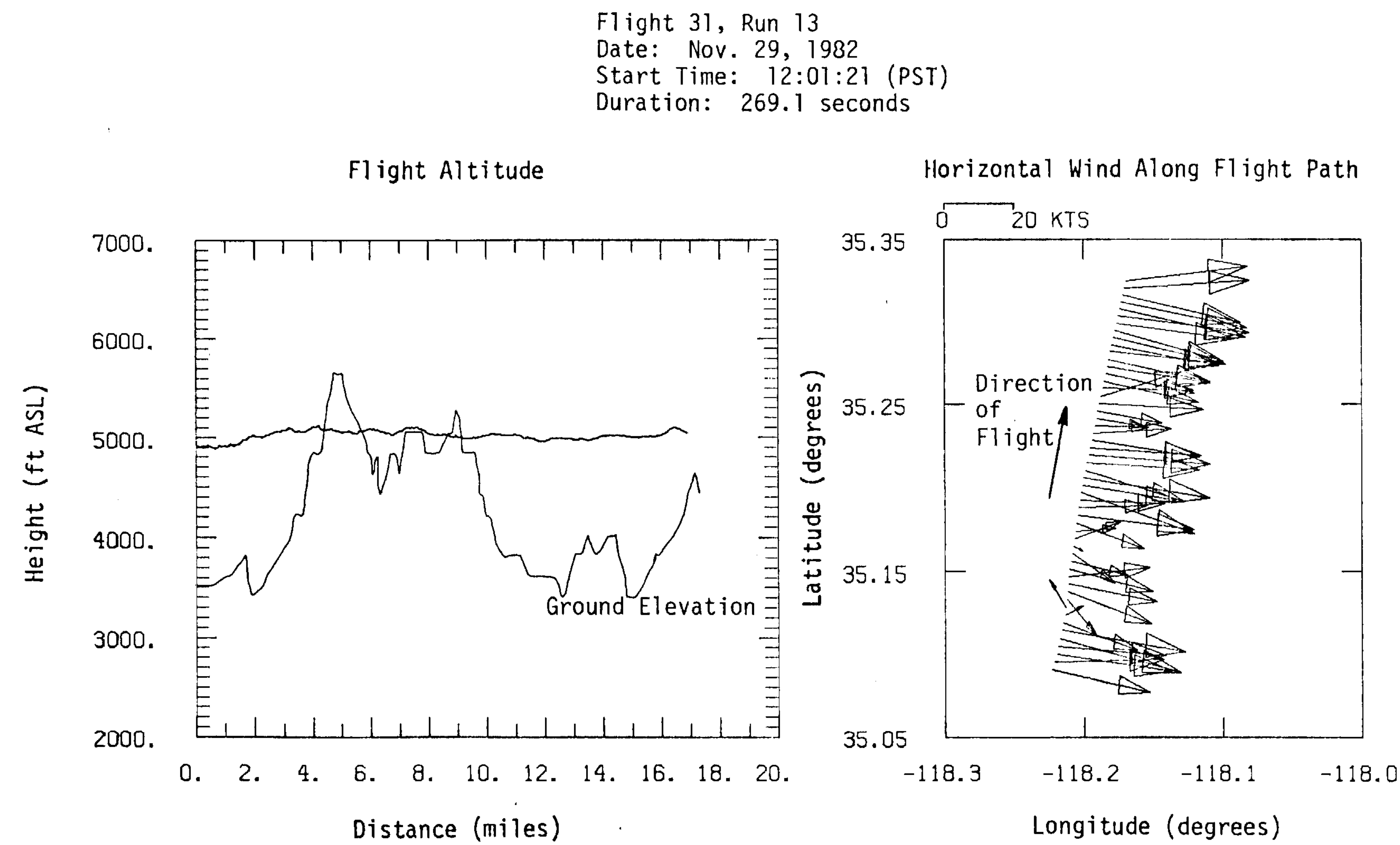

Figure A.61. Flight altitude and horizontal wind along flight path, Flight 31, Run 13.

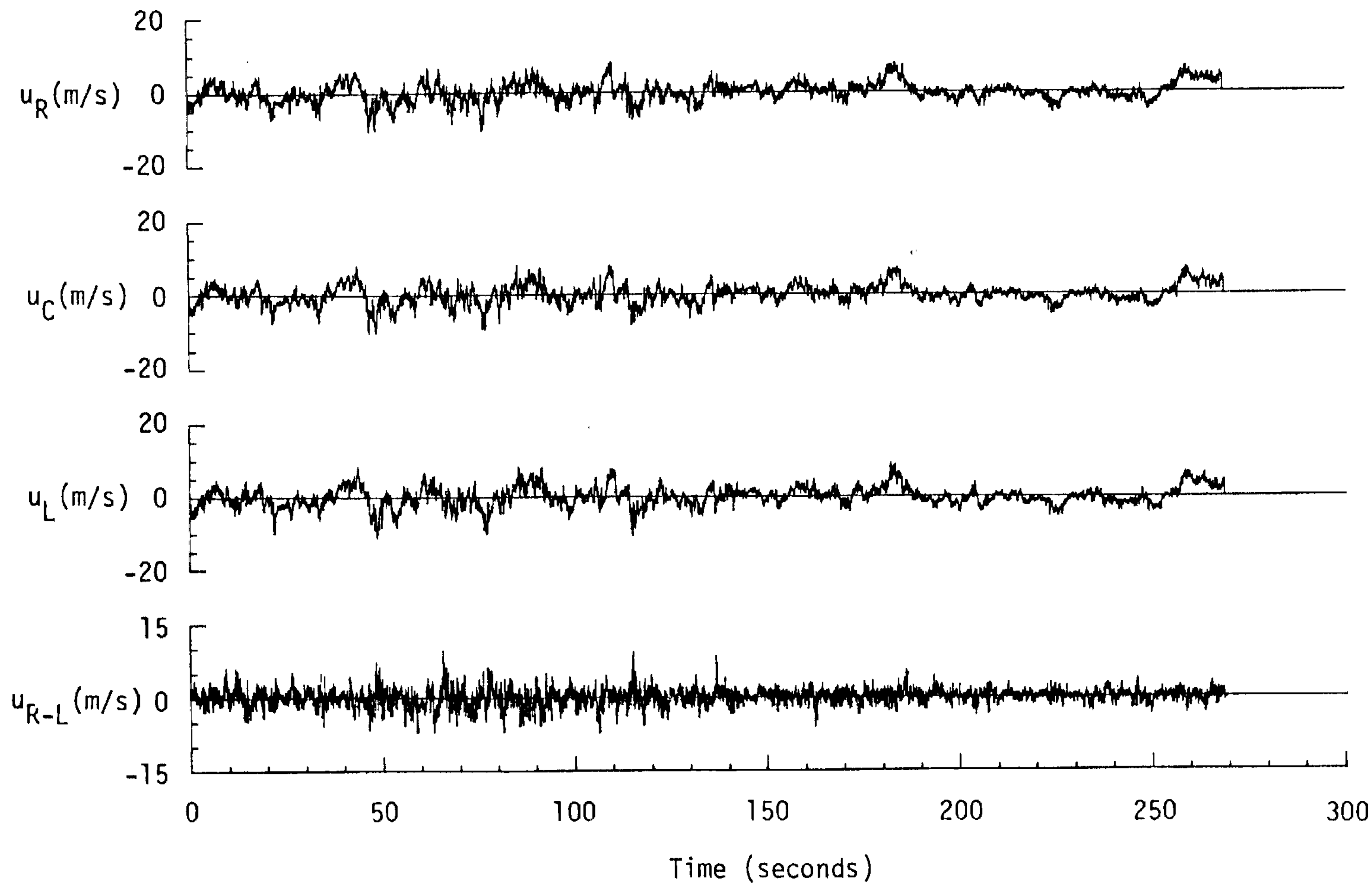

Figure A.62. Time histories of gust velocities, gust velocity differences, and aircraft's normal accelerations, Flight 31, Run 13.

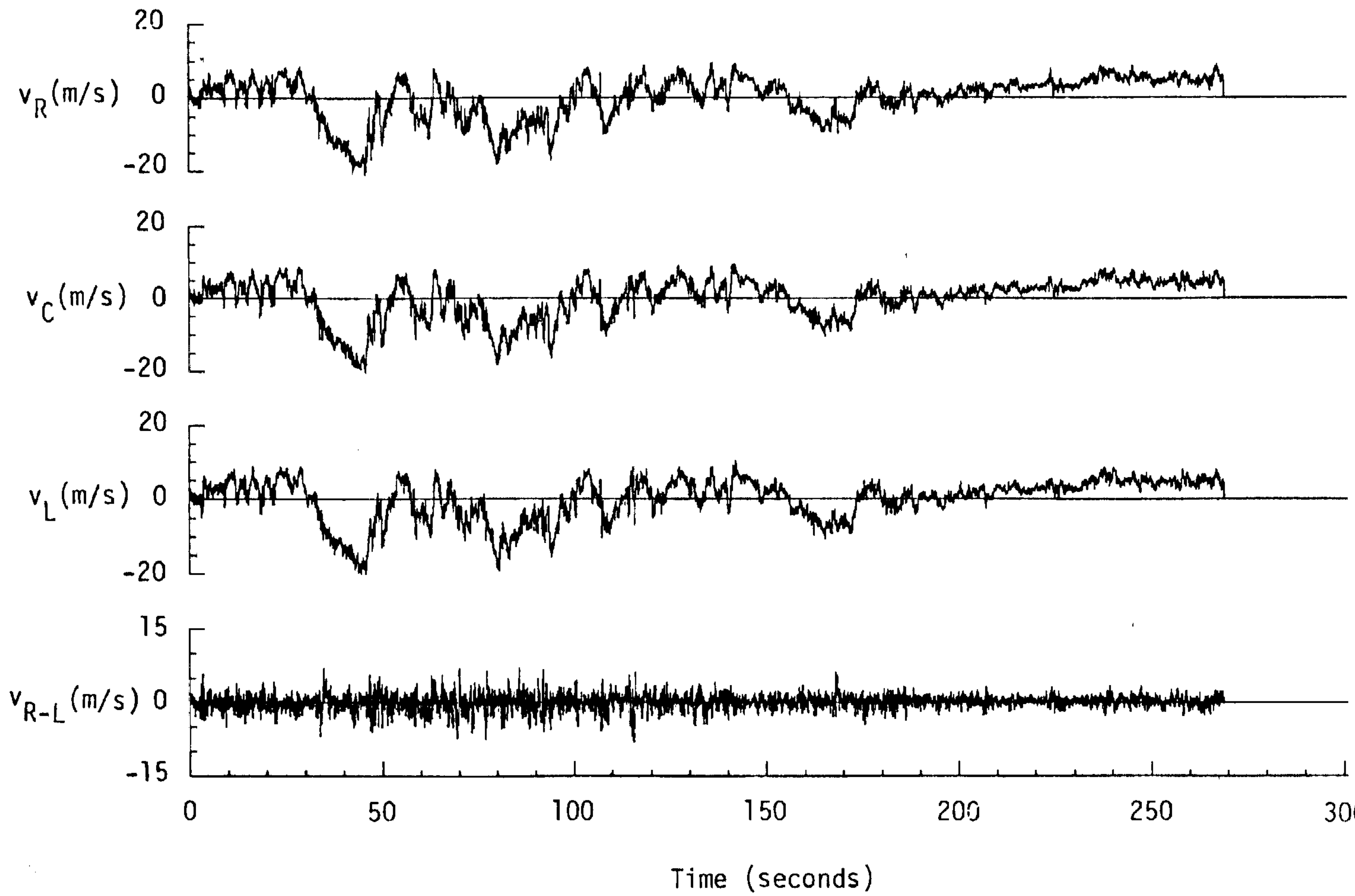

Figure A.62. (continued).

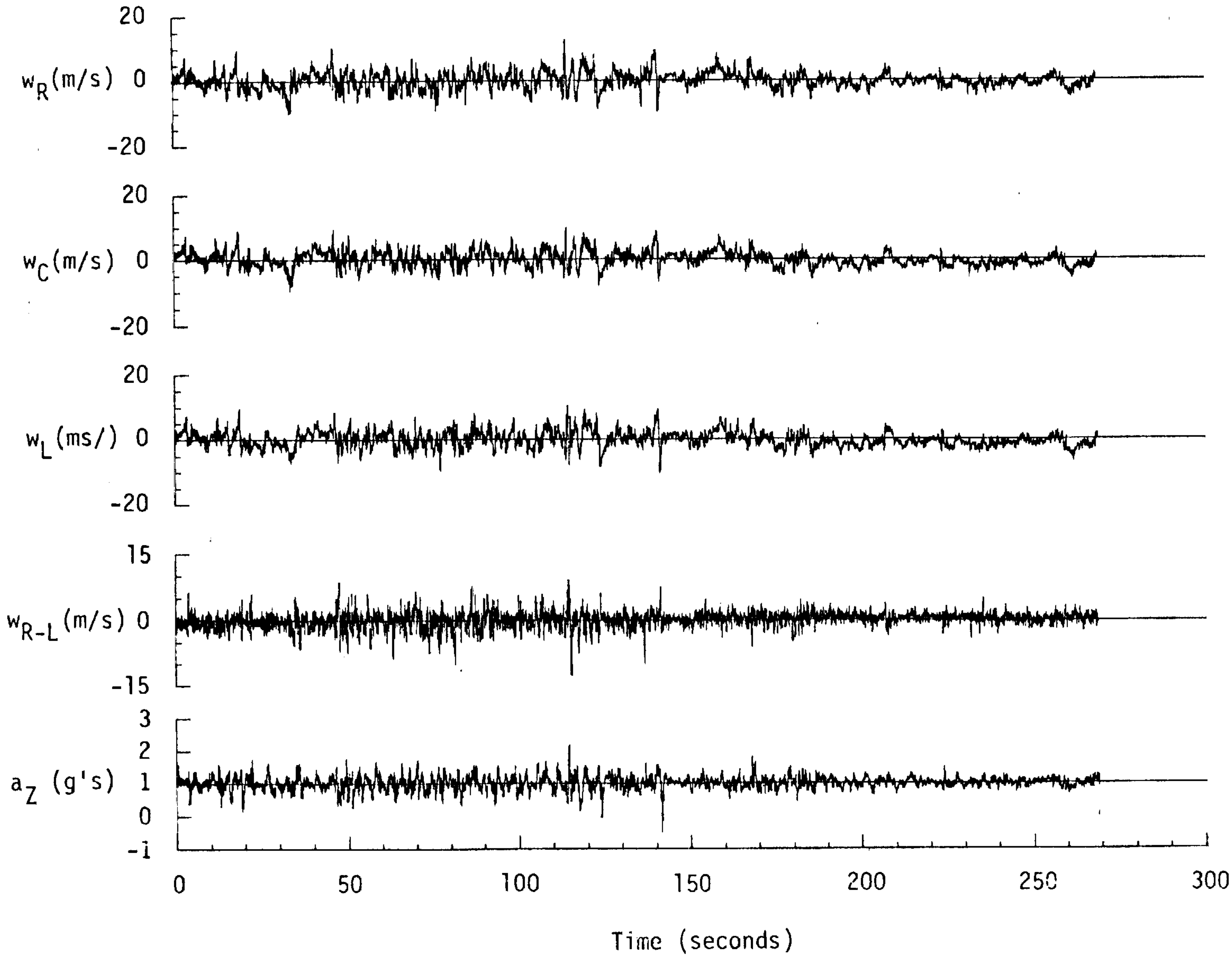

Figure A.62. (continued).

TABLE A.25. Average Turbulence Parameters, Integral Length Scales, and Correlation Coefficients of Gust Velocities, Flight 31, Run 13.

1. Mean Airspeed (m/s):

$\overline{V}_L$	$\overline{V}_C$	$\overline{V}_R$
103.30	101.40	103.30

2. Standard Deviation of Gust Velocities (m/s):

σ_{uR}	σ_{vR}	σ_{wR}
2.49	5.57	2.43

σ_{uC}	σ_{vC}	σ_{wC}
2.48	5.57	2.29

σ_{uL}	σ_{vL}	σ_{wL}
2.59	5.56	2.41

3. Standard Deviation of Gust Velocity Differences (m/s):

$\sigma_{\Delta uRL}$	$\sigma_{\Delta vRL}$	$\sigma_{\Delta wRL}$
1.53	1.39	1.59

4. Integral Length Scale #1 (m):

L_{uR}	L_{vR}	L_{wR}
156.0	428.8	83.7

L_{uRL}	L_{vRL}	L_{wRL}
148.6	424.4	82.6

5. Correlation Coefficient of Gust Velocities:

$\overline{u_R u_L}/\sigma_{u_R}\sigma_{u_L}$	$\overline{v_R v_L}/\sigma_{v_R}\sigma_{v_L}$	$\overline{w_R w_L}/\sigma_{w_R}\sigma_{w_L}$
0.80	0.91	0.79

$\overline{u_R v_R}/\sigma_{u_R}\sigma_{v_R}$	$\overline{v_R w_R}/\sigma_{v_R}\sigma_{w_R}$	$\overline{w_R u_R}/\sigma_{w_R}\sigma_{u_R}$
-0.18	-0.32	0.25

$\overline{u_R v_L}/\sigma_{u_R}\sigma_{v_L}$	$\overline{v_R w_L}/\sigma_{v_R}\sigma_{w_L}$	$\overline{w_R u_L}/\sigma_{w_R}\sigma_{u_L}$
-0.19	-0.32	0.22

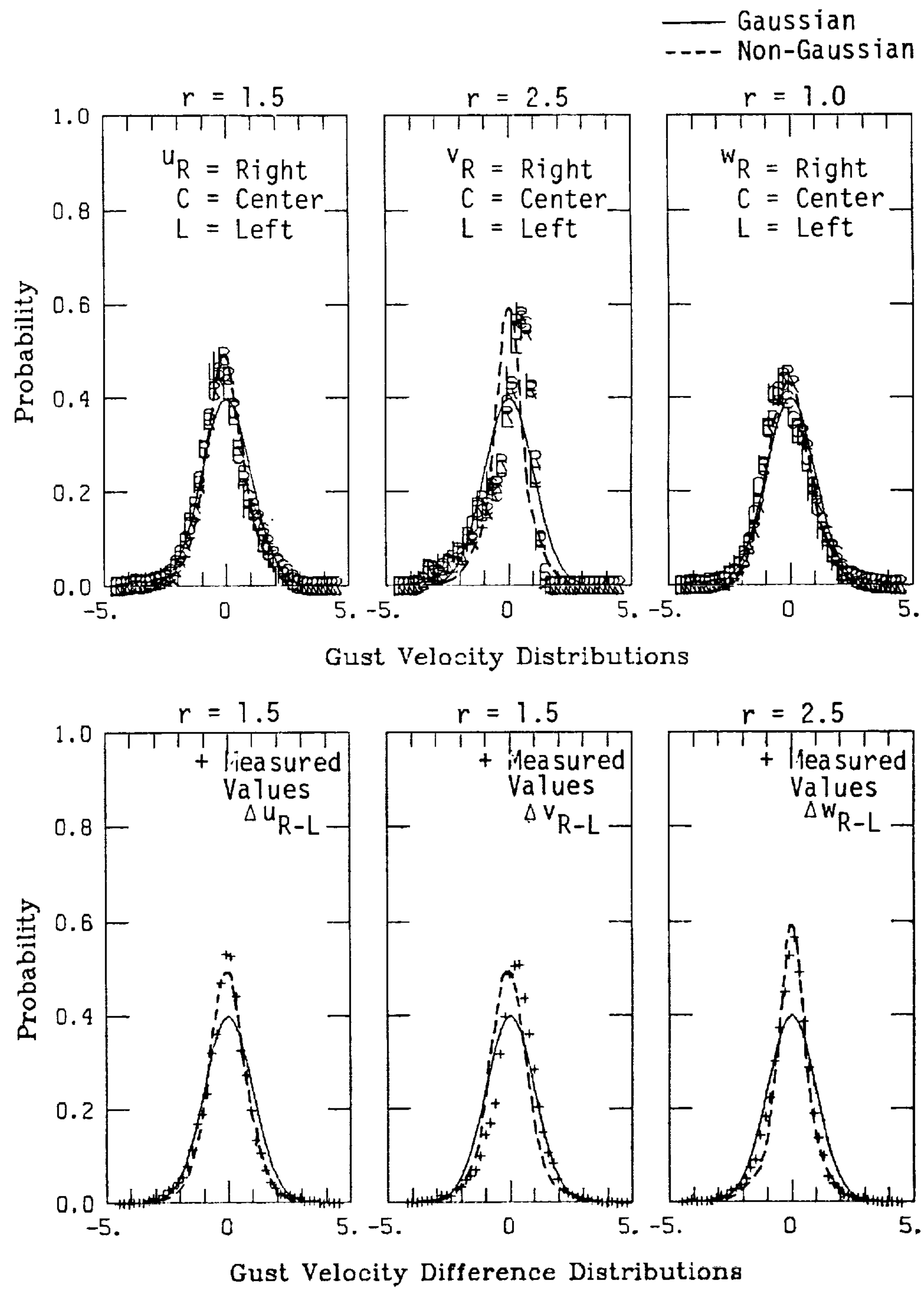

Figure A.59. Probability density functions for gust velocities and gust velocity differences (normalized with the standard deviation), Flight 31, Run 13 (r = degree of non-Gaussian).

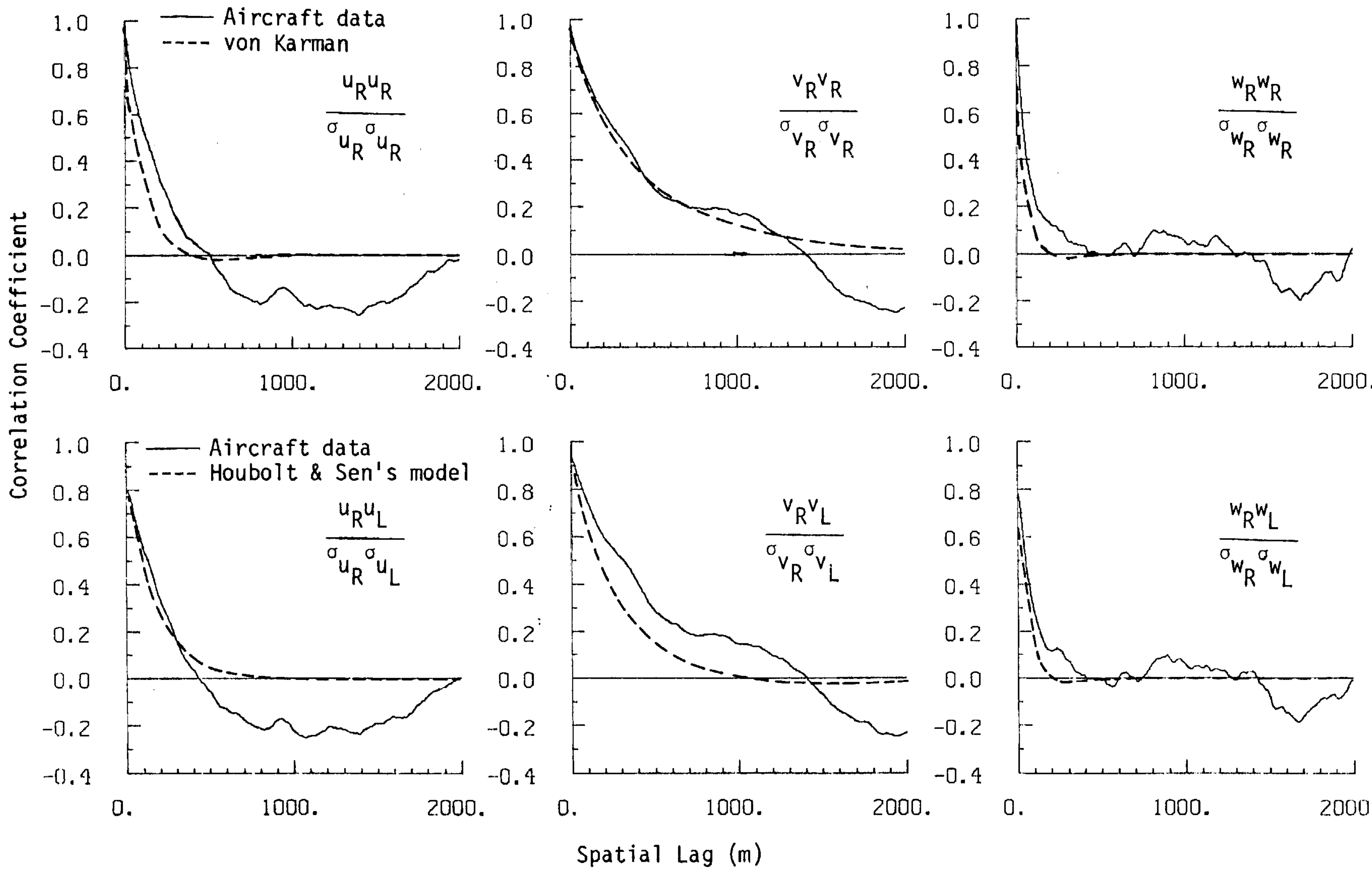

a. One- and two-point common component correlations.

Figure A.64. Comparison of normalized one- and two-point correlation functions for gust velocities with theoretical models, Flight 31, Run 13.

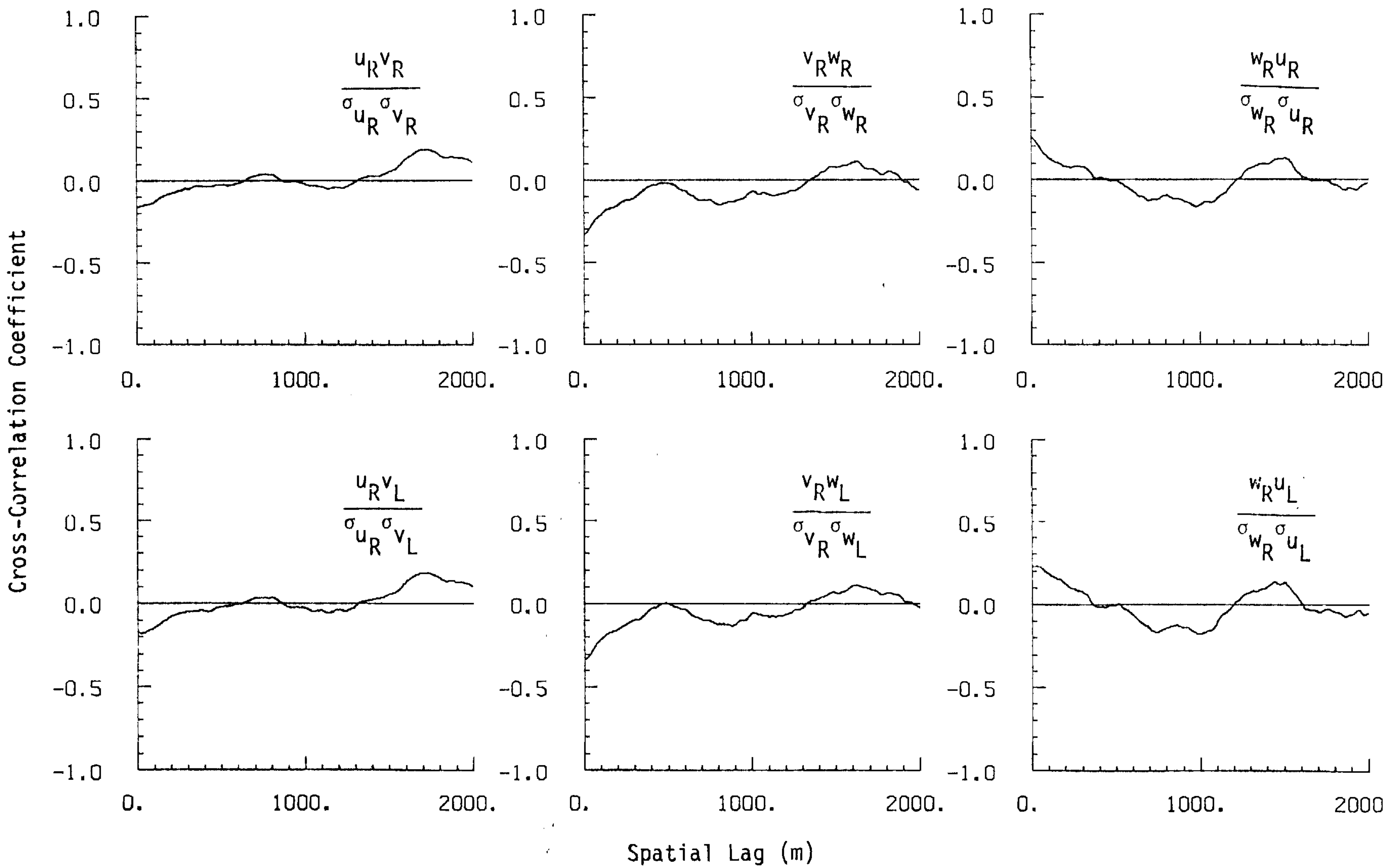

b. One- and two-point cross-correlations.

Figure A.64. (continued).

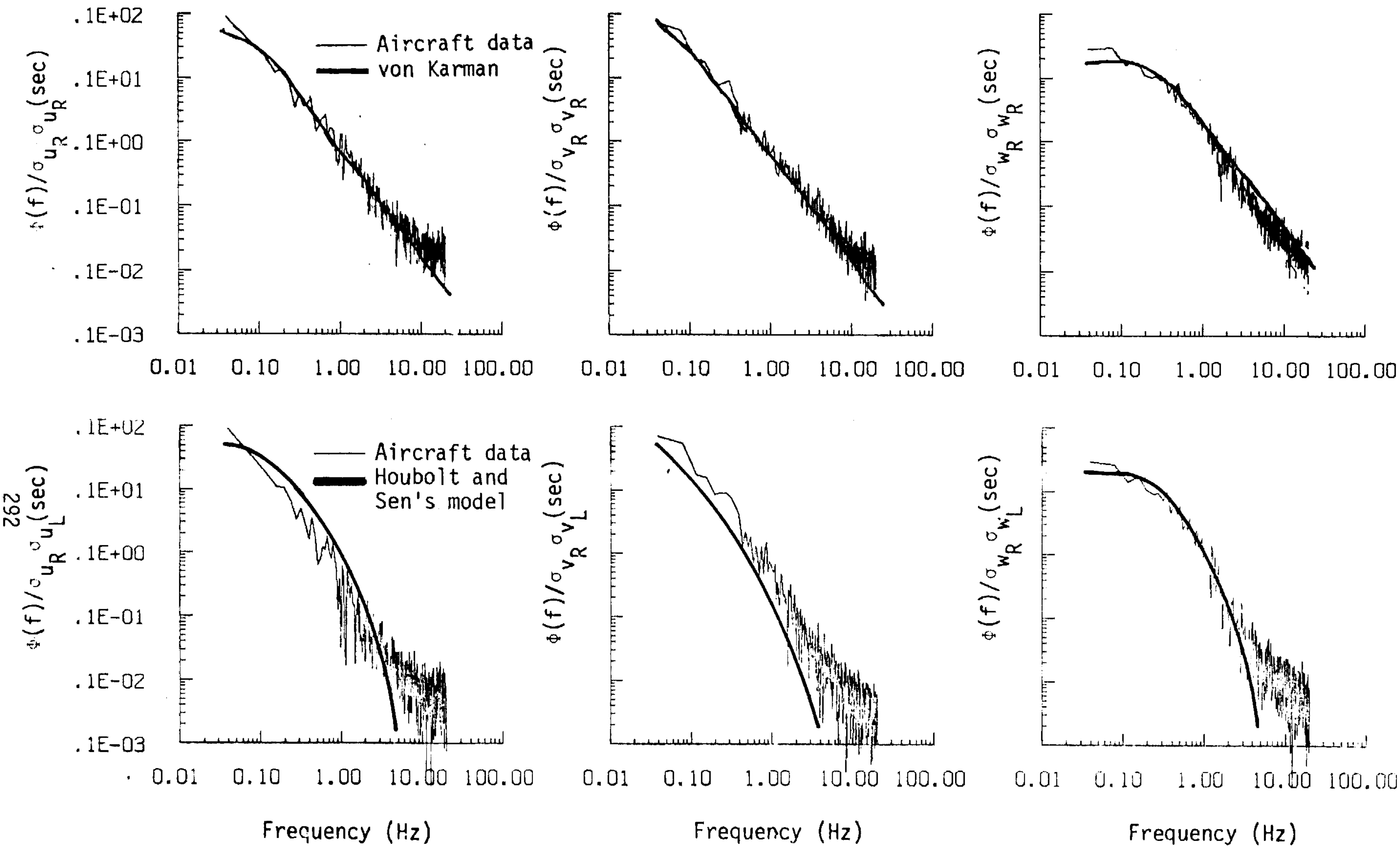

a. One- and two-point common component spectra.

Figure A.65. Comparison of normalized one- and two-point spectral density functions for gust velocities with theoretical models, Flight 31, Run 13.

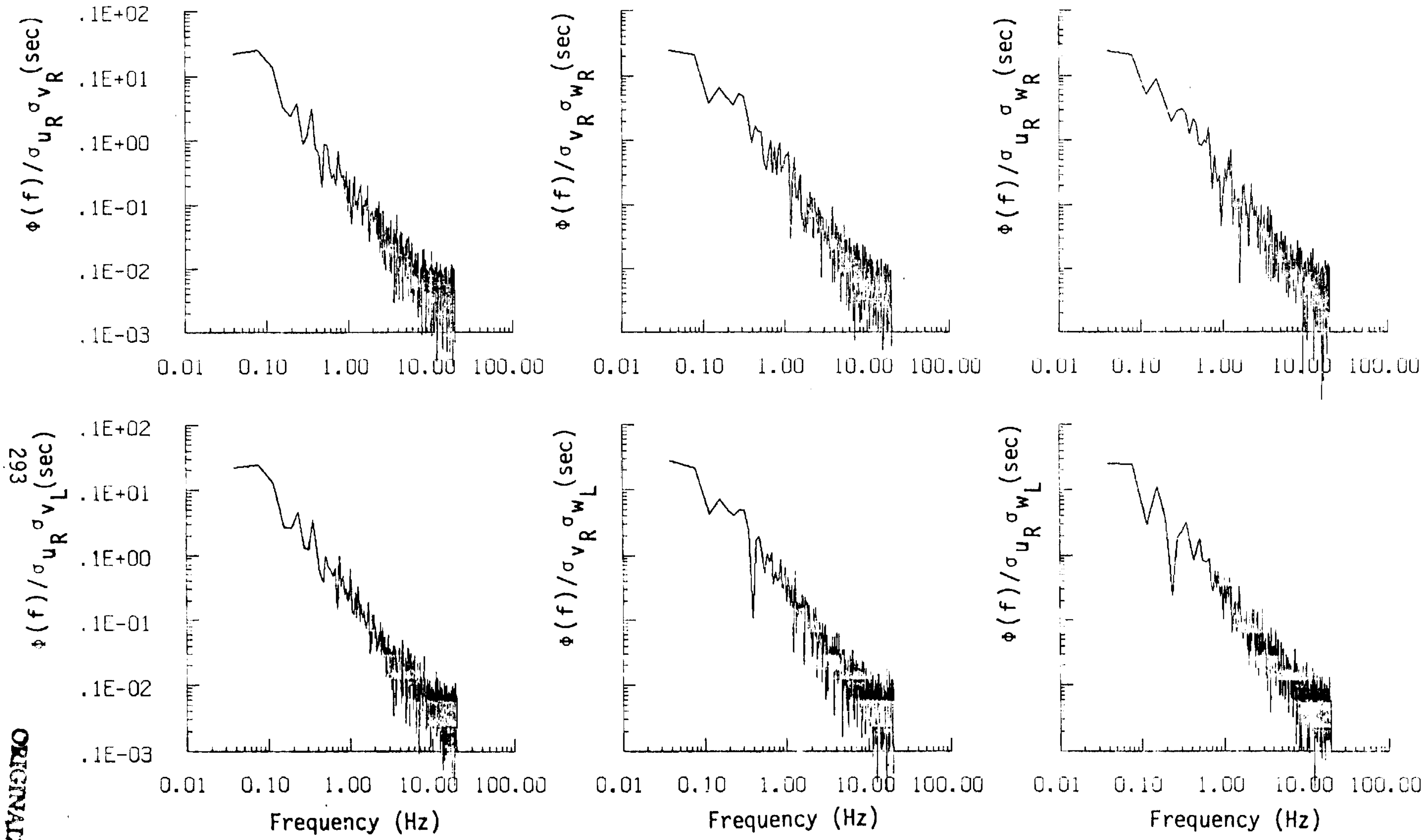

b. One- and two-point cross-spectra.

Figure A.65. (continued).

ORIGINAL PAGE IS
OF POOR QUALITY

TABLE A.26. List of All Parameters Measured and Their Range of Values, Flight 31, Run 13.

CHANNEL	UNITS	HIGH	LOW	MEAN	RMS	STD	POINTS
1 TIME	SECONDS	43549.560	43280.535	43415.04760	43415.11707	77.67165	10762
2 PHI DOT	RAD/SEC	.379	-.233	-.00237	.05375	.05370	10762
3 ACCL N CG	G UNITS	2.088	-.458	1.00261	1.01986	.13681	10762
4 THETA DOT	RAD/SEC	.093	-.112	.00310	.01869	.01843	10762
5 THETA	RAD	.102	-.021	.05051	.05408	.01932	10762
6 PHI	RAD	.193	-.171	.00542	.04822	.04792	10762
7 PSI I	RAD	359.118	-.155	38.48182	113.32492	106.59617	10762
8 DEL PSI 1	DEG	5.049	-10.818	-1.72432	3.00313	2.45887	10762
9 PSI 2	RAD	367.091	351.601	360.46659	360.47449	2.38697	10762
10 DEL PSI 2	DEG	14.988	-4.242	.78272	5.16699	5.10760	10762
11 ACCL N LT	G UNITS	3.175	-1.167	1.01560	1.07715	.35889	10762
12 ACCL N RT	G UNITS	3.304	-1.348	1.01105	1.08550	.39508	10762
13 ACCL X CG	G UNITS	.156	-.039	.04595	.04904	.01714	10762
14 ACCL Y CG	G UNITS	.126	-.163	-.00693	.03096	.03018	10762
15 ALPHA CTR	RAD	.061	-.155	-.03120	.03653	.01899	10762
16 BETA CTR	RAD	.156	-.166	-.00317	.03782	.03769	10762
17 TEMP I	DEG F	76.137	75.418	75.86306	75.86326	.17615	10762
18 TEMP P	DEG F	59.264	59.084	59.12621	59.12625	.06929	10762
19 ACCL Z INS	G UNITS	2.154	-.495	1.00539	1.02288	.15836	10762
20 ALPHA RT	RAD	.093	-.156	-.01916	.02875	.02143	10762
21 BETA RT	RAD	.145	-.136	.00490	.03390	.03354	10762
22 ALPHA LT	RAD	.110	-.138	.00570	.02117	.02038	10762
23 BETA LT	RAD	.151	-.149	.00102	.03468	.03467	10762
24 PSI DOT	RAD/SEC	.136	-.113	.00244	.03092	.03082	10762
25 TEMP TOT	DEG C	14.358	10.518	12.02362	12.05910	.92444	10762
26 QC LT	PSID	1.116	.626	.84037	.84324	.06952	10762
27 QC CTR	PSID	1.035	.588	.80597	.80369	.06610	10762
28 QC RT	PSID	1.068	.619	.83201	.83477	.05785	10762
29 PS	PSIA	12.282	12.152	12.21816	12.21818	.02351	10762
30 TEMP IRT	VOLTS	9.433	7.140	8.24400	8.26329	.56427	10762
31 HYGROM	DEG C	3.928	-8.202	-.37809	2.51954	2.49112	10762
32 QC2 LT	PSID	.056	.050	.05193	.05194	.00125	10762
33 QC2 CTR	PSID	.175	.091	.14999	.15172	.02266	10762
34 QC2 RT	PSID	.156	.097	.12547	.12694	.01925	10762
35 DAR	DEG	-6.595	-7.479	-6.87790	6.88219	.24311	10762
36 DAL	DEG	-6.392	-6.667	-6.48720	6.48759	.07194	10762
37 DELEV	DEG	5.384	4.994	5.15201	5.15328	.11417	10762
38 DSTAB	DEG	-.376	-.399	-.38791	.38797	.00663	10762
39 DRUD	DEG	11.144	10.857	11.06301	11.06335	.08669	10762
40 DTHRR	PCT MAX	67.969	67.578	67.88402	67.88410	.10500	10762
41 DTHRL	PCT MAX	68.164	67.578	67.89650	67.89669	.15867	10762
42 DFLP	POSITION	.262	.242	.25235	.25241	.00520	10762
43 DSB	POSITION	.346	.338	.34137	.34138	.00154	10762
44 D TO G	METERS	7498923.686	7486146.470	***********	***********	3633.20453	10762
45 B TO D	DEGREES	72.883	72.824	72.85235	72.85236	.01749	10762
46 LONG	DEGREES	-118.167	-118.223	-118.19586	118.19586	.01547	10762
47 LAT	DEGREES	35.331	35.089	35.21185	35.21192	.06982	10762
48 TRK ANG	DEGREES	14.560	4.724	10.67592	10.94068	2.39241	10762
49 HDG	RADIANS	.173	-.112	.05671	.06747	.04450	10762
50 VE	M/SEC	27.040	8.476	18.75663	19.21691	4.18092	10762
51 VN	M/SEC	105.977	92.267	99.60717	99.65539	3.11914	10762
52 ALTITUDE	KM	1.575	1.488	1.53037	1.53045	.01566	10762
53 TEMPC	DEGREES C	9.576	5.479	6.89803	6.95030	.85081	10762
54 EW WND SPD	KNOTS	44.353	-12.830	25.87646	28.02785	10.76940	10762
55 NS WND SPD	KNOTS	15.266	-22.245	-2.99359	5.78682	4.95258	10762
56 WIND SPEED	KNOTS	44.732	.359	26.98911	28.61901	9.52072	10762
57 WIND DIREC	DEGREES	354.810	.083	271.19588	273.26223	33.54312	10762
58 WIND DIR2	DEGREES	178.810	-179.917	91.19593	97.16859	33.54314	10762
59 WIND DIR3	DEGREES	358.810	.083	271.19593	273.26228	33.54314	10762
60 WIND DIR4	DEGREES	341.948	-1241.685	-774.85127	975.34834	592.40399	10762
61 AIRSPEED P	M/SEC	116.977	89.678	103.30451	103.38603	4.10504	10762
62 AIRSPEED C	M/SEC	114.795	87.497	101.40045	101.40244	4.07872	10762
63 AIRSPEED L	M/SEC	119.158	96.161	103.80750	103.89158	4.17934	10762
64 DELTA ALT	METERS	75.037	-11.883	30.82562	34.57617	15.66255	10762
65 INRTL DISP	METERS	55.598	-9.398	30.16986	33.21885	13.90286	10762
66 UG RIGHT	M/SEC	8.232	-10.262	.00000	2.49445	2.49456	10762
67 UG CENTER	M/SEC	8.216	-10.157	.00000	2.48049	2.48060	10762
68 UG LEFT	M/SEC	9.032	-10.957	.00000	2.59710	2.59722	10762
69 VG RIGHT	M/SEC	9.241	-20.865	-.00192	5.57921	5.57947	10762
70 VG CENTER	M/SEC	9.569	-20.014	-.00033	5.57528	5.57554	10762
71 VG LEFT	M/SEC	10.411	-20.161	-.00449	5.56625	5.56651	10762
72 WG RIGHT	M/SEC	12.520	-9.954	-.02370	2.43192	2.43191	10762
73 WG CENTER	M/SEC	9.716	-9.319	-.01524	2.29754	2.29759	10762
74 WG LEFT	M/SEC	10.354	-10.302	-.01190	2.41250	2.41258	10762

Flight 31, Run 14
Date: Nov. 29, 1982
Start Time: 12:07:41 (PST)
Duration: 208.9 seconds

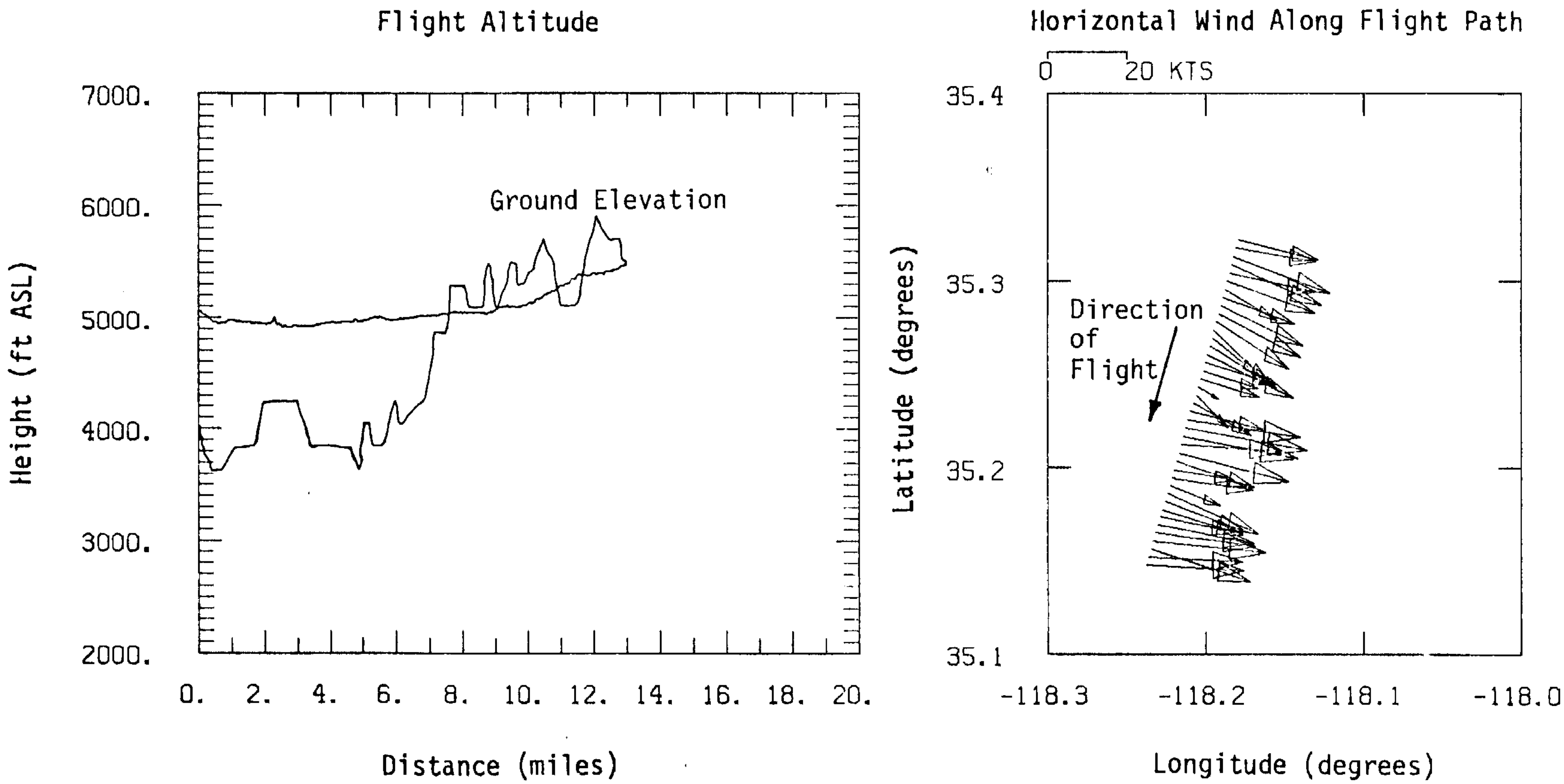

Figure A.66. Flight altitude and horizontal wind along flight path, Flight 31, Run 14.

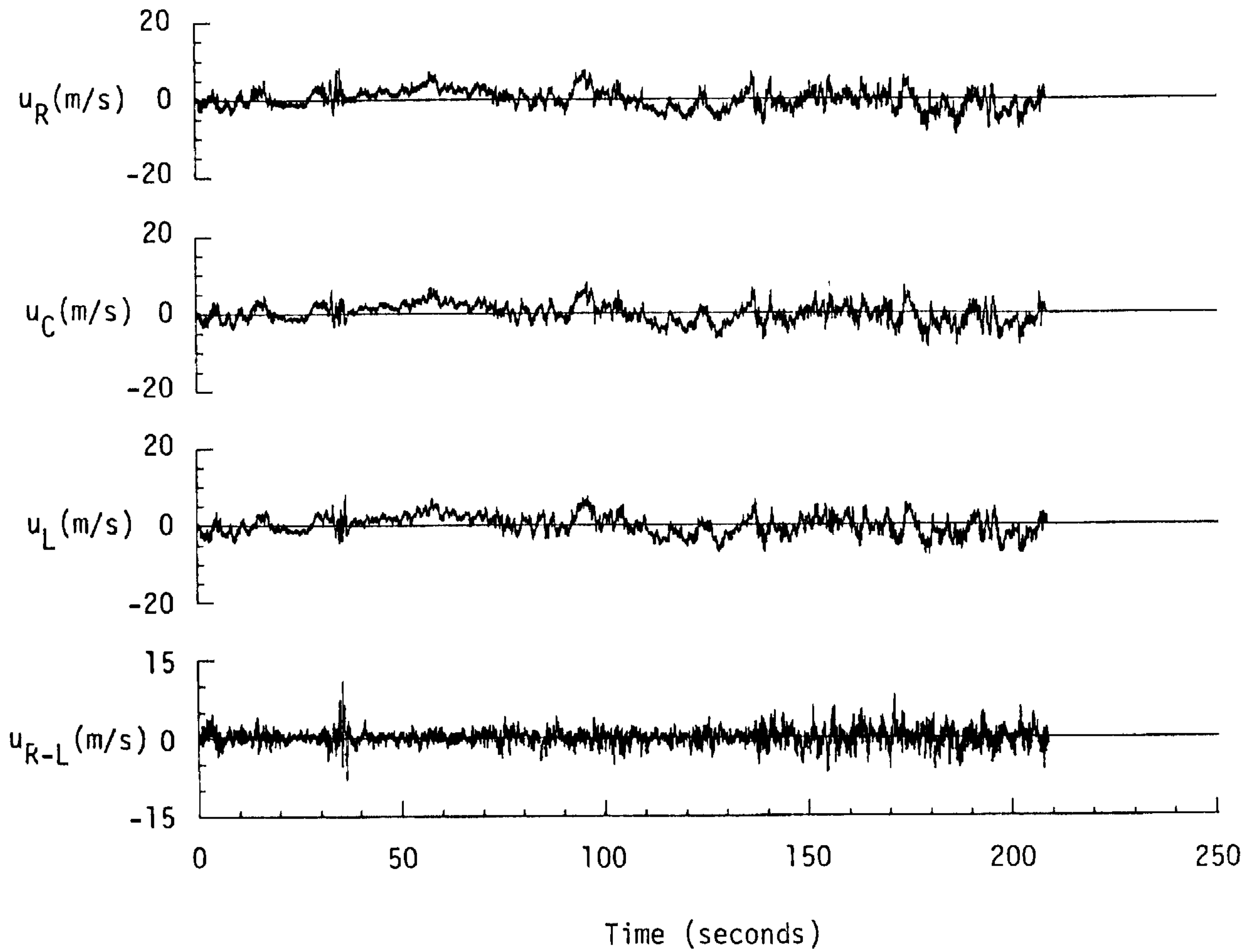

Figure A.67. Time histories of gust velocities, gust velocity differences, and aircraft's normal accelerations, Flight 31, Run 14.

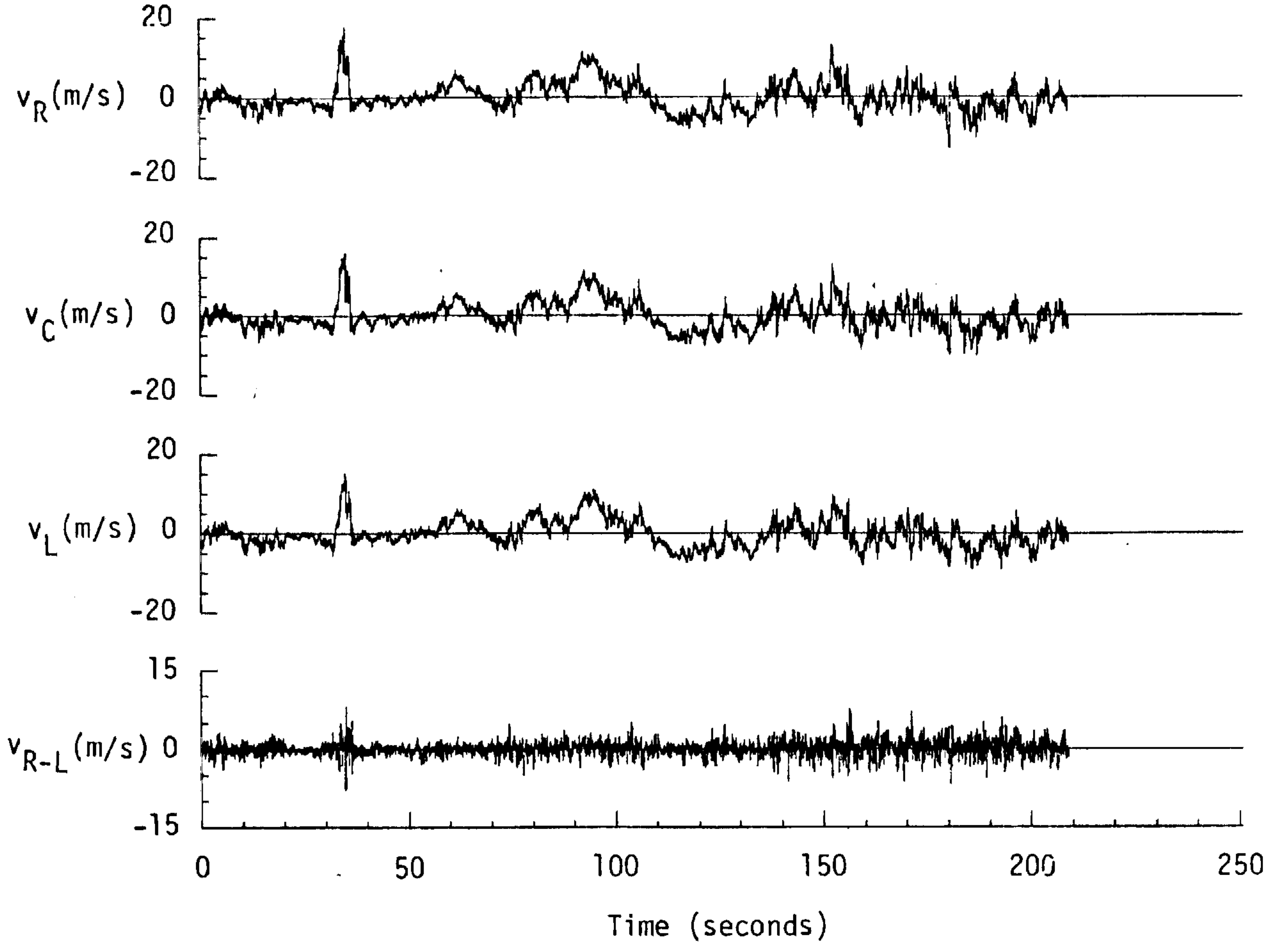

Figure A.67. (continued).

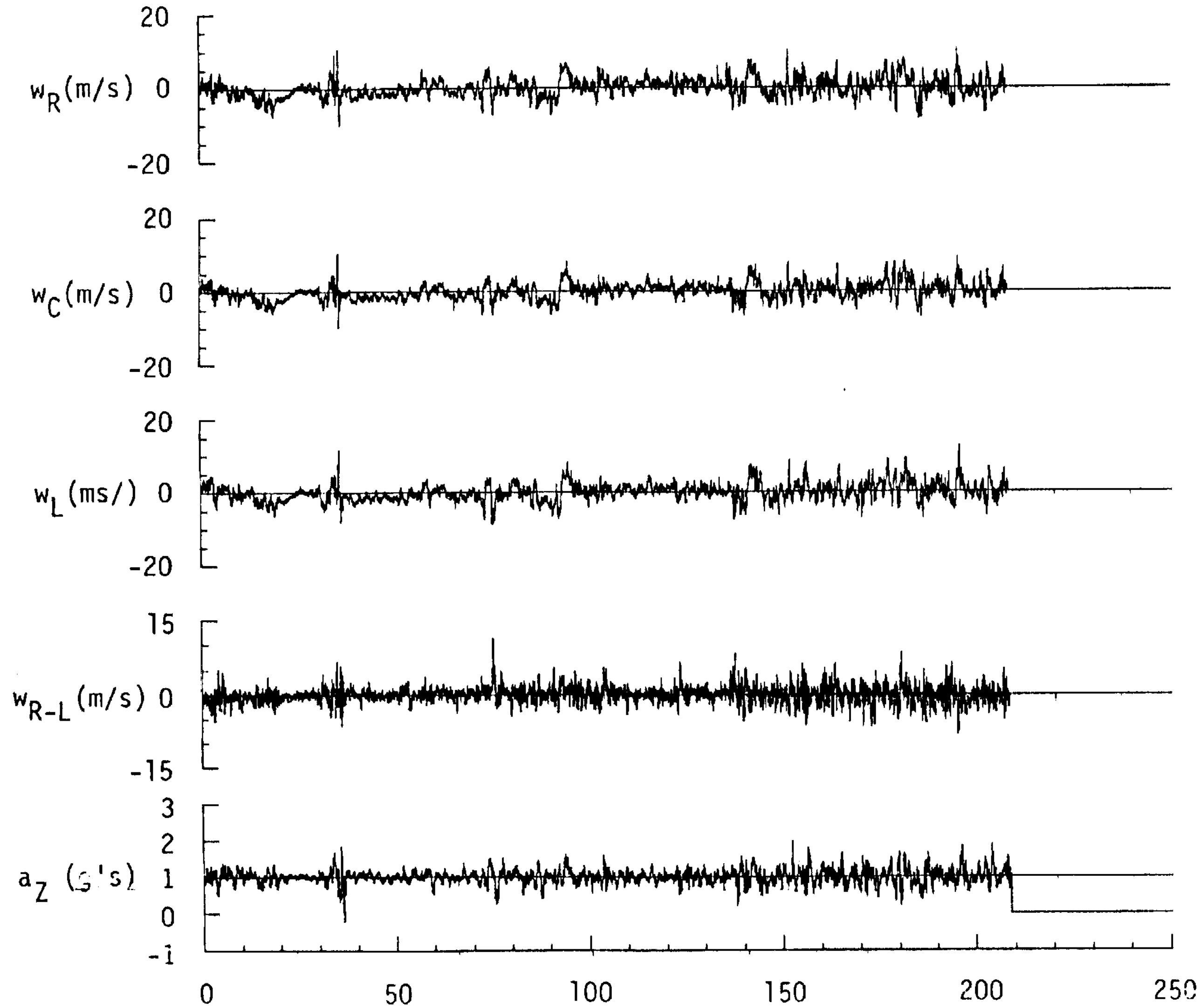

Figure A.67. (continued).

TABLE A.27. Average Turbulence Parameters, Integral Length Scales, and Correlation Coefficients of Gust Velocities, Flight 31, Run 14.

1. Mean Airspeed (m/s):

$\overline{V}_L$	$\overline{V}_C$	$\overline{V}_R$
103.38	101.07	102.99

2. Standard Deviation of Gust Velocities (m/s):

σ_{uR}	σ_{vR}	σ_{wR}
2.51	3.54	2.37

σ_{uC}	σ_{vC}	σ_{wC}
2.47	3.50	2.12

σ_{uL}	σ_{vL}	σ_{wL}
2.52	3.42	2.28

3. Standard Deviation of Gust Velocity Differences (m/s):

$\sigma_{\Delta uRL}$	$\sigma_{\Delta vRL}$	$\sigma_{\Delta wRL}$
1.29	1.12	1.37

4. Integral Length Scale (m):

L_{uR}	L_{vR}	L_{wR}
174.9	204.4	66.8

L_{uRL}	L_{vRL}	L_{wRL}
161.3	205.4	64.5

5. Correlation Coefficient of Gust Velocities:

$\overline{u_R u_L}/\sigma_{u_R}\sigma_{u_L}$	$\overline{v_R v_L}/\sigma_{v_R}\sigma_{v_L}$	$\overline{w_R w_L}/\sigma_{w_R}\sigma_{w_L}$
0.79	0.90	0.77

$\overline{u_R v_R}/\sigma_{u_R}\sigma_{v_R}$	$\overline{v_R w_R}/\sigma_{v_R}\sigma_{w_R}$	$\overline{w_R u_R}/\sigma_{w_R}\sigma_{u_R}$
0.18	0.19	0.10

$\overline{u_R v_L}/\sigma_{u_R}\sigma_{v_L}$	$\overline{v_R w_L}/\sigma_{v_R}\sigma_{w_L}$	$\overline{w_R u_L}/\sigma_{w_R}\sigma_{u_L}$
0.13	0.27	0.07

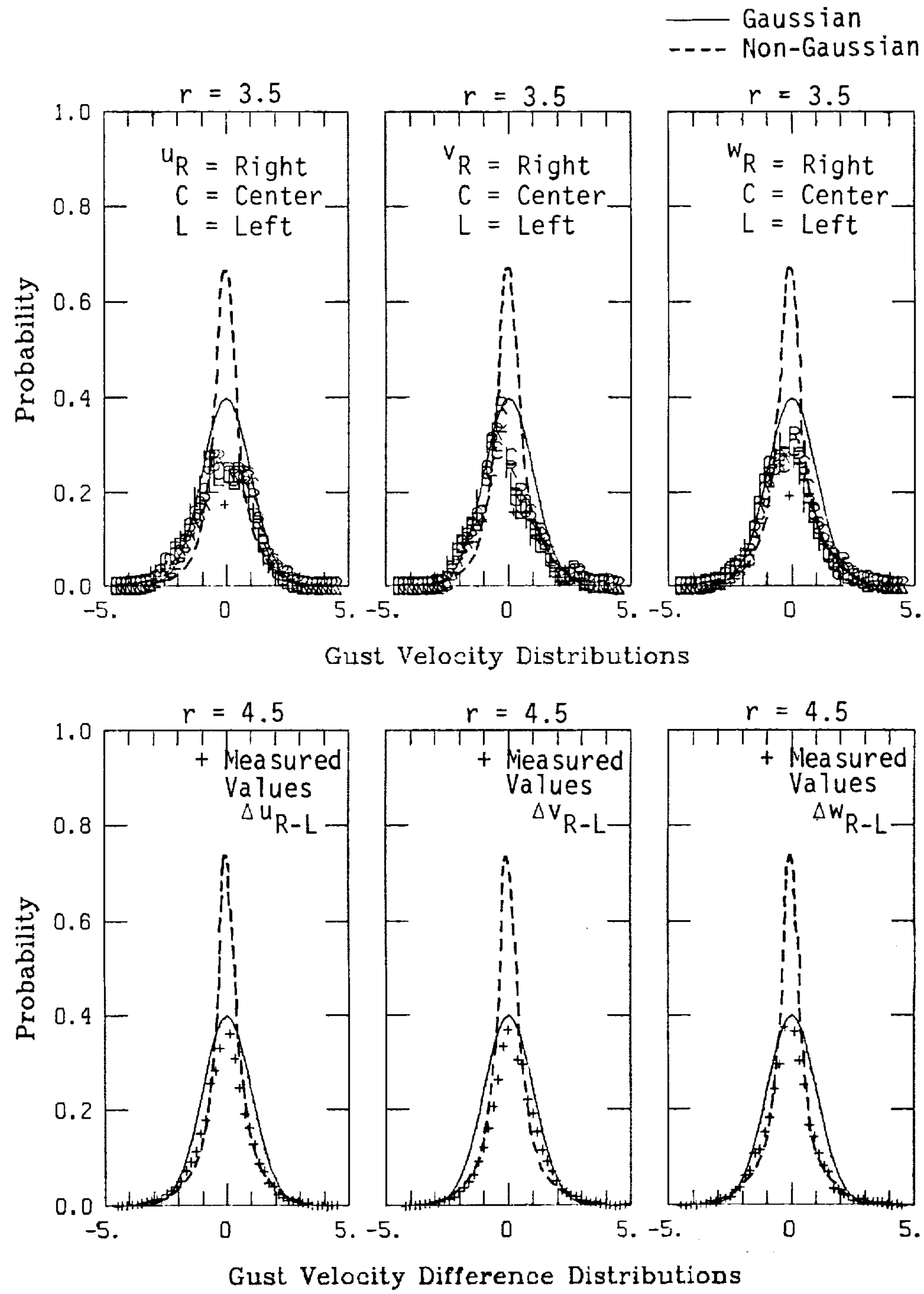

Figure A.68. Probability density functions for gust velocities and gust velocity differences (normalized with the standard deviation), Flight 31, Run 14 (r = degree of non-Gaussian).

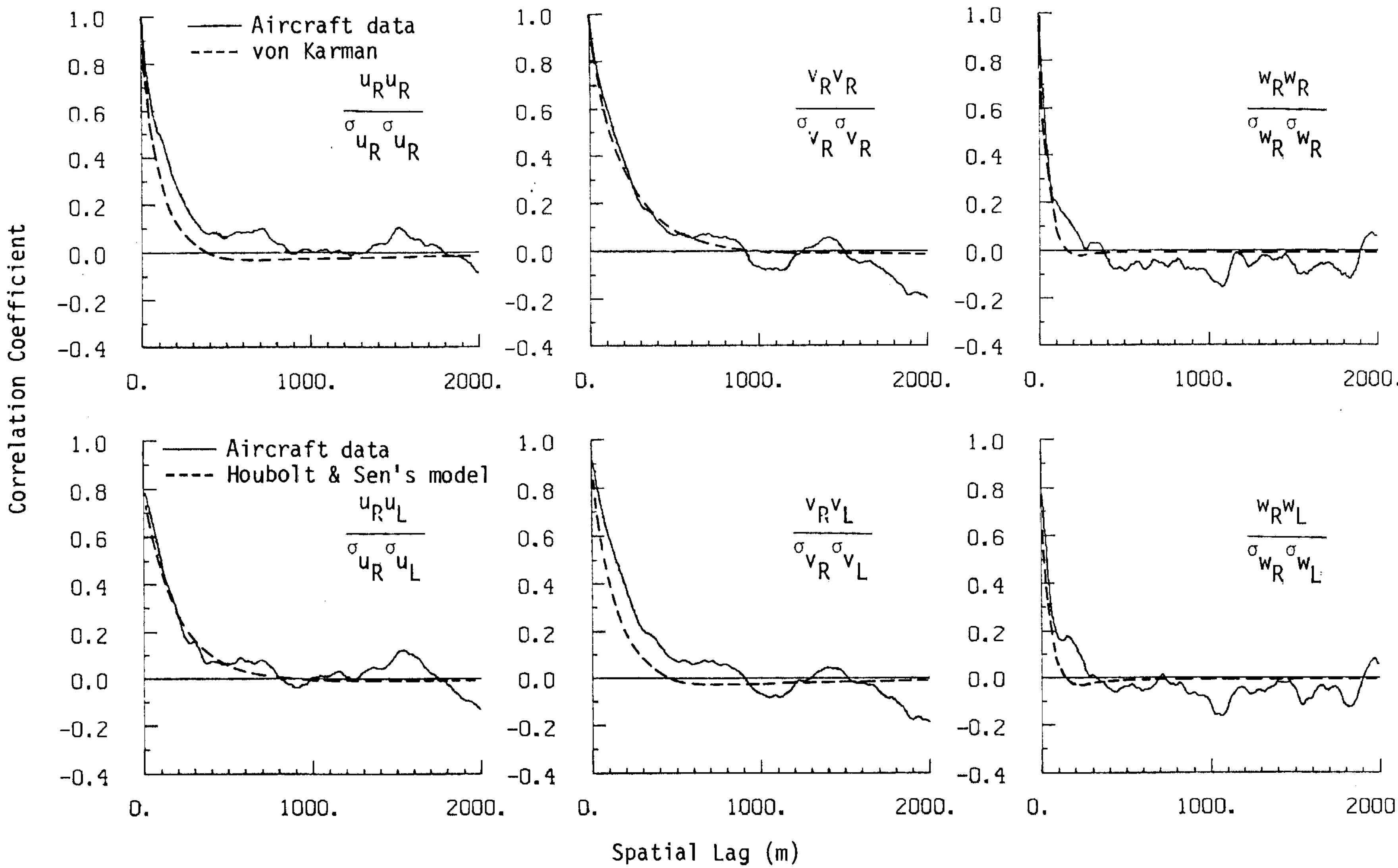

a. One- and two-point common component correlations.

Figure A.69. Comparison of normalized one- and two-point correlation functions for gust velocities with theoretical models, Flight 31, Run 14.

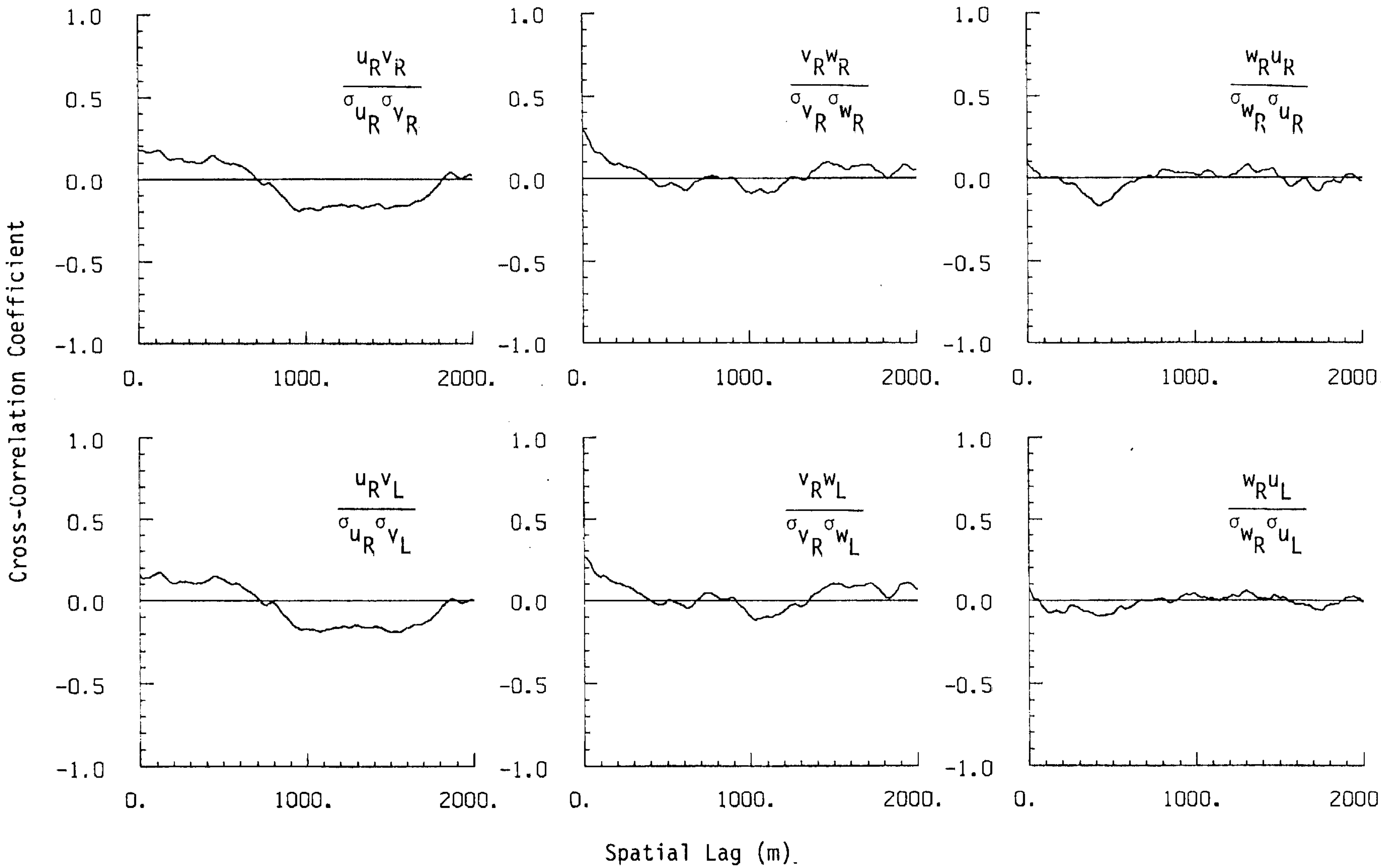

b. One- and two-point cross-correlations.

Figure A.69. (continued).

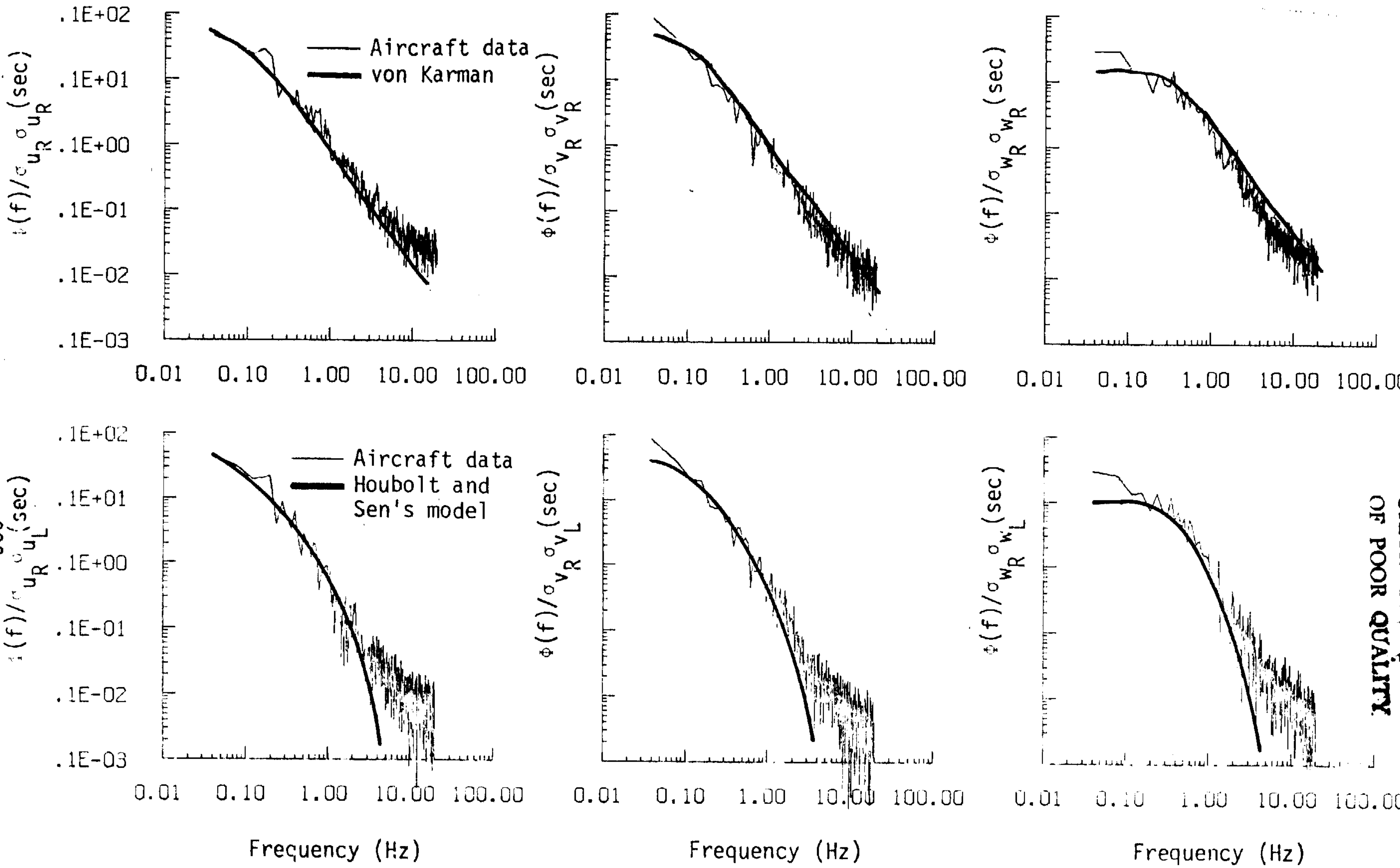

a. One- and two-point common component spectra.

Figure A.70. Comparison of normalized one- and two-point spectral density functions for gust velocities with theoretical models, Flight 31, Run 14.

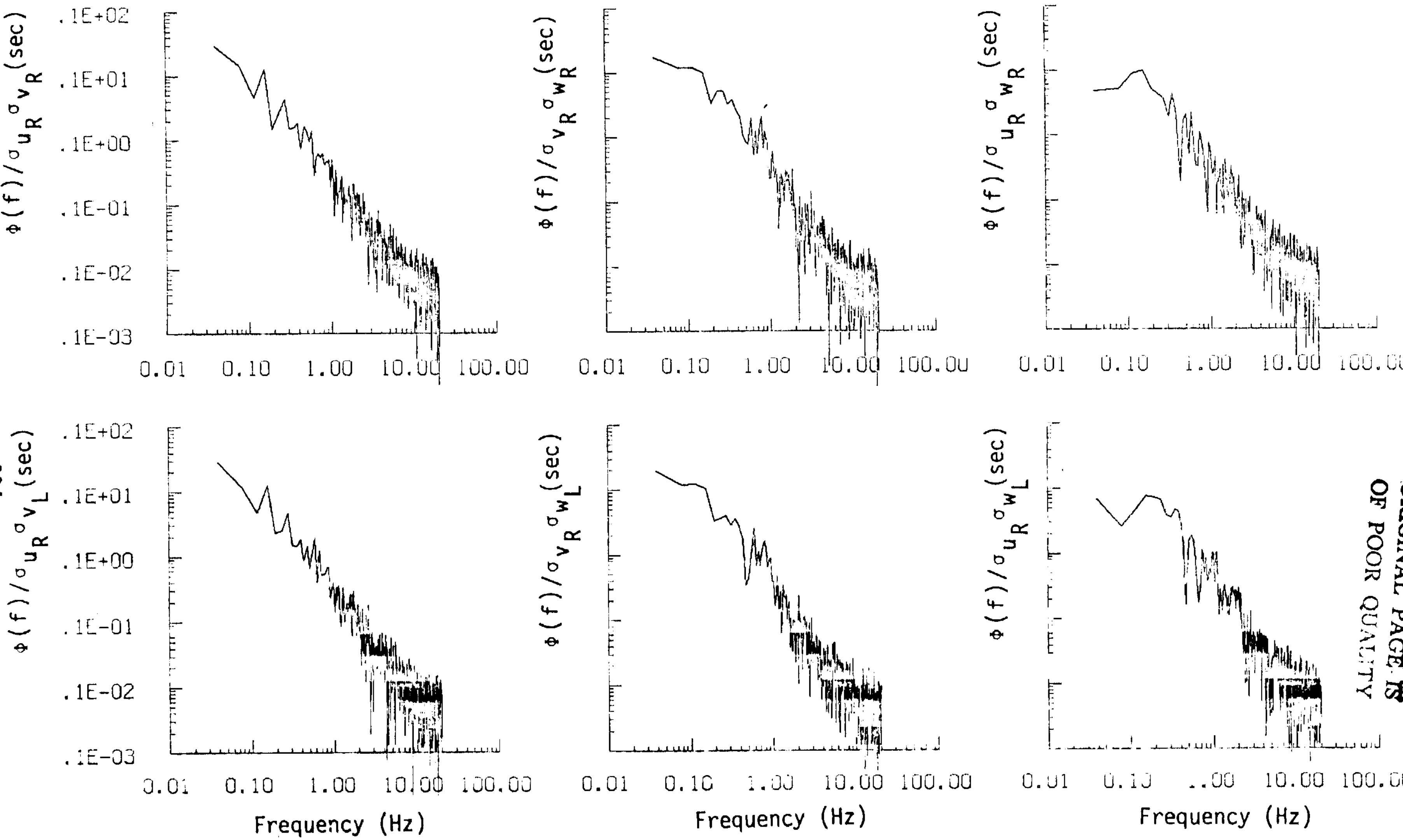

b. One- and two-point cross-spectra.

Figure A.70. (continued).

ORIGINAL PAGE IS OF POOR QUALITY

TABLE A.28. List of All Parameters Measured and Their Range of Values, Flight 31, Run 14.

CHANNEL	UNITS	HIGH	LOW	MEAN	RMS	STD	POINTS
1 TIME	SECONDS	43869.423	43660.573	43764.99780	43765.03934	60.30063	8355
2 PHI DOT	RAD/SEC	.195	-.280	-.00275	.05322	.05315	8355
3 ACCL N CG	G UNITS	1.882	-.047	1.00641	1.02263	.18142	8355
4 THETA DOT	RAD/SEC	.087	-.107	.00350	.01665	.01628	8355
5 THETA	RAD	.112	-.017	.05980	.06283	.01926	8355
6 PHI	RAD	.200	-.197	.00128	.04365	.04364	8355
7 PSI 1	RAD	206.681	190.753	200.87019	200.88491	2.43183	8355
8 DEL_PSI 1	DEG	5.020	-15.081	-.78389	2.73068	2.61590	8355
9 PSI 2	RAD	568.813	548.747	563.09995	563.10573	2.55352	8355
10 DEL PSI 2	DEG	5.379	-10.387	-.40259	2.44284	2.40958	8355
11 ACCL N LT	G UNITS	3.651	-1.016	1.01893	1.07847	.35340	8355
12 ACCL N RT	G UNITS	4.004	-1.172	1.01544	1.08022	.36709	8355
13 ACCL X CG	G UNITS	.179	-.026	.05634	.06047	.02198	8355
14 ACCL Y CG	G UNITS	.107	-.156	.00031	.02915	.02915	8355
15 ALPHA CTR	RAD	.073	-.153	-.03215	.03720	.01872	8355
16 BETA CTR	RAD	.146	-.191	.01173	.03989	.03811	8355
17 TEMP I	DEG F	76.497	75.957	76.30558	76.30566	.10776	8355
18 TEMP_P	DEG F	59.264	59.084	59.11203	59.11206	.06051	8355
19 ACCL Z INS	G UNITS	1.976	-.197	1.01012	1.02673	.18395	8955
20 ALPHA RT	RAD	.111	-.130	-.01699	.02763	.02179	8355
21 BETA RT	RAD	.148	-.177	.01941	.03976	.03470	8355
22 ALPHA LT	RAD	.112	-.094	.00468	.01950	.01893	8355
23 BETA LT	RAD	.129	-.177	.01401	.03729	.03456	8355
24 PSI DOT	RAD/SEC	.165	-.105	.00262	.03197	.03184	8355
25 TEMP TOT	DEG C	14.358	10.420	11.64364	11.66879	.76576	8355
26 QC LT	PSID	.967	.666	.83168	.83326	.04760	8355
27 QC CTR	PSID	.920	.634	.79435	.79563	.04514	8355
28 QC RT	PSID	.947	.682	.82555	.82686	.04654	8355
29 PS	PSIA	12.269	11.993	12.19375	12.19397	.07275	8355
30 TEMP IRT	VOLTS	8.293	6.907	7.31174	7.31627	.25744	8355
31 HYGROM	DEG C	4.123	-8.976	-.18993	3.14426	3.13871	8355
32 QC2 LT	PSID	.066	.056	.06153	.06161	.00307	8355
33 QC2 CTR	PSID	.169	.084	.14043	.14243	.02375	8355
34 QC2 RT	PSID	.147	.117	.12796	.12831	.00960	8355
35 DAR	DEG	-8.446	-9.054	-8.90240	8.90402	.16993	8355
36 DAL	DEG	-7.301	-8.430	-7.96148	7.96819	.32686	8355
37 DELEV	DEG	5.813	5.033	5.43606	5.44035	.21598	8355
38 DSTAB	DEG	-.372	-.399	-.38331	.38339	.00782	8355
39 DRUD	DEG	10.914	10.686	10.75424	10.75447	.07094	8355
40 DTHRR	PCT MAX	67.578	67.383	67.44859	67.44862	.05991	8355
41 DTHRL	PCT MAX	68.066	67.773	67.89629	67.89634	.08283	8355
42 DFLP	POSITION	.250	.238	.24308	.24310	.00312	8355
43 DSB	POSITION	.348	.346	.34722	.34722	.00079	8355
44 D TO G	METERS	7497719.117	7486463.462	***********	***********	3265.93300	8355
45 B TO D	DEGREES	72.651	72.819	72.83578	72.83578	.00908	8355
46 LONG	DEGREES	-118.178	-118.239	-118.20802	118.20802	.01767	8355
47 LAT	DEGREES	35.325	35.142	35.23301	35.23305	.05267	8355
48 TRK_ANG	DEGREES	198.153	192.659	195.25335	195.25736	1.25075	8355
49 HDG	RADIANS	3.630	3.347	3.52647	3.52674	.04334	8355
50 VE	M/SEC	-22.074	-31.592	-26.46176	26.54089	2.04811	8355
51 VN	M/SEC	-92.662	-100.965	-96.87623	96.89158	1.72466	8355
52 ALTITUDE	KM	1.682	1.496	1.54676	1.54753	.04872	8355
53 TEMPC	DEGREES C	9.036	5.402	6.55501	6.59134	.69114	8355
54 EW WND SPD	KNOTS	43.342	-9.144	20.14629	21.36764	7.12102	8355
55 NS WND SPD	KNOTS	10.379	-18.023	-5.49680	6.99665	4.32904	8355
56 WIND SPEED	KNOTS	43.370	.328	21.51716	22.48397	6.52271	8355
57 WIND DIREC	DEGREES	359.435	.046	283.62071	285.11087	29.11357	8355
58 WIND DIR2	DEGREES	179.435	-179.954	103.62077	107.63254	29.11359	8355
59 WIND DIR3	DEGREES	359.435	.046	283.62077	285.11093	29.11359	8355
60 WIND DIR4	DEGREES	797.759	37.990	486.22041	517.76979	177.98612	8355
61 AIRSPEED R	M/SEC	110.401	94.382	102.99972	103.03887	2.84003	8355
62 AIRSPEED C	M/SEC	108.415	91.123	101.07719	101.11596	2.79987	8355
63 AIRSPEED L	M/SEC	111.076	94.632	103.30307	103.42360	2.89518	8355
64 DELTA ALT	METERS	135.311	-50.008	.36671	48.71373	48.71526	8355
65 INRTL DISP	METERS	135.202	-48.052	.09576	47.72420	47.72696	8355
66 UG RIGHT	M/SEC	8.343	-9.114	.00000	2.51904	2.51919	8355
67 UG CENTER	M/SEC	7.811	-8.818	.00000	2.47656	2.47671	8355
68 UG LEFT	M/SEC	8.272	-7.712	.00000	2.52441	2.52456	8355
69 VG RIGHT	M/SEC	17.830	-12.509	-.02267	3.54824	3.54838	8355
70 VG CENTER	M/SEC	15.810	-9.840	-.02292	3.50256	3.50269	8355
71 VG LEFT	M/SEC	15.304	-9.201	-.02535	3.42437	3.42448	8355
72 WG RIGHT	M/SEC	10.708	-9.825	.00089	2.37144	2.37158	8355
73 WG CENTER	M/SEC	10.126	-9.684	.00239	2.12435	2.12447	8355
74 WG LEFT	M/SEC	12.575	-8.528	.00677	2.28809	2.28822	8355

Flight 31, Run 15
Date: Nov. 29, 1982
Start Time: 12:16:41 (PST)
Duration: 234 seconds

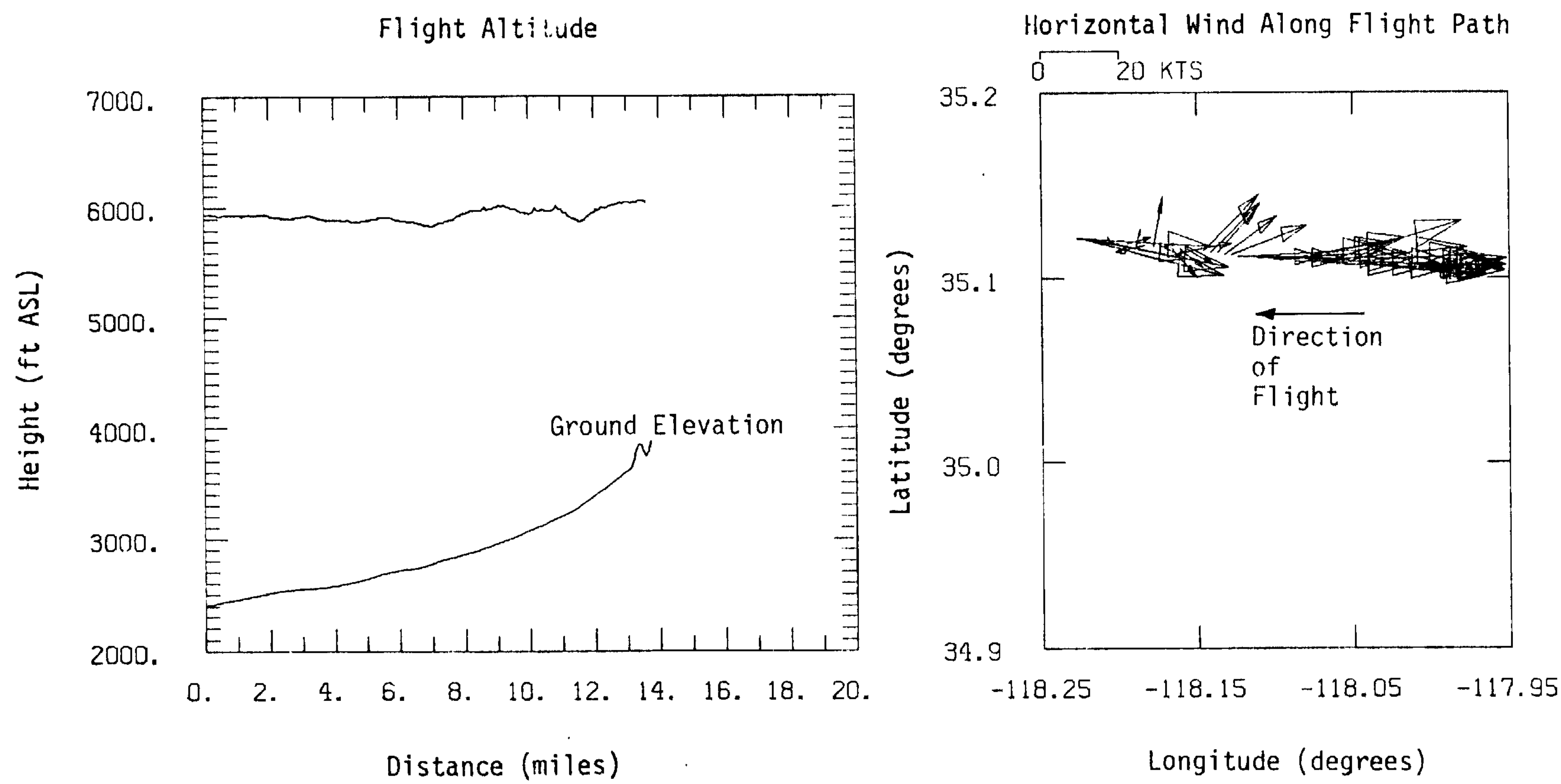

Figure A.71. Flight altitude and horizontal wind along flight path, Flight 31, Run 15.

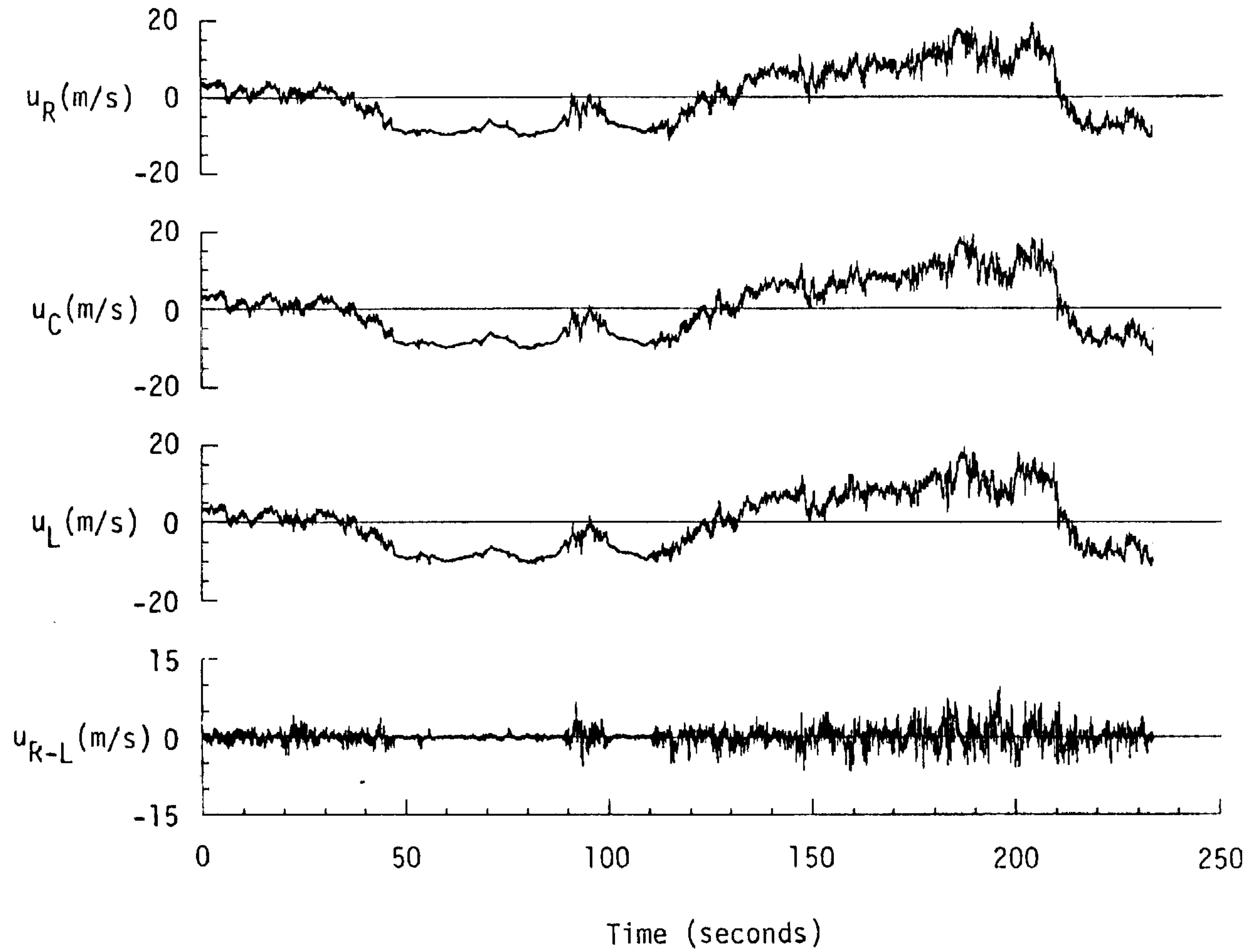

Figure A.72. Time histories of gust velocities, gust velocity differences, and aircraft's normal accelerations, Flight 31, Run 15.

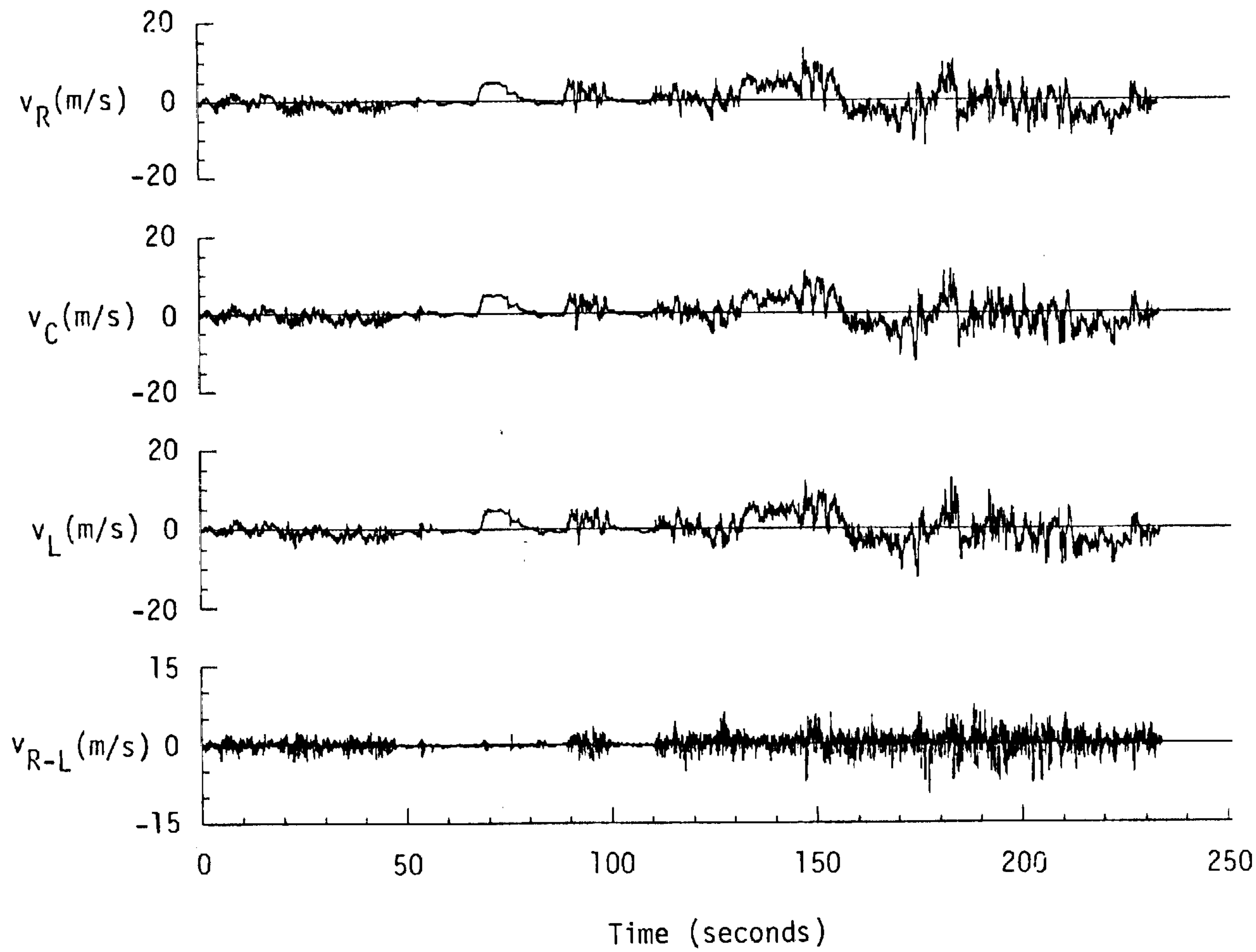

Figure A.72. (continued).

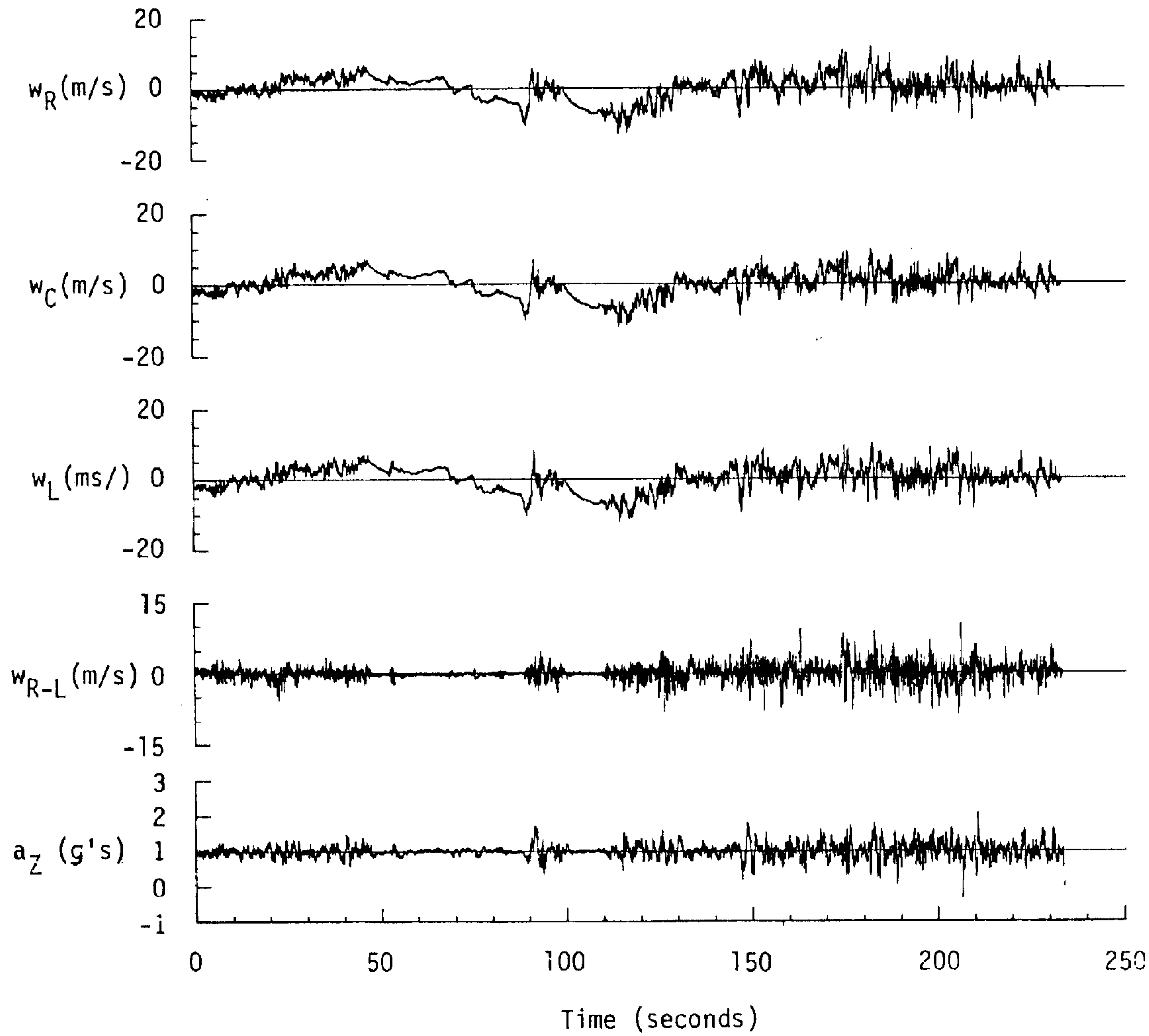

Figure A.72. (continued).

TABLE A.29. Average Turbulence Parameters, Integral Length Scales, and Correlation Coefficients of Gust Velocities, Flight 31, Run 15.

1. Mean Airspeed (m/s):

$\overline{V}_L$	$\overline{V}_C$	$\overline{V}_R$
107.74	105.40	107.23

2. Standard Deviation of Gust Velocities (m/s):

σ_{uR}	σ_{vR}	σ_{wR}
7.46	2.84	3.45

σ_{uC}	σ_{vC}	σ_{wC}
7.31	2.89	3.29

σ_{uL}	σ_{vL}	σ_{wL}
7.32	2.87	3.35

3. Standard Deviation of Gust Velocity Differences (m/s):

$\sigma_{\Delta uRL}$	$\sigma_{\Delta vRL}$	$\sigma_{\Delta wRL}$
1.45	1.24	1.49

4. Integral Length Scale (m):

L_{uR}	L_{vR}	L_{wR}
540.0	225.8	526.1

L_{uRL}	L_{vRL}	L_{wRL}
526.5	225.3	494.0

5. Correlation Coefficient of Gust Velocities:

$\overline{u_R u_L}/\sigma_{u_R}\sigma_{u_L}$	$\overline{v_R v_L}/\sigma_{v_R}\sigma_{v_L}$	$\overline{w_R w_L}/\sigma_{w_R}\sigma_{w_L}$
0.90	0.88	0.88

$\overline{u_R v_R}/\sigma_{u_R}\sigma_{v_R}$	$\overline{v_R w_R}/\sigma_{v_R}\sigma_{w_R}$	$\overline{w_R u_R}/\sigma_{w_R}\sigma_{u_R}$
0.32	0.06	0.02

$\overline{u_R v_L}/\sigma_{u_R}\sigma_{v_L}$	$\overline{v_R w_L}/\sigma_{v_R}\sigma_{w_L}$	$\overline{w_R u_L}/\sigma_{w_R}\sigma_{u_L}$
0.30	0.01	0.00

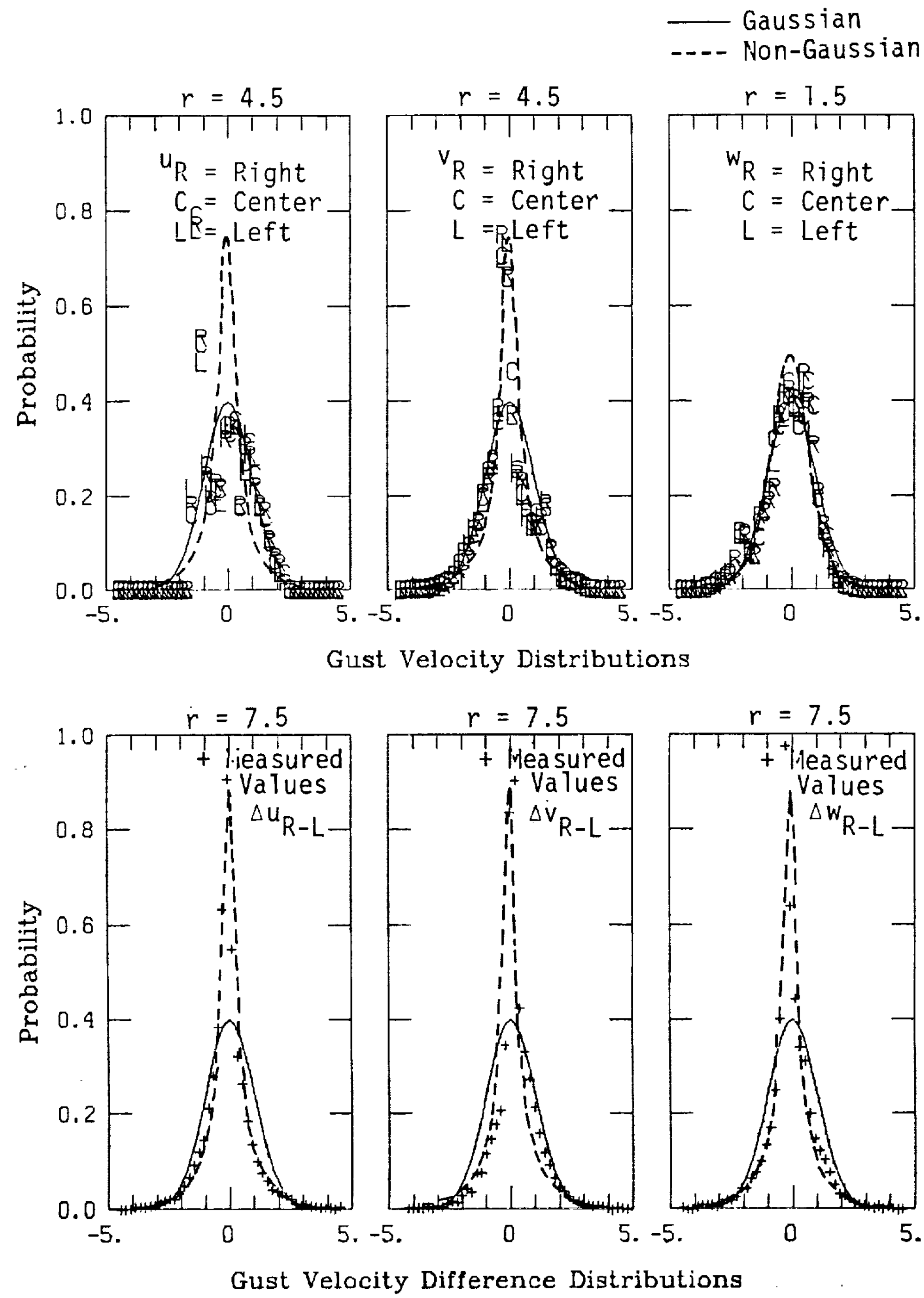

Figure A.73. Probability density functions for gust velocities and gust velocity differences (normalized with the standard deviation), Flight 31, Run 15 (r = degree of non-Gaussian).

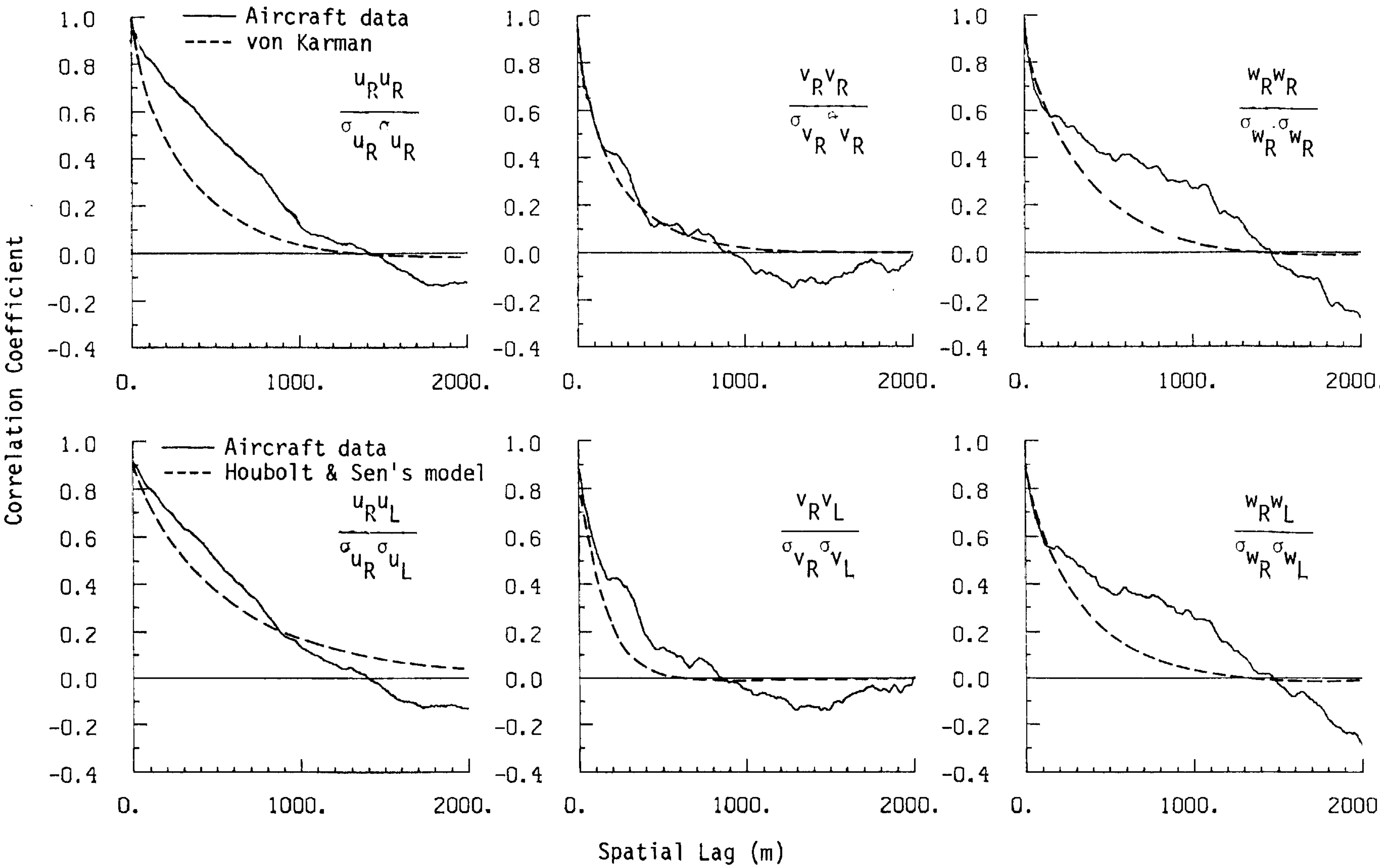

a. One- and two-point common component correlations.

Figure A.74. Comparison of normalized one- and two-point correlation functions for gust velocities with theoretical models, Flight 31, Run 15.

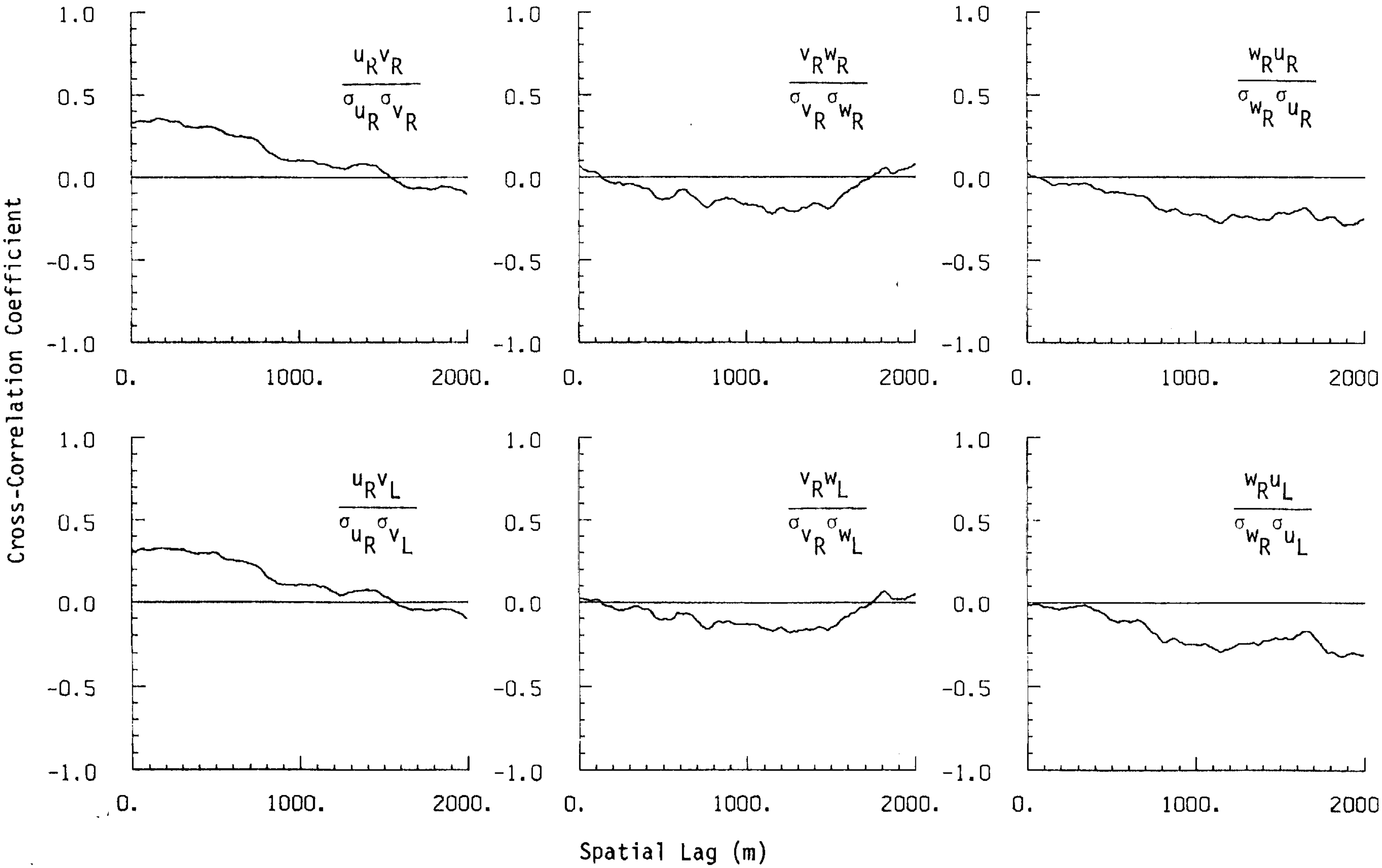

b. One- and two-point cross-correlations.

Figure A.74. (continued).

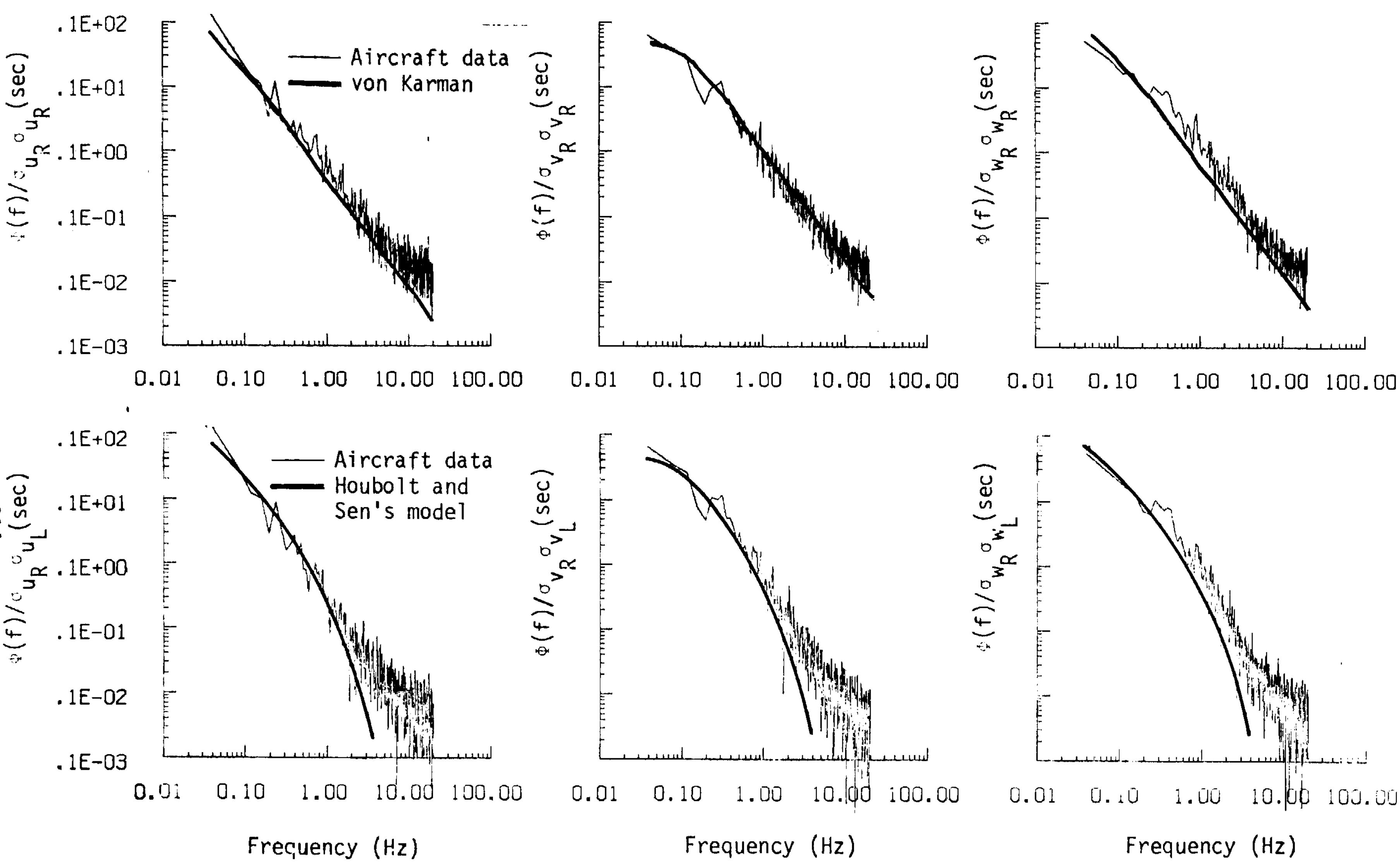

a. One- and two-point common component spectra.

Figure A.75. Comparison of normalized one- and two-point spectral density functions for gust velocities with theoretical models, Flight 31, Run 15.

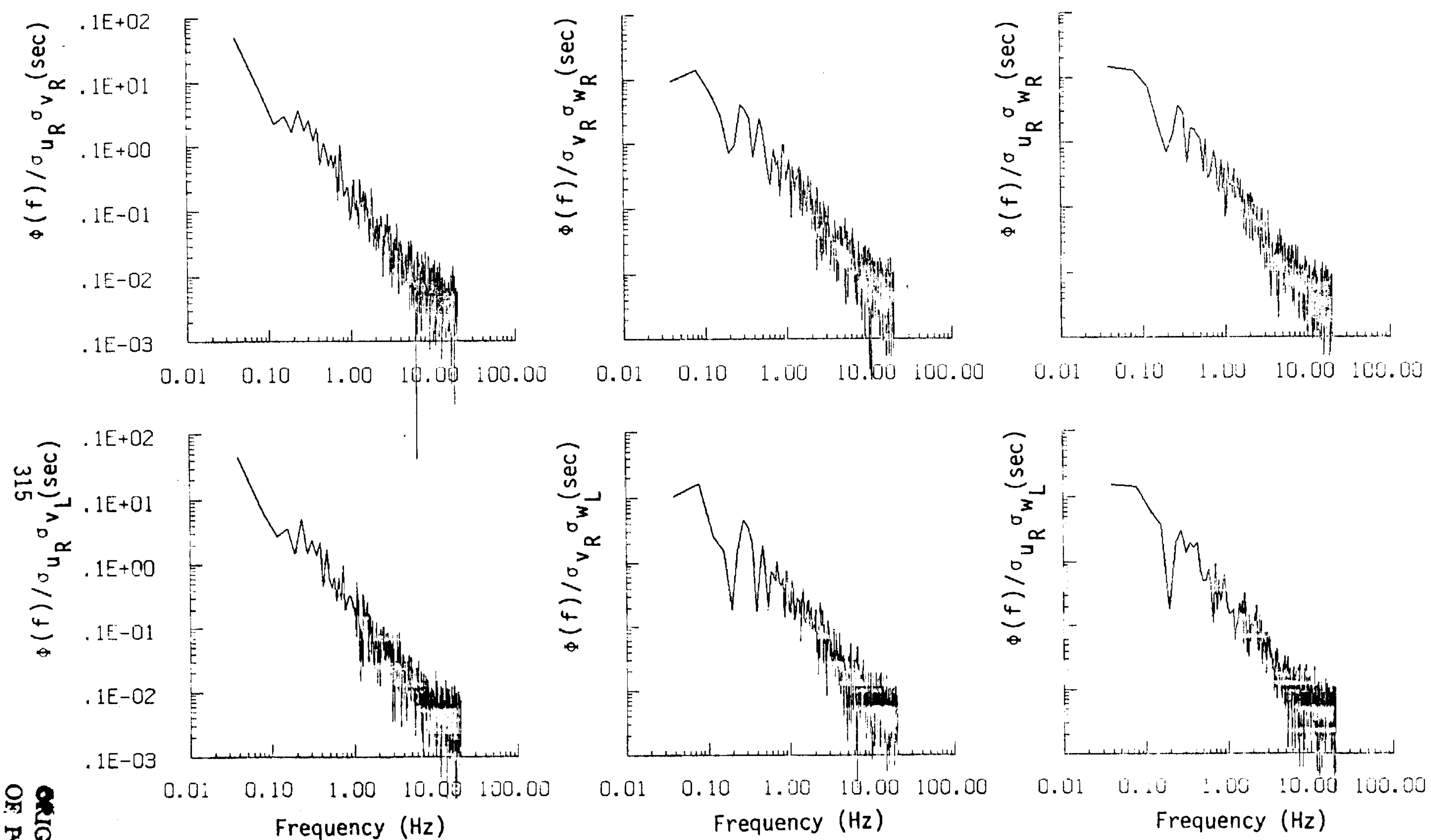

b. One- and two-point cruss-spectra.

Figure A.75. (continued).

ORIGINAL PAGE IS
OF POOR QUALITY

ORIGINAL PAGE IS
OF POOR QUALITY

TABLE A.30. List of All Parameters Measured and Their Range of Values, Flight 31, Run 15.

	CHANNEL	UNITS	HIGH	LOW	MEAN	RMS	STD	POINTS
1	TIME	SECONDS	44434.497	44200.497	44317.49660	44317.54809	67.56081	9361
2	PHI DOT	RAD/SEC	.258	-.259	-.00252	.04622	.04619	9361
3	ACCL N CG	G UNITS	1.973	-.176	1.00100	1.01600	.17390	9361
4	THETA DOT	RAD/SEC	.124	-.087	.00301	.01556	.01567	9361
5	THETA	RAD	.136	-.018	.04794	.05645	.03665	9361
6	PHI	RAD	.148	-.162	.00941	.04198	.04091	9361
7	PSI 1	RAD	280.571	268.947	273.98499	273.99249	2.02717	9361
8	DEL PSI 1	DEG	5.784	-5.765	-.72558	2.13835	2.01014	9361
9	PSI 2	RAD	279.375	267.110	271.87764	271.88473	1.96342	9361
10	DEL PSI 2	DEG	6.196	-5.271	-.28305	2.02320	2.00341	9361
11	ACCL N LT	G UNITS	2.859	-1.796	1.01475	1.06420	.32064	9361
12	ACCL N RT	G UNITS	2.996	-1.476	1.01099	1.06693	.34097	9361
13	ACCL Y CG	G UNITS	.215	-.043	.04556	.06782	.05024	9361
14	ACCL Y CG	G UNITS	.108	-.133	-.00514	.02562	.02509	9361
15	ALPHA CTR	RAD	.071	-.142	-.03523	.04178	.02246	9361
16	BETA CTR	RAD	.135	-.146	.00151	.02585	.02981	9361
17	TEMP T	DEG F	76.857	76.317	76.60817	76.60825	.11384	9361
18	TEMP P	DEG F	59.264	59.084	59.16942	59.16948	.08270	9361
19	ACCL Z INS	G UNITS	2.041	-.326	1.00465	1.02000	.17630	9361
20	ALPHA RT	RAD	.091	-.150	-.03082	.03998	.02547	9361
21	BETA RT	RAD	.142	-.130	.00751	.02838	.02737	9361
22	ALPHA LT	RAD	.107	-.124	.00220	.02422	.02412	9361
23	BETA LT	RAD	.120	-.139	.00500	.02809	.02765	9361
24	PSI DOT	RAD/SEC	.097	-.093	.00275	.02273	.02257	9361
25	TEMP TOT	DEG C	16.327	8.844	11.92158	12.10293	2.08739	9361
26	QC LT	PSID	1.190	.553	.88423	.89858	.15995	9361
27	QC CTR	PSID	1.139	.528	.84526	.85919	.15409	9361
28	QC RT	PSID	1.179	.549	.87560	.89000	.15944	9361
29	PS	PSIA	11.850	11.746	11.80425	11.80427	.02289	9361
30	TEMP TOT	VOLTS	9.433	6.208	7.68652	7.71908	.70825	9361
31	HYGROM	DEG C	-2.329	-13.473	-6.82922	7.17853	2.21213	9361
32	QC2 LT	PSID	.071	.054	.06408	.06429	.00515	9361
33	QC2 CTR	PSID	.166	.079	.12254	.12823	.03777	9361
34	QC2 RT	PSID	.129	.033	.07827	.08415	.03090	9361
35	DAR	DEG	-5.380	-8.032	-6.41164	6.46690	.84367	9361
36	DAL	DEG	-5.868	-8.375	-7.14971	7.19107	.77021	9361
37	DELEV	DEG	6.086	5.228	5.77688	5.78295	.26504	9361
38	DSTAB	DEG	-.411	-.431	-.42533	.42537	.00568	9361
39	DRUD	DEG	11.938	11.768	11.88148	11.88157	.04574	9361
40	DTHRR	PCT MAX	69.238	68.555	69.00506	69.00531	.18824	9361
41	DTHRL	PCT MAX	69.141	68.457	68.84293	68.84321	.19601	9361
42	DFLP	POSITION	.230	.203	.21732	.21742	.00667	9361
43	DSB	POSITION	.361	.348	.35429	.35431	.00380	9361
44	N TO G	METERS	7506561.672	7486279.900	**********	**********	5776.44551	9361
45	N TO D	DEGREES	73.032	72.862	72.94796	72.94798	.04834	9361
46	LONG	DEGREES	-117.994	-118.234	-118.11298	118.11300	.06839	9361
47	LAT	DEGREES	35.123	35.105	35.11276	35.11276	.00544	9361
48	TRK_ANG	DEGREES	279.086	272.356	275.50516	275.51061	1.73247	9361
49	HDG	RADIANS	4.911	4.704	4.79411	4.79425	.03620	9361
50	VE	M/SEC	-77.683	-105.444	-93.57270	93.86247	7.97973	9361
51	VN	M/SEC	14.439	4.191	8.95178	9.34641	2.68733	9361
52	ALTITUDE	KM	1.850	1.779	1.81012	1.81019	.01570	9361
53	TEMPC	DEGREES C	9.555	3.931	6.34655	6.51068	1.45277	9361
54	EW WND SPD	KNOTS	45.621	-14.828	22.29207	26.43351	14.20620	9361
55	NS WND SPD	KNOTS	24.118	-21.987	1.09625	5.76597	5.66517	9361
56	WIND SPEED	KNOTS	45.621	.158	24.22300	27.05593	12.05343	9361
57	WIND DIREC	DEGREES	359.927	.006	254.44940	259.26680	49.74980	9361
58	WIND DIR2	DEGREES	179.927	-179.994	74.44943	89.54048	49.74983	9361
59	WIND DIR3	DEGREES	359.927	.006	254.44943	259.26684	49.74983	9361
60	WIND DIR4	DEGREES	2351.930	534.319	866.11485	996.87545	493.59067	9361
61	AIRSPEED R	M/SEC	124.926	85.596	107.23087	107.67319	9.75021	9361
62	AIRSPEED C	M/SEC	122.693	83.974	105.40077	105.83834	9.61467	9361
63	AIRSPEED L	M/SEC	125.321	86.019	107.74866	108.18868	9.74821	9361
64	DELTA ALT	METERS	40.925	-30.373	.98776	15.72839	15.69818	9361
65	INRTL DISP	METERS	35.362	-31.592	1.40839	14.25622	14.18724	9361
66	UG RIGHT	M/SEC	19.188	-11.361	.00000	7.46476	7.46516	9361
67	UG CENTER	M/SEC	19.115	-12.000	.00000	7.31850	7.31889	9361
68	UG LEFT	M/SEC	19.566	-11.267	.00000	7.32498	7.32537	9361
69	VG RIGHT	M/SEC	13.160	-11.909	.01067	2.89719	2.89732	9361
70	VG CENTER	M/SEC	11.098	-12.221	.03165	2.89623	2.89621	9361
71	VG LEFT	M/SEC	12.780	-12.380	.02179	2.87713	2.87720	9361
72	VG RIGHT	M/SEC	11.645	-12.865	.05385	3.45700	3.45591	9361
73	VG CENTER	M/SEC	9.409	-11.746	.11645	3.30030	3.29842	9361
74	VG LEFT	M/SEC	9.941	-11.933	.10287	3.35332	3.35192	9361

Flight 31, Run 16
Date: Nov. 29, 1982
Start Time: 12:22:31
Duration: 99.8 seconds

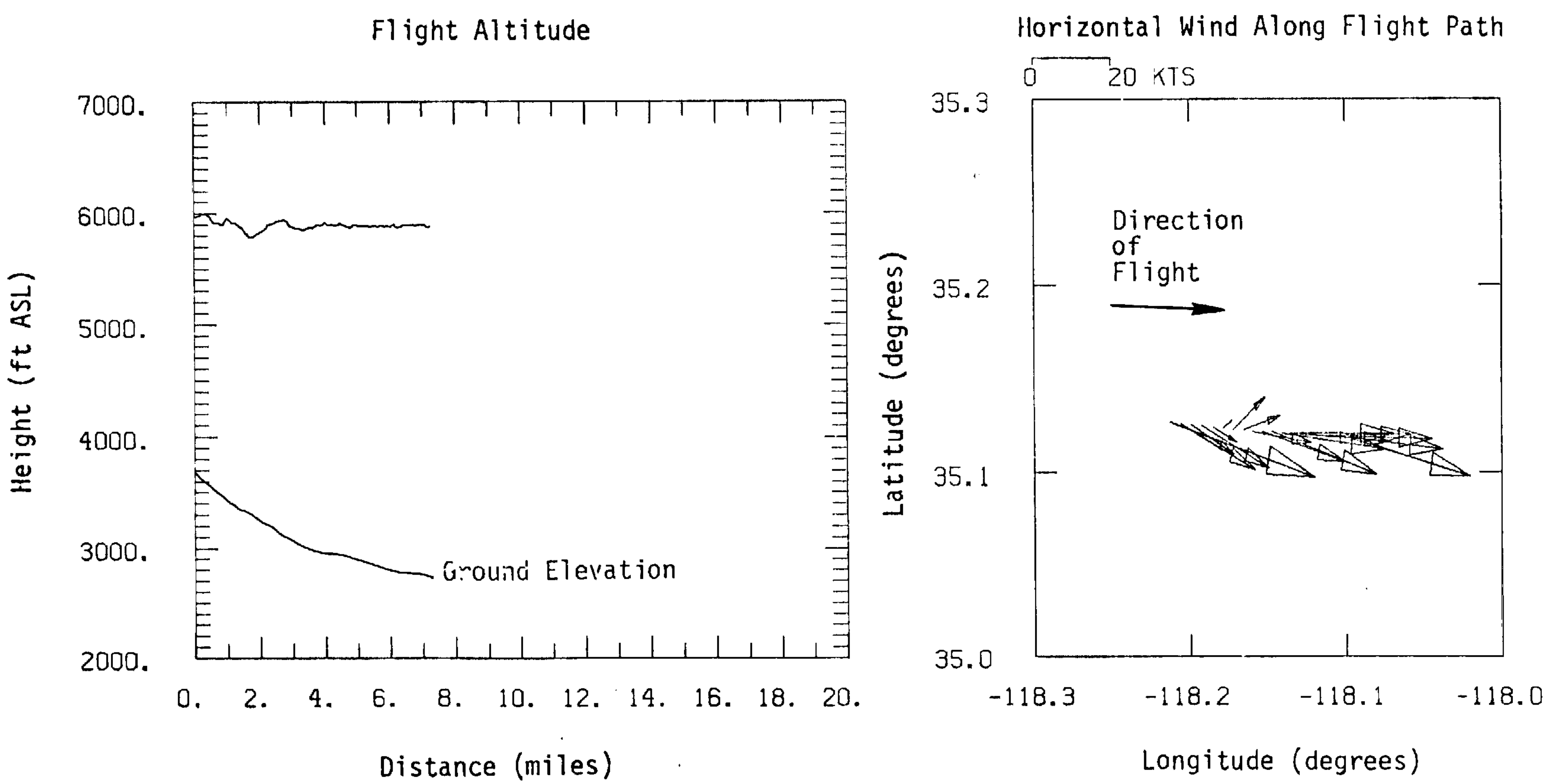

Figure A.76. Flight altitude and horizontal wind along flight path, Flight 31, Run 16.

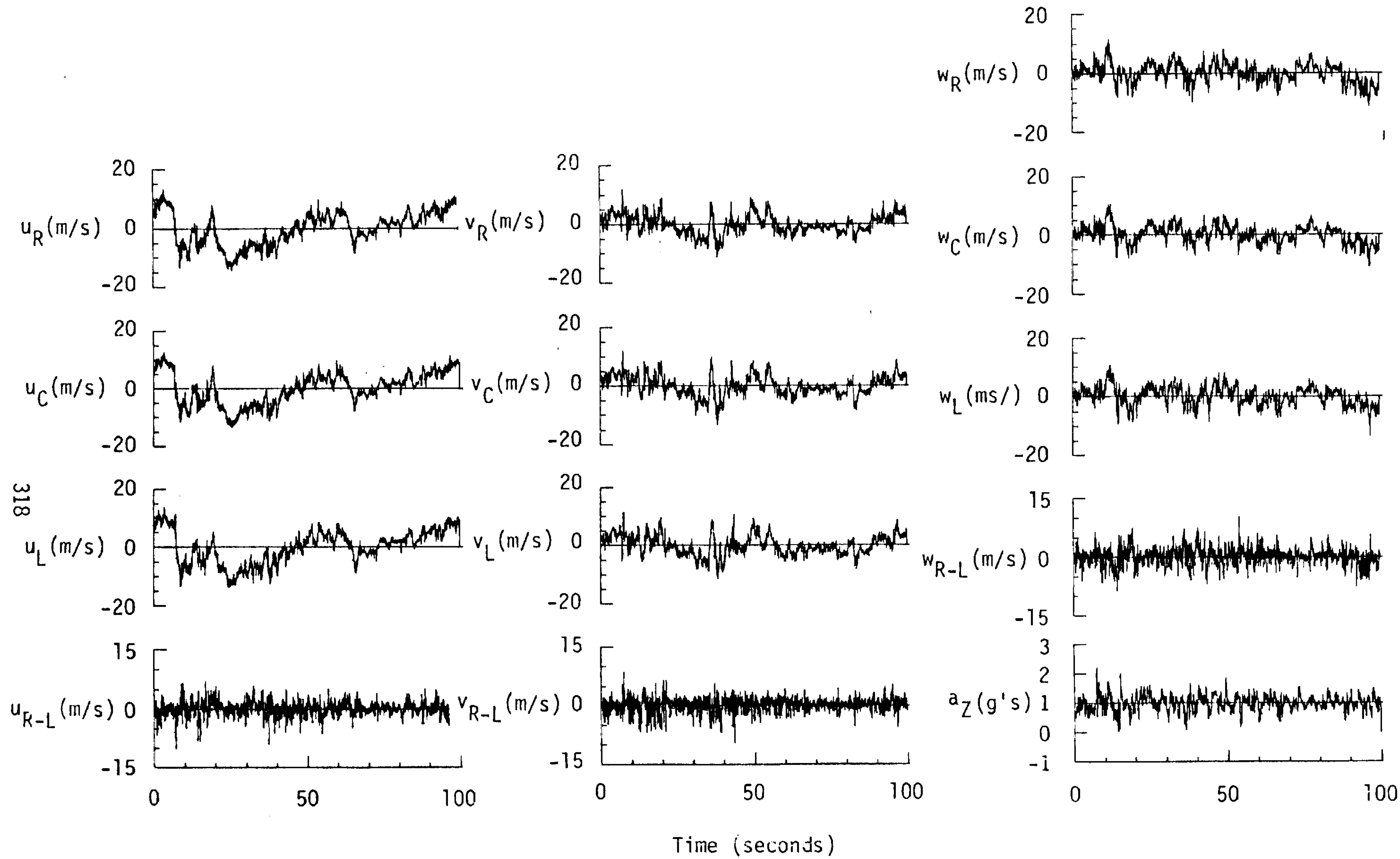

Figure A.77. Time histories of gust velocities, gust velocity differences, and aircraft's normal accelerations, Flight 31, Run 16.

TABLE A.31. Average Turbulence Parameters, Integral Length Scales, and Correlation Coefficients of Gust Velocities, Flight 31, Run16.

1. Mean Airspeed (m/s):

$\overline{V}_L$	$\overline{V}_C$	$\overline{V}_R$
109.41	107.07	108.82

2. Standard Deviation of Gust Velocities (m/s):

σ_{uR}	σ_{vR}	σ_{wR}
5.68	3.21	3.21
σ_{uC}	σ_{vC}	σ_{wC}
5.59	3.44	3.02
σ_{uL}	σ_{vL}	σ_{wL}
5.74	3.29	3.14

3. Standard Deviation of Gust Velocity Differences (m/s):

$\sigma_{\Delta uRL}$	$\sigma_{\Delta vRL}$	$\sigma_{\Delta wRL}$
1.75	1.61	2.00

4. Integral Length Scale (m):

L_{uR}	L_{vR}	L_{wR}
348.1	362.2	95.0
L_{uRL}	L_{vRL}	L_{wRL}
347.5	336.5	115.3

5. Correlation Coefficient of Gust Velocities:

$\overline{u_R u_L}/\sigma_{u_R}\sigma_{u_L}$	$\overline{v_R v_L}/\sigma_{v_R}\sigma_{v_L}$	$\overline{w_R w_L}/\sigma_{w_R}\sigma_{w_L}$
0.85	0.86	0.85
$\overline{u_R v_R}/\sigma_{u_R}\sigma_{v_R}$	$\overline{v_R w_R}/\sigma_{v_R}\sigma_{w_R}$	$\overline{w_R u_R}/\sigma_{w_R}\sigma_{u_R}$
0.49	0.05	-0.10
$\overline{u_R v_L}/\sigma_{u_R}\sigma_{v_L}$	$\overline{v_R w_L}/\sigma_{v_R}\sigma_{w_L}$	$\overline{w_R u_L}/\sigma_{w_R}\sigma_{u_L}$
0.49	0.02	-0.10

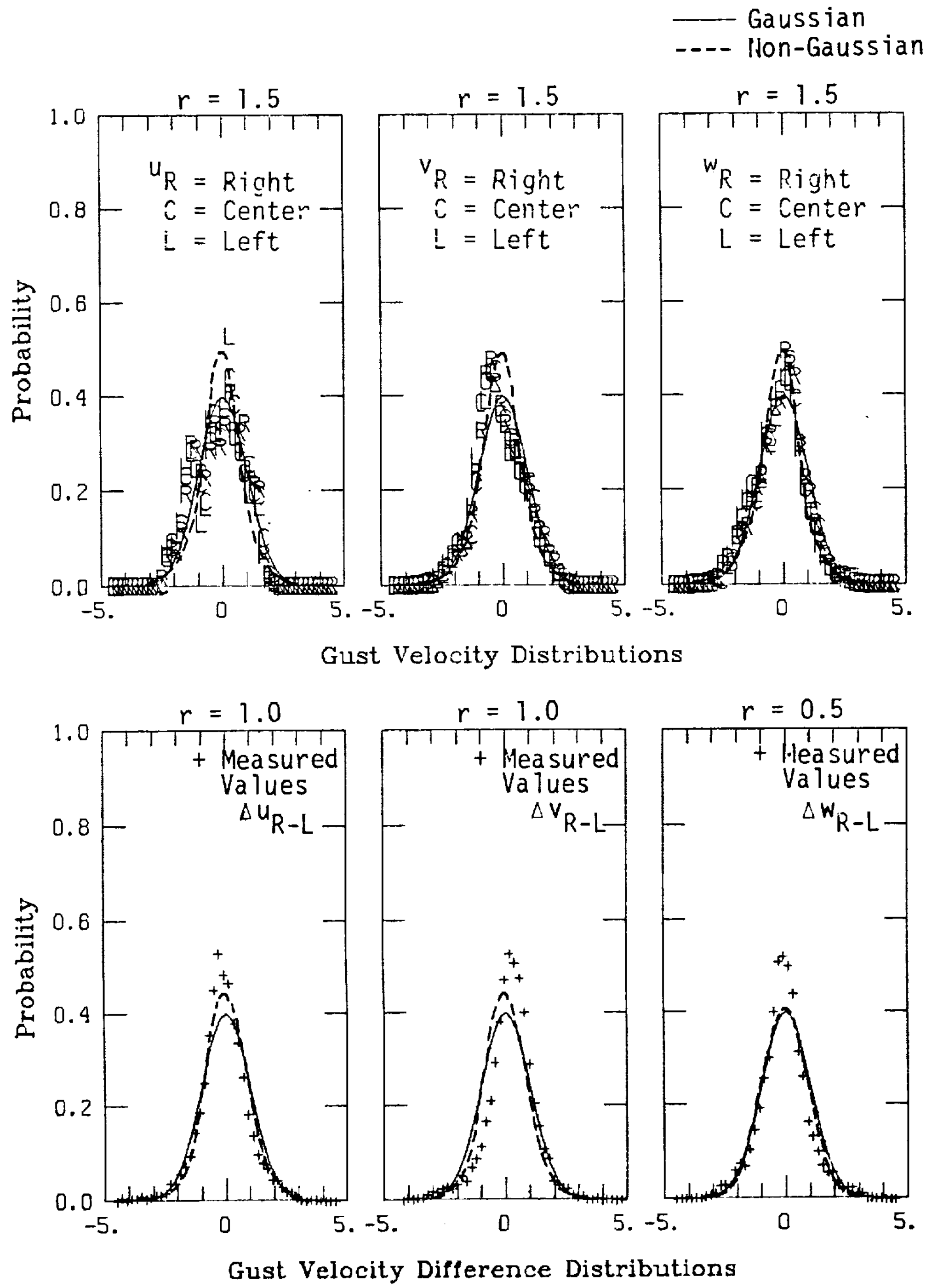

Figure A.78. Probability density functions for gust velocities and gust velocity differences (normalized with the standard deviation), Flight 31, Run 16 (r = degree of non-Gaussian).

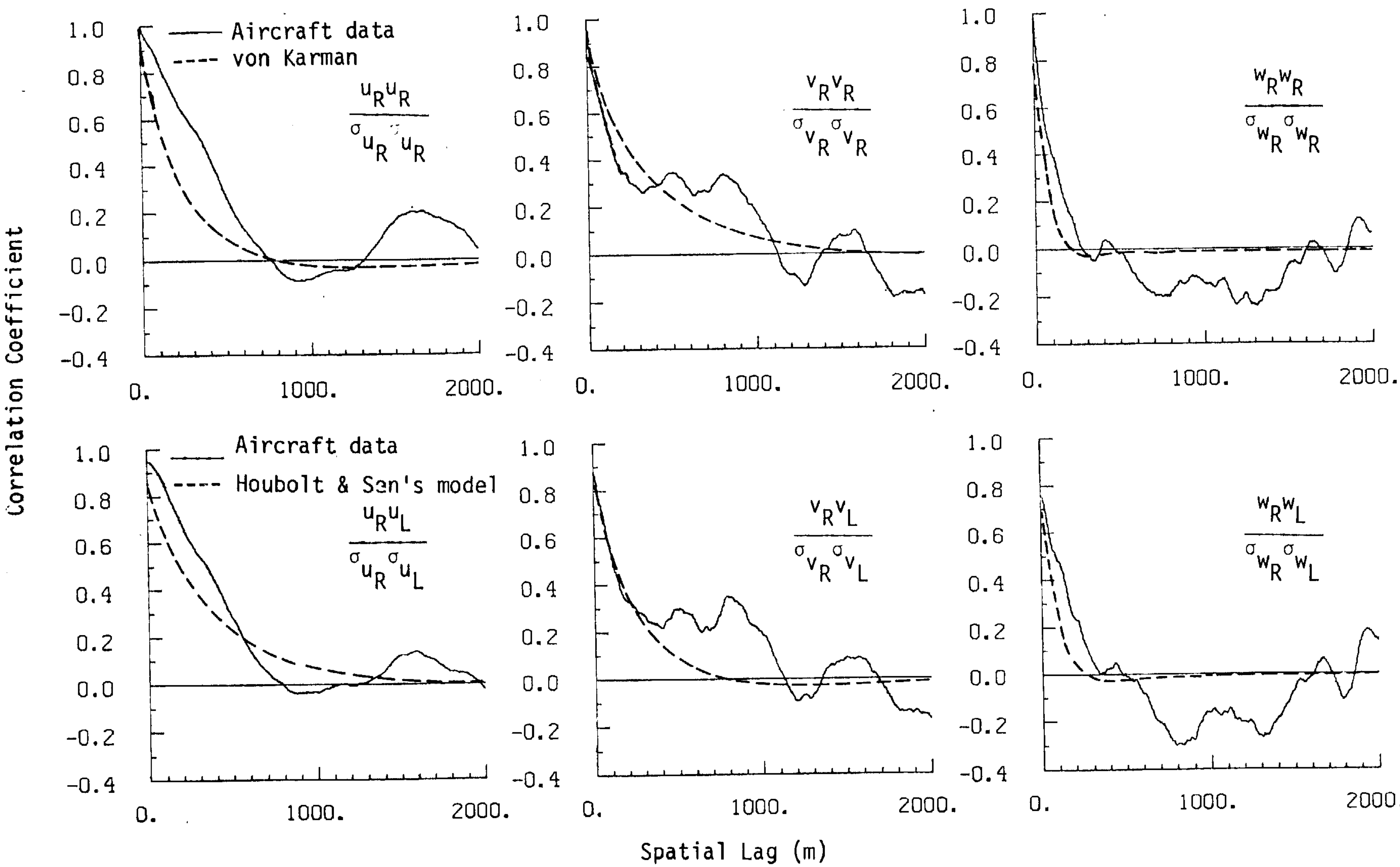

a. One- and two-point common component correlations.

Figure A.79. Comparison of normalized one- and two-point correlation functions for gust velocities with theoretical models, Flight 31, Run 16.

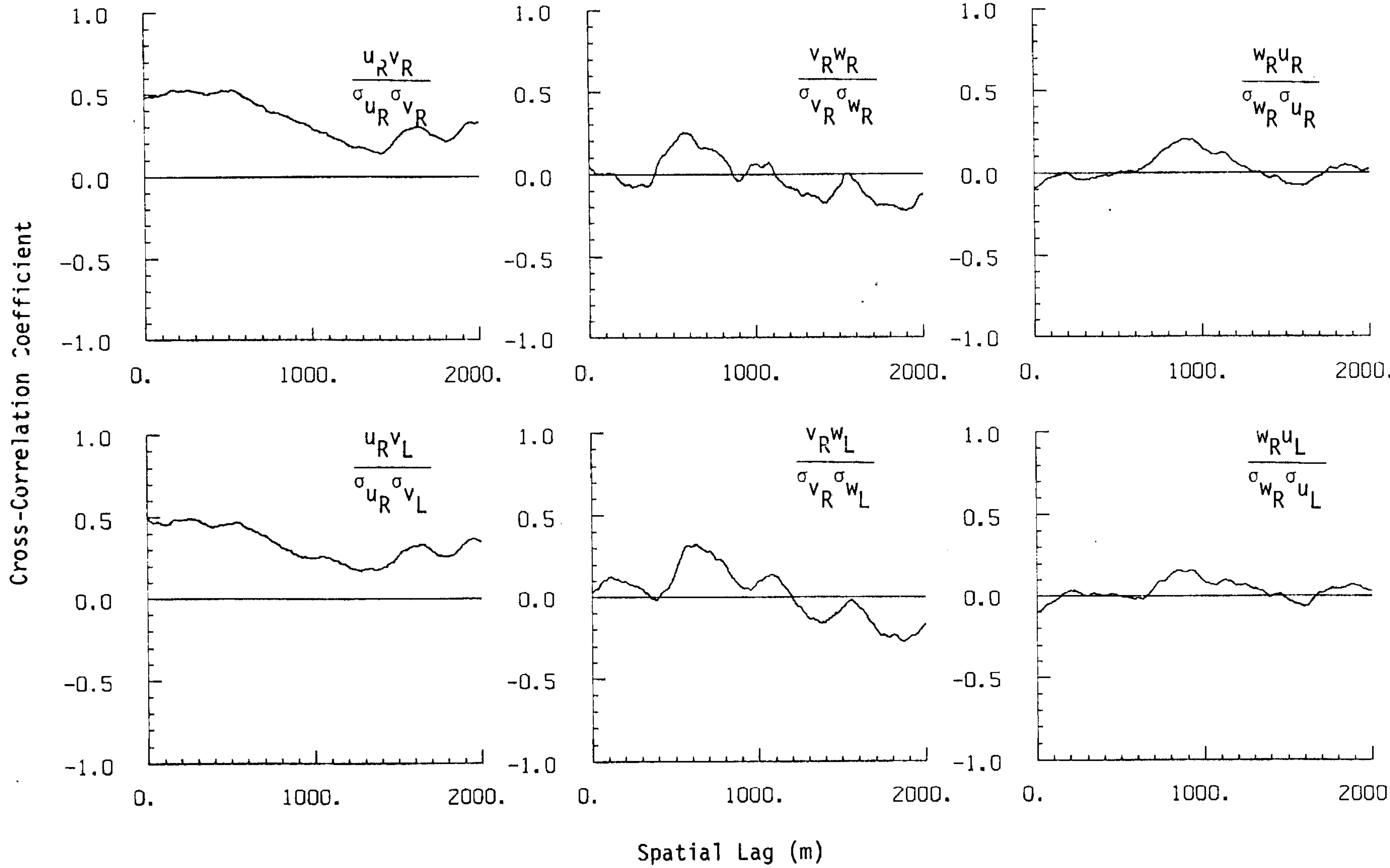

b. One- and two-point cross-correlations.

Figure A.79. (continued).

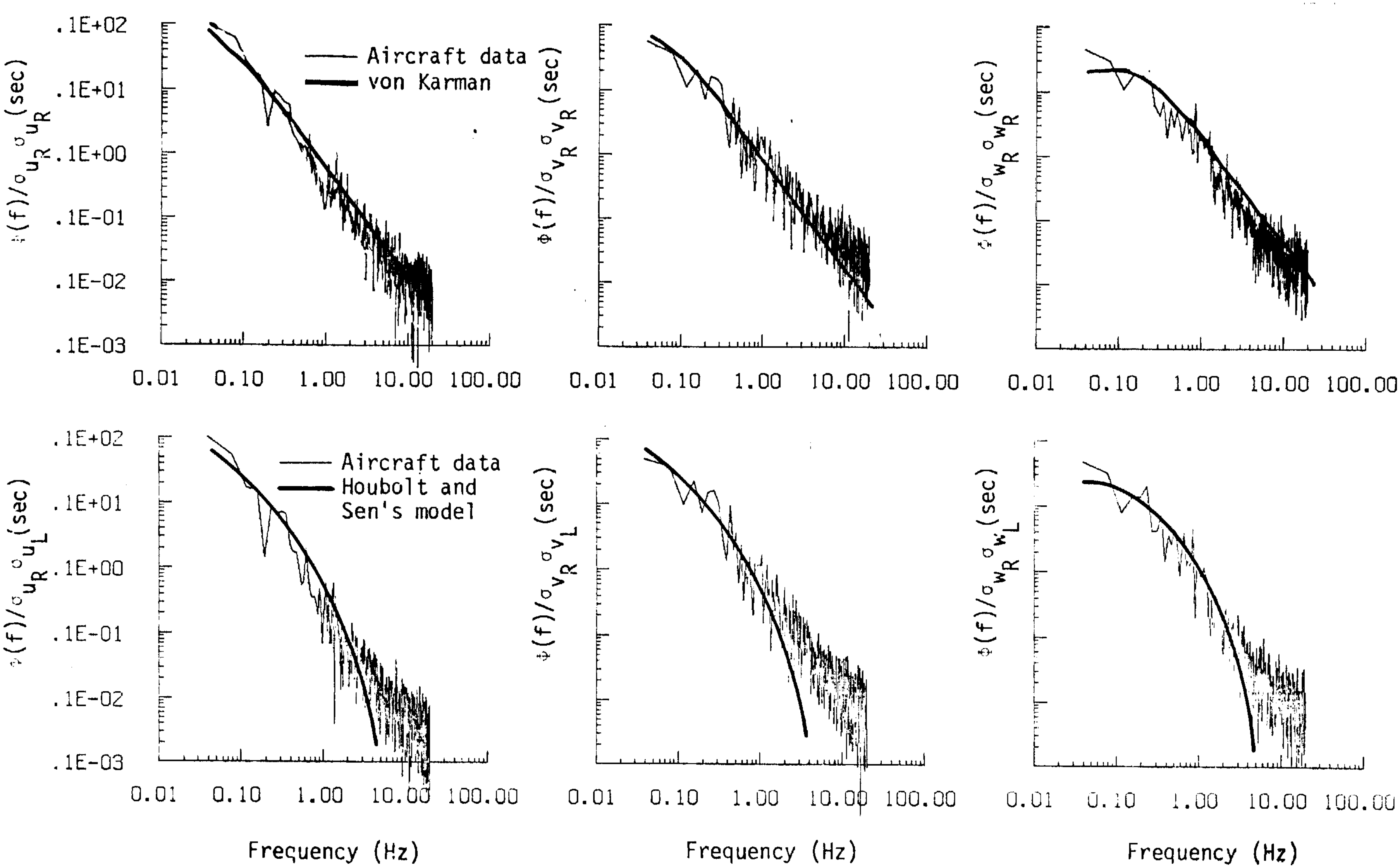

a. One- and two-point common component spectra.

Figure A.80. Comparison of normalized one- and two-point spectral density functions for gust velocities with theoretical models, Flight 31, Run 16.

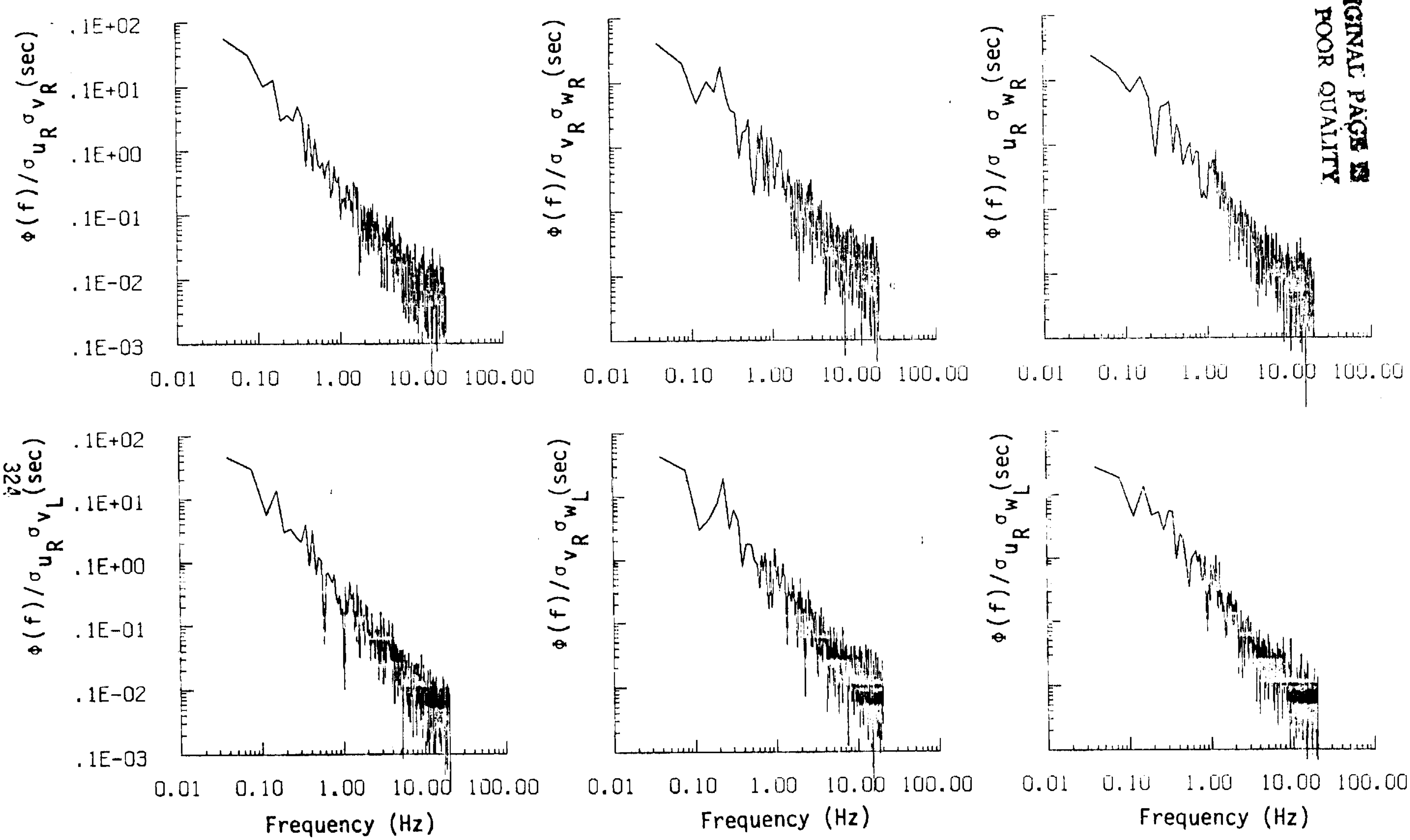

b. One- and two-point cross-spectra.

Figure A.80. (continued).

TABLE A.32. List of All Parameters Measured and Their Range of Values, Flight 31, Run 16.

CHANNEL	UNITS	HIGH	LOW	MEAN	RMS	STD	POINTS
1 TIME	SECONDS	44650.419	44550.619	44600.51910	44600.52841	28.82063	3993
2 PHI DOT	RAD/SEC	.173	-.170	-.00219	.05469	.05465	3993
3 ACCL N CG	G UNITS	1.836	.184	.99295	1.02051	.23560	3993
4 THETA DOT	RAD/SEC	.114	-.115	.00353	.02160	.02132	3993
5 THETA	RAD	.093	-.028	.03568	.04473	.02697	3993
6 PHI	RAD	.124	-.141	.00810	.05303	.05242	3993
7 PSI 1	RAD	98.821	88.254	94.18252	94.20765	2.17604	3993
8 DEL PSI 1	DEG	7.048	-3.444	2.57783	3.36447	2.16232	3993
9 PSI 2	RAD	456.511	446.301	452.21091	452.21583	2.11081	3993
10 DEL PSI 2	DEG	7.402	-3.037	2.94148	3.64665	2.15567	3993
11 ACCL N LT	G UNITS	3.840	-1.764	1.00539	1.09143	.42480	3993
12 ACCL N RT	G UNITS	2.939	-1.890	1.00248	1.09894	.45026	3993
13 ACCL Y CG	G UNITS	.138	-.079	.02342	.05700	.05198	3993
14 ACCL Y CG	G UNITS	.212	-.308	-.00651	.05113	.05072	3993
15 ALPHA CTR	RAD	.035	-.127	-.04022	.04610	.02253	3993
16 BETA CTR	RAD	.126	-.181	.00199	.04261	.04257	3993
17 TEMP T	DEG F	77.217	76.677	76.99361	76.99375	.14330	3993
18 TEMP B	DEG F	59.429	59.084	59.26035	59.26035	.02375	3993
19 ACCL Z INS	G UNITS	2.197	.038	.99566	1.02411	.23972	3993
20 ALPHA RT	RAD	.063	-.114	-.03255	.04116	.02520	3993
21 BETA RT	RAD	.123	-.146	.00732	.03884	.03814	3993
22 ALPHA LT	RAD	.069	-.083	-.00486	.02410	.02361	3993
23 BETA LT	RAD	.118	-.153	.00521	.03848	.03813	3993
24 PSI DOT	RAD/SEC	.141	-.099	.00216	.03507	.03501	3993
25 TEMP TOT	DEG C	13.275	10.124	11.36003	11.38193	.70577	3993
26 QC LT	PSID	1.372	.699	.91431	.92597	.14649	3993
27 QC CTR	PSID	1.299	.660	.87481	.88616	.14142	3993
28 QC RT	PSID	1.377	.667	.90437	.91609	.14579	3993
29 PS	PSIA	11.874	11.774	11.82186	11.82187	.01712	3993
30 TEMP IRT	VOLTS	8.293	6.907	7.74091	7.74587	.27715	3993
31 HYGROM	DEG C	-2.720	-11.519	-5.65175	6.04169	2.13560	3993
32 QC2 LT	PSID	.049	.046	.04738	.04739	.00077	3993
33 QC2 CTR	PSID	.148	.091	.12450	.12556	.01626	3993
34 QC2 RT	PSID	.121	.108	.11176	.11183	.00406	3993
35 DAR	DEG	-6.015	-6.788	-6.42209	6.42615	.22842	3993
36 DAL	DEG	-5.483	-5.896	-5.65123	5.65245	.11733	3993
37 DELEV	DEG	4.643	4.565	4.58025	4.58030	.02080	3993
38 DSTAB	DEG	-.360	-.379	-.36745	.36749	.00538	3993
39 DRUD	DEG	11.312	10.751	11.04139	11.04252	.15799	3993
40 DTHRR	PCT MAX	68.945	68.262	68.61489	68.61509	.16471	3993
41 DTHRL	PCT MAX	69.238	68.945	69.11436	69.11441	.08580	3993
42 DFLP	POSITION	.199	.191	.19540	.19541	.00088	3993
43 DSB	POSITION	.369	.365	.36728	.36728	.00145	3993
44 D TO G	METERS	7498835.904	7488038.669	***********	***********	3088.10998	3993
45 R TO D	DEGREES	72.963	72.873	72.91892	72.91892	.02572	3993
46 LONG	DEGREES	-118.088	-118.216	-118.15034	118.15035	.03649	3993
47 LAT	DEGREES	35.128	35.118	35.12248	35.12248	.00266	3993
48 TRK ANG	DEGREES	97.616	92.672	95.36264	95.37241	1.36528	3993
49 HDG	RADIANS	1.737	1.549	1.65660	1.65705	.03894	3993
50 VE	M/SEC	129.876	110.605	116.93289	117.06536	5.56814	3993
51 VN	M/SEC	-5.153	-17.078	-11.05970	11.54155	3.30188	3993
52 ALTITUDE	KM	1.831	1.763	1.79805	1.79809	.01172	3993
53 TEMPC	DEGREES C	7.254	4.521	5.62056	5.64283	.51212	3993
54 EW WND SPD	KNOTS	43.718	-5.148	20.03804	22.67758	10.61968	3993
55 NS WND SPD	KNOTS	22.902	-26.948	-3.83615	7.99222	7.01227	3993
56 WIND SPEED	KNOTS	46.577	.289	21.62644	24.04471	10.08862	3993
57 WIND DIREC	DEGREES	358.531	.654	272.94353	275.93952	40.55692	3993
58 WIND DIR2	DEGREES	178.531	-179.346	92.94357	101.40453	40.55694	3993
59 WIND DIR3	DEGREES	358.531	.654	272.94357	275.93557	40.55695	3993
60 WIND DIR4	DEGREES	2721.902	1867.900	2079.79556	2080.33551	47.40080	3993
61 AIRSPEED R	M/SEC	133.796	94.165	108.82734	109.14090	8.26821	3993
62 AIRSPEED C	M/SEC	129.918	93.661	107.07751	107.38788	8.15965	3993
63 AIRSPEED L	M/SEC	133.483	96.364	109.41262	109.72337	8.25302	3993
64 DELTA ALT	METERS	12.694	-55.642	-20.15336	23.31478	11.72414	3993
65 INRTL DISP	METERS	9.983	-39.925	-16.67988	19.74180	10.56163	3993
66 UG RIGHT	M/SEC	13.178	-14.235	.00000	5.68439	5.68510	3993
67 UG CENTER	M/SEC	12.729	-13.457	.00000	5.59419	5.59489	3993
68 UG LEFT	M/SEC	13.918	-13.629	.00000	5.74077	5.74149	3993
69 VG RIGHT	M/SEC	11.799	-11.170	-.15232	3.22170	3.21850	3993
70 VG CENTER	M/SEC	12.004	-13.296	-.13133	3.44382	3.44175	3993
71 VG LEFT	M/SEC	11.329	-11.407	-.12924	3.30171	3.29960	3993
72 WG RIGHT	M/SEC	11.274	-11.269	.06866	3.21870	3.21837	3993
73 WG CENTER	M/SEC	10.461	-10.769	.08381	3.02294	3.02216	3993
74 WG LEFT	M/SEC	10.864	-13.718	.07831	3.14724	3.14666	3993

APPENDIX B

DERIVATION OF EQUATIONS

This appendix contains a more complete derivation of the gust equations to compare with the specialized form of those used by the NASA Langley Research Center (LaRC) and to show the significance during certain manuevers, of terms which are not present in the specialized form. The wind velocity vector components at some position $\bar{r}$ measured from the c.g. of a rigid aircraft are designated u_g, v_g, and w_g. These are measured in the coordinate system with the x axis pointing north, the y axis pointing east, and the vertical axis pointing along the local vertical (gravity vector; positive downward). The coordinate system is called the true north coordinate system and is taken as the inertial system in this analysis (however, see Rhyne, 1976).* The u_g, v_g, and w_g components point north, east, and vertical, respectively, and are given by:

$$\begin{bmatrix} u+u_g \\ v+v_g \\ w+w_g \end{bmatrix} = \begin{bmatrix} V_N \\ V_E \\ V_{AZ} \end{bmatrix} + \begin{bmatrix} u_R \\ v_R \\ w_R \end{bmatrix} \quad (B.1)$$

The symbols u, v, and w designate the components of the aircraft velocity vector relative to the air mass measured in the true north coordinate system; V_N, V_E, and V_{AZ} are the inertial velocity vector components of the c.g. of the aircraft; and u_R, v_R, and w_R are the velocity components of the position $\vec{r}$

*Grid north is true north at the platform alignment location, but as the platform moves east or west from its initial alignment point, its north-south axis is not torqued to point at true north but remains parallel to a vertical plane through the meridian at which it was aligned. (The north-south and east-west axes are torqued to be perpendicular to the local vertical at all times, however.) For all practical purposes, the inertial-platform axis system can be assumed to be aligned with true north, considering the latitudes of operation and the east-west distances flown in a preceding project.

relative to the c.g. of the aircraft due to rotation of the frame of reference fixed in the airplane, i.e., the body coordinate system.

The matrix L_{AI} transforms the velocity components in the true north coordinate system to the average flight path coordinates. This transform matrix has the following form: bank angle ($\overline{\phi}$), track angle ($\overline{\psi}$), and elevational angle ($\overline{\theta}$).

$$L_{AI} = \begin{bmatrix} \cos\overline{\theta}\cos\overline{\psi} & \cos\overline{\theta}\sin\overline{\psi} & -\sin\overline{\theta} \\ \sin\overline{\phi}\sin\overline{\theta}\cos\overline{\psi} - \cos\overline{\phi}\sin\overline{\psi} & \sin\overline{\phi}\sin\overline{\theta}\sin\overline{\psi} + \cos\overline{\phi}\cos\overline{\psi} & \sin\overline{\phi}\cos\overline{\theta} \\ \cos\overline{\phi}\sin\overline{\theta}\cos\overline{\psi} + \sin\overline{\phi}\sin\overline{\psi} & \cos\overline{\phi}\sin\overline{\theta}\sin\overline{\psi} - \sin\overline{\phi}\cos\overline{\psi} & \cos\overline{\phi}\cos\overline{\theta} \end{bmatrix} \quad (B.2)$$

The velocity components u_R, v_R, and w_R in Equation B.1 are derived as follows. The velocity of a point $\vec{r} = \ell_x\vec{i} + \ell_y\vec{j} + \ell_z\vec{k}$ measured in the airplane frame of reference (i.e., body coordinates) which is rotating relative to the fixed frame of reference (i.e., inertial frame taken as the true north coordinates in this report) is given by $\vec{\Omega} \times \vec{r}$, where $\vec{\Omega}$ is the angular velocity of the airplane frame of reference relative to the inertial frame of reference. $\vec{\Omega}$ has the components p, q, and r and $\vec{\Omega} \times \vec{r}$ has the components u_R', v_R', and w_R' expressed in body coordinates, i.e.:

$$\vec{\Omega} \times \vec{r} = \begin{vmatrix} \vec{i} & \vec{j} & \vec{k} \\ p & q & r \\ \ell_x & \ell_y & \ell_z \end{vmatrix} = u_R'\vec{i} + v_R'\vec{j} + w_R'\vec{k} \quad (B.3)$$

Note ℓ_z measured down is positive and ℓ_y measured to the right is positive. Expanding Equation B.3 gives:

$$\begin{bmatrix} u_R' \\ v_R' \\ w_R' \end{bmatrix} = \begin{bmatrix} q\ell_z - r\ell_y \\ r\ell_x - p\ell_z \\ p\ell_y - q\ell_x \end{bmatrix} \quad (B.4)$$

In terms of the Euler angles (ψ,θ,ϕ) of the body axis relative to the true north or inertial frame of reference:

$$\begin{bmatrix} p \\ q \\ r \end{bmatrix} = \begin{bmatrix} 1 & 0 & -\sin\theta \\ 0 & \cos\phi & \sin\phi\cos\theta \\ 0 & -\sin\phi & \cos\phi\cos\theta \end{bmatrix} \begin{bmatrix} \dot\phi \\ \dot\theta \\ \dot\psi \end{bmatrix} \tag{B.5}$$

hence

$$\begin{bmatrix} p \\ q \\ r \end{bmatrix} = \begin{bmatrix} \dot\phi - \dot\psi\sin\theta \\ \dot\theta\cos\phi + \dot\psi\sin\phi\cos\theta \\ -\dot\theta\sin\phi + \dot\psi\cos\phi\cos\theta \end{bmatrix} \tag{B.6}$$

Thus, the components of the rotational velocity of the position $\vec{r}$ about the c.g. measured in the body coordinate system are:

$$\begin{bmatrix} u_R' \\ v_R' \\ w_R' \end{bmatrix} = \begin{bmatrix} \ell_z(\dot\theta\cos\phi + \dot\psi\sin\phi\cos\theta) + \ell_y(\dot\theta\sin\phi - \dot\psi\cos\phi\cos\theta) \\ -[\ell_z(\dot\phi - \dot\psi\sin\theta) + \ell_x(\dot\theta\sin\phi - \dot\psi\cos\phi\cos\theta)] \\ \ell_y(\dot\phi - \dot\psi\sin\theta) - \ell_x(\dot\theta\cos\phi + \dot\psi\sin\phi\cos\theta) \end{bmatrix} \tag{B.7}$$

Now since these are velocity components in the body coordinate system they must be transformed to the average flight path coordinates.

$$\begin{bmatrix} \hat{u}_R \\ \hat{v}_R \\ \hat{w}_R \end{bmatrix} = L_{AB} \begin{bmatrix} u_R' \\ v_R' \\ w_R' \end{bmatrix} \tag{B.8}$$

$$L_{AB} = \begin{bmatrix} \cos\hat\theta\cos\hat\psi & \sin\hat\phi\sin\hat\theta\cos\hat\psi - \cos\hat\phi\sin\hat\psi & \cos\hat\phi\sin\hat\theta\cos\hat\psi + \sin\hat\phi\sin\hat\psi \\ \cos\hat\theta\sin\hat\psi & \sin\hat\phi\sin\hat\theta\sin\hat\psi + \cos\hat\phi\cos\hat\psi & \cos\hat\phi\sin\hat\theta\sin\hat\psi - \sin\hat\phi\cos\hat\psi \\ -\sin\hat\theta & \sin\hat\phi\cos\hat\theta & \cos\hat\phi\cos\hat\theta \end{bmatrix} \tag{B.9}$$

where $\hat{u}_R$, $\hat{v}_R$, and $\hat{w}_R$ are the components of the rotation vector expressed in the average flight path coordinates; $\hat\psi$, $\hat\theta$, and $\hat\phi$ are the Euler angles of the body axis relative to the average flight path axis.

The north, east, and vertical inertial velocity components expressed in the average flight path coordinates are denoted with capital letters having a $(\hat{\ })$ are:

$$\begin{bmatrix} \hat{U} \\ \hat{V} \\ \hat{W} \end{bmatrix} = \begin{bmatrix} V_N \cos\bar{\theta}\cos\bar{\psi} + V_E \cos\bar{\theta}\sin\bar{\psi} - V_{AZ}\sin\bar{\theta} \\ V_N(\sin\bar{\phi}\sin\bar{\theta}\cos\bar{\psi} - \cos\bar{\phi}\sin\bar{\psi}) + V_E(\sin\bar{\phi}\sin\bar{\theta}\sin\bar{\psi} \\ \quad + \cos\bar{\phi}\cos\bar{\psi}) + V_{AZ}\sin\bar{\phi}\cos\bar{\theta} \\ V_N(\cos\bar{\phi}\sin\bar{\theta}\cos\bar{\psi} + \sin\bar{\phi}\sin\bar{\psi}) + V_E(\cos\bar{\phi}\sin\bar{\theta}\sin\bar{\psi} \\ \quad - \sin\bar{\phi}\cos\bar{\psi}) + V_{AZ}\cos\bar{\phi}\cos\bar{\theta} \end{bmatrix} \tag{B.10}$$

The values of $\hat{u}$, $\hat{v}$, and $\hat{w}$ which are the true airspeed velocity components in the average frame of reference are not measured directly in the flight experiments. Rather the true airspeed of the aircraft, V, is measured. Therefore, $\hat{u}$, $\hat{v}$, and $\hat{w}$ must be expressed in terms of this variable. The velocity components u', v', and w' (i.e., measured in body coordinates) are related to the true airspeed by the relationship:

$$\begin{bmatrix} u' \\ v' \\ w' \end{bmatrix} = L_{BW}\begin{bmatrix} V \\ 0 \\ 0 \end{bmatrix} \tag{B.11}$$

where

$$L_{BW} = \begin{bmatrix} \cos\alpha\cos\beta & -\cos\alpha\sin\beta & -\sin\alpha \\ \sin\beta & \cos\beta & 0 \\ \sin\alpha\cos\beta & -\sin\alpha\sin\beta & \cos\alpha \end{bmatrix} \tag{B.12}$$

and α and β are the angle of attack ($= \tan^{-1} w'/u'$) and sideslip angle ($= \sin^{-1} v'/V$), respectively. L_{BW} transforms the velocity components measured in a frame of reference for which the x axis is located along the relative velocity vector (Etkin (1972) calls this the "wind" coordinate system) to the body coordinate system. Thus:

$$\begin{bmatrix} u' \\ v' \\ w' \end{bmatrix} = \begin{bmatrix} V \cos \alpha \cos \beta \\ V \sin \beta \\ V \sin \alpha \cos \beta \end{bmatrix} \quad \text{(B.13)}$$

The above assumes that the pitot tube measures actual magnitude of the relative velocity or true airspeed and not some fractional component.

The above values must be rotated into the average flight path frame of reference with the transform L_{AB}, i.e.,

$$\begin{bmatrix} \hat{u} \\ \hat{v} \\ \hat{w} \end{bmatrix} = L_{AB} \begin{bmatrix} u' \\ v' \\ w' \end{bmatrix} \quad \text{(B.14)}$$

The wind velocity measured in the flight path coordinate system is thus given by:

$$\begin{bmatrix} \hat{u}_g \\ \hat{v}_g \\ \hat{w}_g \end{bmatrix} = \begin{bmatrix} \hat{U} \\ \hat{V} \\ \hat{W} \end{bmatrix} + \begin{bmatrix} \hat{u}_R \\ \hat{v}_R \\ \hat{w}_R \end{bmatrix} - \begin{bmatrix} \hat{u} \\ \hat{v} \\ \hat{w} \end{bmatrix} = L_{AI} \begin{bmatrix} V_N \\ V_E \\ V_{az} \end{bmatrix} + L_{AB} \begin{bmatrix} u_R' - u' \\ v_R' - v' \\ w_R' - w' \end{bmatrix} \quad \text{(B.15)}$$

Consider the transform L_{AB} (Equation B.9). The angles $\hat{\phi}$, $\hat{\theta}$, and $\hat{\psi}$ are not measured in the flight program; therefore, L_{AB} must be expressed in terms of ϕ, θ, and ψ which are measured and $\overline{\phi}$, $\overline{\theta}$, and $\overline{\psi}$ which may be determined in post-flight analysis. This is achieved as follows:

$$\vec{V}_A = L_{AI}\vec{V}_I \text{ and } \vec{V}_I = L_{IB}\vec{V}_B \quad \text{(B.16)}$$

hence

$$\vec{V}_A = L_{AI}L_{IB}\vec{V}_B \quad \text{(B.17)}$$

and thus

$$L_{AB} = L_{AI}L_{IB} = L_{AI}L_{BI}^T \quad \text{(B.18)}$$

where the superscript T denotes the transpose. The terms of L_{AB} for the general case are very complex; however, assuming wings level flight, i.e., $\overline{\phi} = 0$, which does not lose any generality for the present problem, results in:

$$L_{AB} = \begin{bmatrix} \cos\theta\cos\bar{\theta}\cos(\psi-\bar{\psi}) + \sin\theta\sin\bar{\theta} & \sin\phi\sin\theta\cos\bar{\theta}\cos(\psi-\bar{\psi}) - \cos\bar{\theta}\cos\phi\sin(\psi-\bar{\psi}) - \cos\theta\sin\phi\sin\bar{\theta} & \cos\phi\sin\theta\cos\bar{\theta}\cos(\psi-\bar{\psi}) + \sin\phi\cos\bar{\theta}\sin(\psi-\bar{\psi}) - \cos\theta\cos\phi\sin\bar{\theta} \\ \cos\theta\sin(\psi-\bar{\psi}) & \cos\phi\cos(\psi-\bar{\psi}) + \sin\phi\sin\theta\sin(\psi-\bar{\psi}) & -\sin\phi\cos(\psi-\bar{\psi}) + \cos\phi\sin\theta\sin(\psi-\bar{\psi}) \\ \cos\theta\sin\bar{\theta}\cos(\psi-\bar{\psi}) - \sin\theta\cos\bar{\theta} & \sin\phi\sin\theta\sin\bar{\theta}\cos(\psi-\bar{\psi}) - \cos\phi\sin\bar{\theta}\sin(\psi-\bar{\psi}) + \cos\bar{\theta}\sin\phi\cos\theta & \cos\phi\sin\theta\sin\bar{\theta}\cos(\psi-\bar{\psi}) + \sin\phi\sin\bar{\theta}\sin(\psi-\bar{\psi}) + \cos\phi\cos\theta\cos\bar{\theta} \end{bmatrix} \quad (B.19)$$

Now assuming ϕ, $\psi-\bar{\psi}$, and $\theta-\bar{\theta}$ are small angles and neglecting high order terms, Equation B.19 reduces to:

$$L_{AB} = \begin{bmatrix} 1 & -(\psi-\bar{\psi})\cos\bar{\theta} & \theta-\bar{\theta} \\ (\psi-\bar{\psi})\cos\theta & 1 & -\phi \\ -(\theta-\bar{\theta}) & \phi - (\psi-\bar{\psi})\sin\bar{\theta} & 1 \end{bmatrix} \quad (B.20)$$

Substituting L_{AB} from above into Equation B.15 and similar assuming small angles (or angle differences) with second order terms neglected in the expressions $u_R' - u'$, $v_R' - v'$, and $w_R' - w'$ (see Equations B.7 and B.13) the second term on the right-hand side of Equation B.15 becomes:

$$L_{AB}\begin{bmatrix} u_R' - u' \\ v_R' - v' \\ w_R' - w' \end{bmatrix} = \begin{bmatrix} \ell_z\dot{\theta} - \ell_y(-\dot{\theta}\phi + \dot{\psi}\cos\theta) - V - (\psi-\bar{\psi})\cos\bar{\theta}[\ell_x\dot{\psi}\cos\theta - V\beta - \ell_z(\dot{\phi} - \dot{\psi}\sin\theta)] + (\theta-\bar{\theta})[\ell_y(\dot{\phi} - \dot{\psi}\sin\theta) - \ell_x\dot{\theta} - V\alpha] \\ (\psi-\bar{\psi})\cos\theta[\ell_z\dot{\theta} - \ell_y\dot{\psi}\cos\theta - V] + \ell_x(-\theta\dot{\phi} + \dot{\psi}\cos\theta) - V\beta - \ell_z(\dot{\phi} - \dot{\psi}\sin\theta) - \phi[\ell_y(\dot{\phi} - \dot{\psi}\sin\theta) - \ell_x\dot{\theta} - V\alpha] \\ -(\theta-\bar{\theta})[\ell_z\dot{\theta} - \ell_y\dot{\psi}\cos\theta - V] + [\phi - (\psi-\bar{\psi})\sin\bar{\theta}][\ell_x\dot{\psi}\cos\theta - V\beta - \ell_z(\dot{\phi} - \dot{\psi}\sin\theta)] + \ell_y(\dot{\phi} - \dot{\psi}\sin\theta) - \ell_x(\dot{\theta} + \dot{\psi}\phi\cos\theta) - V\alpha \end{bmatrix} \quad (B.21)$$

The derivation of the equations currently used in the data reduction algorithms at the NASA Langley Research Center computer laboratory treats the values of $\dot{\phi}$, $\dot{\theta}$, and $\dot{\psi}$ as small. Moreover, assuming the position vector $\vec{r} = \ell_x\vec{i} + \ell_y\vec{j} + \ell_z\vec{k}$ lies in the x-y plane of the body coordinate system, i.e., $\ell_z = 0$ and introducing these assumptions into Equation B.21 gives upon neglecting higher order terms:

$$L_{AB}\begin{bmatrix} u_R' - u' \\ v_R' - v' \\ w_R' - w' \end{bmatrix} = \begin{bmatrix} -\ell_y\dot{\psi}\cos\theta - V + (\psi-\overline{\psi})\,V\beta\cos\overline{\theta} - (\theta-\overline{\theta})\,V\alpha \\ -(\psi-\overline{\psi})\,V\cos\theta + \ell_x\dot{\psi}\cos\theta - V\beta + V\phi\alpha \\ (\theta-\overline{\theta})\,V + [\phi - (\psi-\overline{\psi})\sin\overline{\theta}]\,V\beta + \ell_y\dot{\phi} - \ell_x\dot{\theta} - V\alpha \end{bmatrix} \tag{B.22}$$

Recalling that we have assumed wings level flight, i.e., $\overline{\phi} = 0$, the first term on the right-hand side of Equation B.15 becomes:

$$\begin{bmatrix} \hat{U} \\ \hat{V} \\ \hat{W} \end{bmatrix} = \begin{bmatrix} V_N\cos\overline{\theta}\cos\overline{\psi} + V_E\cos\overline{\theta}\sin\overline{\psi} - V_{AZ}\sin\overline{\theta} \\ -V_N\sin\overline{\psi} + V_E\cos\overline{\psi} \\ V_N\sin\overline{\theta}\cos\overline{\psi} + V_E\sin\overline{\theta}\sin\overline{\psi} + V_{AZ}\cos\overline{\theta} \end{bmatrix} \tag{B.23}$$

Therefore, under the following assumptions:

1. Wing level flight, i.e., $\overline{\phi} = 0$.
2. ϕ, $\theta-\overline{\theta}$, $\psi-\overline{\psi}$, α, and β are small (<10 deg, cos () = 1, sin () = (); error <2%) and high order terms of the products of these angles are negligible (error <3%).
3. The wind velocity probe is measured at a given point in the x-y plane of the body coordinate system (i.e., $\ell_z = 0$).
4. The values of $\dot{\phi}$, $\dot{\theta}$, and $\dot{\psi}$ are small (<10 deg/sec, error <2%) and high order terms of the products of these values are negligible (error <3%).

The wind velocity vector components expressed in the average flight path coordinate system is given by adding Equation B.22 and Equation B.23:

$$\begin{bmatrix}\hat{u}_g\\ \hat{v}_g\\ \hat{w}_g\end{bmatrix} = \begin{bmatrix} V_N\cos\bar{\theta}\cos\bar{\psi} + V_E\cos\bar{\theta}\sin\bar{\psi} - V_{AZ}\sin\bar{\theta} - \ell_y\dot{\psi}\cos\theta \\ \quad - V + (\psi-\bar{\psi})V\beta\cos\bar{\theta} - (\theta-\bar{\theta})V\alpha \\ -V_N\sin\bar{\psi} + V_E\cos\bar{\psi} - (\psi-\bar{\psi})V\cos\theta + \ell_x\dot{\psi}\cos\theta - V\beta + V\phi\alpha \\ V_N\sin\bar{\theta}\cos\bar{\psi} + V_E\sin\bar{\theta}\sin\bar{\psi} + V_{AZ}\cos\bar{\theta} + (\theta-\bar{\theta})V \\ \quad - [\phi-(\psi-\bar{\psi})\sin\bar{\theta}]V\beta + \ell_y\dot{\phi} - \ell_x\dot{\theta} - V\alpha\end{bmatrix} \qquad (B.24)$$

The NASA LaRC algorithm assumes level flight given by $\theta = \bar{0}$ which implies the angle θ is small, Equation B.24 then becomes:

$$\begin{bmatrix}\hat{u}_g\\ \hat{v}_g\\ \hat{w}_g\end{bmatrix} = \begin{bmatrix} V_N\cos\bar{\psi} + V_E\sin\bar{\psi} - \ell_y\dot{\psi} - V + (\psi-\bar{\psi})V\beta - V\theta\alpha \\ V_E\cos\bar{\psi} - V_N\sin\bar{\psi} - (\psi-\bar{\psi})V + \ell_x\dot{\psi} - V\beta + V\phi\alpha \\ V_{AZ} + V\theta - V\phi\beta + \ell_y\dot{\phi} - \ell_x\dot{\theta} - V\alpha\end{bmatrix} \qquad (B.25)$$

These equations represent the total wind velocity components, however, interest is generally in the fluctuations about the mean, hence the terms in Equation B.25 are expressed as a mean quantity plus a fluctuation quantity, i.e., $A = \overset{+}{A} + \tilde{A}$

$$\begin{bmatrix}\overset{+}{\hat{u}}_g\\ \overset{+}{\hat{v}}_g\\ \overset{+}{\hat{w}}_g\end{bmatrix} + \begin{bmatrix}\tilde{\hat{u}}_g\\ \tilde{\hat{v}}_g\\ \tilde{\hat{w}}_g\end{bmatrix} = \begin{bmatrix} \overset{+}{V}_N\cos\bar{\psi} + \overset{+}{V}_E\sin\bar{\psi} - \overset{+}{V} \\ \quad - \overset{+}{V}\,\overset{+}{\theta}\,\overset{+}{\alpha} \\ \overset{+}{V}_E\cos\bar{\psi} - \overset{+}{V}_N\sin\bar{\psi} \\ \\ \overset{+}{V}_{AZ} + \overset{+}{V}\,\overset{+}{\theta} - \overset{+}{V}\,\overset{+}{\alpha} \\ \end{bmatrix} + \begin{bmatrix} \tilde{V}_N\cos\bar{\psi} + \tilde{V}_E\sin\bar{\psi} - \tilde{V} - \ell_y\dot{\psi} \\ \quad + \tilde{\psi}V\beta - V\theta\alpha \\ \tilde{V}_E\cos\bar{\psi} - \tilde{V}_N\sin\bar{\psi} - V\tilde{\psi} + \ell_x\dot{\psi} \\ \quad - V\beta + V\phi\alpha \\ \tilde{V}_{AZ} + V\tilde{\theta} + \tilde{V}\overset{+}{\theta} - V\phi\beta + \ell_y\dot{\phi} \\ \quad - \ell_x\dot{\theta} - (V\tilde{\alpha} + \tilde{V}\overset{+}{\alpha})\end{bmatrix} \qquad (B.26)$$

Note $\overset{+}{\psi} = \bar{\psi}$, $\tilde{\dot{\psi}} = \dot{\psi}$, $\tilde{\dot{\theta}} = \dot{\theta}$, $\tilde{\dot{\phi}} = \dot{\phi}$, $\overset{+}{\phi} = \overset{+}{\beta} = 0$ (thus, $\tilde{\beta} = \beta$ and $\tilde{\phi} = \phi$): $\overset{+}{\theta}$ and $\overset{+}{\alpha}$ are not necessarily zero. The right-hand most term is the velocity fluctuation about the mean where the mean is given by the expression immediately following the equal sign.

The equations used in the NASA LaRC algorithm for the fluctuating gust velocities are given by:

$$\begin{bmatrix} \tilde{\hat{u}}_g \\ \tilde{\hat{v}}_g \\ \tilde{\hat{w}}_g \end{bmatrix} = \begin{bmatrix} \tilde{V}_N \cos \overline{\psi} + \tilde{V}_E \sin \overline{\psi} - \ell_y \dot{\psi} - \tilde{V} \\ \tilde{V}_E \cos \overline{\psi} - \tilde{V}_N \sin \overline{\psi} - V\tilde{\psi} + \ell_x \dot{\psi} - V\beta + V\phi\tilde{\alpha} \\ \tilde{V}_{AZ} + V\tilde{\theta} - V\phi\beta + \ell_y \dot{\phi} - \ell_x \dot{\theta} - V\tilde{\alpha} \end{bmatrix} \tag{B.27}$$

In the NASA LaRC algorithm, the signs of β, $\tilde{V}_{AZ}$, and $\tilde{\hat{w}}$ are defined opposite to those used in the previous derivation. Therefore, to obtain the exact form of the NASA LaRC equations, one has to change the signs of β, $\tilde{V}_{AZ}$, and $\tilde{\hat{w}}_g$ in Equation B.27. Also, it must be noted that the values of α and β in Equation B.12 are measured relative to the body axis of the aircraft whereas α and β measured in the NASA Gust Gradient Program are relative to the axis of the boom. To obtain the angle of attack, α, in Equation B.12 one must add the angle between the projection of the boom in the body x-z plane and the body x-axis to the measured α. Since for the full equations α must be the value relative to the body axis, the angle between the boom and the body x-axis was estimated by subtracting the average measured value of α from the average value of pitch angle for the total number of straight and level runs of Flight 31 and Flight 21. This value was determined to be approximately 4.4 degrees for the center probe.

There are some differences in Equation B.26 and B.27 that can be explained as follows. The terms $\tilde{\psi}V\beta$ and $\tilde{V}\theta\alpha$ in Equation B.26 are neglected in Equation B.27. This is consistent with the assumption that second-order small terms are negligible. However, based on this reasoning, the terms $V\phi\tilde{\alpha}$ and $V\phi\beta$ should also be neglected but it is not. The reason is that in early studies, $V\phi\tilde{\alpha}$ and $V\phi\beta$ were found not to be small compared to the other terms in the equation (Rhyne, 1976) and have therefore been retained. Also, the expressions $V\tilde{\alpha} + V\tilde{\alpha}_{\perp}$ and $V\tilde{\theta} + V\tilde{\theta}_{\perp}$ in Equation B.26 are simply written $V\tilde{\alpha}$ and $V\tilde{\theta}$ in Equation B.27. Justification for this is that since $\overset{\perp}{\alpha}$, in $\widetilde{V\alpha}$ + $\overset{\sim\perp}{V\alpha}$ for example, is a small angle even on the average, then $\overset{\sim\perp}{V\alpha}$ is negligible compare to $\widetilde{V\alpha}$. This is reasonable in view of the fact that $\widetilde{V\alpha}$ may be 1 to 2 orders of magnitude larger than $\overset{\sim\perp}{V\alpha}$ because V is typically two orders of magnitude larger than $\tilde{V}$ whereas $\overset{\perp}{\alpha}$ is probably of the same order of magnitude as $\tilde{\alpha}$. Finally, if second-order terms are strictly neglected, then $\widetilde{V\alpha}$ should actually be $\overset{\perp\sim}{V\alpha}$; however, there is no saving in computing $\overset{\perp\sim}{V\alpha}$ since it is just as easy to compute $\widetilde{V\alpha}$. This is true of $\widetilde{V\theta}$ and $V\beta$ as well.

Standard Bibliographic Page

1. Report No.	2. Government Accession No.	3. Recipient's Catalog No.
NASA CR-178288		

4. Title and Subtitle Analyses and Assessments of Spanwise Gust Gradient Data from NASA B-57B Aircraft	5. Report Date August 1987
	6. Performing Organization Code
7. Author(s) Walter Frost, Ho-Pen Chang, Erik A. Ringness	8. Performing Organization Report No.
9. Performing Organization Name and Address FWG Associates, Inc. Rt. 2, Box 271-A Tullahoma, TN 37388	10. Work Unit No.
	11. Contract or Grant No. NAS1-17989
12. Sponsoring Agency Name and Address National Aeronautics and Space Administration Washington, DC 20546	13. Type of Report and Period Covered Contractor Report
	14. Sponsoring Agency Code

15. Supplementary Notes

Langley Technical Monitor: Hal Murrow
Final Report

16. Abstract

Analysis of turbulence measured across the airfoil of a Cambera B-57 aircraft are reported. The aircraft is instrumented with probes for measuring wind at both wing tips and at the nose.

Statistical properties of the turbulence are reported. These consist of the standard deviations of turbulence measured by each individual probe, standard deviations and probability distribution of differences in turbulence measured between probes and auto-and two-point spatial correlations and spectra.

The report addresses procedures associated with calculation of two-point spatial correlations and spectra utilizing digitized data. Methods and correction procedures for assuring the accuracy of aircraft measured winds are also described.

Results are found, in general, to agree with correlations existing in the literature. The velocity spatial differences fit a Gaussian/Bessel type probability distribution. The turbulence agrees with the von Karman turbulence correlation and with two-point spatial correlations developed from the von Karman correlation.

17. Key Words (Suggested by Authors(s))	18. Distribution Statement
Gust Gradient, atmospheric turbulence, spectral analysis	Unclassified - Unlimited

19. Security Classif.(of this report)	20. Security Classif.(of this page)	21. No. of Pages	22. Price
Unclassified	Unclassified	335	

For sale by the National Technical Information Service, Springfield, Virginia 22161

NASA Langley Form 63 (June 1985)